Leucogranites of the NW Himalaya: crust-mantle interaction beneath the Karakoram and the magmatic evolution of collisional belts.

A Thesis

submitted for the degree of

Doctor of Philosophy

in the

Faculty of Science of the University of Leicester

by

Mark B. Crawford B.A. (Oxon)

July 1988

UMI Number: U010043

All rights reserved

INFORMATION TO ALL USERS
The quality of this reproduction is dependent upon the quality of the copy submitted.

In the unlikely event that the author did not send a complete manuscript
and there are missing pages, these will be noted. Also, if material had to be removed,
a note will indicate the deletion.

UMI U010043
Published by ProQuest LLC 2015. Copyright in the Dissertation held by the Author.
Microform Edition © ProQuest LLC.
All rights reserved. This work is protected against
unauthorized copying under Title 17, United States Code.

ProQuest LLC
789 East Eisenhower Parkway
P.O. Box 1346
Ann Arbor, MI 48106-1346

X791496595

Leucogranites of the NW Himalaya: mantle-crust interaction beneath the Karakoram and the magmatic evolution of collisional belts.

M. B. Crawford B.A. (Oxon.) July, 1988.

The Karakoram Axial Batholith in N. Pakistan records the magmatic development of the Eurasian continental margin since the late Jurassic. Magmatism prior to the collision of India with Eurasia at c.45Ma is represented by subduction-related, calc-alkaline granodiorite plutonism. The chemical variation within these plutons is caused by high-level fractionation processes. However, heterogeneous isotope data suggests that the source of these magmas was the mantle wedge, enriched by a subducted slab component, with the melts being contaminated by a ^{87}Sr-rich crustal component.

There are two types of post-collisional leucogranite. The Sumayar pluton is related to restricted partial melting of sillimanite-grade metapelites triggered by fluxing of fluids from the underthrust Indian crust. This water-saturated, minimum melt is considered to be an analogue of the High Himalayan leucogranites.

The other Karakoram leucogranites are related by fractionation to a more basic monzogranitic parent, whose geochemistry indicates a lower crustal source. However, melting of typical crust cannot explain the anomalously high large ion lithophile element (LILE) content of the monzogranites. Associated with the granites are ultra-potassic, LILE-enriched lamprophyres. This LILE-enrichment is attributed to alteration of the mantle wedge by fluids and/or siliceous melts from the slab. Amphibole in the resulting metasomatic assemblage acts as a sink for the otherwise incompatible LILE. As a result of heating and thermal relaxation beneath the thickened continental crust, enriched amphibole, stable in the pre-collisional mantle wedge beneath the Karakoram, dehydrated or melted some 20Ma after collision to give the lamprophyres. Fluid precursors to this melting contaminated the source region of the granites selectively enriching it in LILE and triggering/promoting melting.

The identification of the above magma-types, which have different generative processes and magmatic triggers, in other collisional environments will lead to information about the evolution of similar orogenic belts.

Acknowledgements.

I would like to thank the following people:

Dr. A.D. Saunders and Prof. B.F. Windley for setting up this project and guiding me through many pitfalls.

Dr. A.J. Rex, Dr. M.P. Searle, Dr. M.J. Norry, Dr. C.J. Moon, Prof. J. Tarney and D.J. Prior for useful discussion and comments, donation of samples (AJR, MPS, DJP) and proof reading (AJR, MPS and JT).

Ibrahaim Baig, Abdul Ghani and the people of Hunza for making me feel welcome. Prof. Qasim Jan at the N.C.E. in Geology at the University of Peshawar for his help with logistics during my field work.

Dr. G. Davies and everybody else at the isotope laboratories at Leeds University.

R.N. Wilson, N.G. Marsh, A. Holmes, C. Cunningham, S. Button and the other technical staff at Leicester University.

Steve, Mark, Simon and John for being shuffling dossers.

In no particular order, Bob, Tim, Bill, Shona, Ann, Lee, Simon P., Simon M., Wayne, Martin, Mark W., Mark W., Mark A., Richard, Paul, Norbert, Elson and Dave for being co-sufferers.

My family for their support.

Finally, I acknowledge NERC grant GT4/85/GS/47 which has kept me in beers.

Page.

CONTENTS.

CHAPTER ONE: Introduction.

1.1: General Introduction and Thesis layout. 1
1.2: Logistics. 5
1.3: Nomenclature. 6

1.3.a: Element nomenclature. 7
1.3.b: Isotope nomenclature. 9

1.4: Classification of granitoid rocks. 10

CHAPTER TWO: Plutonic development of the NW Himalaya; a review.

2.1: Introduction. 13
2.2: General Himalayan Geology and Plutonic Development. 14

2.2.a: Zone 1; The Karakoram and north of the Transhimalayan belt. 14
2.2.b: Himalayan Evolution. 19
2.2.c: Zone 2; The Transhimalaya. 20
2.2.d: Zone 3; The Indus-Tsangpo Suture Zone. 24
2.2.e: Zone 4; The High Himalaya. 25
2.2.f: The MCT and inverted metamorphism. 26
2.2.g: Leucogranites of the High Himalaya. 27
2.2.h: Zone 5; The Lesser Himalaya. 28
2.2.i: Zone 6; Sub-Himalaya or Siwaliks. 29
2.2.j: Nature and extent of post-collisional underthrusting. 29

2.3: Possible tectonic models for the magmatic evolution of the NW Himalaya. 30

Page.

CHAPTER THREE: Field relationships in the Hunza Valley, N. Pakistan; description and interpretation.

3.1: Introduction. 32
3.2: Country rock north of the plutonic complex. 32
3.3: South of the plutonic complex. 34

3.3.a: The Hunza Group. 35
3.3.b: The Chalt Group (phyllite zone). 40

3.4: The Hunza Plutonic Complex. 41

3.4.a: The main rock types and relationships. 42
3.4.b: The northern contact. 46
3.4.c: The southern contact. 46
3.4.d: Inclusions. 48

3.5: Minor intrusions outside the plutonic complex. 49
3.6: Structure. 52
3.7: Discussion of the evolution of the Hunza area. 55

CHAPTER FOUR: Pre-collisional magmatism of the Karakoram.

4.1: Introduction. 58
4.2: Isotope systematics for the pre-collisional magmatism. 59
4.3: Mineralogy. 63

4.3.a: The Hunza Plutonic complex. 63
4.3.b: Chemistry of the common HPC phases. 64
4.3.c: Other areas. 67

4.4: Internal Chemical Trends. 68

4.4.a: The Hunza Plutonic Complex. 68
4.4.b: The HPC mixing zone. 75
4.4.c: Khunjerab and Sost. 77
4.4.d: Batura. 79

Page.

CHAPTER FOUR continued.

4.5: Spatial magmatic variations on the northern margin of the subducting Neo-Tethys ocean, and possible petrogenesis of the pre-collisional calc-alkaline pluton of the HPC. 80

4.6: Summary. 84

CHAPTER FIVE: Post-collisional granites of the Baltoro Plutonic Unit: mantle-crust interaction beneath the Karakoram.

5.1: Introduction. 86

5.2: Field relationships and tectonic setting of the BPU. 87

5.3: Mineralogy. 88

5.4: Internal Chemical Trends. 90

5.5: Possible sources. 93

5.6: The Baltoro lamprophyres. 98

5.7: Mantle-crust interaction beneath the Karakoram. 102

5.8: Summary. 110

CHAPTER SIX: Post-collisional granites of the Hunza Valley, North Pakistan: magmatic variation in process and product.

6.1: Introduction. 112

6.2: Field relationships and geological setting. 112

6.3: Mineralogy. 114

6.3.a: Garnet chemistry. 115

6.4: Geothermometry and barometry: constraints on melting conditions within the Hunza meta-sediments. 117

6.5: The Hunza Dykes and HPC aplite sheets - chemistry and possible petrogenesis. 121

Page.

CHAPTER SIX continued.

6.5.a: The Hunza Dykes. 121
6.5.b: The HPC aplite sheets. 127

6.6: The Sumayar Pluton: Chemistry and petrogenesis - a Manaslu analogue? 128

6.6.a: Chemistry. 128
6.6.b: The Hunza Valley sillimanite-grade metasediments; a source for the Sumayar leucogranites? 131

6.7: Discussion: a tentative crustal cross section through Hunza. 133

CHAPTER SEVEN: Leucogranites of the NW Himalaya: implications for study of leucogranite petrogenesis and magmatic evolution within collisional belts.

7.1: Introduction. 137
7.2: Leucogranites in collisional belts; the problems of recognition and interpretation. 138

7.2.a: Field relationships and emplacement style. 143
7.2.b: Mineralogy. 143
7.2.c: Isotope geochemistry. 144
7.2.d: Element geochemistry. 145
7.2.e: Summary: what to look for? 147

7.3: The magmatic evolution of collisional belts: the generation of leucogranites in both space and time. 149
7.4: Discussion: Leucogranites; a collisional signature? 153

Page.

CHAPTER EIGHT: Summary of conclusions.

8.1: Introduction. 156
8.2: Pre-collisional or syn-subduction magmatism. 156
8.3: Post-collisional magmatism; type-a. 157
8.4: Post-collisional magmatism; type-b. 158
8.5: Leucogranites; the global context. 159
8.6: Suggestions for further work. 160

BIBLIOGRAPHY. 161

APPENDIX ONE: Analytical Techniques.

A1.1: X-ray fluorescence (XRF). A1-1
A1.2: REE analysis. A1-5
A1.3: Isotope analysis. A1-42
A1.4: Electron microprobe analysis. A1-45

APPENDIX TWO: Sample localities. A2-1

LIST OF TABLES.

CHAPTER ONE: Introduction.

Table 1.1: Normalising values. 8

CHAPTER THREE: Field relationships in the Hunza Valley.

Table 3.1: Evolution of the Hunza Valley (after page) 57

CHAPTER FOUR: Geochemistry of pre-collisional magmatism.

Table 4.1: Modal mineralogy. 64
Table 4.2: Representative analyses (after page). 68

Page.

CHAPTER FIVE: Geochemistry of the Baltoro Plutonic Unit.

Table 5.1: Modal mineralogy. 90
Table 5.2: Representative analyses (after page). 90
Table 5.3: PETMIX modelling results. 92

CHAPTER SIX: Geochemistry of post-collisional Hunza granites.

Table 6.1: Modal mineralogy. 115
Table 6.2: Garnet rim compositions. 116
Table 6.3: Temperature and pressure estimates for the Hunza Valley metasediments. 118
Table 6.4: Representative analyses (after page). 121
Table 6.5: Comparison of Sumayar and Manaslu. 129

CHAPTER SEVEN: Leucogranites; discrimination and discussion.

Table 7.1: Comparison of leucogranites from different tectonic environments (after page). 155

APPENDIX ONE: Analytical techniques.

Table A1.1: Comparison of analyses from two preparations of the same sample. A1-1
Table A1.2: Comparison of analyses from two fusion beads of the same samples. A1-2
Table A1.3: Comparison of analyses from two pellets of the same samples. A1-3
Table A1.4: Comparison of analyses from pellets after the powder for one has been re-temed. A1-3
Table A1.5: Comparison of XRF and INAA data. A1-4
Table A1.6: Comparison of trace element analyses run on pellets and fusion beads. A1-4
Table A1.7: Comparison of REE analyses for standards from this study and other sources. A1-6

Tables of XRF & REE results for all samples. A1-9
Tables of isotope analyses. A1-43
Tables of electron microprobe analyses. A1-46

After Page.

LIST OF FIGURES.

CHAPTER ONE: Introduction.

Figure 1.1: Comparison of classification schemes for plutonic rocks. 11
Figure 1.2: Debon and Le Fort (1982) characteristic minerals diagram. 11

CHAPTER TWO: Plutonic development of the Himalaya.

Figure 2.1: Geological map of the Himalayan belt. 14
Figure 2.2: Geological map of the western Himalaya. 14
Figure 2.3: Compliation of Cretaceous-Tertiary radiometric ages for the Karakoram. 30
Figure 2.4: Two tectonic models for the post-Jurassic evolution of the Karakoram. 30
Figure 2.5: Coward et al.'s (1986) model for the structural evolution of Kohistan. 30

CHAPTER THREE: Field relationships in the Hunza Valley.

Figure 3.1: Geological map of the western Himalaya. 32
Figure 3.2: Geological map of the Hunza Valley. 32
Figure 3.3: Logged section through the sillimanite-grade zone of the Hunza Valley. 37
Figure 3.4: Schematic cross section through Hunza. 52
Figure 3.5: Stereonets of foliation direction. 53

CHAPTER FOUR: Geochemistry of pre-collisional magmatism.

Figure 4.1: Geological map of the western Himalaya. 59
Figure 4.2: Isochron for the HPC isotope data. 61
Figure 4.3: Calcic amphibole classification diagrams. 64
Figure 4.4: [Al]iv vs. (Na+K) for HPC amphiboles. 65
Figure 4.5: [Al]iv vs. $(Na+K)_A$+Alvi+Fe^{3+}+2Ti for the HPC amphiboles. 65
Figure 4.6: HPC biotite classification diagram. 65
Figure 4.7: Ab-Or-An triangle for HPC feldspars. 65
Figure 4.8: Classification diagram for HPC Fe-oxides. 66

After Page.

CHAPTER FOUR continued.

Figure 4.9: Classification diagram for HPC pyroxenes. 66
Figure 4.10(a): Debon and Le Fort (1982) classification diagram for the main phase of the HPC. 68
Figure 4.10(b): AFM trend for the HPC. 68
Figure 4.11: Harker variation diagrams for the HPC. 68
Figure 4.12: Debon and Le Fort (1982) characteristic mineral diagram for the HPC. 70
Figure 4.13: Major element modelling for the HPC. 74
Figure 4.14: Rayleigh fractionation model using trace elements for the HPC. 75
Figure 4.15: Main REE patterns and fractionation model for the main phase of the HPC. 75
Figure 4.16: REE patterns for first fractionation assemblage of the HPC. 75
Figure 4.17: Harker variation diagrams for the HPC mixing zone. 76
Figure 4.18: Spider diagrams for related lithologies within the HPC mixing zone. 76
Figure 4.19: REE patterns for mixing zone samples. 76
Figure 4.20(a): Debon and Le Fort classification diagram for Khunjerab and Sost. 77
Figure 4.20(b): AFM trend for Khunjerab and Sost. 77
Figure 4.21: Harker variation diagrams for Khunjerab and Sost. 78
Figure 4.22: LILE quadrant plots for Khunjerab. 79
Figure 4.23: REE patterns and fractionation model for Khunjerab. 79
Figure 4.24: REE patterns for N. Sost. 79
Figure 4.25: Harker variation diagrams for Batura. 79
Figure 4.26: REE patterns for Batura. 79
Figure 4.27: Spider diagrams for the main pre-collisional plutons of the Karakoram. 80
Figure 4.28: Harker variation diagrams for the pre-collisional plutons of the Karakoram. 81
Figure 4.29: Mixing model for the origin of the HPC. 83
Figure 4.30: AFC model for the evolution of the HPC. 84

After Page.

CHAPTER FIVE: Geochemistry of the Baltoro Plutonic Unit.

Figure 5.1: Geological map of the Baltoro area. 87
Figure 5.2: Normative Ab–Or–Qtz plot for the BPU. 90
Figure 5.3: Harker variation diagrams for the BPU. 90
Figure 5.4: Spider diagrams for the main BPU lithologies and K2 Gneiss. 91
Figure 5.5: REE patterns for the BPU lithologies. 91
Figure 5.6: LILE quadrant plots and models for the BPU. 92
Figure 5.7: Spider diagram for the BPU showing in situ fractionation trends. 93
Figure 5.8: Fractionation modelling of REE patterns. 93
Figure 5.9: εNd vs. εSr for the BPU granites. 94
Figure 5.10: Spidergram of monzogranite normalised to lower crust. 95
Figure 5.11: Modelled spider diagram for melting of a tonalite compared to fig. 5.10. 97
Figure 5.12: Pearce et al. (1984) discrimination diagram for the BPU. 98
Figure 5.13: Spidergrams for the Baltoro lamprophyres. 98
Figure 5.14: Nb vs. Ba and Nb/Ba vs. Rb/Ba biaxial plots for the Baltoro lamprophyres. 101
Figure 5.15: Simple mixing models for a relationship between the BPU and the lamprophyres. 105
Figure 5.16: P–T section through a hypothetical mature subduction zone. 107
Figure 5.17: Hypothetical 20Ma section through the mantle beneath the Karakoram (model 1). 107
Figure 5.18: Hypothetical 20Ma section through the mantle beneath the Karakoram (model 2). 108

CHAPTER SIX: Geochemistry of the Hunza post-collisional granites.

Figure 6.1: Chemical variation in garnets. 115
Figure 6.2: Location of metasediments in P–T space. 117
Figure 6.3: Location of metasediments in P–T space with respect to melting curves. 117
Figure 6.4(a): Granitic melting curves in P–T space. 119
Figure 6.4(b): Melting of hydrous phases in P–T space. 119

CHAPTER SIX continued.

Figure 6.5: Debon and Le Fort (1982) characteristic mineral diagram for the Hunza dykes. 121
Figure 6.6: Normative Ab-Or-Qtz phase triangle for the Hunza dykes. 121
Figure 6.7: Harker variation diagrams for Hunza dykes. 121
Figure 6.8: Total alkali vs. silica biaxial plots to illustrate reduction of scatter. 123
Figure 6.9: LILE quadrant plots for the Hunza dykes. 124
Figure 6.10: Sensitivity of LILE quadrant plots to fractionating assemblage changes. 124
Figure 6.11: Ba/Nb vs. Sr/Nb quadrant plot for the Hunza dykes with fractionation models. 124
Figure 6.12: REE patterns for the Hunza dykes. 126
Figure 6.13: REE pattern modelling for Group one Hunza dykes. 126
Figure 6.14: REE pattern modelling for Group two Hunza dykes. 126
Figure 6.15: Comparative spider diagrams for post-collisional monzogranites. 127
Figure 6.16: Comparative spider diagrams for post-collisional leucogranites. 127
Figure 6.17: εNd vs. εSr diagram for post-collisional granites. 127
Figure 6.18: REE patterns for the HPC aplite sheets. 127
Figure 6.19: Harker diagrams for the HPC aplite sheets. 127
Figure 6.20(a): Normative Ab-Or-Qtz diagram for the Sumayar pluton. 128
Figure 6.20(b): Debon and Le Fort (1982) classification diagram for Sumayar. 128
Figure 6.21: Harker diagrams for the Sumayar pluton. 130
Figure 6.22: REE patterns for the Sumayar pluton. 130
Figure 6.23: AFM plot for the Sumayar pluton. 130
Figure 6.24: Ba vs. Sr quadrant plot and model for the Sumayar pluton. 130
Figure 6.25: Pelite melting modelled spidergrams compared to the Sumayar pluton. 133
Figure 6.26: REE modelled patterns for same pelite in fig. 6.25, compared to Sumayar. 133

After Page.

CHAPTER SIX continued.

Figure 6.27: Schematic crustal cross section through Hunza. 134

CHAPTER SEVEN: Leucogranites; discrimination and discussion.

Figure 7.1: Three dimensional plot of LILE for the Baltoro Plutonic Unit. 140
Figure 7.2: Comparative spidergrams for different types of leucogranite. 140
Figure 7.3: Harris et al. (1986) discrimination diagram for the Karakoram granites. 141
Figure 7.4: εNd vs. εSr diagram for the Karakoram post-collisional granites. 141
Figure 7.5: Rb/10 vs. Zr vs. Nb triangular plot for various leucogranites. 147
Figure 7.6: Geotherms at selected times during collision and extension. 150
Figure 7.7: Schematic diagram for the four-fold evolution of a collisional belt. 152
Figure 7.8: Possible discrimination diagrams for type-b and A-type peraluminous magmas. 154

APPENDIX ONE: Analytical techniques.

Figure A1.1: Comparison of REE patterns from double runs of the same sample. A1-6

LIST OF PLATES.

CHAPTER THREE: Field relationships in the Hunza Valley.

Plate 3.1: Sediment layering. 35
Plate 3.2: Calc-schist. 35
Plate 3.3: Mineral assemblage in a calc-gneiss. 35
Plate 3.4: Scapolite replacing feldspar. 35
Plate 3.5: Sillimanite-biotite-garnet schist. 38

After Page.

CHAPTER THREE continued.

Plate 3.6: Augen gneiss. 38
Plate 3.7: View of sillimanite-grade zone. 38
Plate 3.8: P and Q zones in a kyanite schist 38
Plate 3.9: Kyanite in a two-mica schist. 39
Plate 3.10: Staurolite porphyroblast. 39
Plate 3.11: Rotated inclusions in garnet. 39
Plate 3.12: Syn-tectonic chloritoid porphyroblast. 39
Plate 3.13: Interfingering granodiorite and quartz diorite. 42
Plate 3.14: Three views of mixing zone features. 42
Plate 3.15: Group 2 aplite sheet. 44
Plate 3.16: Zoned leucogranite pegmatite. 44
Plate 3.17: Anastomosing network of dykes. 44
Plate 3.18: Parallel sheets of dykes. 44
Plate 3.19: Southern contact of the HPC. 47
Plate 3.20: Boudinaged feldspar bands in quartz diorite at southern contact. 47
Plate 3.21: Igneous inclusion in HPC. 47
Plate 3.22: Metasedimentary xenoliths in HPC. 47
Plate 3.23: Basic dyke in HPC. 49
Plate 3.24: Large xenolith in granodiorite sheet. 49
Plate 3.25: Roof of the Sumayar pluton. 49
Plate 3.26: Aplite dykes in sillimanite-zone. 49
Plate 3.27: Isoclinally folded sandstone layer. 53
Plate 3.28: Rotated boudins in the HPC. 53
Plate 3.29: Brecciated gneiss band in carbonate. 53
Plate 3.30: Late, secondary fold in sillimanite-zone. 53

CHAPTER FOUR: Geochemisty of the pre-collisional magmatism.

Plate 4.1(a): Sphene associated with biotite. 63
Plate 4.1(b): Clinopyroxene in the HPC. 63
Plate 4.1(c): Zoisite in an igneous inclusion (HPC). 63
Plate 4.1(d): Mineralogy of a calcareous inclusion. 63

After Page.

CHAPTER FIVE: Geochemistry of the Baltoro Plutonic Unit.

Plate 5.1(a): Interstitial biotite and myrrmekite texture in a monzogranite. 89
Plate 5.1(b): Secondary muscovite growth. 89
Plate 5.1(c): Strings of garnet crystals. 89
Plate 5.1(d): Xenocrystic sillimanite. 89

CHAPTER SIX: Geochemistry of the Hunza post-collisional granites.

Plate 6.1(a): Tourmaline in the Sumayar pluton. 114
Plate 6.1(b): Biotite enclosed by muscovite. 114

CHAPTER ONE: Introduction.

1.1: General Introduction and Thesis layout.

Granitoid rocks are important constituents of the Earth's crust and occur in a wide variety of tectonic settings. Pitcher (1983) stated that 'the connection between environment and granite type is inescapable. This is because each granite arises as a result of several generative processes and different source rocks, each process and source being appropriate to a particular environment'. However, there is still much controversy over the processes involved in granitoid genesis, and how the geochemical signature of a granitoid can be related to a particular environment. Studies of granitoid rocks involve processes such as high level fractionation and contamination, multi-component, heterogeneous melting sources and are hampered by a paucity of experimental data when compared to the data available for the basaltic system. Such problems often make it impossible to identify a primary magma or definite source. This thesis is concerned mainly with leucogranites, which comprise a small but important part of the broad granite spectrum. As will be seen below, some leucogranites are true crustal melts, with a definite source exposed within a distinctive tectonic environment. Studies of such cases, where good control is available, will prove invaluable when considering a more complete picture of granitoid genesis.

The term leucogranite was defined by Johannsen (1932) as a rock containing less than 5% mafics, having enough quartz to form between 5 and 50% of the leucocratic portion and having an orthoclase to oligoclase-andesine ratio between 5:95 and 50:50. Hence, leucogranites differ from "normal" granites in the scarcity of mafic phases and consist predominantly of quartz, alkali feldspar (microcline or perthite) and oligoclase or andesine. They differ from alaskites in not having albite as their plagioclase component. The most common accessory minerals are muscovite, which can be primary or secondary, and biotite, with the appearance of other accessories such as garnet, zircon, apatite, cordierite, aluminosilicates, tourmaline, spinel and corundum being controlled by pressure, temperature, $a(H_2O)$, $f(O_2)$, and magnesium, iron and alumina contents of the melt (Clarke, 1981). SiO_2, Al_2O_3, and the alkalis typically make up over

96% of leucogranite whole rock chemistry with Na_2O and K_2O showing a negative correlation with each other. This means that leucogranites are strongly peraluminous, with A/CNK ratios over 1.1, and are corundum normative. Because of their low content of mafic minerals they tend to plot at the alkali-rich end of calc-alkaline trends in AFM plots although few are actually related to such a trend. Trace element abundances in leucogranites can be quite variable due to their dependence on the nature of the source, but generally amongst the large ion lithophile elements (LILE) rubidium is enriched and strontium and barium are depleted. Rare earth elements (REE) are depleted with respect to other granitoid rocks with the light rare earths (LREE) generally being more depleted than the heavier rare earths (HREE).The two main petrogenetic groups of leucogranites are outlined below.

Group 1: Some leucogranite suites have been related by fractionation to a more basic parent. Cawthorn et al. (1976) demonstrated that peraluminous magmas could be produced by fractional crystallisation of amphibole from calc-alkaline granodiorites, and this would seem to be a likely explanation for those leucogranites found in association with such plutons. Taylor et al. (1968) showed that the Snowy Mountains leucogranite in New South Wales was the result of feldspar fractionation of a granodiorite. Similarly, Petterson and Windley (submitted) demonstrate that the Shirot leucogranite in Pakistan is a late-stage fractionate of the Shirot granodiorite pluton. These leucogranites could occur in any tectonic setting that involves the production of suitable parental magmas, and their chemistry will depend entirely on the parent. Therefore, this type of leucogranite is of little interest when considering the relationship between tectonics and magma processes.

Group 2: Many leucogranites occur in areas associated with high heat flow, commonly as late magmatic intrusions in intracontinental orogenic belts. These belong to the second group where leucogranites are considered to represent primary, or near primary, crustal melts and it is this type of leucogranite that is of most interest, since the particular conditions that these magmas form under are directly related to the tectonic environment. Steepening of the geotherms by crustal thickening in collisional settings may be sufficient to promote melting of metapelitic material or, at greater depths, high-

grade metamorphic basement (see England and Thompson, 1986). Clemens and Wall (1981) show that partial melting of a muscovite-quartz-feldspar assemblage could occur between 4-10 kb. and below 700°C to produce a water-aluminosilicate-rich melt which could account for many muscovite-garnet leucogranites found intruding kyanite-sillimanite regional metamorphic belts. Similarly, Thompson (1982) notes that widespread melting should occur in the kyanite-sillaminite facies series due to the great overlap of the quartz + muscovite dehydration with initial melting reactions in P-T space. These melts would lie close to the granite eutectic and show little change in composition due to the steepness of the liquidus isotherms. Thus voluminous melts would only be produced if the melting assemblage also lay close to the eutectic. Only at much higher temperatures would the melts migrate away from the eutectic when one melting phase is exhausted i.e. become non-minimum melts. Alternatively, such high temperatures would not be necessary if an excess of fluid was present to lower the solidus to the wet melting curve. Whilst fluid saturation is unlikely in granulite-facies metamorphic terranes under normal circumstances (e.g. Clemens and Vielzeuf, 1987), fluid influx has been invoked to induce melting in lower-grade (amphibolitic) terranes e.g. along strike-slip faults in Brittany (Strong and Hanmer, 1981) and from beneath thrusts in the Himalaya (Le Fort, 1981).

Scattered along the Himalayan range from Nanga Parbat in the NW to Bhutan in the east are 10 or more major Cenozoic leucogranite plutons, often forming some of the highest peaks of the Higher Himalaya e.g. Lhotse, Makalu and Manaslu. Of these the Manaslu pluton has been extensively studied e.g. Le Fort (1981), Vidal et al. (1982), Cuney et al. (1984), Le Fort et al. (1987) and from this work has come the classic model for the generation of Himalayan leucogranites. The granite has been shown geochemically to be the result of remelting of the Tibetan Slab gneisses, caused by sillimanite-grade metamorphism and local high heat flow due to high concentrations of heat producing elements (Le Fort et al., 1987). Melting was initiated by crustal thickening as a result of thrust movement on the Main Central Thrust (MCT) with subsequent dehydration of the underlying sediments and upward movement of the fluids (Le Fort, 1981). The magmas are water-saturated, minimum melts and consequently have not migrated far from their source. The Bhutan

leucogranites have similarly been attributed to crustal anatexis due to tectonic shortening and intracrustal thickening which also gave rise to regional Barrovian-type metamorphism (Dietrich and Gansser, 1981). Residual Barrovian heat and fluid fluxing have also been invoked to cause anatexis of metamorphic crystalline basement giving rise to the leucogranitic lit-par-lit intrusions, plutons and dykes and vast migmatite terrane in Zanskar and Kishtwar (Searle and Fryer, 1986).

The High Himalayan leucogranites have, therefore, formed under special conditions and provide much information about their tectonic setting. They represent one of the few true examples of "S-type" granites as defined by Chappell and White (1974) in that they have been generated by melting of a crustal, metasedimentary protolith. However, the question arises as to whether this is the only mechanism which can generate leucogranites in collisional belts. Vielzeuf and Holloway (1988) recently demonstrated that about 40% of "S-type" granitic liquid can be produced by the dehydration reaction of biotite in a metapelite, under fluid absent conditions between 850-875°C. These liquids are likely to leave behind a residue of quartz, garnet sillimanite and plagioclase which will resemble an aluminous granulite. This amount of melt surpasses the estimates of Clemens and Vielzeuf (1987) and Wickham (1987) for the percentage of partial melting needed for a magma to be able to separate from its source. However, the models of England and Thompson (1986) predict only 5-20% melting at the base of collision-thickened crust. Both Clemens and Vielzeuf (1987) and Rutter and Wyllie (1988) consider that a mantle input of heat is necessary to generate sufficient partial melting at the base of the crust for pluton development.

It should, therefore, be possible to generate leucogranites at the base of the crust under fluid absent conditions if an external heat supply is available. Such a mechanism is most likely in a collisional setting where the base of the crust has already started to melt. Whilst many granites in Andean-type settings are considered to have a ultimate mantle origin, few leucogranites have been related to mantle processes. The Cabo leucogranite in Brazil is an exception (Long et al., 1986) but this lies in an extensional, rather than collisional, setting and is probably related to a mantle plume. However, the association of mantle magmas and granites has recently

been noted in many areas (e.g. Rock and Hunter, 1987; MacDonald et al., 1985), and it has been suggested that the Cornubian Batholith, previously considered to be an "S-type" melt with a similar origin to the Himalayan leucogranites, is a fractionate of its associated potassic mantle magmas (Leat et al., 1987).

The original aim of this project was to study a group of leucogranites in the Skardu region of N. Pakistan. These granites are part of the Karakoram Axial Batholith (KAB) and occupy a tectonic position which parallels that of the High Himalaya. It was hoped that study of these would ascertain whether they conformed to the High Himalayan model of generation or whether another model was more appropriate. However, due to the political situation and logistics the field area was switched to a different section of the KAB in the nearby Hunza Valley which is much more accessible via the Karakoram Highway. Chapter 2 of this thesis reviews the general geology of the Himalaya and discusses how the KAB represents the magmatic evolution of the Eurasian margin since the mid-Cretaceous. Because of this, field work spread over two seasons (chapter 3) revealed that the Karakoram Axial Batholith in Hunza was composed of a number of plutonic episodes of which leucogranites were only the latest. Therefore, the geochemistry of the plutonic rocks of Hunza is divided into two sections. Chapter 4 considers the pre-collisional phase and compares it with other sampled plutons in the Karakoram, whilst chapter 6 concentrates on the post-collisional phases including the leucogranites. When the field samples from Hunza were delayed in arriving back in Britain, some leucogranite samples from the Baltoro Plutonic Unit (BPU) 100km east of Hunza were donated by Tony Rex and Mike Searle (University of Leicester) to provide an additional data base. The geochemistry of these and related rocks is discussed in chapter 5, and the comparison of the leucogranites from the BPU, Hunza and the High Himalaya forms the basis for a more general discussion in chapter 7 of the implications of this work for leucogranite study elsewhere.

1.2: Logistics

This project is part of a large-scale research program being carried out in the NW Himalaya and Karakoram at Leicester University. Two field seasons were spent in the Hunza Valley of N. Pakistan, the

first of two months duration in 1985, and a second of four months in 1986. The climate is generally dry and hot so few days were lost due to bad weather. However, the relief is extremely mountainous (vertical relief from 4000' to 25000') and so most work is restricted to valley exposure and mappable units have to be extrapolated from valley to valley. One main road, the Karakoram Highway, runs through the Hunza valley and cuttings along this road expose a good section through the Karakoram Axial Batholith. With the use of a jeep most geochemical samples of the batholith were collected along this road section. The police presence in Hunza is not as obvious as in other areas of N. Pakistan but care must be taken not to enter restricted areas.

Samples of 1-2kg were collected for geochemical analysis, ensuring that they were as fresh as possible. Smaller samples (1-2" cubed) were collected for microprobe and thin sections. All samples were taken to the N.C.E in Geology, Peshawar University in order to be packed for shipping back to the UK. In hindsight it is advisable to send all samples back via surface post in parcels weighing <10kg. Whilst this may require a large number of parcels, the time in transit is in the order of three months as opposed to eight months by ship freight.

1.3: Nomenclature

The shortening of definitive sequences (SODS) for units and structures is employed in this thesis for conciseness. Each abbreviation is defined when first used in each chapter, but the most important three are given below:

KAB = Karakoram Axial Batholith
HPC = Hunza Plutonic Complex
BPU = Baltoro Plutonic Unit

Rock type abbreviations are defined in appendix 1.1 but important ones are; grd = granodiorite, mzg = monzogranite, lcg = leucogranite, 2mg = two mica granite, ap = aplite, peg = pegmatite. Where plots show groups of different rock types the samples included in each group are again listed in appendix 1.1.

1.3.a: Element nomenclature

Element symbols rather than full names are used in the text. In addition various elements are assigned to groups according to their abundance or properties:

Major elements: Si, Al, Fe, Mg, Ca, Na, K.
Usually quoted as oxides in %, and are the main rock and common mineral forming elements.

Minor elements: Ti, P, Mn.
Also usually quoted as oxides in %, and are important constituents of minor phases such as sphene, apatite and garnet.

Trace elements: usually given in ppm (generally <1000ppm) and include (after Saunders et al., 1980).
Large ion lithophile elements (LILE): Rb, Ba, Sr, Th, U, and also K.
These elements have ionic radii larger than the common rock forming elements.
High field strength elements (HFSE): Zr, Nb, Hf, Ta and also Ti, P.
Refractory elements: Ni, Cr, V.

Rare earth elements (REE).
These form their own group (the Lanthanides) in the periodic table, and are also given in ppm.
Light rare earth elements (LREE): La, Ce, Pr, Nd.
Middle rare earth elemnts (MREE): Sm, Eu, Gd, Dy.
Heavy rare earth elements (HREE): Ho, Er, Yb, Lu.

For some plots it is necessary to convert % oxide to ppm element and this is done by calculating the amount of the element in the oxide using atomic weight, multiplying this by 10,000, and then multiplying by the oxide %. Some conversion factors are given below:

K_2O (%) to K (ppm) * 8301.5
TiO_2 (%) to Ti (ppm) * 5995.0
P_2O_5 (%) to P (ppm) * 4294.0

The term 'spider diagram' is often used in place of multi-element variation diagram with individual traces being 'spidergrams'

(after Thompson et al., 1983). Where such diagrams are normalised to primordial mantle the normalising values of Taylor and McLennan (1985) are used (table 1.1). REE spidergrams are often normalised to chondrite using values from Taylor and McLennan (1981), (table 1.1). The letter 'n' indicates a value is normalised to another, defined value.

Primitive mantle (ppm)		Chondrite (ppm).	
Na	2500	La	0.367
K	180	Ce	0.957
Ti	960	Pr	0.137
Rb	0.55	Nd	0.711
Sr	17.8	Sm	0.231
Y	3.4	Eu	0.087
Zr	8.3	Gd	0.306
Nb	0.56	Dy	0.381
Ba	5.1	Ho	0.085
La	0.551	Er	0.249
Ce	1.436	Yb	0.248
Nd	1.067	Lu	0.038
Hf	0.27		
Ta	0.04		
Pb	0.120		
Th	0.064		
U	0.018		
P_2O_5	0.024 by extrapolation		

Table 1.1: Normalising values for primitive mantle and chondrite (Taylor and McLennan, 1985, 1981 resp.).

Modelling equations used include:

Batch melting (Hanson, 1978): $C_L/C_O = 1/[D_O+F(1-P)]$

Rayleigh fractional crystallisation: $C_L/C_O = F^{(D-1)}$

Equilibrium crystallisation: CL/CO = product(1 to n) [1/f(D-1)+1] (McCarthy and Hasty, 1976)

where: CL = concentration in liquid; CO = initial concentration; D = bulk distribution coefficient; P = bulk distribution coefficient of melting assemblage; F = proportion of liquid; f = size of equilibrium increment; n = number of increments.

1.3.b: Isotope nomenclature.

Decay constants used in isotopic calculations are from Steiger and Jager (1977);

$$\lambda^{87}Rb = 1.42 * 10^{-11} \text{ years}^{-1}$$
$$\lambda^{147}Sm = 6.54 * 10^{-12} \text{ years}^{-1}$$

87Rb/86Sr and 147Sm/144Nd ratios were calculated from the Rb/Sr ratio from XRF data and the Sm/Nd ratio from ICP data using;

$$^{87}Rb/^{86}Sr = (2.6929 + (0.283 * (^{87}Sr/^{86}Sr))) * Rb/Sr$$

$$^{147}Sm/^{144}Nd = (0.531497 + (0.142521 * (^{143}Nd/^{144}Nd))) * Sm/Nd$$

Where $^{87}Sr/^{86}Sr$ and $^{143}Nd/^{144}Nd$ are the measured isotopic ratios (appendix 1.3). Epsilon (εSr and εNd) values were calculated using the equations of DePaolo (1979);

$$\varepsilon Sr_t = (((^{87}Sr/^{86}Sr(x,t))/(^{87}Sr/^{86}Sr(UR,t))) -1) *10000$$

where: $^{87}Sr/^{86}Sr(x,t)$ is the isotopic ratio of sample x at time t; $^{87}Sr/^{86}Sr(UR,t)$ is the isotopic ratio of a uniform reservoir at time t. These two variables are calculated by;

$$^{87}Sr/^{86}Sr(x,t) = ^{87}Sr/^{86}Sr(x,m) - (^{87}Rb/^{86}Sr(x,m)*(e^{\lambda t}-1))$$

$$^{87}Sr/^{86}Sr(UR,t) = ^{87}Sr/^{86}Sr(UR,0) - (^{87}Rb/^{86}Sr(UR)*(e^{\lambda t}-1))$$

where: $^{87}Sr/^{86}Sr(x,m)$ and $^{87}Rb/^{86}Sr(x,m)$ are the measured ratios for the sample x; $^{87}Sr/^{86}Sr(UR,0)$ and $^{87}Rb/^{86}Sr(UR)$ are the present day values for the uniform reservoir.

Analogous equations are used to calculate ENd. Present day

values for the uniform reservoir used here are;

$^{87}Sr/^{86}Sr(UR,0)$ = 0.7045 (DePaolo, 1979)
$^{87}Rb/^{86}Sr(UR)$ = 0.0839 (DePaolo, 1979)
$^{143}Nd/^{144}Nd(UR,0)$ = 0.51264 (Hawkesworth and Norry, 1983)
$^{147}Sm/^{144}Nd(UR)$ = 0.1967 (Jacobssen and Wasserburg, 1980)

1.4: Classification of granitoid rocks

There are two main methods used in the literature to approach the problem of classifying granitoid rocks. These methods are not mutually exclusive and both must be used with their limitations in mind (Bowden et al., 1984). The first approach is to use accurately defined mineralogical and/or geochemical boundaries to delimit fields for individual rocktypes. Trends shown by rock suites in such systems can also be used in classification as well as giving information about petrogenetic processes. The second method is to use mineralogical and geochemical characteristics to define a genetic classification based on source and tectonic environment.

Many of the first classifications used mineralogy and petrology (e.g. Johannsen, 1932) but many names then used have since become redundant (leucogranite being a notable exception). More recently the main system for mineralogical classification has been devised by Streckheisen (1976) working with the IUGS. This uses a QAP triangular plot with QAP representing the modal proportions of quartz, alkali and plagioclase feldspar in the rock. The main criticism of this system is that no account is taken of the mafic phases present which can constitute up to 40% of some granitoids, and that the albitic feldspar component is assigned to the alkali feldspar rather than being split between A and P. Some workers tried to use other minerals, e.g. Pupin (1980) used zircon morphology, but the QAP diagram does work well owing to the considerable variation of its three components in granitoids. More recently Lameyre and Bowden (1982) have recognised the diagram's potential for identifying trends in rock suites.

The other criticism of the QAP plot beside those mentioned above, is the time consuming nature of modal analysis, particularly if a large rock suite is studied. Therefore several workers have

devised similar systems which can be calculated using geochemical data (Streckheisen and Le Maitre, 1979; La Roche et al., 1980; Debon and Le Fort, 1982). The Streckheisen and Le Maitre (1979) system involves the use of norms and so is not used here as, unless the FeO/Fe_2O_3 ratio is measured for each sample, this will lead to errors. The system devised by Debon and Le Fort (1982) is favoured in this thesis. As well as being quicker and easier to calculate than the modes needed for the QAP diagram, it classifies each sample, and then can also be used to identify trends within a suite of samples using a second diagram. The classification diagram is based on a QPA triangle, but it can be considered as a biaxial plot. The two parameters Q and P are calculated from major cation values which in turn are calculated from the major element oxide analysis of the rock, and they are proportional to the amount of weight % quartz and plagioclase, respectively, in the rock (Q=Si/3-(K+Na+2Ca/3); P=K-(Ca+Na); fig. 1.1(a)). The diagram has been constructed so that the fields coincide as much as possible with the fields in the QAP diagram. However, there are differences with the Debon and Le Fort granite group including the syenogranites and some of the monzogranites of Streckheisen. The rest of the monzogranites fall in the Debon and Le Fort adamellite field which is an equivalent term. As with the QAP diagram no distinction is made between tonalite and trondhjemite or peralkaline and other granitoids. To check that the two systems are comparable figure 1.1 is a comparison to show where some of the main rock types from this thesis fall in the QAP and Debon and Le Fort nomenclature diagrams. In general there is good agreement, although there are some differences such as R4 plotting in the syenogranite field in the QAP diagram and in the monzogranite or adamellite field in the Debon and Le Fort diagram. These discrepancies are probably a result of misidentification of the A and P components during point counting, since if a feldspar does not display lamellar twinning it is hard to determine whether it has $>An_5$. The second diagram (fig. 1.2) is a characteristic minerals diagram and this plots A (Al-(Na+K+2Ca); proportional to the felsic component of the rock) against B (Fe+Mg+Ti; proportional to the mafic component). It is divided into a peraluminous and meta-aluminous domain with each domain further divided into characteristic mineral areas. The diagram is useful in that it identifies likely mafic mineralogy, shows certain trends and has a field for leucogranites.

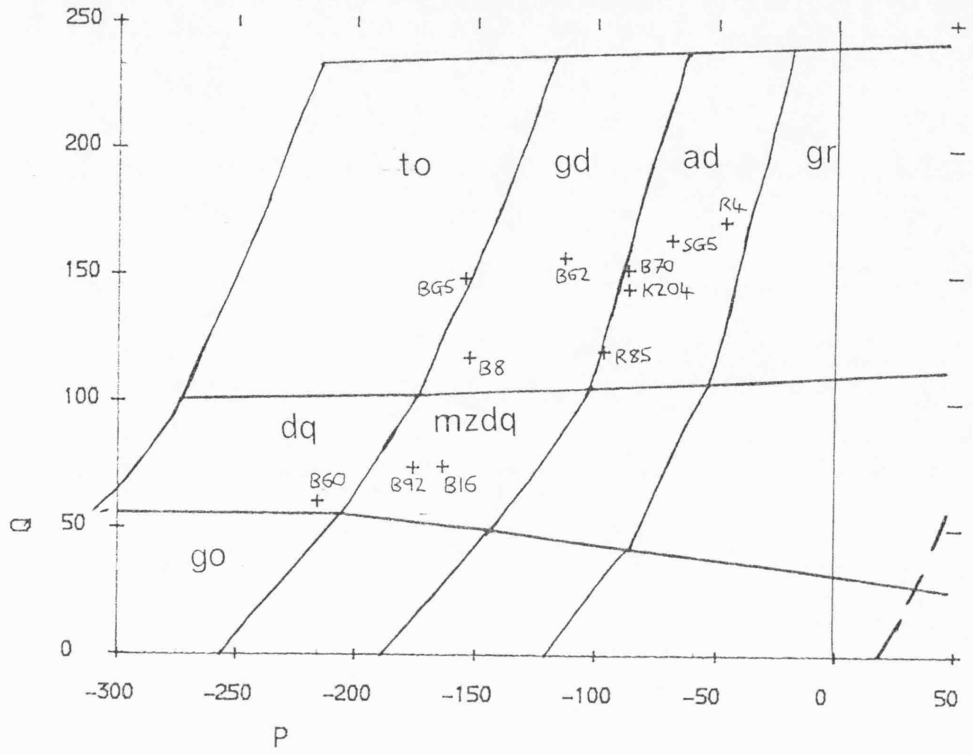

Fig. 1.1(a): Debon and Le Fort (1982) classification diagram.
P = K − (Na + Ca)
Q = Si/3 − (K + Na + 2Ca/3)

Fig. 1.1(b):

Streckheisen (1976)
Q = modal quartz
A = modal alkali feldspar
P = modal plagioclase

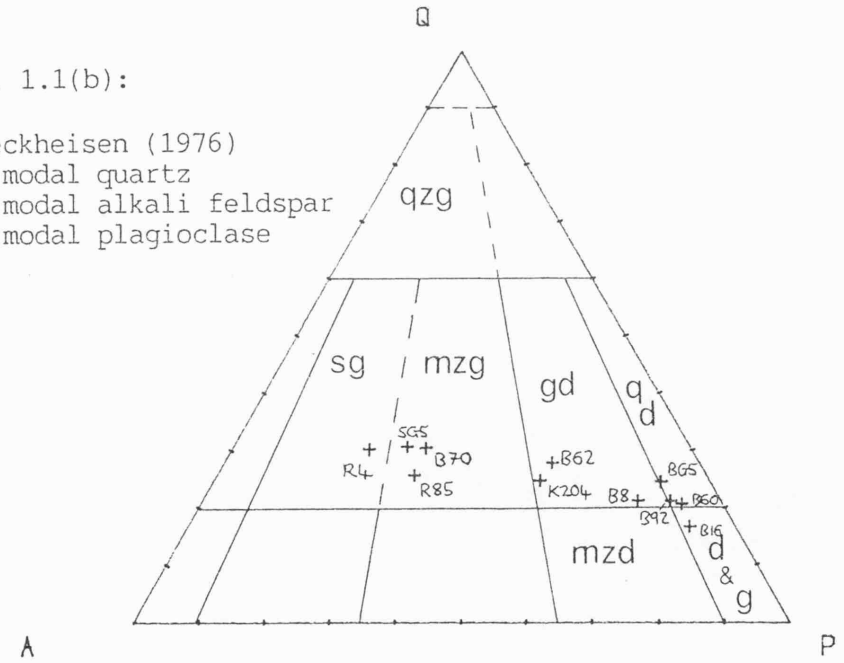

Figure 1.1: Comparison of Debon and Le Fort (1982) chemical and Streckheisen (1976) modal classifications for granitoid rocks.
to=tonalite; gd=granodiorite; ad=adamellite; gr=granite; dq=quartz diorite; go=gabbro; mzdq=monzo-quartz diorite; mzg=monzogranite; sg=syenogranite; mzd=monzodiorite; qzg=quartz granite.

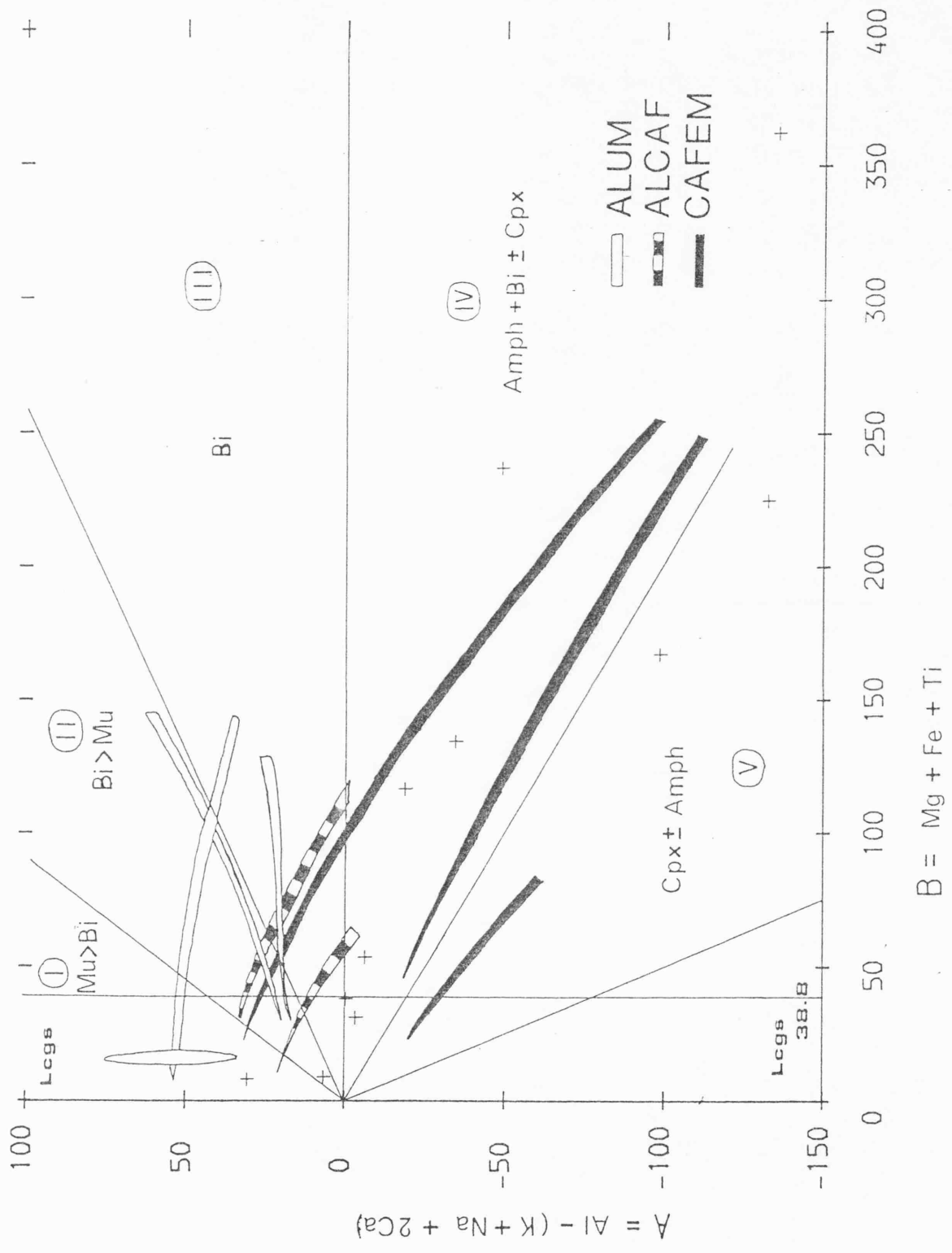

Figure 1.2: Debon and Le Fort (1982) characteristic minerals diagram showing main domains, the leucogranitoid field and the trends for main rock associations (ALUM = aluminous; ALCAF = alumino-cafemic; CAFEM = cafemic). Crosses are analyses from figure 1.1.

Genetic classification schemes (e.g. Chappell and White, 1974; Read, 1956; Pitcher, 1983, 1987; Barker, 1984; Didier (1982); Brown et al., 1984; Pearce et al., 1984; Harris et al., 1986) are not used in this thesis to identify a suites' tectonic affinity or source, since in a number of cases they have been shown to be unreliable (e.g. Dickson, 1986; Twist and Harmer, 1987; Arculus, 1987). However, some of the more sophisticated schemes are used where useful information can be gained from them, and these are discussed further at the appropriate juncture.

CHAPTER TWO: Plutonic development of the NW Himalaya; a review.

2.1: Introduction.

The geology of the Himalaya provides evidence of an orogenic belt which has gone through the complete Wilson cycle from a stable continental phase, through rifting and ocean spreading to subduction and collision. The latter part of this cycle began with northward subduction and closure of Neo-Tethys from the Cretaceous, which generated Andean-type magmatism, with associated platform and basinal sediments, on the margin of the Eurasian plate. Oceanic subduction was terminated in the Eocene by continent-continent collision between India and Eurasia and intracontinental thrusting, crustal thickening and underplating followed. These processes caused deformation, metamorphism, nappe emplacement, and crustal anatexis within the Indian and Eurasian basement and sedimentary cover. Because of the young age and rapid uplift rates (e.g. Zeitler, 1985) of the belt many features formed by this cycle such as the Karakoram Axial Batholith (KAB) are now exposed at the surface and one of the unique characteristics of the chain is the continuity of its major units from Pakistan in the west to Burma in the east - a distance of some 3000km (Gansser, 1964).

To the north of the Himalayan chain within the Eurasian plate there are a number of older sutures and blocks which record earlier accretion events prior to the main collision. Most of these blocks have Precambrian cratonic basement and represent small microcontinents that separated from Gondwana before the opening of Neo-Tethys. Some of the sutures show deepening sedimentary sequences, unconformities and volcanism related to the opening and closing of marginal basins.

This thesis is concerned with the magmatic evolution of the Karakoram Axial Batholith (KAB) in N. Pakistan, particularly after collision, and since this lies along the edge of the Eurasian craton it is intimately linked with the overall evolution of the Himalayan belt. This chapter, therefore, initially reviews how the Karakoram came to be the Eurasian margin prior to the main Himalayan cycle. It then briefly reviews the general geology of the Himalaya, concentrating on areas most relevant to the KAB. Due to the length of

the belt there are tectonic differences between the eastern and western ends, with an island arc developing in the west. Therefore, the latter part of the chapter considers tectonic models for the evolution of the Karakoram/Kohistan/Ladakh area only. Figure 2.1 is a general map of the Himalaya from Searle (1982), and figure 2.2 is a more detailed map of the NW Himalaya from Searle et al. (in press).

2.2: General Himalayan Geology and Plutonic Development.

The Himalaya can be divided into six main zones in a north-south direction (Gansser, 1964; Windley, 1983). Each zone runs parallel to the general trend of the belt.

2.2.a: Zone 1; The Karakoram and north of the Transhimalayan belt.

In the west, where the Indus-Tsangpo Suture Zone (ITSZ) divides into the Shyok Suture Zone (SSZ) to the north and the Main Mantle Thrust (MMT) to the south, this zone lies north of the SSZ. The area includes northern Afghanistan to the far west and the Karakoram in N. Pakistan and Ladakh. It represents the southern edge of the Eurasian plate and is separated from the Pamirs further north by the Rushan-Pshart suture (Searle et al., in press). The major strike-slip Karakoram fault separates the Karakoram from the Tibetan Plateau which forms the eastern part of this zone. There has been an estimated 150km of dextral movement on the fault due to a northward projecting promontory of Indian crust to the west (Molnar and Tapponier, 1978). The Tibetan plateau is composed of the two main Qangtang and Lhasa blocks with the Kun-Lun range to the NW.

In Afghanistan this zone has been divided into three domains (Debon et al., 1987a) which record the pre-Himalayan evolution of the Eurasian margin:

a: The South Central Domain which is equivalent to the Karakoram and consists of Wakhan, the Central Mountains, the southern Pamirs, eastern Hindu Kush and western Nuristan. This domain is separated by the Panjao Suture from;

b: The North Central Domain which contains the Farah Rod and central Pamirs.

c: The Northern Domain which lies to the north of the Wanj-

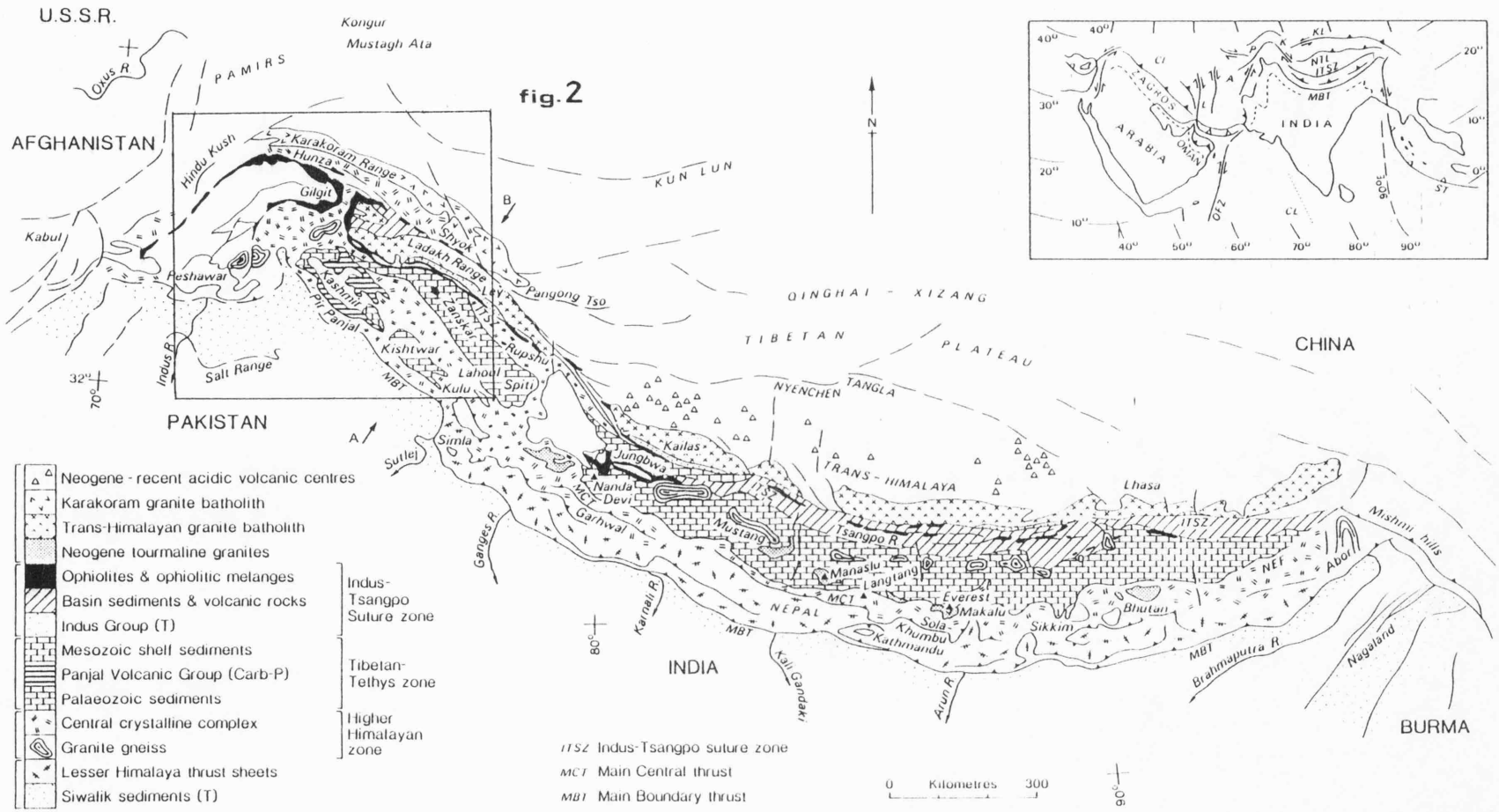

Figure 2.1: Geological map of the Himalayan belt from Searle (1982). Box shows area covered by figure 2.2.

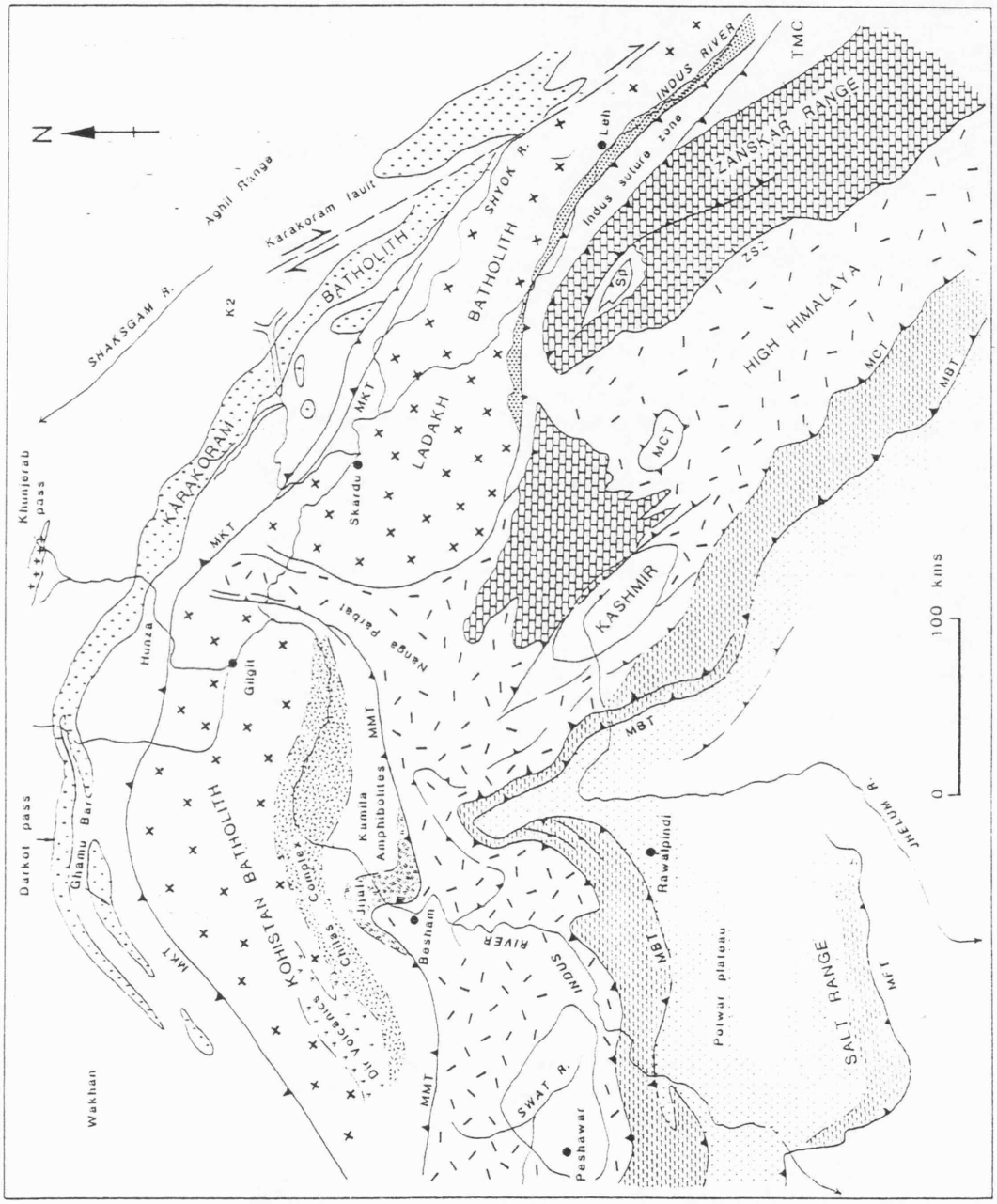

Figure 2.2: Geological sketch map of the western Himalaya and the Karakoram from Searle et al. (in press). MKT, Main Karakoram Thrust; MBT, Main Boundary Thrust; MMT, Main Mantle Thrust; ZSZ, Zanskar Shear Zone; Sp, Spontang Ophiolite.
Phanerozoic sediments of the Indian continental margin in the Zanskar range (bricks) lie structurally above the High Himalayan gneisses and granites (stipple). The Kohistan-Ladakh batholith (large crosses) is bounded to the south by the Indus Suture Zone and MMT, and to the north by the Shyok Suture Zone or MKT. The composite Karakoram Axial Batholith is shown in small crosses.

Aqbaytal Fracture and includes the northern Pamirs, western Hindu Kush and Badakhshan.

In the Northern Domain there is evidence of Palaeozoic orogeny that is not present to the south showing that this area was the margin of Eurasia prior to the Mesozoic. Large scale folds in lower to middle Palaeozoic sediments are unconformably overlain by shallow water carbonates of Carboniferous-Permian age (Tapponier et al., 1981a) and are probably related to the Hercynian orogeny. Intra-Hercynian events may have been caused by the closure of small oceans or basins (Boulin, 1981).

The Mesozoic history of Afghanistan is related to accretion of crustal blocks which were part of Gondwana in the Palaeozoic (Tapponnier et al., op.cit.). These blocks had basement which had been consolidated in the Precambrian and were intruded by c500Ma old granitoids related to crustal thinning and anatexis (Debon et al., 1987a) which seems to have been widespread throughout Gondwana at this time (see later). Northward subduction was initiated along the Herat fault and Wanj-Aqbaytal fracture causing the intrusion of 230Ma old (Rb-Sr WR) Triassic calc-alkaline plutons into the then Eurasian margin of the western Hindu Kush and Badakhshan (Debon et al., 1983; 1987a). Subduction ceased with the collision of the Northern and North Central Domains causing tectonic compression in the Hindu Kush in the early Jurassic.

Subduction then switched to the Panjao Suture, closure of which was marked by the emplacement of the Panjao Ophiolite and the accretion of the South Central Domain to Eurasia in the late Jurassic. This domain contains Cretaceous (100Ma) calc-alkaline batholiths in the Arghandab and Helmand belts on either side of the Central Mountains and also in Wakhan, Safed Kher and western Nuristan (Debon et al., 1987a). These intrusions are related to the same phase of northward subduction of Neo-Tethys that gave the early phases of the KAB. The Spin Boldak belt represents later, Cenozoic (60Ma) plutonism related to the same subduction period (Debon et al., op.cit.). The Kandhar volcanics to the south of the Central Mountains date from the upper Jurassic to the Aptian and are overlain by shallow water carbonates (Tapponier et al., 1981a). These are indicative of a marginal arc that may have been present to the south

during the early stages of subduction.

The domains and accretion events in Afghanistan can be correlated with structures in Tibet whose Mesozoic history was controlled by the accretion of the Qangtang and Lhasa blocks to Eurasia. The Kun-Lun represent the Hercynian boundary of Eurasia (Laurasia) and so correlate with the Northern Domain in Afghanistan. Folding of lower Mesozoic rocks in the Kun-Lun corresponds to a Cimmerian event seen in the Hindu Kush (Tapponier et al., op.cit.).

The North Central Domain is equivalent to the Qangtang block and the BNS is therefore the analogue of the Panjao suture, forming in late Jurassic times. This means that the Lhasa block is equivalent to the South Central Domain and the Karakoram. This is supported by palaeomagnetic data which shows south Tibet to be near Gondwana in the southern hemisphere during the Triassic but to be near the southern Asian margin at 15-20°N by the mid-Cretaceous (Westphal, 1983). Allegre et al. (1984) postulate that Tibet had become detached from Gondwana by as early as the Permian.

The first closure, between the Northern domain or Kun-Lun and the North Central Domain or Qangtang block respectively, probably represented the demise of Palaeo-Tethys. At the same time rifting signalled the opening of Neo-Tethys. The second closure represents a Cimmerian crisis. Work on the Donqiao ophiolite in the BNS (Giradeau et al., 1984) shows a typical ophiolite sequence but reduced in thickness. Geochemistry points to a small ocean or marginal basin environment. Folding of Jurassic flysch followed by thrusting and emplacement of Palaeozoic metasediments over the top dates the obduction phase of the ophiolite as Upper Jurassic with Upper Jurassic and Lower Cretaceous sediments being deposited on top. This correlates with work by Blaise et al. (1978) on the Panjao suture which shows that folding of the flysch and emplacement of the Waras ophiolite took place before the late Cimmerian, as they are overlain by red molasse of Lower Cretaceous age. This all suggests that the second closure was of a small ocean (the Tanggula-Waser ocean) splitting a Cimmeride microcontinent which had crossed Neo-Tethys (Sengor, 1986).

Concerning the igneous activity in this zone in Tibet, a

513±14Ma granite gneiss in the north of the Lhasa block (Xu et al., 1985) is of the same age as Palaeozoic gneisses in Afghanistan (Debon et al., 1987a; 502±24Ma) confirming the Gondwanan origin of this block. Plutonic rocks of Triassic age, related to the first closure, have not been reported in Tibet. Two belts of intrusions, the Bange (121±2Ma) and the Anduo (120-140Ma) belts were thought to represent the Cimmerian subduction phase (Xu et al., op. cit.) but Ar/Ar dates on northern volcanic rocks give ages of 110-80Ma (Coulon et al., 1986) which postdates the Cretaceous red beds overlying the BNS. Coulon et al. (op. cit.) suggested the belts were related to the later, main Gangdese subduction further south. However, Gariepy et al. (1985) plotted $^{207}Pb/^{204}Pb$ versus $^{206}Pb/^{204}Pb$ for these belts and found that both plotted solely in the field for crustal basement. This showed that neither belt is related to subduction but that both are a result of anatexis following crustal thickening, possibly as a result of thrusting. Allowing time for crustal re-equilibration this would date the deformation period as Lower Jurassic, the same time as formation of the BNS and the second collision.

Following the second closure the Karakoram formed the southern margin of Eurasia in, what is now, N. Pakistan and Ladakh. The area north of the SSZ can be broadly divided into three domains (Searle et al., in press):

1). The Northern Domain consisting of low-grade sedimentary rocks and culminations of high-grade gneiss.
2). The Karakoram Axial Batholith (KAB).
3). The southern Karakoram Metamorphic Complex composed of a variety of metamorphic rocks from low pressure chlorite, biotite, and chloritoid-bearing greenschists up to kyanite and sillimanite-grade gneisses. These have been uplifted by the Main Karakoram Thrust (MKT) to the south, which represents re-activation of the SSZ following collision. The juxtaposition of the low-grade rocks to the north with the high-grade rocks to the south has led Rex et al. (in press) to infer the presence of a major N-dipping normal fault, the Karakoram Batholith Linament (KBL). This is thought to form as a result of culmination collapse during and following the uplift of the metamorphic complex, and has an analogue in the Zanskar Himalaya (see later).

The KAB consists of a number of plutonic centres and stretches E-W for over 600km but only reaches a width of upto 30km. The batholith has been the locus of activity since the Jurassic and Rex et al. (in press) consider that its position may be controlled by the inferred KBL. The oldest component of the KAB is the Hushe Complex composed of foliated orthogneiss interlayered with amphibolites and felsic gneisses (Searle et al., in press). This gives Jurassic ages of 208±8Ma and 163±7Ma supported by Ar/Ar step heating analyses on amphiboles which give integrated ages of 205±1.4 and 203±0.6Ma (K-Ar Hbl; Rex et al., in press). Associated with this magmatism is a low-pressure metamorphism (M1; Searle et al., in press).

The main phase of the KAB is late Cretaceous, granodioritic, calc-alkaline plutonism related to the subduction of Neo-Tethys. Ages from this phase include 95±5Ma (U-Pb, Hunza; Le Fort et al., 1983) and 111±6Ma (Rb-Sr, Darkot Pass; Debon et al., 1987b). The Darkot Pass unit consists of monzodiorites through to leucogranites and appears to be composite (Debon et al., 1987b). The Hunza unit is a large quartz diorite-granodiorite pluton and is the subject of a later chapter. Following this c.100Ma event there was a quiet period until collision of India with Eurasia around 45Ma (see below). The next phase of plutonism may be represented by the Batura unit which gives a Rb-Sr age of 43±3Ma and consists predominantly of an unfoliated granite (Debon et al., 1987b).

The collision caused a major thermal event due to crustal thickening and crust stacking, leading to widespread Barrovian-type metamorphism (M2; Searle et al., in press). This metamorphism was syn-tectonic to the main deformation phase and is now exposed in the uplifted Karakoram Metamorphic Complex. This event had ceased by 36my as its structures are cut by the Mango Gusar pluton of this age (Rex et al., in press). Later post-collisional magmatism is represented by monzogranites and leucogranites intruded as dykes in Hunza and as a pluton in the Baltoro. The Baltoro Plutonic Unit gives a U-Pb age of 21Ma (Parrish and Tirrul, in press) whilst the Hunza dykes give K-Ar ages of 16.9-4.5Ma (Debon et al., 1987b). These units are the main subject of the rest of this thesis. Local thermal effects from these magmas superimpose an M3 metamorphism on the main M2 assemblages (Searle et al., in press).

2.2.b: Himalayan Evolution.

After the Cimmerian closure the Neo-Tethys ocean crust started to be subducted beneath the Eurasian margin. Collision between the Eurasian and Indian plates occurred in the Eocene and since then the northward movement of the Indian plate has been accommodated by underplating, intracontinental thrusting, crustal thickening, block rotation along lateral strike-slip faults and E-W extension in the north.

The timing of major events in the Himalaya is loosely constrained by palaeomagnetic data. Peirce (1978) noted a change in the relative motion of India northward, with respect to the south pole from, 14.9±4.5cm/y between 70-40Ma to a slower rate of 5.2±0.8 cm/y which has continued to the present. This change corresponds to the major collision in the mid-Eocene. In the late Cretaceous the southern margin of Tibet moved south to palaeolatitudes of 7-10°N due to clockwise rotation as a result of Africa moving towards Asia in the west (Westphal, 1983). Since collision it has moved northwards again as a rigid, triangular, indenting block (Tapponier et al., 1981b) which undergoes little internal deformation but causes block rotation and deformation in the regions surrounding it.

The age of collision has been more accurately defined by later work. Besse et al. (1984) sampled early Cenozoic limestones deposited on the shallow northern margin of India and found that they had been laid down between anomalies 26 and 25 giving them an age of 57±1Ma. They acquired a primary magnetisation at this time showing a palaeolatitiude of 2.5°S±4°. A re-magnetisation is observed at latitude 6°N±5° and when the apparent polar wandering path (APWP) for India intersects this latitude is taken as the time of collision i.e. 50Ma but with errors this could be as late as 36Ma. Patriat and Achache (1984) state that collision started at anomaly 22 (50Ma) but the change in motion of India occurred at anomaly 20 (44Ma). This 6Ma gap corresponds to the subduction of approx. 400km of Indian crust until the opposing buoyancy force was too great and the subduction was blocked. However, palaeomagnetic data shows that there has been over 2600±900km of shortening between India and Tibet. Patriat and Achache (op.cit.) account for several hundred more kilometres of shortening by continental thrusting, internal deformation and lateral

slip between 44-37Ma (anomalies 20-13). They invoke block rotation and lateral extrusion from anomaly 13 as the most efficient method of shortening, taking up some 1500km. Prior to anomaly 22 Patriat and Achache (op.cit.) show that the rate of northward movement of India varied between 15-25cm/y and this then decreased to a stable value of around 4cm/y after anomaly 13. Blocks such as Indo-China and S. China have rotated clockwise due to the pushing northwards of Tibet, and E-W extrusion is along N-S orientated grabens and normal faults.

The nature of the collision and subsequent shortening along intracontinental thrusts means that the other five zones of the Himalayan chain (Gansser, 1964) are separated by major thrust or suture zones. As described above, the KAB consists of subduction related, pre-collisional phases and post-collisional granites. The two zones below which have most relevance to the evolution of the KAB are the Transhimalayan terranes of Kohistan and Ladakh, and the High Himalaya. This zone exhibits inverted metamorphism along the Main Central Thrust zone, and post-collisional leucogranite magmatism, as seen in the Karakoram.

2.2.c: Zone 2; The Transhimalaya.

To the east, this zone lies along the southern margin of the Lhasa block and represents the former Eurasian margin during the subduction of Neo-Tethys. To the west the zone lies between the Shyok Suture Zone (SSZ) and the Main Mantle Thrust (MMT) i.e. the areas of Kohistan and Ladakh separated by the Nanga Parbat Syntaxis. These represent a former island arc (Bard, 1983) off the Eurasian margin of the Karakoram.

In Tibet the Transhimalayan batholith is termed the Gangdese plutonic belt. This belt is comparable to the Andean chain in that it intruded the continent-ocean crust junction of the Eurasian margin and was related to subduction of oceanic crust. There appears to be two main stages of emplacement with the oldest plutons at 110-90Ma (Ar/Ar; Maluski et al., 1985) and the youngest around 60my. The plutons intrude sediments of Palaeozoic to early Tertiary age. To the north is Precambrian gneissic continental basement overlain by Carboniferous to Jurassic sediments covered by lower Cretaceous red beds. To the south these red beds (Takena Formation) show open

folding equivalent to a maximum of around 40% shortening (England and Searle, 1986).

Associated with the younger Gangdese plutons are the Lingzizong calc-alkaline volcanics which unconformably overlie the folded Mesozoic sediments. These have been dated as 60Ma by Maluski et al. (1982) and overlie most of the plutons but are intruded by a few. The large volume of ignimbrites and restriction of the 60Ma volcanic zone to the south points to a steep subduction zone (Coulon et al., 1986). An earlier, broader zone of volcanism is indicated by some basalts to the north, which suggests a shallower dip to the zone from 90-80my. The Lingzizong volcanics may not mark the final subduction phase seen in the Transhimalaya since a peak in volcanism occurred in the Maqiang area between 15-10Ma. This volcanism was potassic and enriched in incompatibles i.e. a post-subduction signature and may be related to either late thermal updoming and tension (Coulon et al., op.cit) or crustal thickening.

In Ladakh the Transhimalayan batholith shows the same two phases of evolution with U-Pb ages of 103Ma (Honegger et al., 1982), 101±2Ma and 60.7±0.4Ma (Scharer et al., 1984). Brookfield and Reynolds (1981) reported a $^{39}Ar/^{40}Ar$ age of 82±6Ma for a syenite cutting the ophiolitic melange and Dras volcanics in the Kargil Thrust which is equivalent to the Indus-Tsangpo Suture Zone (ITSZ). This led to to the conclusion that the suture formed in the Cretaceous, but ophiolites can be emplaced prior to closure (Coward et al., 1986). Marine sediments up to the lower Eocene (50Ma) are found in Ladakh suggesting that the suture closed after 50Ma with the ophiolites being emplaced earlier (see later; Searle, 1986). The Transhimalaya batholith intrudes the Dras volcanic series which represents a Jurassic-Cretaceous island arc (Dietrich et al, 1983) showing that the arc had become attached to the continental margin prior to 100Ma. The volcanics range from basalts to dacites and resemble island arc tholeiites from the present day SW Pacific (Honegger et al., 1982). The Transhimalaya batholith ranges from gabbro through to granite with a predominance of granodiorite. The plutons define a calc-alkaline trend on an AFM diagram with plagioclase, olivine, pyroxene, amphibole and magnetite being fractionating phases. Late leucogranite dykes are enriched in Ba, Sr and Zr with respect to the rest of the batholith (Honegger et al., 1982). Initial Sr isotope ratios are low

(0.7048; Honegger et al., op.cit.) but zircons show an inherited crustal component (Scharer et al., 1984) and isotopic values are heterogeneous. There is a close similarity between the mafic plutons and the Dras volcanics suggesting a similar source, which appears to be mantle lherzolite with a small component of subducted ocean crust (Honegger et al., op.cit.).

In Kohistan the Transhimalayan batholith also intrudes the same island arc sequence (Bard, 1983) but the section is more complete than in Ladakh. Again, the batholith shows the two phases of intrusion. The first phase forms a series of basic to tonalitic deformed plutons with a Rb-Sr age of 102±12Ma (Matum Das; Petterson and Windley, 1985). The second phase cuts early structures and ranges from gabbro to leucogranite with ages from 54-40±6Ma i.e. immediately prior to the main collision (Shirot and Gilgit plutons; Petterson and Windley, op.cit.). Within the early phase of plutonism is a series of low-K gneisses interpreted to be partial melts of the Chalt volcanics (see below; Petterson and Windley, 1986). The other plutonics are envisaged as melts of a mantle wedge enriched in large ion lithophile elements and light rare earths. Variations in acidity are related to fractionation with the leucogranites representing the final, most evolved liquid. Initial Sr isotope ratios are all low (0.7039-0.7044; Petterson and Windley, 1985).

The second phase of plutonism was preceded by the intrusion of a swarm of basic hornblende-plagioclase dykes. This is in contrast to the KAB which is unusual in having no associated basic dykes. After collision swarms of leucogranite dykes giving Rb-Sr ages of 34±14Ma and 29±8Ma were intruded (Petterson and Windley, op.cit.). The low initial Sr isotope ratios of these dykes (0.7042-0.7045) preclude them from having a similar source to the leucogranites of the High Himalaya (see later) but may correlate them with those of the KAB.

The Jijal ultramafic complex represents the deepest part of the Kohistan sequence and lies immediately north of the MMT. It consists of high pressure garnet granulites which give P-T conditions of 700°C and 12-14kb (Jan and Howie, 1981) suggesting that they formed at depth along the suture. These rocks correspond with the Chilas complex which consists of stratiform, layered norites and noritic gabbros metamorphosed to granulite facies. It is thought that these

may represent the sub-arc magma chamber for the first phase plutons (Petterson and Windley, 1986). These two groups are structurally separated by the Kamila amphibolites. Bard (1983) interprets these as relics of the oceanic crust on which the arc was built but Coward et al. (1986) consider them to be highly deformed plutonics, metasediments and volcanics which may be the along strike equivalent of the Dras volcanics or a second, parallel, older arc sequence.

Above the Kohistan batholith and south of the SSZ or Northern Suture are the Chalt volcanics which represent primitive arc tholeiites succeeded by calc-alkaline andesites and rhyolites (Petterson and Windley, 1986). Overlying the volcanics is the Yasin Group of sediments containing Albian-Aptian fossils (Pudsey, 1986). These comprise turbidites, volcaninlastics and deep water limestones probably formed in an intra-arc basin (Coward et al., 1986).

The age of formation of the SSZ in Pakistan can be constrained to around 100-80Ma on the following evidence. Firstly, Cretaceous volcanics and Albian-Aptian sediments are the youngest rocks in the suture (Pudsey, 1986). Secondly, a basic dyke dated at 75Ma (Ar/Ar) cuts deformed volcanic sequences (Petterson and Windley, 1985) and the earliest deformation phase is recognised to be mid-Cretaceous (Coward et al., 1986). The closure of this suture is taken by Coward et al. (1986) to be the cause of the first deformation phase with the main deformation phase being associated with the major collision at c.45Ma. This gave the large south-vergent thrusts which brought deep levels of Kohistan to the surface in a 'pop-up' structure. Later shear movement along the SSZ caused re-orientation of local structures.

Pudsey (1986) has shown that associated with the SSZ is a melange unit (e.g. the Maiun melange in Hunza) which consists of a slaty matrix with exotic blocks of limestone, serpentinite, volcanics, schists and sandstones. The slate is distinct from other units either side of the suture in Asia and Kohistan, and some limestones and conglomerates occur as beds rather than blocks. The preservation of these depositional contacts and lack of strong deformation indicates that the melange is sedimentary rather than tectonic in origin. The blocks can be matched with Kohistan lithologies and few are derived from Asia. Therefore the melange is

interpreted as an olistostrome derived largely from Kohistan in a back-arc environment. Therefore the SSZ represents the closure of a back-arc basin between Kohistan and the Karakoram.

2.2.d: Zone 3; The Indus-Tsangpo Suture Zone (ITSZ).

This suture, which runs the length of the Himalayan chain, represents the junction between the Eurasian and Indian plates, and the former margin of Eurasia along which Neo-Tethys was subducted. In the west it divides into the SSZ and the MMT between which lie the Transhimalayan batholiths of Kohistan and Ladakh. As seen above, in these areas the MMT represents the c.45Ma suture between India and Eurasia. The suture contains belts of ophiolites, high pressure metamorphic rocks, granulites, basic volcanics and molasse (Gansser, 1964).

In Tibet, the Xigaze flysch structurally overlies the Xigaze ophiolite, although most contacts are tectonised. The ophiolite is unusual in that the mafic part of the sequence is devoid of plutonics except for a few cumulates (Nicholas et al., 1981). Diabases and dolerites are rotated and give the appearance of sills rather than sheeted dykes. The mafic section is thin and serpentinised harzburgites are abundant only 5km below the sedimentary interface. This may be the result of truncation of the sequence by thrusting. The ophiolite has an N-type MORB-like chemistry (Nicholas et al., op.cit.) suggesting that it formed at an oceanic spreading ridge rather than in a marginal basin related to subduction (Saunders and Tarney, 1984). It seems likely that the Xigaze ophiolite represents Tethyan ocean crust and is, therefore, probably similar to the ocean crust subducted beneath the Karakoram.

In Zanskar the emplacement of the Spongtang ophiolite represent the first observed deformation phase from 75-60Ma (T1; Searle, 1986). The ophiolite lies 30km south of the suture and rests on allocthonous sediments and melange from the Lamayuru complex within the suture zone. Little geochemical work has been published on this ophiolite and so its tectonic affinity is unknown. Also located within the suture are the Dras volcanics (see earlier) and the oldest rocks are Permian and Triassic exotic blocks of deep water limestone and Triassic basltic volcanics (Searle, 1986). Overlying all this is

Tertiary molasse.

South of the ITSZ, and overthrust in places by klippen from the suture, is the Tethyan sedimentary terrane. These sediments display an epicontinental sequence some 10km thick, ranging from the Cambrian to the Cretaceous, and represent mainly shelf, and shelf-edge, facies deposited on the Indian northern margin (Baud et al., 1984; Gaetani et al., 1983). There are no unconformities and they pass northwards into deep sea sediments deposited from the Triassic to the early Tertiary within the ITSZ. The sequence is intruded by Tertiary leucogranites (see later) as well as the porphyritic granites of lower Palaeozoic age (Debon et al., 1986; Dietrich and Gansser, 1981).

In NW India the Tethyan sediments outcrop along the Zanskar Range. The Palaeozoic Lahoul Supergroup is separated from the Mesozoic Zanskar Supergroup by the Permo-Carboniferous Panjal volcanics (Searle, 1986). These form a sequence of continental tholeiites, alkali basalts and marine tholeiites related to the break-up of Gondwana. Collision caused a major period of southward thrusting (T2; Searle, 1986) which carried the earlier T1 Spontang and Lamayuru thrust sheets 'piggy back' style.

2.2.e: Zone 4; The High Himalaya.

This zone lies south of the Tethyan shelf sequence and north of the major structure of the Main Central Thrust (MCT). It consists of a belt of high-grade metamorphic rocks termed the Cental Crystallines (CC) or Tibetan Slab. It was widely thought that the Tethyan sediments were unconformable on the gneisses but Stocklin (1980) stated that there is some transition between the two, and Baud et al. (1982) suggested a thrust contact. More recent mapping (Burg et al., 1984) has demonstrated a north-dipping, low-angle normal fault zone to be the contact in E. Nepal. In Zanskar the contact lies along the Zanskar Valley and has been shown to be a listric normal fault caused by culmination collapse during and following the uplift of the High Himalaya (Searle, 1986). This fault, the Zanskar Shear Zone (ZSZ), strikes NE-SW, dipping to the north, and has a vertical displacement of c.19km (Herren, 1987).

The CC range from Precambrian through Palaeozoic to Mesozoic in age with biotite gneisses in the Rohtang Pass area giving an age of 581±9Ma (Rb-Sr WR; Mehta, 1977). Gneisses from the Kangmar window in the Tethyan sedimentary zone give a U-Pb age of 562±4Ma (Scharer and Allegre, 1983). These gneisses represent deformed granites and are related to the porphyritic Cambrian granites found along the length of the belt. The rest of the CC is made up of amphibolite facies pelitic and psammitic schists and gneisses with some marbles, amphibolites and orthogneisses. The sequence exhibits divergent isograds with metamorphic grade increasing upwards from the MCT to garnet-sillimanite gneisses and then decreasing again into low-grade metasediments again. Along the northern margin of the CC are a number of Miocene leucogranite plutons and dyke suites associated with the sillimanite-grade metamorphism (see later; Le Fort, 1981).

2.2.f: The MCT and inverted metamorphism.

Following closure of the ITSZ in the Eocene thrusting propogated southwards across the N. Indian plate margin to the High Himalaya and the MCT zone which evolved into an intracontinental shear zone or subduction zone. The timing of this is not certain but leucogranite plutons associated with the MCT are dated as upper Oligocene-Miocene. Within the MCT zone there is a metamorphic inversion with sillimanite-grade rocks overlying staurolite and kyanite-grade rocks. Associated with this metamorphism there are Miocene leucogranites which have been shown to be anatectic melts of the sillimanite-grade rocks (Le Fort, 1981).

A number of models have been proposed to account for the inverted metamorphism such as heat from the intruding leucogranites or thrust imbrication of pre-existing normal metamorphic sequences. However, the leucogranites are unlikely to be the cause because they are intruded to the north of the sequence and impose a secondary, contact metamorphism on the country rocks they intrude (Le Fort et al., 1987). Large amounts of shear heating along the MCT, as modelled for other thrusts by Graham and England (1976), is unlikely to have played a major role due to the wet nature of the underlying sediments and the resultant fluid circulation. A popular model was put forward by Le Fort (1975) where the thrusting speed of the MCT exceeded thermal re-equilibration rates causing recumbent folding of the

isotherms into an S-shape across the thrust.

This mechanism of thrusting and syn-deformational metamorphism is now widely accepted as the cause for inversion and the metamorphic history of the CC has recently been divided into a number of stages (Hodges et al., in press). The P-T-t paths for the sequence show two main metamorphic events. The first occurred between the mid-Eocene and the early Oligocene as a result of subduction of the Indian margin (B- or A-type). This gave a high P and T metamorphism with the base of the sequence being buried to depths in excess of 30km. Following this there was about 10km of uplift through erosion and, possibly, tectonic denudation. In the late Oligocene several kilometres of further burial due to higher thrust imbrications led to a moderate P and high T metamorphism. This was strongest in the upper portion of the Tibetan slab and was intimately associated with the formation of the leucogranite plutons in the early Miocene. After the mid-Miocene, tectonic denudation on N-dipping normal faults led to rapid uplift and prevented re-equilibration of the rocks.

2.2.g: Leucogranites of the High Himalaya.

The exact relationship between anatectic melting and movement on the MCT with its associated metamorphism still remains unclear. The High Himalayan leucogranites have been related geochemically to the melting of the sillimanite-grade rocks of Formation 1 in the Tibetan Slab (e.g. Le Fort, 1981; Vidal et al., 1982; Cuney et al., 1984; Le Fort et al., 1987). The plutons have been dated at 24 and 21.9Ma by U-Pb methods on zircons and monazite which appear to be most reliable since other isotope systems show heterogeneity and long cooling histories (Scharer et al., 1986). These ages correlate the granites with the formation of the MCT. The water-saturated minimum melts have high initial Sr ratios (0.74-0.78) and are chemically depleted in most trace elements (Deniel et al., 1985; Le Fort et al., 1987). All these features are reflective of their metasedimentary source which retains many elements in residual accesory phases such as monazite (Cuney et al., 1984). The chemistry of the granites is discussed in more detail, and compared with the leucogranites of the KAB, in a later chapter.

The melts were relatively immobile and Jaupart and Provost

(1985) suggested that they ponded at the junction between the high-grade gneisses and the Tethyan sediments due to the thermal contrast across this contact. These authors considered that this contrast could also have been the cause of melting by maintaining a high heat flow leading to unusually high temperatures. However, predicted temperatures across the contact are not high enough to give the observed metamorphic break (Hodges et al., in press). One of the favoured models for the leucogranite generation involves the release of fluids from the overthrust Midland Formation sediments fluxing the gneisses which were still hot enough for wet melting (e.g. Le Fort, 1981; Vidal et al., 1982; Searle and Fryer, 1986). This model does not appear to explain why a group of leucogranites in Kangmar to the north give younger ages, when they should have been produced first as thrusting proceeded southwards (Pinet and Jaupart, 1987). However, as thrusting later proceeded southwards from the MCT across the Lesser Himalaya, out-of-sequence breakback thrusting to the north resulted in crustal thickening and elevated temperatures, and this could have been the cause of the late generation of the Kangmar leucogranites (Hodges et al., in press; M. Searle pers. comm.). The spatial restriction of the High Himalayan leucogranite plutons may be related to local, high concentrations of heat producing elements which were necessary to keep the temperature high enough for melting (Pinet and Jaupart, 1987; Hodges et al., in press).

2.2.h: Zone 5; The Lesser Himalaya.

This zone is overthrust by the High Himalaya to the north, and is itself thrust to the south along the Main Boundary Thrust (MBT) which is still active and dates from the Pliocene (Gansser, 1964; Stocklin, 1980). It consists of a thick pile of Proterozoic gneisses, thick Palaeozoic and thin Mesozoic sediments which indicate a shelf origin based on the Indian platform and thickening towards Tethys in the north.

The MCT has brought nappes rooted in the Central Crystallines to overlie the Lesser Himalaya and these are termed the Outer Crystallines (Thakur, 1981). These klippe often consist of Precambrian metasediments and gneisses overlain by Palaeozoic sediments. The porphyritic Mandi granodiorite in the Chail nappe gives a Rb-Sr age of 545±12Ma (Mehta, 1977) whilst the Palung granite

in Nepal gives a U-Pb age of 470±4Ma (Scharer and Allegre, 1983). These ages correspond with those for similar granites found in the High Himalaya and Afghanistan, and all are related to widespread Cambrian plutonism prior to the break-up of Gondwana (Debon et al., 1987a).

2.2.i: Zone 6; Sub-Himalaya or Siwaliks.

This zone is located south of the MBT and marks the front of the Himalayan belt. The Siwaliks represent a molasse basin recording the unroofing history of the Himalaya, and are dominated by detritus from the Central Crystallines where uplift is higher (Windley, 1983). The rocks themselves are gently folded and cut by short displacement thrusts.

2.2.j: Nature and extent of post-collisional underthrusting.

As outlined earlier, deformation and northward movement of India since collision has been accommodated by strike-slip, block rotation and the development of intracontinental thrusts such as the MCT and MBT. Ni and Barazangi (1984) note that the present day earthquake centres are concentrated in a 50km wide zone just south of the MCT. This zone has a curvature relating to a small circle of radius 1650±50km and suggests little change in the geometry of the underthrusting Indian plate. This is supported by the simple bimodal distribution of the fault plane solutions and focal data indicates that the basal fault plane dips at 5-30°±5-15° to the north. The MBT is now the most active structure.

Beneath the High Himalaya the Moho dips at 15-20° suggesting a steepening of the underthrust plate which would account for the greater uplift rates. In Tibet to the north deformation style changes from thrusting to normal faulting. This is related to the increased elevation and crustal thickening which changes the vertical stress component from being the minimum to being the maximum principal stress. The velocities of propogation of Pn and Sn waves beneath Tibet and beneath the Himalayas and Indian shield are comparable suggesting that the underthrust Indian lithosphere reaches as far as the Tibetan Plateau (Barazangi and Ni, 1982). Major discontinuities in the Moho depth beneath Tibet are interpreted as a result of later

strike-slip disruptions on E-W lithospheric fractures such as old sutures (Hirn et al, 1984). That underplating reaches so far north may have implications for the Neogene volcanic belt in Tibet which seems to coincide with a model of 15° rotation of the leading edge of the underthrust plate assuming a pivot point around the Nanga Parbat syntaxis (Bingham and Klootwijk, 1980).

Coward and Butler (1985) demonstrated through balancing and restoring cross-sections that a minimum of 470km shortening has occurred between the MMT and the Pakistani foreland. This was used to suggest that the lower Indian crust had underthrust Eurasia as far north as the Pamirs. However, Treloar et al. (1987) and Searle et al. (in press) suggest that this shortening is accommodated in the lower crust by thickening and thrust stacking. If the Indian crust was thin (15-20km) at its northern margin as suggested by the thickness of its shelf sediments (3-4km; Searle et al., op.cit.) then it need only underthrust Eurasia as far as the Karakoram.

2.3: Possible tectonic models for the magmatic evolution of the NW Himalaya.

Figure 2.3 is a summary of age dates from the Karakoram, Kohistan and Ladakh after Searle et al. (in press). Prior to the publication of many of these dates, models for the evolution of the area involved the MMT forming before the SSZ through the collision of India and Kohistan/Ladakh (e.g. Reynolds and Brookfield, 1983; Bard, 1983). This was based on the dating of the ophiolitic melange as pre-80Ma, but as already mentioned, this may reflect the age of emplacement during initial thrusting and not necessarily date closure. Such a model also required the continual switching of subduction direction to explain the similar ages given by the Kohistan and Karakoram batholiths.

Recent work (e.g. Petterson and Windley, 1985; Coward et al., 1986; Pudsey, 1986) has shown that the SSZ closed sometime between 100-80Ma. The MMT marks the position of the subduction zone beneath Kohistan and has a long history as shown by associated blueschists on its hanging wall with an age of 84±1.7Ma (K-Ar Musc; Shams, 1980). However, the suture zone later acted as a major thrust zone during collision between India and Eurasia around 45Ma and is the analogue

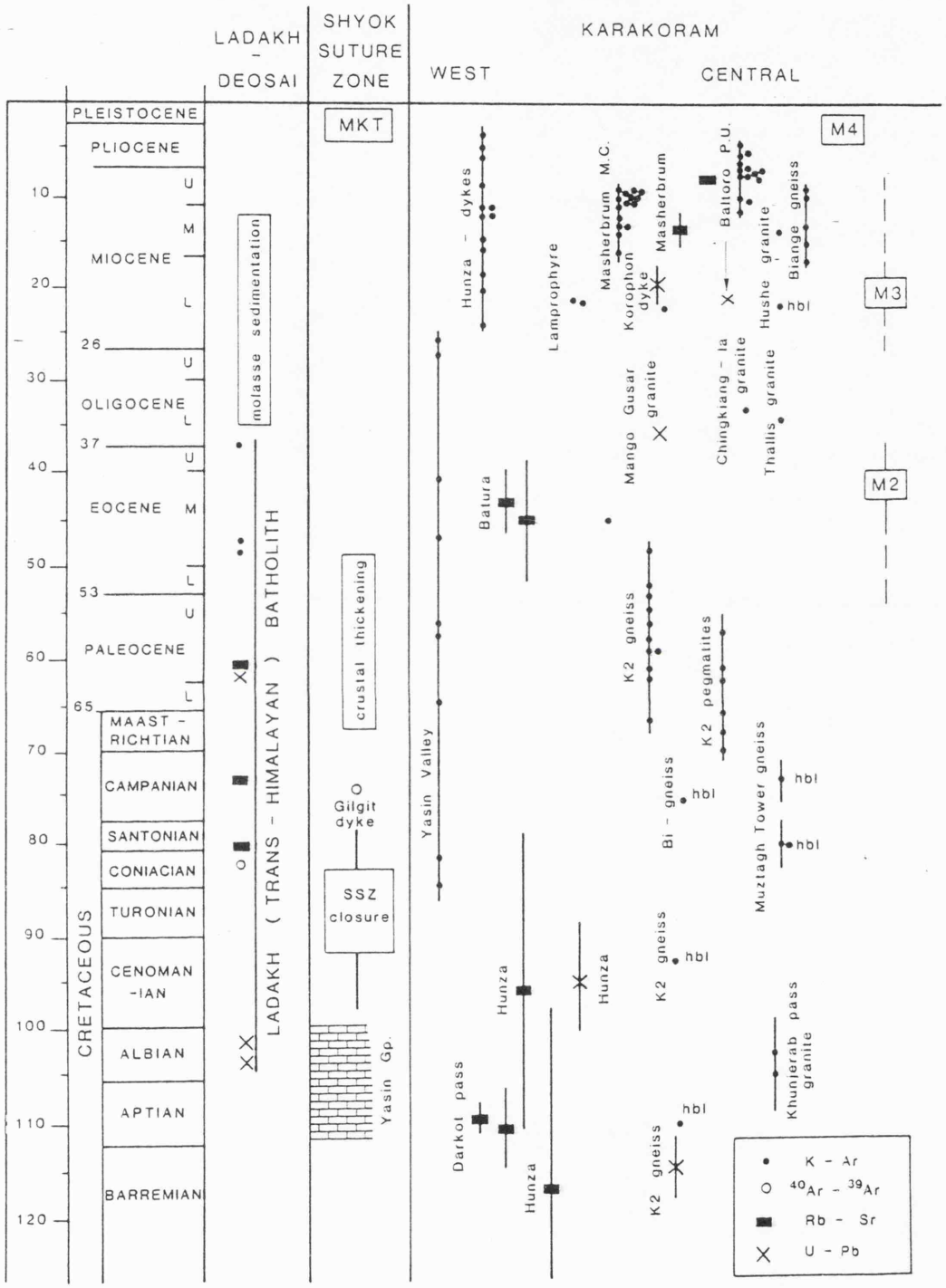

Figure 2.3: Compilation of Cretaceous-Tertiary radiometric ages for the Ladakh (Kohistan) and Karakoram areas from Searle et al. (in press). Other sources of data: Debon et al. (1986; 1987b); Honegger et al. (1982); Le Fort et al. (1983); Parrish and Tirrul (in press); Petterson and Windley (1985); Coward et al. (1986).

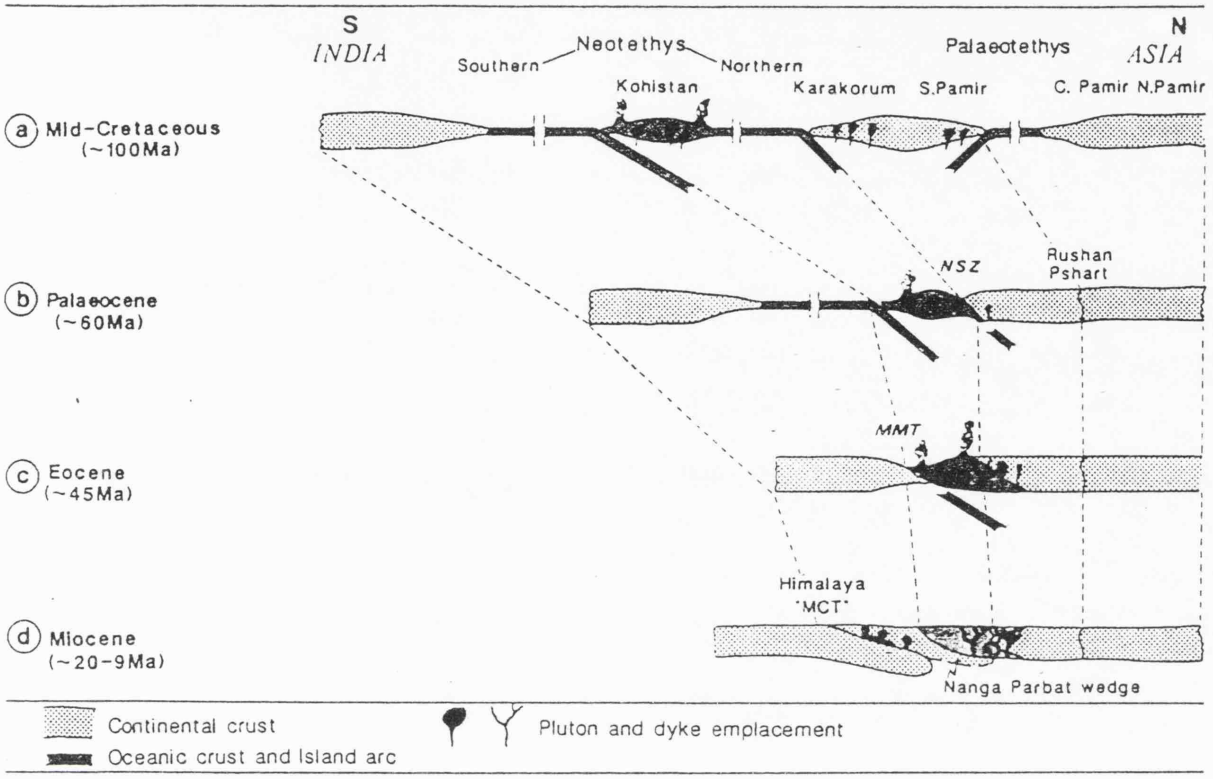

(a)

(b)

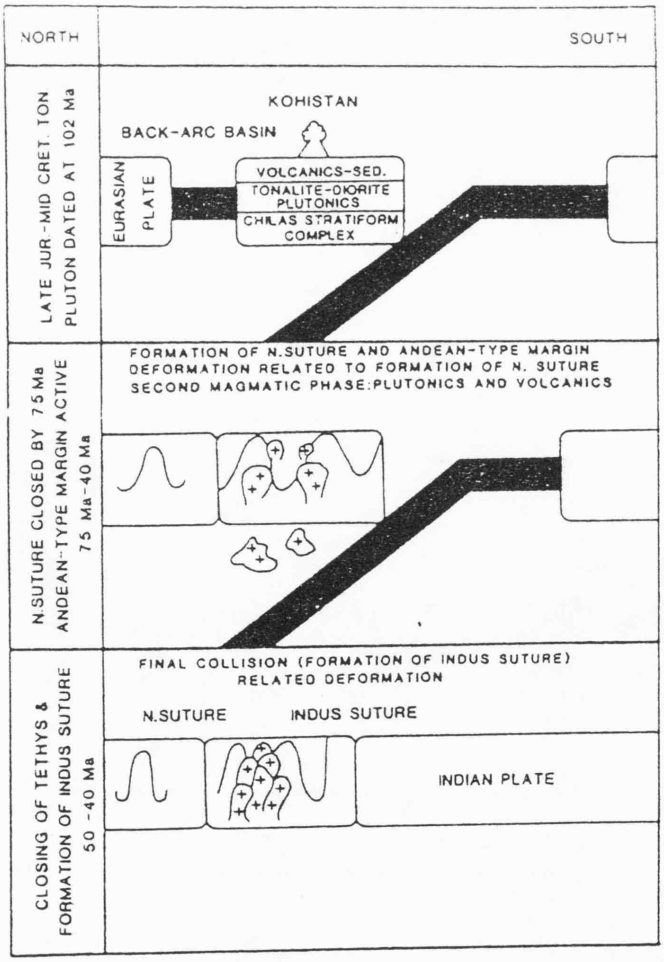

Figure 2.4: Two tectonic models for the post-Jurassic evolution of the Karakoram. Model (a) is from Debon et al.(1987b); model (b) is from Petterson and Windley (1985). See text for discussion.

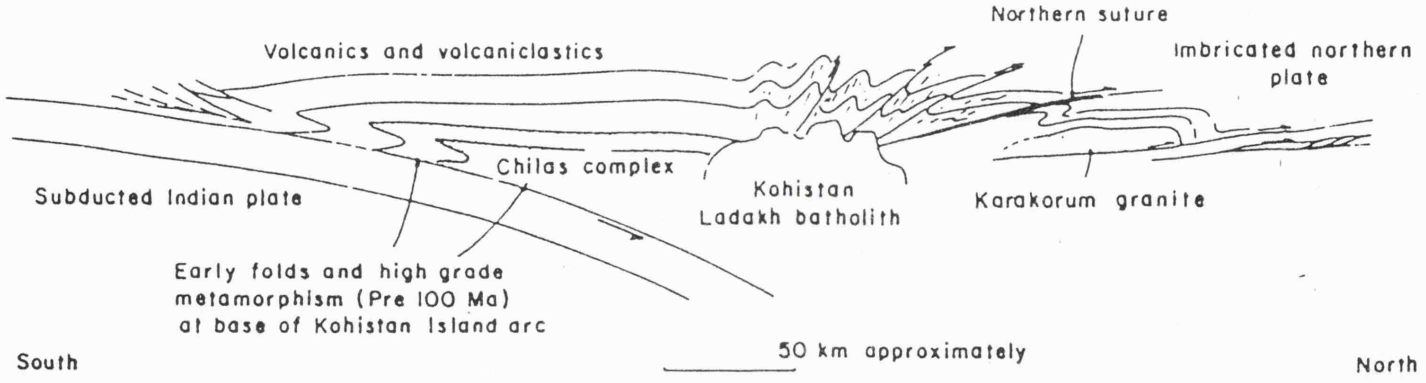

Suggested cross-section through Kohistan in Late Cretaceous times, after the closure of the Northern Suture.

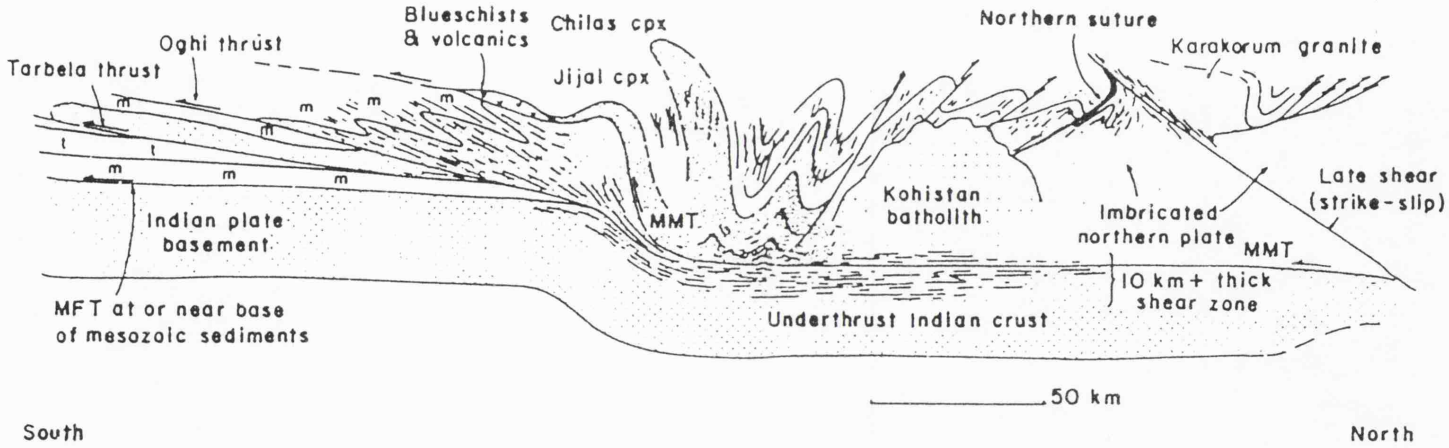

Section through Kohistan after the closure of the Southern Suture. m and t represent the Mesozoic and Tertiary sediments, respectively. The thrust structures on the Indian Plate are highly oversimplified.

Figure 2.5: Model for the structural evolution of Kohistan from Coward et al. (1986). Northern suture = MKT and Oghi thrust = MCT in text.

of the ITSZ in Tibet. Two recent models have been proposed to explain the magmatic evolution of the area in the light of this evidence (fig. 2.4; Petterson and Windley, 1985; Debon et al., 1987b). Both models have Kohistan as an island arc docking onto the Karakoram at around 80Ma, and then continued subduction giving the younger plutons in the Transhimalayan batholith. Collision at 45Ma was followed by the generation of post-collisional leucogranites. The two models differ in their interpretation of the relationship between Kohistan and the Karakoram prior to 80Ma. The Debon et al. (1987b) model has two northward subduction zones to explain the contemporaneous plutonism in both terranes. However, Pudsey (1986) has shown that the SSZ probably represents closure of a back-arc basin. The Petterson and Windley (1985) model shows this, and is preferred here.

Structurally, minor deformation may have been experienced in the Karakoram during the formation of the SSZ, whilst a stronger deformation event is seen in Kohistan. The main collision around 45Ma caused the main deformation phase and high-grade Barrovian-type metamorphism in the Karakoram. These high-grade rocks were brought to the surface along southward verging thrusts (e.g. reactivation of the SSZ to give the the MKT), which also affected Kohistan (fig. 2.5 from Coward et al., 1986). Large-scale backthrusting some time after collision also occurred in some areas (e.g. T3 <15Ma in Zanskar; Searle, 1986). Culmination collapse has led to the juxtaposition of upper and mid-crustal rocks along N-dipping normal faults (the Zanskar Valley, Herren, 1987; the KBL?, Rex et al., in press). One problem which is still apparent is that considering Kohistan lay between India and the Karakoram and was heavily deformed during collision, why is the major c.45Ma metamorphic event seen in the Karakoram not observed in Kohistan?

CHAPTER THREE: Field relationships in the Hunza Valley, N. Pakistan; description and interpretation.

3.1: Introduction

The Hunza Valley lies in northern Pakistan just south of the Chinese border, roughly between 36° and 36.5°N and 74° and 75°E. The area of study is the middle third of the valley from Chalt up to Pasu and Shimshal. Geologically this is part of the southern margin of the Eurasian Craton and lies to the north of the Shyok Suture passing through Chalt. South of this is the Chalt Volcanic group of the Kohistan sequence which represents a deformed island arc sequence uplifted when Pakistan/India collided with Eurasia approx. 45ma ago (figs. 3.1 & 3.2). Chapter 2 outlined how the Karakoram Axial Batholith (KAB) represents the magmatic evolution of the Eurasian margin since the Jurassic/Cretaceous. The Hunza unit of the KAB runs E-W across the valley between Serrat and Gulmit giving it a width of about 15km, and because it is composed of a number of different plutonic episodes it is referred to hereafter as the Hunza Plutonic Complex (HPC). This chapter is a summary of the field observations made during five months in the Hunza Valley with details of previous work in the area and interpretations where possible. The maps provided are based on Landsat 2 satellite photographs with localities and heights from the US Army U502 map series, sheets NS14 and NS15.

3.2: Country rock north of the plutonic complex

A large succession of slates and limestones, together with a few minor intrusions, are exposed all the way up the upper Hunza Valley as far as the Khunjerab Pluton, just south of the Khunjerab Pass and 120km north of the KAB. A large amount of work was done in this area by Desio and Martina (1972) from Baltit up to the Chinese border resulting in the sequence given below:

1. Axial batholith - south
2. Pasu Slates |
3. Gujhal Dolomite |
4. Gircha Formation |
5. Kilik Formation |
6. Misgar Slates - north

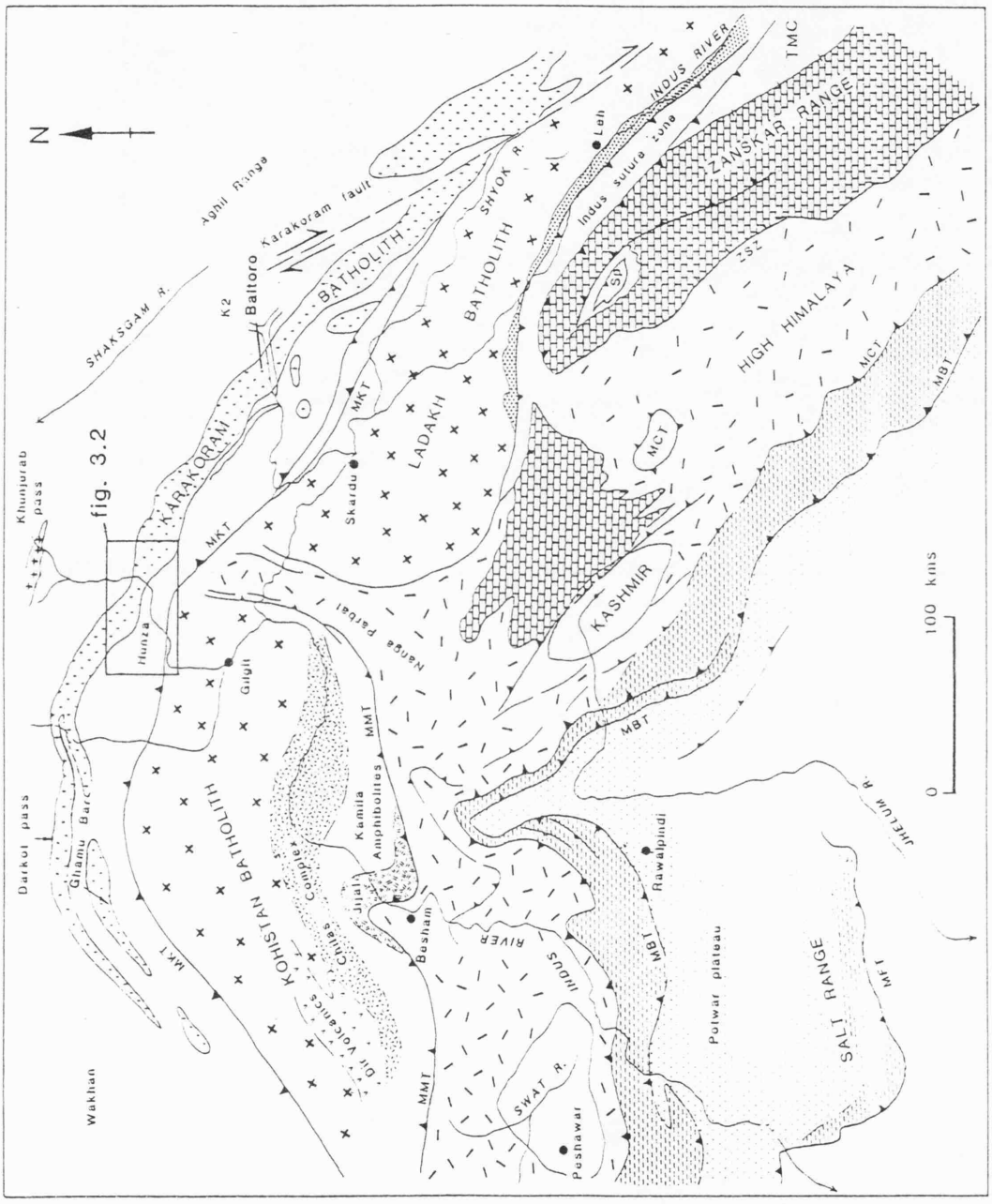

Figure 3.1: Geological sketch map of the western Himalaya and the Karakoram from Searle et al.(in press). MKT, Main Karakoram Thrust or Shyok Suture Zone; MBT, Main Boundary Thrust; MMT, Main Mantle Thrust; ZSZ, Zanskar Shear Zone; Karakoram Axial Batholith is shown in small crosses. Rest of features are discussed in chapter 2 (refer to fig. 2.2). Box shows area covered by figure 3.2.

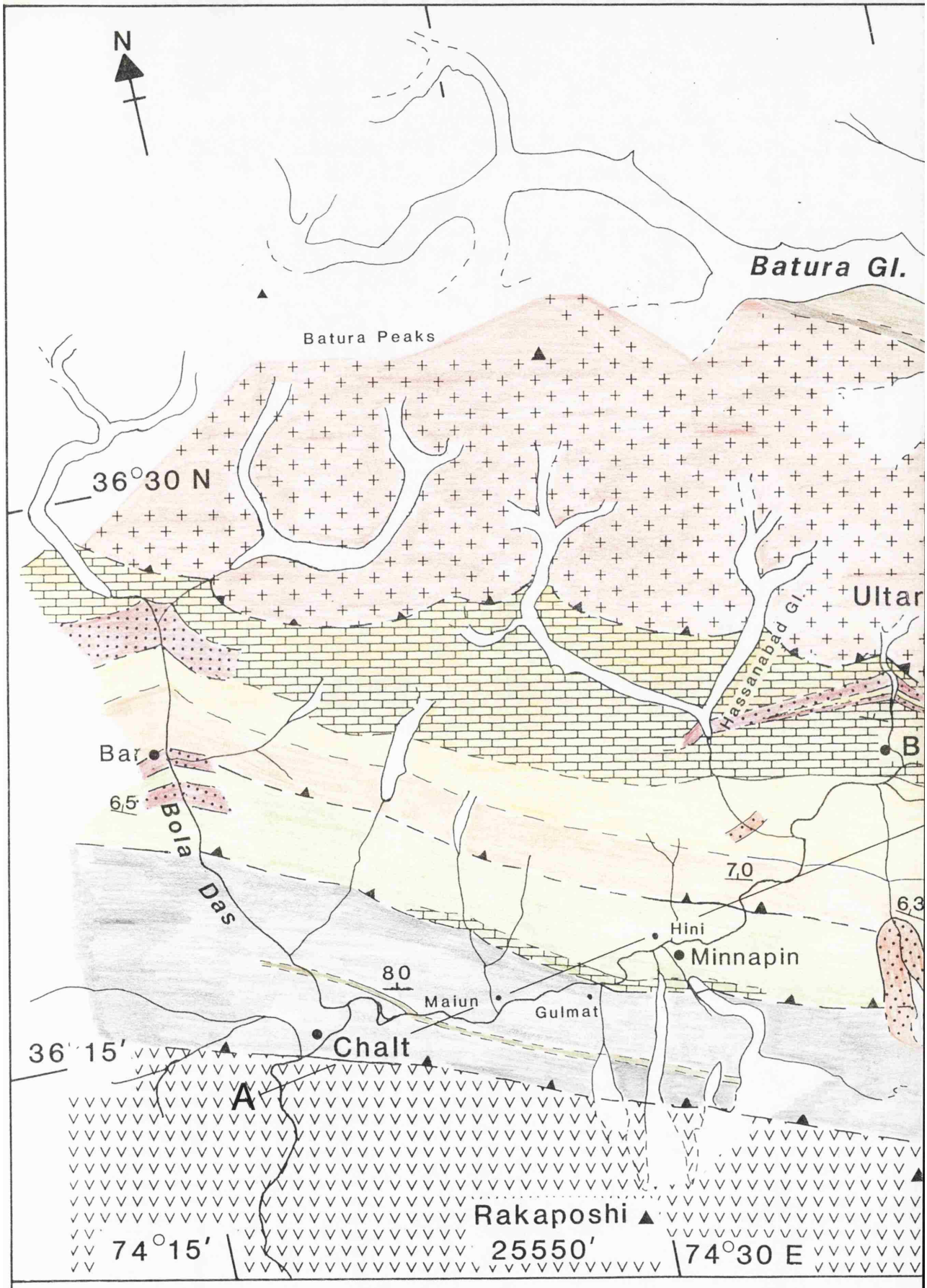

Figure 3.2: Geological map of the middle Hunza Valley and s

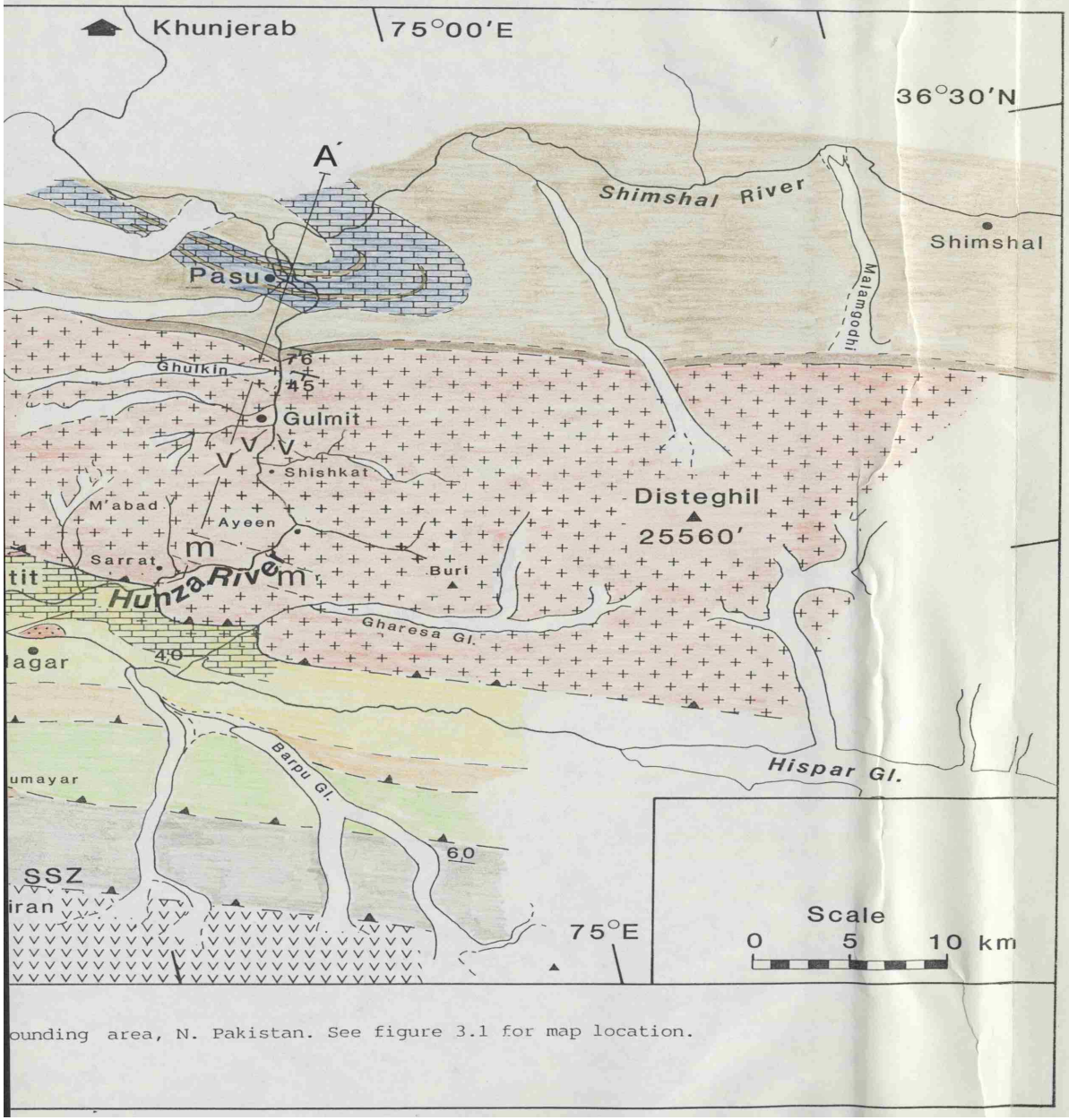

ounding area, N. Pakistan. See figure 3.1 for map location.

	Pasu Slates	Pasu
	Pasu Limestone	Group
	Chiastolite slate (contact aureole)	
	Hunza Plutonic Complex (KAB)	
m	Mixing Zone	HPC
V–V–	Northern Limit of Dykes	
	Granodiorite intrusion outside HPC	
	Leucogranite intrusion outside HPC	
	Sillimanite-grade zone (marble dominated)	
	Sillimanite-grade zone (schist dominated)	Hunza
	Kyanite-grade zone	Group
	Staurolite-grade zone	
	Chalt Group phyllites	Chalt
	Chalt Melange	Group
	Chalt Volcanics (Kohistan Arc)	

Thrust (triangles on upthrown side)

Geological contact (observed)

Geological contact (inferred)

Foliation dip and strike

SSZ = Shyok Suture Zone

The whole sequence north of the complex is collectively called the 'Darkot Group' correlating it with the sequence seen in the Yasin Valley further to the west. No ages have been given to the Pasu and Gujhal rocks because they are unfossiliferous. However, the Gircha Formation gives lower Permian ages and, despite a tectonic contact with the Gujhal Dolomite, it is likely that the Pasu Slates and the dolomite are also Palaeozoic, possibly Carboniferous.

As far north as the Batura Glacier only the Pasu Slates and the Gujhal Dolomite, here collectively referred to as the Pasu Group, are encountered. Scattered boulders of the Sost granite, which outcrops further north, and is characterized by large, pink, porphyrytic crystals of potassic feldspar, are also found.

The Pasu Slates are, for the most part, black and argillaceous with occaisional more arenaceous, sandy or calcareous beds. They are dominated by quartz, biotite, muscovite, chlorite and opaque minerals aligned parallel to the foliation. Small quartz and opaque porphyroblasts show rotation and recrystallisation shadows. Where a crenulation cleavage is developed (section 3.6) there is development of P and Q zones with the P zones being rich in biotite and defining the cleavage and the Q zones containing recrystallised quartz. The original foliation is defined by muscovite and chlorite in places.

Along the northern margin of the HPC there is a 1km contact aureole in which the main metamorphic mineral is chiastolite. The growth of chiastolite is dependent upon the aluminium content of the rock and it follows that the composition of the slates must be quite variable since the sizes of the chiastolite needles vary from bed to bed and some beds do not contain any at all. None of the needles are larger than 1cm. Andalusite/chiastolite indicates a low pressure which would be expected if the batholith is a high level intrusion as is suggested by the rest of the country rocks to the north being relatively unmetamorphosed. The narrow width of the aureole and the lack of baking at the contact suggest a low temperature of intrusion.

Some slates, particularly at the entrance to the Shimshal valley, are rich in iron as shown by the growth of pyrite. In these areas the sandstone layers are either red or green depending upon the oxidation

state of their iron content.

On the road section, halfway between Sesoni and Pasu, where the foliation becomes vertical adjacent to the Pasu Synform (section 3.6) there is a small, amphibole rich intrusion dissimilar to any other igneous rock seen in Hunza. Here the slates are more graphitic and interbedded with a number of grey quartzite and white calcareous bands and the whole zone is shot through by quartz veins which are boudinaged parallel to the foliation.

The Pasu Limestones are homogeneous, recrystallised and dolomitised (Desio and Martina, 1972). The only variation seen is in colour from dark to light, and in grain size due to inhomogeneous recrystallisation. No accessory minerals were observed and, due to the recrystallisation, few fossils have been preserved except for some crinoid stems which cannot be used to date the rocks.

3.3: South of the plutonic complex

The rocks to the south of the KAB or Hunza Plutonic Complex have been given various names in the past. Both Desio and Martina (1972) and Pudsey (1986) prefer to regard the rocks as still part of the Darkot Group on the basis that they may be subdivisible at a later date. Desio and Martina (1972) provided the name 'Dumordu Formation', and in 1979 Desio assigned a Permian-Cretaceous age to the rocks immediately south of the HPC using laterally equivalent, fossiliferous rocks. Tahirkheli (1982) follows Stauffer in using the term 'Baltit Group' for the more northern rocks and 'Chalt Melange' for the southern ones. The Baltit Group is divided into the Ganesh Marble in the north and the Minnapin Formation in the south.

This study prefers to use local names to maintain clarity. The phyllites to the south are referred to as the Chalt Group and not melange since this constitutes only part of the sequence. The higher grade metamorphics to the north are termed the Hunza Group and further subdivision is only possible using metamorphic grade and not by using stratigraphy.

3.3.a: The Hunza Group

Little work has been published on these high-grade rocks rocks immediately to the south of the complex. Okrusch (1976) calculated PT conditions in the sillimanite grade rocks from a ruby (corundum) in the marbles and obtained a temperature of 600-620°C and pressure of 6kbar with 20 mole% of CO_2 in the vapour phase. Broughten et al. (1985) described a series of iso-reaction grads and gave maximum metamorphic conditions of 632°C at 5.5kbar for the metapelites and 669°C for the siliceous dolomites which compare favourably with Okrusch. These P-T estimates place the rocks well into the amphibolite facies. Powell and Vernon (1979) described rotated garnet porphyroblasts which grew during the main metamorphism and record changes in the metamorphic conditions through time. The garnets in the metapelites show rotation of up to 520°.

The Hunza Group, which comprises the amphibolite grade rocks, is bounded to the south by a thrust which runs parallel to the Shyok Suture and separates them from the greenschist grade Chalt Group (fig. 3.2). This thrust runs through Maiun and Gulmat following the southern edge of a carbonate band, and where it was seen above Gulmat it is a brecciated zone about 1m wide and parallel to the main foliation. Prior (submitted) has shown through P-T work that this thrust was after the peak of metamorphism and emplaced hotter rocks over the phyllites of the Chalt Group beneath. This caused the reaction garnet + chlorite + muscovite = biotite + andalusite + quartz + water and generated an andalusite-biotite contact hornfels on the south side. The northern edge of the Hunza Group is defined by the HPC.

Before metamorphism the gneisses, schists and marbles were probably alternating beds of muds, muddy limestones and limestones with some basic igneous layers (plate 3.1), possibly belonging to the same sequence as the Pasu Group to the north. The initial sedimentary sequence may have formed in shallow seas or a basin with water level fluctuations, and some volcanic activity to give the igneous layers. The calc-schists only occur as layers separating the gneisses and schists (metabasites and metapelites) from the marbles indicating there was some sediment mixing during deposition (plate 3.2). The marbles are most heavily concentrated in the north adjacent to the

Plate 3.1

Small scale layering of marbles and metapelitic schists within sillimanite grade rocks.
Vertical scale = 1.5m

Plate 3.2

Calc-schist, interlayered with marble, separating a thick marble unit from a gneiss unit in the Ultar Valley section (see fig. 3.3)

Plate 3.3

General mineral assemblage of a calc-gneiss in the sillimanite-grade zone, with clinopyroxene, feldspar, calcite, feldspar and sphene.

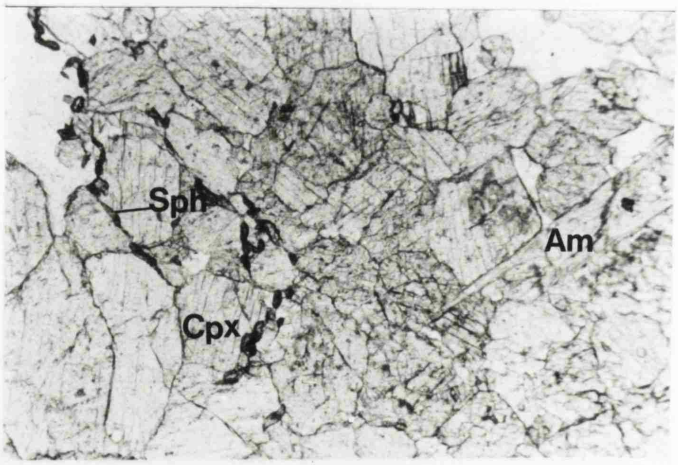

Plate 3.4

Scapolite replacing feldspar in a calc-gneiss collected from near to the HPC contact.

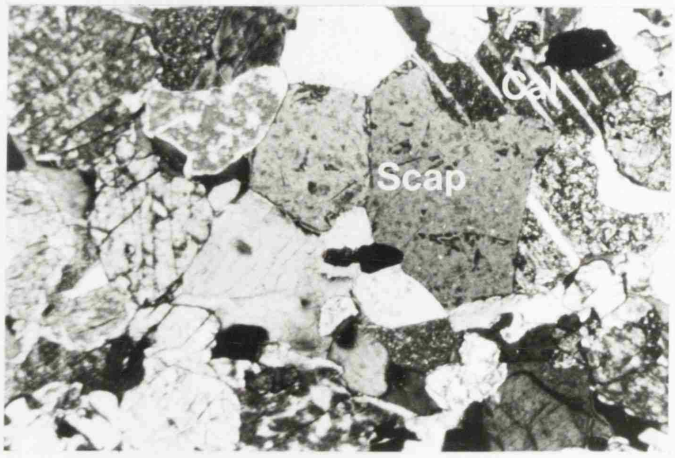

1mm

complex where they form thick units. Elsewhere schists and gneisses are dominant with only thin and discontinuous carbonate layers.

The metamorphic grade increases northwards from staurolite-garnet schists through kyanite-biotite to sillimanite-biotite schists and gneisses. Muscovite is present in the staurolite schists but after this biotite is the dominant mica. These grades are identified only in the pelites, and to some extent psammites, because the purity of the marbles inhibited the growth of recognisable metamorphic assemblages. The calc-schists do show one reaction where the higher grades contain forsterite instead of, or together with, diopside, but the scarcity of these rocks prevents accurate location of the isograd.

The pelitic isograd studied in detail was the staurolite-out isograd because of its easy identification in the field. It is marked by the disappearance of the black/brown, prismatic crystals of staurolite and seems to be parallel to the foliation in three dimensions. This means that metamorphic grade increases with structural height (section 3.6) which could be due to one of the following:

a. The metamorphism is a primary inverted sequence in that it grew in response to inverted isotherms, possibly during 'hot over cold' thrusting.

b. The isograds could be controlled by variations in the pelitic chemistry and not be true iso-reaction grads at all but merely compositional boundaries following bedding planes, which are sub-parallel to the foliation, giving the appearance of inversion.

c. The staurolite-out isograd appears to be marked by a thrust and so the sequence could have been reversed by southward thrusting and may not have originally been inverted.

The evidence supports option c. and Coward et al. (1982) also favours this idea as a means of telescoping the sequence to give the large metamorphic grade increase seen in such a short distance. Prior (submitted) considers the mineralogical changes that are parallel to the foliation are compositionally dependent and are not related to

palaeo-isotherms. However, Prior also considers the increase in metamorphic grade from south to north to be thrust-related and shows that metamorphism and schistosity development were synchronous in the south. The thrusts post-date schistosity development, and represent a period of major southward thrusting which brought hotter, deeper rocks to the surface over the top of cooler, shallower rocks. However, thrusts in the north are syn-metamorphic because on P-T-t paths (England and Richardson, 1977) higher-grade rocks reach their peak metamorphic temperatures later during thermal relaxation. This is also illustrated by the metamorphism starting to post-date the schistosity going northwards, as staurolite porphyroblasts show orientated textures whilst sillimanite crystals are unaligned. Such a model is supported by K-Ar ages younging northwards suggesting rocks in the north were last to cool. This differential uplift must have ceased with peak metamorphism since fission track data (Zeitler, 1985) does not show the same feature. Such rapid uplift would also account for the lack of retrogressive metamorphic assemblages.

The sillimanite grade rocks contain the majority of intrusive dykes and bodies outside of the complex and are probably the most important concerning information on the magmatic evolution of the area. Figure 3.3 shows a typical section through part of this zone in the Ultar Valley above Baltit. There are six main rock types to be considered in this zone:

1. The marbles: these form large homogeneous layers and are composed of entirely recrystallised calcite and/or dolomite. The only impurity commonly seen is a red/brown, calcium rich, mica. Rarely, other impurities e.g. ruby are found and exploited in local mines. During deformation the marbles were most mobile resulting in boudinaged and brecciated layers of more competent gneiss and schist within the marble bands (see plate 3.29, section 3.6). Another feature within the marbles are boudinaged pods rich in clinopyroxene which may have grown as a result of local high silica content in the original carbonate.

2. Calc-gneisses: located between gneiss and marble bands, these are composed of leucocratic gneisses and marbles interlayered on a small scale. The gneisses are rich in pale brown clinopyroxene (diopside), plagioclase feldspar, acicular amphibole (tremolite),

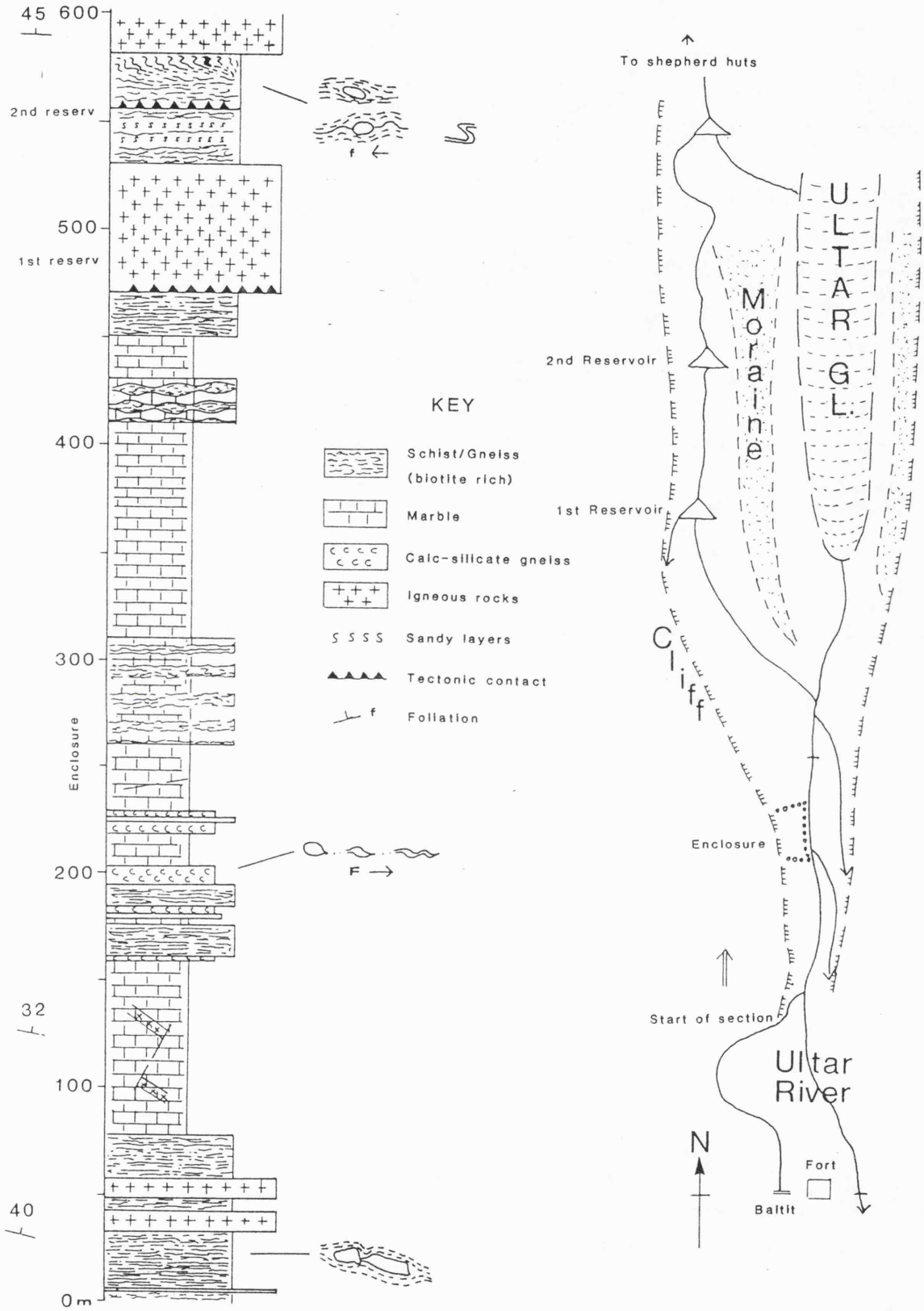

Figure 3.3: Logged section through the sillimanite-grade gneisses, marbles and other lithologies in the lower part of the Ultar Valley above Baltit (see fig. 3.2 for location). Section heights are approximate and the map accompanying the section is not to scale. This illustrates the varied nature of the rock-types in this zone.

garnet, calcite, quartz, a little sphene (plate 3.3), and, nearer to the complex, scapolite replacing feldspar (plate 3.4) and occasional forsterite. The absence of wollastonite indicates a medium pressure and regional metamorphism.

3. Biotite schists and gneisses (metapelites): by far the most abundant rock type south of Baltit, these tend to decrease in dominance towards the complex. They are rich in biotite, plagioclase and quartz with other common minerals being hornblende and garnet. Accessory minerals include opaque phases, apatite, sphene and calcite. Sillimanite occurs as tiny needles often replacing or growing around biotite, and is hard to observe in the field. The feldspar and garnet often form large porphyroblasts between biotite-rich layers parallel to the foliation, and show rotation and recystallisation trails (plate 3.5). Where the rocks are finer grained they are better termed schists, and they often contain pods stretched out along the foliation rich in megacrystic hornblende and quartz.

4. Augen gneisses: which are generally medium-fine grained and rich in biotite (often chloritised) and quartz with bands and rotated augen of feldspar in them (plate 3.6). Muscovite, apatite, sphene, zoisite, secondary calcite, and relic amphibole also are found in small quantities. These probably represent deformed granite sheets (see chapter 4.4) and must have been intruded prior to deformation and so may be related to the first phase of the HPC.

5. Amphibolite gneisses (metabasites): nearer to the HPC, usually occurring as thin sheets sandwiched between thick marble units, are hornblende rich gneisses with other common minerals being plagioclase, zoisite, sphene and apatite with some clinopyroxene and quartz. They contain little or no biotite and often show layering of felsic and mafic portions. These are much more mafic than the biotite gneisses and probably represent metamorphosed basic rocks such as basalts.

6. Igneous intrusions: the sillimanite zone is rich in pegmatite and aplite dykes and larger igneous sheets (plate 3.7), two of which are seen crossing the Ultar Valley parallel to the foliation. These sheets were presumably intruded after the deformation as they are

Plate 3.5

Sillimanite-bearing, biotite schist with the orientated biotites being deflected by the garnet porphyroblast.

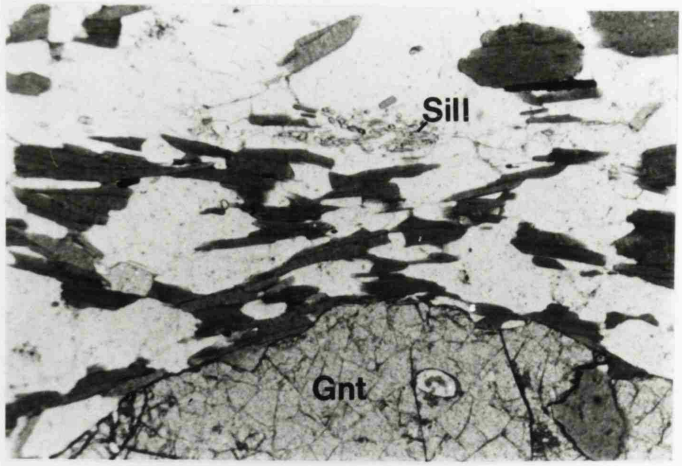

1mm

Plate 3.6

Augen gneiss from the sillimanite-grade zone near Baltit. This represents a deformed granite sheet.

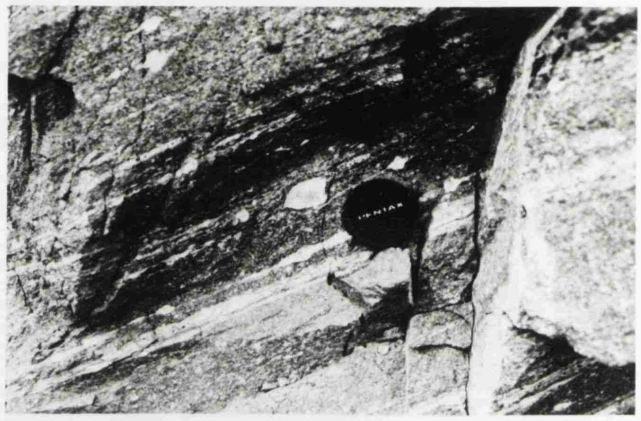

Plate 3.7

View of sillimanite-grade zone in Hassanabad showing numerous igneous intrusions on all scales, and large scale boudinisation of gneissic layers.

Vertical scale = 400m approx.

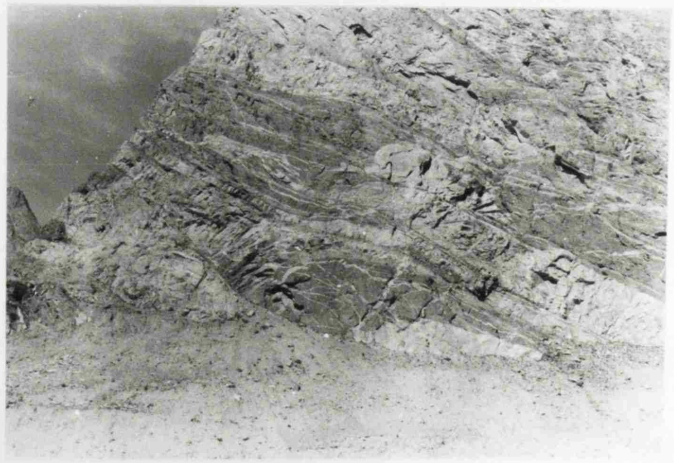

Plate 3.8

P and Q zones developed in a kyanite-bearing schist.

P zones, represented by the micas, are deflected by the feldspar-rich Q zones.

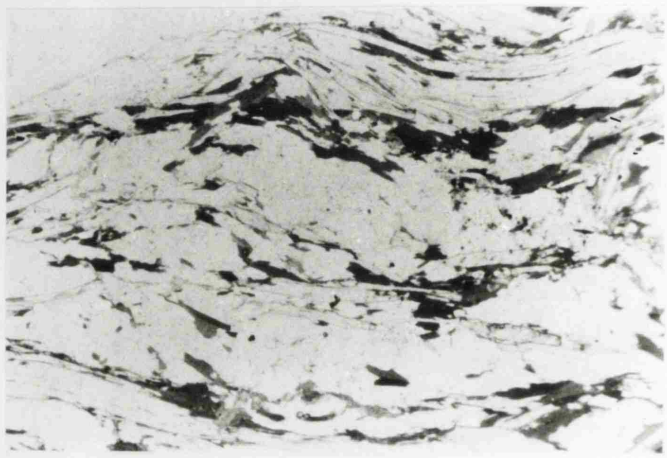

1mm

undeformed and have not developed into augen gneisses. The gneisses adjacent to the dykes do not show any signs of partial melting and do not contain any granitic pods. Whilst the larger sheets are definitely thrust or intruded into the gneisses and are probably related to the complex, the gneisses adjacent to these sheets do show signs of migmatisation. The temperature estimate of around 620°C by Broughten et al. (1985) is too low for conditions to have been suitable for partial melting in Hunza assuming water-undersaturated conditions (see chapter 6.4).

The kyanite-biotite zone is dominated by biotite gneiss containing biotite, plagioclase feldspar, muscovite, opaques, quartz and often garnet. P and Q zones are well developed in places with micas in P zones being wrapped around feldspar augen (plate 3.8). The kyanite occurs as small, regular white crystals (plate 3.9) but again is hard to see amongst the feldspar. Marble layers occur above Hindi but are thin and discontinuous. Within the gneisses there are thin, mica-rich schist layers and also calc-schist layers with a green mica and sporadic garnet. More acidic layers tend to be the richest in kyanite, and the growth of this mineral clearly depends upon the rock type and chemistry. Near the staurolite isograd there is a different type of gneiss which appears recrystallised as it does not show a strong foliation. It contains garnet, hornblende, biotite, plagioclase, quartz, opaques, apatite, and sphene and may have originally been an igneous intrusion.

Below a large thrust are the first staurolite-garnet micaschists. Next to the thrust they are layered with psammitic bands on a centimetre scale and have large garnet porphyroblasts. Going structurally down from the thrust the layers increase in thickness and the staurolite crystals increase in size. The metapelites are rich in muscovite which, with some biotite, defines the foliation and is deflected by large garnet and staurolite porphyroblasts (plate 3.10). These porphyroblasts show rotation up dip (southwards) and contain rotated inclusion trails (plate 3.11). This zone marks the northern limit where muscovite is the dominant mica over biotite. Carbonates reappear in the staurolite zone near the southern contact where they form large continuous bands which can be traced by sight across the valley marking the thrust against the Chalt Group. These carbonates contain garnet in places and are not as

Plate 3.9

Kyanite in a metapelitic two-mica schist halfway between Hindi and Aliabad.

1mm
2

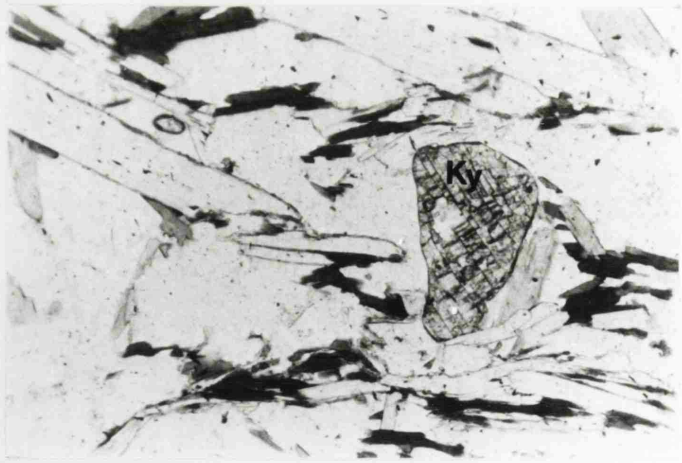

Plate 3.10

Staurolite porphyroblast deflecting the foliation defined by muscovite in a micaschist.

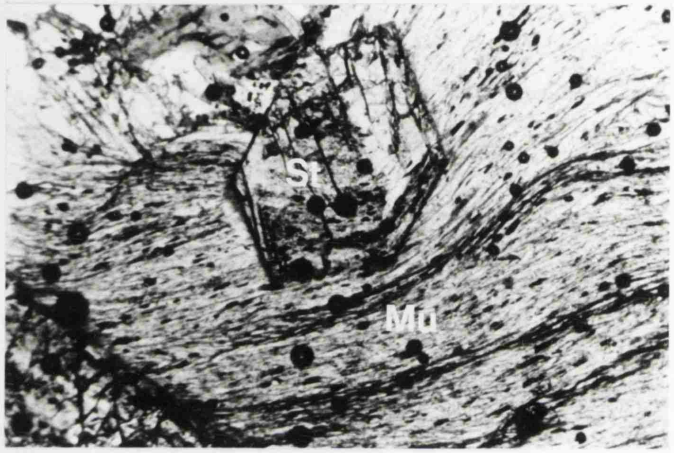

Plate 3.11

Rotated inclusion trails or snowball texture in a garnet (x polars) within a staurolite-garnet micaschist.

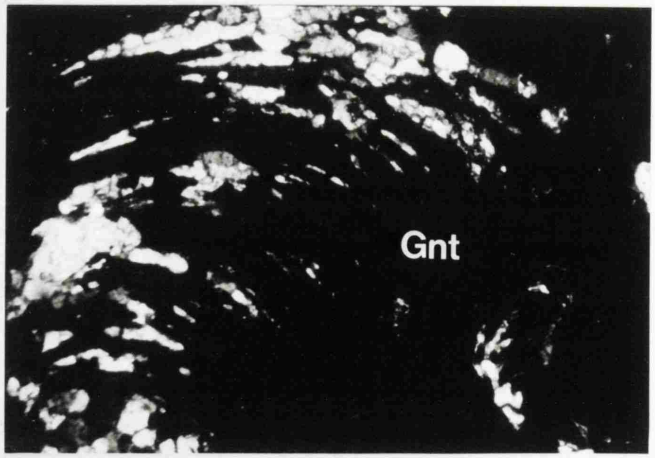

Plate 3.12

Chloritoid porphyoblast showing syn-tectonic growth and deflection of the foliation in a Chalt Group phyllite.

1mm

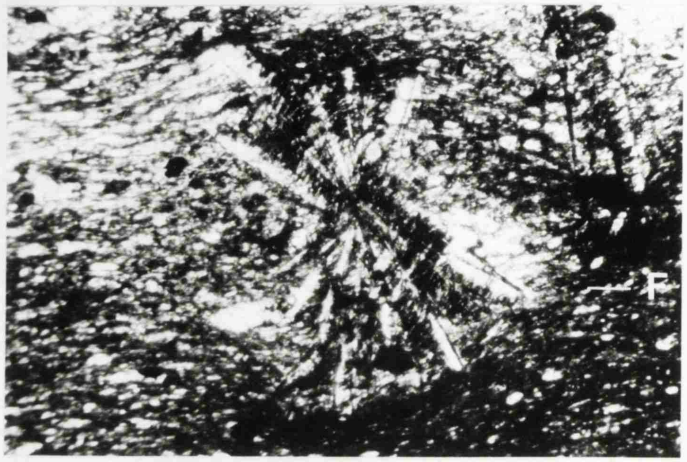

pure as the northern marbles.

The metamorphic sequence is similar to that of the Barrovian zone in Scotland. Staurolite indicates a high Fe/Mg ratio and the preference of staurolite over cordierite and kyanite over andalusite indicates a medium pressure. Possible metapelitic reactions are:

chlorite + garnet => staurolite + biotite

31chloritoid + 5musc. + quartz => 8staurolite + 4biot. + 27water

6staurolite + 4musc. + 7quartz => 31kyanite + 4biot. + 3water

musc. + quartz => K-feldspar + sillimanite + water

biotite + sillimanite + quartz => garnet + K feldspar + water

The last reaction may not have occurred and has certainly not proceeded to completion indicating granulite facies conditions were not reached.

3.3.b: The Chalt Group (phyllite zone)

A lot of work has been done on these rocks immediately north of Chalt by Prior (1987; submitted) and Pudsey (e.g. 1986). They consist of a succession of slates metamorphosed in the greenschist facies, bounded by the Shyok Suture and Chalt Volcanics (Kohistan Arc Sequence) to the south and by the Hunza Group to the north. Adjacent to the Shyok Suture the slates contain chloritoid but no garnet, and are black in colour. Going north garnet appears and there are also some conglomerates near Gulmat which show deformation of their clasts. The matrix of the phyllites is dominated by muscovite and quartz ± biotite, chlorite, ilmenite, plagioclase and graphite. Porphyroblasts, which are syn-tectonic, include chloritoid, biotite, chlorite, ilmenite, and garnet (Prior, 1987). These porphyroblasts show syn-tectonic growth and deflect the foliation (plate 3.12).

Prior (submitted) has divided the Chalt Group into four zones on the basis of their metamorphic mineralogy. These zones roughly follow the main foliation. Zone 4 is only exposed in the Bar Valley and

represents a contact hornfels beneath the thrust which separates the Hunza and Chalt groups.

From south to north:

Zone 1: Ctd-Bi-Chl
Zone 2: Ctd-Gt-Chl
Zone 3: Gt-Chl-Bi
Zone 4: Gt-And-Bi

Also within the Chalt Group is the Chalt or Maiun Melange which, in Hunza, forms a band some 500m wide just north of Chalt. This is composed mainly of greenschists, limestones,red shales and mafic lenses and is related to the formation of the Shyok Suture (Pudsey, 1986). One large serpentinite body is located on the road just opposite the Bar stream junction.

3.4: The Hunza Plutonic Complex

The term Karakoram Axial Batholith (KAB) was first used by Desio (e.g. 1964) and later by Le Fort et al. (1983). The first date on the complex was given by Desio et al. (1964) at 8.6Ma using Rb/Sr data. Zeitler (unpublished) obtained a $^{39}Ar/^{40}Ar$ date from hornblende near Shishkat of 38ma and a K/Ar from biotite of 13Ma. Debon et al. (1987b) got an ill-defined Rb-Sr WR isochron date of 117±22Ma, but when they added a sample from the basic dyke (2.4.d.) this decreased to 96.6Ma with a high initial ratio of 0.7094 (see chapter 4.2). Le Fort et al. (1983) obtained a U/Pb discordia line from zircons which intercepted the concordia line at 95±5Ma and 1500Ma (old lead component) and this is probably the most reliable date so far. They also obtained two pseudo-isochrons using K/Ar of 46.3±1.2Ma from hornblendes and 26±0.3Ma from biotites. The hornblende ages may represent resetting by a thermal event around the collisional period or a long cooling history. Many K/Ar ages on biotites come out at less than 15Ma which probably means there has been at least one recent thermal episode. Ages for the leucogranites range from 16.9 to 4.5Ma (Debon et al., 1987b) which are probably cooling rather than emplacement ages.

3.4.a: The main rock types and relationships

The rocks of the complex can be divided into three main groups or magmatic phases with the later phases intruding the earlier ones.

Group 1: The main plutonic rocks

These make up the bulk of the complex with the other two groups intruding this group, mostly as dykes. There is an increase northwards in acidity going from quartz diorites to granodiorites, and there is a corresponding decrease in mafics with clinopyroxene only present in the south and hornblende becoming less abundant northwards. At Shishkat bridge a mesocratic granodiorite gives way to a zone where the interfingering leucocratic Gulmit granodiorite and Gulmit quartzdiorite predominate (plate 3.13) until Gulmit where the northern granodiorite, similar to the leucocratic granodiorite, takes over. This interfingering is on the scale of wispy layers only cm's wide up to large bodies which can be over 100m wide. Debon et al. (1987b) considers the mafic parts of this sequence to be igneous inclusions (3.4.d.), but they could also be an earlier pluton brecciated by later intrusives. At the northern contact the rock is a leucocratic granodiorite with biotite as its main mafic mineral. Debon et al. (1987b) show through chemical analysis that the rocks also change northwards from being met- to per-aluminous and assume this to be a single magmatic trend. However, this may not be the case as the Gulmit quartzdiorite and granodiorite appear to be separate intrusive phases.

The rocks in the south have recrystallised in response to deformation, whilst the northern granodiorite is undeformed and fairly homogeneous. The general primary assemblage is composed of andesine, biotite, hornblende, some clinopyroxene, alkali feldspar and quartz with accessory apatite, allanite, zircon and sphene. Zoisite is a common secondary alteration product, and garnet was seen in the field. Debon et al. (1987b) have estimated the recrystallisation temperature from garnet-biotite pairs and the pressure from garnet-plagioclase-sillimanite-quartz assemblages to get values of 580-640°C and 5.0±0.5kbar which compare well with estimates for the metamorphism to the south indicating the two events were probably synchronous. The southern rocks contain bands of

Plate 3.13

Interfingering qtz. diorite and granodiorite near Shishkat bridge.

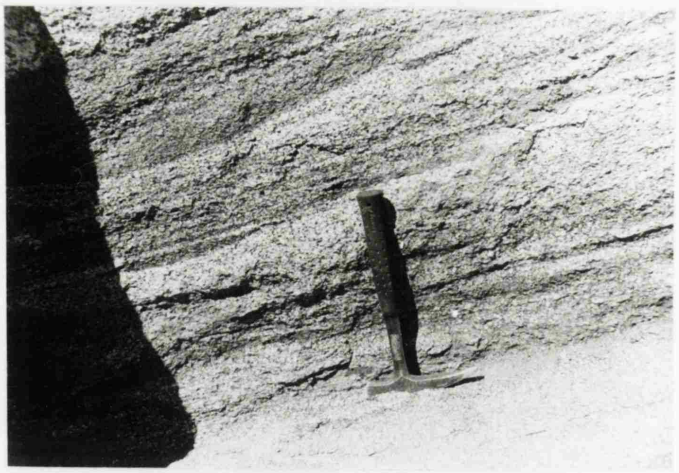

Plate 3.14

Three views of mixing zone features where:

A = Original granodiorite

B = Gneissic layers which can be basic or acidic

C = Megacrystic granodiorite

D = Sweat-type pegmatitic layers.

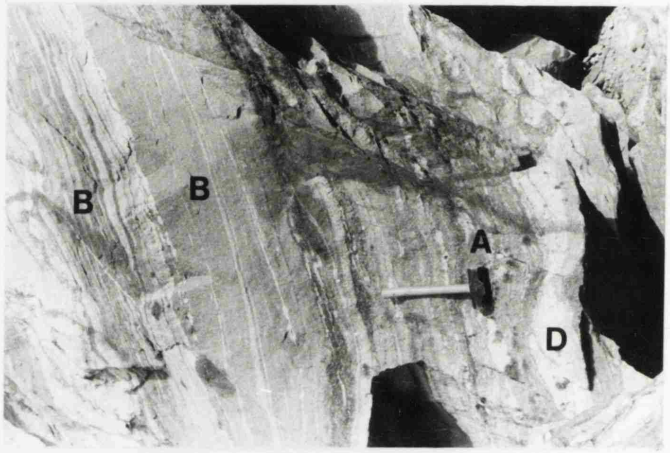

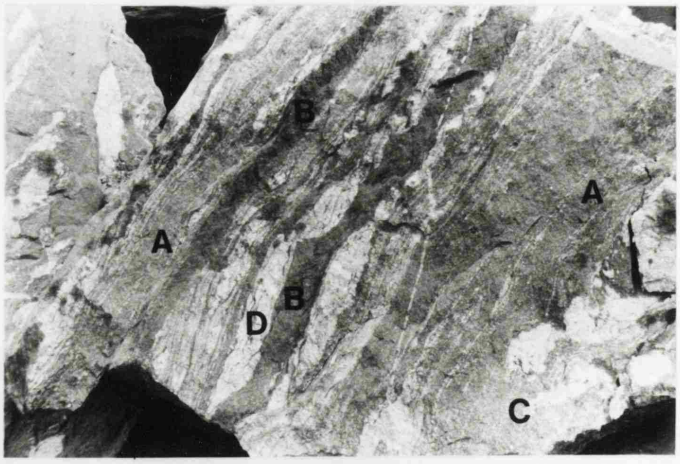

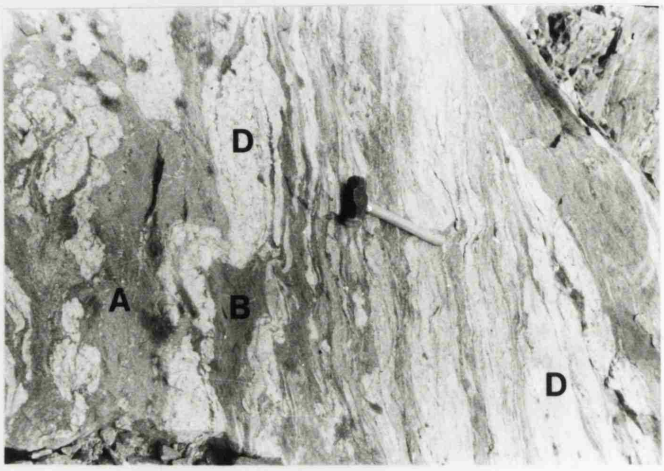

gneissic material caused by shearing and different amounts of recrystallisation within them. They also contain hornblende rich pods which are not seen further north.

The Mixing Zone.

This zone is a conspicuous part of the complex and so deserves separate consideration. It is composed of a complicated and intricate mixture of rock types and is located in the southern part of the complex about 2km from the southern contact. The main zone is about 2km wide but traces of it are seen as far north as Ayeen (fig. 3.2)

Whilst there are many patterns and rock textures observed, most of the features can be resolved down to mixtures of a small number of rock types, hence the term mixing zone (plates 3.14 a,b,c). The zone could be caused by either the mixing of an acid and basic magma, or the result of localized intense heating and migmatisation. The main rock types are:

A: Quartz diorite and granodiorite representing the original plutonic rock. Occasional garnet and green clinopyroxene occur and there are some pegmatitic, sweat-type bands parallel to the foliation.

B: Gneissic layers which can be basic but are usually more mesocratic. The more basic gneiss is rich in leucogranitic sweats, often banded with the mesocratic gneiss and has sharp contacts with type A. The mesocratic gneiss usually has an acidic vein separating it from type A and sometimes has feldspar porphryoblasts in it. Garnet and hornblende are common, but the mineralogical difference between layers is essentially the proportion of mafic phases present.

C: A more acidic, plutonic granodiorite with feldspar megacrysts in it. Often separates types A and B.

D: Sweat-type layers. These usually have irregular boundaries and are often boudinaged. They are always pegmatitic in the basic rocks and are leucogranitic. In the more acidic rocks they are sometimes aplitic but never layered.

E: Late aplite/pegmatites cut and disrupt all the above types and are considered to be part of group 3 (see later).

It could be that type A has undergone migmatisation to give types B and D as palaeosome and leucosome with type C being a secondary or intermediate feature, or the sequence may have resulted from the mixing of two magmas. The structure on a small scale is very complex as all the rocks are intricately folded together, and this could be a magmatic or ductile deformation feature. The whole zone is affected by the main foliation with good rotation structures.

Further north the features gradually decrease with small leucocratic layers or sweats being the result of local deformation and recrystallisation.

Group 2: The Aplitic Sheets.

This group appears to be related to the mixing zone. No sheets are seen in the zone but either side of it they decrease in abundance away from it and dip back into it. The sheets strike N-S and so they dip E to the west of the zone and W in the east.

The sheets are composed of fine-medium grained granodiorite/ monzogranite with biotite as the main mafic mineral, and also a little muscovite and opaques. They are usually tens of metres wide and often have pegmatitic rims rich in garnet and muscovite, sometimes layered with thin aplite bands. The sheets are intrusive and have large xenoliths of host, group one rocks in them. Whilst the sheets cut the foliation and the dykes parallel to it, they are in turn cut by later leucogranitic aplite/pegmatite dykes (plate 3.15). There are two generations of material within the sheets, the earlier being slightly more mesocratic than the later. Tourmaline is a secondary feature forming radiating patterns on 060° fracture planes indicating a secondary fluid origin.

Group 3: The Leucogranite Dykes.

There are two main sets of these, both having pegmatite, aplite and layered dykes and both composed of monzogranites and leucogranites, with the later set slightly more evolved. The

Plate 3.15

Large, group 2 aplite sheet cutting the main HPC foliation and being cut by later leucogranite dykes.

Scale = 5m across.

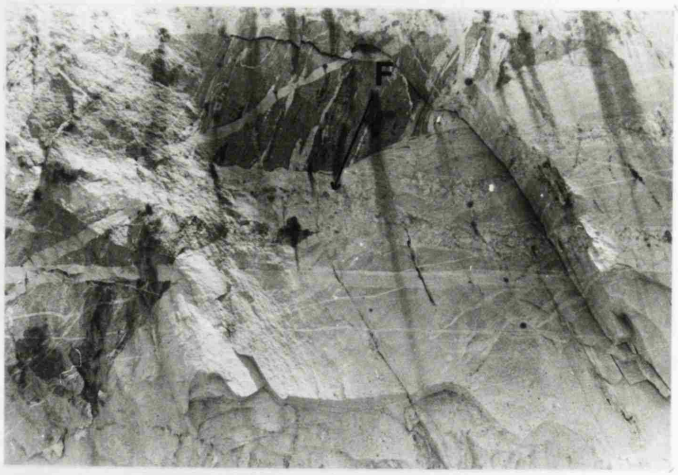

Plate 3.16

Leucogranite pegmatite showing mineral zonation with biotite-rich margins and muscovite-rich centres with stringers of small garnets (near Gulmit).

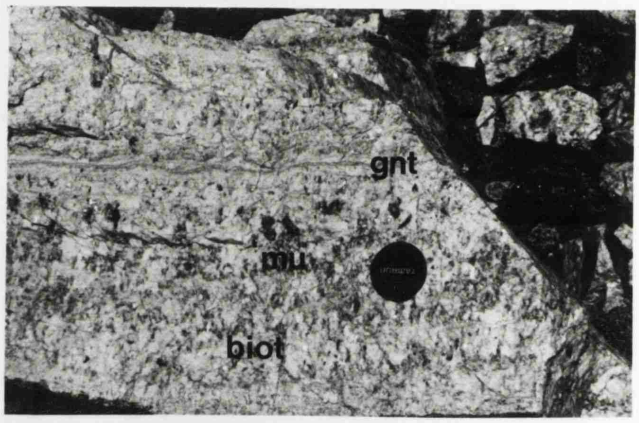

Plate 3.17

Anastomosing network of leucogranitic dykes intruding the first phase of the HPC in Gharesa.

Vertical scale = 200m

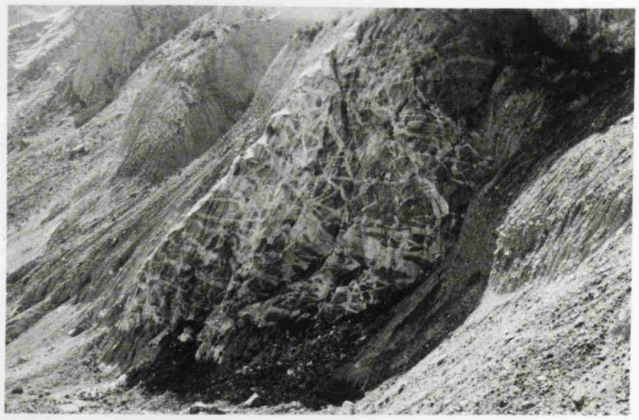

Plate 3.18

Parallel intrusion of leucogranite dykes trending 030 near to the limit of deformation in the HPC at Shishkat bridge. Road for scale = 10m wide.

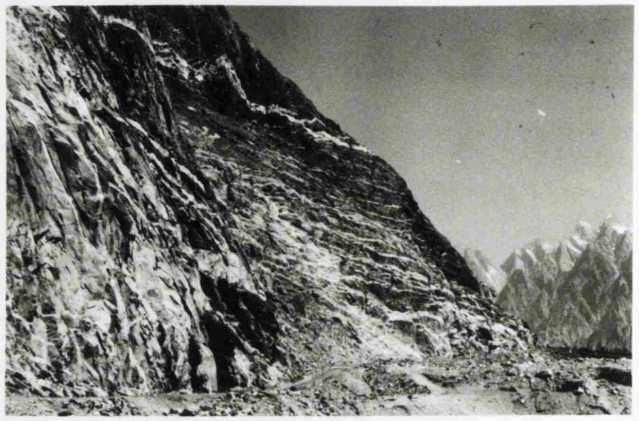

pegmatites tend to have garnet and muscovite-rich centres and biotite-rich rims (plate 3.16) but some only contain biotite. Tourmaline is rare and the only other visible accessory mineral.

The earlier dykes are generally parallel to the foliation which means they strike E-W and dip south in the north and vice versa. They are smaller than the later set but occur throughout the complex. They are cut by later dykes and boss-like pegmatites may also fit in this group.

The later group tend to be larger, more continuous and cut all other structures including the southern contact. However, they are only present in the deformed part of the complex and die out just south of Gulmit. They often show layered structures and form great swarms, making up to 40% of the batholith by volume and showing more than one generation. In the south the swarms are anastamosing (plate 3.17) but to the north around Shishkat they trend towards parallel sheets with a general strike of 030° dipping gently to the northwest (plate 3.18). Despite the cross-cutting relationships seen, the fact that all the dykes post-date the deformation suggests that they are roughly contemporaneous and belong to the same magmatic phase.

Magmatic evolution.

There are three intrusive phases in the HPC represented by the three groups. Group 1 rocks form the main plutonic phase and are calc-alkaline and presumably subduction related. Group 3 dykes seem to represent later crustal melts, with group 2 being ambiguous in origin.

The problem with the migmatisation model for the mixing zone is its localisation as it would be expected that migmatisation would be centred on the zone of greatest deformation and metamorphism i.e. around the southern contact. This could be explained, however, by the zone being generated by heat from the intruding group 2 magmas, or the zone being centred on a later, post-metamorphic, high-level brittle thrust. The two magma mixing model may be preferable as there are no such constraints on where the second magma would intrude the complex. However, the gneissic rocks are not so readily explained by this model, but could be due to deformation within the zone.

3.4.b: The northern contact

Desio and Martina (1972) state that the complex has a tectonic contact dipping south against the Pasu Group, whilst Debon et al. (1987b) say that it is intrusive dipping steeply NE parallel to the slate foliation.

The contact was examined across the Hunza River from Ghulkin, and on a ridge above Boreet Lake. In both places it was intrusive and parallel to the regional foliation of the slates. However, this makes it vertical or steeply south dipping and not NE as Debon et al. (op.cit.) stated. In Hunza it strikes 110° and then bends gently north to strike 135° above Boreet. The contact was also observed from a distance passing across the top of the Pasu Glacier towards Batura, and across the top of the Malamgodhi Glacier in Shimshal going east towards Kurdopin Pass and Snowlake allowing it to be confidently defined on the sketch map (fig. 3.2).

At the contact the leucocratic granodiorite is the dominant plutonic rock. It does not show an appreciable decrease in grainsize towards the contact again indicating a cool emplacement temperature. Whilst there are no veins coming off the complex into the slates, there are rafts of slates incorporated into the granodiorite next to the contact. These rafts can be quite large and often show a foliation still parallel to the main regional foliation and do not show any alteration except for chiastolite growth in places. A stoping mechanism is favoured for removing these rafts from the wall into the magma, but this is not suggested as a general mechanism for emplacement. A narrow contact aureole of andalusite-bearing slate suggests that the pluton was emplaced at a fairly high level and was relatively cool.

3.4.c: The southern contact

Debon et al. (1987b) state the southern contact dips at around 55° to the NE but do not say that it is a thrust. The contact was examined in several places and only in Ultar was it not clearly a thrust.

The contact is best exposed below Sarrat (fig. 3.2, plate 3.19). Here there is a thick sequence of marbles leading up to the thrust which is parallel to the foliation dipping 40°N striking 080°. Just before the contact is a thin calc-gneiss layer and then 20cm of garnet-rich gneiss. A metre-thick sheared gneiss also rich in garnet marks the thrust zone, and then the quartz diorite of the complex above is rich in feldspar bands boudinaged parallel to the thrust (plate 3.20). These bands decrease in abundance away from the contact and have hornblende rich patches associated with them. There are also some secondary green-weathering porphyroblasts which seem to be characteristic of the contact quartz diorite since they are also seen in Ultar.

The contacts in Mohammedabad and along the road are comparable. The thrust is not exposed along the road but there is a thick sequence of marbles and then there is the quartz diorite with many boudinaged feldspar bands and hornblende rich pods. There are some aplites parallel to the foliation and later, layered aplite/ pegmatites cutting the foliation. In Mohammedabad the marbles and thin calc-gneiss layer are present, but there is a thicker gneiss layer before the banded quartz diorite. There is also a fine grained margin to the diorite and the gneiss is not as sheared next to it, with a more sheared area about 50cm further down the sequence. This may represent some original contact material truncated by the thrust.

A common feature of the Mohammedabad and road exposures is that both have a wedge or sheet of gneiss about 30m wide in the complex about 50-100m back from the contact. In Mohammedabad both the contacts of the sheet are thrusts, but on the road only the upper contact is an obvious thrust and the lower is ill-defined. The quartz diorite above the sheet is again rich in boudinaged feldspar bands. The bounding thrusts are parallel to the regional foliation so the sheet was presumably emplaced during the major deformation episode.

The contact was also seen in detail in Gharesa where it showed the same features as the road exposure. It was observed in less detail in Hassanabad and the Bar Valley, but in both places it was parallel to the foliation and had a sequence of marbles leading up to it. It was followed up the Hispar Valley, where it is inaccessible, using binoculars so that its position could be further constrained on

Plate 3.19

Thrust contact between the southern margin of the HPC and sillimanite grade marbles and gneisses near Sarrat.
RH vertical scale = 3m

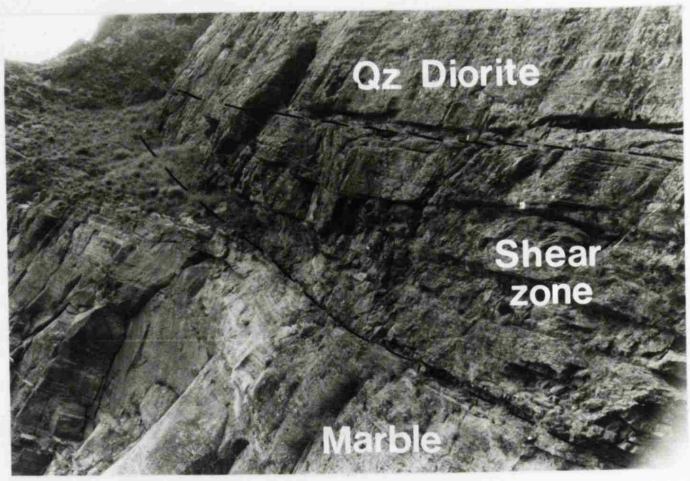

Plate 3.20

Boudinaged feldspar bands within quartz diorite at the southern margin of the HPC near Sarrat. Rotation indicates shear movement up dip i.e. towards the south

Plate 3.21

Igneous inclusion of diorite within the Gulmit granodiorite near Shishkat.

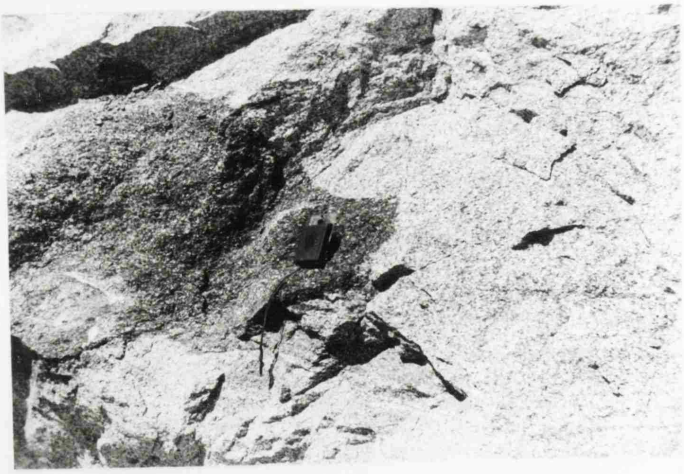

Plate 3.22

Metasedimentary xenoliths orientated as ellipses along the foliation in the northern granodiorite.

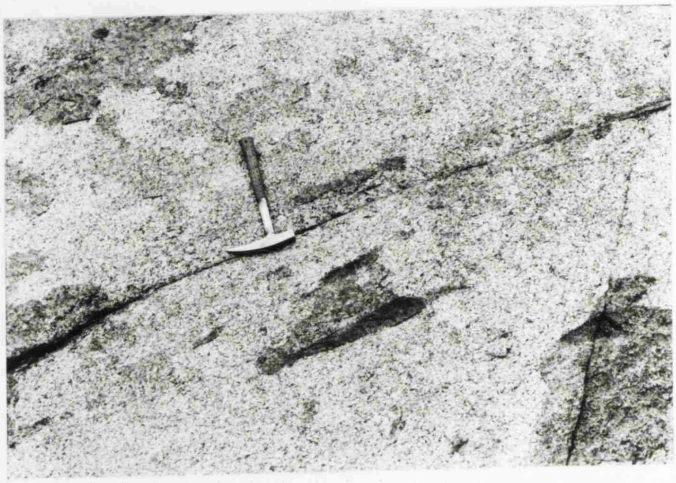

the map. Only in Ultar was a different sequence seen, as the large acid sheets (section 3.5, gp.1) seemed to complicate the situation. Between the upper sheet, with an intrusive upper contact, and the complex are a series of gneisses and no marbles. Because these gneisses resemble the contact quartz diorite, no thrust was identified and the contact was located at the first obvious plutonic rock, which had green porphyroblasts in it. Between Ultar and Mohammedabad the acid sheets must die out or abut against the complex.

The evidence above suggests that there was an original intrusive contact which has been truncated and inverted by later thrusting. The feldspar bands in the contact quartz diorites show asymmetric rotation of boudins which constrain the direction of thrusting as southwards.

3.4.d: Inclusions.

There are three main groups of xenoliths or inclusions in the complex. These are mostly found near the contacts and the centre of the complex is xenolith free.

Group 1: These are the igneous inclusions and there is one major type which is mafic and rich in hornblende and biotite with accessory sphene, apatite and clinopyroxene. They are especially common around Ghulkin and just south of Gulmit and are usually irregularly shaped but have sharp and rounded edges (plate 3.21). These inclusions either represent an earlier intrusion through which the granodiorite was intruded or restite material. Debon et al. (1987b) include the large mafic bodies and layers seen interfingering the northern granodiorite within this group.

Group 2: These are the most common metasedimentary inclusions and are biotite and feldspar-rich septa which occur as ellipses elongated along the foliation (plate 3.22). They often contain hornblende and, sometimes clinopyroxene and even garnet. Zoisite is a common replacement mineral. Ratios of long axes to short axes vary enormously but usually in the range 1:2 to 1:10. They are found near the contacts and probably represent assimilated gneisses or mafic selvages from a metasedimentary protolith.

Group 3: These are rarer metasedimentary inclusions which are more variable in composition. Some are rich in clinopyroxene and often have mica rich rims whilst some are dominated by tremolite or talc. However, they all contain calcite and some quartz, are generally larger than group 2, irregularly shaped and appear to represent assimilated marbles.

Opposite Gulmit there is a strange dyke about 2m wide, which is made up of coarse grained hornblende, feldspar and quartz. This contains quartzite, granitoid and other xenoliths (plate 3.23). Debon et al. (1987b) state that the quartzite xenoliths indicate the complex has a metasedimentary floor. Whilst this is not unlikely since all the country rocks are sedimentary, one dyke is insufficient evidence to prove this.

3.5: Minor intrusions outside the plutonic complex

Most of the minor intrusions are located in the sillimanite zone of the Hunza Group and can be related to the plutonic complex. No intrusions emanate from the batholith into the Pasu Group in the north although there is the small amphibole rich intrusion mentioned earlier (section 3.2) and the only basic dykes found in the area studied were intruded in the carbonates in Shimshal. These are rich in amphibole phenocrysts within a quartz-feldspar-amphibole-opaques matrix and resemble the small intrusion. They trend 040° i.e. they follow the main trend of the second phase of deformation (section 3.6) and they appear to represent the same magmatic phase as the intrusion, but no evidence was seen to connect them with the HPC. No basic dykes are seen associated with the complex which is unusual considering its calc-alkaline nature.

In the south the intrusive phases can be divided into four main groups:

1. Large sheets of medium-coarse-grained, intermediate rocks.
2. Plutons or sheets of leucogranitic material.
3. Aplites in dykes of metre or more scale and essentially monzogranitic.
4. Pegmatites and aplites, generally of leucogranitic material, and forming dykes which vary widely in scale.

Plate 3.23

Basic dyke within the HPC containing sedimentary xenoliths within a hornblende and plagioclase rich matrix.

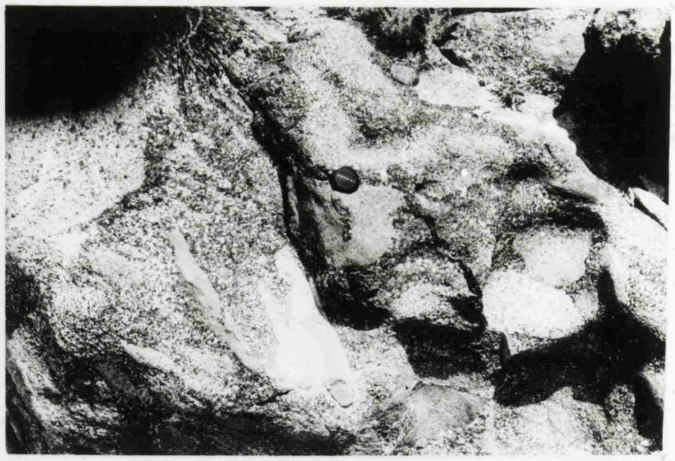

Plate 3.24

Xenolith of country rock incorporated in a granodiorite sheet (Hassanabad).
Xenolith is approx. 70m across.

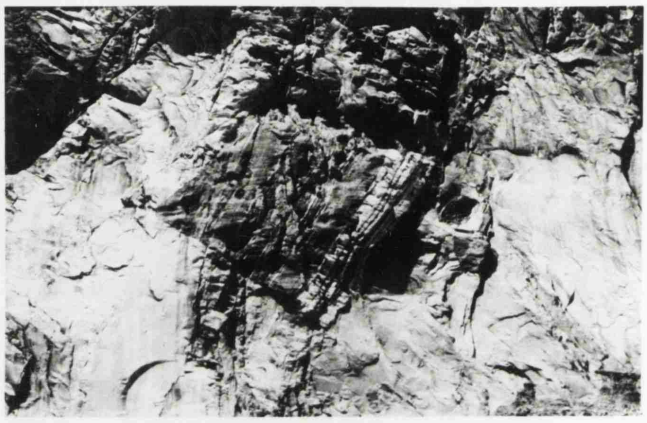

Plate 3.25

Ridge forming the cap to the Sumayar pluton. Rocks forming the top of the ridge are staurolite/kyanite grade metapelites.
Vertical height approx. 500m

Plate 3.26

Aplite dykes intruded parallel to the foliation into sillimanite-grade schists (Hassanabad).
Vertical height approx. 50m

Groups 1 and 2 are on a much larger scale than 3 and 4 and may extend for many kilometres. The exposures across mountainsides are usually inaccessible and the rocks are all the same weathered brown colour so it is hard to follow the sheets using binoculars. Whilst this was done where possible e.g following contacts up valley sides by eye, the sheets were generally located by valley exposures. Because the valleys are often a long way apart, when drawing the sketch map it was very hard to link exposures up and so define the shape of the sheets. This was only done when the exposures show such similarities as composition, texture and field relations so as to be almost certainly part of the same sheet.

Group 1: In Ultar two large sheets cross the valley parallel to the main foliation. These can be correlated through composition and texture with another exposure in Hassanabad (fig. 3.2). It is possible that one sheet splits into two between the valleys. The sheet is coarse-grained and is composed of about equal amounts of plagioclase and alkali feldspar, 20% biotite with a little apatite, quartz and relict clinopyroxene. Schneider (1957) classifies this as a lamprophyre but granodiorite is preferred as the rock is very comparable to the plutonic rocks in the southern part of the complex except that it is more coarsely crystalline and the mafics occur in larger clumps. This suggests the sheets are directly related to group one of the HPC (section 3.4.a).

In Hassanabad there are small veins from the sheet intruding the country rock and there are large xenoliths of the country rock, still showing original textures and banding, incorporated in the sheet (plate 3.24). In Ultar the lower contact gneisses show rotation up dip, and the sheet does not get finer-grained nearer its margins. This evidence shows the sheet was intruded and probably cool when emplaced and it was intruded along the foliation causing shearing and fracture in the contact gneisses.

One other sheet which probably falls in this group on the basis of composition is exposed in the Bar valley. It is unique in that it has large, regular phenocrysts or megacrysts of white alkali feldspar in a biotite-hornblende-plagioclase-titanaugite-muscovite-sphene matrix. The contacts were not seen close up but appear to be parallel

to the foliation. This sheet cannot be correlated with any other exposure so its extent is unknown, but boulders with the same texture and megacrysts were found on the Hassanabad Glacier. The megacrysts do not appear to be aligned so they may be secondary features.

Group 2: In Sumayar and Nagar there are large bodies composed of leucogranite i.e. feldspar and quartz with common accessory muscovite and garnet. Whilst they resemble the aplite/pegmatites in the complex and country rocks in their mineralogy, and probably have a similar origin, they are the largest intrusions of such magmas seen in Hunza and they show no association with the dykes and no dykes emanate from them.

The two intrusions are not linked together because of one major difference in mineralogy. The Sumayar Pluton shows large blotches of black tourmaline evenly distributed throughout the rock, and there are pegmatitic growths of tourmaline along fracture planes, suggesting an origin from fluids flowing along planes of weakness.

The Nagar exposure is in the form of a sheet whilst Sumayar appears plutonic, with no lower contact being seen. The contacts of the Sumayar Pluton are heavily altered and baked staurolite/kyanite grade gneisses. These form a cap and can be seen lying on top of the pluton along the ridges either side of the valley (plate 3.25). Next to the contact the gneisses are brecciated suggesting a forceful intrusion. The Nagar sheet contacts appear to be intrusive with large rafts of the gneiss (sillimanite-grade) incorporated in the sheet. The direction of the contacts was hard to establish, but the northern contact appeared to strike E-W. The Aliabad leucogranite body which strikes approximately E-W across the front of the Hassanabad valley closely resembles the Nagar sheet, but its contacts were not observed.

Group 3: On a smaller scale, throughout the sillimanite zone a series of aplitic dyke-like bodies cut the gneisses and marbles. These are fairly fine-grained consisting of feldspar, quartz and biotite with rare muscovite. Tourmaline grows on secondary cleavage planes indicating a later origin, and garnet is occasionally found. In general, however, the rocktype is granodioritic to monzogranitic. The dykes are intrusive with small veinlets coming off them into the

country rock and are rarely more than 20m wide. They either have irregular shapes and orientations or form regular sheets roughly parallel to the foliation (plate 3.26).

As with the large, late aplite sheets in the complex (section 3.4.a), they show at least two types of material in them, the earlier being darker than the later. They also often have thin pegmatitic margins. It is by no means certain that they are related to the complex sheets but they may be related to the same phase of magmatic activity.

Group 4: The large dyke swarms cutting through the complex are seen throughout the sillimanite zone as well, but not in the kyanite-grade rocks. The majority are leucogranitic and often show layering with aplitic centres and pegmatitic margins or more complicated multi-layered patterns. The pegmatites show the same textures and zones as those in the complex. Orientations are very variable although a number follow the foliation. No indications were seen that these dykes were caused by partial melting of the sillimanite grade rocks despite their absence at lower grades. Indeed, dykes from the complex cross the thrusted southern contact into the country rocks indicating a post-deformational age and a common origin for the dykes in the complex and sillimanite zone.

These four groups cover all intrusions seen except for two sheet intrusions, each over 100m wide, seen in the Bar Valley. The sheets were parallel to the foliation, both were in the kyanite zone and the most southerly one had a baked, probably intrusive, lower contact which seemed to mark the staurolite-out isograd, putting it in the same structural position as the Sumayar Pluton. The contact of the northern sheet was intrusive with many assimilated xenoliths of kyanite gneiss at the margin and it resembled the group 1 intrusions.

3.6: Structure

Figure 3.4 shows a schematic cross section through the study area along the Hunza River (line A-A' on fig. 3.2). The main structural trend of the area is a foliation which roughly strikes E-W throughout Hunza and to which bedding planes are sub-parallel. At Pasu this foliation defines the Pasu Synform changing from south-

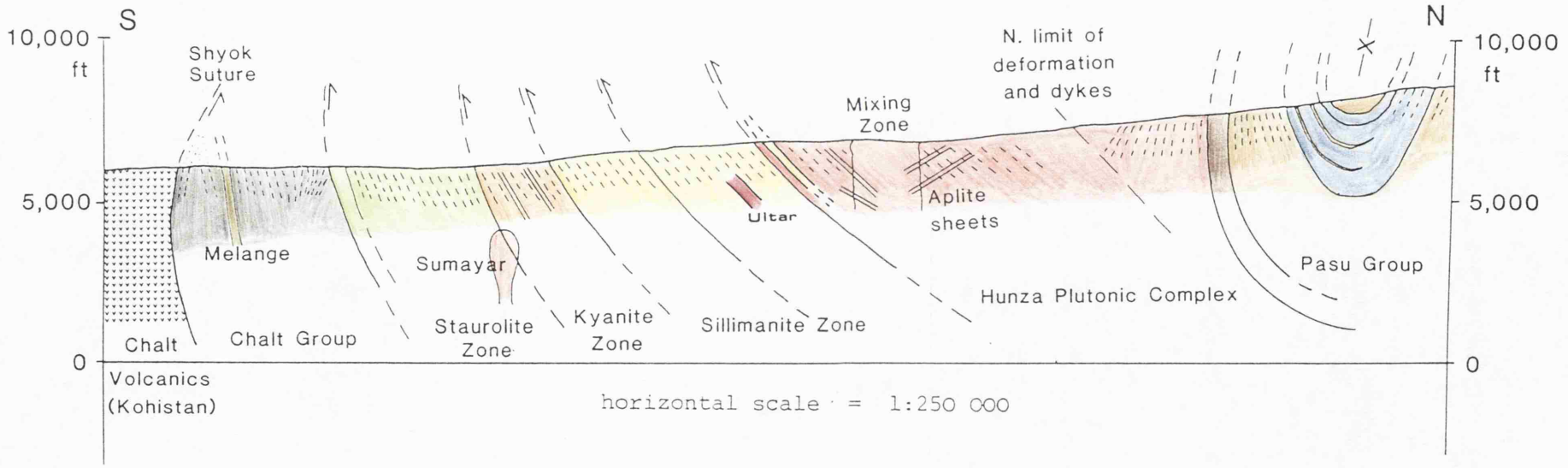

Figure 3.4: Schematic cross section through the middle Hunza Valley following the river to avoid major vertical relief variation (line A - A' on fig. 3.2). Small dashed lines just below the surface show the foliation direction. For colour key refer to figure 3.2.

dipping to north-dipping and then it steepens southwards passing through vertical so that it is south dipping at around 70° at the batholith contact (fig. 3.5(a)). It seems that the original bedding of the Pasu Group is parallel to this foliation since the carbonate and slate beds also define the Pasu Synform. This structure has an axial plane running E-W bending gently north and plunging west. The change through vertical by the foliation may represent a fan or overturning of the Pasu fold at a higher, eroded off level.

Near the contact, sandstone layers show isoclinal folding with the fold axes parallel to the foliation but with the axial planes cutting it (plate 3.27). They also show boudinage parallel to the foliation as a result of being more competent than the surrounding slates. Around each fold in the sandstone layers the slates show a crenulation cleavage for a distance of nearly 30m. These crenulations trend 060° and plunge at 40° to the horizontal on the foliation surfaces, but near the folds they form a divergent fan.

Elsewhere there is little disruption. Cleavage traces are common but do not seem to have a dominant trend although most are vertical and fall between 020° and 060°. The best structures were observed in Shimshal where there were a series of kink bands and chevrons consistently giving directions 40°W of the foliation. Three dominant partings were seen in Shimshal:

1. The main foliation (E-W to 120° south-dipping)
2. An 060° vertical cleavage
3. A later 160° cleavage dipping 45°W. This last cleavage is often filled with quartz (pressure solution cleavage) and is not deflected by the other two.

Also in Shimshal a large anticline with a carbonate core was observed. This trended 040°, bent to the SW and defines a second, later folding episode after the initial deformation episode had formed the Pasu Synform with compression in a roughly north-south direction.

South of the complex the structure of the Hunza Group is relatively straightforward. The main foliation always dips north at varying, but generally quite steep, angles. The strike varies from

Plate 3.27

Isoclinally folded sandstone layer in Pasu slates, with associated crenulation cleavage.

Plate 3.28

Rotated boudins in the HPC showing compression and shear movement up dip, i.e towards the south.
Field of view = 10m across.

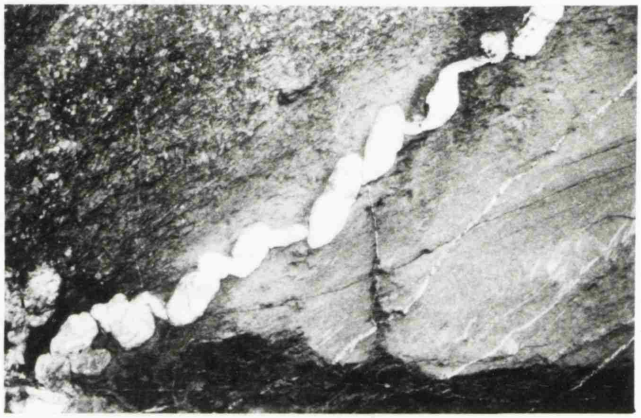

Plate 3.29

Brecciated gneiss band in carbonate showing rotation and shear movement towards the south (F=foliation).

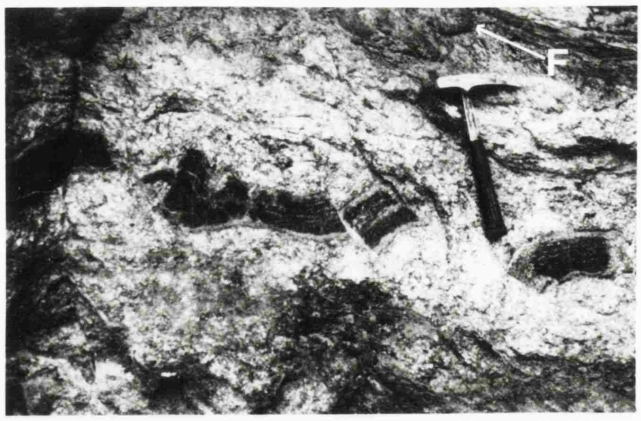

Plate 3.30

Late, 030 fold in sillimanite-grade rocks south of the HPC.
Field of view=20m across.

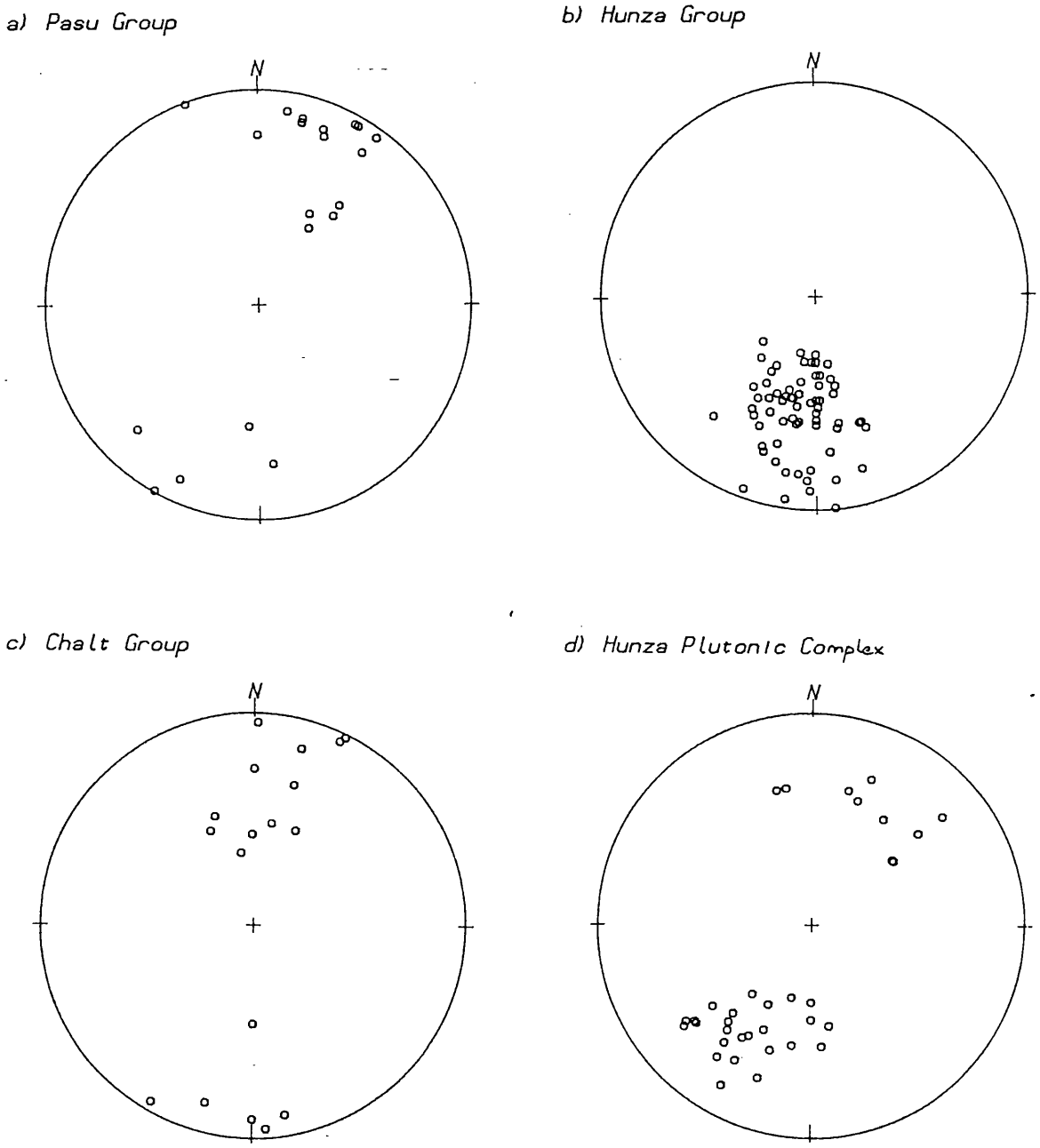

Figure 3.5: Stereoplots of poles to foliation for the main units of the middle Hunza Valley, N. Pakistan.

070° to 140° but is mainly 100° approx. (fig. 3.5(b)). All the shear zones are parallel to this foliation and rotated boudins and folded bands show movement up dip (plates 3.28 and 3.29) showing that they acted as thrusts rather than faults.

There are some later minor folds which deflect the foliation and these have axes which trend N-S to 030°, so they are probably related to the late phase of deformation seen in the north (plate 3.30). Faults are more variable in their direction and do not show a common trend. Lineations occur along the foliation surfaces dipping by variable amounts to the west.

The structure of the Chalt Group is more complicated. Next to the Shyok Suture are sheared rocks with a steep, south-dipping foliation, which is parallel to the suture and the foliation further north i.e. roughly E-W. The foliation then appears to be isoclinally folded to become north-dipping approaching the steep, north-dipping thrust which marks the margin of the Hunza Group (fig. 3.5(c)). The lenses in the melange are orientated parallel to the foliation.

According to Coward et al. (1986) this zone is controlled by steeply inclined, northward verging folds. Lineations dip south down the foliation surfaces showing that this zone was not affected by the later deformation phases which caused westward reorientation of the lineations in the north.

Within the HPC there is a sudden change in the dip of the foliation from south dipping in the north to north dipping in the south whilst maintaining a strike of E-W. The change occurs around the centre of the complex (Shishkat) where the foliation is indistinct. Various models can be proposed for this structure e.g the complex being intruded so that it expanded upwards giving a fountain shape, or unequal tilting of an original intrusion with a uniform foliation. However, such models assume that the foliation is a primary magmatic feature. The foliation in the north is parallel to that in the country rocks and all the group 2 xenoliths are aligned along it, so it may be primary and caused by convection in the pluton (Wickham, 1987). Alternatively, it may be related to an early regional deformation event. In the south the foliation in the country rocks was caused by later thrusting and this seems to be the case in

the complex with boudinage and rotation structures. Hence, the complex probably had an initial foliation parallel to the early regional foliation, which is still prevalent in the north, and then a secondary foliation, caused by southward thrusting, overprinting this foliation in the south. This is supported by only the rocks in the south of the complex having undergone deformation and recrystallisation, boudinage and rotation, and the stereonet data which show a distinct bimodal distribution in the dips from the north and south, rather than a gradual change from one to the other (fig. 3.5(d)).

The later dykes have a complicated structure, particularly in the south where they form large swarms and show practically all orientations. However, in the north before they die out they show a more consistent trend striking around 030° and dipping gently to the NW. Where they cut other structures, e.g. earlier dykes, they do not displace them so there has been no fault or thrust movements along them. The dykes die out along the line marking the northward extent of the major deformation phase.

3.7: Discussion of the evolution of the Hunza area

The preserved history of the area commenced with a thick pile of carbonates and muds being deposited during the Upper Palaeozoic, either in a shelf sea or basin, possibly with some interlayered basic volcanic rocks.

Around 95Ma (Middle Cretaceous) the first plutonic rocks were emplaced, related to Andean type subduction as shown by their calc-alkaline chemistry (Debon et al., 1987b). There may have been more than one intrusion but acidity generally increases with structural height. The intrusion was cool at its present exposed level and caused only low-grade contact metamorphism, and only assimilated country rocks at its margins. Little restite material is apparent and the rocks resemble I-type granitoids as defined by Chappell and White (1974). The southward-dipping foliation still preserved in the north of the complex must pre-date the major deformation event and post-date the intrusion. The most likely event which fits these constraints is the formation of the Shyok Suture (chapter 2) at around 100-80Ma (Pudsey, 1986), and this is in

agreement with Coward et al.'s (1986) model for the structural evolution of N. Pakistan (see fig. 2.5).

Before the next magmatic event there was a major thrusting episode which sheared the southern part of the complex, overprinted the early southward-dipping foliation with a north-dipping one, and probably inverted and thrusted its southern contact upwards and southwards. Prior to thrusting metamorphism and deformation during crustal thickening caused the plutonic rocks in the south to recrystallise and the similar PT conditions given by the recrystallised complex rocks and the metamorphic rocks immediately to the south indicate that this was also the period of the high grade metamorphism which affected the Hunza Group. Prior (1987) has shown deformation and metamorphism to be synchronous through studies of the growth and rotation of the prophyroblasts in the Chalt Group with the thrusting being later. The thrusts telescoped and inverted the metamorphic sequence by placing deeper rocks over shallower ones. This episode can be linked with the major India-Asia collisional phase 50-45Ma ago (Searle et al., in press)

After, or roughly contemporaneous with, the main episode of deformation, there was a second phase of magmatism which caused the mixing zone and aplite sheets in the HPC. The sheets are undeformed, but the mixing zone itself is deformed and so might be related to the intense deformation and heating causing partial melting. Alternatively, the zone may have been caused by a pulse of new magma a lot later than the deformation.

A further, smaller episode of deformation followed to give the 020°-060° trends of minor folds, faults, and re-orientation of S-lineations to a westerly dip in the Hunza group.

Finally, probable crustal melting gave the large, late leucogranite dykes and the Sumayar Pluton and Nagar Sheet. This magmatic episode was post-collisional and caused by the Indian Plate being subducted under Asia, with the time delay possibly being the time needed for the crustal geotherms to re-equilibrate to melting temperatures. It is felt that all the dykes are roughly contemporaneous with the earlier dykes being intruded parallel to the foliation which would provide planes of weakness.

Table 3.1 is a summary of this history based only upon the above and previous work. The rest of this thesis concentrates only on the geochemistry and origin of the magmatic rocks and there is still scope for a lot more work on the metamorphic and structural evolution of Hunza.

20 - 0 ma	Uplift and cooling	Setting of K/Ar ages in biotites and possible small deformation event giving 040° trend.
Uncertain: around 20ma.	Crustal anatexis.	Formation of the late leucogranite dyke swarms and plutons
Uncertain: post 40ma	Could be related to either collision and crustal melting or mantle magmas coming from the residual slab.	Formation of the mixing zone, and generation of the aplitic granodiorite sheets. Undeformed. Requires an input of heat from somewhere.
40 - 50ma	Collision and formation of the Indus Suture	Major deformation period. Amphibolite grade metamorphism, recrystallisation of the southern complex rocks and development of main foliation. Major southward thrusting followed.
Around 80ma	Closure of a back-arc basin and formation of the Shyok Suture.	Minor deformation may have given the regional foliation seen in the north of the complex and Pasu Slates.
95ma	Andean type subduction under the Karakoram	Generation of the main quartz diorites and granodiorites of the complex.
Upper Palaeozoic	Shelf sea or basin with some volcanic activity.	Deposition of the carbonates, muds, and basalts which are now the metamorphic country rocks.

Table 3.1: Tentative sequence for the evolution of the middle Hunza Valley based upon field evidence and previous work.

CHAPTER FOUR: Pre-collisional magmatism of the Karakoram.

4.1: Introduction.

The Karakoram block was accreted onto Eurasia in the Jurassic as shown by the Waras ophiolite emplacement onto the laterally equivalent South Central Domain in Afghanistan. Folding of flysch and overlying red molasse of lower Cretaceous age date this as occurring before the late Cimmerian (Blaise et al., 1978). To the east, folding of Jurassic flysch, followed by thrusting and emplacement of Palaeozoic metasediments on top, dates the obduction phase of the Donqiao ophiolite within the Bangong-Nujiang Suture as Upper Jurassic (Giradeau et al., 1984). This marks the collision of the Lhasa and Qangtang blocks which Sengor (1986) considers to represent the demise of a small ocean between splitting a Cimmerian microcontinent which had crossed Neo-Tethys.

Following this accretion event, Neo-Tethyan ocean crust continued to be subducted northwards beneath the new Eurasian margin. To the east this generated the Trans-Himalayan Andean-type batholith along the edge of the Lhasa block (e.g. Coulon et al., 1986). In the west the Trans-Himalaya is represented by the Kohistan and Ladakh terranes (Petterson and Windley, 1985; Honegger et al., 1982) which formed during the subduction phase. Kohistan was formed as an island arc with a back-arc basin separating it from the Karakoram (Petterson and Windley, 1985; Pudsey, 1986) This basin closed and Kohistan was accreted onto the Karakoram between 100-80Ma (Pudsey, 1986) with subduction continuing beneath the new continental margin. Dating has established that many of the granitoid plutons in Kohistan and the Karakoram were intruded during this subduction phase prior to the collision at around 45ma.

The study of granitoid plutons generated at destructive plate margins has benefited greatly from work on the currently active of the Andean chain (e.g. Harmon and Barreiro, 1984). Components that need to be considered in the genesis of such granitoids are:

a) The subducting slab comprising ocean crust basalts and sediments which may have been altered by seawater.
b) Mantle which can be both sub-oceanic or sub-continental

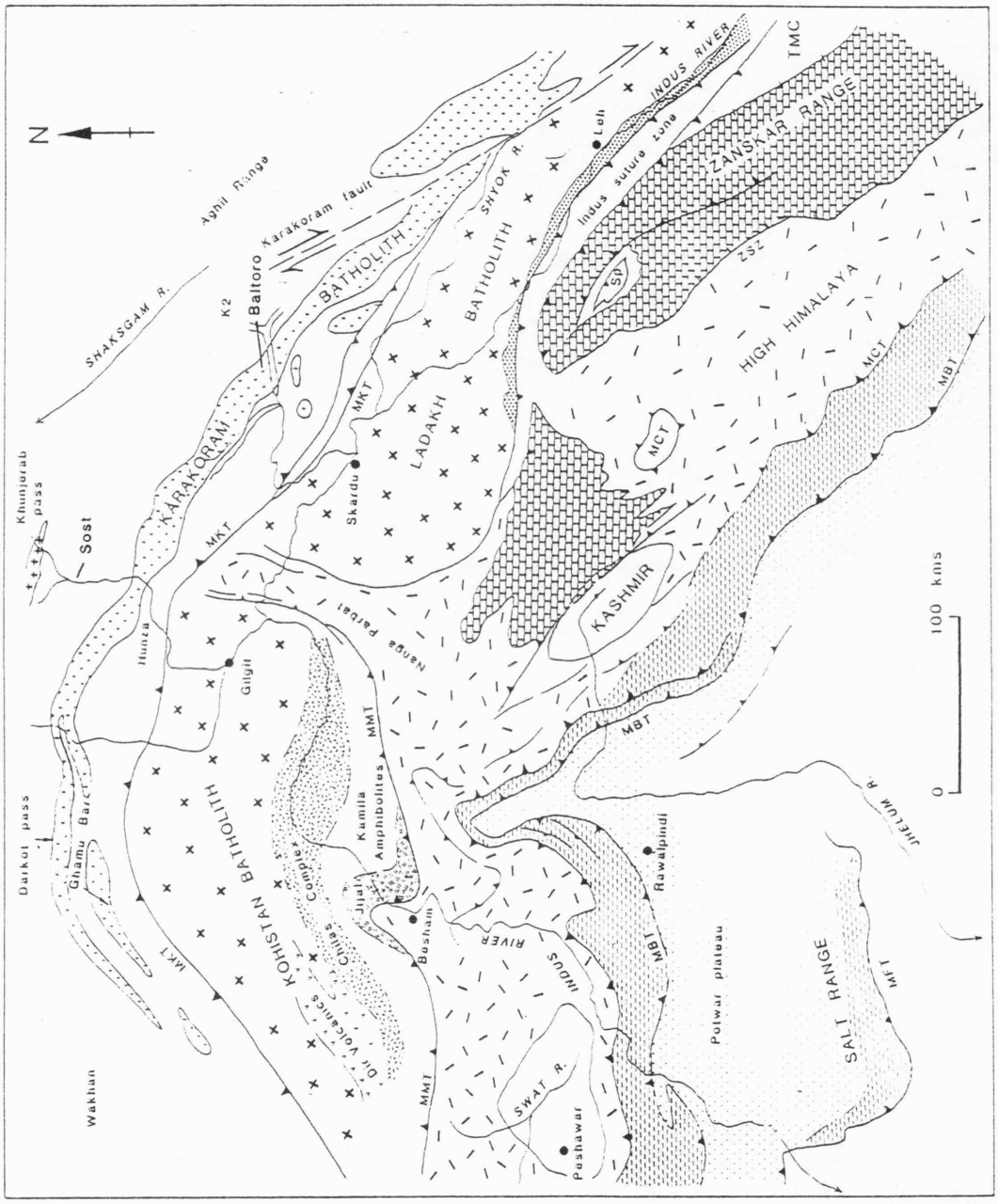

Figure 4.1: Geological sketch map of the western Himalaya and the Karakoram to show the location of the main pre-collisional plutons (from Searle et al., in press). MKT, Main Karakoram Thrust; MBT, Main Boundary Thrust; MMT, Main Mantle Thrust; ZSZ, Zanskar Shear Zone. The Kohistan-Ladakh batholith is shown in large crosses bounded to the south by the Indus Suture Zone or MMT, and to the north by the Shyok Suture Zone or MKT. The composite Karakoram Axial Batholith is shown in small crosses with the Khunjerab Pluton to the north of this. Baltoro and Hushe are located in the K2 area.

lithosphere or asthenosphere, all of which may have undergone earlier enrichment or depletion.
c) Continental crust which could contribute lower crustal melts or upper crust through assimilation.
d) Fluids which transport elements from one region to another.

In addition to this high number of possible components the chemistry of the plutons may be strongly affected by high and low pressure fractionation (Wyllie, 1984). A large amount of geochemical and mineralogical data on a wide variety of related plutons has helped reveal some information about the relative importance of these components and processes in the Andes. Unfortunately such an amount of data is not available for N. Pakistan.

This chapter looks at the new data available for those plutons in the Karakoram that have been dated and appear to be temporally related to the subduction phase. Initially mineralogy and internal geochemical trends are discussed for the first phase of the Hunza Plutonic Complex (HPC) within the Karakoram Axial Batholith (KAB), and the Khunjerab and Batura suites (fig. 4.1) to illustrate the difficulties imposed on any inter-pluton comparison by fractionation and heterogeneity. It will then be seen that whilst all the plutons show subduction-related signature such as calc-alkaline trends (e.g. Brown et al., 1984; Debon and Le Fort, 1982), a high LILE/HFSE ratio (e.g. Tarney and Saunders, 1979; Pearce et al., 1984) and a negative Nb anomaly (e.g. Bartholomew and Tarney, 1984) there is little significant spatial variation in the data available. A lot more work is needed in this area before any conclusions can be drawn in terms of possible source/petrogenetic variation that existed beneath the Eurasian margin prior to collision.

4.2: Isotope systematics for the pre-collisional magmatism.

Dating Himalayan plutons using isotope systems has been found to be fraught with problems due to the heterogeneity and thermal history of the rocks. U-Pb based dating systems appear to be the most reliable due to the high blocking temperature of U and Pb in accessory minerals. This is estimated to be 650-700°C for monazite and even higher in zircon (Parrish and Tirrul, in press). This prevents post-magmatic resetting of isotope values and so preserves

the primary crystallisation age allowing for slow cooling rates. This was demonstrated by Scharer et al. (1983) who obtained a primary Palaeozoic U-Pb age of 470±4Ma for the Palung granite in the Outer Crystalline nappes whereas other isotope systems had been reset and gave Alpine ages. Problems with this system are experienced for young rocks since the trajectory of lead loss lies very close to the concordia line so all data yield concordant ages. Additionally, certain minerals such as monazite have Th/U ratios greater than those of the magma and so have an excess of ^{206}Pb not produced by radioactive decay from ^{238}U. However, these problems apart, reliable and consistent ages have been obtained using this system for all main groups of Himalayan granitoids.

Ar-Ar methods are very useful for dating metamorphic events (e.g. Maluski and Matte, 1984) and there has been limited success in their use for dating plutons (e.g. Reynolds and Brookfield, 1983). However, $^{40}Ar/^{39}Ar$ ages on biotites, muscovites and K-feldspar are often lower than the true age, through either long cooling histories or re-setting by metamorphic events, due to the low closure temperatures of argon in these minerals (e.g. Faure, 1986). Similarly, K-Ar dating on biotites always gives younger ages than those from hornblende from the same rock due to the higher blocking temperature of Ar in amphibole, but both are prone to resetting by later thermal events. Rb-Sr measurements on individual minerals experience the same problem and Rb-Sr whole rock data is often scattered (e.g. Le Fort et al., 1987) due to heterogeneity or lack of equilibrium, although fortuitous isochrons may be obtained e.g. 97.7±9.4Ma for Makalu as opposed to the U-Pb ages of 24 and 21.9Ma (Scharer et al., 1986). However, careful measurement has led to what appear to be reliable isochrons in certain cases such as work on the Transhimalaya (Honegger et al., 1982) and Kohistan (Petterson and Windley, 1985) although the ages obtained from these often have large error limits. At present little dating has been done using the Sm-Nd decay system but this appears to give the same problems as the Rb-Sr system (Deniel et al., 1985).

The most reliable age so far on the pre-collisional part of the HPC comes from a U-Pb determination on zircons of 95±5Ma by Le Fort et al. (1983). Previous determinations by Rb-Sr on biotite (Desio et al., 1964) and K-Ar whole rock (Windley and Jan, 1981) gave much

younger ages of 8.6 and 52Ma respectively. Le Fort et al. (op.cit.) also obtained two pseudo-chrons of 26 and 46Ma for K-Ar measurements on biotites and amphiboles respectively and they attributed these ages to later thermal events. The zircon age corresponds with the U-Pb age (101±2Ma, Scharer et al., 1984) and Rb-Sr whole rock age (102±12Ma, Petterson and Windley, 1985) of the older plutonic phase of the Transhimalaya batholith. The Khunjerab granodiorites also give an age of 105-107±5Ma by K-Ar on biotite (D. Rex, pers. comm.) and this appears not to have been reset, unlike the HPC further south (K-Ar biotite ages of 12-18Ma), because Khunjerab lies north of the main Eocene deformation front (fig. 4.1).

For this study Rb-Sr and Sm-Nd isotopic measurements were made on three samples from the main part of the HPC and on one xenolith found within the northern granodiorite (appendix 1.3). The only other comprehensive study of the Rb-Sr systematics of the area was made by Debon et al. (1987b). These authors took eight samples from along the road section of the HPC and, since they considered them to represent a single pluton, tried to construct an isochron. They experienced large errors in trying to obtain a best fit line and obtained an age of 117±22Ma with a very high mean square of weighted deviates (MSWD) of 22. Because this age was higher than the zircon U-Pb age of Le Fort et al. (1983) they then took a sample of the basic dyke (B6, appendix 1) which lies well off the trend and is unlikely to be comagmatic and included it in the isochron. This gave an age of 97±17mma with an even larger MSWD of 28, and this was taken to be representative.

The samples from the present study gave a wide range of initial $^{87}Sr/^{86}Sr$ ratio values from 0.7055-0.7157 when calculated for an age of 95Ma. These samples are plotted along with the Debon et al. (1987b) data, except for the dyke sample, on a $^{87}Sr/^{86}Sr$ vs. $^{87}Rb/^{86}Sr$ graph (fig. 4.2) with a best-fit regression line and confidence limits to show the scatter. Using the method of McIntyre et al. (1966) the scatter is initially assumed to be due to experimental error and the samples are weighted to reduce this scatter and give an isochron. The data gave a model age of 769.9±2.5Ma, but with a MSWD > 5000. Assuming that the scatter is geological and not experimentally related, and setting the MSWD to one, the data gives a model age of 289.0±237.6Ma with an initial Sr

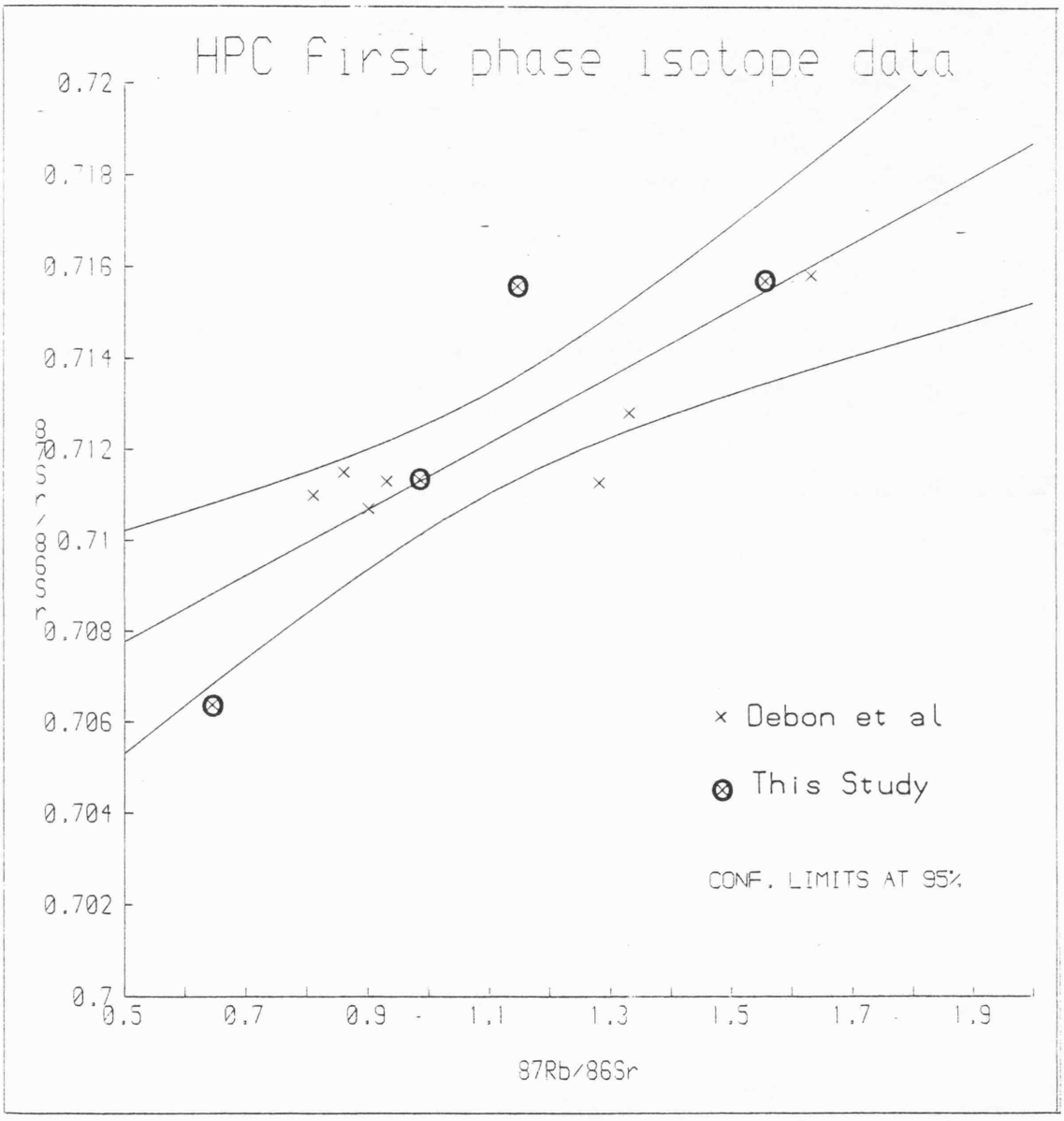

Figure 4.2: Unweighted isotope data for the main Cretaceous phase of the HPC. Data are from this study and Debon et al. (1987b). Best-fit regression line with 95% confidence limits is shown.

isotope ratio of 0.708. This shows that a reliable Rb/Sr isochron cannot be constructed for the HPC and must cast doubt on any similar isochron obtained for a Karakoram pluton which has a large MSWD. The reason for the heterogeneity seen in the Rb-Sr systematics for the HPC will be considered later (section 4.5).

One piece of information that can be derived from Debon et al. (1987b) is the average initial Sr isotopic value of the HPC of 0.7094 for an age of 97Ma. This is very high compared to the Kohistan and Ladakh batholiths which have mantle-like values of 0.7034-0.7048 (Petterson and Windley, 1985; Honegger et al., 1983) but similar to values from the Muztagh Tower Unit of the KAB (0.711-0.7127, T. Rex, pers. comm.) which has K-Ar (Hbl) ages of 82-75±3mma and is thought to be an along strike equivalent to the HPC (Rex et al., in press). Debon et al. (1987b) obtained a reasonable Rb-Sr WR isochron (MSWD=2.7) for the Darkot Pass unit of the KAB which gave an age of 109±4Ma with an initial Sr isotope ratio of 0.7044 which is comparable with the Kohistan values. Mafic, foliated gneisses and quartz diorites of the Hushe Valley section of the KAB give Jurassic K-Ar ages on hornblende of 208±8Ma and 163±7Ma which slightly pre-date cross-cutting monzogranitic pegmatite dykes with an age of 142±6ma (K-Ar; Musc) (Rex et al., in press). U-Pb zircon ages on the Hushe gneiss, and the K2 gneiss north of the Baltoro Plutonic Unit, lead the same authors to consider that both are deformed, early constituents of the KAB. These zircons (Parrish, writ. com.; from Rex et al., op.cit.) show an older crustal component.

Therefore, on the basis of field evidence and age dating the main phase of pre-collisional, calc-alkaline magmatism at around 100ma in N. Pakistan is represented by the first HPC phase, Darkot Pass, Khunjerab and the early Kohistan plutons (e.g. Matum Das). Earlier plutonism is recorded by the Hushe Complex of the KAB (Jurassic) and later plutonism is represented in Kohistan by the second phase granites of Petterson and Windley (1985). These granites such as the Gilgit and Shirot plutons (54±4Ma and 40±6Ma respectively; Rb-Sr WR) were intruded just before collision during what appears to have been a quiet magmatic period in the Karakoram. Possibly one pluton in the KAB dates from this period and that is the Batura to the NW of the HPC dated at 43±3Ma by Debon et al. (1987b) (Rb-Sr WR, MSWD=0.7, Sr_i=0.7056).

This chapter now concentrates on the new data available for the HPC, Khunjerab and Batura plutons. The Sost pluton, which lies between Khunjerab and Hunza (fig. 4.1) is included because of its similar characteristics, although no date is available for this pluton. First the mineralogy is discussed followed by modelling of the internal chemical trends so that these are not confused with source characteristics. Then it remains to be seen if there are any significant spatial and temporal variations between the pre-collisional plutons intruding the Karakoram margin. Such variations might yield valuable information on the source components of the granitoids, and on the nature of the mantle beneath the Karakoram.

4.3: Mineralogy.

4.3.a: The Hunza Plutonic Complex.

Table 4.1 shows the modal mineralogy of some common HPC pre-collisional granitoids. The mafic component is dominated by amphibole and biotite which are discussed further below. Sphene is usually associated with biotite (plate 4.1(a)) and apatite and allanite are other accessory phases. Clinopyroxene is present in small quanities in the more basic rocks (plate 4.1(b)) and opaque phases become more common in the acidic rocks. Zoisite is a common alteration product of plagioclase which varies from labradorite to oligoclase with andesine being dominant (see below). This variation occurs from the basic rocks up to the more acidic samples and is accompanied by a decrease in the amphibole and biotite content and an increase in K-feldspar and quartz. The igneous xenoliths (chapter 3.4.d) are composed of amphibole, biotite, a little clinopyroxene, and plagioclase with zoisite alteration (plate 4.1(c)). The sedimentary enclaves are extremely variable in their metamorphic assemblages due to the original heterogeneity in their composition. However, they tend to be dominated by zoisite with tremolite being common in the more calcareous samples (plate 4.1(d)).

Plate 4.1(a)

Sphene associated with biotite (sample B8).

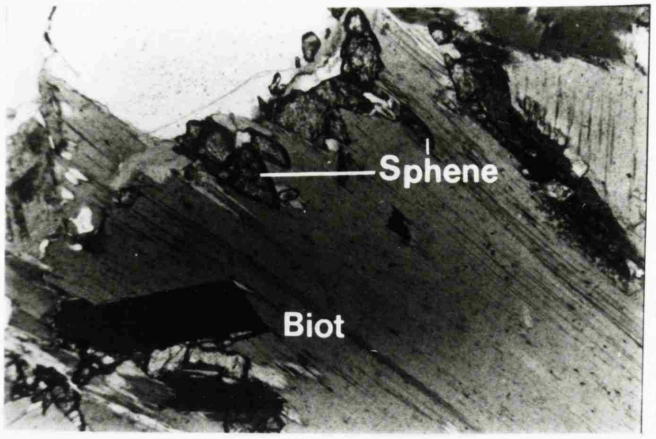

Plate 4.1(b)

Clinopyroxene, hornblende and biotite in the Gulmit quartz diorite (sample B8).

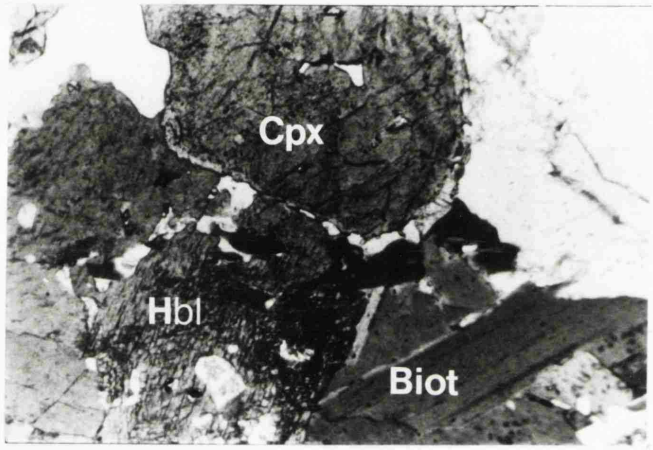

Plate 4.1(c)

Zoisite, amphibole, and biotite (with associated sphene) in an igneous inclusion (sample 2PS8)

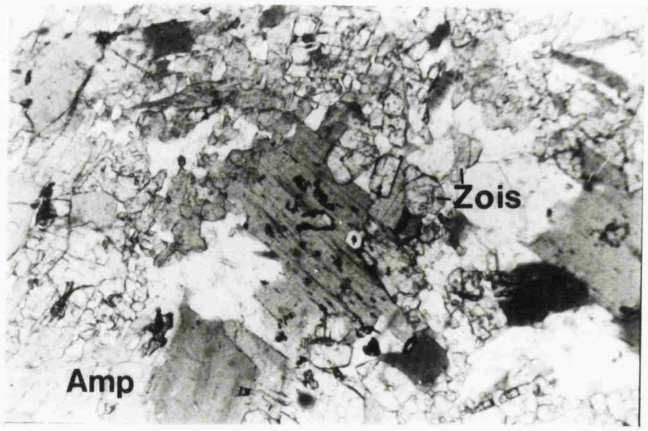

Plate 4.1(d)

Acicular amohibole, zoisite, clinopyroxene and calcite in a calcareous inclusion (sample 1PS6)

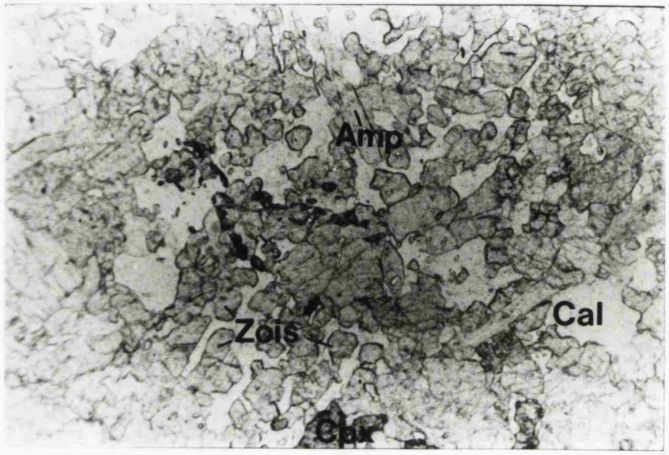

1mm

Sample	B8	B16	B60	B92	1PS3	K204	BG5
Type	Grd	QzDi	QzDi	Xen	Grd	Grd	Grd
Location	HPC	HPC	HPC	HPC	HPC	Khunj.	Batura
Points (n)	493	434	494	425	467	500	425
Quartz	13.3	8.7	14.5	8.2	16.0	19.4	19.9
Plag.fsp.	45.0	40.0	51.5	25.8	48.5	39.1	55.4
(comp.)	An34	An54	An41	An46	An38	An39	An39
(K,Na)fsp	4.9	3.7	4.5	4.9	8.2	20.2	6.1
Biotite	18.4	20.1	18.8	21.4	-	13.2	10.8
Amphibole	14.3	22.4	9.3	38.1	24.9	7.5	6.6
Cpx	1.6	2.6	-	-	-	-	-
Sphene	2.2	1.0	1.2	1.4	1.6	tr	0.6
Apatite	tr	1.6	0.2	tr	tr	0.6	0.3
Opaques	tr	-	-	-	0.6	-	-

Table 4.1: Modal mineralogy for some pre-collisional Karakoram granites

4.3.b: Chemistry of the common HPC phases.

1). Amphibole.

For the amphibole analyses (appendix 1.4) Fe_2O_3 has been calculated from FeO by recalculating the formula unit to total 13 cations excluding Ca, Na and K and then adjusting the Fe^{2+}/Fe^{3+} ratio to bring the O anion total up to 23. This gives a maximum estimate of Fe^{3+} following the procedure recommended by Leake (1978). The HPC amphiboles are exclusively calcic in composition ($(Ca+Na)_B>1.34$, $(Na)_B<0.67$; Leake, 1978) and are classified according to Leake (op.cit.) on two ($Mg/Mg+Fe^{2+}$) vs. Si cation diagrams which split the analyses according to whether $(Na+K)_A$ is higher or lower than 0.5. Most of the analyses range from edenite through edenitic hornblende to ferro-pargasitic hornblende (fig. 4.3(a)). Analyses from one of the more basic rocks and from a xenolith range from actinolite to magnesian hornblende (fig. 4.3(b)), although the actinolite may be

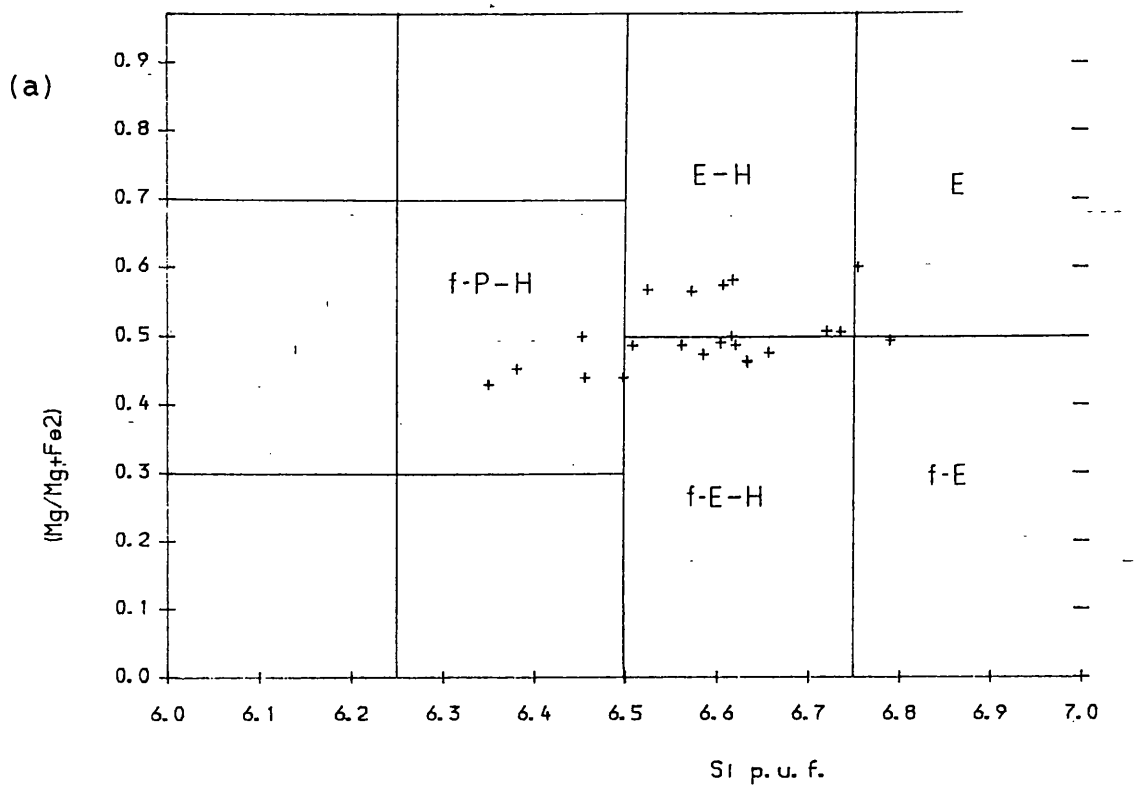

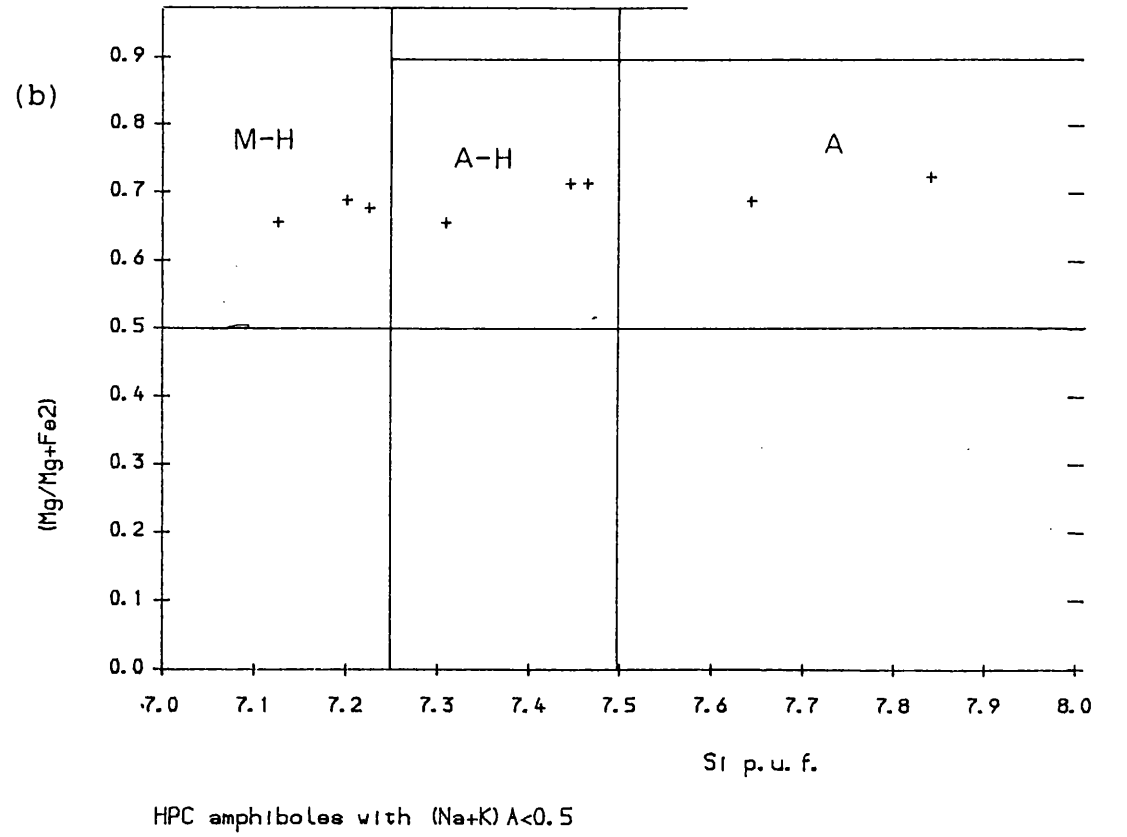

Figure 4.3: Classification diagrams for calcic amphiboles from Leake (1978). See appendix 1.4 for method of calculating Fe^{2+}. Figure (a) represents the main set of HPC amphibole analyses with figure (b) showing analyses from a xenolith and a more basic samples which have $(Na+K)_A$<0.5. E = edenite; H = hornblende; A = actinolite; P = pargasite. M = magnesian and f = ferro-varieties.

secondary in origin. The compositional variation on these diagrams is due to the substitution of Fe^{2+} for Mg and this may in part reflect the changing magma composition. However, it is also dependent on other amphibole substitution schemes which require complementary substitutions to balance the charges.

Figure 4.4 shows a straight line correlation between Al in the tetrahedral site and alkalis in the A site and this shows that the edenitic substitution $(Na+K)_A + Al^{iv} = [\ ]_A + Si$ is operational. However, the slope of approximately 2:1 indicates an excess of Al over the alkalis, and so this is not the only substitution taking place. Other schemes which involve Al^{iv} and which would therefore explain the excess are the Al-Tschermakite ($2Al^{iv}$ (or $Fe^{3+} + Al^{iv}$) = Mg + Si) and the Ti-Tschermakite ($Ti + 2Al^{iv} = Mg + Si$) substitutions (Czamanske and Wones, 1973). These authors point out that if a combination of these three schemes was dominant then a 1:1 relationship should exist between Al^{iv} and $((Na+K)_A+Al^{vi}+Fe^{3+}+2Ti)$. Figure 4.5 shows that this is the case for the HPC amphiboles, with the deviation towards the right being caused by either using the maximum Fe^{3+} value given by the recalculation (see above), or by a less important process involving Na+K such as the glaucophane subsitution.

In summary the HPC amphiboles are calcic and hornblendic in composition forming a trend from actinolite (possibly secondary) to edenite and pargasite. Variation probably reflects magmatic evolution during crystallisation and also the operation of the edenite and Ti- and Al-Tschermakite substitution schemes. Analyses from enclaves are indistinguishable from those of the main pluton suggesting they are either co-magmatic or complete re-equilibration has taken place between magma and xenolith. The calcic content of the amphiboles is very consistent (10.78 to 13.16%) and overall the analyses are comparable with those from the calc-alkaline plutons of the Aleutian arc (Kay et al., 1983).

2). Biotite.

Chemical analyses of the HPC biotites are plotted on a Si vs. Fe/Fe+Mg (Fe^*) graph (fig. 4.6; from Deer et al., 1966) using total FeO to calculate the Fe cation (appendix 1.4). The Fe^* value is

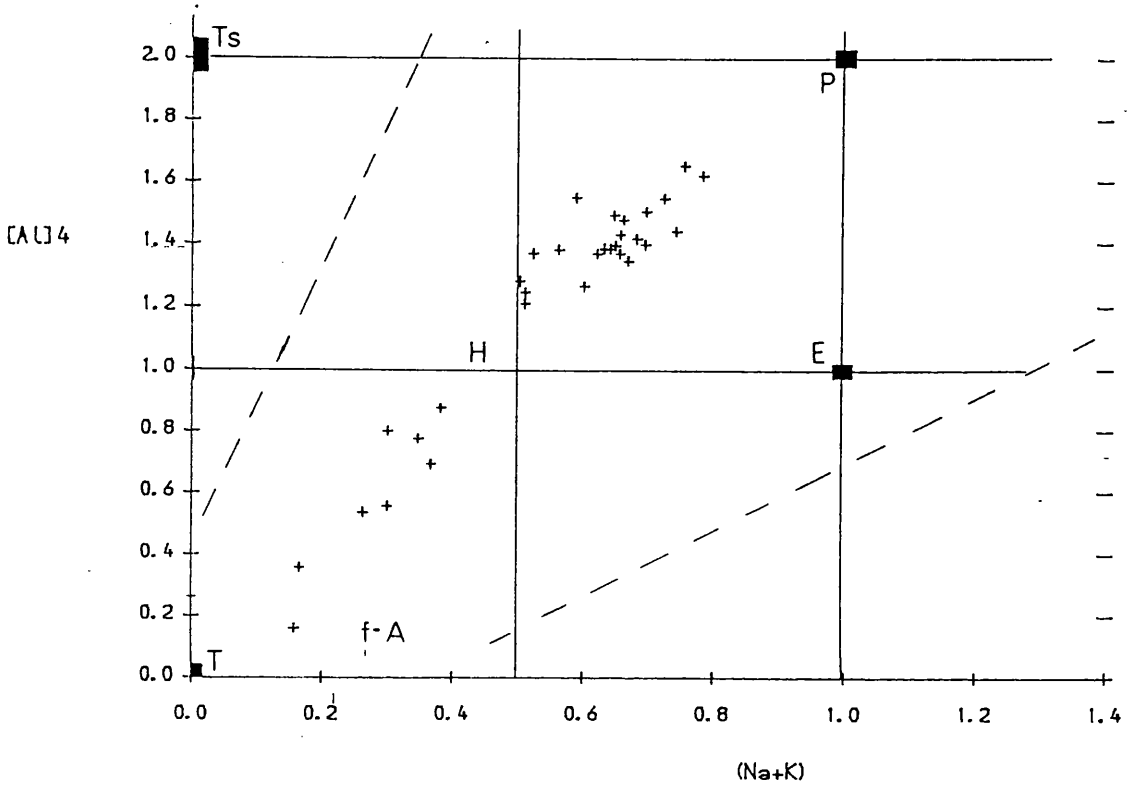

Figure 4.4: Straight line correlation between [Al]iv and (Na+K) for the HPC amphiboles indicates the operation of the edenite substitution. Excess of [Al]iv must be explained by another substitution scheme (see below).

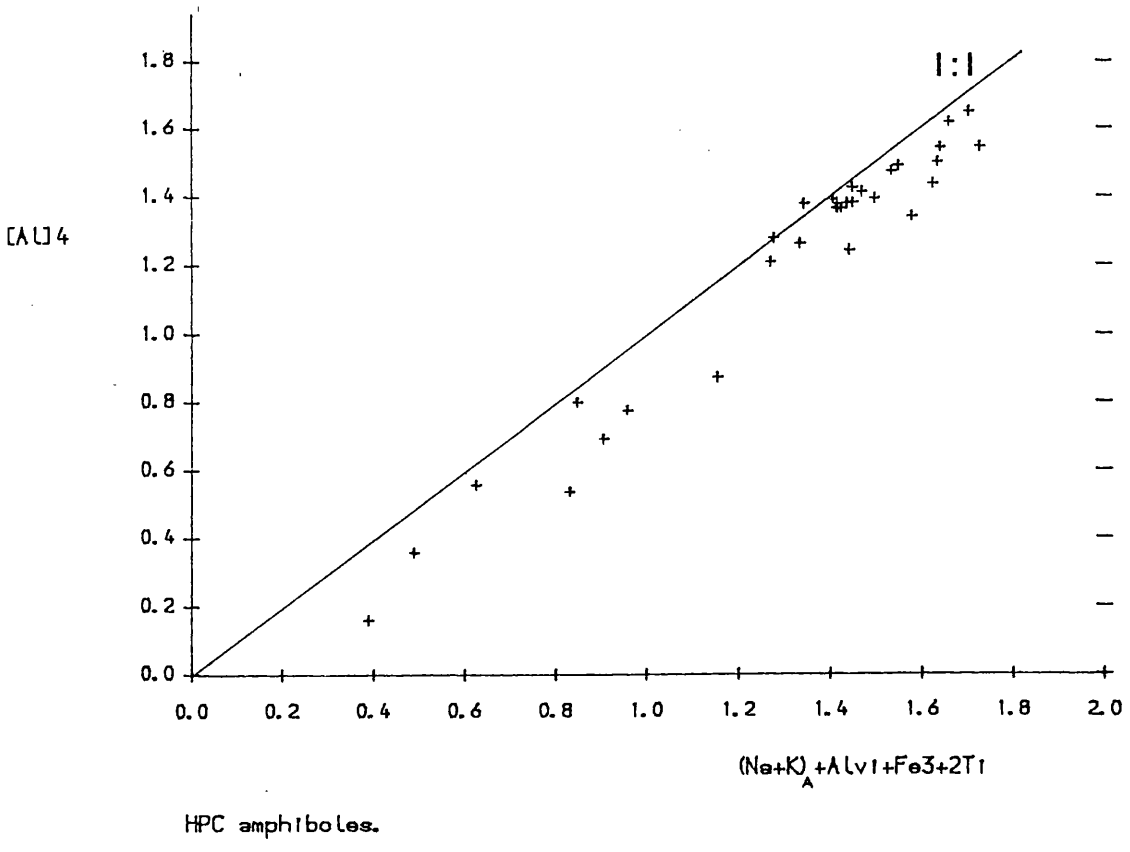

Figure 4.5: 1 to 1 straight line correlation of [Al]iv with $(Na+K)_A$ + [Al]vi + Fe^{3+} + 2Ti shows that the edenite and tschermakite substitution schemes are dominant in the HPC amphiboles.

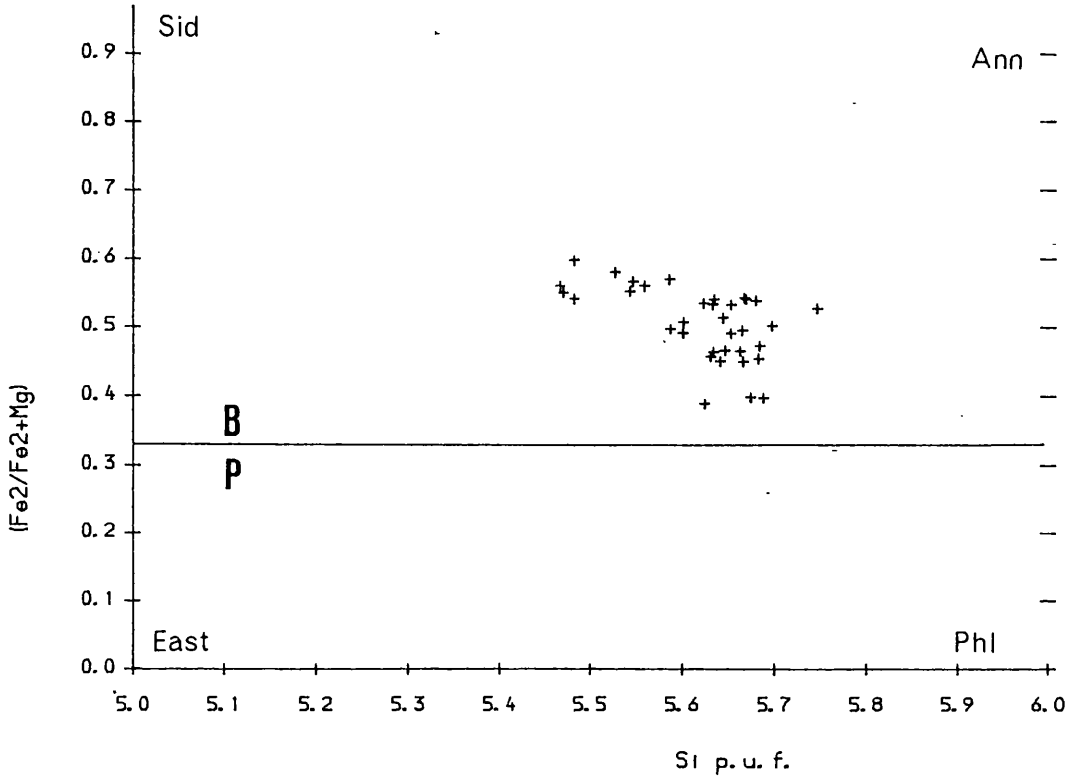

HPC first phase biotites.

Figure 4.6: Biotite classification diagram for the HPC biotites after Deer et al. (1966). B = biotite; P = phlogopite; East = eastonite; Sid = siderophyllite; Ann = annite.

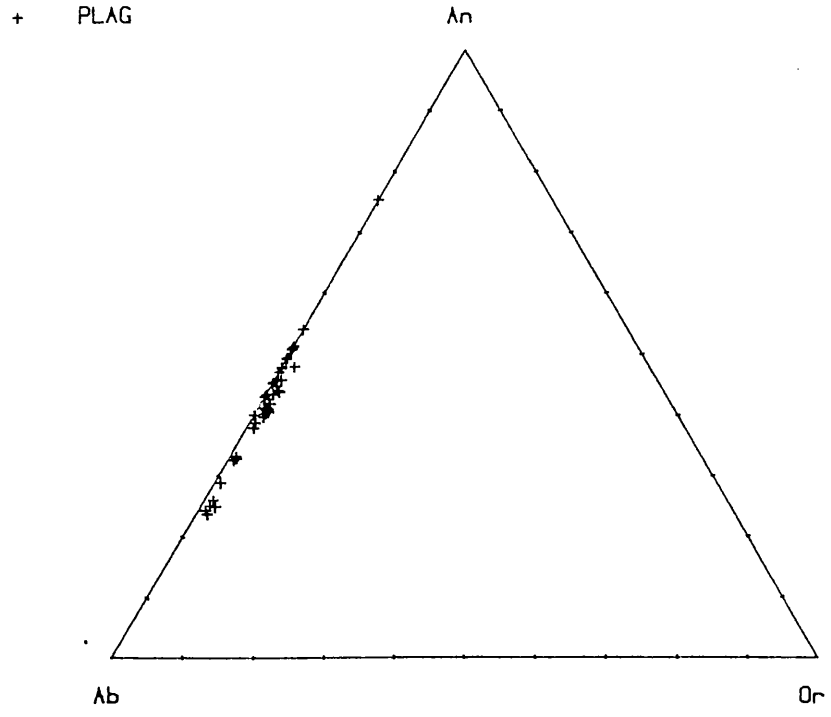

HPC first phase plagioclases

Figure 4.7: Albite (Ab) - orthoclase (Or) - anorthite (An) classification diagram for the HPC plagioclases. Ab, Or and An are calculated from molecular proportions of Na, K and Ca respectively.

always >0.33 indicating the micas are true biotites and not phlogopites. There is little variation in the analyses and, as with the amphiboles, there is no separation of host rock and enclave compositions indicating either complete re-equilibration between the two or a co-magmatic relationship. There is a slight increase in the Fe content of the biotites with acidity and according to Wones and Eugster (1965) this could reflect a decrease in oxygen fugacity (fO_2) during crystallisation. This is consistent with the late crystallisation of ilmenite (see below).

3). Plagioclase.

Compositions of HPC plagioclases are plotted on a An-Ab-Or phase triangle (fig 4.7) calculated from the molecular proportions of Ca, Na and K respectively (appendix 1.4). Apart from one analysis the feldspars cluster between An_{55-25} with very little Or component. Again, there is no apparent difference between analyses from the main body and from enclaves.

4). Fe-oxides.

All the opaque phases of the HPC analysed are Fe-oxides and are plotted on a $FeO-Fe_2O_3-TiO_2$ classification triangle (fig. 4.8; after Deer et al., 1966). Fe_2O_3 is estimated from the total FeO by the charge balance method of Carmichael (1967; appendix 1.4). Opaque phases are most common in the acidic granodiorites and they are scarce in the more basic rocks. The Fe-oxides in the acidic rocks are ilmenites which show no hematite component (fig. 4.8). The analyses lie slightly away from the ideal ilmenite endmember towards the TiO_2 apex, and this may be a result of a small amount of secondary alteration. Only one opaque phase was analysed in a more basic rock (B8) and this gave poor totals, but plots at magnetite with no ulvospinel component. The slight deviation towards the FeO apex is probably due to the low totals resulting in low apparent abundances of elements substituting for FeO.

Whereas these analyses are not sufficient to base too much interpretation on, it appears that there is a change in oxide mineralogy from magnetite to ilmenite as acidity increases. Ishihara (1977) showed that the stability of these two phases was controlled

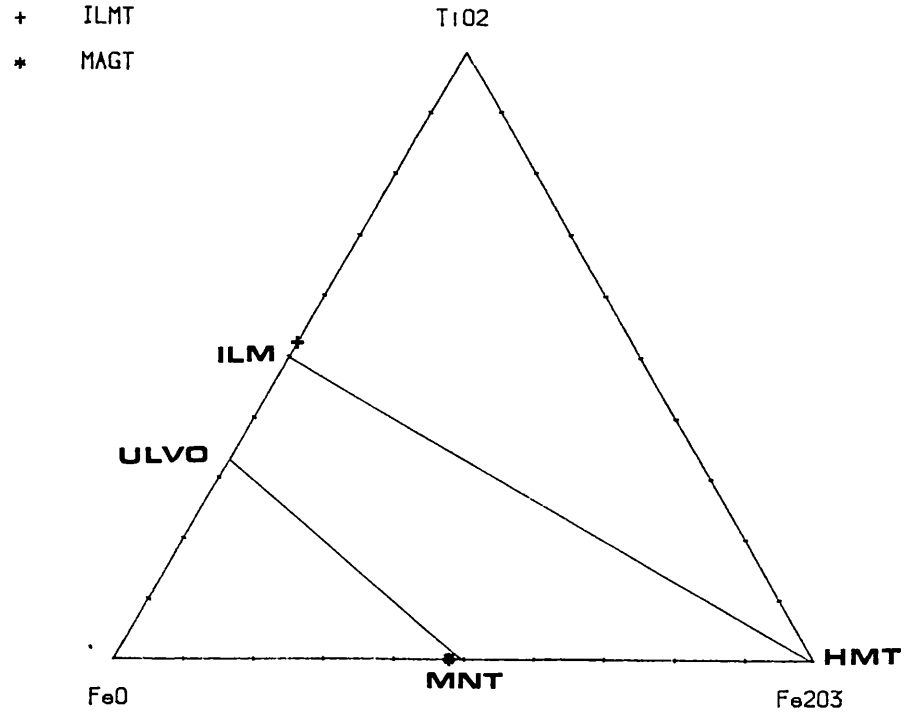

Figure 4.8: Classification diagram for HPC Fe-oxides after Deer et al. (1966). All endmembers are calculated in molecular proportions by dividing the oxide analyses by the molecular weight. For the magnetite (MNT) - ulvospinel (ULVO) analyses, FeO is calculated from the excess which remains when the necessary amount required to balance the charges for TiO_2, SiO_2 and Al_2O_3 substitution has been removed according to the method of Carmichael (1967). The ilmenite (ILM) analyses have an excess of TiO_2 over FeO and so this is not necessary for the ilmenite - hematite (HMT) solution series.

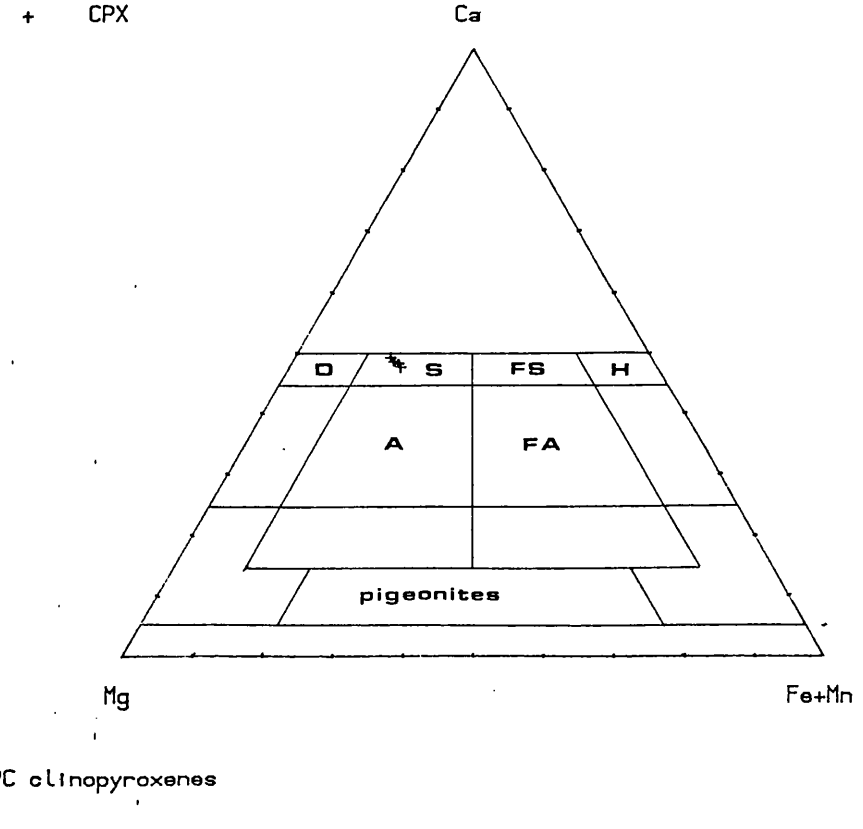

Figure 4.9: Classification diagram for the HPC clinpyroxenes from Deer et al. (1966) calculated from molecular proportions of Ca, Fe, Mn and Mg. All analyses plot in the salite (S) field. D = diopside; A = augite; H = hedenbergite; F = ferro-varieties.

by oxygen fugacity, with the boundary separating the two being near to the Ni-NiO buffer. Magnetite represents higher oxygen fugacities and is typically found in calc-alkaline batholiths. It is proposed here that magnetite was originally precipitated in small quantities during the early stages of fractionation in the HPC. As fractionation proceeded the oxygen fugacity decreased causing the crystallisation of ilmenite rather than magnetite. The limited occurrence of magnetite, and to some extent ilmenite, compared to other phases suggests that Fe and Ti are being controlled by the precipitation of other phases such as amphibole, biotite and sphene.

5). Clinopyroxene.

Clinopyroxene is only found in the more basic rocks and all the analyses here come from one sample (B16, southern contact). On the Ca:Fe+Mn:Mg nomenclature triangle calculated from molecular proportions (fig. 4.9; taken from Deer et al., 1966, p.99) the pyroxenes are Ca-rich and plot in the salite field. Whereas there are too few analyses to observe any trends, Kay et al. (1983) report similar pyroxenes from the calc-alkaline plutons of the Aleutian arc which show only limited Fe-enrichment. Early amphibole crystallisation in these plutons, as seen in the HPC, is thought to reflect low crystallisation temperatures and high water pressure. These factors have the effect of suppressing the pyroxene solidus thus reducing its stability field. Therefore, Ca-rich pyroxene which crystallises from a hydrous, mafic-intermediate pluton will become unstable early in the fractionation process and will be replaced by amphibole and possibly biotite. The residual magma will be depleted in Fe and enriched in Si giving a typical calc-alkaline trend.

4.3.c: Other areas.

The mineralogy of the Khunjerab pluton is similar to the bulk of the HPC (table 4.1; K204) with the main differences being more K-feldspar and the scarcity of sphene. The rocks are coarse grained, fresh and the only alteration seen is the sericitisation of feldspar. The main mafic minerals are again biotite and hornblende, which decrease in abundance in the monzogranites. The xenolith (K208) trends in the opposite direction and consists of large grains of hornblende, biotite and plagioclase surrounded by smaller amphibole

and biotite crystals. The Sost pluton associated with the Khunjerab pluton shows the same assemblage with the only difference being the alteration of biotite by chlorite. A 'Shap-type' granite sample found in the vicinity of Sost is dominated by large crystals of perthitic K-feldspar, and is also rich in euhedral sphene and opaque phases.

The Batura granodiorite has an identical mineralogy to the granodiorites of the HPC except that it is fresh and does not show the growth of zoisite. The trend from the xenoliths to the more evolved rocks is again one of decreasing mafics and plagioclase and increasing K-feldspar and quartz.

4.4: Internal Chemical Trends

4.4.a: The Hunza Plutonic Complex.

Figure 4.10 shows a Debon and Le Fort (1982) classification diagram and an AFM trend for the main 100ma batholith phase of the HPC whilst figure 4.11 shows a number of Harker type variation diagrams for various major and trace elements. Silica is considered a suitable abscissa since it is likely to increase with differentiation in acidic rocks as most crystallising mineral phases will be silica saturated. The behaviour of other elements is then more straightforward to interpret than would be the case if a differentiation index involving a number of elements was used. The 78 rocks chosen for these diagrams are considered to be representative of a complete traverse of the batholith and should show any variation from north to south as well as within the HPC as a whole. To this end the rocks have been grouped according to geographical location and in the case of Gulmit the analyses are split on the basis of mafic content giving the Gulmit granodiorite and quartz diorite groups. Samples that may have been affected by later processes in the mixing zone (chapter 3.4.a) are not plotted here.

Also included are analyses of the Ultar, Bar and Hassanabad granodiorite sheets (chapter 3.5) since these show affinities with the HPC. The augen gneisses SLG4, 5 and 7 have identical geochemical signatures to the HPC granodiorites except in their Sr content which is slightly lower. This is attributed to the samples having an unrepresentative number of augen, which being plagioclase will

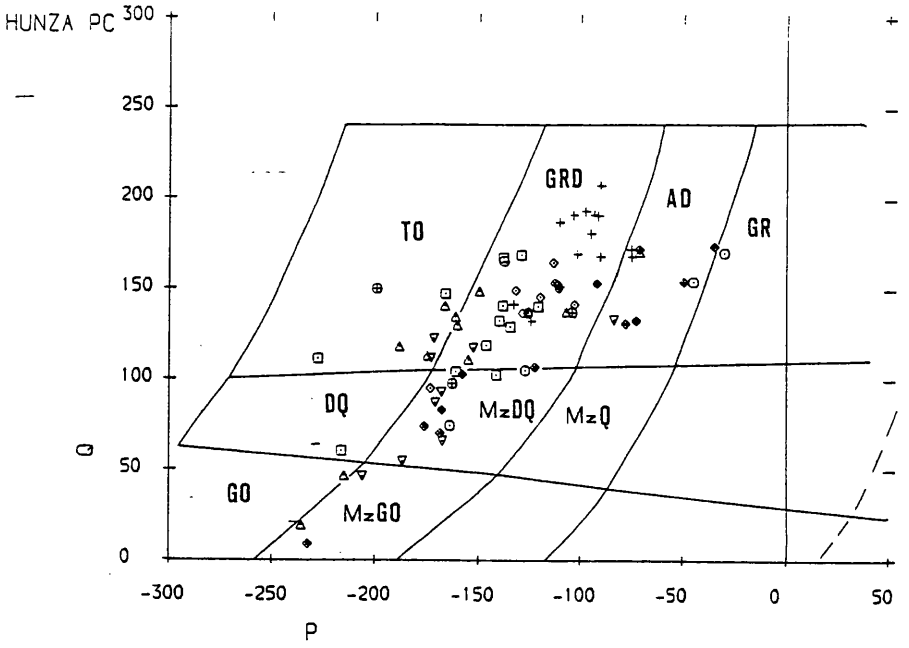

Figure 4.10(a): Debon and Le Fort (1982) classification diagram for the main 95Ma phase of the HPC. P = K-(Na+Ca); Q = Si/3-(K+Na+2Ca/3); TO, tonalite; GRD, granodiorite; AD, adamellite; GR, granite; DQ, quartz diorite; MzDQ, monzo-quartz diorite; MzQ, quartz monzonite; GO, gabbro; MzGO, monzo-gabbro.

Figure 4.10(b): AFM Trend for the HPC first phase

A = Na_2O+K_2O

F = Fe_2O_3

M = MgO

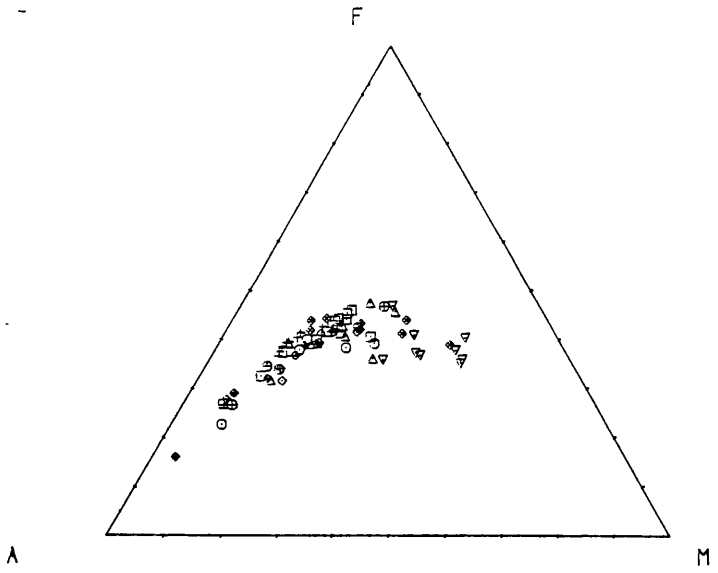

+ NORTHERN GRD
△ GULMIT GRD
▽ GULMIT QZ.DI.
⊡ N OF MIX. ZONE
◇ S OF MIX. ZONE
⊙ S. CONTACT
◆ GRD. SHEETS
⊕ AUGEN GNEISSES
◆ XENOLITHS

Figure 4.11: 'Harker-type' biaxial plots for the main Cretaceous phase of the Hunza Plutonic Complex (HPC). (Major elements).

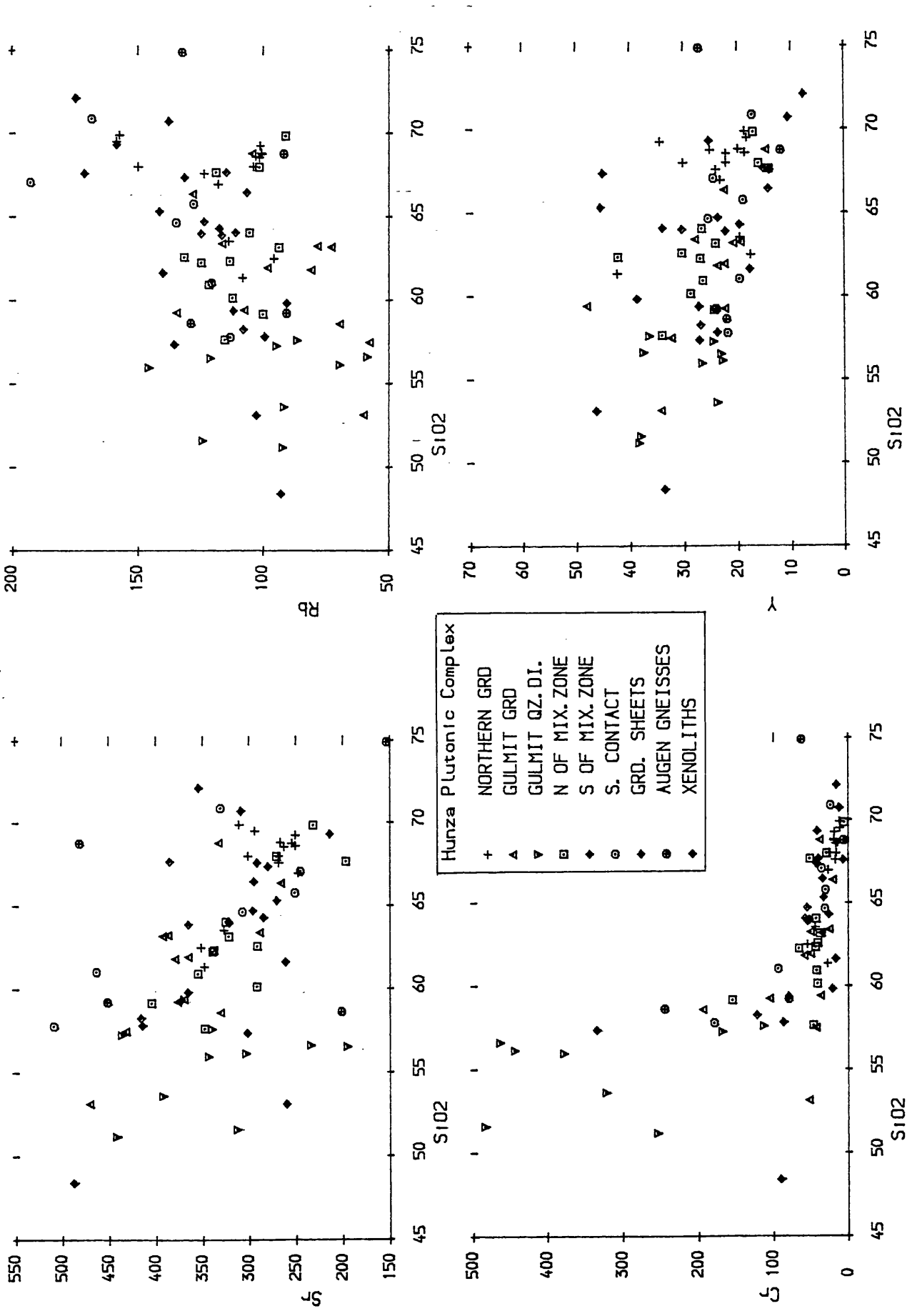

Figure 4.11: continued. (Trace elements).

Rock No.	B8	B16	B52	B111	B115	K203	BG4
Type	QzDi	QzDi	Grd	Grd	Xen	Grd	Grd
SiO2	57.2	57.5	63.6	68.1	59.9	60.3	67.0
TiO2	1.05	0.69	0.77	0.69	1.01	0.73	0.60
Al2O3	15.9	14.7	16.2	15.4	16.2	16.2	14.8
Fe2O3	8.2	7.1	5.8	4.4	6.8	5.5	4.8
MnO	0.11	0.13	0.09	0.07	0.10	0.09	0.09
MgO	4.8	5.1	2.4	1.4	2.6	3.0	2.0
CaO	6.7	7.4	5.1	3.9	4.8	5.1	4.1
Na2O	2.5	3.0	3.0	2.8	2.2	2.9	1.4
K2O	2.09	2.97	2.59	2.56	3.71	3.54	3.58
P2O5	0.22	0.23	0.20	0.18	0.21	0.34	0.11
LOI	0.76	0.45	0.42	0.98	2.81	0.83	0.35
Total	99.44	99.30	100.18	100.45	100.28	98.45	98.75
Trace elements in parts per million							
Rb	86.5	113.3	108.6	100.6	140.4	126.7	155.6
Ba	668.0	537.2	533.0	633.1	563.7	963.2	631.8
Th	23.4	18.0	13.4	9.8	9.5	11.5	13.5
Pb	13.8	24.1	-	-	-	11.5	29.0
Nb	13.5	12.0	16.9	12.9	15.1	10.9	15.2
Sr	340.0	509.1	319.5	254.4	261.5	529.3	253.5
Zr	188.5	96.7	161.5	183.2	146.3	176.3	160.7
Y	36.5	21.9	18.4	25.1	17.8	25.7	36.5
V	191.6	156.8	112.0	53.8	105.6	137.1	91.0
Cr	113.0	179.3	35.6	19.0	17.1	71.7	30.3
Ni	25.1	24.4	7.0	4.8	5.1	6.6	6.4
Cu	14.0	33.3	-	-	-	-	0.5
Zn	72.2	68.1	72.1	70.4	103.4	54.6	59.5
Ga	15.1	18.2	19.6	17.8	18.9	20.2	19.2
La	68.4	34.5	46.6	36.4	30.4	40.0	40.6
Ce	119.7	66.9	93.9	72.8	60.7	91.4	79.9
Pr	12.58	7.64	11.31	8.18	6.91	9.39	8.66
Nd	45.6	27.2	34.3	31.4	27.5	35.0	32.8
Sm	7.52	4.7	6.66	5.38	4.94	6.06	5.9
Eu	1.47	1.23	1.39	1.36	1.53	1.48	1.07
Gd	9.42	4.67	4.56	6.09	5.05	6.5	5.94
Dy	6.88	3.64	4.66	3.82	3.47	4.56	5.65
Ho	1.38	0.73	-	0.68	0.6	0.89	1.13
Er	3.79	2.37	2.61	1.97	1.59	2.54	3.7
Yb	3.25	1.93	2.11	1.34	0.97	2.06	3.81
Lu	0.58	0.4	0.29	0.23	0.13	0.4	0.6
$^{87}Sr/^{86}Sr$	-	0.7064	0.7113	0.7156	0.7157	-	-
$^{143}Nd/^{144}Nd$	-	0.51255	0.5122	0.51209	-	-	-

Table 4.2: Representative analyses from the calc-alkaline phase of the HPC, Khunjerab (K203), and the Batura pluton (BG5). All analyses by XRF techniques except for the REE measured by ICP and the isotopic ratios by mass spectrometry (see appendix 1 for further details).

contain a lot of Sr. The xenoliths are all from the Gulmit/Northern granodiorite groups and are included as possible residual melting/fractionation assemblages being carried within the more acidic magmas.

Whether the groups represent the same magma or separate pulses of different magmas is debatable. The Gulmit granodiorite and quartz diorite are intimately related in the field and so it is likely that they belong to the same trend. However, these two groups interfinger with the group identified as 'North of the mixing zone' and this could be interpreted as indicative of two magma pulses. No field evidence was seen to suggest that the groups south of the mixing zone represented a different magma to the group north of the mixing zone, but it is possible that the Northern granodiorite is a separate magma on the basis of its homogeneous geochemical signature. Additionally, the undeformed nature of the sheets outside the HPC compared to the strongly deformed augen gneisses indicates that these two groups represent two magmas intruded at different times.

With the likelyhood of different magma pulses it has to be considered that the trends seen might simply be a consequence of all the groups having similar signatures because of their calc-alkaline nature. However, the trends cannot be related to mixing of two magmas since they show changes in direction during evolution. For the same reason, the simple liquid-restite mixing trends of White and Chappell (1977) can be ruled out. The problems of modelling granitic liquids are discussed in greater detail in chapter 6.5.a. For the purposes of this chapter it will be assumed that the data represent a single trend. More data, particularly detailed isotopic analyses, is needed before the overall trend can be confidently split up into discrete magmatic phases, which can then be modelled individually. However, the uniformity of the general trends suggests that, if there are separate magmas, then they are all controlled by roughly the same processes which are modelled below.

The trends seen in granitoid plutons can often be explained in terms of either partial melting or fractional crystallisation, although neither mechanism need be mutually exclusive. One of the major arguments against fractionation was the lack of observed cumulate bodies that should be present due to crystal settling.

However, granitoid magmas are generally too viscous to allow crystal settling and fractionation probably proceeds via in situ growth of crystals which squeezes out the remaining liquid towards warmer parts of the crystallising body (filter pressing; e.g. Tindle and Pearce, 1981). As well as explaining the lack of cumulates, this mechanism allows the fractionation of phases such as biotite, which could not be explained by crystal settling. High level fractionation has been invoked by a number of authors to explain trends seen in calc-alkaline plutons (e.g. Stephens and Halliday, 1979; Pankhurst, 1979; Atherton et al., 1979; Thompson et al., 1984).

The high LILE/HFSE ratio and negative Nb anomaly of these granitoids suggests that the ultimate source for the magmas lies in the subducted slab as these features are related to stable phases in the slab (e.g. Tarney and Saunders, 1979). Wyllie et al. (1976) showed that compositions as acidic as the most evolved HPC granitoids cannot be in equilibrium with a mantle source, and must be produced by contamination or differentiation from a more basic magma. Therefore, if these granitoids are coming from the mantle it seems unlikely that they are directly related to partial melting. Additionally, since Sr increases from the adamellites towards the tonalites and quartz diorites, plagioclase must be stable in the source in order to make Sr a compatible element. Large degrees of melting would be required and it is unlikely that any source rock in the mantle contains sufficient plagioclase to do this. Thus, whilst a degree of partial melting amongst the tonalites and quartz diorites is not ruled out as an explanation for local trends, it is considered here that the simplest explanation for the main trend of the HPC is one of fractional crystallisation. If this cannot be modelled in terms of filter pressing, i.e. only observed phases are modelled, then an alternative mechanism will have to be sought.

On the Debon and Le Fort (1982) classification diagram (fig. 4.10(a)) most of the rocks cluster in the granodiorite field with the more basic rocks trending through quartz monzodiorite towards monzogabbro. There is some scatter into the tonalite and adamellite fields. The first point to be noticed is the calc-alkaline trend defined on both the AFM (fig. 4.10(b)) and the Debon and Le Fort (1982) characteristic mineral plot (fig. 4.12) by the HPC. Together with its calc-alkaline mineralogy of hornblende, biotite ± cpx and

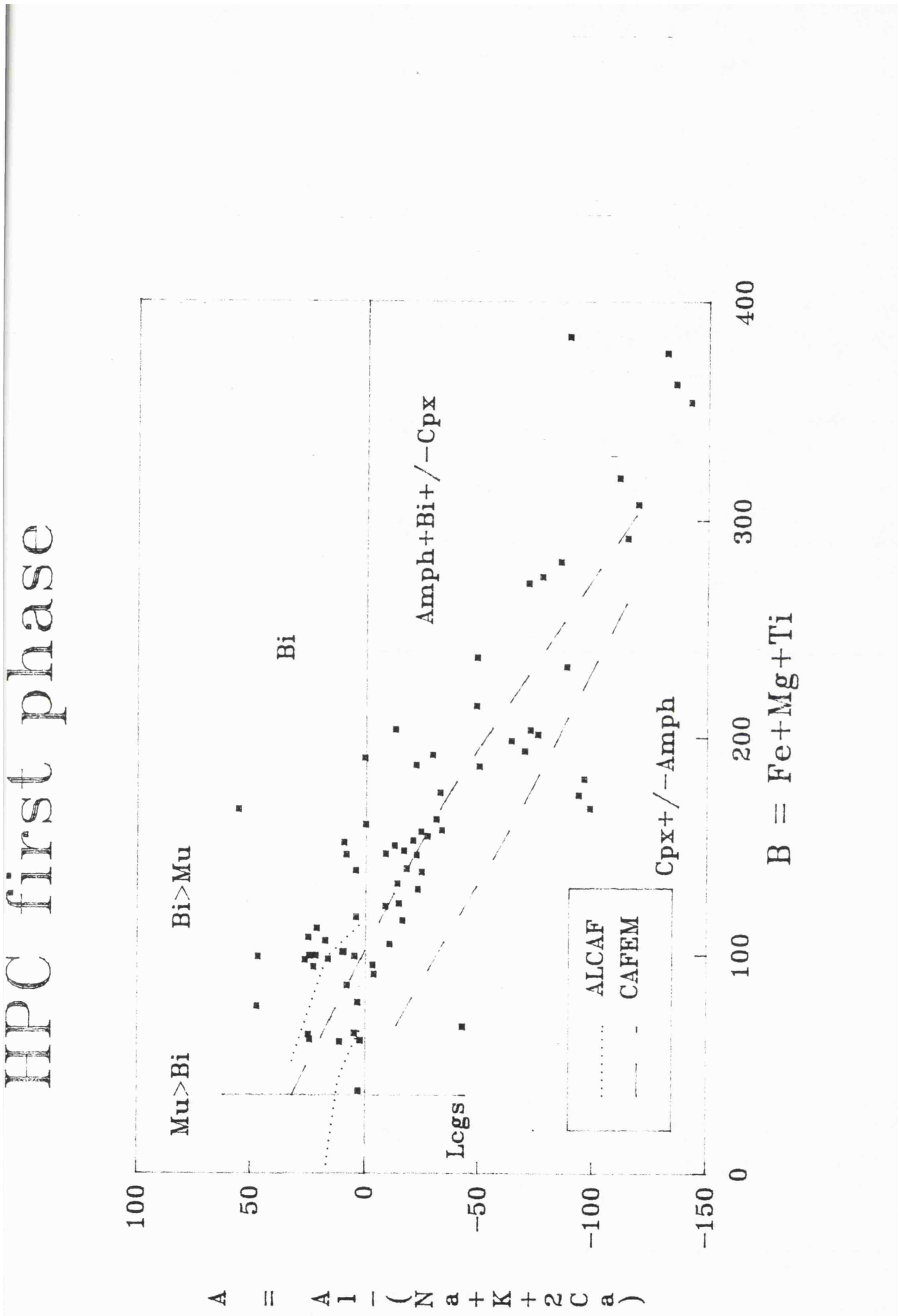

Figure 4.12: Debon and Le Fort (1982) characteristic mineral diagram for the main Cretaceous phase of the HPC which defines a cafemic (CAFEM) or calc-alkaline trend.

its high LILE/HFSE ratio (see later) this confirms that the Cretaceous phase of the HPC has a subduction-related signature. Secondly from all the major element plots as well as the AFM and classification plots it can be seen that whilst the Northern granodiorite is a very homogeneous group always plotting near the end of each trend, the Gulmit granodiorite and diorite plot near the mafic end of trends, thus negating the observation of Debon et al. (1987b) that acidity in the HPC increases northwards with structural height. In their model they considered the HPC to be a single magma pulse whereas it seems more likely that at least two and possibly three pulses are involved.

Considering the major element plots (fig. 4.11) CaO decreases at a constant rate through the crystallisation of amphibole, plagioclase ± clinopyroxene (cpx) and indicates that if there are any changes in the crystallising assemblage then the CaO/SiO_2 ratio remains the same. Al_2O_3 is scattered initially but shows a slight increase and then starts to decrease above 60% SiO_2. For CaO to decrease and Al_2O_3 to increase clinopyroxene must be crystallising since this is the only phase with a large Ca/Al ratio. Above 60% SiO_2 plagioclase and/or amphibole must become dominant for Al_2O_3 to decrease. MgO shows a steep initial depletion until 60% SiO_2 when it decreases more gradually and this is consistent with pre-60% SiO_2 fractionation being dominated by cpx and/or amphibole and post-60% SiO_2 fractionation being dominated by plagioclase ± hornblende and biotite. TiO_2 and Fe_2O_3 show continuous depletion due to removal first of cpx and then hornblende and biotite together with sphene. A steeper depletion in both elements above 67% SiO_2 is probably the result of the appearance in the crystallising assemblage of ilmenite ($FeTiO_3$). Na_2O and K_2O are scattered but the general trend is one of increasing alkalis with silica. Na_2O gives flatter patterns possibly as a result of buffering by crystallising plagioclase.

Most of the trace element data is scattered but Cr, Ni, Sr and Y show decreasing, compatible trends, whilst Rb, La, Zr, and Ba show scattered increases with increasing silica (fig. 4.11). Sr does not show a decrease until 60% SiO_2 following the same pattern as Al_2O_3 indicating the importance of plagioclase (D_{Sr}=6.0) as a crystallising phase above this silica value. Both Cr and Ni show strong depletion prior to 60% SiO_2 and then a more gradual decrease. Ni depletion is

usually associated with olivine crystallisation but no olivine is seen in the HPC and olivine could not be in equilibrium with the more acidic rocks in the sequence. Cpx is therefore probably responsible for the strong depletions in the basic rocks (D_{Ni}=2.6, D_{Cr}=8.4 for cpx, Henderson, 1984). However, both Ni and Cr still have bulk D values >1 above 60% SiO_2 and, as with olivine, cpx cannot be in equilibrium with the liquid at such silica levels (see above; 4.3.b: no. 5), and so other phases such as hornblende (D_{Cr}=1.6) and biotite (D_{Cr}=19, Henderson, 1982) must be removing these elements. Y is probably being removed in amphibole (D_Y=1.0) and possibly sphene.

The above evidence points to three main fractionating assemblages controlling the evolution of the HPC. The proportions of minerals in these assemblages may change from group to group but not markedly enough to significantly change the general bulk distribution coefficients of elements within each assemblage. The most basic rocks are controlled by clinopyroxene fractionation, probably together with amphibole and plagioclase. Above 60% SiO_2 cpx stops crystallising and plagioclase becomes dominant with amphibole and biotite. Because most of the samples have >60% SiO_2 this is the dominant fractionating assemblage within the HPC. Above 67% silica ilmenite starts to crystallise. Apatite and sphene are probably important minor crystallising phases in all three assemblages and quartz and K-feldspar may become more important at the more acidic end of the trends.

A few basic points may be assumed from the trace element data. One method of calculating crystallising proportions is to calculate a number of bulk distribution coefficients and use these to derive a series of simultaneous equations with mineral proportions being the unknown variables. For the main crystallising assemblage B20 and B25 from the southern contact were taken and using the Rayleigh fractionation equation the concentrations in B20 were taken as C_o and those in B25 as C_1. On the Zr vs. SiO_2 plot (fig. 4.11) Zr appears to be very incompatible between these two rocks and so D_{Zr} was assumed to be zero. Therefore, the degree of fractionation, F, can be calculated and following this bulk D values were calculated for the least scattered trace elements, Ni, Cr, Sr and Rb. Unfortunately distribution coefficients for Ni could not be found in the literature for amphibole, biotite or plagioclase but assuming that these three

phases control the distribution of the other three elements, three simultaneous equations can be set up and solved for three unknowns:

Rayleigh fractionation $\frac{C_l}{C_o} = F^{(D-1)}$

$B25 = C_l$: $B20 = C_o$

For Zr $\frac{140.8}{157.4} = \frac{1}{F}$ F=0.89

Considering elements which show the least scattered trends,

Using F=0.89, $D_{Sr} = 2.72$, $D_{Cr} = 1.25$, $D_{Rb} = 0.61$, $D_{Ni} = 2.38$

Using distibution coefficient data from Henderson (1982):

(6.0*x) + (0.57*y) + (0.3*z) = 2.72 Sr (1)
(0.2*x) + (1.6*y) + (19.0*z) = 1.25 Cr (2)
(0.1*x) + (0.25*y) + (3.5*z) = 0.61 Rb (3)

where: x = plagioclase proportion
y = amphibole proportion
z = biotite proportion

However, these equations do not solve to give reasonable answers (e.g. y = -6.96). This is presumably due to two factors:

a) The assumption that $D_{Zr} = 0$ is incorrect leading to a miscalculation of F.
b) The D values for individual minerals from Henderson (1982) are not valid for the HPC. D values change with temperature, pressure and composition of the melt which can result in a wide scatter of values (Henderson, op.cit.). The only way to be confident that a set of D values is suitable is to measure them for each suite of rocks, and this is time consuming and not very feasible. The high D_{Cr} of 19.0 in biotite is responsible for the large negative value of y in these equations suggesting a lower distribution coefficient is more likely in the HPC. Using the simplistic assumptions that all Rb enters biotite and all Sr enters plagioclase gives D_{Cr} for biotite from the

above equations as 3.2.

A least squares modelling technique of major elements based on the method of Wright and Doherty (1970) failed to give consistent results for the main intermediate assemblage. The model for B20 - B25 gave a negative proportion for amphibole and biotite was the main fractionating mineral. This is probably partly a consequence of scatter in the data, and partly due to probe analyses not accurately reflecting the continually changing composition of the crystallising phases. Calculated errors were, however, small because a large number of phases were involved. Because of this it was decided to reduce the number of phases and variables and use a modelling technique from Cox et al. (1979).

Ten analyses from the main intermediate trend of the HPC representing rocks collected all the way through the batholith were selected. On biaxial plots of major elements against silica, least square best-fit lines with 95% confidence limits were drawn through the data points. The slope and standard error on the slope were calculated for each line. Only the three main phases probably controlling fractionation i.e. amphibole, biotite and plagioclase were considered and the three least scattered major elements controlled by these phases, CaO, MgO and Fe_2O_3, were used. Sphene and apatite are considered to be present in too small a quantity to have a major effect on these elements. For each of these oxides only one rock out of the ten lies outside the 95% limits for the best fit line (fig. 4.13). Also plotted on the graphs are averages and standard errors of 28 plagioclase, 19 biotite and 18 amphibole probe analyses from similar rocks. Where the best fit lines cut the triangles formed by the three phases, ratios and errors on ratios were measured between phases. These ratios were used to plot the best fit lines on a plagioclase-biotite-amphibole equilateral triangle (fig. 4.13). The three lines from the three graphs did not meet at a single point but lines from the $CaO-SiO_2$, $MgO-SiO_2$, and $CaO-Fe_2O_3$ graphs did giving a fractionation assemblage of 13% biotite, 43% plagioclase and 44% amphibole. When these proportions are inserted into eqns. (1) and (3) above they give bulk D values of 2.87 and 0.61 which agree well with the calculated D values (2.72 and 0.61 respectively). In eqn. (2) these proportions would give D_{Cr} for biotite as 3.5. The lack of correlation of the Fe_2O_3 line might be a result of having to treat

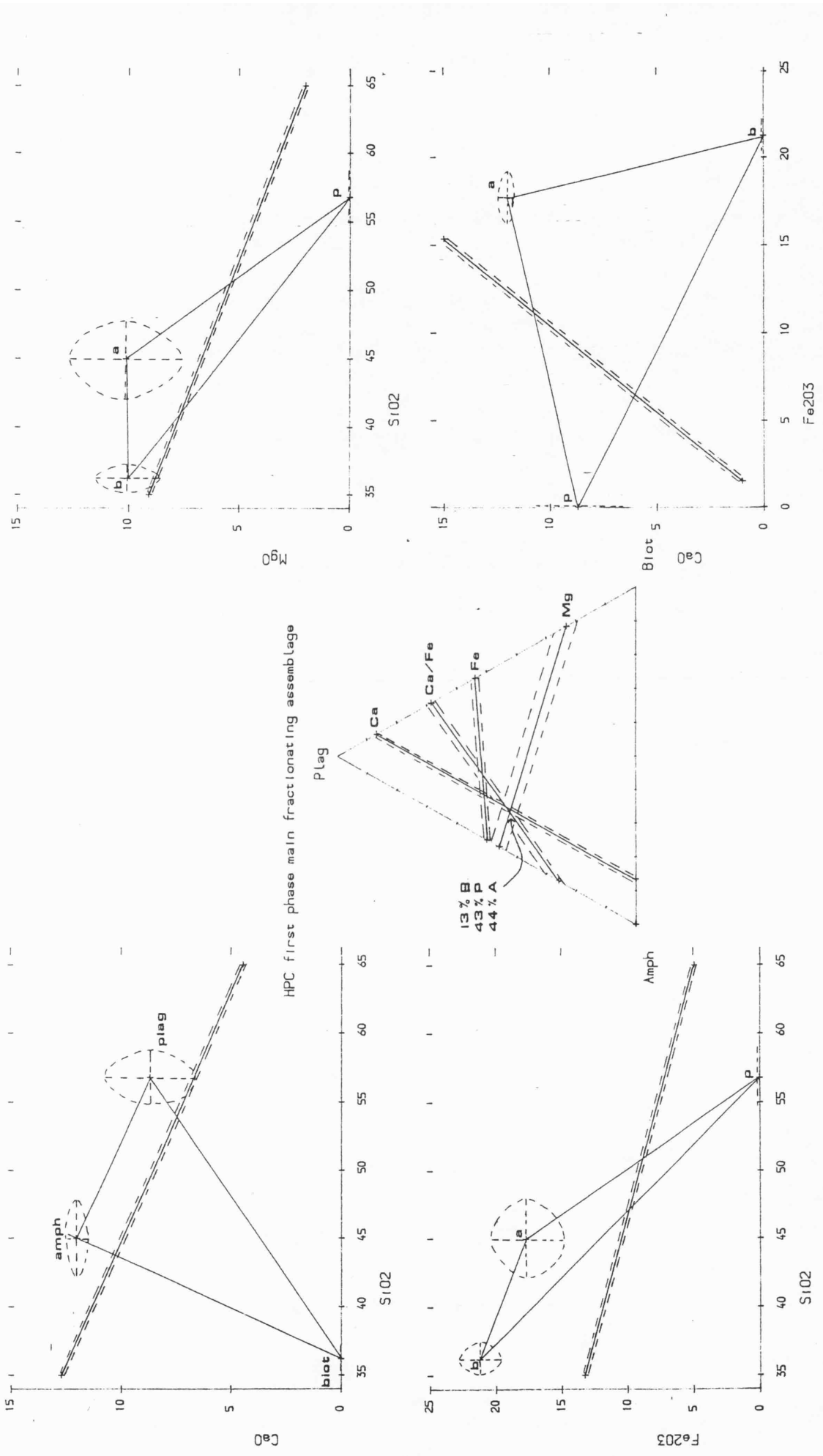

Figure 4.13: Major element modelling for the main trend of the HPC. The ratios of where the best-fit lines with errors (dashed lines) cut the phase triangle on the individual graphs are plotted on the central triangle. (B = biotite, A = amphibole, P = plagioclase).

all the iron as Fe^{3+} as no FeO/Fe_2O_3 ratios have been measured for these rocks.

Unfortunately, this method does not yield a solution for the first fractionating assemblage assuming the three major phases are clinopyroxene, plagioclase and amphibole. This may be due to the greater scatter of data at the basic ends of the trends, or due to biotite also being a fractionating phase. Figure 4.14 shows a spidergram of sample B20 normalised to B17 from the southern contact. The lines show a Rayleigh fractionation model using the assemblage obtained above and D values from Henderson (1982). This model shows a good fit for all the trace elements except La and Ce, and the major element K. The discrepancies in the REE can be explained by modelling the evolution of the REE patterns in figure 4.15. This figure shows the pattern for B99 (crosses) and the range of values for eight other samples from the HPC. In order to lower the LREE during fractionation a small amount of allanite has to be added to the above fractionating assemblage (modelled liquid is shown by squares). Some samples (B8 and B9) do not show this LREE depletion (fig. 4.16) and their evolution from B99 can be modelled approximately by 15% fractionation of 30% cpx, 20% amphibole and 50% plagioclase followed by a further 20% fractionation of 20% cpx, 30% amphibole and 50% plagioclase. These results may be an approximation of the first fractionating assemblage.

4.4.b: The HPC mixing zone.

The mixing zone within the HPC (chapter 3.4.a) consists of an igneous melange of rock-types that appear to have been derived from a protolith of the calc-alkaline granodiorites described above. Because the rocks in this 2km wide zone have obviously been affected by later processes, they are considered separately from the rocks forming the main trends of the HPC.

At first sight, the mixture of granodiorites, acidic and basic gneisses, feldspar megacrystic granodiorites and pegmatitic sweat-type layers resemble the development of migmatites. However, the localization of this zone suggests that the features are not entirely related to the c.45ma deformation event, otherwise the whole area would be expected to have been affected in the same way. Temperature

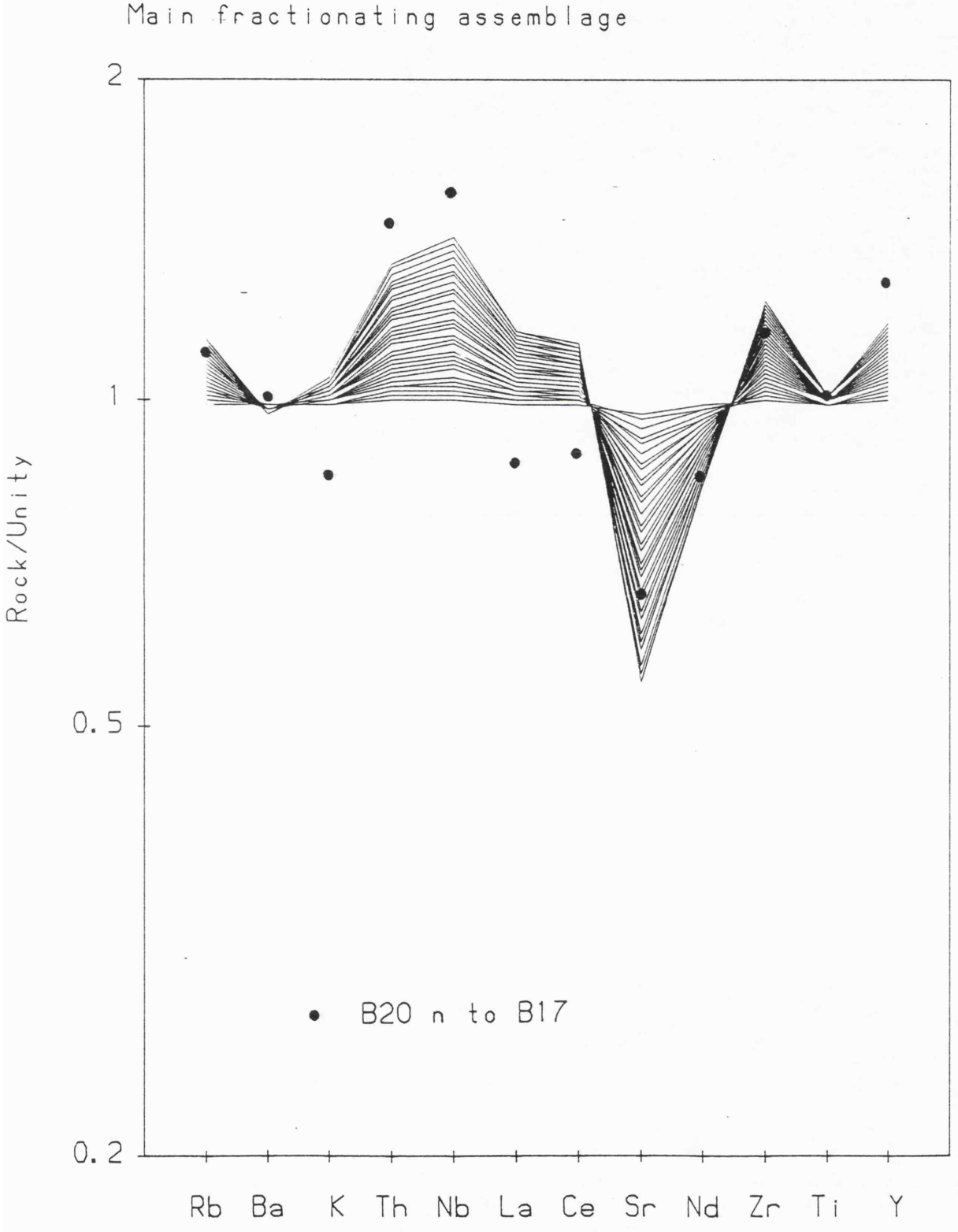

Figure 4.14: Modelled Rayleigh fractionation assemblage of 43% plagioclase, 44% amphibole and 13% biotite starting from unity and increasing in 1% increments up to 30%. Dots show evolved sample B20 normalised to B17 from the southern contact.

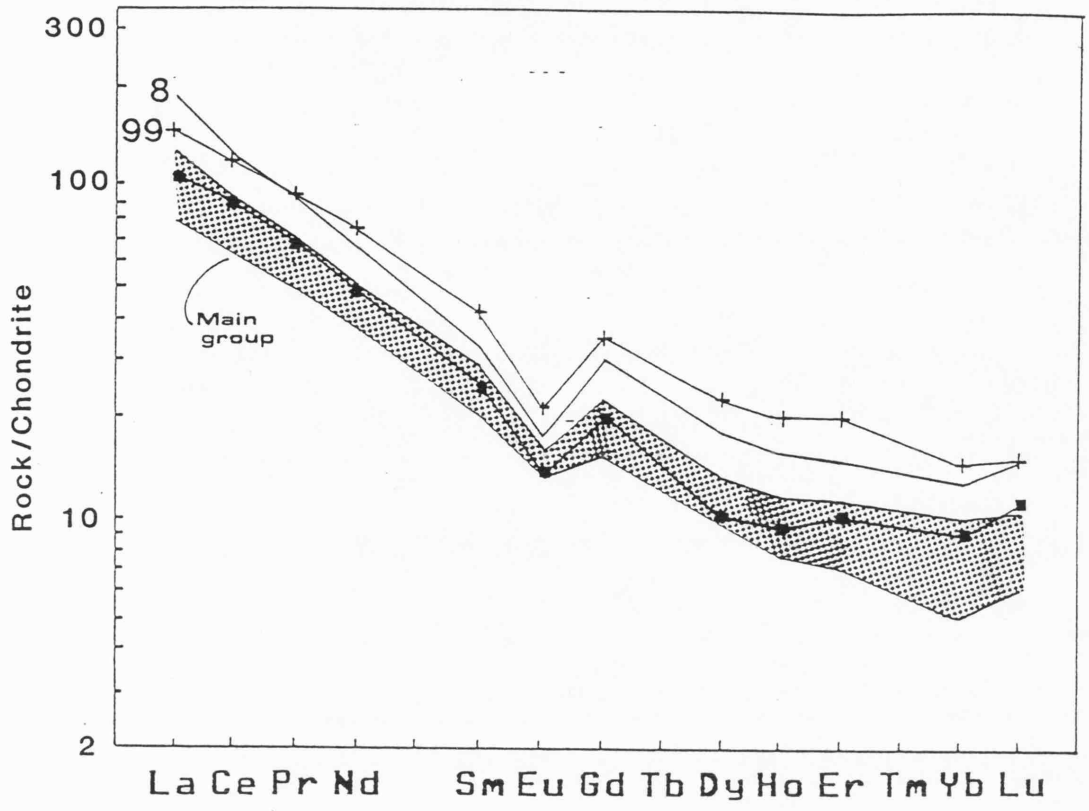

Figure 4.15: Main REE patterns for the 95Ma phase of the HPC. Shaded area contains eight analyses. Crosses show sample B99 from Gulmit, line shows B8, and the squares show the modelled fractionation liquid from B99 discussed in the text.

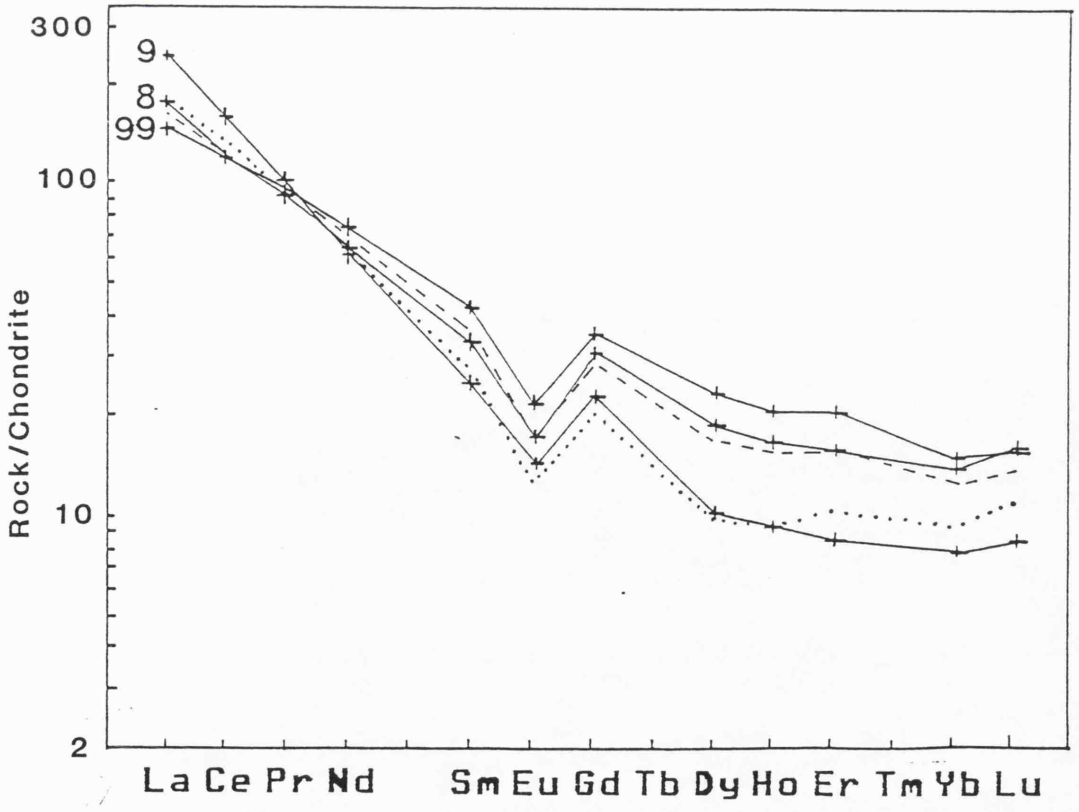

Figure 4.16: REE patterns for samples B99, B8 and B9 from the Gulmit area within the HPC. Dashed line represents 10% fractionation of 30% clinpyroxene, 20% amphibole and 50% plagioclase from B99. Dotted line represents a further 20% crystallisation of 20% clinopyroxene, 30% amphibole and 50% plagioclase.

estimates from two samples (BPS33 and B83) using the garnet-biotite geothermometer of Hodges and Spear (1982) give slightly higher values than the country rocks to the south (692-710°C compared to 626-684°C at 6kb; see chapter 6.4 for further details). The aplite sheets intruding the HPC (chapter 6.5.b) appear to be centred on the mixing zone, and perhaps extra heat from the intrusion of these magmas caused migmatitic development in the granodiorites, which were already hot due to the regional metamorphism. That the development of this zone was syn-deformational is indicated by some layers being parallel to the foliation whereas others are folded. It was suggested in chapter 3 that magma mixing between the aplite sheets and the granodiorites might have generated the features, but no chemical evidence has been found to support this. The simplest explanation appears to be separation of the pegmatite sweats from the granodiorite leaving the gneissic layers as palaeosomes. The feldspar megacrysts in some samples could be related to K-rich fluid activity.

In theory, such a hypothesis should be easily tested using chemical data, with the basic gneisses and pegmatite sweats lying on opposite ends of trends through the protolith granodiorite. However, whilst the pegmatite sweats always lie at the silica-rich end of trends, the basic gneisses tend to plot in the same place as the host granodiorites, and the acidic gneisses plot between the two groups (fig. 4.17). Additionally, a pegmatite sweat sample (B85) gave a Sr isotope ratio of 0.71 whilst a feldspar megacrystic granodiorite collected next to it (B84) gave a value of 0.718, showing that the two cannot be related by a simple separation process. However, because of the heterogeneous Sr isotope values found in the HPC this does not preclude the sweat coming from another part of the granodiorite.

Metamorphic minerals such as garnet are found locally in both the gneisses and pegmatite sweats, but generally the difference between layers is generally only in the proportion of the same mafic phases, particularly biotite. Therefore, the samples give linear trends on biaxial plots of major element oxides (fig. 4.17). Most trace elements are scattered but Cr shows a similar trend to that of the main HPC group (see above). On the Sr vs. CaO graph the aplite sheets lie at higher Sr abundances showing that the trends are not related to mixing of this magma.

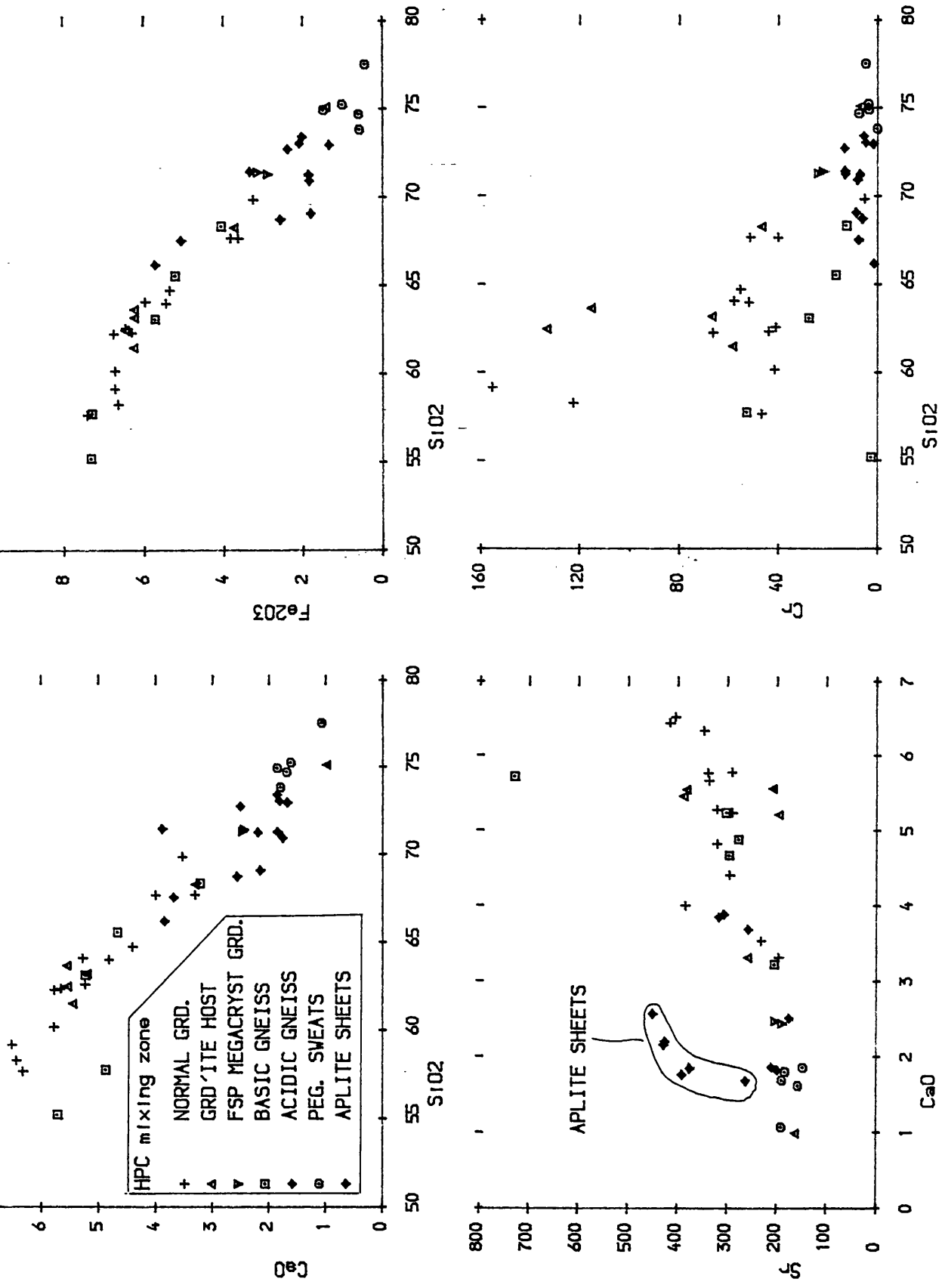

Figure 4.17: 'Harker-type' variation diagrams for the mixing zone within the HPC. Note aplite sheet field lies off the main trend on the Sr vs. CaO graph precluding magma mixing of this group.

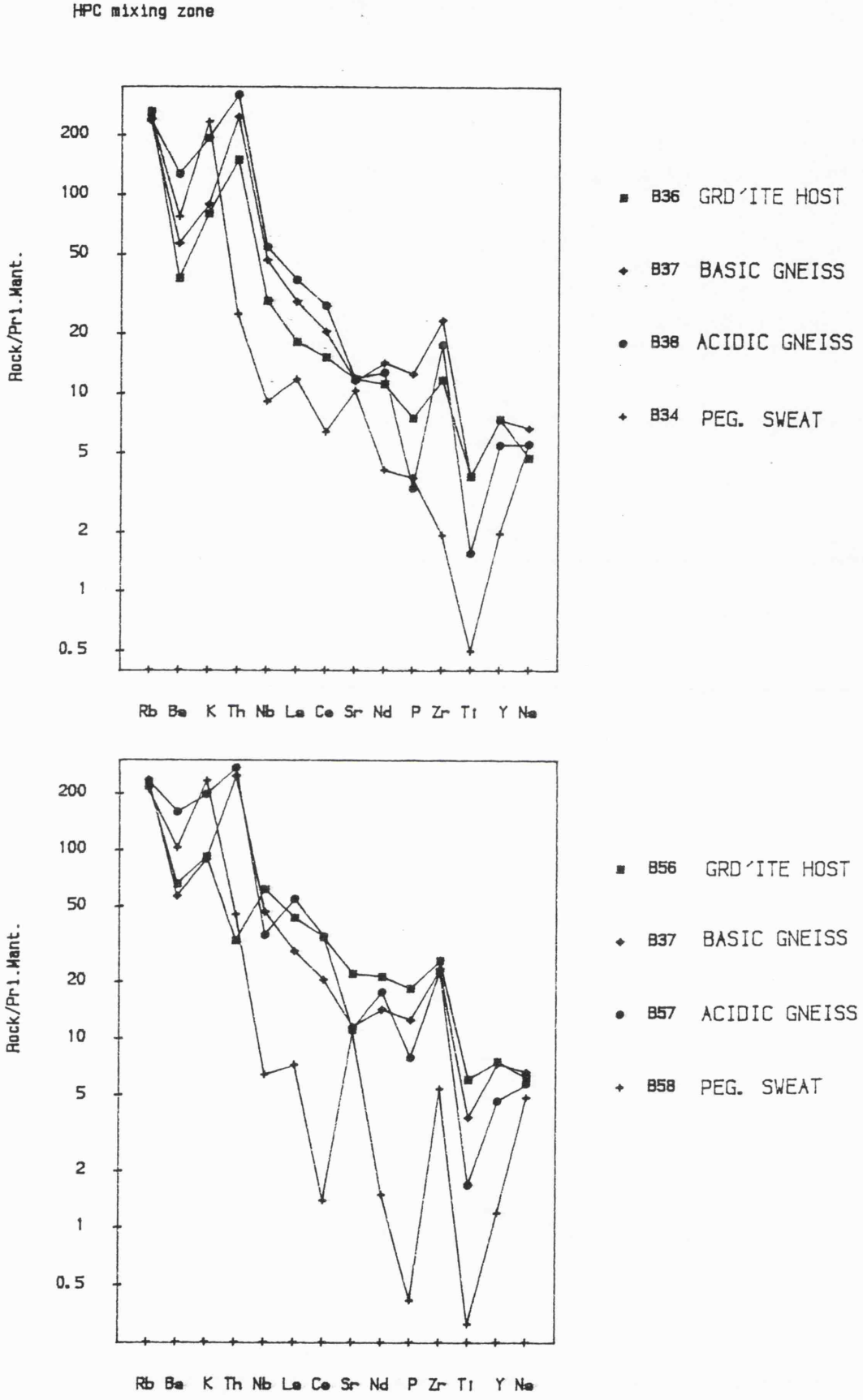

Figure 4.18: Spider diagrams for related lithologies in the HPC mixing zone. Note the positive Sr anomaly in the pegmatite sweats.

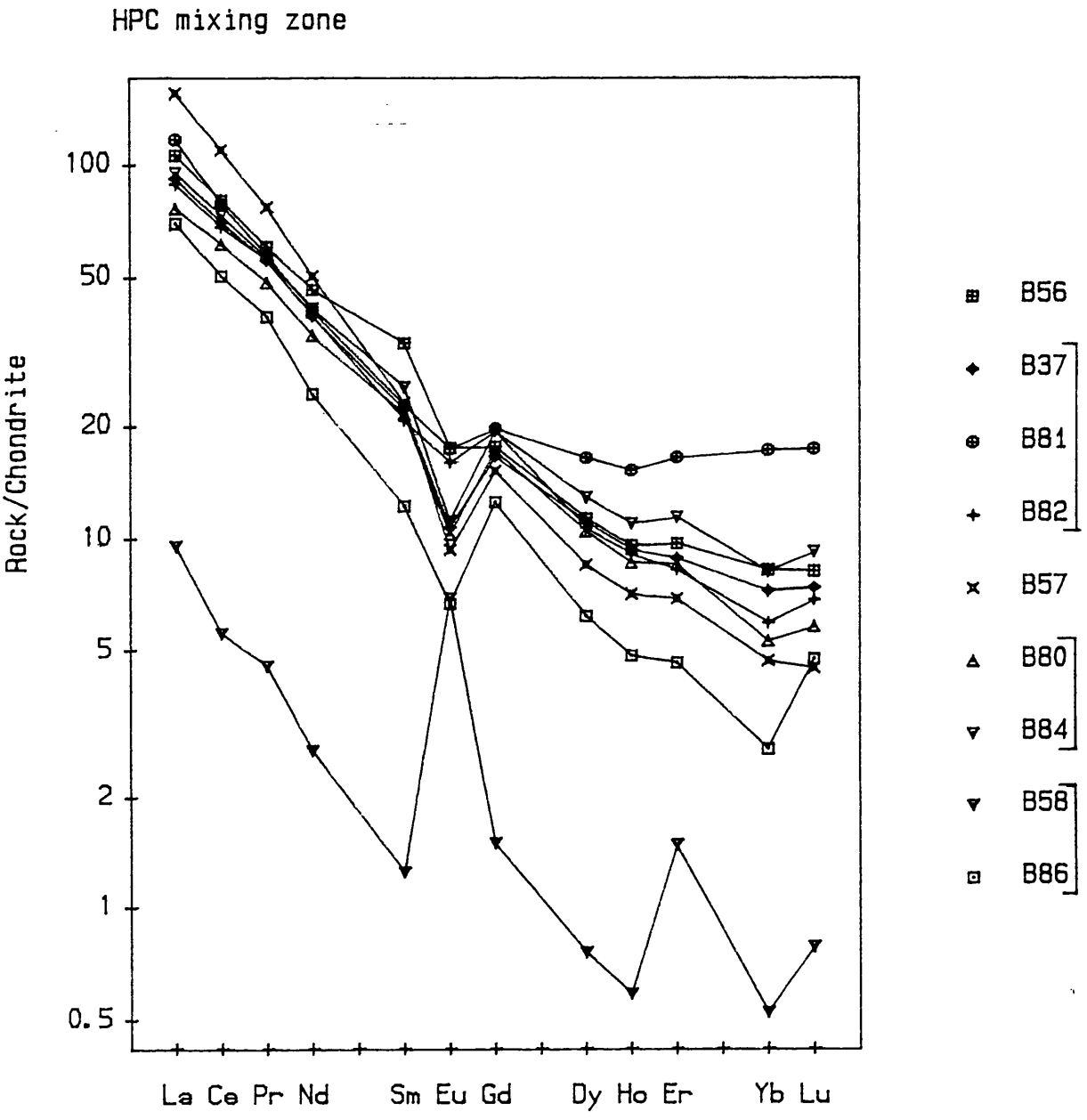

Figure 4.19: REE patterns for lithologies from the mixing zone of the HPC.

B56 = Host granodiorite
B37, B81, B82 = Basic gneiss
B57 = Acidic gneiss
B80, B84 = Feldspar megacrystic granodiorite
B58, B86 = Pegmatite sweats.

REE and spider diagram patterns (figs. 4.18 and 4.19) are not much help in resolving this problem. In general the pegmatite sweats are more depleted in most trace elements but there is no consistent variation between the gneissic layers and the host granodiorite. Both Sr and Eu show positive anomalies in the pegmatite sweats and have similar abundances to the granodiorites. This suggests that the pegmatite chemistry is controlled by the movement of the feldspar component, and because D<1 for most trace elements in feldspar the pegmatites are depleted. K and Ba show variable behaviour and this may relate to the fluid activity which caused the growth of the feldspar megacrysts. Rb is also fairly constant in all the rock-types and this suggests a bulk D value approaching unity, possibly controlled by the biotite in the gneisses. The LREE do not show much variation in the gneisses and granodiorites and the overall patterns are similar to those of the unaltered HPC granodiorites (fig. 4.19; cf fig. 4.14). HREE show more variation and the high abundances in B37 may reflect cumulus garnet in this sample.

Whilst the above does not rule out a separation process to explain the relationship between the rock-types, it would appear that the mechanism is more complex than is understood at present. As R.H. Dana stated, 'geology is a particularly alluring field for the premature interpretation of imperfectly understood data'. Much more data, particularly isotopic analysis, is needed before this author will be prepared to present a confident interpretation of this zone.

4.4.c: Khunjerab and Sost.

Whilst no dates are available on the Sost pluton it is included here as its similarity and close proximity to the Khunjerab pluton suggest that it belongs to the same period of magmatism. To confirm this, Sost and Khunjerab both lie on the same line at the alkali rich end of a calc-alkaline trend on an AFM diagram (fig. 4.20(b)). Both plutons have a similar mineralogy to the HPC being dominated by hornblende, plagioclase and biotite with lesser amounts of K-feldspar, quartz in the more acidic rocks and cpx in the basic rocks. On a Debon and Le Fort classification diagram (1982, fig. 4.20(a)) the Khunjerab rocks fall in the granodiorite and monzogranite fields except for the xenolith which borders the gabbro field. The Sost

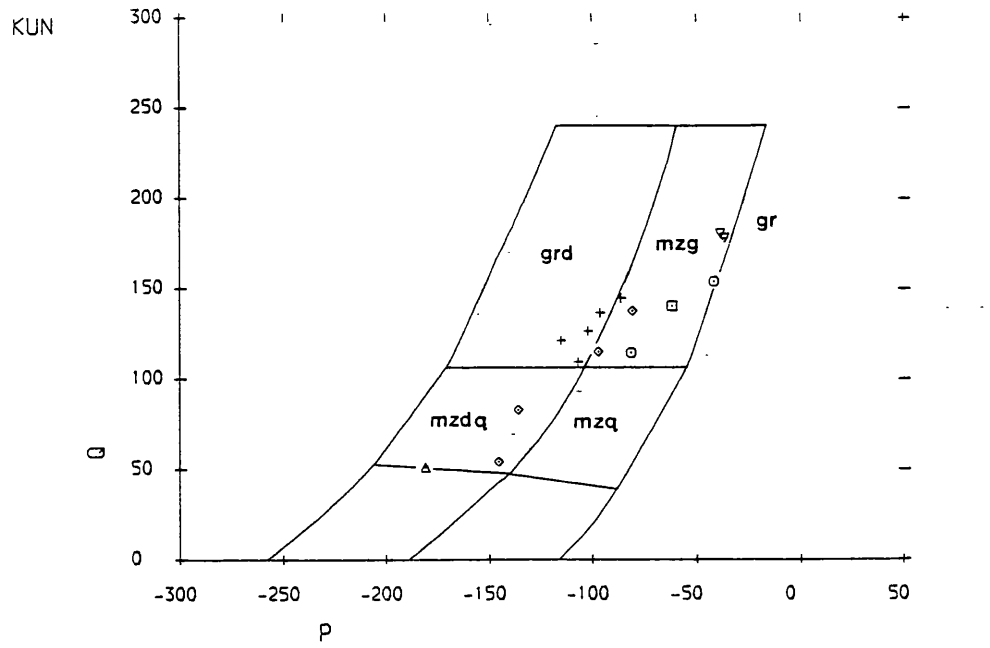

Figure 4.20(a): Debon and Le Fort (1982) classification diagram for the Khunjerab and Sost plutons (see below for key)
P = K-(Ca+Na); Q = Si/3-(Na+K+2Ca/3); grd = granodiorite; mzg = monzogranite or adamellite; gr = granite; mzdq = monzo-quartz diorite; mzq = quartz monzonite.

Figure 4.20(b): AFM Trend for Khunjerab and Sost.
A = Na_2O+K_2O

F = Fe_2O_3

M = MgO

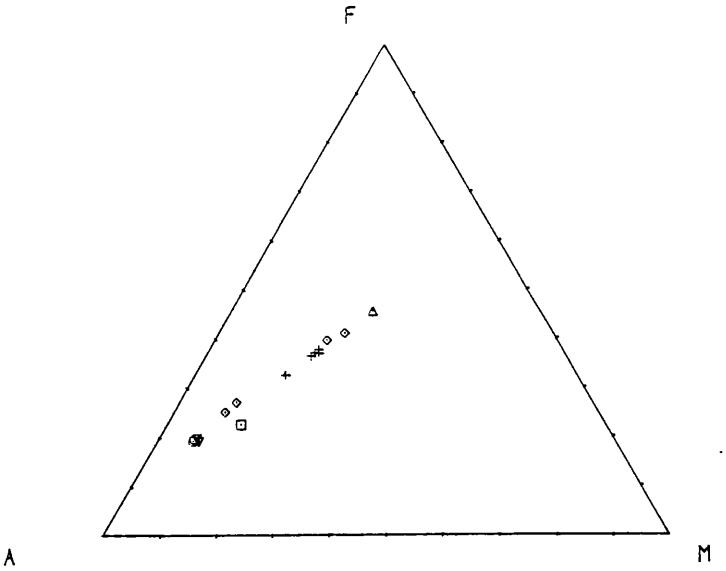

+ KHUNJ. GRANODIORITE
△ KHUNJ. XENOLITH
▽ KHUNJ. MZGRANITE
⊡ N. SOST SHAP TYPE
◇ N. SOST PLUTON
⊙ S. SOST MZG PLUTON

North Pluton trends from the quartz monzodiorite field to the monzogranite field, whilst the South Pluton lies in the monzogranite field.

On Harker variation diagrams, plotted against silica all elements show good trends (fig. 4.21). The Khunjerab and N. Sost plutons define different trends for many elements, particularly trace elements, and so represent different magmas. Similarly, the S. Sost and N. Sost 'Shap-type' granites often fall off both trends and so do not seem to be related to either of the main plutons. Because of the lack of samples for these two types they are not considered further. However, the Khunjerab monzogranites plot at the end of all the trends defined by the granodiorites and so these two lithologies may well be consanguinous.

For the same reasons as outlined for the HPC, the simplest explanation for the trends shown by the plutons is taken to be high level fractionation. Not surprisingly, considering their comparative mineralogies, the Khunjerab and N. Sost plutons show similar fractionation trends to the HPC. Both show constantly decreasing CaO, MgO, P_2O_5, TiO_2 and Fe_2O_3 and increasing K_2O. Although the lack of the kink seen in the HPC at 67% SiO_2 in the Fe2O3 and TiO2 trends suggests the crystallisation of ilmenite does not occur, this might also be due to a lack of data. The Al_2O_3 trend for Sost shows a slight increase until 60% SiO_2 and then decreases and this same trend in the HPC was attributed to a dominance of clinopyroxene in the initial fractionating assemblage.

Unlike the HPC, both plutons show a gradual decrease in Cr rather than a rapid initial depletion. This might be due to a lack of data at more basic silica values or it might indicate cpx is not as dominant as in the early stages of the fractionation of the HPC. Ni, Cr and V all decrease throughout fractionation suggesting they are taken into phases such as amphibole and biotite at high silica values (>60%). Sr decreases throughout fractionation suggesting plagioclase is important and, unlike the HPC, so does Ba suggesting K-feldspar is also fractionating. Ba is also taken up in biotite but Rb increases showing biotite cannot be a major fractionating phase (D_{Rb} for biotite = 3.5 in acidic magmas; Henderson, 1982). Nb decreases and this can be attributed to its removal in sphene. As in the HPC Zr

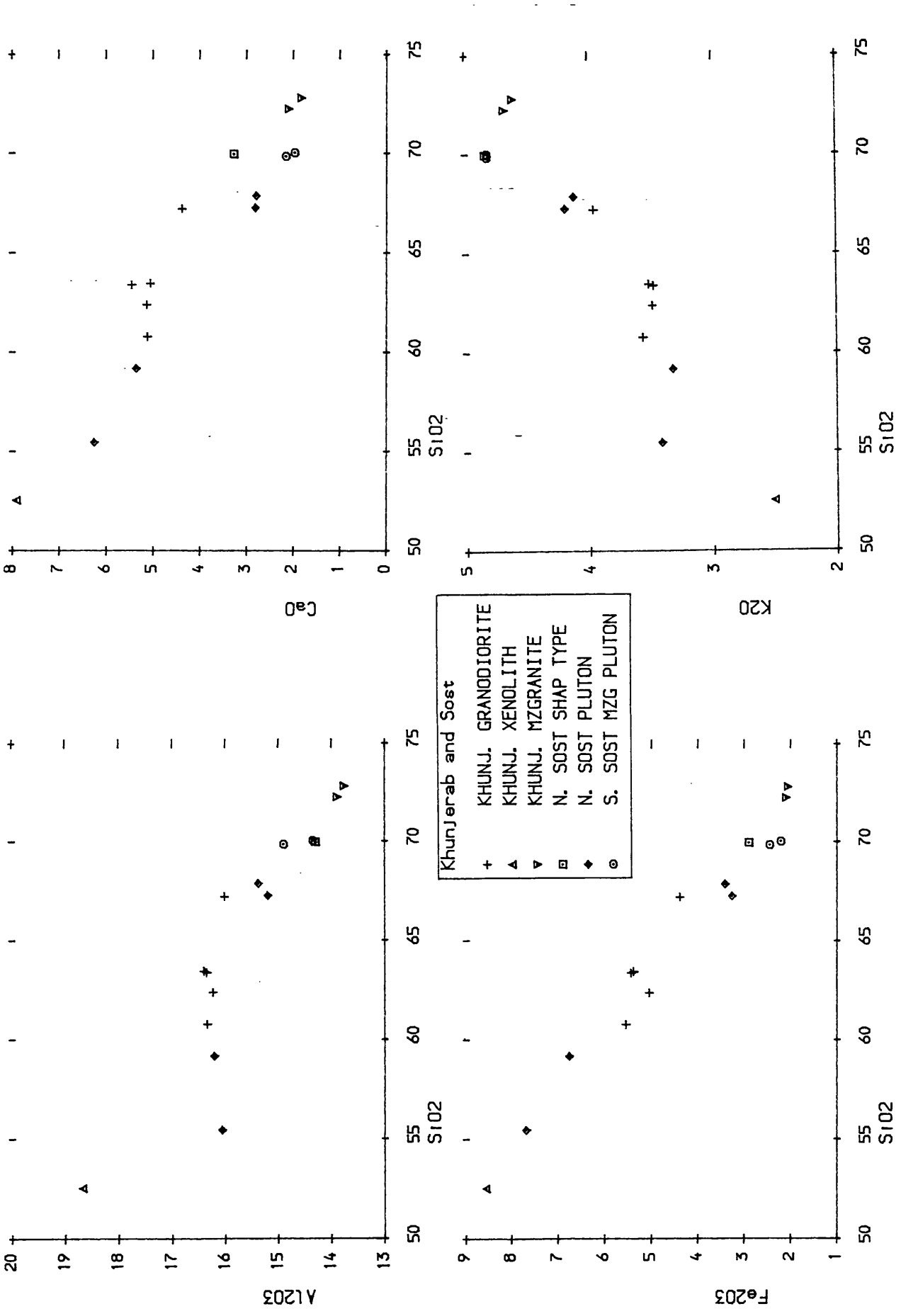

Figure 4.21: 'Harker-type' biaxial plots for the Khunjerab and Sost plutons (major elements).

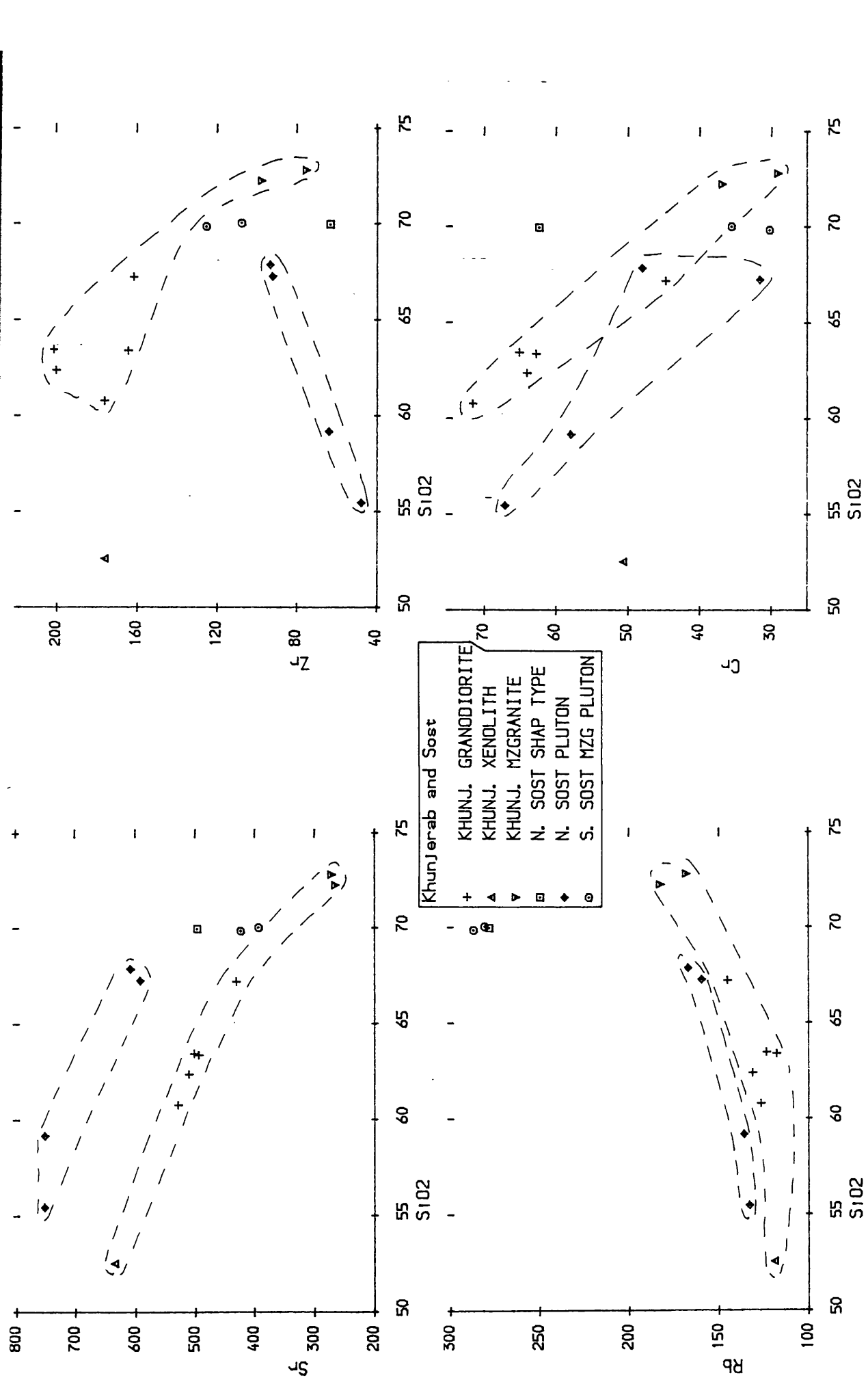

Figure 4.21: continued (trace elements). Note separate trends for Khunjerab and N.Sost, and lack of correlation of S. Sost samples.

increases in the N. Sost pluton, but it decreases in the Khunjerab pluton and so the magma must have been saturated in Zr so that zircon started to precipitate (Watson and Harrison, 1984).

Figure 4.22 shows logarithmic plots of Rb/Sr vs. Sr and Ba vs. Sr for the Khunjerab samples, after they have been normalised to the sample with the highest Sr abundances (K203). The best-fit lines for these two trends can be approximated to a fractionating assemblage of 30% K-feldspar, 40% plagioclase, 20% amphibole and 10% biotite. The inclusion of K-feldspar in the assemblage is supported by the decrease in Ba with increasing silica, and the greater modal abundance of this phase in Khunjerab when compared to the HPC (section 4.3). The REE patterns (fig. 4.23) show an evolving trend from K208 (a xenolith) to K203 and then on to K210 (a monzogranite). These conform with the above assemblage with the dashed lines showing modelled trends for fractionation of 27.9% K-feldspar, 40% plagioclase and 30% amphibole, with 1% apatite and sphene and 0.1% allanite being necessary to lower the LREE abundances.

Only four data points are available for the N. Sost pluton which precludes an accurate crystallisation model. However, the similar Harker variation diagrams and REE patterns (fig. 4.24; cf fig. 4.14) suggests a similar assemblage for Sost as that modelled for the main trend of the HPC.

4.4.d: Batura.

The Batura samples were collected from boulders on the terminal moraine of the Batura Glacier. Whilst representative lithologies were concentrated on, because the rocks were not seen in situ their relationships are unknown. The reason for collecting these samples is that similar samples collected by Debon et al. (1987b) gave an isochron with a younger age and lower initial Sr isotope ratio than the HPC (43±3Ma; Sr_i=0.7056). This suggests that a separate pluton may exist to the NW of the HPC, at the head of the Batura Glacier.

Because the relationships of the rocks are not clear, there is little point in modelling the trends shown by the samples, as more than one magmatic phase might be represented. Harker variation diagrams (fig. 4.25) show that the granodiorites tend to cluster, but

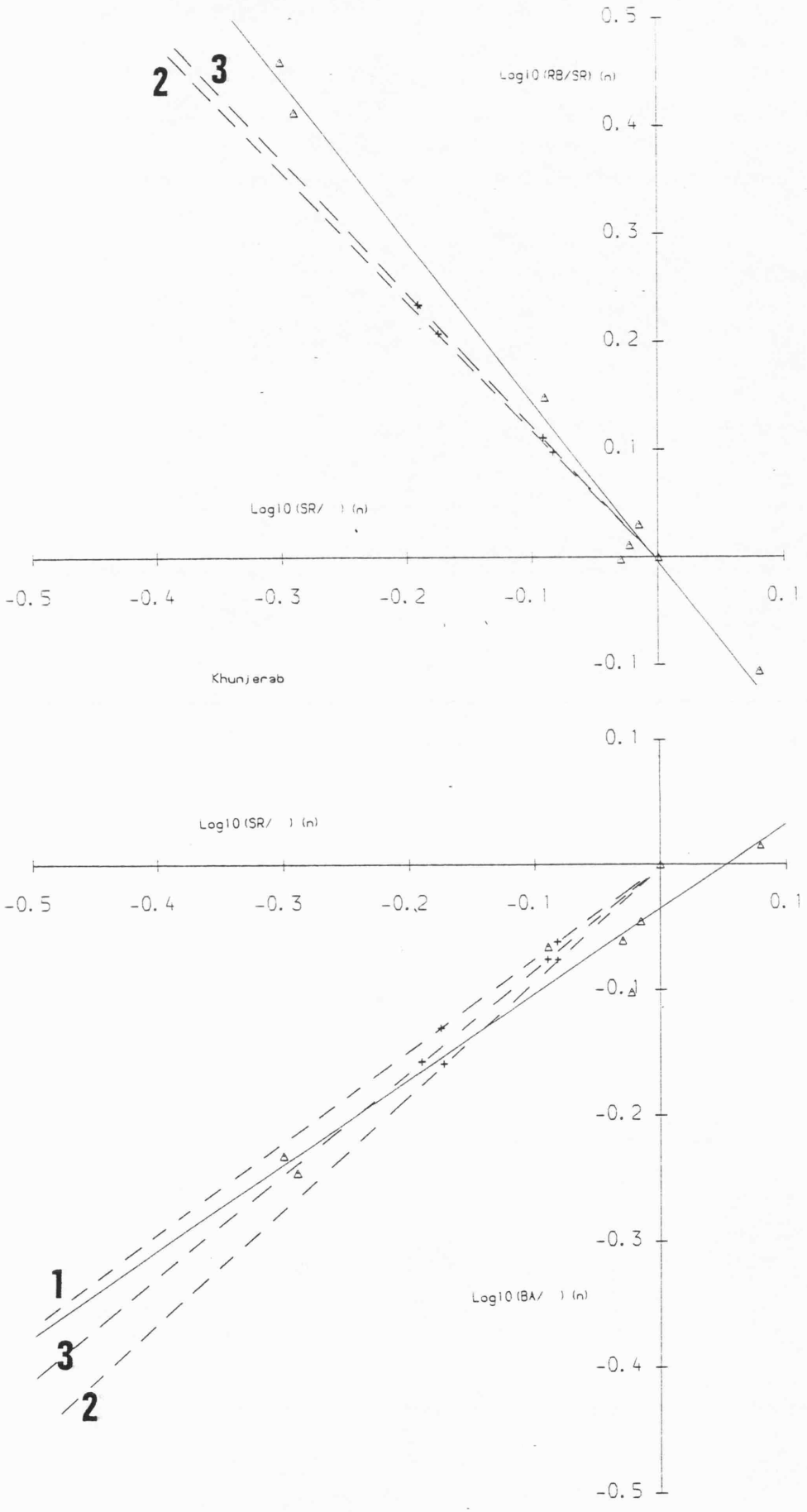

Figure 4.22: Log(Rb/Sr) and log(Ba) vs. log(Sr) quadrant plots for the Khunjerab pluton samples normalised to K203. Solid line is best fit to data. 1 = 20% amph, 15% biot, 45% plag, 20% Kfsp.
2 = 20% amph, 15% biot, 40% plag, 25% Kfsp.
3 = 20% amph, 10% biot, 40% plag, 30% Kfsp.
calculated using D values from Hanson (1978). Crosses represent 10% and 40% crystallisation away from the origin.

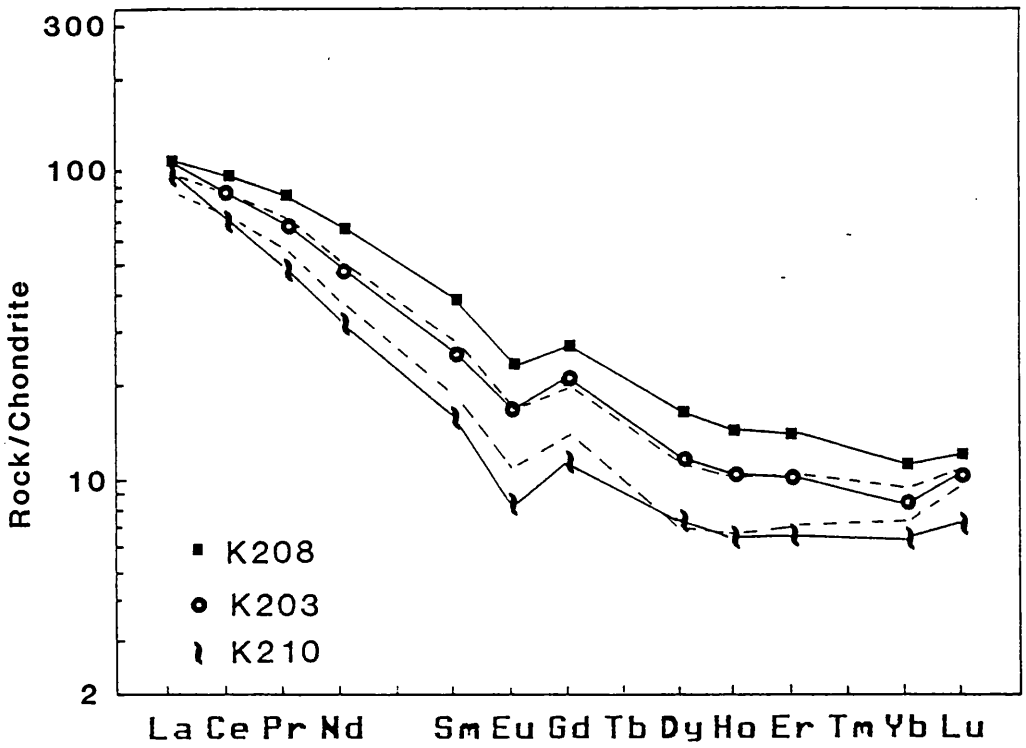

Figure 4.23: REE patterns for the Khunjerab pluton. K208=xenolith, K203=granodiorite; K210=monzogranite. Dashed lines represent 12% and then a further 15% fractionation of 27.9% Kfsp., 40% plag., 30% amph. and 1% apatite, 1% sphene and 0.1% allanite from sample K208. D values from Henderson (1984).

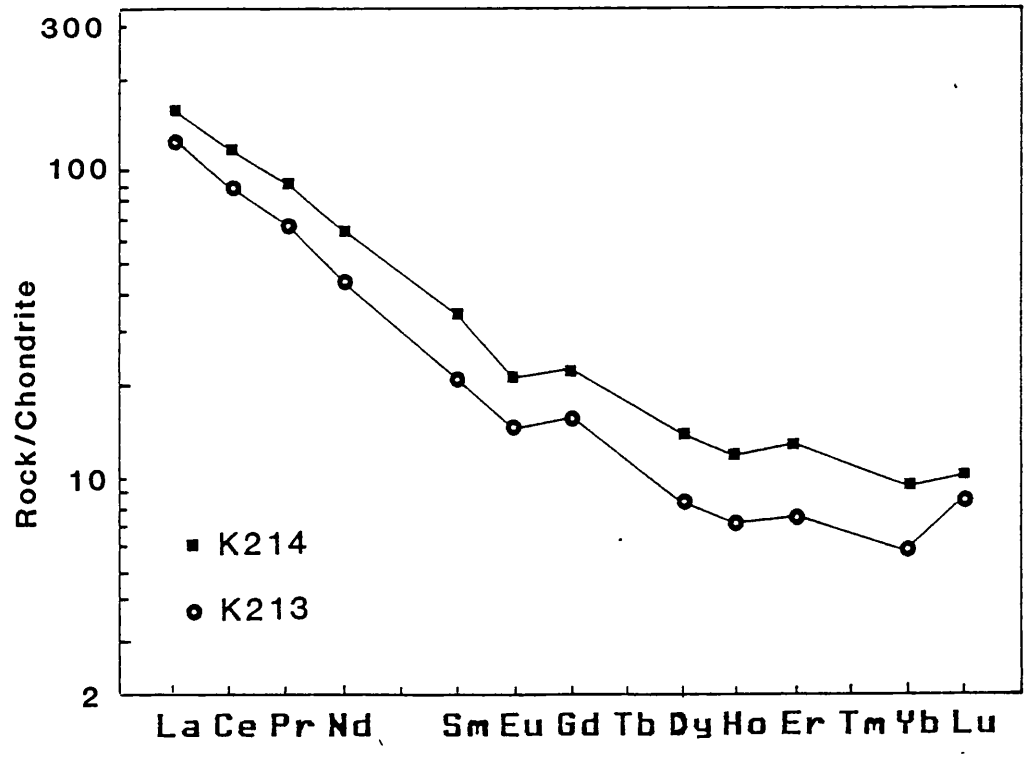

Figure 4.24: REE patterns for the N. Sost pluton.

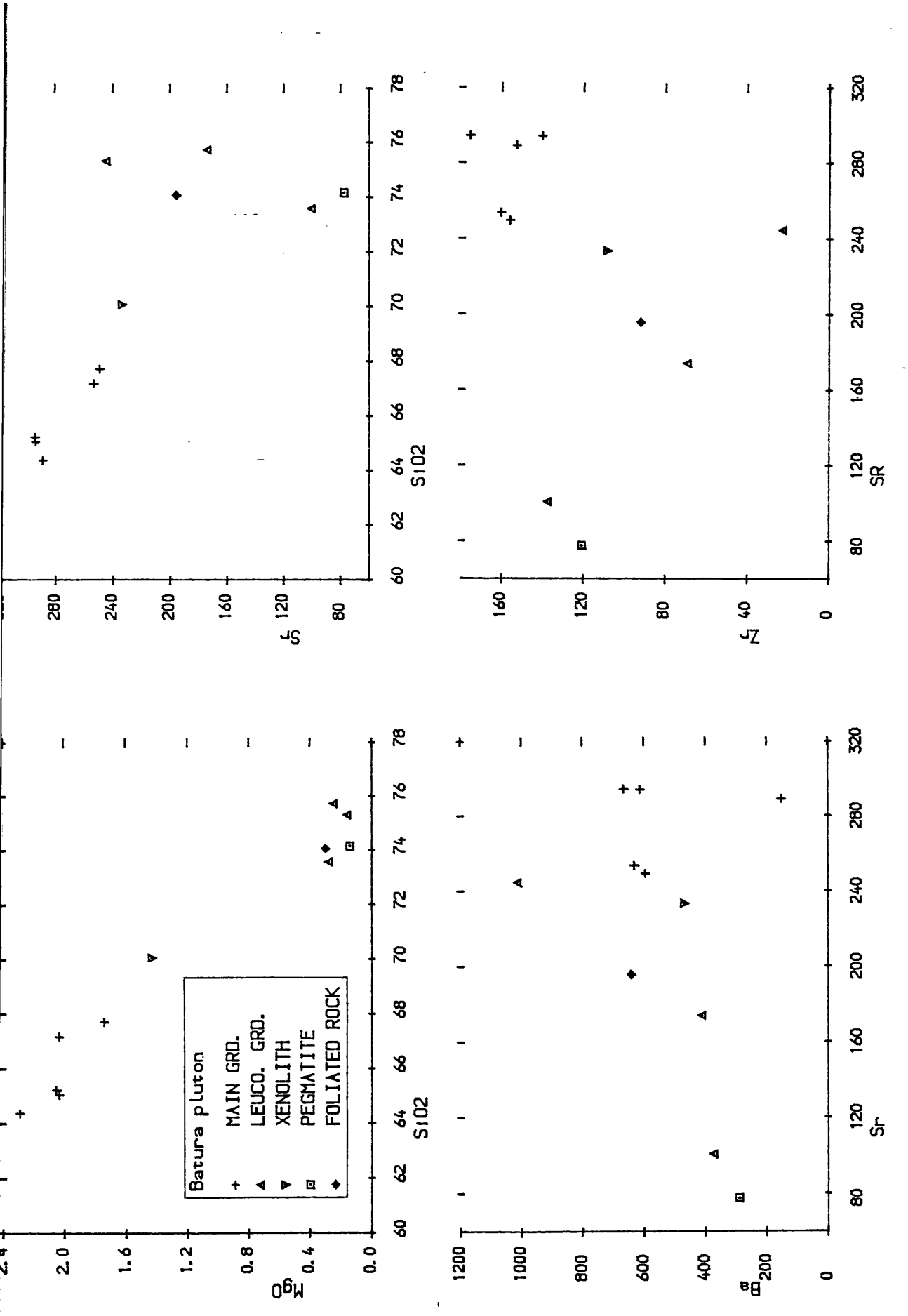

Figure 4.25: 'Harker-type' biaxial plots for the Batura pluton. Note leucogranitoids lie off any trends on the Sr and Zr plots.

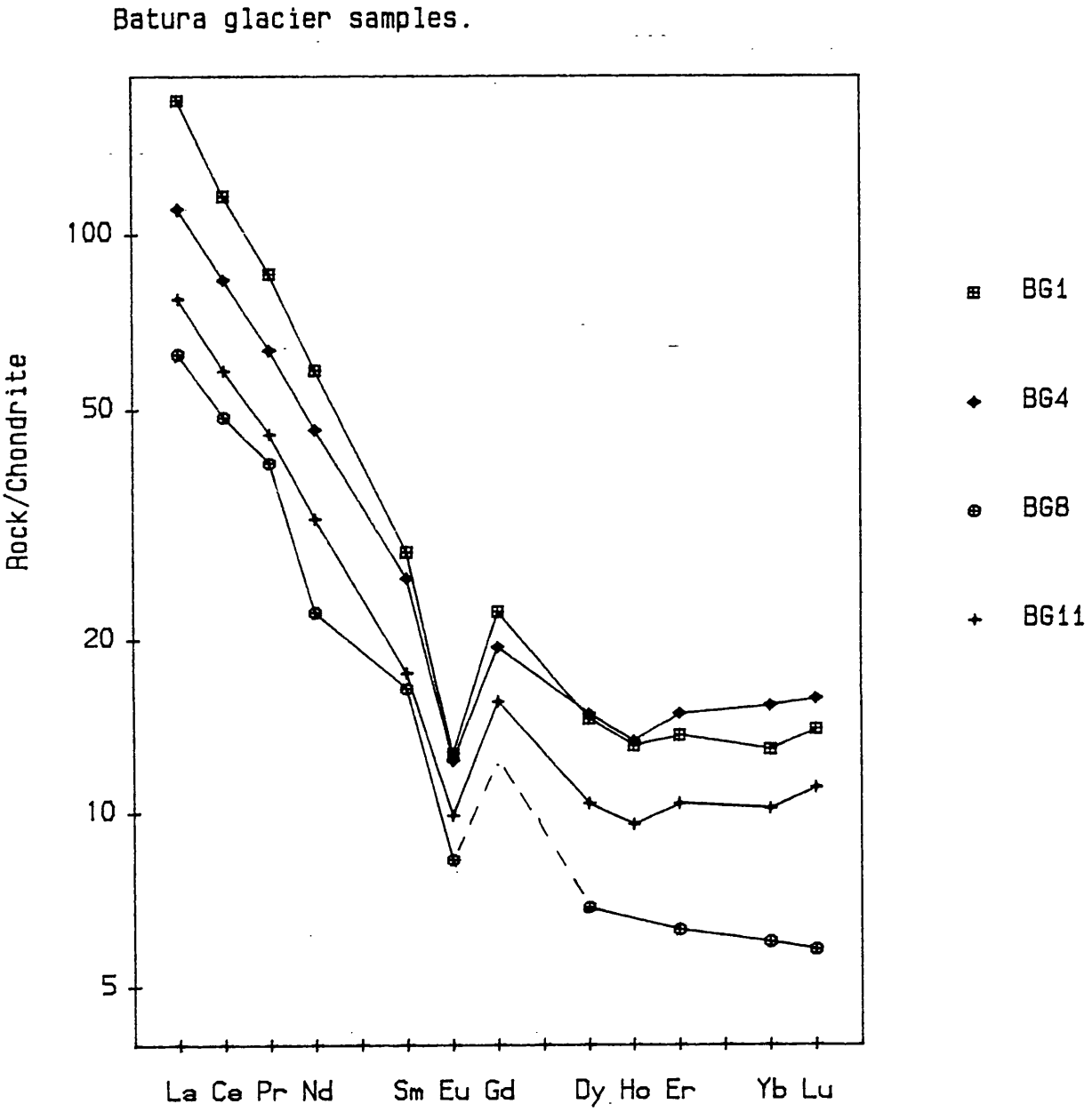

Figure 4.26: Rare earth element patterns for the Batura pluton. BG1 and BG4 are granodiorites, BG8 is a foliated sample and BG11 is a xenolith.

show general compatible trends for Sr, Ba, Zr and the LREE. Sample BG5 is depleted in Ba compared to the rest of the samples, and within the granodiorites the LILE in general are too scattered for accurate trends to be defined. However, the compatiblity of the above elements suggests the crystallisation of plagioclase and alkali feldspar, with some accessory zircon and probably, based on the mineralogy, some biotite and amphibole. The xenolith and foliated sample may also lie on the same trends as the granodiorites although it is unusual that the xenolith is more evolved. The leucogranitoids collected do not appear to belong to the same trends.

The average silica contents of the samples collected by Debon et al. (1987b) are all >70% and so it is possible that they have concentrated on the leucogranitoid phase. If these rocks are related to the post-collisional leucogranites of the HPC then it is not surprising that they give a younger age. The granodiorites could then be related to the northern granodiorite of the HPC, as they are similar in many respects.

One feature noted by Debon et al. (op.cit) and also observed here is the evolution of the REE patterns within the granodiorite with depletion of LREE and slight enrichment of HREE (BG1 to BG4, fig. 4.26). This is different to the patterns observed for the HPC where the HREE were removed by amphibole, although overall abundances are similar. The Batura pattern can still be explained in terms of the fractionation of allanite (around 0.5%) but with a much lower amphibole to feldspar ratio. If the xenolith (BG11) and foliated rock (BG8) are also related to the evolutionary trend then, in order for further fractionation to produce the HREE depletion seen (fig. 4.26), either more amphibole or another accessory phase such as zircon must enter the crystallising assemblage.

4.5: Spatial magmatic variations on the northern margin of the subducting Neo-Tethys ocean, and possible petrogenesis of the pre-collisional calc-alkaline pluton of the HPC.

Figure 4.27 shows spider diagrams for the main Karakoram pre-collisional granodiorite plutons discussed above. All show typical calc-alkaline signatures with high LILE/HFSE ratios and a negative Nb anomaly. All the patterns are similar and differences can be

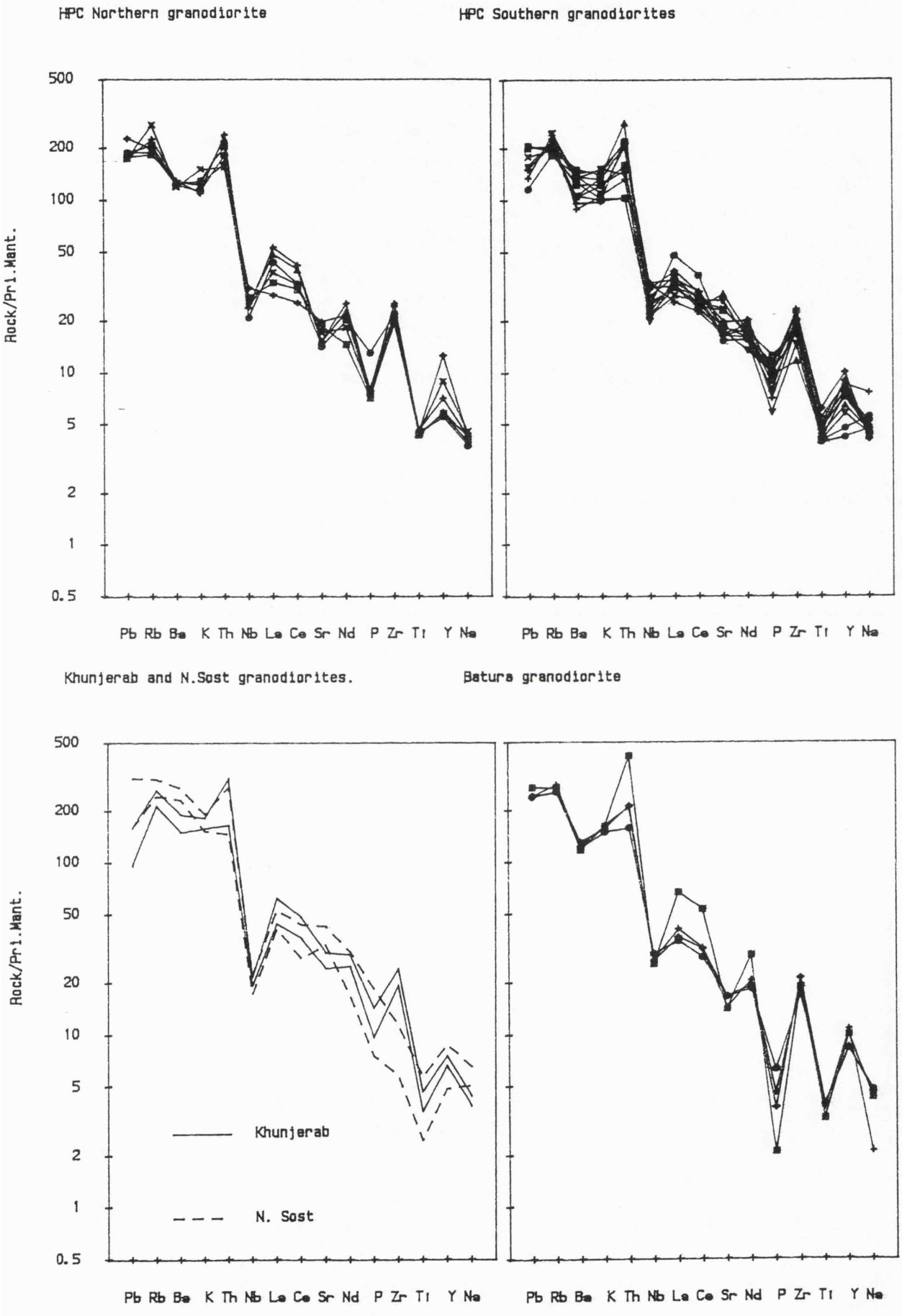

Figure 4.27: Spider diagrams for the main, pre-collisional granodiorite plutons of the Karakoram.

explained by varying degrees of the high level fractionation processes modelled above. The close spatial and temporal proximity of the plutons probably means that they share common source components and petrogenetic histories. The resultant lack of variety is, however, not condusive to study of possible sources and mantle heterogeneity beneath the Karakoram.

The large number of possible source components for a batholith at a destructive plate margin were outlined in the introduction. The trace element signature of calc-alkaline magmas has been useful in identifying an ultimate source in the subducting slab. The high LILE/HFSE ratio and negative Nb anomaly can be explained by accessory phases such as rutile, sphene and garnet retaining the HFSE and Nb in the slab whilst LILE are released into the overlying mantle during dehydration or small-scale partial melting (e.g. Tarney and Saunders, 1979; Saunders et al., in press).

However, unless such distinctive features or definite variations can be found, trace element chemistry is often limited in its use to infer source characteristics. Figure 4.28 shows biaxial plots of some trace element ratios for the Karakoram plutons. Most of the ratios, such as Rb/Y, show no separation of the plutons for similar silica abundances. However, LILE/HFSE ratios such as Sr/Ti and Rb/Nb do show that N. Sost, and to some extent Khunjerab, have higher ratios than Batura and the HPC. Also Zr shows some discrimination with Khunjerab being rich in Zr and N. Sost being relatively depleted compared to the HPC. Possible explanations for this include source heterogeneity on a local scale or different degrees of partial melting and enrichment of LILE from the dehydrating slab. The higher LILE/HFSE ratio might also be related to distance from the trench, as the same feature is also observed to an extent with K_2O and this has been noted at other destructive plate margins as the K-h relationship (e.g. Dickinson, 1975). This relationship is thought to reflect the increased contamination of the mantle wedge by the subducted slab input with depth. The LILE/HFSE ratio in magmas also tends to increases with arc maturity as the contamination signature builds up with time (Saunders and Tarney, 1984). Therefore, the fact that Sost, which is nearer to the former Eurasian margin, has a higher ratio than Khunjerab could be explained by Sost being younger, as no age dating has been done on this pluton. However, Batura is younger than

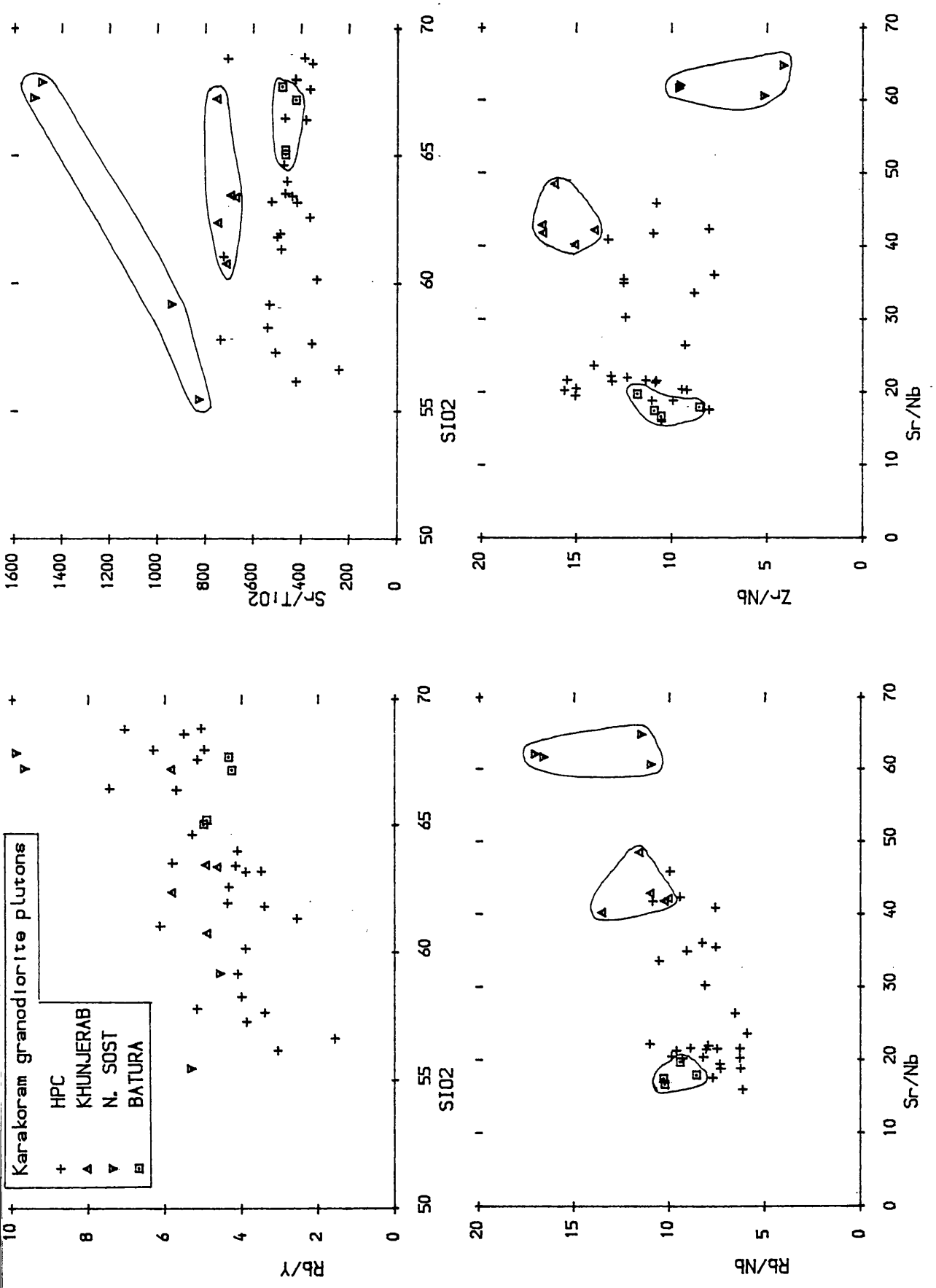

Figure 4.28: 'Harker-type' biaxial plots for the main pre-collisional plutons of the Karakoram. Note the N. Sost, and to some extent Khunjerab, plutons lie at higher LILE/HFSE ratios for similar silica values.

the HPC and does not show the same enrichment as Sost.

Isotope systems have proved extremely useful in identifying source components in granitoid rocks. Little data are available for the Karakoram plutons and much more work is needed before any conclusions can be reached with a large degree of confidence. However, a possible interpretation of the data for the HPC is outlined below, with the intention that further work may confirm or rule out this model.

It has already been seen (section 4.2) that the Sr isotope data for the HPC are heterogeneous and an isochron cannot be constructed. Four possible mechanisms could explain this heterogeneity:-

a). Source heterogeneity: whilst this cannot be disproved, if the ultimate source of the HPC is the mantle it is debatable whether the $^{87}Sr/^{86}Sr$ values of up to 0.718 can be generated by this mechanism. Hawkesworth (1979) states that values of up to 0.71 can be generated in the mantle, but the majority of HPC analyses lie above this. Additionally the heterogeneity would have to be on a local scale, as opposed to the heterogeneity seen on a large scale such as that between the sources of magmas found on ocean islands and ocean ridges.

b). During fractionation the crystallising phases could become dis-equilibrated from the melt and the melt could become preferentially contaminated in radiogenic Sr (Stephens and Halliday, 1979). However, this would result in rocks with higher silica values having higher Sr isotope ratios which is not always the case in the HPC, and would also require large degrees of contamination.

c). If fractional crystallisation occurred over a long period and Rb was enriched in the residual liquid then this could increase the Sr isotope ratio in the more evolved rocks. However, even if crystallisation took 20Ma, this would require a Rb/Sr ratio of around 423 in the melt in order to increase the ratio from 0.706 to 0.718, which is clearly unrealistic.

d). The original magma could have been contaminated by a more radiogenic (crustal?) melt/rock, and this possibility seems most

plausible at present.

Sr isotopic ratios of calc-alkaline magmas have already been shown, in some cases, to be higher than those predicted by the mantle array because of input from the more Sr radiogenic subducting slab (e.g. Hawkesworth, 1979). In addition to this process, magmas have been shown to be further contaminated by crustal rocks (e.g. Thorpe and Francis, 1979). It has already been noted that zircons from the HPC contain an inherited 1500Ma component (Le Fort et al., 1983; chapter 2). Figure 4.29 shows a plot of initial $^{143}Nd/^{144}Nd$ vs. $^{87}Sr/^{86}Sr$ for the few samples from the HPC. Whilst there are only three points (crosses) it can be seen that the data may define a hyperbolic curve trending away from MORB. Also plotting on this possible curve is the field defined by the two metabasite country rock samples, SLG2 and SLG6 (corrected to 100Ma; $^{87}Sr/^{86}Sr$=0.705, $^{143}Nd/^{144}Nd$ = 0.5127-0.5128). These two samples were probably basalts prior to metamorphism, and may have been extruded shortly before the intrusion of the main batholith. If this is the case then they could represent mantle magmas coming from the same source region as the HPC. They plot off the mantle array towards the line representing a 50:50 mixture of MORB-type mantle and the 87Sr/86Sr (=0.707) released from the subducted slab (taken from Hawkesworth, 1979). This indicates that the slab is a probable source component for the HPC.

In order to produce the HPC values on figure 4.29 from the metabasites it would be necessary to mix them with an extremely Sr radiogenic magma. The only analysed sample from the Karakoram which fits this criterion is the Dassu Gneiss (R-109; $^{87}Sr/^{86}Sr$=1.05 corrected to 100Ma) from the Baltoro area (see fig. 5.1, next chapter). The solid lines on figure 4.29 show mixing between SLG6 and R-109 calculated from the equation given in Faure (1986, p.148). The different lines represent different assumed Nd isotope values for R-109, and other conditions are fixed (SLG6; Sr=405ppm, Nd=43.8ppm: R-109; Sr=87.5ppm, Nd=214ppm). The line for $^{143}Nd/^{144}Nd$ (R-109) = 0.511 shows a better fit to the data if the Nd isotope ratio of SLG2 (0.5127) is used as one endmember (dashed line) and a steeper curve could be obtained by lowering the Sr/Nd ratio of the Dassu Gneiss endmember. However, this diagram is only meant to illustrate that it is possible to explain the present data by mixing a mantle-derived basalt with a subucted slab input, with a Sr radiogenic crustal rock

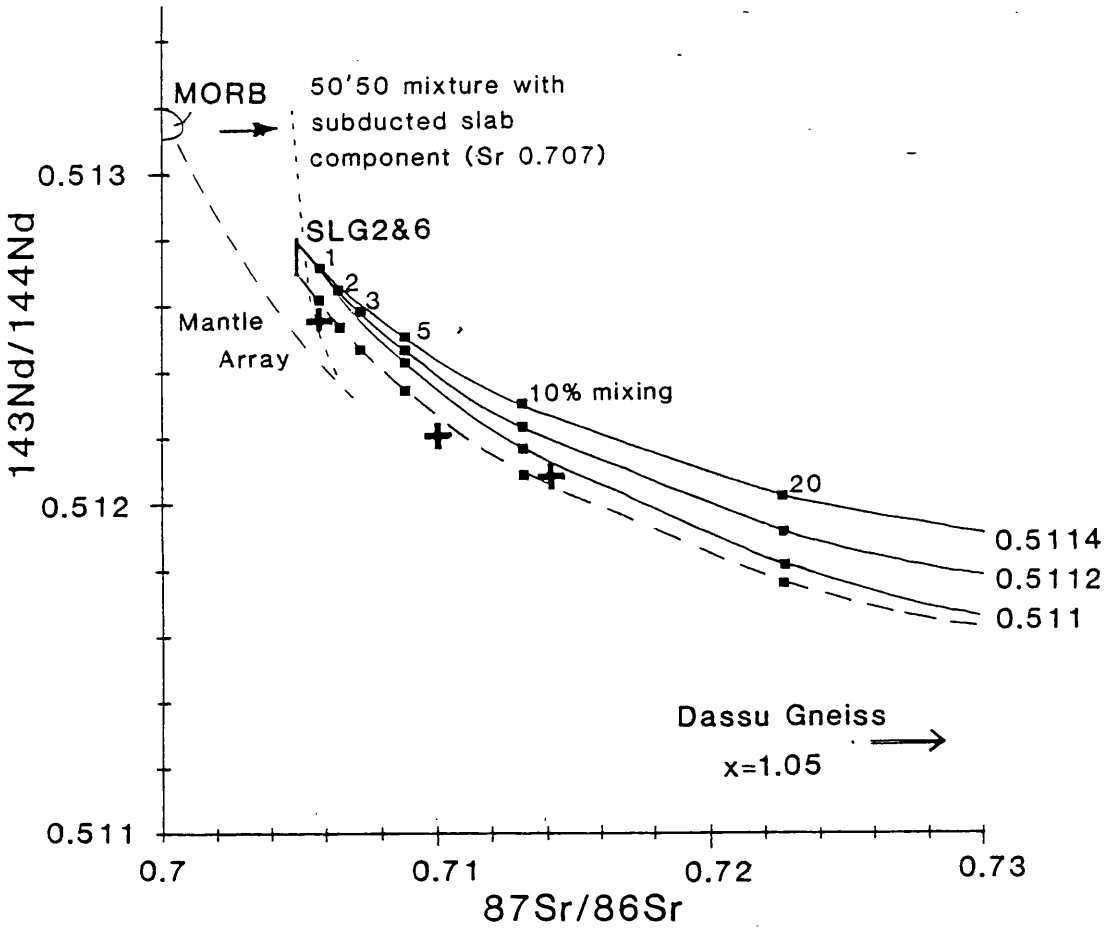

Figure 4.29: Modelled mixing curves between metabasalts SLG2 & 6 and the Dassu Gneiss ($^{87}Sr/^{86}Sr$ = 1.05 at 100Ma) in an attempt to fit the data for the HPC (large crosses) calculated back to 100Ma. Solid lines assume SLG has $^{143}Nd/^{144}Nd$ of 0.5128 whereas the dashed line represents 0.5127. Different solid lines represent different assumed $^{143}Nd/^{144}Nd$ ratios for the Dassu Gneiss. Mantle array and 50:50 mixing line taken from Hawkesworth (1979). Squares and numbers refer to percentage mixing of Dassu Gneiss component.

similar to the Dassu Gneiss.

At first, such a mixing relationship would seem to contradict the fractional crystallisation relationship between the samples modelled earlier. However, the two processes need not be mutually exclusive. Firstly, the squares on figure 4.29 show 1,2,3,5 and 10% mixing and it can be seen that only about 10% mixing is necessary, which may not greatly effect the rest of the HPC chemistry, although it may explain some of the scatter seen. Secondly, R-109 tends to plot at the high silica end of many of the HPC trends and so mixing may enhance, rather than detract from, the fractionation trends. The contamination of the main HPC magma by crust similar to R-109 may not be a simple binary mixing relationship, but could have occurred by an assimilation-fractional crystallisation (AFC) process as described by DePaolo (1981). Figure 4.30 shows data from this study and from Debon et al. (1987b) plotted on a $^{87}Sr/^{86}Sr$ vs. Sr graph. The line through the data is modelled using an assimilation to crystallisation ratio (r) of 0.2 between the Dassu Gneiss and a mantle magma with the same parameters as SLG2 except that the magma is assumed to have fractionated some clinopyroxene prior to assimilation in order to raise the Sr content to 600ppm. Equations for the model were taken from DePaolo (op.cit) and the bulk distribution coefficient for Sr (2.7) was taken from section 4.4. This is oversimplified as the ratio (r) and D_{Sr} would probably change during fractionation, but the model illustrates that a possible AFC relationship for the data exists.

4.6: Summary.

Despite dating problems it is now clear that there was a major period of plutonism in the Karakoram around 100Ma which, together with other sporadic plutonism in the area, was related to northward subduction of Neo-Tethys.

The plutons are dominated by granodiorite, but show an evolutionary sequence from quartz diorites and tonalites through to granites. All show typical calc-alkaline signatures with AFM trends, high LILE/HFSE ratios and negative Nb anomalies. The mineralogy is also typically calc-alkaline being dominated by plagioclase, hornblende and biotite, with clinopyroxene present in the more basic rocks (<60% SiO_2). The amphiboles of the HPC are generally edenitic

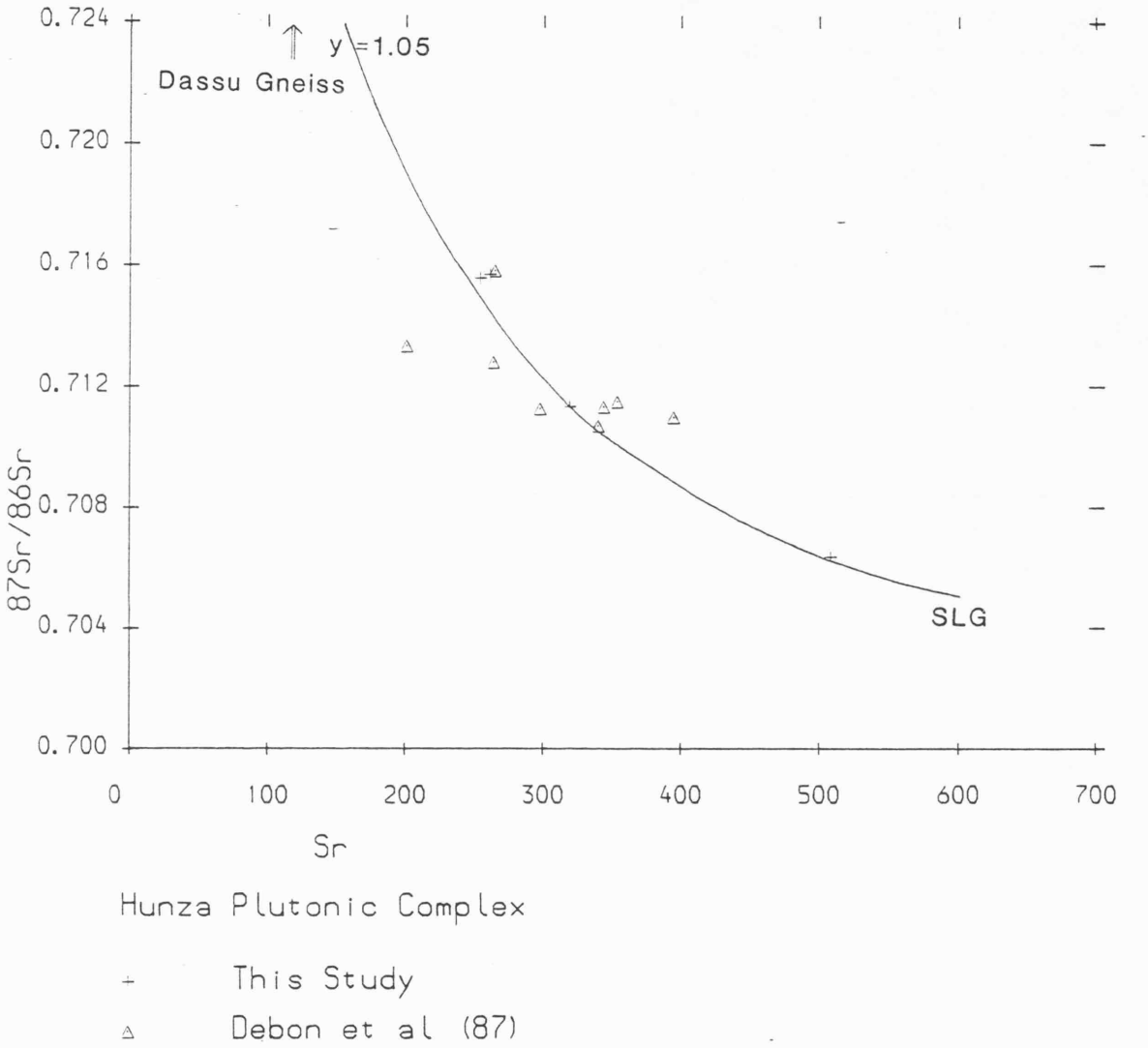

Figure 4.30: Assimilation-fractional crystallisation (AFC) modelling line for Sr isotope data for the HPC 95Ma phase. Conditions are assimilation to crystallisation ratio (r) = 0.2; D_{Sr} = 2.7; Dassu Gneiss - $^{87}Sr/^{86}Sr$ = 1.05, Sr = 87.5ppm; SLG - $^{87}Sr/^{86}Sr$ = 0.705, Sr = 600ppm after fractionation. Modelling equations were taken from DePaolo (1981). See text for further discussion of endmembers.

and show chemical variation through the edenite and tschermakite substitution schemes. Both biotite and opaque phases indicate there was a drop in the oxygen fugacity during crystallisation.

The chemical trends shown by the plutons are often scattered, but are most easily explained by fractional crystallisation proceeding via a filter pressing mechanism. The HPC, whilst not necessarily representing one magma batch, appears to be controlled by three general fractionating assemblages. The first probably involved 20-30% clinopyroxene, until this phase became unstable at 60% SiO_2, together with amphibole and plagioclase. The main assemblage consisted of 44% amphibole, 43% plagioclase and 13% biotite, possibly with some sphene and apatite. REE chemistry was controlled by the accessory phase allanite. Above 67% silica ilmenite becomes important in controlling some elements such as Fe and Ti.

The Khunjerab pluton contains more K-feldspar than the HPC and this was an important fractionating phase, whilst the REE were dominated by sphene and apatite crystallisation. The N.Sost pluton appears to have had a similar evolution to the HPC. It is not clear whether the Batura samples represent a discrete pluton or whether they are merely the NW extension of the HPC northern granodiorite.

Little inter-pluton chemical variation is seen which cannot be explained by differing degrees of fractionation. N.Sost and Khunjerab tend to exhibit higher LILE/HFSE ratios and this may be related to distance from the trench, maturity or different sources and degrees of partial melting. The heterogeneous isotopes within the HPC could be explained by mixing mantle magmas, similar to exposed metabasites, with a Sr radiogenic crustal rock such as the Dassu Gneiss. This would also explain the inherited crustal component observed in some zircons. The mixing may have proceeded by an AFC-type model with an assimilation to crystallisation ratio of around 0.2. Mixing of up to 10% may have been necessary, but this process is not mutually exclusive and probably enhanced the fractionation trends. Therefore, the source components of the HPC, and possibly the other plutons, appear to have been the subducting slab and the overlying mantle wedge, with an upper crustal contaminant. This is consistent with the source invoked for the equivalent Kohistan plutons by Petterson and Windley (1986).

CHAPTER FIVE: Post-collisional granites of the Baltoro Plutonic Unit: mantle-crust interaction and mantle evolution beneath the Karakoram.

5.1: Introduction

There has long been controversy over how the nature and chemistry of various granite types relate to their environment (e.g. Read, 1957; Chappell and White, 1974; Pearce et al., 1984; Harris et al., 1986; Lameyre and Bowden, 1982; Pitcher, 1983). Many leucogranites, including those of the High Himalaya, have been interpreted as crustal melts following orogenic collision, crustal thickening and resultant elevated heat flow, with anatexis often being aided by heat focusing and fluid fluxing along fault or thrust planes (e.g. Le Fort, 1981; Dietrich and Gansser, 1981; Searle and Fryer, 1986; Pinet and Jaupart, 1987; Strong and Hanmer, 1981). Only a few leucogranite suites have been related to fractionation from a more basic parent (e.g. Taylor et al., 1968; Schemerhorn, 1987) and none of the crustal melting models for leucogranite petrogenesis within collisional belts have invoked the need for a mantle component or precursor in order to promote melting. This is despite recent observations by Clemens and Vielzeuf (1987) and Rutter and Wyllie (1988) that underplating of the crust by mantle-derived magmas may be necessary to generate the high temperatures needed to cause sufficient partial melting for a granitic magma to be able to separate from its source and rise through the crust. This chapter looks at the geochemistry of the leucogranites and associated rocks of the Baltoro Plutonic Unit (BPU) within the Karakoram Axial Batholith (KAB) of N. Pakistan. Despite being post-collisional and occupying a tectonic position that parallels that of the High Himalayan leucogranites this suite has a distinctly different isotopic signature. The BPU is also spatially and temporally related to ultra-potassic lamprophyre magmatism, a situation seen elsewhere with granites in post-collisional settings (e.g. SW England, Leat et al., 1987; Criffell, Henney, 1987). This chapter is therefore concerned with the nature of the leucogranites, their possible petrogenesis, and their relationship with the ultra-potassic magmatism.

For geochemical purposes, leucogranites, as defined in chapter

1.1, can generally be considered to be a result of one of two main processes; either they represent the acidic end member of a fractionation series from a more basic parent, e.g. the Snowy Mountains suite (Taylor et al., 1968), or they represent a primary, acidic partial melt, probably as a result of crustal anatexis and migmatisation, e.g. Manaslu (Le Fort, 1981). The latter situation can be complicated by fractionation within the melt during cooling. Leucogranites are unlikely to be a direct result of large scale magma mixing since there are few magmas sufficiently acidic to form one end member of the mixing series, unless all the mixing components are leucogranitic. For the same reason, if a multiple source is envisaged for a primary leucogranite melt then contamination from the secondary sources must be small enough so as not to affect the leucogranitic nature of the main melt. However, mixing could produce a more basic magma which could then fractionate to produce a leucogranite. Therefore it is very important to identify any internal fractionation trends within a suite so that information about the more basic parental magma can be obtained. Petrology is important in assisting this by identifying plausible fractionation phases, particularly accessory minerals, which could control a suite's trace element and REE chemistry. Only when such internal trends have been characterized from the chemistry can inferences about source be made. In aiding such inferences isotope data and knowledge of the chemistry of possible source components or contaminants are invaluable. Finally, consideration of separation and emplacement mechanisms is essential, since it is of little value invoking a lower crustal source if there is no plausible way of getting the magma from the lower crust to its present intrusive level.

5.2: Field relationships and tectonic setting of the BPU.

The geology of the BPU has been extensively dealt with by Searle et al. (in press) and the main points are summarized below and in figure 5.1. To the north the BPU is bounded by a hornblende-rich tonalitic complex (the Muztagh Tower Unit, MTU) and low grade regional metamorphic rocks displaying a small contact aureole. To the south are Barrovian series metamorphic rocks ranging from chlorite-biotite grade phyllites up to sillimanite-grade gneisses which represent the main M2 metamorphic phase associated with the Eocene collisional deformation. The age of M2 is constrained by the Mango

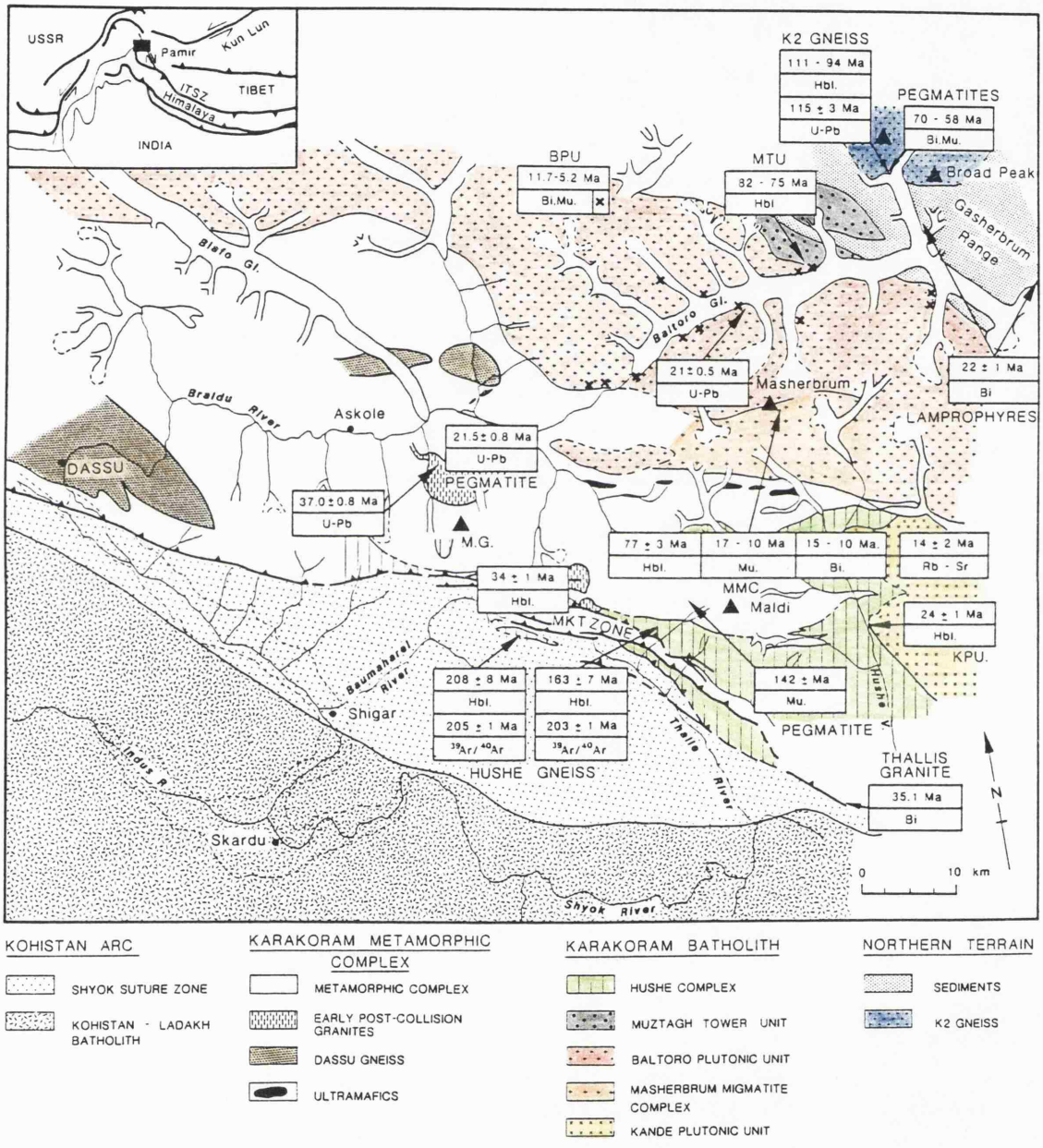

Figure 5.1: Geological sketch map of the Skardu/Baltoro/K2 area, northern Pakistan, showing the important radiometric dates. From Rex et al. (in press).

Gusar pluton which cuts syn-M2 foliation and is dated at 36.4±1Ma (U-Pb, R. Parrish, writ. comm. in Rex et al., in press). The BPU has vertical intrusive contacts, shows little deformation or foliation and is also clearly post-collisional. It represents the final magmatic phase of the KAB which records the post-Jurassic magmatic development of the Eurasian margin through subduction of Neo-Tethys and continental collision. The unit is restricted in composition to monzogranites and leucogranites cut by later leucogranitic dykes. A precise age of 21±0.5Ma has been obtained from U-Pb analysis of zircons (Parrish and Tirrul, in press) which also showed a large inherited Precambrian component. Eleven K-Ar (biotite) dates reported by Searle et al. (in press) range between 12 and 5±0.5Ma for BPU granites and these are interpreted as recording uplift and cooling events. Rb-Sr data are scattered on a $^{87}Sr/^{86}Sr$ vs. $^{87}Rb/^{86}Sr$ plot and do not yield an isochron (Rex et al., in press).

Some melting is seen within the sillimanite-K feldspar gneisses in the south, but not in great enough volume to be an important source for the BPU unless much more melting is hidden at depth. Along the southern margin of the BPU is the Masherbrum Migmatite Complex (MMC) comprising an anastomosing set of leucogranite dykes cutting host biotite- and hornblende-orthogneisses and minor amphibolites, marbles and paragneisses. A Rb-Sr isochron on the dykes yields an age of 14.1±2Ma with an $^{87}Sr/^{86}Sr$ initial ratio of 0.7084 (Searle et al., in press) whilst K-Ar determinations (biotite and muscovite) give a range of ages between 17-10Ma. Rafts of the MMC are found in the batholith around the Yermanandu Glacier but otherwise there is little evidence of assimilation except for high level xenoliths near the margins of the batholith. Another important lithology in the area is the K2 Gneiss to the north which has a U-Pb zircon age of 115±3Ma (R. Parrish, writ.comm. in Rex et al., in press), and probably represents a thrust culmination of mid-crustal gneiss.

The BPU is inferred to be intruded along the Karakoram Batholith Linament (KBL); a major crustal linament which has localized the magmatic activity of the KAB since the Cretaceous.

5.3: Mineralogy.

The mineralogy of the leucogranites and associated monzogranites

is fairly constant and the main differences tend to be in the type and amount of accessory phases present (table 5.1). All of the rocks contain 80-90% feldspar and quartz. These phases show a granular habit with quartz usually forming smaller interstitial grains indicating it is the later crystallising phase of the three. Occasional myrrmekitic texture suggests, however, that occasional co-precipitation of alkali feldspar and quartz may have occurred. Of the feldspars, alkali feldspar, including albite, is usually dominant occasionally occurring as perthite or microcline. The plagioclase feldspar component varies from An_{30} in the monzogranites to about An_{14} in the leucogranite dykes, putting it in the oligoclase field. K-feldspar megacrysts occur in some granites and these are considered to result from localized potassium metasomatism during the final stages of crystallisation (Searle et al., in press).

The monzogranites differ from the leucogranites in having biotite as their main accessory phase. Sometimes sphene is associated with the biotite suggesting some titanium exchange reaction between the two. Some monzogranites from the BPU (e.g. R63) also contain muscovite and euhedral garnets although the muscovite appears to be secondary. The biotite often has an interstitial habit between the feldspars showing it crystallised later (plate 5.1.a) which is indicative of a low water content in the magma (Wyllie et al., 1976).

The leucogranites often have scattered crystals of biotite but muscovite is the dominant mica. Muscovite occurs either as large laths which are primary, or as smaller, irregular crystals growing along grain boudaries and within feldspar crystals which suggests that these are secondary growths, probably as a result of the later K-rich fluids mentioned above migrating through the rocks (plate 5.1.b). The other common accessory mineral in the leucogranites is garnet which often occurs as strings of crystals in the middle of the later pegmatitic dykes (plate 5.1.c). Garnet only contains inclusions of quartz and is a late crystallising phase.

Other, rarer accessory minerals include allanite, apatite, sphene, zircon which is usually found as inclusions in biotite within the monzogranites, opaques and monazite. Allanite, opaques and sphene only occur in the monzogranites. Tourmaline and thorite were not observed, though thorite must be present since it was used for dating

Plate 5.1(a)
Interstitial biotite and myrrmekite texture in a monzogranite (R85), (cross polars).

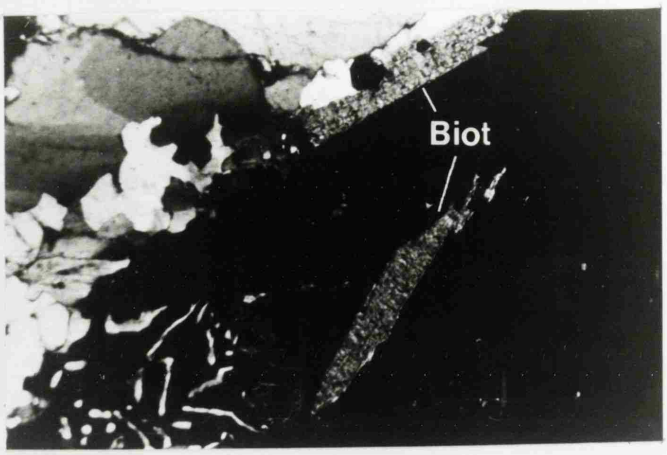

Plate 5.1(b)
Secondary muscovite growth within a plagioclase crystal in monzogranite R63, (cross polars).

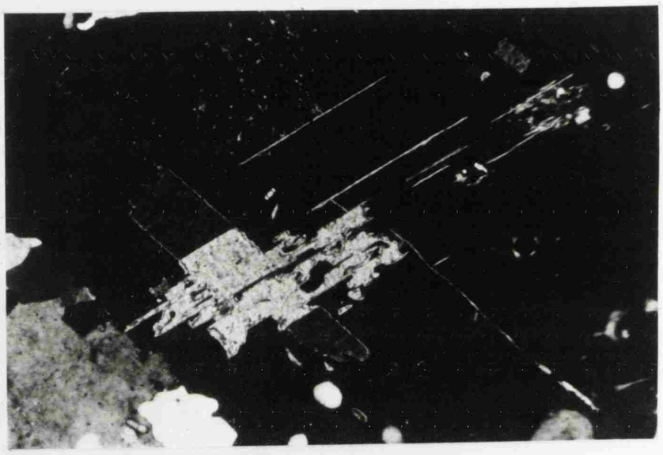

Plate 5.1(c)
Strings of garnet crystals within a leucogranite pegmatite (R68).

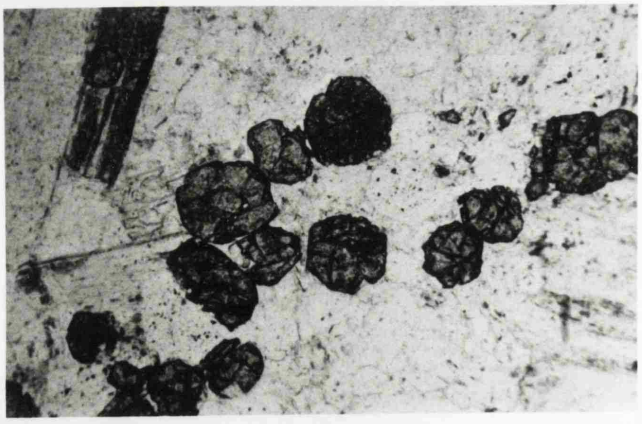

Plate 5.1(d)
Xenocrystic sillimanite, possibly representing restitic material.

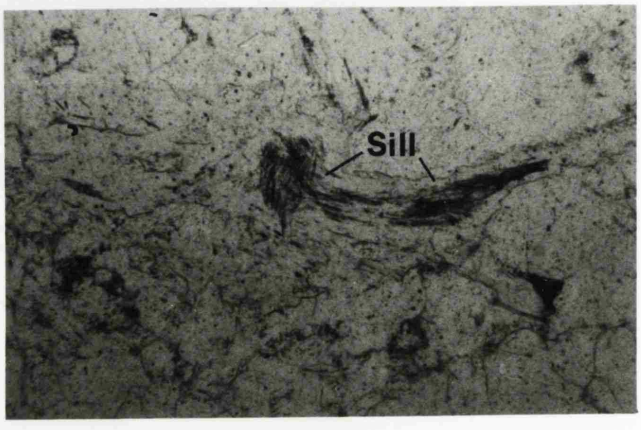

1mm

(Parrish and Tirrul, in press). The lack of tourmaline suggests that the BPU was depleted in volatiles, particularly boron. One section contains sillimanite overgrown by retrograde muscovite which may represent xenocrysts from the source of the BPU (plate 5.1.d).

Sample	R1	R4	R50	R63	R68	R85	R94
Type	LCG	LCG	PEG.	MZG	PEG.	MZG	MZG
Points (n)	472	430	254	466	407	426	392
Quartz	23.3	28.8	23.6	18.7	24.8	23.3	17.6
Plag. fsp	23.0	20.0	16.3	34.6	16.8	27.4	26.7
(comp.)	An25	An20	?	An30	An14	An25	An27
(K,NA)fsp	43.7	46.8	44.2	28.1	45.9	40.5	44.2
Biotite	0.8	1.0	-	8.1	-	6.5	10.2
Muscovite	6.7	2.0	10.6	8.6	10.7	-	-
Garnet	2.2	1.8	5.1	1.8	1.5	-	-
Apatite	-	-	tr	-	-	0.6	1.0
Sphene	-	-	-	-	-	1.5	-
Zircon	-	-	tr	tr	-	tr	tr
Opaques	-	-	-	-	-	-	-

Table 5.1: Modal mineralogy of various leucogranites and monzogranites from the BPU.

5.4: Internal Chemical Trends.

Table 5.2 shows a representative selection of 65 XRF analyses and 19 accompanying REE analyses for rocks from the Baltoro area. All of the granites and late dykes contain between 67-77% SiO_2, are generally corundum-normative and peraluminous. They mostly plot in the leucogranite field of the Debon and Le Fort (1982) classification system, and lie close to the eutectic in the Ab-Or-Qtz system but trend away from it (fig. 5.2). Most of the major elements show straight line correlations on Harker variation diagrams, particularly when plotted against total iron indicating consanguinuity within the pluton (fig. 5.3). However, K_2O shows scatter, probably as a result

Rock No.	R33	R85	R35	R51	R68	R-53	R11
Type.	Mzg	Mzg	Lcg	Lcg	Dyke	K2 Gneiss	Lamp.
SiO2	69.4	67.9	73.9	75.5	73.6	70.6	52.9
TiO2	0.42	0.41	0.12	0.05	0.02	0.28	1.62
Al2O3	14.7	15.6	14.2	13.6	14.5	16.2	10.3
Fe2O3	2.1	2.3	1.0	0.7	1.1	2.2	6.9
MnO	0.04	0.03	0.05	0.05	0.36	0.06	0.12
MgO	0.7	0.8	0.1	0.1	0.0	0.4	11.1
CaO	1.7	2.3	0.8	0.7	0.4	2.1	6.0
Na2O	5.0	4.6	4.6	4.7	4.0	3.8	1.1
K2O	3.98	4.10	3.87	3.50	4.24	3.76	7.95
P2O5	0.19	0.20	0.10	0.07	0.09	0.13	1.70
LOI	0.18	0.24	0.42	0.72	0.44	0.21	-
Total	98.35	98.39	99.21	99.66	98.78	99.77	99.69
Trace elements in parts per million							
Rb	233.6	188.4	271.6	262.3	273.2	181.9	358.4
Ba	2317.0	1369.4	442.4	305.8	9.8	624.8	3679.5
Th	61.7*	36.1	13.3*	6.4	8.2*	19.0*	76.0
U	11.2*	-	8.3*	-	40.6*	2.8*	7.2
Pb	92.4	55.5	45.8	49.3	22.2	-	105.9
Nb	21.8	15.4	21.1	18.5	20.9	16.9	46.3
Sr	795.6	821.9	155.8	87.3	8.8	209.9	1221.4
Zr	244.2	218.9	70.8	37.5	29.9	120.9	692.3
Y	15.9	10.4	13.7	16.0	13.0	11.4	34.3
V	31.9	32.2	5.1	1.6	1.5	25.3	134.9
Cr	22.6	15.0	15.8	15.7	11.7	7.0	580.5
Ni	10.3	5.2	2.6	1.0	1.3	3.5	402.8
Cu	4.1	6.3	5.0	4.0	3.6	-	0.0
Zn	54.5	50.0	33.4	18.3	16.2	44.5	153.3
Ga*	19.6	21.0	22.3	18.3	27.0	15.7	18.7
Ta*	1.7	-	3.5	-	2.2	1.4	-
Hf*	8.4	-	2.7	-	3.3	4.5	-
La	66.1	76.1	19.7	3.8	5.7	36.4	114.1
Ce	141.0	145.4	44.6	10.9	20.2	84.1	265.6
Nd	56.8	51.4	18.3	4.6	13.5	32.0	135.6
Sm	8.9	6.9	3.0	-	1.6	5.4	-
Eu	1.9	1.3	0.6	-	1.0	0.9	-
Tb	0.4	-	0.3	-	0.2	0.5	-
Yb	1.2	0.7	0.6	-	1.3	1.0	-
Lu	0.1	0.1	0.1	-	0.2	0.2	-
$^{87}Sr/^{86}Sr$	0.7128	0.7098	-	-	-	0.7112	0.7166

Table 5.2: Representative chemical analyses for BPU lithologies and associated rocks. Analysis by XRF techniques except for data marked * which were measured by INAA methods. All REE data for R33, R35, R68, and R-53 were analysed by INAA. REE data for R85 by ICP (see appendix 1. for further details).

Baltoro granites, K2 Gneiss and porphyries.

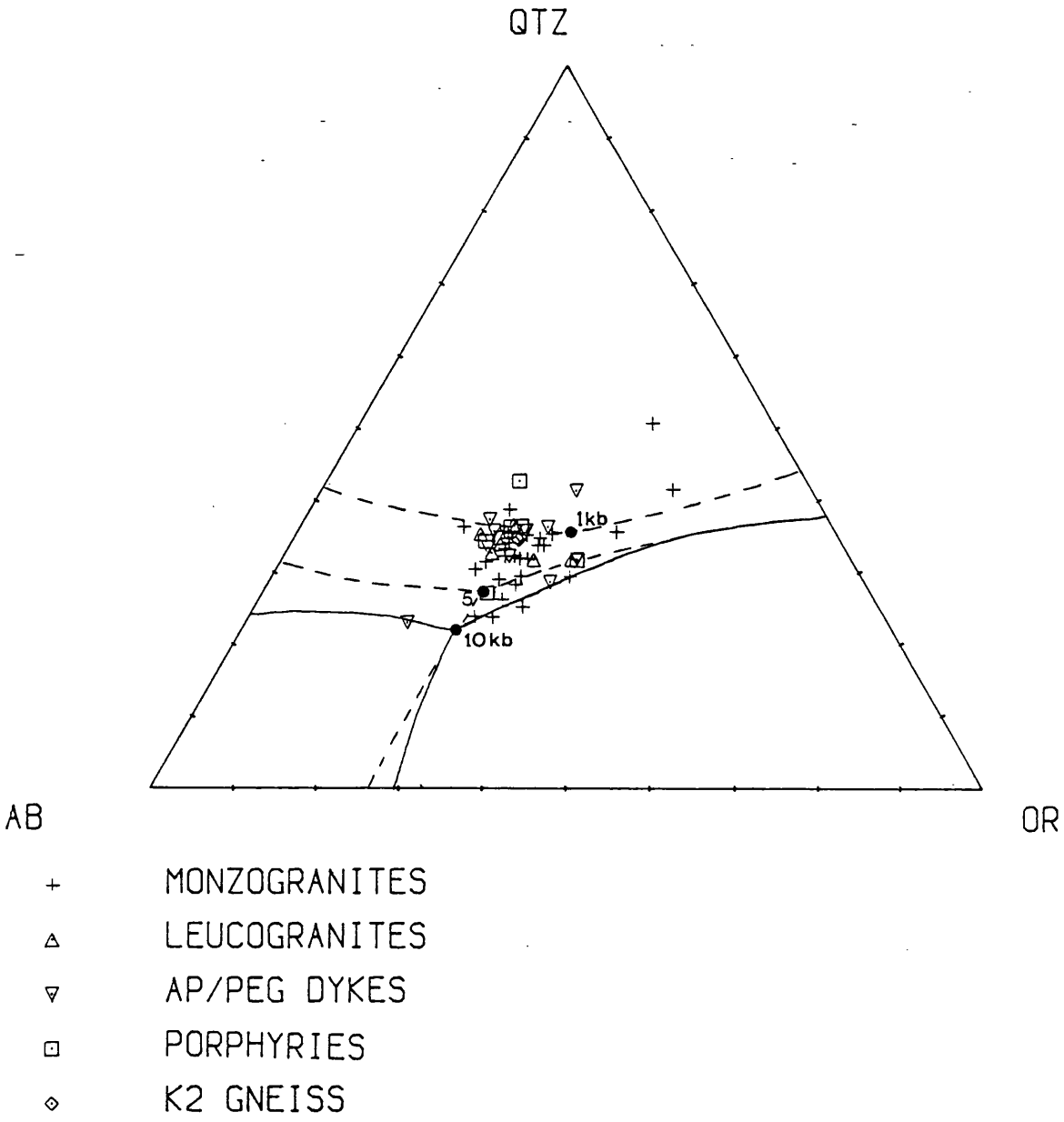

Figure 5.2: Normative albite (AB) - orthoclase (OR) - quartz (QTZ) ternary diagram for the BPU granites, K2 Gneiss and Broad Peak porphyries. Position of the granite minimum/eutectic with correspondin cotectic lines is marked for PH_2O = 1, 5, and 10kb (taken from Johannes, 1985).

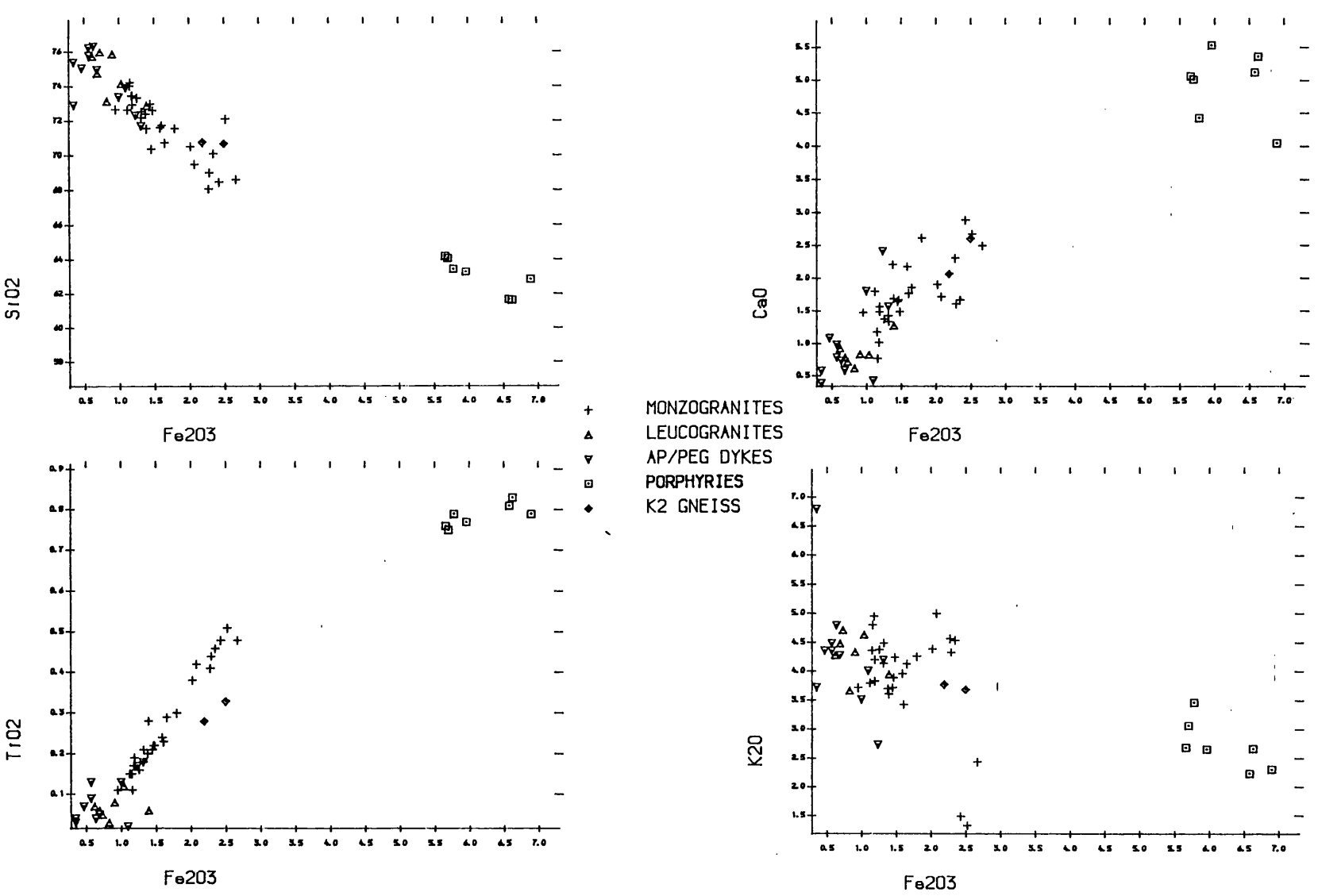

Figure 5.3: Major element 'Harker' variation diagrams for the BPU granites, K2 Gneiss and Broad Peak porphyries.

of later mobility during K-metasomatism associated with the growth of localised potassium feldspar megacrysts.

The least-siliceous (least-evolved?) granites in the BPU are the monzogranites. These have high abundances of Ba (315-2300 ppm, mean = 1100ppm, n = 28), Sr (100-800, av = 515 ppm) and other large ion lithophile elements (LILE) such as K and Th (Th: 5-85 ppm, av = 23 ppm). However, Rb abundances tend to be low (90-260 ppm, av = 160 ppm) compared to other crustally derived melts (cf Pearce et al., 1984). Trace element spidergrams (fig. 5.4.a) show calc-alkaline type patterns with high (LILE/HFSE) ratios and a pronounced negative Nb anomaly as well as negative spikes for P and Ti and a positive spike for Th. The monzogranites have a LREE enrichment with respect to the HREE but show no Eu anomaly (fig. 5.5). In moving to higher silica values towards the leucogranites (fig. 5.4.b) and later dykes (fig. 5.4.c) only Rb, K and the HREE show increases in abundance. All the other trace elements become depleted. There are three possible relationships between the monzogranites and leucogranites to account for this:

a) The monzogranites and leucogranites are unrelated and the leucogranites come from a more depleted source than the monzogranites. The intimate association of the two rock types in the field means that the two magmas would have to be intruded at approximately the same time. However, the similarity between initial Sr isotope ratios for the two and the consideration that they give coherent trends suggests the two groups are related.
b) The leucogranites are related to the monzogranites by fractionation, and the decreasing element abundances relate to phase extraction.
c) The two groups are related by partial melting with the leucogranites representing the first, highly silicic, eutectic melts and the monzogranites being higher percentage melts of the same source. However, using such a model it is hard to explain how the leucogranites are consistently more depleted.

The linear trends and trace element variations described above could be interpreted as due to either partial melting or fractionation and one or other of the models b) and c) has to be discriminated against. A program called PETMIX based on Wright and

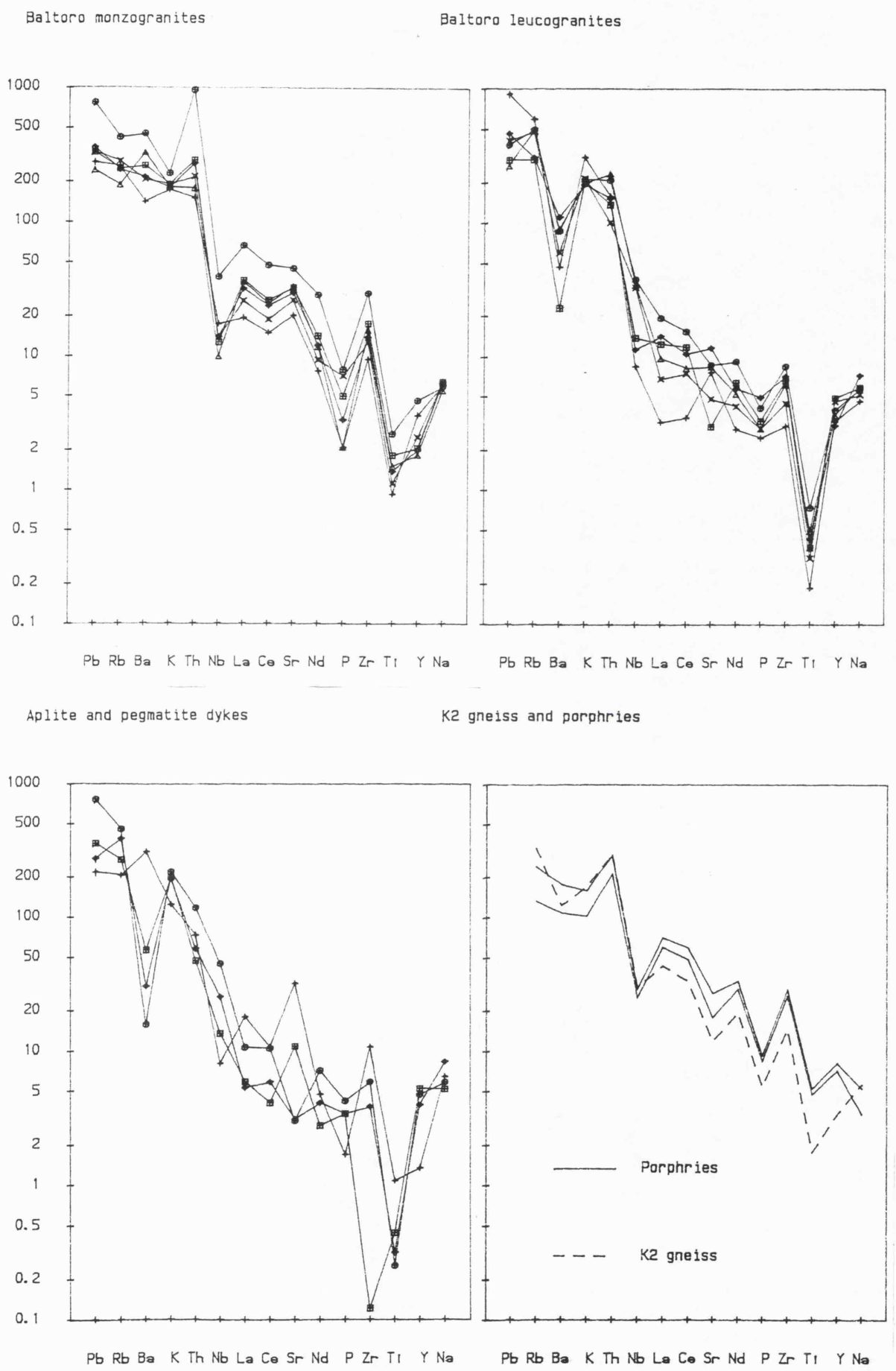

Figure 5.4: Representative 'spider diagram' multi-element variation plots for the BPU granites, K2 Gneiss and Broad Peak porphyries.

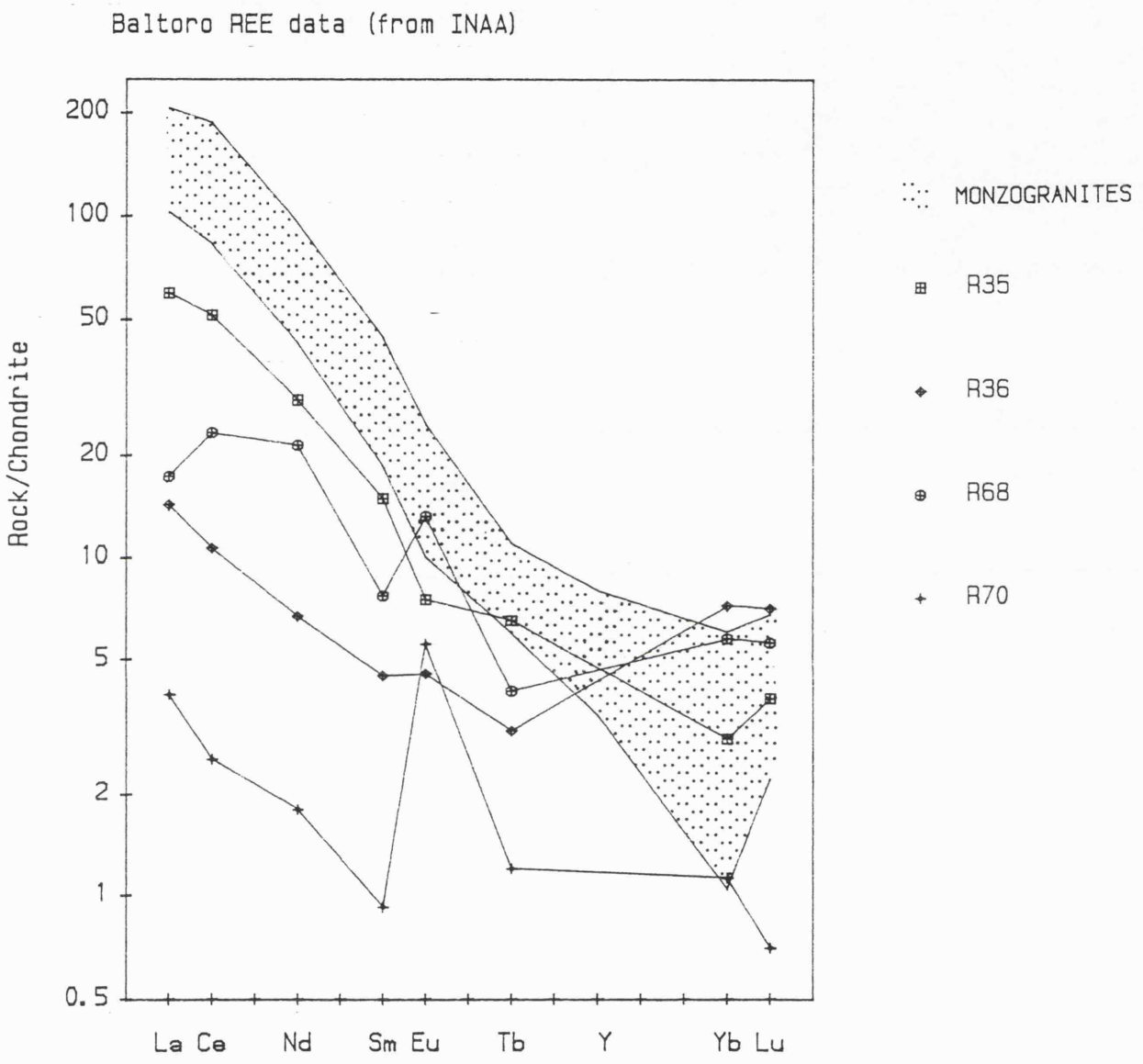

Figure 5.5: Rare earth element (REE) variation diagram for the BPU lithologies. Dots show the field for the monzogranites; R35 and R36 are leucogranites; R68 and R70 are leucogranitic pegmatite dykes.

Doherty (1970) was used in which probe analyses of mineral phases in the granites were entered together with the XRF major oxide analyses of two rocks, one at either end of the evolutionary trend. In general the results consistently showed that fractionation of around 65% plagioclase, 18% biotite, 12% orthoclase, 3% sphene and 2% apatite will produce the more evolved leucogranites from the monzogranites, with the sums of the squares of the residuals being sufficiently small to indicate a good degree of accuracy (table 5.3).

	Evolved rock	K-fsp	Plag An30	Biot	Sphn	Apat	Zircon	Parent rock?
	R1							R85
Wt.Fr	0.7474	0.0348	0.1359	0.0486	0.0095	0.0039	0.0003	
Wt%	76.2	3.5	13.9	5.0	0.97	0.4	0.03	
Fr%		14.7	58.4	21.0	4.1	1.7	0.12	

Sum of square of residuals = 0.4555

	R51							R85
Wt.Fr	0.7106	0.030	0.1718	0.0488	0.0079	0.0017	0.0002	
Wt%	72.7	3.1	18.2	5.0	0.81	0.17	0.02	
Fr%		11.4	66.7	18.3	3.0	0.6	0.07	

Sum of square of residuals = 0.5233

Table 5.3: Results for two runs of PETMIX where R85 is a basic monzogranite and R1 and R51 are leucogranites. Wt.Fr = weight fraction, Fr% = fractionating percentage proportions of minerals that are needed to get evolved rock from parent rock.

These results are borne out when modelling the LIL elements and studying the spidergrams of trace elements. Figure 5.6 shows plots of Rb/Sr and Ba versus Sr after the values have been normalised against those of one of the more basic monzogranites (R85, table 5.2). The lines show trends for Rayleigh fractionation (Hanson, 1978) with total % crystallisation amounts marked. Distribution coefficient data for phases in equilibrium with acidic magmas was taken from Hanson (1978). It can be seen that trends for a 60% plagioclase, 20% biotite

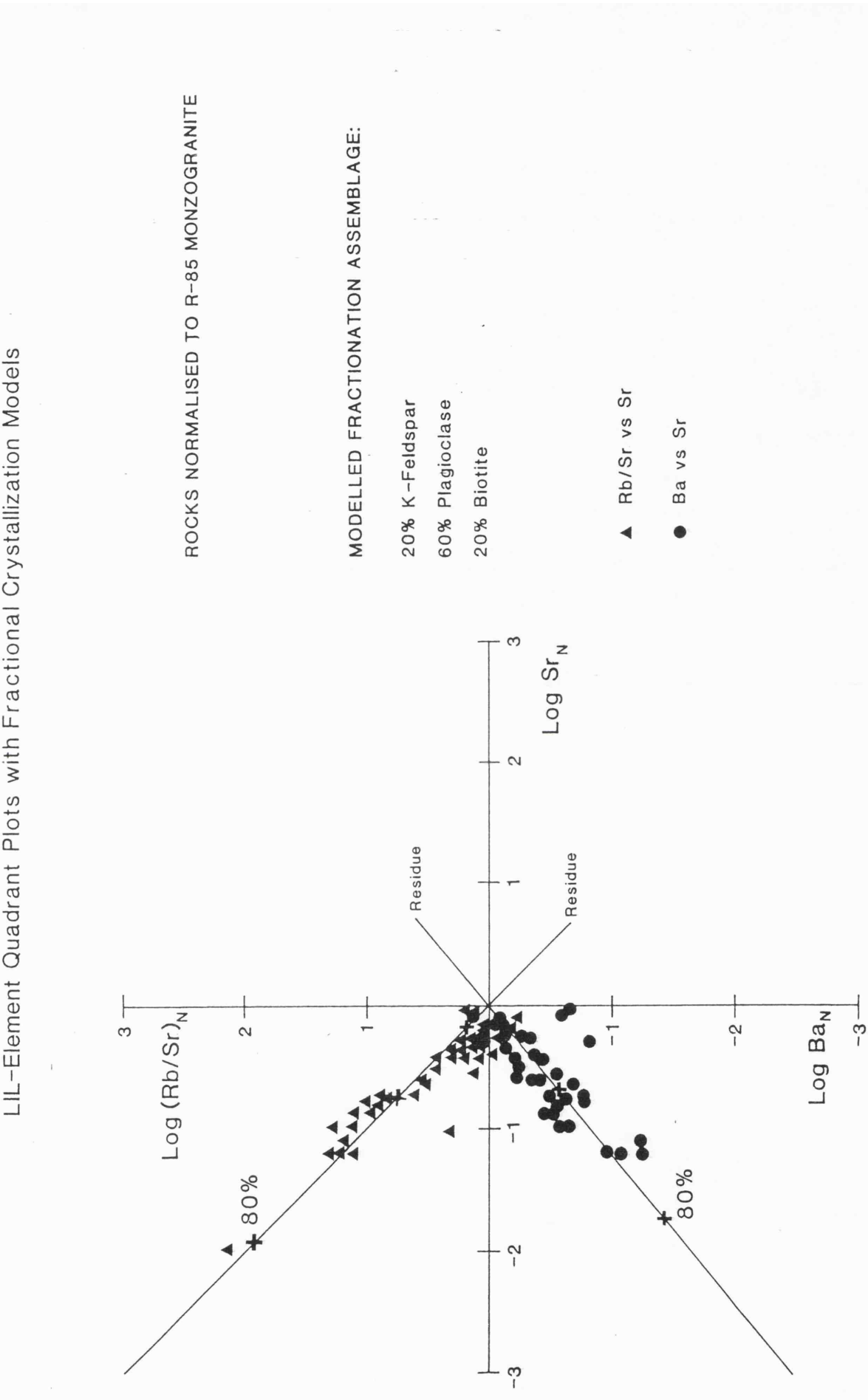

Figure 5.6: LILE trends on logarithmic quadrant plots where the samples are normalised to sample R85. Crosses represent 10%, 40% and 80% Rayleigh fractional crystallisation away from the origin.

and 20% potassium feldspar fractionating assemblage fit the data well. Whilst this diagram does not provide a unique answer (see chapter 6.4) it does support the PETMIX model. Studying the spidergram plots (fig. 5.7), as the rocks evolve from monzogranites to leucogranites and finally to the dykes, Ba and Sr decrease due to feldspar fractionation, and P and Ti also fall due apatite and sphene being removed. Zr shows a degree of compatibility in the more basic rocks and this is probably due to precipitation of zircon in oversaturated conditions (Watson, 1979).

For these trends to be due to partial melting Ba and Sr would have to increase with melting by a factor of 5 to 6 from the leucogranites to the monzogranites. This is unlikely for moderate degrees of melting in a source which, if crustal (see later), probably contains feldspar, since feldspar in the residue will buffer the Sr content of the melt. Therefore the fractionation relationship outlined above between the monzogranites and leucogranites (model b) is favoured. This is given further weight by the fact that only phases seen in the rocks were used in the model.

One feature which does not conform with the fractionation trend is the evolving REE pattern (fig. 5.5) which shows decreasing LREE and a small positive Eu anomaly which is not expected with fractionation dominated by feldspar. However, it has been shown that REE patterns in acidic magmas can be dominated by the precipitation of accessory phases (e.g. Gromet and Silver, 1983; Watson and Harrison, 1984) and using distribution coefficient data estimated from data from Henderson (1984) it can be shown that fractionation of less than 0.5% monazite together with the feldspars would produce the general pattern of the observed trends (fig. 5.8), and this would also explain the decreasing Th values (fig. 5.7). The lack of data for monazite precludes a more accurate model but in reality the proportion of monazite needed is probably much less than this.

5.5: Possible sources.

From the above it appears that the leucogranites of the BPU are related by fractionation to a more basic monzogranite parent. It is, therefore, the geochemistry of the monzogranites that is most relevant when trying to infer source characteristics. The

Figure 5.7: Representative Lithologies of the B.P.U Showing In-Situ Fractionation Trends

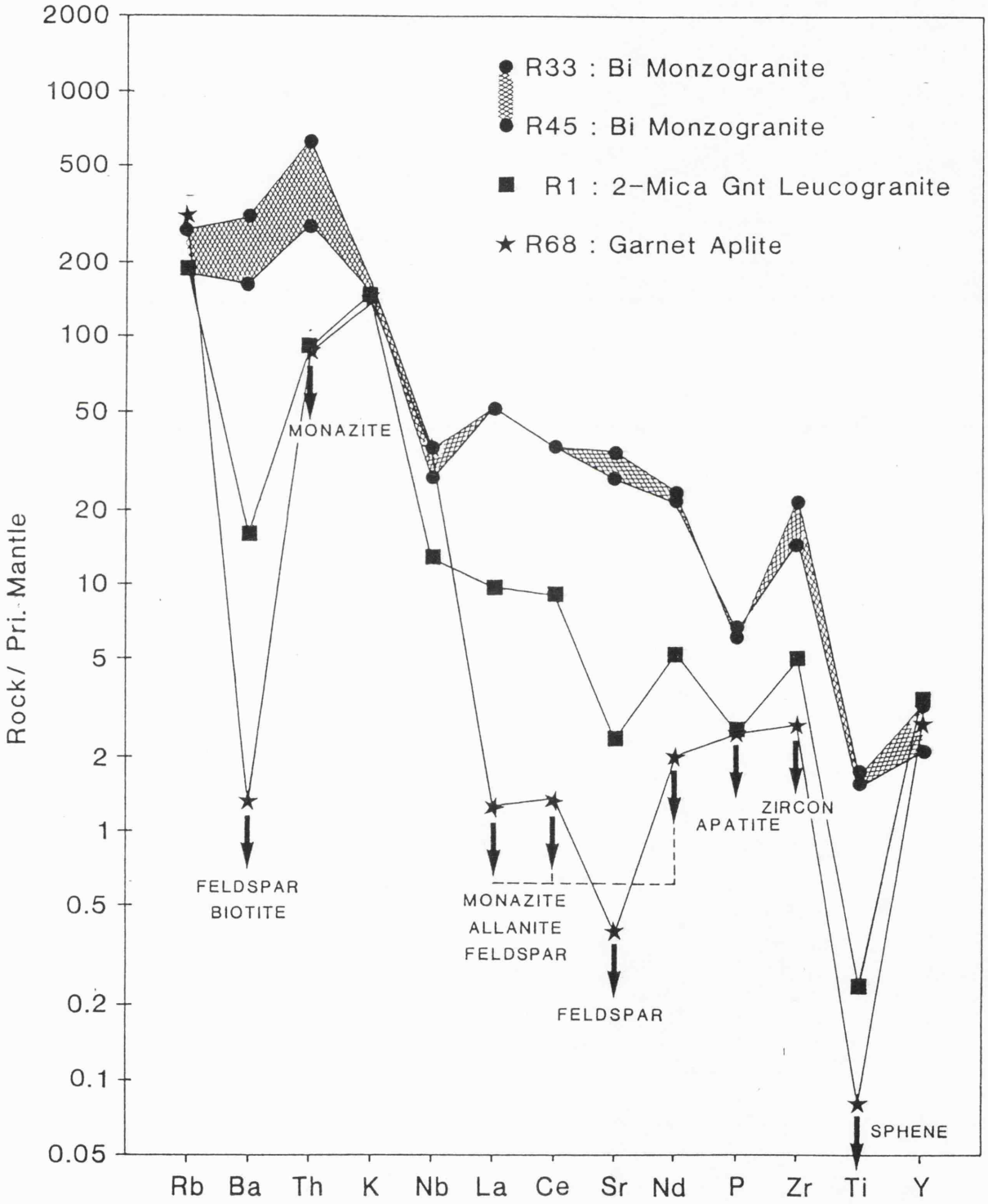

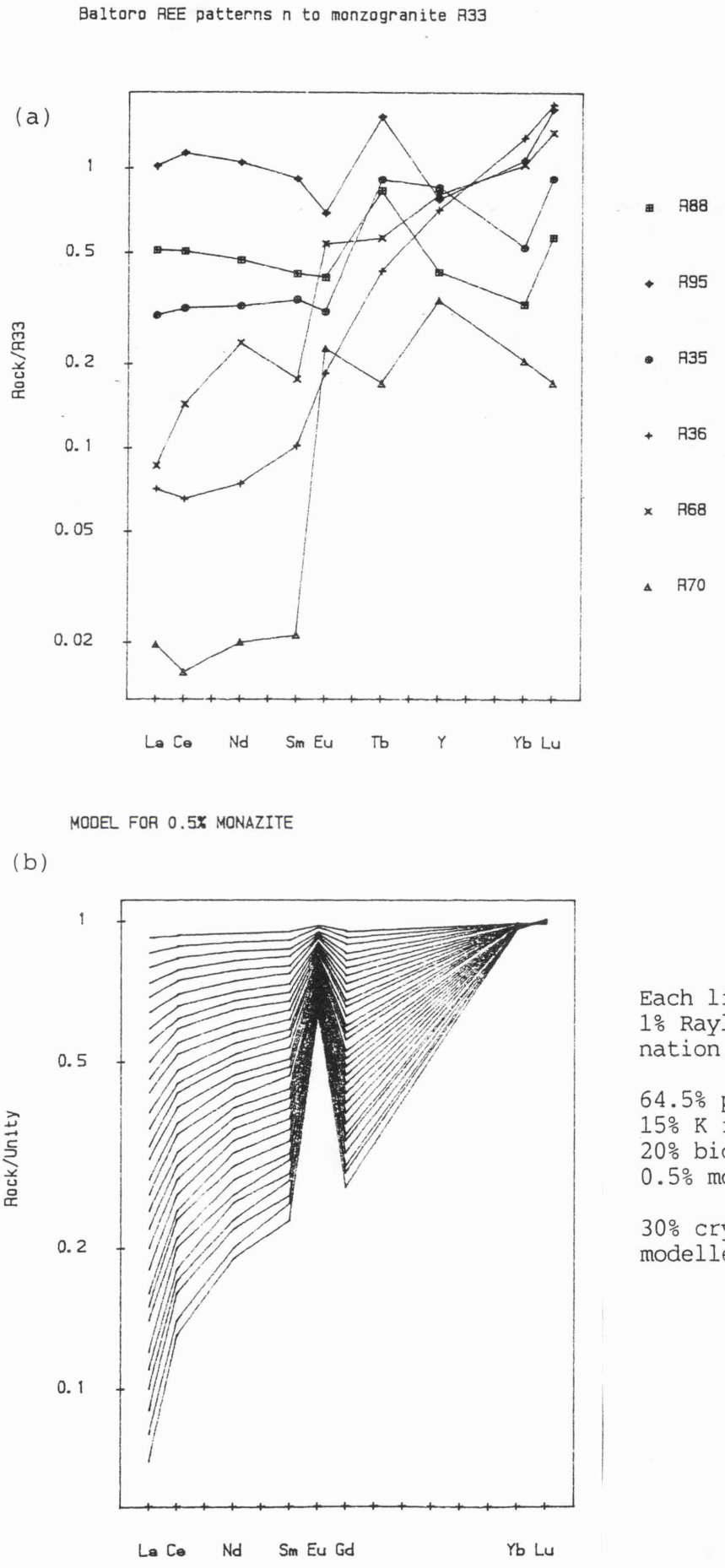

Figure 5.8: (a) Evolving REE patterns for the BPU granites normalised to monzogranite R33. R88 and R95 are monzogranites; R35 and R36 are leucogranites; R68 and R70 are leucogranitic pegmatite dykes.
(b) Modelled REE patterns for 0.5% crystallisation of monazite.

monzogranites have heterogeneous initial Sr isotope ratios of 0.707-0.712 (Rex et al., in press) which are higher than unmodified mantle values but lower than those which might be expected for mature upper crust. Heterogeneous initial Nd isotope ratios of 0.5121-0.5122 are consistent with this. Zircons show an inherited Precambrian component suggesting that at least part of the source must be this old. εSr and εNd values calculated for an age of 21Ma (40 to 118.5 and -6.8 to -8.5 (two samples only) respectively) lie in the enriched quadrant with respect to bulk earth on a εNd vs εSr diagram, but at lower values of εSr than would be expected if the granites had a pelitic source (fig. 5.9). $\delta^{18}O$ values are enriched with respect to the mantle with values of +9 to +11 (T. Rex, pers.comm.). In terms of trace elements (figure 5.4.a) the source is likely to be in equilibrium with a LILE-enriched melt with a LREE/HREE >1.0. The source must either have a negative Nb anomaly itself or contain a residual phase, such as sphene, which retains Nb.

The nature of the BPU in the field shows that the magma has been sufficiently mobile to separate from its source. The Dassu Gneiss to the south of the BPU has low abundances of Sr (87.5ppm) and contains feldspar. On melting residual feldspar would hold back the strontium and so this rock type could not melt to give a magma with the high Sr contents of the monzogranites. Additionally, the Dassu gneiss has a much higher Sr isotope ratio (1.058 at 21Ma) than the initial ratios for the BPU. The K2 Gneiss and quartz porphyries of the K2 region show very similar geochemical signatures to the BPU monzogranites (fig. 5.4.d), but this in itself precludes them as a source since all the elements would have to be released in proportionally equal quantities during melting; this is unrealistic. It is, however, possible that these two rock types are related to the same source as the monzogranites, despite the difference in age (K2 Gneiss=115±3Ma). Therefore, the source of the monzogranites does not appear to be exposed and its nature must be assumed in order to try to model the above features.

On the basis of the isotopic evidence there is little or no unmodified mantle component in the monzogranites, and if they are primary or near primary magmas then they must be crustal melts since there are no suitable protoliths that could be in equilibrium with such a melt in the mantle (Huang and Wyllie, 1981). Their

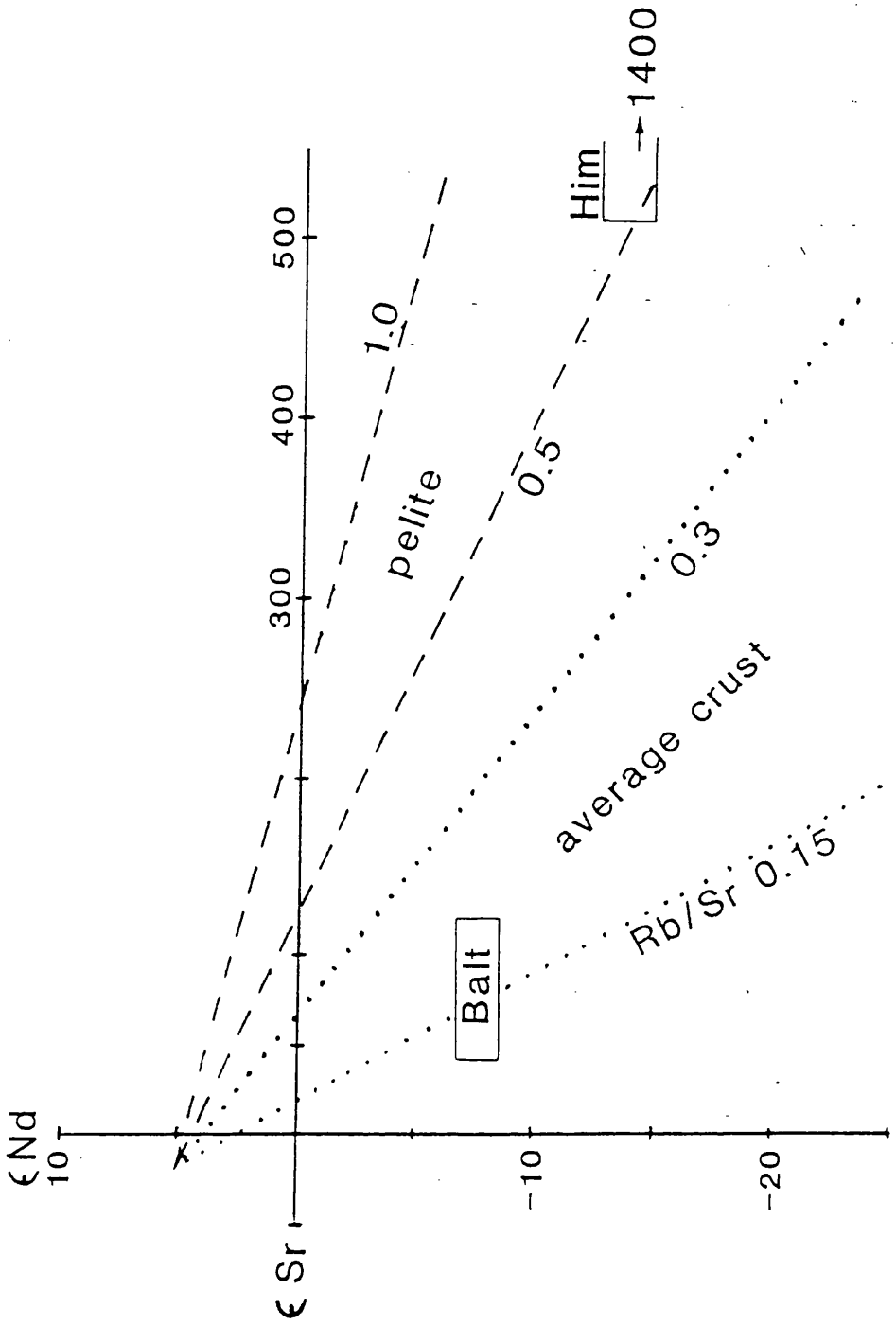

Figure 5.9: εNd vs. εSr diagram showing the position of the BPU granites. Also shown are evolution lines from depleted mantle for various Rb/Sr ratios representative of pelites and average crust (taken from Miller, 1985). Field for the High Himalayan leucogranites (HIM) is calculated with data from Allegre and Othman (1980).

peraluminous nature and near minimum melt composition also indicate a crustal derivation. Continental crust has a negative Nb anomaly (Taylor and McLennan, 1985) due to retention of this element in the subducting slab (Saunders et al., in press), and a source containing quartz and feldspar would provide the necessary $\delta^{18}O$ values. The Precambrian component in the zircons precludes a young source, but an older source would have to be poor in Rb to explain the low Sr isotope ratios. This description fits lower crust which has low Rb abundances (av = 5.3 ppm) and low Rb/Sr ratios (0.023) with respect to the upper crust (Taylor and McLennan, 1985). The gneisses to the south of the BPU indicate a former mid-crustal level for intrusion (Searle et al., in press) and so on the basis of the above evidence the source is most likely to be lower crust.

Figure 5.10 shows one of the more basic monzogranites (R33) normalised to typical lower crust (Taylor and McLennan, 1985) and, if the monzogranites are near primary magmas, this is the signature that must be produced by melting. In order to facilitate source modelling the assumption that the monzogranites are primary, crustal melts is made below. If this is shown not to be feasible, then a suitable, more basic parent which can produce the monzogranites by fractionation must be identified. Even if the monzogranites can be modelled by crustal melting this possibility must be considered and is discussed later.

If excess fluid is present crustal rocks will melt extensively at around 650°C (granitic wet solidus) and yet this is rarely observed in upper amphibolite-grade facies terranes. High-grade metamorphic terranes have low porosities (0.1% or less) and if these were filled with water this would still amount to only 0.03% H_2O in the rock by volume (Clemens and Vielzeuf, 1987). Any fluid initially present will be quickly used up during melting leading to fluid-absent conditions and many granitoid bodies are, therefore, water-undersaturated. It is, therefore, reasonable to assume that melting in the lower-middle crust occurs under fluid-absent conditions. Huang and Wyllie (1981) demonstrated that it is possible to melt a variety of crustal rocks under vapour-absent conditions via dehydration reactions of hydrous minerals (micas and amphiboles) to produce granitic liquids. These primary liquids will have moderate H_2O contents, with the exact nature of the melt being dependent on the

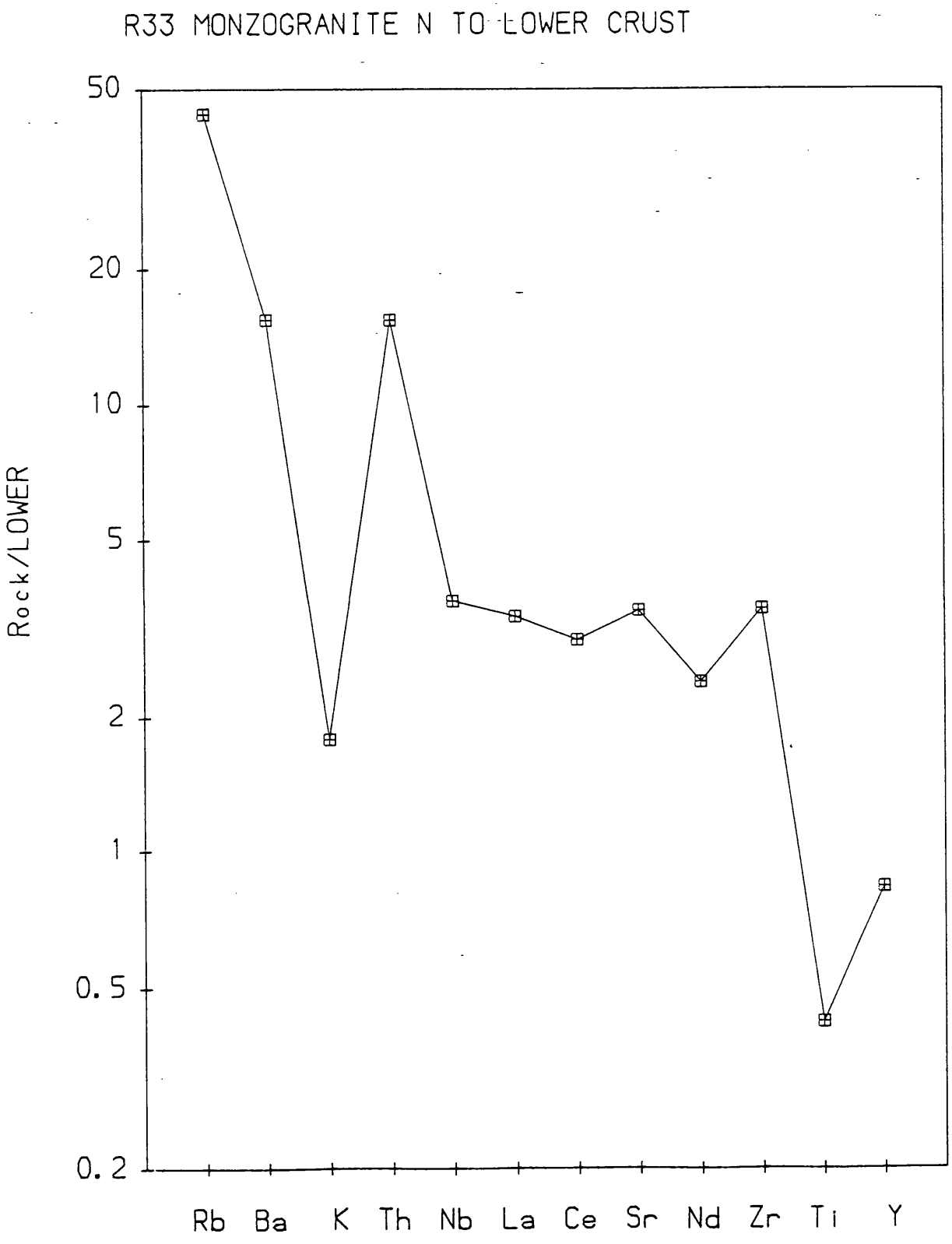

Figure 5.10: R33, one of the least evolved BPU monzogranites, normalised to lower crustal abundances (from Taylor and Mc Lennan, 1985). This is the spidergram pattern that needs to be produced by melting if the BPU monzogranites are primary melts (see text).

type and amount of residual crustal minerals present.

It has already been noted that the BPU was mobile and may have ascended for some distance through the crust along the KBL. Clemens and Vielzeuf (1987) considered that the main controlling factor over magma ascent was viscosity of the melt which, in turn, is dependent on melt composition, water content, pressure, temperature and crystal content. Ascent may be facilitated by tensional stress regimes and crustal fractures. However, in order for a magma to separate from its source the amount of partial melting has to exceed the rheologically critical melt proportion (RCMP, Clemens and Vielzeuf, op.cit.) or critical melt fraction (CMF, Wickham, 1987) in order for convective overturn to occur. This convective motion is then capable of generating large magma bodies, and, if these melts lie well above their solidus i.e. they are water-undersaturated, then they will be able to rise considerable distances through the crust. Wickham (1987) estimated the CMF to be between 30-50% melt while Clemens and Vielzeuf (1987) gave lower estimates of 20-30% for the RCMP and suggested that certain lithologies such as quartzo-feldspathic rocks generated more mobile magmas where the RCMP may be <20%. To generate enough melt to exceed the RCMP Clemens and Vielzeuf (op.cit.) showed that pelites would have to reach the biotite breakdown reaction (850°C approx.) and intermediate lithologies such as tonalites would have to reach the amphibole breakdown temperatures (900°C approx.). Dehydration of muscovite in a pelite at lower temperatures would only yield about 6% melt. The same authors also noted that intermediate rock types at high temperatures are the most fertile sources producing the hottest and wettest melts, but they considered that the most likely source rocks for large, primary, peraluminous, muscovite bearing syntectonic granites are pelites. Melting of such pelites at 10kb would give a magma with a water content of 3.7%.

Rutter and Wyllie (1988) took Wickham's (1987) estimate of the CMF and tried to model melting of a garnet tonalite as a lower crustal source for the southern Sierra Nevada batholith. They found that at between 850 and 900°C biotite dehydrates and reacts out but only produces a 22% partial melt. Further dehydration of hornblende to give clinopyroxene between 925 and 975°C is required to give a 35% partial melt containing 2.3% water at 1000°C. Similar temperatures would be required if the source was amphibolitic but pelitic gneisses

could yield sufficient melt in the range 850-900°C due to the higher percentage of biotite present.

Both set of authors above have reached essentially the same conclusion that whatever the source rock for granitic plutons (probably pelitic in the case of the BPU) temperatures in excess of 800-850°C are required to generate sufficient melt in water-undersaturated conditions to allow mobility, and that this melt will itself be undersaturated. Lower temperatures would be capable of inducing sufficient melting if the system was fluid-saturated as might be the case where wet sediments are overthrust and start to dehydrate e.g. the High Himalaya (Le Fort, 1981). However, it is unlikely that this is the situation in the lower Karakoram crust. It is debatable whether such high temperatures can achieved at the base of the Karakoram crust by the crustal thickening and P-T-t path models predicted for continental collision zones by England and Thompson (1986). These models predict that the most deeply buried rocks in young (Mesozoic-Cenozoic) orogenic terranes may achieve 20% melting via dehydration reactions with an average of around 5% melt for the lower half of the crust. Therefore, it is not surprising that both Clemens and Vielzeuf (1987) and Rutter and Wyllie (1988) consider that an additional heat source or fluid from the mantle beneath the crust is required.

Another question to be answered is whether the melting of such a tonalite or pelitic gneiss is capable of producing the BPU signature. Rutter and Wyllie (1988) started with an assemblage of K-feldspar-plagioclase-quartz-biotite-hornblende-garnet-magnetite. K-feldspar melted out first producing orthopyroxene, and sphene also appeared as a new phase. Using available distribution coefficients a 12 element spidergram was calculated using Hanson's (1978) batch melting equation and starting concentrations of unity. Whilst this is fairly simplistic and is only meant as an illustration, it can be seen that the melting process given in figure 5.11 gives good agreement between the theoretical melt and the crustally normalised BPU monzogranite for Th, Nb, Zr and the LREE. Muscovite was not included in the melting assemblage due to the lack of distribution coefficient data available for this phase, so all the dehydration melting is through breakdown of biotite and hornblende. There may also be a minor quantity of unmodelled aluminosilicate in the source as indicated by

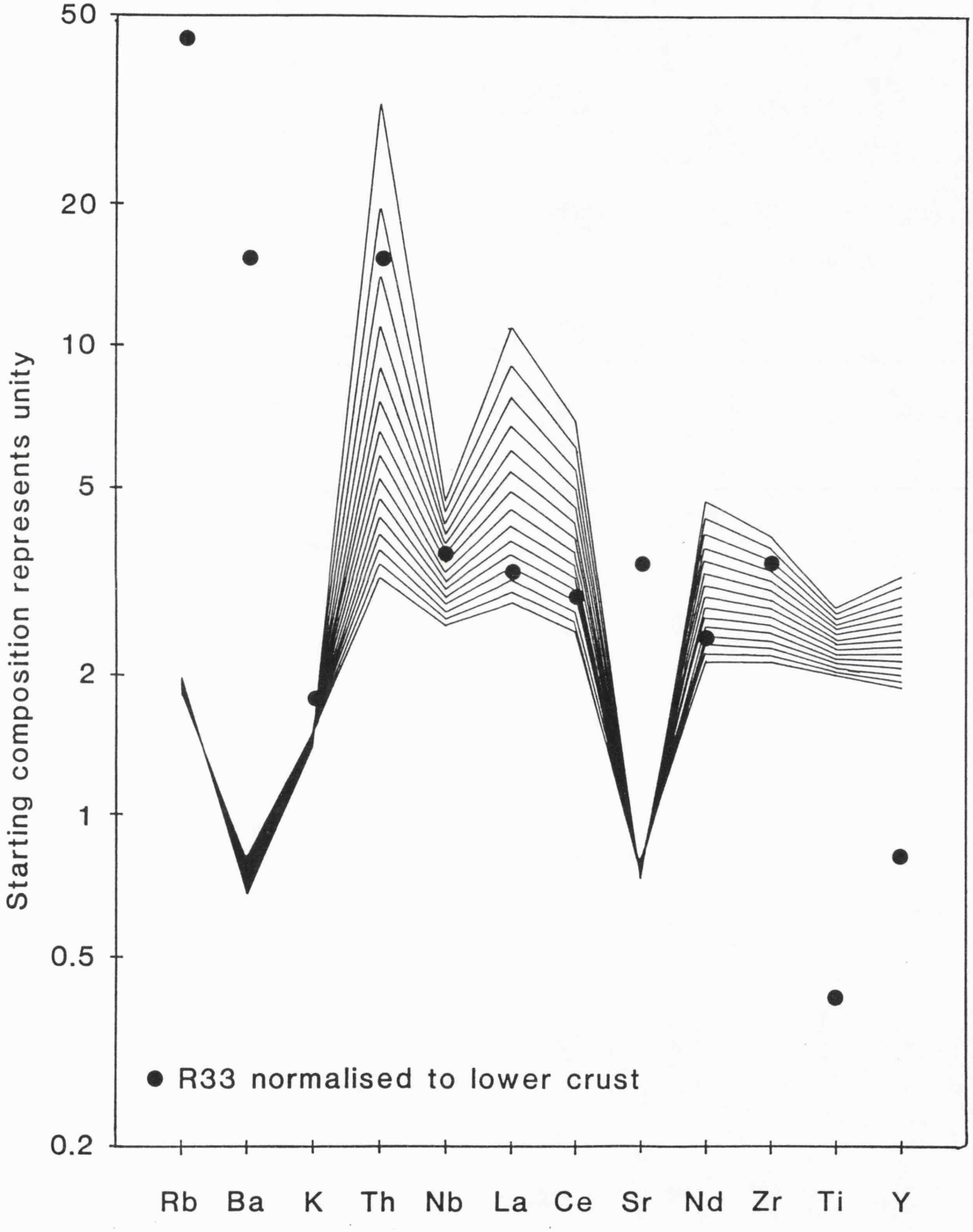

Figure 5.11: Modelled spidergrams for partial melting of tonalitic lower crust compared with the actual spidergram of monzogranite R33 (circles) when normalised to lower crust (Taylor and McLennan, 1985). Each line represents a 2% batch melt using the equation of Hanson (1978) upto 30% melting. Distribution coefficients from Henderson (1982). Tonalitic assemblage = 10% biotite, 10% hornblende, 20% plagioclase, 20% K-feldspar, 20% quartz, 10% garnet and 10% clinopyroxene. Melting proportions = 20% biotite, 20% hornblende, 10% plagioclase, 25% K-feldspar and 25% quartz.

the xenocrystic sillimanite (plate 5.1(d)). The HFS elements Ti and Y could be depleted further by residual sphene, magnetite, and garnet, but there is no obvious mechanism for the necessary enrichment of the LILE concentrations because the crust has much lower concentrations than the BPU and biotite and plagioclase are possible residual phases. A more accurate model is precluded by insufficient knowledge of the starting composition and the likelihood that the monzogranites have fractionated and changed their composition slightly prior to emplacement.

The high Rb content of similar magmas from Barouse, Yunnan and the High Himalaya was noted by Pearce et al. (1984) resulting in the syn-collisional granite field on their Rb vs. (Y+Nb) discrimination diagram being placed at high Rb values (fig. 5.12). Pearce et al. (op.cit.) could not explain this by simple melting of greywacke or quartz diorite and invoked addition of a fluid component rich in Rb and poor in Y+Nb into these granites. This is valid because these granites are related to volatile-induced melting at the base of hot thrust sheets. The Baltoro granites plot on the lower boundary of the syn-collisional field (fig. 5.12) suggesting that this fluid component was not as prevalent in their genesis, and this is supported by their volatile depleted nature. However, such a fluid could explain the enrichment of Rb relative to crust seen in the BPU. A mechanism is still required, however, to explain the high values of Ba and Sr in the BPU, otherwise it must be taken that the assumption that the BPU is a lower crustal melt is incorrect.

5.6: The Baltoro lamprophyres.

Spatially and temporally associated with the BPU are biotite minette dykes (fig. 5.1, Rex et al., in press). Petrographically they are unusually fresh carrying phenocrysts of orthopyroxenes and feldspars with pseudomorphs after olivine. Their K-Ar ages on biotite of 24-22±1Ma (cf 21Ma for the BPU) and their nature of forming a 'shadow zone' about the BPU, with no dykes actually intruding the pluton, suggests that they are genetically related to the BPU. Geochemically they are enriched in trace elements, especially the LIL elements Sr, Ba, Th, U, K and the LREE (fig. 5.13, table 5.2) which are usually incompatible in the mantle. They also show enriched initial $^{87}Sr/^{86}Sr$ ratios (0.7163-0.7206, Rex, pers. comm.) despite

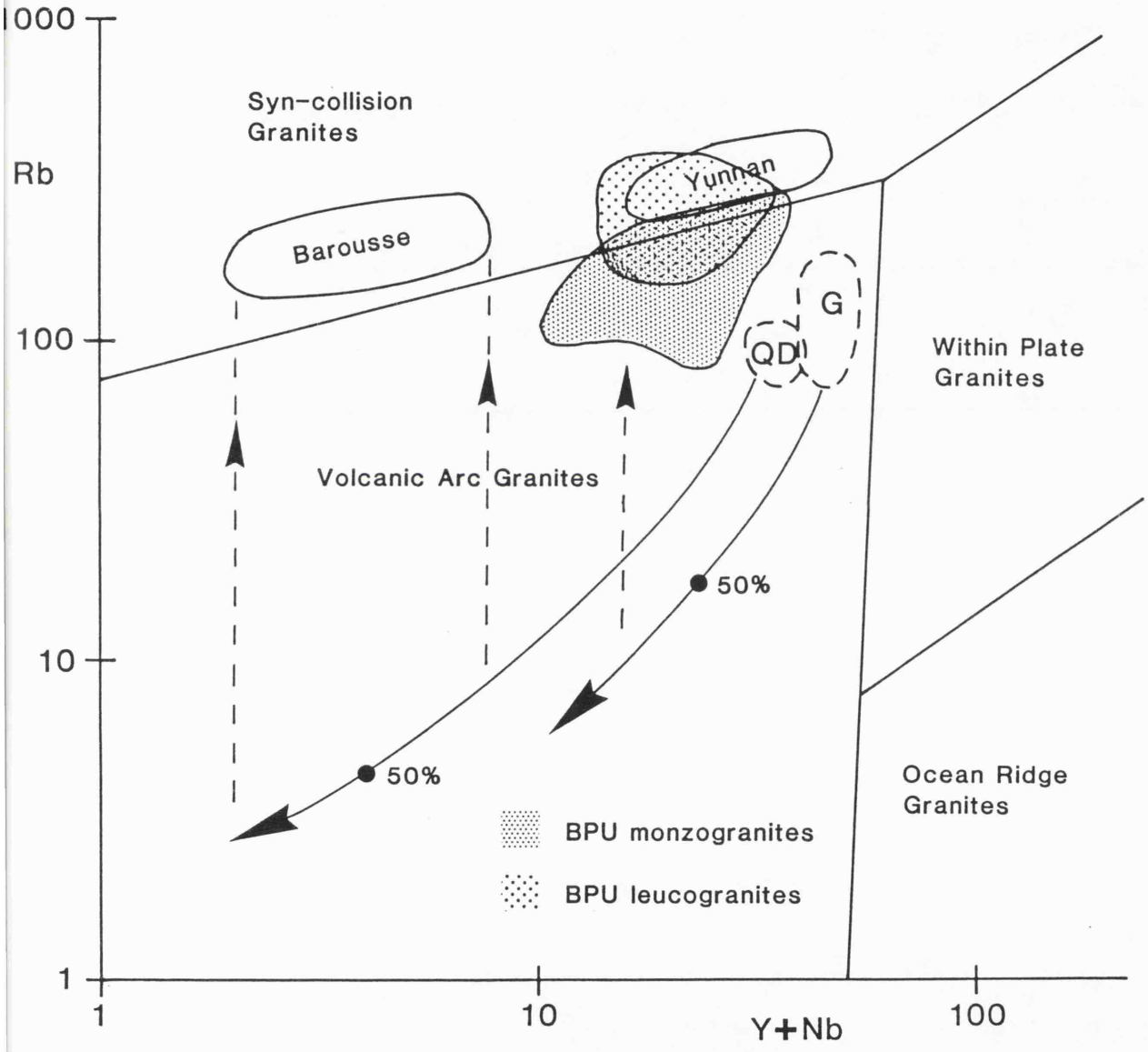

Figure 5.12: Pearce et al. (1984) Rb vs. Y+Nb tectonic discrimination diagram showing the position of the BPU monozogranites and leucogranites. Barousse and Yunnan are syn-collisional granites whose position cannot be explained by partial melting of the greywackes (G) or quartz diorites (QD) (solid curves and arrows) and require the addition of a Rb-rich fluid (dashed lines and arrows).

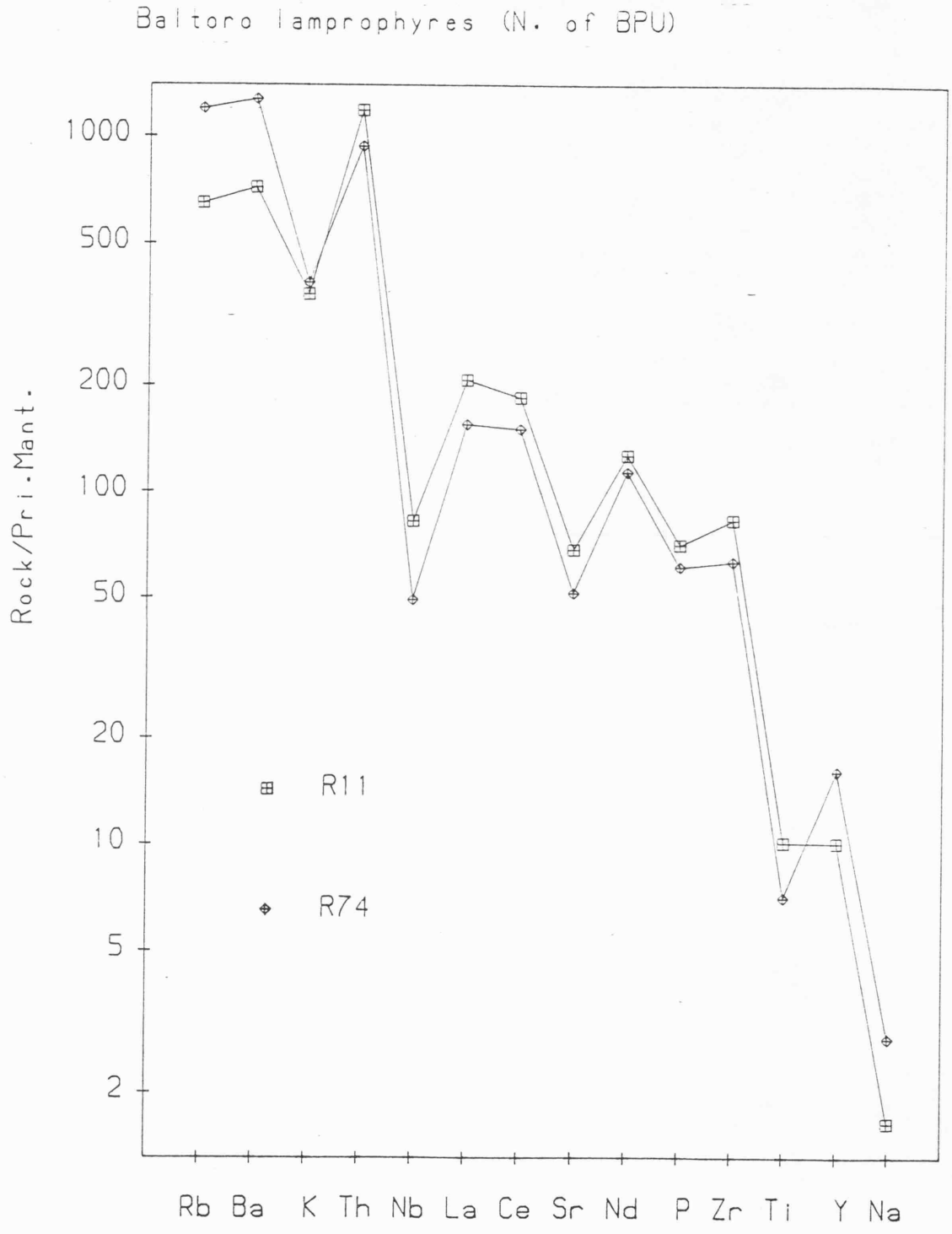

Figure 5.13: Multi-element variation plot or 'spider diagram' for the Baltoro lamprophyres.

not being enriched in Rb with respect to Sr. Their high concentrations of V, Ni and Cr together with their high Mg number preclude a crustal source or major contaminant, and so they must have been derived from a $^{87}Sr/^{86}Sr$ and LILE-enriched mantle source. The spidergram patterns of figure 5.13 are very similar to those for the calc-alkaline lamprophyres of N. England which are also subduction related and spatially and temporally associated with post-collisional granites (Macdonald et al., 1985).

The lamprophyres lie in group IV of Foley et al.'s (1987) classification which is transitional between the low Ca, Al and high Mg number group I found in stable continental or orogenic areas, and the high Ca, Al and low Mg number group III found in active orogenic areas. Foley et al. (1987) consider the enrichment seen in lamprophyres to represent enrichment of their mantle source by small melts rich in incompatible elements being trapped as they rise by the crystallisation of amphibole, or phlogopite at greater depths. These phases can later melt to give magmas with high K/Na ratios. Variations within the lamprophyre group can be attributed to one of the following processes:

a) Mantle heterogeneity prior to enrichment due to the removal of basaltic melts leaving a residue depleted in Al, Ca and Na. The amount of clinopyroxene left in the source region and the volume of earlier melts will cause variation in the above elements.
b) Variation at the enrichment stage either due to the stability of incompatible element-rich phases such as K-richterite, rutile or Cr-titanates or due to the type of enriching agent, water being a richer carrier than carbon dioxide. The varying stability of phases would lead to a zoned mantle.
c) Chemical variations during melting due to different residual phases.

Many authors have recognised the need for a LILE-enriched high Sr and low Nd radiogenic component in the source of ultra-potassic and/or post-collisional magmas (e.g. Fraser et al., 1985; Rogers et al., 1985; Varne, 1985; Nelson et al., 1986; Thorpe et al., 1986). This component must be mantle in origin due to the high Mg number and refractory element concentrations in the magmas. A similar component is recognised in the source of certain OIB magmas in the southern

hemisphere and is designated as EM II (where EM is enriched mantle) as opposed to EM I which has the same chemical characteristic as EM II except that it has low rather than high $^{87}Sr/^{86}Sr$ isotope values (Zindler and Hart, 1986). EM I and EM II are thought to represent depleted MORB mantle (DMM) that has been accreted onto the lithosphere during subduction and has then been subsequently enriched by fluids (Saunders et al., in press). Menzies (1983) proposed that the high Rb/Sr character of EM II is due to the incorporation of a hydrous fluid whilst EM I signatures are produced by CO_2-rich fluids based on the much higher solubility of H_2O compared to CO_2 in mantle melts. It is debatable whether the asthenosphere can provide the hydrous fluids for EM II-type enrichment since the asthenosphere has much lower (LILE/Nb) ratios than those seen in many ultrapotassic magmas. This can, however, be explained by having a Ti-rich phase such as perovskite stable in the source region which would retain Nb with respect to the LILE.

The isotopic characteristics of EM II have a strong similarity with upper continental crust or sediment (Zindler and Hart, 1986) and so hydrous fluids from subducted continental material metasomatising the DMM above a subducting slab are a likely enriching agent. The subducting slab releases fluids/melts rich in incompatible LILE preferentially retaining Nb and the HFS in a Ti rich phase (Saunders et al., in press) so explaining the observed high (LILE/Nb) ratios mentioned above. Rogers et al. (1985) recognise two such subduction components in the source of the Vulsini lavas of the Roman region. One is a low-K component from water-rich slab fluids mixing with E-type MORB mantle to give one mixing end member. The other component comes from melts from the slab interacting with the overlying mantle. Sekine and Wyllie (1982) showed that hybridisation of such hydrous siliceous melts with a simplified peridotite causes solution of the peridotite component with little change in liquid composition. Hybridisation products include phlogopite (at pressures and temperatures where phlogopite is stable) ± enstatite ± quartz. The precipitation of phlogopite will remove all the potassium and presumably a large quantity of LILE compatible in phlogopite from the melt. Later melting of this phlogopite-rich component gives the high Rb/Sr, Rb/Ba, K/Ti ratios in the magmas. Because the source is enriched in Rb, K, and Th and depleted in Ti, Ta, Nb and P it has a typically high Th/Yb subduction-related ratio (Pearce, 1983). In

terms of compatible elements there is no difference between the high and low-K magmas showing that these elements are not affected by the enrichment process.

Varne (1985) notes the EM II-type component present in the post-collisional magmas of the Sunda arc. Here the component becomes more involved towards the collision zone and is also evident in the within-plate magmatism of W. Australia. Varne (op.cit.) therefore considers the ancient subcontinental lithosphere beneath the Australian craton to be the source of the EM II component. This lithosphere presumably became enriched during an older subduction event when it underplated the craton and has been stable there since. The difference between the within plate and collisional magmas is that the intraplate magmas are not depleted in the Ti-group elements. Varne considers this to be a result of a stable Ti phase in the residue of the collisional magmatism depleting the melts in the Ti group. Another possibility is that mantle plumes from the OIB reservoir, which will be rich in the Ti group elements as these are retained in the residual slab component which feeds the reservoir (Saunders et al., in press), could intrude and re-enrich the subcontinental lithosphere in these elements.

The Baltoro lamprophyres plot with the same high ratios as the Australian lamproites and W. Sunda Arc magmas on a Nb vs. Ba diagram (Varne, op.cit.) showing that have typically enriched Ba signatures (fig. 5.14(a)). However, on a Nb/Ba vs. Rb/Ba plot (fig. 5.14(b), Rogers et al., 1985) they show unusually low Rb/Ba ratios compared to the Italian Roman lavas and mantle peridotite xenoliths containing phlogopite, and actually lie in the destructive plate margin terrain of circum-Pacific lavas. This implies that the source region for the lamprophyres is not as enriched in Rb as it is in the other LILE.

In Baja California, Mexico Upper Miocene-Recent volcanic rocks provide a record of magmatism both during active subduction and after subduction had ceased (Saunders et al., 1987; Rogers and Saunders, in press). Geophysical evidence indicates that at 12.5Ma subduction stopped along much of Baja either due to ridge abandonment or subduction. Between 25 and 10Ma syn-subduction basaltic andesites and andesites formed the Comondu Formation and these magmas define calc-alkaline trends and are similar to other destructive plate margin

Figure 5.14: Biaxial variation diagrams for the Baltoro lamprophyres (large stars), Caledonian lamprophyres (triangles; Rock and Hunter, 1987) and SW England minettes (circles; Leat et al., 1987).

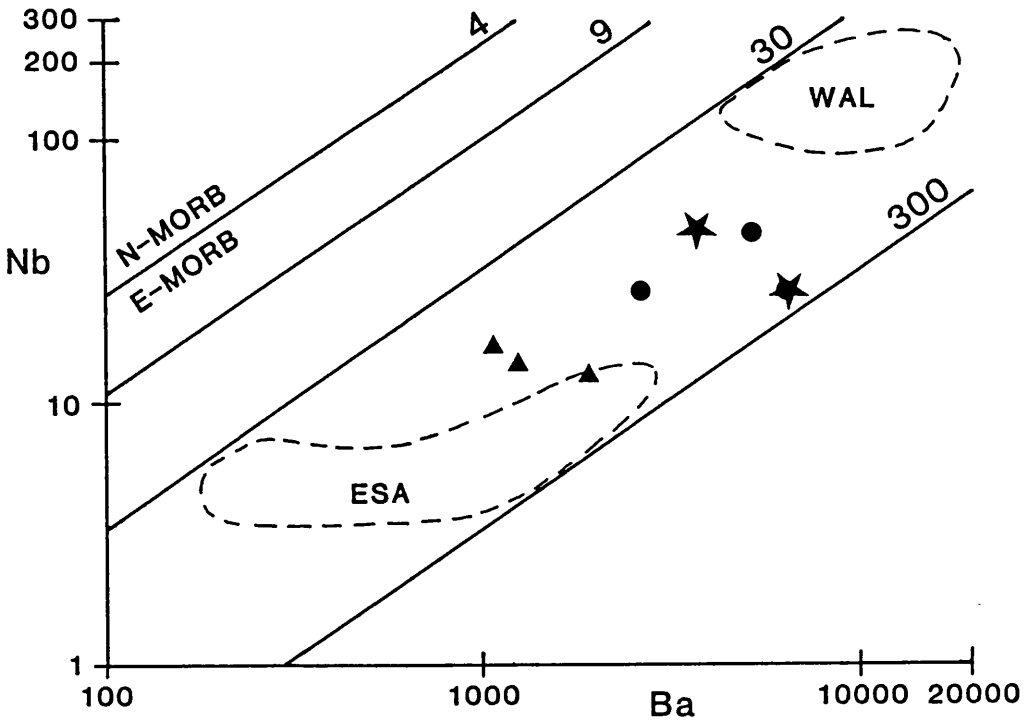

5.14(a): Lines and numbers show constant Ba/Nb ratios. Baltoro lamprophyres plot with the same high ratios as East Sunda arc lavas (ESA) and western Australian lamproites (WAL) (after Varne, 1985).

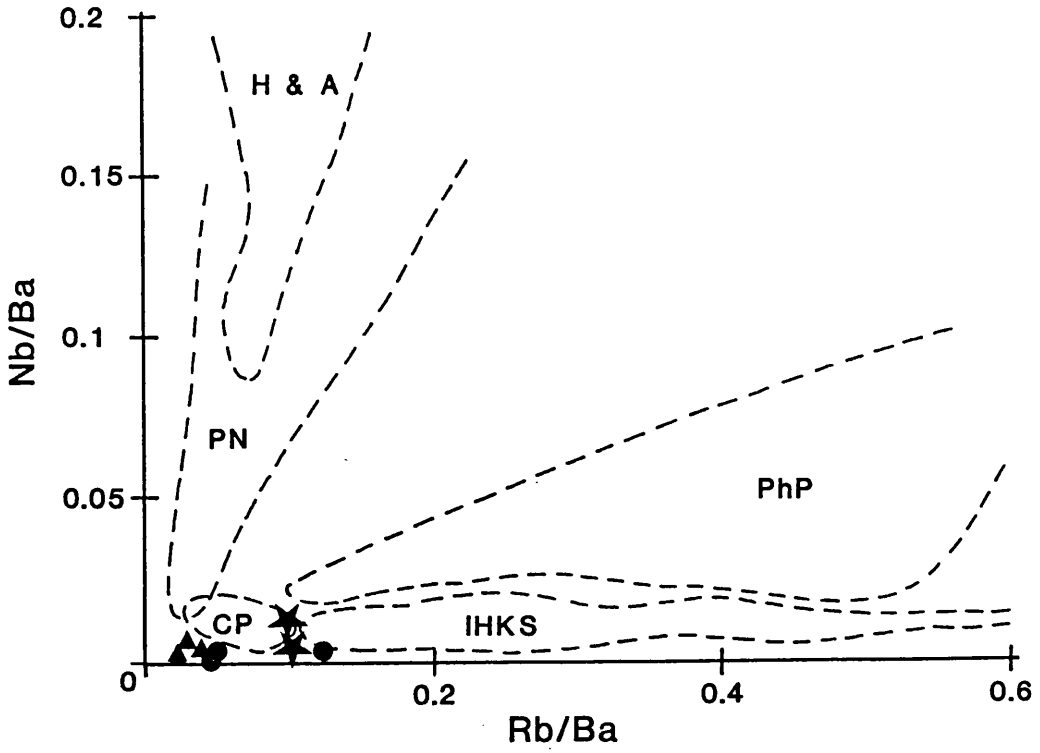

5.14(b): Lamprophyres plot with low Rb/Ba ratios compared to the Italian high-K series lavas (IHKS) and phlogopite-bearing mantle xenoliths (PhP), but with similar ratios to magmas of circum-Pacific destructive margins (CP), non-phlogopite-bearing xenoliths (PN) and magmas from Hawaii and the Azores (H&A); (after Rogers et al., 1985).

lavas. Incorporation of subducted sediment into the source of the Comondu Fm best explains their isotopic signature (εSr=-17 to +23, εNd=+3 to -3.6). The most abundant and widespread post-subduction magmas are magnesian basaltic andesites and andesites termed 'bajaites' which range in age from 11.1Ma to Recent. The bajaites have many of the calc-alkaline features displayed in the Comondu lavas with high (LILE/HFSE) ratios. However, the bajaites also exhibit unusually high Sr and P_2O_5 abundances and high K/Rb, Na_2O/K_2O and $(La/Yb)_N$ ratios. Baja differs from the above examples in that the post-collisional magmas are enriched in Ba and Sr but not in Rb. This is attributed to the stable, modified mantle wedge phase being amphibole and not phlogopite, amphibole being stable at lower temperatures and pressures. The amphibole acts as a sink for K, Sr and Ba but Rb is not trapped and so appears in the pre-collisional magmas. The Baltoro lamprophyres are not enriched in Rb with respect to the other LILE and so a similar situation is envisaged beneath the Karakoram. However, either ancient subcontinental mantle lithosphere or the modified mantle wedge related to the post-Jurassic subduction beneath the Karakoram could be the source for the lamprophyres.

Arc magmas become progressively more enriched in LILE as the subduction zone matures (Saunders and Tarney, 1984), and this shows that the enrichment of the mantle wedge by the slab component is gradual. In the case of the Sunda arc and Baja California the signature of the enriched mantle only started to appear immediately prior to, and after, collision, with more normal arc-type magmatism prior to this. This is also the case in the Baltoro with the lamprophyres being post-collisional. This must be because conditions in the mantle have to change from those during 'normal' subduction i.e. an increased heat flow, in order to melt or breakdown the previously stable amphibole.

5.7: Mantle-crust interaction beneath the Karakoram.

It was established earlier that a pelitic (or tonalitic) source containing biotite and hornblende together with quartz and feldspar ± pyroxene ± muscovite ± sillimanite could produce a 30% partial melt similar to the BPU monzogranites under high temperatures at the base of the crust. Residual sphene and/or garnet must be invoked to explain the depletion in Ti and Y. However, difficulties were

experienced in trying to model the high concentrations of Ba and Sr in the monzogranites. With the lamprophyres there is an obvious contaminant, especially considering their spatial and temporal relationship to the BPU. Despite being depleted in Rb relative to the other LILE the lamprophyres still contain more Rb (av = 509 ppm, n=2) than the BPU monzogranites (av = 160 ppm, n=28) and so could also contaminate the BPU to give the observed high Rb abundances relative to lower crust (Taylor and McLennan, 1985). This would negate the need for the Rb-rich fluid mentioned earlier (section 5.5) and is more plausible since melting probably occurred under anhydrous conditions (see earlier). However, a K-rich fluid was a late-stage feature of the BPU (see section 5.3) and this could have carried Rb. Therefore, the Rb abundances in the BPU may be a result of the mixture of the two processes.

The questions that now need to be answered are: can the lamprophyres mix with a crustal source to give the monzogranites, how did the mixing take place bearing in mind the field relations, and what change in conditions initially caused the melting in both the crust and mantle?

Three mechanisms can be considered whereby the LILE-enriched signature of the lamprophyres could appear in the BPU monzogranites:

a) The BPU is a direct fractionate of the lamprophyre magmas. This was an idea recently pursued by Rock and Hunter (1987) who considered that co-intruded, Inner Hebridean lamprophyres and microgranite porphyries within composite dykes were co-genetic and related by fractionation. This conclusion was based upon their close relationships in the field, linear chemical trends, similar initial Sr isotope ratios and least squares fractionation modelling. Discontinuities in some trends and disturbed isotopic systems also suggested a degree of crustal contamination. The authors also considered that the lamprophyres could be the parent magma for the Ross of Mull granite pluton due to the similar Sr isotope ratios and high LILE contents of the two.

It was mentioned earlier that the monzogranites might not be primary melts as assumed, but fractionates of a more basic parent, and at first sight the lamprophyres would appear to be suitable

parental magmas. In order for the Baltoro lamprophyres to fractionate to form the BPU they would have to precipitate olivine and orthopyroxene, two observed phenocryst phases, to reduce the Ni, Cr (and V) contents of the melt. Taking distribution coefficients from Henderson (1982) and assuming Rayleigh-type fractionation (Hanson, 1978), an assemblage of 50% olivine and 50% opx would need to fractionate until 45% of the liquid was used up in order to reduce the Ni contents from 380 ppm (lamprophyre average) to 10 ppm (the concentration in R33, table 5.2). For the same assemblage 49% of the liquid would have to crystallise to reduce the Cr contents from 540 ppm to 22 ppm. During this fractionation $D_{Ba} << 1$ and so Ba contents will increase from an average of 4500 ppm to over 8000 ppm. Assuming the fractionating assemblage changes to something similar to that which was modelled to generate the leucogranites from the monzogranites (5.4, 65% plag, 20% biot, 15% K-fsp) D_{Ba} will rise to about 2.5. This means a further 57% of the remaining liquid will have to crystallise to lower the Ba content of the melt down to 2317 ppm (R33). Whilst the above calculations are simplistic they represent one of the most efficient methods of reducing the high elemental abundances in the lamprophyres. They show at least 75% of the lamprophyre magma must crystallise before concentrations in the melt will be similar to those of the BPU. This is a conservative estimate since the presence of phenocrysts in the sampled lamprophyres suggest that they have already fractionated to some extent. This means a huge quantity of basic magma would be necessary to create the voluminous BPU, and this is in contrast to the apparent sparsity of lamprophyres exposed. Another point which opposes this model is the difference in initial Sr isotope ratios between the lamprophyres and the BPU.

b) The lamprophyres assimilate crust and then fractionate, or the crustal melt discussed above mixes with the lamprophyre magmas to give the BPU. Whether one considers the crust to be contaminating the lamprophyres or vice versa depends upon which is the dominant component, but the principle of each forming a end member on a mixing curve remains the same. Leat et al. (1987) considered the source of the SW England granite to be fractionated potassic magmas from subduction-enriched mantle which were contaminated, as they rose through the crust, by assimilating pelites. This is analagous to considering lamprophyre magmas contaminating pelitic melts. Leat et al. (1987) invoked the potassic magmas as a source because they have

high Rb/Th ratios. This ratio is higher in the SW England granite than can be explained by contamination by typical basaltic magmas, but it is lower than that seen in other syn-collisional granites such as Manaslu. However, this reasoning might be erroneous since the high Rb/Th ratios in the Manaslu granite are not just related to a Rb-rich fluid typical of many crustally derived syn-collisional granites (Pearce et al., 1984), as considered by Leat et al. (op.cit.), but they are also due to residual monazite in the source holding back the Th (Cuney et al., 1984). Fractionation is necessary to lower some of the high elemental abundances (e.g. Zr) of the potassic magmas to granitic values.

It was shown above that at least 45% crystallisation of olivine, orthopyroxene ± plagioclase in the Baltoro lamprophyres is needed to lower the Ni and Cr abundances. Therefore, for a simple mixing model a fractionated lamprophyre melt, which is by now only enriched in LILE not removed in the fractionation, can be considered as one endmember. The other endmember can be considered to be either the crustal melt modelled earlier or typical lower crust (Taylor and McLennan, 1985). Figure 5.15(a) shows a plot of Ba vs. Sr for these two possible mixing endmembers. The BPU monzogranites plot between the two endmembers and lie nearer the crustal end indicating this is the dominant component. On a similar plot for Cr vs. Ni (fig. 5.15(b)) it can be seen that the lower crust has much higher abundances of Ni and Cr (135 and 235 ppm respectively) than the BPU. This indicates that it is more probably a crustal melt rather than the crust that is the mixing endmember, and this crustal melt must be depleted in Ni and Cr with respect to the crust. The Ni and Cr must be kept in the residue by phases such as biotite (D_{Cr} = 19 in acidic magmas; Henderson, 1982) and amphibole. However, this could not be modelled since no Ni distribution coefficients could be found for biotite and amphibole in equilibrium with an acidic melt. Alternatively, after mixing further fractionation of pyroxene removes these elements. However, pyroxene would not be in equilibrium with a melt as acidic as the BPU.

No Nd isotope data are available for the lamprophyres. However, lower crust has heterogeneous εSr values around zero and these plot on the opposite side of the εSr values for the BPU (40 to 118.5) to those for the lamprophyres (170.5 and 235). Hence, mixing between a

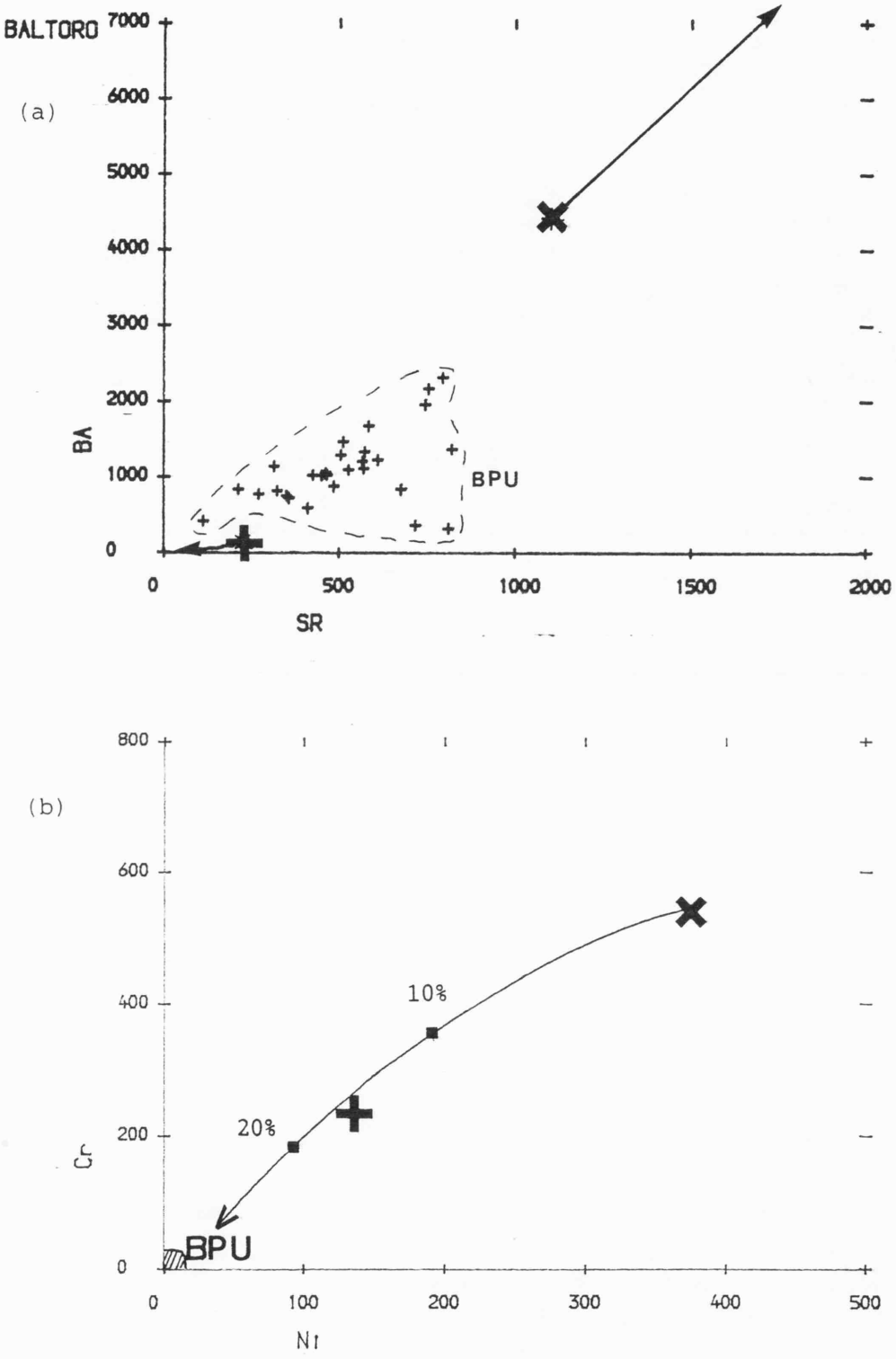

Figure 5.15: Tests to see if a simple mixing model can explain the relationship between the Baltoro granites and lamprophyres.
Large cross (x) shows the lamprophyre magma and the line and arrow show fractionation of 50% olivine, 40% orthopyroxene and 10% plagioclase. Plus sign (+) shows position of average lower crust (Taylor and Mc Lennan, 1985) with the line and arrow in (a) representing the melt of fig. 5.11. This could not be modelled in (b) due to a lack of distribution coefficient data (see text).

fractionated lamprophyre melt and lower crust or crustal melt is a strong possibility for the petrogenesis of the BPU monzogranites, although the mixing process is probably more complex than that outlined above[1]. It was thought that this mixing process might be akin to models for assimilation-fractional crystallisation (AFC) described by DePaolo (1981). These models predict that the mixing products will lie on a line between the original magma and the assimilated material on a 87Sr/86Sr vs. Sr graph. The shape of this line is dependent on D_{Sr} in the magma and the ratio of assimilation to fractionation, but on such a plot the BPU monzogranite data are scattered and so this model cannot be pursued.

c) The crustal source region of the BPU is metasomatised and contaminated by mantle-derived, LILE-only enriched fluid precursors to the lamprophyre magmatism. The fluid would come from dehydration of amphibole to produce pyroxene in the mantle wedge (see below) prior to the melting which produced the lamprophyres. Because of this the fluid will be enriched only in the elements that were compatible in the amphibole but are incompatible in the pyroxene i.e. the LILE. This cannot be modelled due to insufficient knowledge of amphibole composition in the mantle and pyroxene/fluid partition coefficients, but such a fluid would probably plot in the same place as the fractionated lamprophyre endmember in the graphs of model b) and so could also explain the mixing trends seen.

Having shown that the BPU could be produced by the mixing processes discussed above there are a number of possible mechanisms to explain the initialisation of melting and how the mixing/ contamination could have taken place, with the lamprophyres still forming a shadow zone around the BPU despite their older crystallisation age:

(1). After collision, as the Indian plate underthrusts the Karakoram

---

[1]Postscript: Recent Nd isotope data for the lamprophyres (June, 1988; T.Rex pers.comm.) supports the mixing possibility. On an εNd vs. εSr diagram the BPU granites lie between the field for lower crust taken from Taylor and McLennan (1985) and the lamprophyres, and the three groups define an approximate hyperbolic curve.

plate, the mantle will effectively be pushed both laterally and downwards. Initially the isotherms and solidus reactions will be depressed as well, but later thermal relaxation will cause the isotherms to rise to higher levels in the mantle, and also in the crust, due to thickening above. The isotherms will also be relaxing back towards the steady state geotherm as the cold slab input is removed. This will mean that the garnet lherzolite solidus will start to encompass a large region of mantle which was below the solidus during subduction. The same principle is illustrated in the differences between the warm mantle and cold mantle subduction zone models of Wyllie (1984). If PH_2O is high then the geotherm will intersect the wet garnet lherzolite solidus at a relatively shallow depth (fig. 5.16). Amphibole is stable above the wet solidus and will contribute to the melt. However, as the slab input has been removed it is more likely that the PH_2O of the system decreases and the melting front tends towards the dry solidus which lies above the amphibole-out reaction. If the geotherm is elevated so that it is hotter than usual at shallower depths, either due to the overlying thickened continental crust or through input of magmas from below, then it will intersect the amphibole-out curve causing dehydration of amphibole to give pyroxene and a water-rich fluid. Initially, the composition of this fluid will be buffered by the remaining amphibole according to the mineral/fluid partition coefficients. Eventually, however, the system will become oversaturated as more amphibole dehydrates and the fluids will start to become enriched in the most incompatible elements. These fluids will then flux the overlying mantle, lowering the solidus towards wet melting. The resultant melts will inherit the enriched signature of the fluids and may resemble lamprophyres. Figure 5.17 shows a hypothetical mantle structure beneath the Karakoram at 20Ma. It shows the area in which amphibole will dehydrate as the amphibole-out curve rises in response to thermal re-equilibration. Above this is the area of the mantle that will be able to melt if PH_2O rises. The 20Ma gap from collision to magmatism is explained by the time taken for crustal thickening, re-equilibration and also the time needed to saturate the system.

Three models can explain the subsequent evolution of the system. In all cases it can be seen from the crustal section in figure 5.17 (Rex et al., in press) that the lower Karakoram crust is the most likely source for the BPU. Incipient melting had probably already

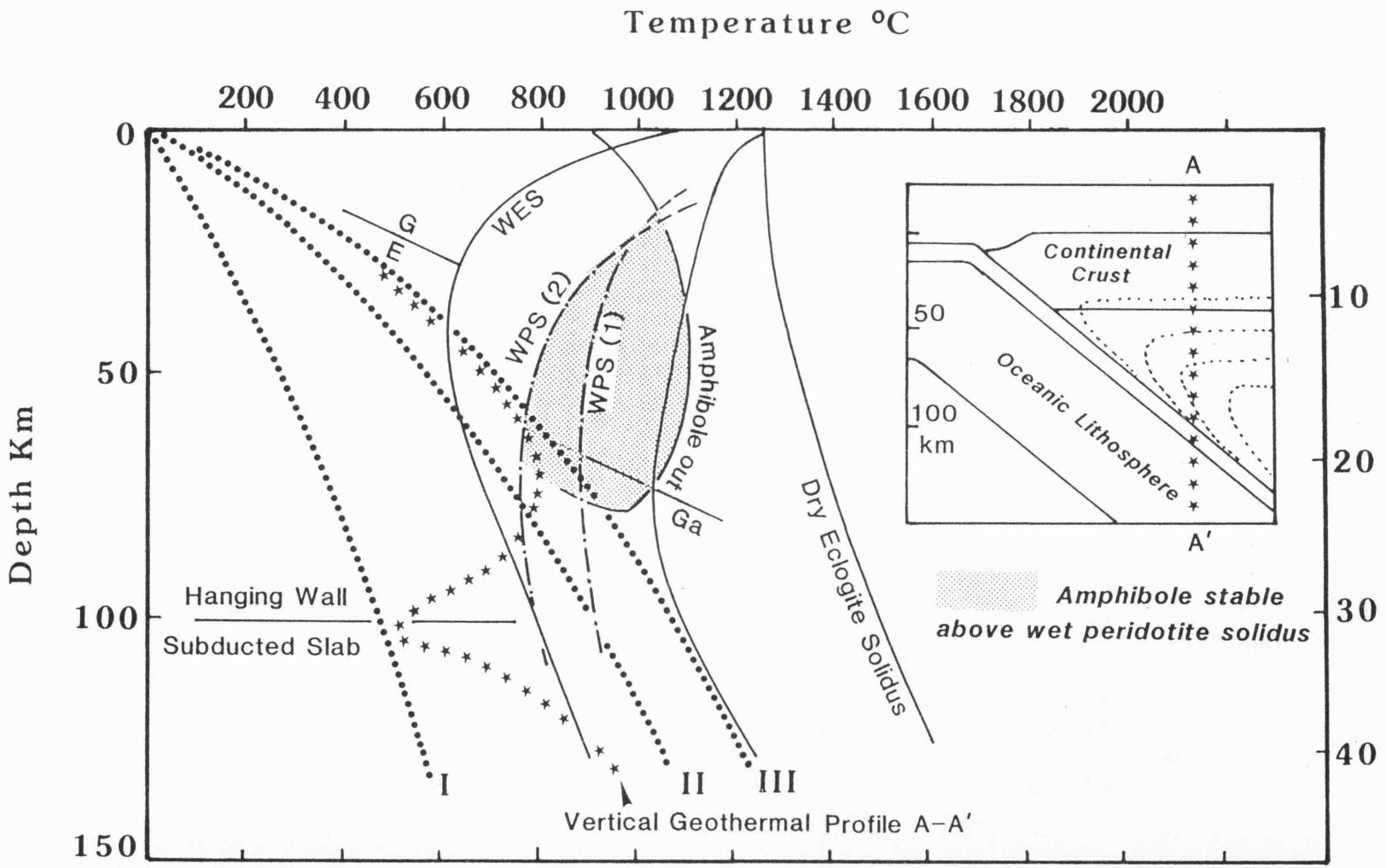

Figure 5.16: Pressure-temperature profile through a hypothetical mature subduction zone (cold crust, cold mantle; Wyllie, 1984). WPS = wet peridotite solidus; WES = wet eclogite solidus; Ga = garnet stable; G/E = gabbro to eclogite transition. Curve I = geotherm within the slab; curves II and III are shield and oceanic geotherms respectively. Taken from Rogers and Saunders (in press).

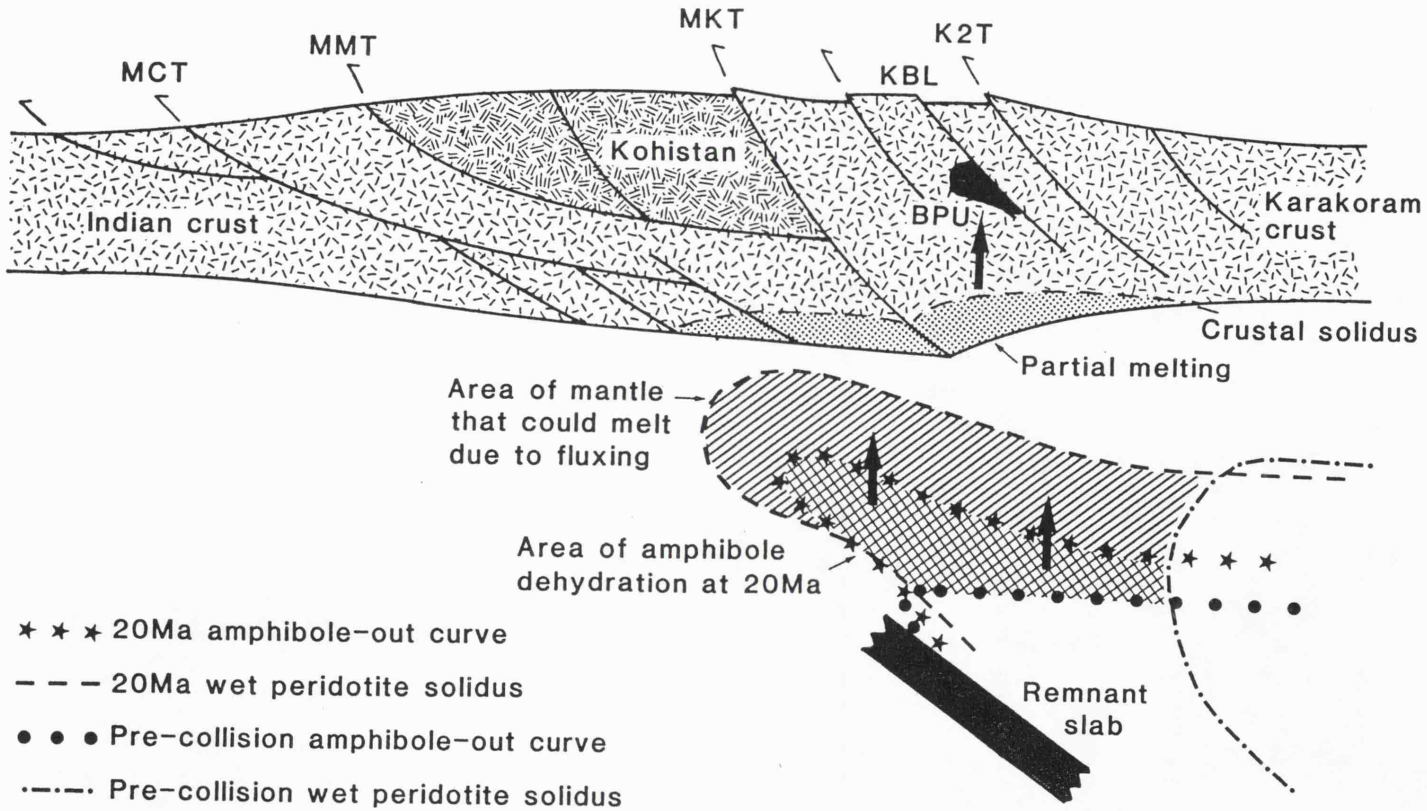

Figure 5.17: Hypothetical cross section through the mantle beneath the Karakoram at 20Ma. The continental crust has been homogeneously thickened, and the crustal structure is taken from model A of Rex et al. (in press). MCT = Main Central Thrust; MMT = Main Mantle Thrust; MKT = Main Karakoram Thrust; KBL = Karakoram Batholith Lineament; K2T = K2 thrust. Not drawn to scale.

started at the base of the crust in response to thickening. This melting would roughly correspond in time to the melting in the mantle beneath, although this would depend on the relative relaxation rates of the isotherms in the crust and mantle. However, it is probable that heat from a mantle input into the crust was necessary to generate sufficient partial melt to allow the BPU to separate from its source.

a) LILE enriched fluids (model c) above) from either amphibole dehydration or melting rise and metasomatise the base of the crust. This promotes melting to give the contaminated BPU magma and is, in effect, a trigger mechanism. The magma separates from its source and starts to rise but as the mantle continues to melt lamprophyre magmas rise, overtake the BPU and are intruded first. The slower ascent and crystallisation of the BPU accounts for the the older age of the lamprophyres despite the fact the BPU formed first. The shadow zone is formed through the inability of the lamprophyres to penetrate the silicic BPU magma.

b) Lamprophyres underplate the crust but their intrusion is inhibited by the melt already formed there and so they start to fractionate due to the temperature contrast. The heat from these lamprophyres promotes large scale melting of the base of the Karakoram crust and convective overturn is initiated. This convection causes the crustal melt and fractionated lamprophyre melt to mix giving the BPU (model b above). As the BPU rises a second pulse of lamprophyre magma is intruded around it to form the shadow zone.

c) If the BPU had already formed through melting at the base of the Karakoram crust then lamprophyre magmas could simply be intruded with those magmas meeting the BPU mixing directly with it and contaminating it and the rest of the magmas forming the shadow zone. This model is not favoured because, as outlined earlier, it is unlikely temperatures were high enough to generate the large quantity of melt needed for the BPU under fluid absent conditions. Additionally, there is no evidence for direct assimilation in the BPU.

(2) As the Indian plate underthrusts the Karakoram plate a sliver of modified mantle is trapped between the two (fig. 5.18). Fluids from

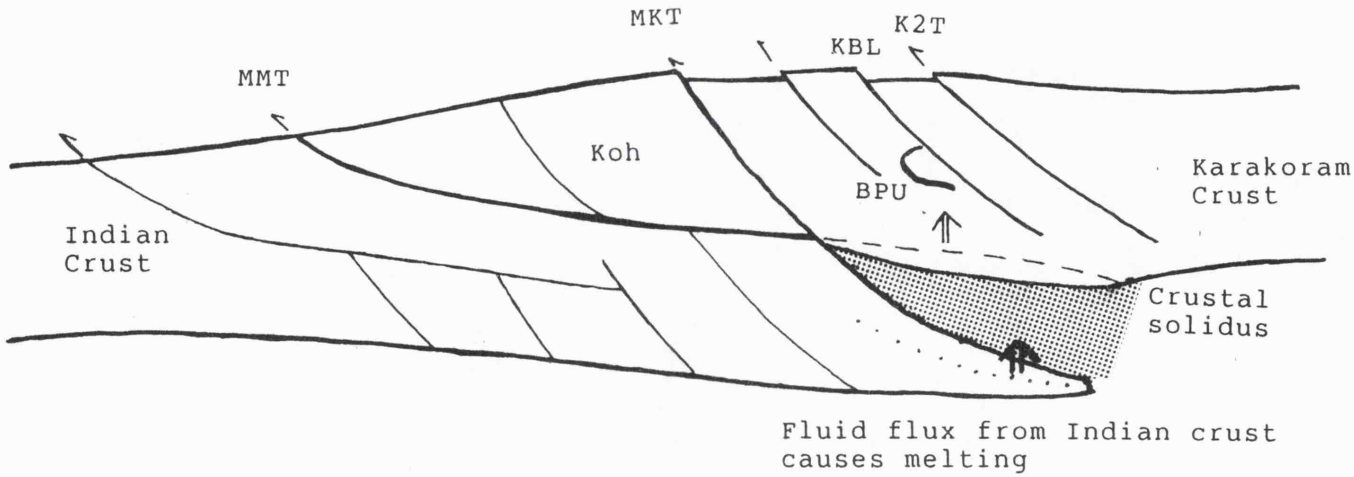

Figure 5.18: Hypothetical cross section through the Karakoram/Indian collision zone at 20ma for model (2) in the text. This differs from figure 5.17 in that northward movement of India has been accomodated by crust-mantle imbrication and not crustal thickenening (taken from model B of Rex et al., in press; and Searle, pers.comm). This results in a sliver of enriched mantle (subcontinental lithosphere?) being trapped between India and the Karakoram (dotted area) which is then fluxed and can melt. Symbols as for figure 5.17. Not to scale.

the Indian crust lower the solidus in the mantle sliver, which contains amphibole, and promote melting. Then, as above, either the precursor fluids or lamprophyre magmas themselves cause melting of the base of the Karakoram crust and contaminate the BPU magma. If it was the intrusion of the lamprophyres that triggered crustal melting then there would need to be more than one lamprophyre pulse in order to get the shadow zone.

In this model (fig. 5.18) it can be seen that the crustal structure of the area (Rex et al., in press) precludes the mantle sliver underlying Kohistan. Hence the leucogranites in this area, which also have enriched Sr and Ba values (Petterson and Windley, 1986), could not be a result of this process, whereas the first model could explain both sets of leucogranites with Indian crust being the source of the Kohistan leucogranites. However, this is not conclusive proof for the first model since melting of the mafic Kohistan crust might also be able to produce the leucogranites seen.

The three models, 1(a), 1(b) and 2, all could explain the petrogenesis of the BPU and its relationship with the ultra-potassic magmatism and no available evidence discriminates between the models. Once the contaminated BPU magma had formed and was of sufficient volume to separate from its source, then it could have risen along the inferred Karakoram Batholith Linament (KBL) whilst fractionating to give the leucogranites. The KBL, if present, imposes upper crustal rocks against mid-crustal gneisses (Rex et al., in press) and according to modelling by Pinet and Jaupart (1987) the conductivity contrast across such a boundary will act as a thermal barrier leading to localized high heat flow. This would slow down the rate of cooling and crystallisation in the BPU allowing ascent to higher levels. Therefore, no problem is envisaged in getting the BPU from its source near the base of the thickened Karakoram crust to its observed intrusion level. For the simple homogeneous thickening in model 1 (fig. 5.17) this will be a vertical distance of 50-60km but in model 2 (fig. 5.18) the crust is not thickened to the same degree due to the imbricated slice of mantle between the Karakoram and Indian plates, and this distance is reduced to about 30km (Rex et al., in press).

5.8: Summary.

1). The BPU leucogranites are related to the BPU monzogranites by fractionation and so are not primary melts. The fractionating assemblage is dominated by plagioclase with biotite, K-feldspar and lesser amounts of apatite and sphene ± zircon. The REE patterns of the BPU are dominated by the precipitation of a small amount of monazite.

2). The BPU monzogranites appear to represent a near primary melt from the lower Karakoram crust. They have low initial Sr isotope ratios, moderate $\delta^{18}O$ values, an inherited Precambrian component in their zircons and a negative Nb anomaly. The most likely source is a metapelite (or tonalite) which underwent anhydrous melting via dehydration of biotite ± hornblende to generate a hot, undersaturated magma. Other likely phases in the source are quartz and feldspar ± sphene, garnet, muscovite and sillimanite. However, such a source cannot generate the Rb, Ba and Sr contents of the BPU monzogranites, with the BPU Ba and Sr abundances being particularly high for crustal melts.

3). Spatially and temporally associated with the BPU are lamprophyres representing a phase of ultra-potassic magmatism. These lamprophyres are mantle melts which have high $^{87}Sr/^{86}Sr$ and are enriched in LILE. They are related to the metasomatic enrichment of the mantle wedge or sub-continental lithosphere beneath the Karakoram by hydrous siliceous melts from the subducting slab. Crystallisation of amphibole traps K and LILE (except Rb) in the metasomatic mantle assemblage.

4). Post-collisional melting of this enriched mantle occurs either due to elevated mantle heat flow or due to a sliver of the mantle being trapped above, and being fluxed by fluids from the subducted Indian crust. During melting/dehydration amphibole releases its LILE-enriched signature and generates the lamprophyres. Rb is not so enriched in the lamprophyres because the amphibole does not trap this element.

5). Either fluid precursors to this melting or the lamprophyre magmas themselves intrude the base of the Karakoram crust. This crust

is already hot due to thickening above and may have started to melt. Heat from the mantle input will generate sufficient melting to allow the BPU to form and separate from its source.

6). Either fractionated lamprophyre magmas enriched in only the LILE or the LILE-enriched mantle fluids mix with the BPU giving the monzogranites a contaminated high-LILE signature. This explains the discrepancies between the modelled lower crustal melt and the crustal normalised signature of the monzogranites. The Rb abundances in the BPU may be generated by this process or by addition of a Rb-rich fluid.

7). The BPU rose 30-60km through the crust along the heat-focusing KBL and was overtaken by a pulse of lamprophyric magma which formed a shadow zone around the pluton.

This model differs from others put forward in the relationship between the ultra-potassic magmatism and the post-collisional granites (e.g. Leat et al., 1987; Henney, 1987). In this model the granite is essentially crustally derived but it is initiated and contaminated by mantle input. Other models have so far preferred to have the mantle magma as the dominant mixing member with the crust as a contaminant. However, the Criffell pluton (Henney, 1987) is more basic than the BPU and so this may well be the case. Obviously the nature of many post-collisional granites may be dependent upon whether the crust or enriched mantle is the dominant component in their history, but what factors control this is unclear. A similar relationship between post-collisional, highly silicic granites and lamprophyres has been observed in the Proterozoic of Finland (Nurmi and Haapala, 1986). The implications for finding leucogranites with a mantle component occupying a similar tectonic position to purely crustally-derived leucogranites (e.g. Manaslu; Le Fort et al., 1987) will be discussed in chapter 7.

CHAPTER SIX: Post-collisional granites of the Hunza Valley, North Pakistan: magmatic variation in process and product.

6.1: Introduction.

This chapter looks at the geochemistry of the post-collisional Hunza granites of N. Pakistan. On the basis of field evidence alone three groups can be recognised. The earliest group comprises the large aplite sheets found within the Hunza Plutonic Complex (HPC) (chapter 3.4) whereas the main group consists of the later, aplitic monzogranite and pegmatitic leucogranite dykes intruding the HPC and the sillimanite-grade country rocks to the south. The third group is represented only by the Sumayar Pluton to the south of the HPC (chapter 3.5). In the last chapter it was shown that the Baltoro monzogranites and leucogranites were lower crustal melts promoted by a mantle input. Therefore the Baltoro Plutonic Unit (BPU) and the Manaslu granite (Le Fort, 1981) represent two types of leucogranite with different petrogenetic processes, but which both occur in collisional settings. Although difficulties are experienced in modelling such granite suites, the mineralogy and chemistry of the Hunza granites discussed in this chapter indicates that the first two Hunza groups conform to the Baltoro-type model whereas the Sumayar Pluton is of Manaslu-type. The implications of finding both types of leucogranite in the same area are discussed in chapter 7, but a structural model is proposed in the final part of this chapter to explain the spatial relationships and source location of the two types.

6.2: Field relationships and geological setting.

The detailed field relationships and setting of the Hunza granites were described in chapter 3, but the main points are outlined again below. All the intrusions cross-cut the foliation and are undeformed, so they were intruded after the c.45Ma collision which caused the main deformation and metamorphism (Rex et al., in press). The aplite sheets within the HPC are the earliest post-collisional magmas since they are cut by later leucogranite dykes. One K-Ar WR age on a "dark aplite" which might represent this group was given by Debon et al. (1987b) as 24.3±1.4Ma. Although K-Ar ages usually represent uplift and cooling ages, this is some 10Ma before

the average age of 15Ma for the leucocratic dykes. The sheets are on a scale of tens of metres and are restricted to the HPC where they are intrusive as shown by the assimilation of host granodiorite. They often have pegmatitic or layered margins which can be rich in garnet and muscovite, but the bulk of the sheets consists of biotite-rich, aplitic (grain size <1mm) granodiorite/monzogranite in two generations, the first being darker. Secondary tourmaline growing on fracture planes is a common feature suggesting the circulation of fluids, possibly derived from the nearby metamorphic country rocks. The sheets strike N-S, dip back into, and decrease in abundance away from, the mixing zone (chapter 3.4) suggesting some relationship. Perhaps the intrusion of the aplite sheet magma provided the heat which generated the mixing features (chapter 4.4.b).

The leucogranites of Hunza represent the third and final magmatic phase seen in the HPC. K-Ar age dates (WR, Mu and Bi) give variable results that indicate a prolonged thermal history (2.7 to 16.9Ma). However, they are interpreted to be Mid-Miocene in age (Debon et al., 1987b) with a poorly defined K-Ar maximum at 15Ma. With the exception of the Sumayar pluton the leucogranites usually form a dense, anastomosing network of dykes intruding the deformed part of the batholith and the sillimanite-grade metamorphic rocks to the south of the HPC. The dykes are on a scale of tens of centimetres to a few metres wide and constitute up to 40% of the rock by volume. The leucogranite dykes are associated with another set of aplitic dykes of granodiorite/monzogranite composition. These aplites are on a smaller scale than the aplite sheets and are also located outside the HPC. The dykes have sharp, intrusive contacts and are often layered, with pegmatitic rims and aplitic centres. Where the pegmatites are well developed they show a mineral zonation with biotite-rich rims and garnet-muscovite-rich centres. There is more than one intrusive phase as later dykes cross-cut earlier ones but all are post-collisional and only a short time span is envisaged between each phase. Two intrusions, the Nagar Sheet and Aliabad body (chapter 3.5) are exceptional in that they are on a much larger scale than the dykes. The Nagar Sheet is some 200m wide and regular in shape whereas the Aliabad body is more irregular and is exposed on both sides of the Hassanabad Valley (a distance of some 2km). Both are intrusive, cross-cut the foliation and consist of a homogeneous leucogranite with an abundance of garnet and muscovite.

The Sumayar Pluton differs from the other leucogranites in that it is intruded outside the sillimanite-grade zone into staurolite-grade rocks. No age dating has been done on this pluton. It is a large homogeneous body about 4km across with sharp, intrusive contacts and a small contact aureole shown by a 50m wide zone of baked and altered country rock. A dyke network emanates from the roof of the pluton, but there is no evidence for assimilation. The leucogranite contains little garnet, except near the margins, but is characterised by evenly distributed growths of tourmaline throughout.

6.3: Mineralogy.

The mineralogy of the Hunza granites is similar to those of the BPU (table 6.1; cf table 5.1). The rocks are usually granular in habit and are dominated by quartz, alkali feldspar (including albite) and plagioclase (oligoclase). Again the main differences between rock types are the type and amount of accessory minerals present.

The HPC aplite sheets contain biotite as their main mafic phase with up to 10 modal%. Accessory muscovite, sphene, apatite and opaque phases are found and the differentiated rims of some of the sheets are leucogranitic and rich in muscovite and garnet.

There is a compositional evolution within the Hunza dykes from biotite-bearing aplitic granodiorites and monzogranites through two-mica granites to pegmatitic, garnet-muscovite bearing leucogranites. The biotite-monzogranites sometimes contain a little muscovite and garnet, and the leucogranites often contain a few small laths of biotite. Biotite has an interstitial habit indicating that it was a late crystallising phase which in turn indicates a low water content in the magma (Wyllie et al., 1976). Apatite is a common accessory in all rock types but sphene and opaque phases are confined to the monzogranites. A little tourmaline was observed in some of the larger pegmatites.

The Sumayar Pluton differs from the other leucogranites in its abundant tourmaline (>2 modal%). This forms euhedral crystals with inclusions of quartz and appears to be a primary phase (plate 6.1(a)). A little biotite, often preserved as relics within muscovite

Plate 6.1(a)

Tourmaline crystal with quartz inclusions, surrounded by feldspar and quartz (Sumayar Pluton).

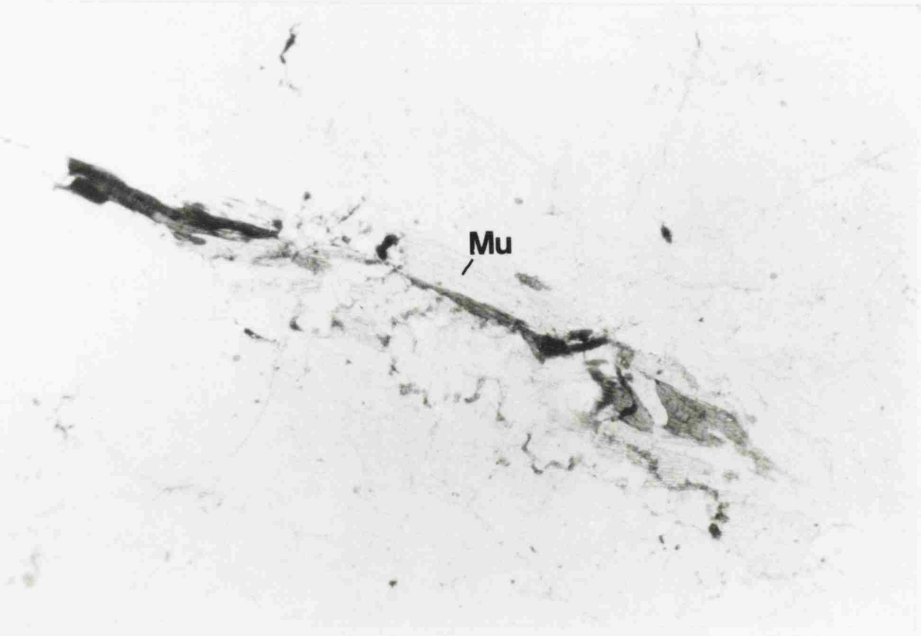

Plate 6.1(b)

Biotite enclosed by muscovite, surrounded by feldspar and quartz. The texture indicates early crystallisation (Sumayar Pluton).

1mm

laths, appears to be an early phase (plate 6.1(b)) and this suggests the Sumayar magma contained significantly more water than the magma which generated the Hunza dykes.

Sample	B27	B62	SLV24	B70	B121	NSG5	SG5
Type	Sheet	Sheet	MZG AP	MZG AP	LCG PG	LCG	LCG
Location	HPC	HPC	Sl zone	HPC	HPC	Nagar	Sumayar
Points (n)	469	463	480	450	374	402	313
Quartz	21.9	25.0	30.0	27.3	25.8	35.7	27.4
Plag. fsp	49.4	45.0	25.0	26.4	22.3	15.1	23.7
(comp.)	?	An48	?	An30	An15	An28	An15
(K,Na)fsp	20.6	20.0	36.7	36.2	38.4	40.0	38.5
Biotite	6.8	9.0	7.0	8.9	1.0	tr	tr
Muscovite	1.0	tr	0.6	-	8.3	8.0	6.3
Garnet	-	-	-	-	4.2	1.0	tr
Apatite	tr	0.6	0.6	0.6	-	tr	1.0
Sphene	tr	-	tr	0.3	-	-	-
Tourmaline	-	-	-	-	-	-	2.8
Opaques	tr	tr	-	-	-	-	-

Table 6.1: Modal mineralogy for a selection of Hunza granites.

6.3.a: Garnet chemistry.

Table 6.2 lists some average garnet rim compositions for the post-collisional granites and figure 6.1 shows the chemical variation from rim to core (0.0-1.0 distance) for a garnet in SG6 near the margin of the Sumayar pluton.

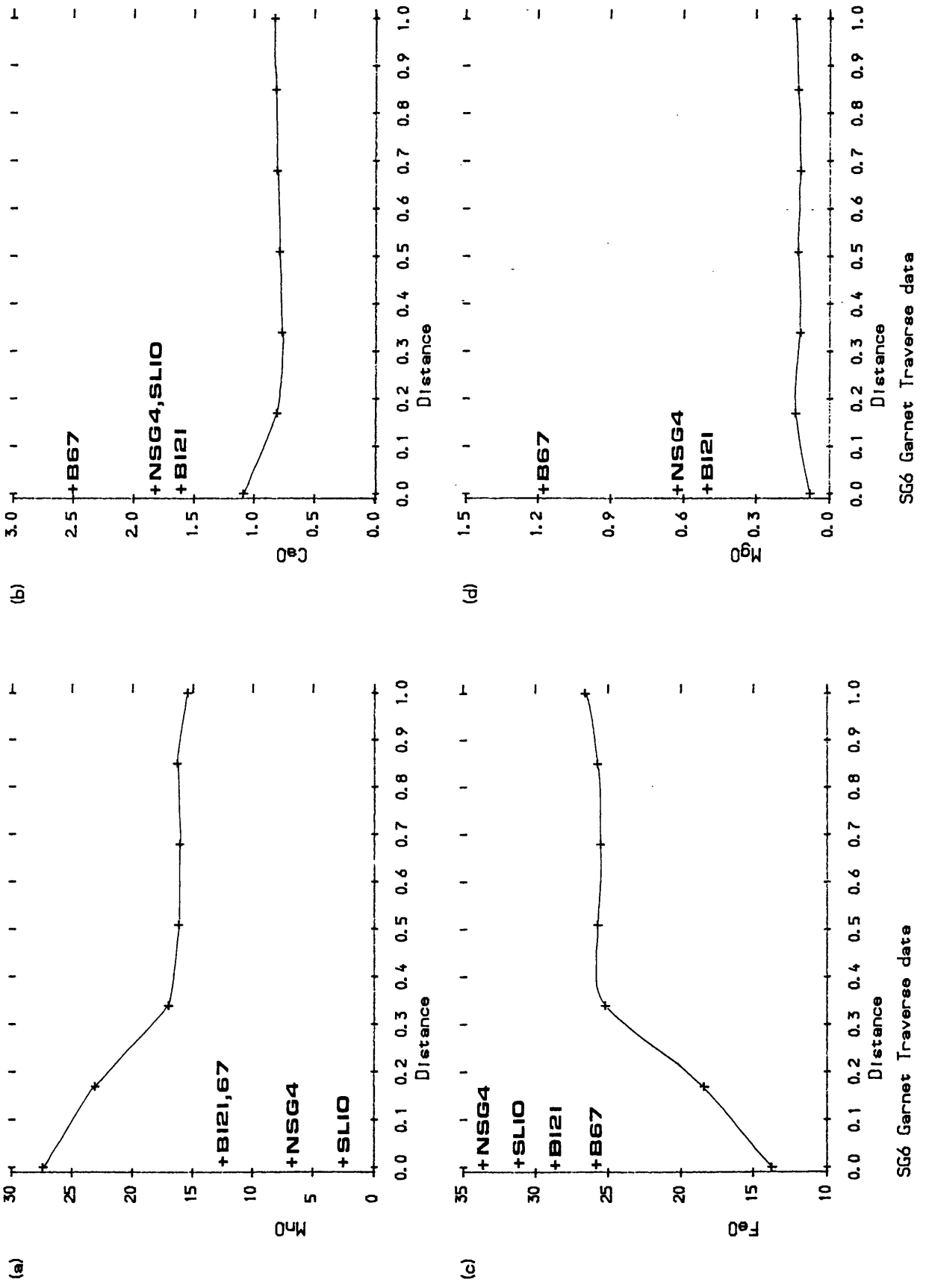

Figure 6.1: Chemical variation from core to rim (1.0-0.0) in a garnet from the Sumayar pluton. Also shown are rim analyses of garnets from B121 (HPC leucogranite dyke), B67 (leucogranite rim to HPC aplite sheet), NSG4 (Nagar Sheet leucogranite), SL10 (Hunza sillimanite-grade biotite-garnet schist).

Sample and location	Alman	Spess	Gross	Pyrope
SG6 Sumayar - Rim	31.2	65.2	3.2	0.3
SG6 Sumayar - Core	61.0	36.0	2.4	0.6
B121 HPC Lcg Dyke (n=8)	64.6	28.5	4.8	2.1
NSG4 Nagar Lcg (n=4)	76.4	15.8	5.2	2.6
B67 Edge, HPC sheet (n=6)	59.1	28.9	7.2	4.8
SILL10 metapelite (n=11)	68.8	5.6	4.9	20.5
SL13 metapelite (n=6)	78.9	0.7	8.7	11.6
SL59 metabasite (n=4)	51.8	4.8	33.9	9.5

Table 6.2: Average garnet rim (except for SG6 core) compositions for some Hunza granites and sillimanite-grade country rocks.

With the exception of SG6 the garnets are almandines with a high spessartine content, and the Nagar garnet has a similar composition to those of the Kilar leucogranites in Zanskar ($Al_{77}Gr_2Py_5Sp_{15}$; Searle and Fryer, 1986). The garnets from the country rocks have much lower spessartine contents showing that the garnets in the leucogranites are magmatic and not xenocrysts from assimilation. Miller and Stoddard (1981) showed that garnets in silicic liquids precipitate in response to high Mn relative to Mg and Fe and therefore usually contain greater than 10% spessartine, as is observed here. The garnet is precipitated at the expense of biotite which explains the rare occurrence of biotite in garnet-muscovite leucogranites.

The SG6 garnet has a core composition similar to the other rim analyses. However, towards the rim MnO shows a sharp increase whilst FeO shows an antipathetic decrease (fig. 6.1). CaO shows a small increase after slightly decreasing and MgO drops fractionally. Green (1977) demonstrated that the amount of MnO (or spessartine) in garnet strongly affects the stability of the phase with respect to pressure. Garnets with <10 mol% spessartine indicate depths of >18km whilst those with >25 mol% can be in equilibrium with a magma as shallow as 12km or 3kb. All the garnets in the Hunza granites therefore indicate high levels of emplacement. The SG6 zonation is considered to be a

result of the magma increasing its (Mg/Ca+Mn+Fe) ratio with differentiation and Mn preferentially entering the garnet at the expense of Fe which would be sequestered in the muscovite. The resultant high MnO content of the rim allowed garnet stability at extremely high levels of emplacement. This is consistent with the observation of Pichavant and Manning (1984) that tourmaline will not crystallise at pressures above 3kb.

Benard et al. (1985) state that Mn-enrichment and a high Fe/Fe+Mg ratio in a magma will promote garnet crystallisation relative to tourmaline. Therefore tourmaline will be favoured in magmas crystallising muscovite which will remove Fe. The crystallisation of tourmaline will inhibit the appearance of garnet explaining the relative abundance of garnet in the Hunza dykes compared to the Sumayar pluton. In summary, the presence of tourmaline and Mn-rich garnet in Sumayar suggest a shallower level of emplacement than the Hunza dykes whose garnets indicate a cooling depth of 12-15km. The garnets also probably reflect a higher abundance of Mn in the Sumayar magma compared to the dykes. A combination of higher pressure, lower boron content and garnet-muscovite crystallisation inhibited the growth of tourmaline in the dykes.

6.4: Geothermometry and barometry: constraints on melting conditions within the Hunza metasediments.

The localisation of the Hunza dykes to the sillimanite-grade zone and the parallel nature of some of the dykes to the foliation suggests that there may be some genetic relationship between the country rocks and the dykes. However, there is little evidence for partial melting in the metasediments so this observation needs to be investigated further.

Figure 6.2 shows the positions of some sillimanite-grade metapelitic samples in P-T space. These are calculated by taking the intersection between the straight lines representing calculated temperature from the garnet-biotite geothermometer of Hodges and Spear (1982) and the lines representing calculated pressure from the garnet-biotite-muscovite-plagioclase geobarometer of Hodges and Crowley (1985) (table 6.3; see appendix 1.4 for further details). For

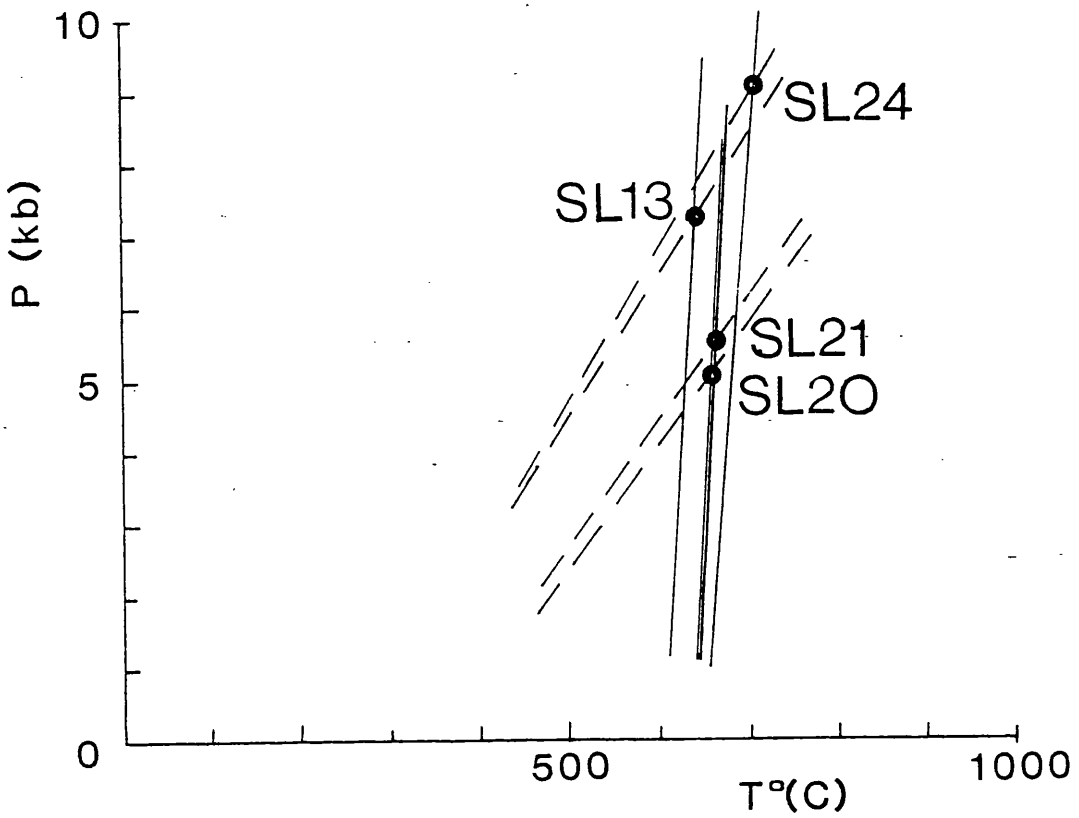

Figure 6.2: To show the location of four samples of sillimamite-grade metapelitic, biotite-garnet gneisses in P-T space. Points are located by the intersection of the temperature gradient line (solid), with the pressure gradient line (dashed), See text for futher details.

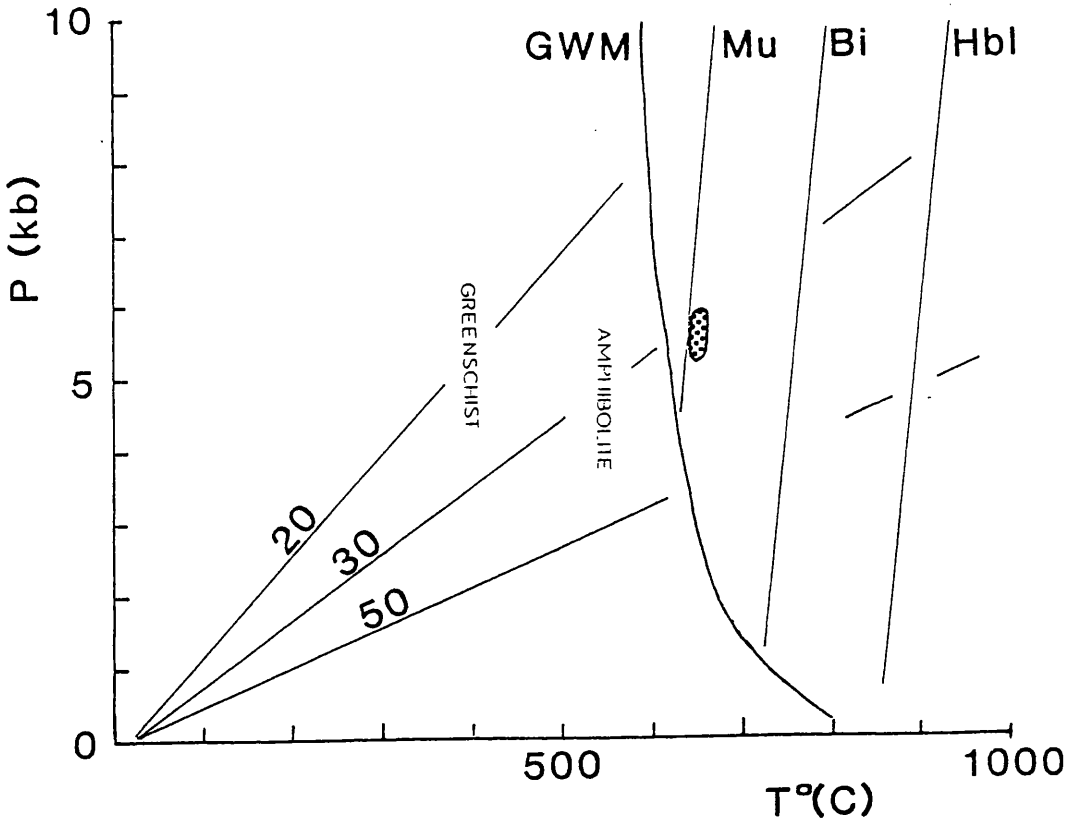

Figure 6.3: Location of selected samples (SL20 and 21) from figure 6.2 in P-T space (dotted area). Also shown is the granitic wet melting curve (GWM) and the muscovite (Mu), biotite (Bi), and hornblende (Hbl) dehydration melting curves. 20, 30 and 50 refer to geothermal gradients in °C/km. Figure adapted from Fyfe (1970).

sample SL32 temperatures were compared with those calculated from Graham and Powell's (1984) garnet-hornblende geothermometer and show good agreement (table 6.3). Since these samples come from locations close to the batholith contact they represent the highest metamorphic grade. The temperatures from all eight samples (650°C approx.) are probably representative since averages of a number of garnet and biotite analyses were used. However, the four samples which were used to calculate pressure divide up into two groups. It is considered that the samples which give high pressures (SL24 and SL13, fig. 6.2) are erroneous because of poor muscovite analyses (see appendix 1.4). Samples SL20 and SL21 are taken to be representative since more muscovite analyses were taken from these samples and they give results which agree well with Broughten et al.'s (1985) estimates for Hunza Valley pelites of 632°C and 5.5kb. Broughten et al. (op.cit.) used a different barometer based on the garnet-plagioclase-sillimanite-quartz equilibrium reaction.

Sample	Temperature (°C) at:-		Pressure (kb) at:-	
	4kb	6kb	500°C	700°C
SL24	676	684	4.73	8.95
SL32	620	626	-	-
SL38	655	662	-	-
SL36	633	641	-	-
SL20	650	659	2.37	5.72
SL13	622	630	4.51	8.60
SL21	656	664	2.69	6.18
SILL10	652	660	-	-
Garnet/hornblende geothermometer (Graham and Powell, 1984).				
SL32	655	655		

Table 6.3: Temperatures and pressures calculated for some Hunza sillimanite-grade metasediments using the garnet-biotite geothermometer of Hodges and Spear (1982) and garnet-biotite-muscovite-plagioclase geobarometer of Hodges and Crowley (1985). See appendix 1.4 for further details.

Figure 6.3 shows these positions with respect to metamorphic facies fields. Superimposed on figure 6.3 are also the granitic wet melting curve and approximate dehydration melting curves for some hydrous minerals. The degree and temperature of onset of partial melting in anatectic environments depends upon the availability of H_2O (e.g. Fyfe, 1970). If the system is saturated with respect to water then melting will begin along the minimum melting curve. In the case of quartz-feldspar-bearing assemblages such as metapelites this will be equivalent to the granite wet solidus. Melts produced here will be water-saturated and have a minimum melt composition as defined by the eutectic in the Qz-Ab-An-Or-water system and will only evolve if the temperature rises sufficiently to allow the melting to continue after one phase has been exhausted (usually K-feldspar). Otherwise the melt will remain at the eutectic and melting will cease when the least abundant phase runs out. Therefore, large volume melts will only be produced if the source composition is close to that of the eutectic. Also, because the melts are wet and are just above solidus temperatures they will not be able to move far without cooling and solidifying.

Where there are no hydrous phases present e.g. the system Qz-Ab-An or Qz-Ab-Or, if the system is water-undersaturated the melting curves develop positive P-T slopes and with decreasing %water content move to progressively higher temperatures at constant pressure until the extreme limit of a dry system (fig. 6.4(a)). Melts produced under such conditions will be drier and because of the higher temperatures they will have non-minimum compositions. By lying well above the solidus they will be able to cool through a larger temperature range before complete crystallisation and so will be able to ascend further than a minimum melt.

If a hydrous phase is present then dehydration melting can occur under water-undersaturated conditions. Hydrous phases will produce melts on breakdown when their dehydration stability curve lies above the wet melting curve (fig. 6.4(b)). If the pressure is higher than that of the resulting vapour pressure in the melt (line Z-W) then the melting will not involve production of a vapour phase since all the vapour will be dissolved in the melt (vapour-absent reactions). In the case of Hunza and many other amphibolite terranes it seems unlikely that an excess of fluid could be present at such

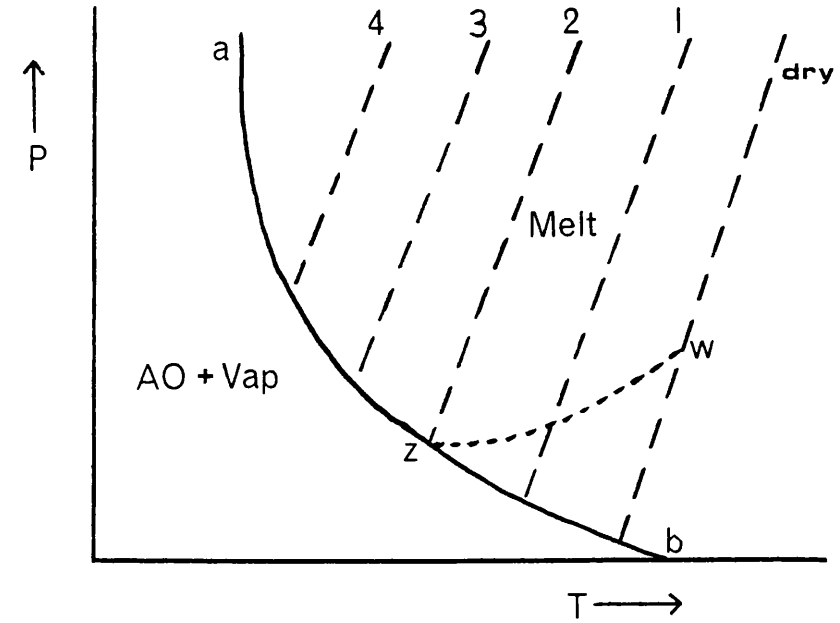

Figure 6.4(a): Granitic melting in P-T space with a-b representing the water-saturated melting curve and the dashed lines representing melting with 4% to 1% water present and melting under dry conditions (after Fyfe, 1973).

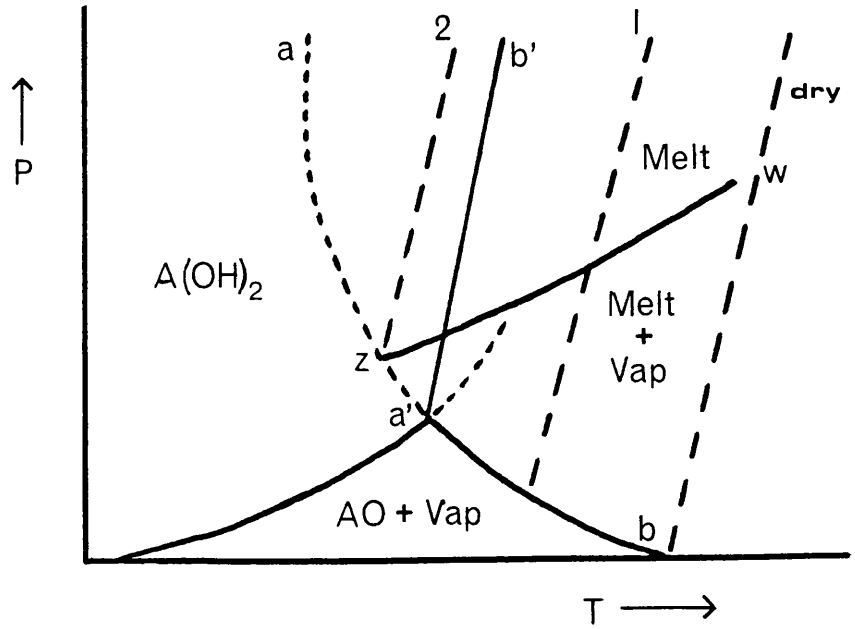

Figure 6.4(b): Granitic melting in P-T space as in figure 6.4(a) except a'-b' represents the melting curve when the stablity curve of a hydrous phase ($A(OH)_2$) intersect the wet solidus.

temperatures and pressures in the heavily compacted rocks. Additionally, Fyfe (1973) states that the character of high grade metamorphic assemblages suggests internal control of $f(H_2O)$.

Between 4-10 kb dehydration partial melting of qtz-alkali feldpar-muscovite will occur below 700°C to produce extremely H_2O-rich and strongly peraluminous melts (saturated in Al_2SiO_5). Such melts would crystallise muscovite, Al_2SiO_5, and garnet or cordierite depending on the pressure and would resemble garnet-muscovite leucogranites as seen in Hunza. The low temperature and high water content of the melt would preclude much mobilisation and the melt would probably solidify at high (>3kb) pressures (Clemens and Wall, 1981).

In Hunza very little muscovite is seen in the rocks above the staurolite-out isograd, and this explains why the above melting process is not seen because of the lack of a key reagent. The reason for the absence of muscovite could be due to a number of processes:

a: The melting reaction has proceeded to completion in the higher grade rocks and all the muscovite has reacted. This would leave a restite rich in K-feldspar and sillimanite, and although these two phases are present they are not abundant. Additionally, migmatites, the expected products of such a reaction, are not observed. However, this process could account for getting rid of any small, local concentrations of relic muscovite, leading to development of the small pods of pegmatitic quartz and feldspar which are observed in places.

b: The rocks are not potassic enough for the growth of muscovite and all the K_2O is contained in biotite. Again this is not likely since the lower grade rocks are rich in muscovite and are similar in lithology to the higher grades.

c: The muscovite has disappeared in lower grade sub-solidus reactions. The two most favoured reactions are:

ctd + musc + qtz = staurolite + biot + water

staurolite + musc + qtz = kyanite + biot + water

Under muscovite-absent conditions, the next dehydration reaction would involve biotite. However, it is apparent from figure 6.3 that the metasediments did not reach sufficient temperatures for this, and hence extensive partial melting did not develop. Therefore, the presently exposed metasediments are not considered to be the source for the post-collisional Hunza granites.

6.5: The Hunza Dykes and HPC Aplite Sheets - chemistry and possible petrogenesis.

The field relationships and mineralogy of the Sumayar pluton distinguish it from the rest of the Hunza leucogranites, and so it is considered separately later.

6.5.a: The Hunza Dykes.

The Hunza dykes cluster in the monzogranite or adamellite field on the Debon and Le Fort (1982) classification diagram, but trend from granodiorites to granites. On the characteristic minerals diagram from the same classification scheme, the dykes cluster in the peraluminous leucogranitoid field, but form a scattered trend away from it (fig. 6.5). This trend is not aluminous like that of the High Himalaya, but is transitional towards a calc-alkaline trend i.e. it is alumino-cafemic (fig. 6.5 after Debon et al., 1987b). On a normative Qtz-Ab-Or triangle the dykes again show considerable scatter, but the bulk of the data plot in a similar position to the BPU granites just off the eutectic (fig. 6.6; cf fig. 5.2).

Representative analyses of the Hunza dykes and aplite sheets are given in table 6.4. On Harker variation diagrams for the Hunza dykes (fig. 6.7) Fe_2O_3, Al_2O_3, CaO, MgO, TiO_2, Zr, Th, Ba, and Sr all show decreasing trends with increasing silica as would be expected if they are co-magmatic. However, all the trends, particularly those of the trace elements, are scattered and this makes the Hunza dykes a good illustration of the difficulties encountered when trying to interpret trends in silicic liquids. These difficulties, already encountered to some extent in chapter 4.4, are discussed below.

In the BPU the leucogranites appear to be related to the

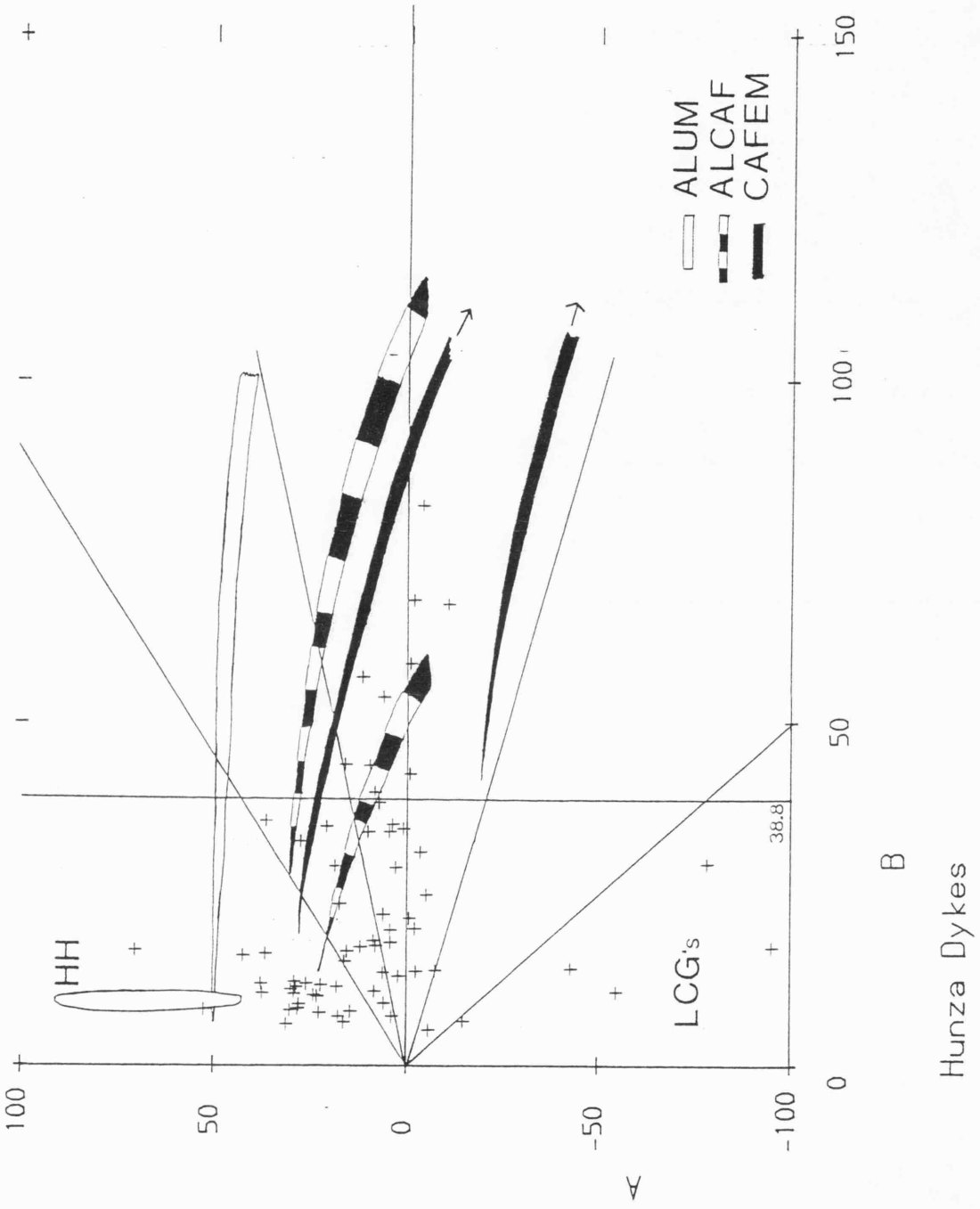

Figure 6.5: Characteristic minerals diagram for the Hunza dykes after Debon and Le Fort (1982). A = Al-(Na+K+2Ca); B = Fe+Mg+Ti calculated from molecular proportions. HH = High Himalayan leucogranites; LCG's = leucogranitoid field. The dykes define an alumino-cafemic (ALCAF) trend.

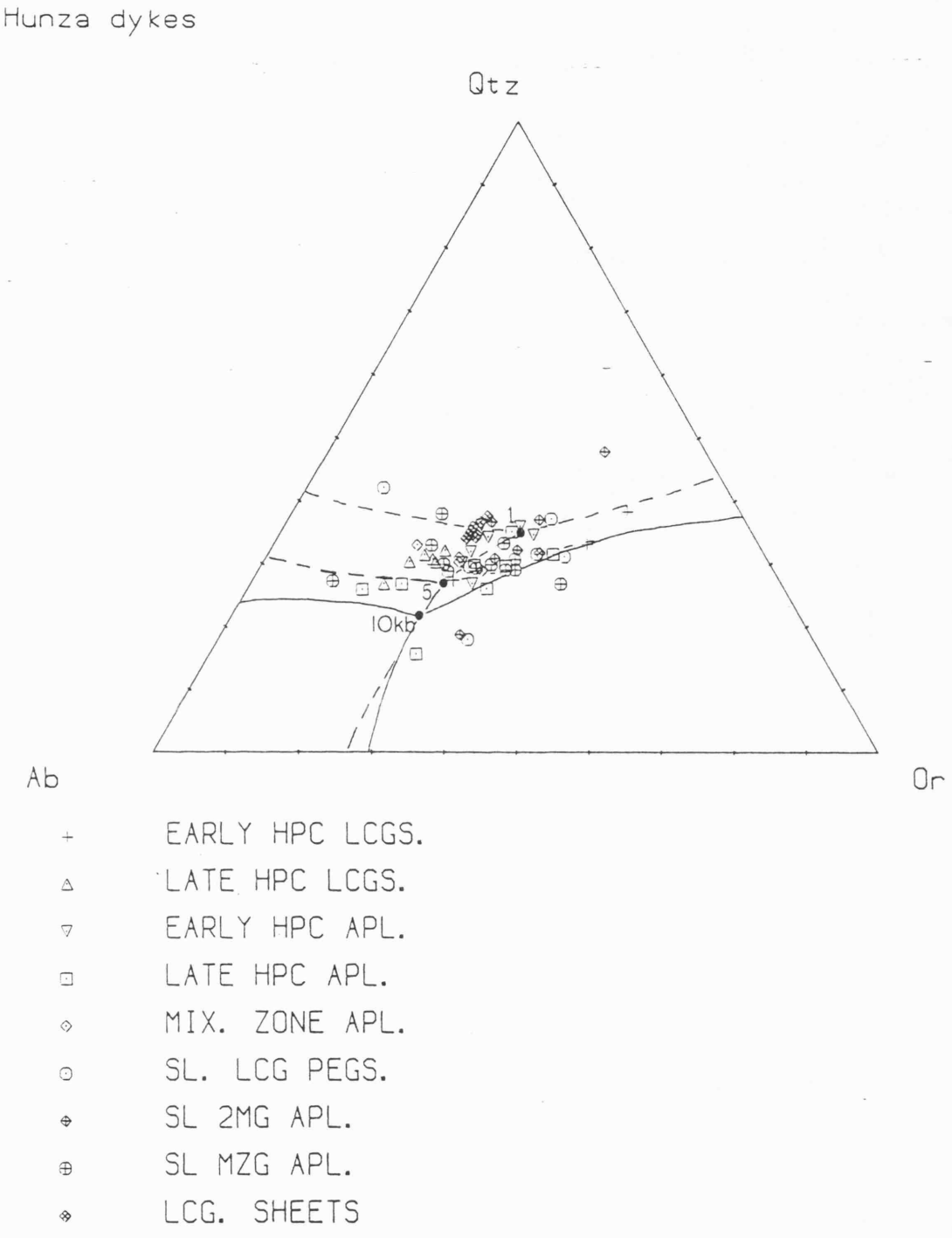

Figure 6.6: Albite (Ab) - Orthoclase (Or) - Quartz (Qtz) normative ternary diagram with the position of the granite minimum/eutectic at 1, 5 and 10kb taken from Johannes (1985).

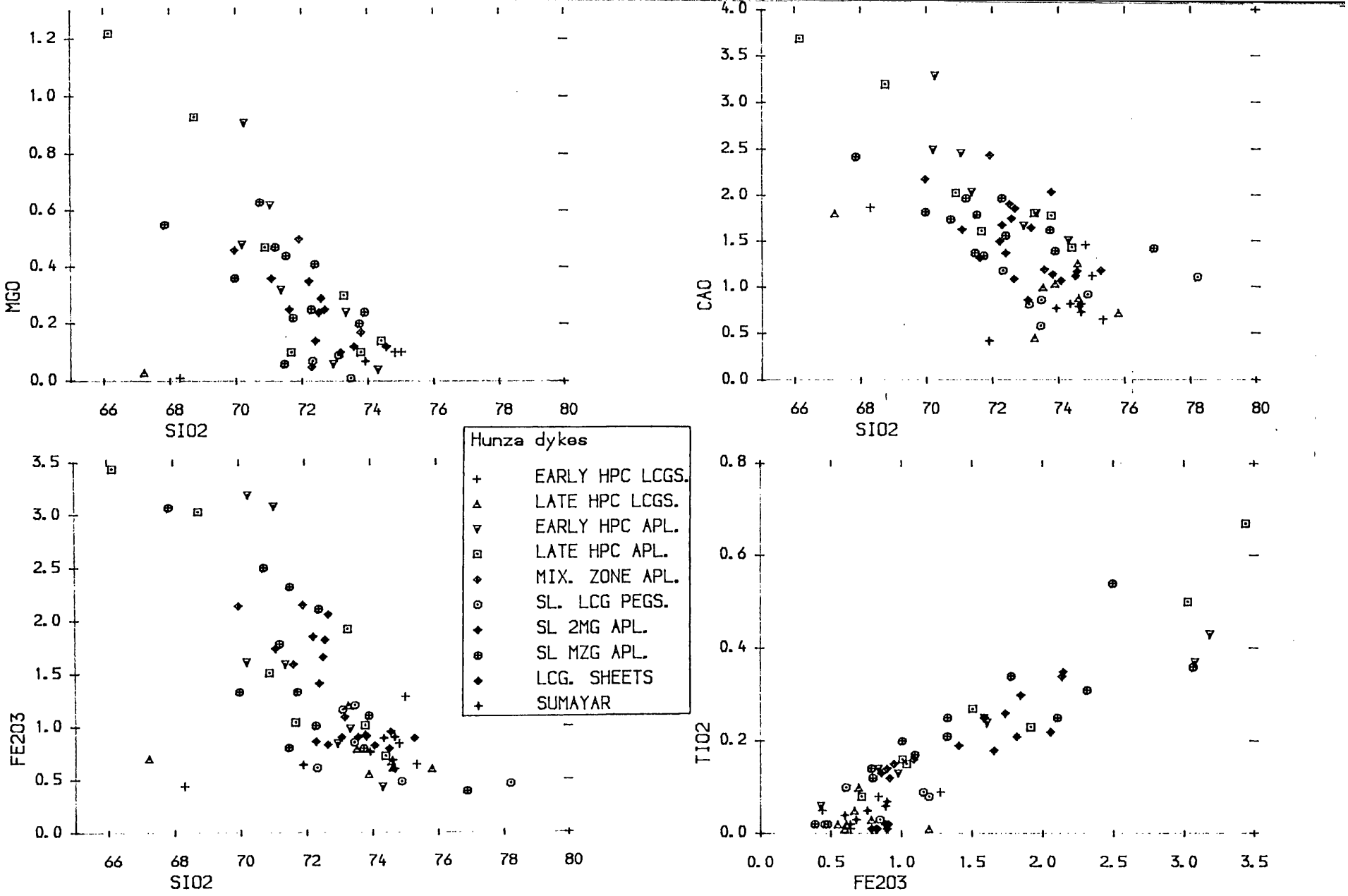

Figure 6.7: 'Harker-type' variation diagrams for the Hunza dykes and Sumayar.

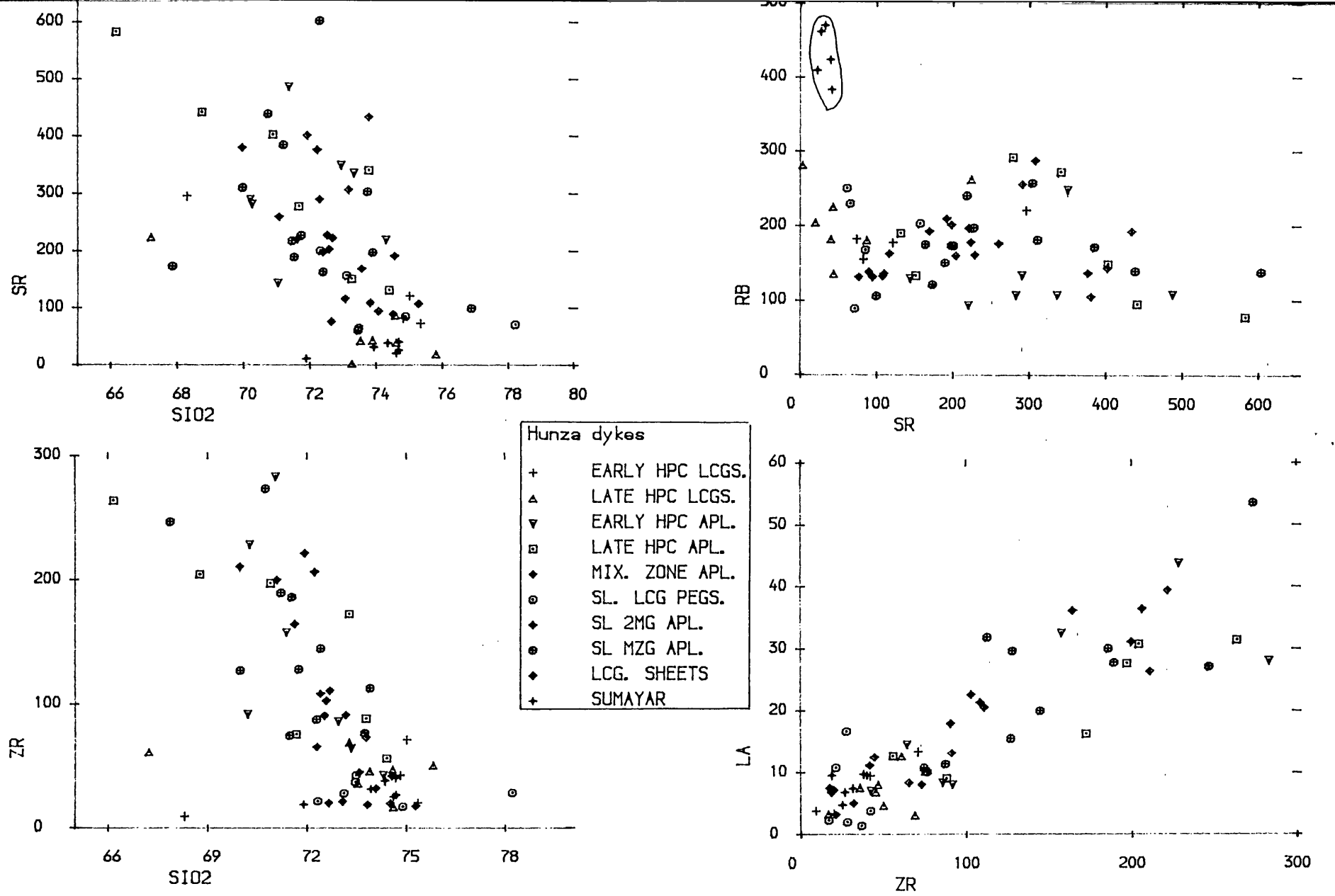

Figure 6.7 continued: note the separation of Sumayar from the dykes on the Rb vs. Sr diagram.

Rock No.	B62	B67	B70	B121	SLV13	SLV5	NSG1
Type.	Sheet	Sh.rim	Mzg.Ap	Lcg.Pg	Mzg.Ap	2MG.Ap	Nagar
SiO2	70.9	74.6	71.2	73.2	70.4	74.1	73.7
TiO2	0.31	0.04	0.25	0.03	0.54	0.15	0.01
Al2O3	14.7	13.8	14.7	14.7	14.8	14.0	14.3
Fe2O3	1.8	0.5	1.6	0.8	2.5	0.9	0.8
MnO	0.02	0.04	0.03	0.16	0.03	0.02	0.09
MgO	0.4	0.0	0.3	0.0	0.6	0.1	0.0
CaO	2.2	1.4	2.0	1.0	1.7	1.2	1.1
Na2O	4.5	4.2	4.3	5.0	3.6	1.4	4.1
K2O	3.24	4.31	3.98	3.33	5.12	5.62	4.00
P2O5	0.09	0.00	0.08	0.02	0.15	0.11	0.12
LOI	0.52	0.24	0.28	0.43	0.50	0.59	0.47
Total	98.80	99.11	98.71	98.70	99.96	98.33	98.78
Trace elements in parts per million							
Rb	83.5	144.7	108.4	225.7	139.8	210.1	131.8
Ba	1444.2	471.4	1649.1	17.2	1576.0	498.8	102.1
Th	7.2	4.8	15.1	9.3	28.3	12.9	4.9
Pb	-	-	-	-	28.5	59.0	37.2
Nb	4.3	6.3	6.5	15.4	12.2	8.0	22.3
Sr	425.9	187.0	487.4	43.5	438.8	192.0	95.1
Zr	198.1	40.5	158.0	36.0	273.7	41.9	32.0
Y	6.3	9.5	6.0	38.7	8.1	14.1	27.2
V	22.9	2.0	16.7	0.0	35.4	3.3	0.0
Cr	7.1	0.4	4.2	1.6	12.4	4.0	5.8
Ni	1.3	0.0	1.3	2.2	2.7	1.1	0.4
Cu	-	-	-	-	4.5	1.0	0.5
Zn	49.0	11.7	28.7	25.6	69.2	24.9	21.0
Ga	20.2	19.5	15.4	26.3	20.7	18.5	22.6
La	56.7	12.3	32.6	7.6	53.6	11.2	5.1
Ce	91.5	20.1	46.6	12.1	104.0	21.2	10.7
Pr	9.2	2.14	-	1.96	-	4.44	1.67
Nd	21.1	6.6	13.3	7.18	33.8	16.0	6.45
Sm	3.7	1.04	-	1.76	-	3.24	1.79
Eu	0.9	0.4	-	0.06	-	0.73	0.26
Gd	-	1.5	-	3.16	-	3.45	2.91
Dy	0.8	1.14	-	4.35	-	2.27	4.37
Ho	-	0.23	-	0.88	-	0.34	0.82
Er	1.2	1.0	-	3.03	-	0.81	1.72
Yb	0.07	1.0	-	3.56	-	0.4	1.5
Lu	0.01	0.18	-	0.55	-	0.08	0.19
$^{87}Sr/^{86}Sr$	0.7065	-	-	0.7134	-	-	0.7144
$^{143}Nd/^{144}Nd$	0.51252	-	-	-	-	-	0.51238

Table 6.4: Representative analyses for the post-collisional granites of the Hunza Valley. B-samples from HPC (B62 & B67 = aplite sheets); SLV from sillimanite-zone; NSG1 from Nagar Leucogranite sheet. All analyses by XRF technique except for full range of REE from ICP technique and isotope ratios from mass spectrometry (appendix 1).

monzogranites by fractionation (chapter 5.4). Such a connection is not so apparent in Hunza since the two magma types occur in discrete dykes, albeit with some layering, rather than being co-intruded in a pluton as with the BPU. The field relationship of the magmas and their similar chemistry and linear trends seem to preclude the magmas being unrelated. Magma mixing seems an unlikely relationship since it is hard to envisage an endmember magma that could be more acidic than the leucogranites. If the trends were due to partial melting and the granites were primary melts then the source would almost certainly contain feldspar and quartz, and plagioclase would be a likely residual phase (e.g. Rutter and Wyllie, 1988). This plagioclase would buffer the Sr content of the melt and so would prevent the much higher abundances of Sr seen in the more basic rocks. The lack of identifiable restite in the dykes precludes the trends being related to a mixture of melt and basic restite (White and Chappell, 1977). Therefore, a fractionation relationship is still the simplest explanation of the trends in figure 6.7 and is considered below.

Fractionation in a silicic liquid cannot proceed by simple crystal settling to form cumulates due to its high viscosity. A more likely mechanism is filter pressing whereby the growth of the crystals in situ pushes out the remaining liquid. This allows accessory phases and phases such as biotite, which cannot accumulate by crystal settling (Tindle and Pearce, 1981), to grow and contribute to the fractionation process, and explains the absence of large cumulate bodies. It is likely that only the surface of the crystals are in equilibrium with the contact liquid and so the fractional rather than equilibrium crystallisation equations of McCarthy and Hasty (1976) are preferred for modelling.

Scatter in the data might be due to the presence of intercumulus liquid trapped between the crystals during cooling. During ideal fractionation the liquid and cumulate will evolve along parallel but separate lines, so trapped liquid will push the overall composition of the cumulates off their trend towards the liquid trend. Therefore, variable amounts of trapped liquid will cause scatter in the data trend. Volatile activity towards the end of the crystallisation process will affect some elements, such as K and Rb in the case of the BPU, and cause scatter in the data set for these elements. Finally, inhomogeneous crystallisation might lead to overestimates of

the importance of a particular phase in a particular sample and cause scatter from the main trend. For example, if a fractionating assemblage is representative of 60% plagioclase crystallising, but in one area more plagioclase nucleates and grows at the expense of other phases, then a sample of this area might contain over 60% plagioclase. This will lead to the analysis of this sample lying above the main trend for elements contained in plagioclase. This is illustrated by figure 6.8(a) where certain samples lie well above the main trend of Na_2O+K_2O vs. SiO_2. This may be caused by an excess of feldspar in these samples and, assuming all Sr is contained in the feldspar, when the alkali content is divided by the Sr abundance (fig. 6.8(b)) the samples lie much nearer the trend and the scatter is reduced. This emphasises the usefulness of carefully chosen ratios rather than single elements in biaxial plots.

When the data is scattered the major elements are not very useful for modelling fractionating assemblages. Least squares modelling based on the method of Wright and Dohertey (1970) gives inconsistent results for the Hunza dykes since individual rocks will only give compatible solutions for their evolution from a common source if the trend is tightly defined, as in the case of the Baltoro. However, minor elements such as Ti and P might be more useful when considering accessory phases such as sphene and apatite.

Trace elements are much more sensitive to fractionation changes and consequently show more scatter as a result of the processes outlined above. In basic liquids it is often possible to find a truly incompatible element (i.e. $D<<1$) and use this element to determine the degree of fractionation (F). Such a method was attempted in chapter 4 and this illustrated the inherent problems in its application to more silicic liquids since it is rare to find a truly incompatible element. Most trace elements will enter one of the accessory phases common in granitoids, and this will lead to an incorrect estimate of F.

When two trace elements from a granitoid suite are plotted against each other, they must both be considered to have $D>0$. Therefore, the trend produced is a combination of both D values for the particular fractionating assemblage and each assemblage will produce a different trend. Many trace elements such as Th, Zr, REE

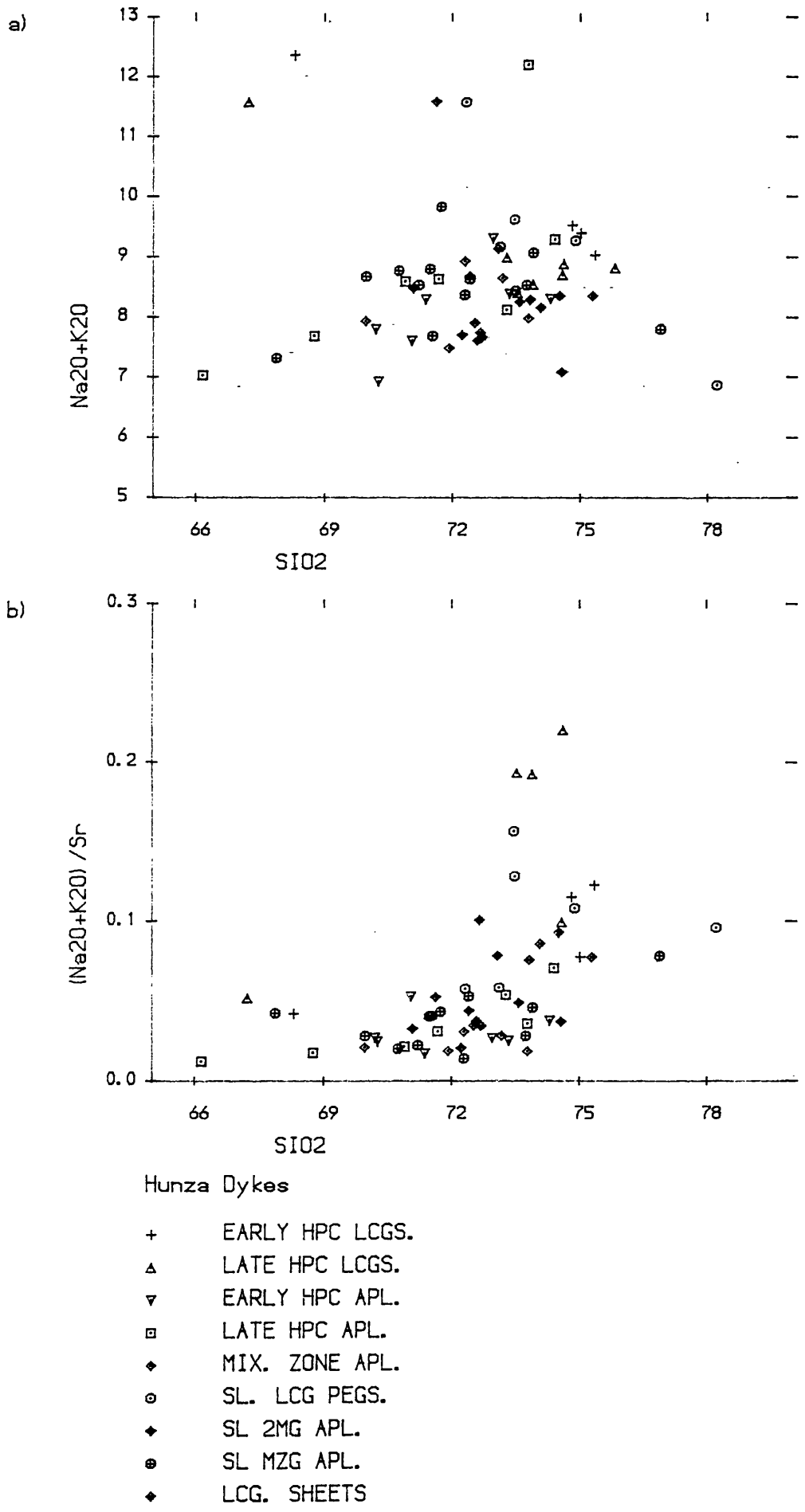

Figure 6.8: Plots of total alkalis and (total alkalis/Sr) vs. silica for the Hunza dykes to illustrate the scatter caused by heterogeneous samples, and the reduction of this scatter by plotting appropriate ratios.

are not suitable for modelling major phase fractionation since they are controlled by accessory phases. However, the LILE Rb, Sr and Ba are generally controlled by the major phases such as feldspar, biotite and amphibole and were used to support the PETMIX model for the BPU fractionation.

On the LILE quadrant plots used for the BPU (fig. 6.9; cf fig. 5.6) the Hunza dykes give similar straight line trends when normalised against the sample with the highest Sr abundance (B70, 1649ppm). However, as would be expected, these trends are scattered and the best-fit line is subject to large errors. Figure 6.10 shows that the Rb/Sr vs. Sr plot is not very sensitive to changes in a fractionating assemblage dominated by feldspars, quartz and biotite, and so should not be used for modelling scattered trends. The Ba vs Sr plot is much more sensitive (fig. 6.10) and therefore potentially much more useful. However, any set of granitoids dominated by feldspar and biotite will plot with similar trends on the same diagram, and so subtle differences in fractionating assemblages will only be detected if the trends are tightly defined. Indeed, on a scattered diagram two sets of similar but completely unrelated granites could be modelled as one fractionation sequence. This is the case in Hunza where the aplite sheets plot within the scattered data of the Hunza dykes.

It must, therefore, be stressed that the dykes are assumed to be related on the basis of field evidence, linear trends and similar overall isotopic and chemical signatures, and that fractionation seems to be the simplest plausible relationship. The LILE quadrant plot is only used to obtain an estimate of the fractionating assemblage due to the inability of other methods to do this. The plot is not taken as proof that the dykes do represent a fractionating series. As shown earlier the scatter can be reduced by using ratios rather than single elements, and using Nb as a denominator on both axes further constrains the Ba vs. Sr trend (fig. 6.11). The best-fit line for this data corresponds to a crystallising assemblage of 10-15% biotite, 60-55% K-feldspar and 30% plagioclase using distribution coefficient data from Hanson (1978) and assuming $D_{Nb} << 1$. If distribution coefficient from Henderson (1982) is used then the line would correspond to an assemblage of 50% biotite, 26% K-feldspar and 24% plagioclase (fig. 6.11). This is clearly unrealistic since

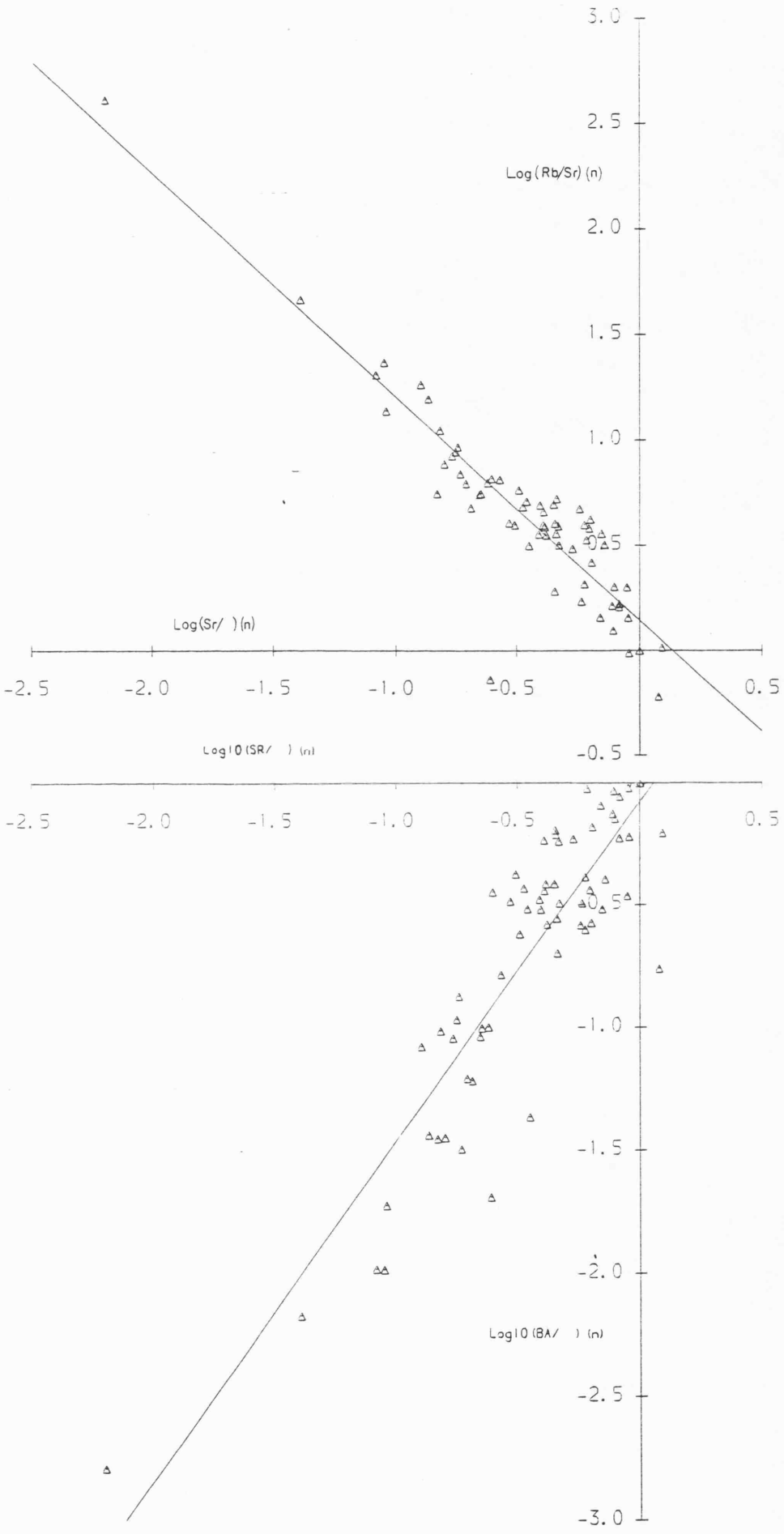

Figure 6.9: LILE quadrant plots for the Hunza dykes. Values are logarithmic and normalised to B70 (a monzogranite aplite dyke). Lines are regression best-fits for the data.

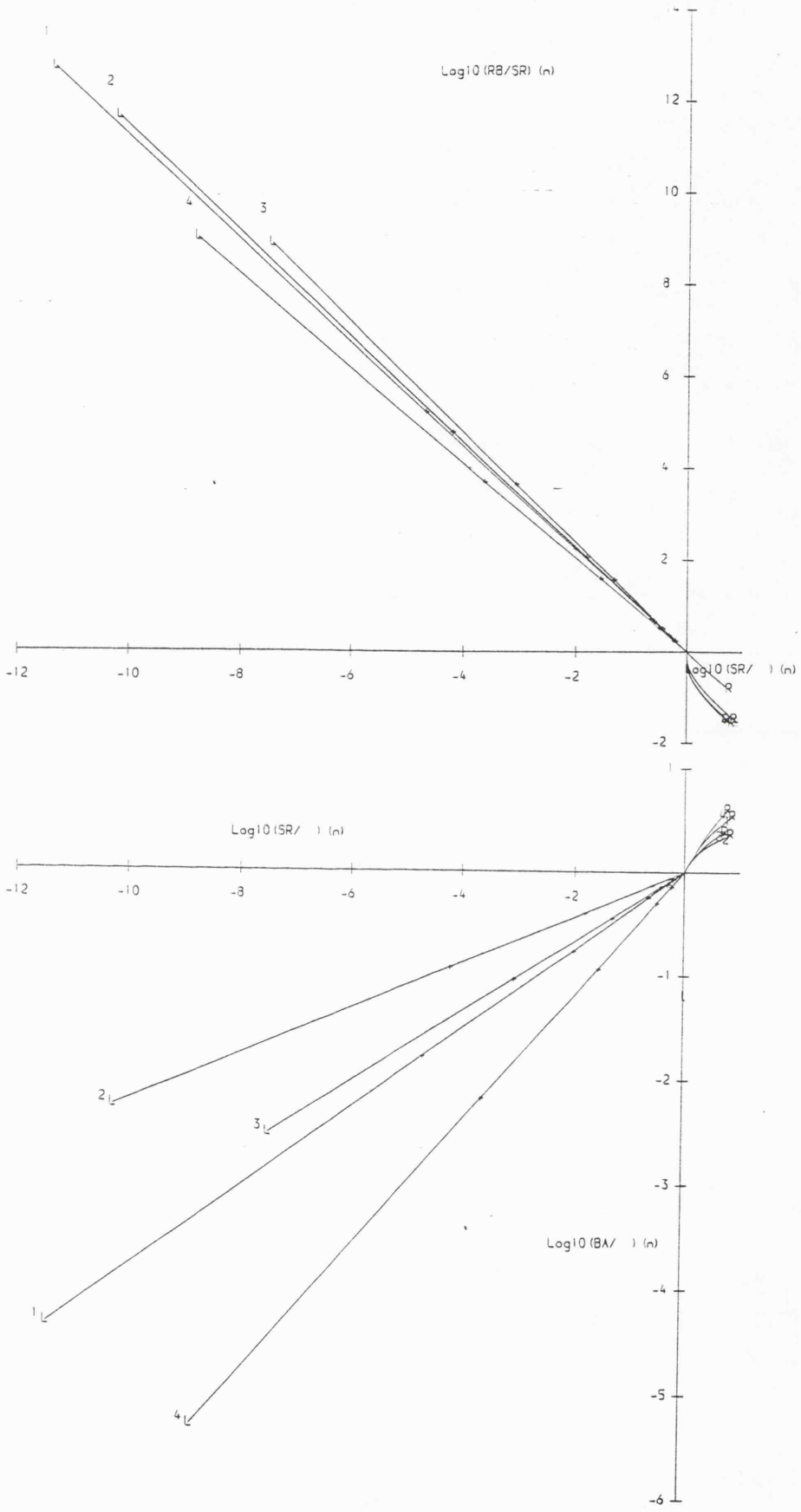

Figure 6.10: To illustrate the effect of changing fractionation assemblages on trends plotted on the LILE quadrant plots.
Line 1 = 50% plagioclase, 50% K feldspar
Line 2 = 70% plagioclase, 30% K feldspar
Line 3 = 35% plagioclase, 35% K feldspar, 30% quartz
Line 4 = 35% plagioclase, 35% K feldspar, 30% biotite
Distribution coefficient data from Henderson (1982).

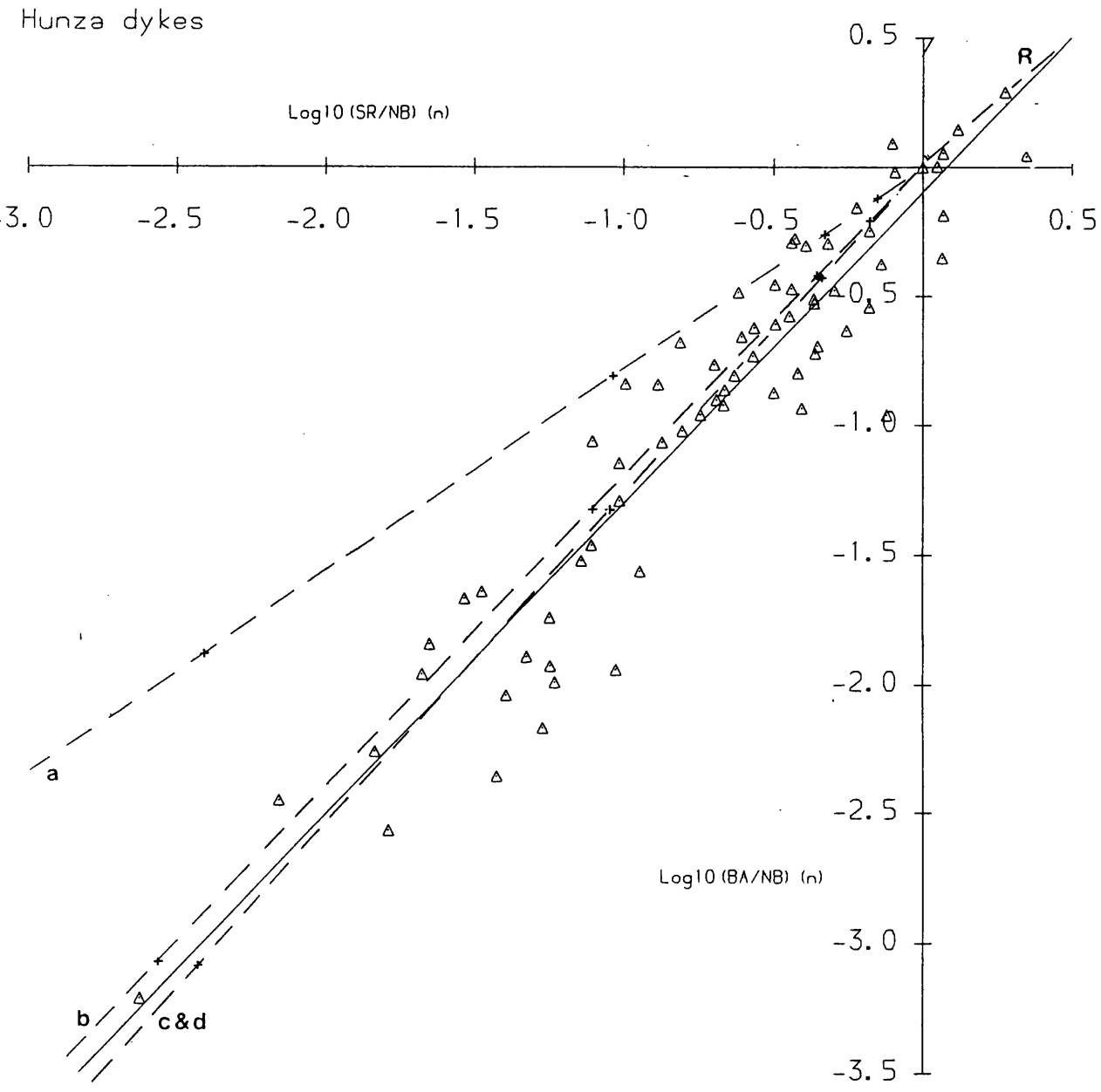

Figure 6.11: Log(Ba/Nb) vs. log(Sr/Nb) for the Hunza dykes normalised to B70. Solid line is regression best-fit for the data. Dashed lines a, b and c correspond to Rayleigh fractionation of assemblages 20% biotite, 20% K feldspar, 60% plagioclase; 10% biotite, 60% K feldspar, 30% plagioclase; 15% biotite, 55% K feldspar, 30% plagioclase respectively using D values from Hanson (1978). Line d correspond to fractionation of 50% biotite, 26% K feldspar, 24% plagioclase using D values fron Henderson (1982). Crosses = 10%, 20% and 40% crystallisation away from the origin.

the most basic dykes contain about 10 modal% biotite and illustrates the importance of using appropriate K_D's. K_D values in granitoids are very variable and also increase with acidity or fractionation (Henderson, 1982). Therefore, any modelled assemblage can only be treated as accurate if a high degree of confidence can be placed on the distribution coefficients used. However, it is not feasible to measure K_D's for each individual rock suite and so a compromise has to be reached where a set of values from the literature has to be chosen which best explain the behaviour of the data.

Other trace elements, whilst they cannot be used for major phase modelling, are useful in identifying the presence of accessory phases. Within the Hunza dykes decreases of Zr, P and Ti indicate the precipitation of zircon, apatite and sphene or ilmenite. These phases have trace elements as major stoichiometric components and will crystallise when the magma is oversaturated in these elements. Watson and Harrison (1984) have shown that, for apatite and zircon at least, this saturation level is dependent on silica activity and temperature. Hence, due to their high silica content and low crystallisation temperatures many granitoids are oversaturated and rich in accessory phases. Additionally, as the magma cools the saturation level will decrease causing further precipitation of these phases. Apatite will crystallise in melts with >70% SiO_2 at levels of 0.02-0.15 wt% P_2O_5 depending upon temperature (Watson and Harrison, 1984). The same authors showed the dependence of Zr saturation on temperature and the cation ratio M=(Na+K+2Ca)/(Si*Al). The monzogranite SLV13 (M=1.04) has the highest abundance of Zr among the Hunza dykes (273ppm) and, assuming this is the saturation level and none of this Zr is contained in xenocrystic zircon, this would correspond to a temperature of about 860°C. The precipitating proportion of zircon needed to lower the Zr abundances from the value of SLV13 to those of the leucogranites (around 40ppm) cannot be modelled because of the difficulty of estimating a distribution coefficient for Zr, as it is not a trace element in zircon. Additionally, there is the likelihood of dis-equilibrium between crystal and melt due to slow diffusion rates, as indicated by the preservation of old zircon cores in younger rocks.

The same problems are experienced with REE since these are generally controlled by accessory phases. The granodiorite and

monzogranite dykes show a consistent LREE enriched pattern with a small, negative Eu anomaly, which is similar to the BPU monzogranites (fig. 6.12; cf fig. 5.5). However, as the rocks evolve the patterns become more irregular and can generally be divided into two groups. Both groups show gradual depletion in LREE and variable enrichment in HREE, but one group develops a positive Eu anomaly whilst the other develops a larger, negative Eu anomaly (fig. 6.12). The development of a positive Eu anomaly was also observed in the BPU and can be accounted for by addition of a small amount of monazite to the fractionating assemblage (fig. 6.13). This cannot be modelled accurately since La and Ce are stoichiometric components in monazite and so Henry's Law and trace element modelling equations are not strictly valid, but the evolving pattern can be seen to approximately fit the data. The other group cannot have evolved by monazite fractionation due to their negative Eu anomaly but they still show decreasing LREE. This can be modelled, again approximately by comparing patterns, using small amounts of allanite (fig. 6.14). Such a model cannot, however, explain the extreme enrichment of HREE seen in some samples (e.g. B121). This is attributed to the presence of cumulus garnet since B121 is a leucogranite pegmatite with a garnet-rich centre. The presence of cumulus accessory phases, leading to an overestimate of the abundance of elements contained within these phases for a sample, probably effects all the REE patterns to a greater or lesser degree, and makes accurate interpretation of REE data for granites extremely problematic.

The precipitation of zircon would lead to a rapid depletion in the HREE which is not seen, and so perhaps Zr is being removed in the garnet and not zircon as suggested above. The dominance of allanite in some cases and monazite in others suggesting local control on phase stablity. Using these accessory phases, the patterns can still be modelled using the main assemblage of feldspars and biotite and so do not preclude a fractionating relationship between the monzogranites and leucogranites.

The probable fractionation relationship of the leucogranites to the monzogranites is a common feature to both Hunza and the BPU. Figure 6.15 shows the similarity in trace element patterns between the HPC aplite sheets, the later monzogranite dykes, the monzogranite dykes in the sillimanite-grade rocks to the south, and the Baltoro

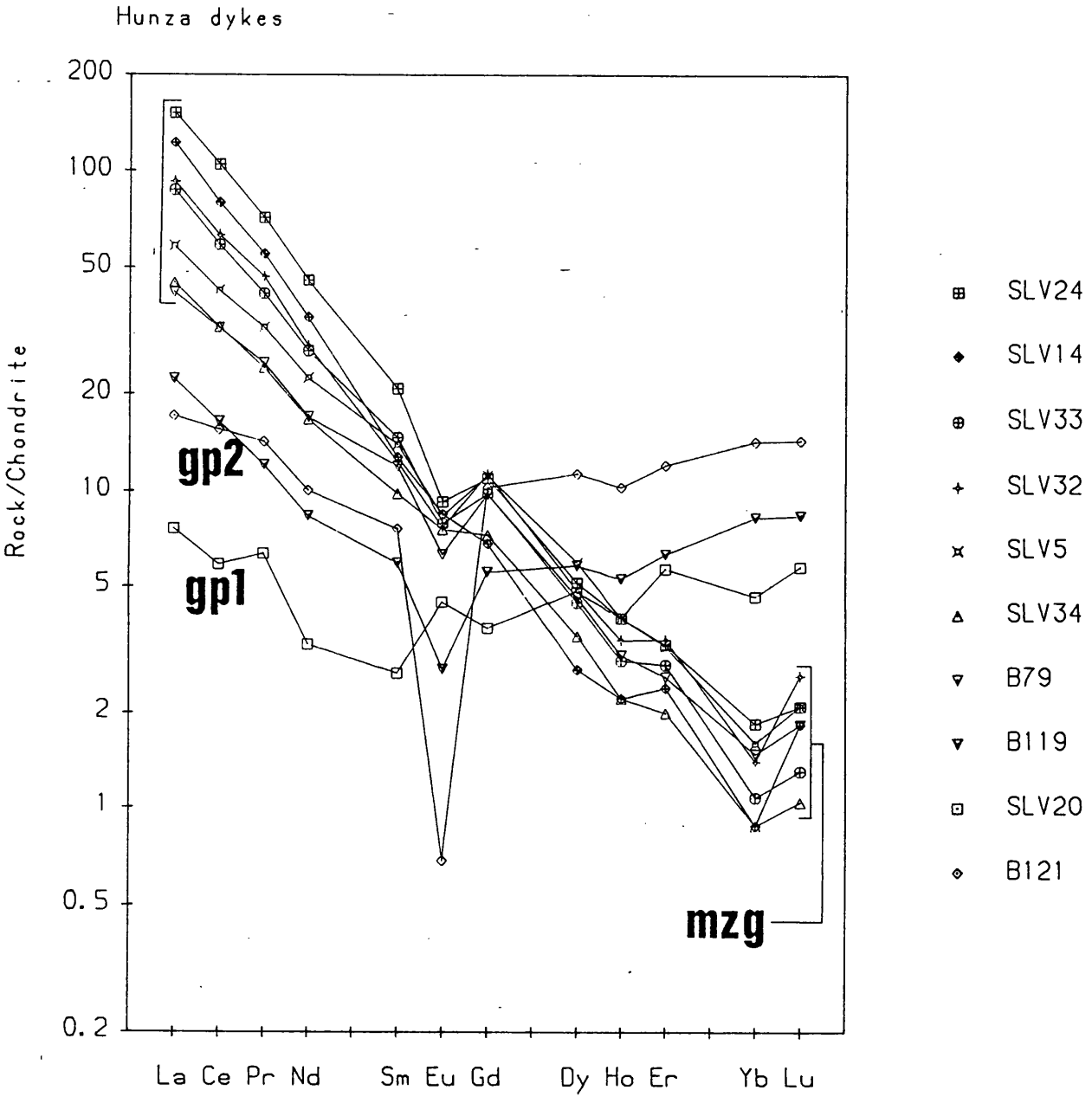

Figure 6.12: Rare earth element patterns for the Hunza dykes:
mzg = monzogranite dykes
gp1 = leucogranites with a positive Eu anomaly
gp2 = leucogranites with a negative Eu anomaly

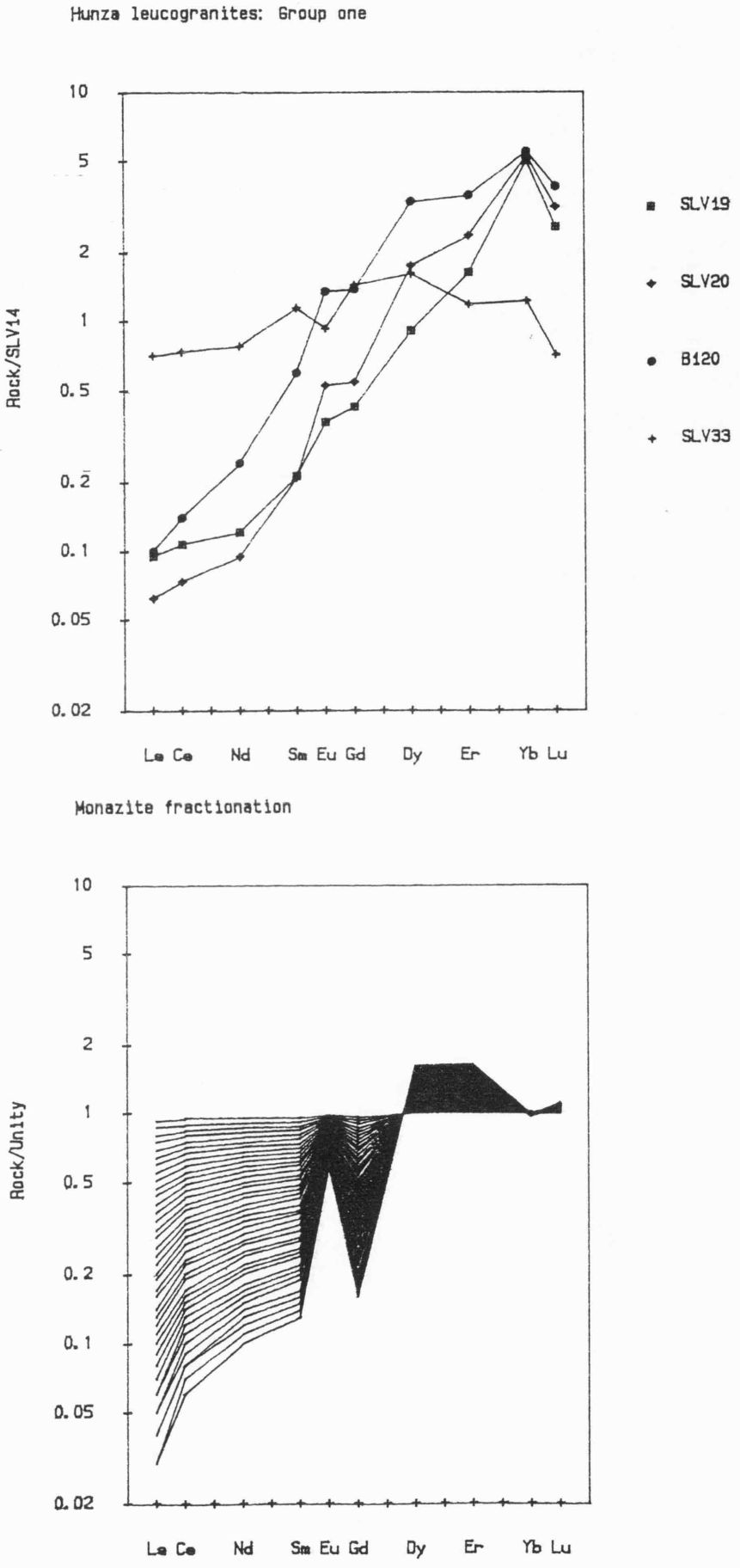

Figure 6.13: Upper diagram shows Group 1 leucogranites from the Hunza dykes normalised to monzogranite SLV14. Lower diagram shows modelled pattern for 40% Rayleigh fractionation of 10% biotite, 30% plagioclase, 59.8% K feldspar, 0.2% monazite. Each line = 1% crystallisation.

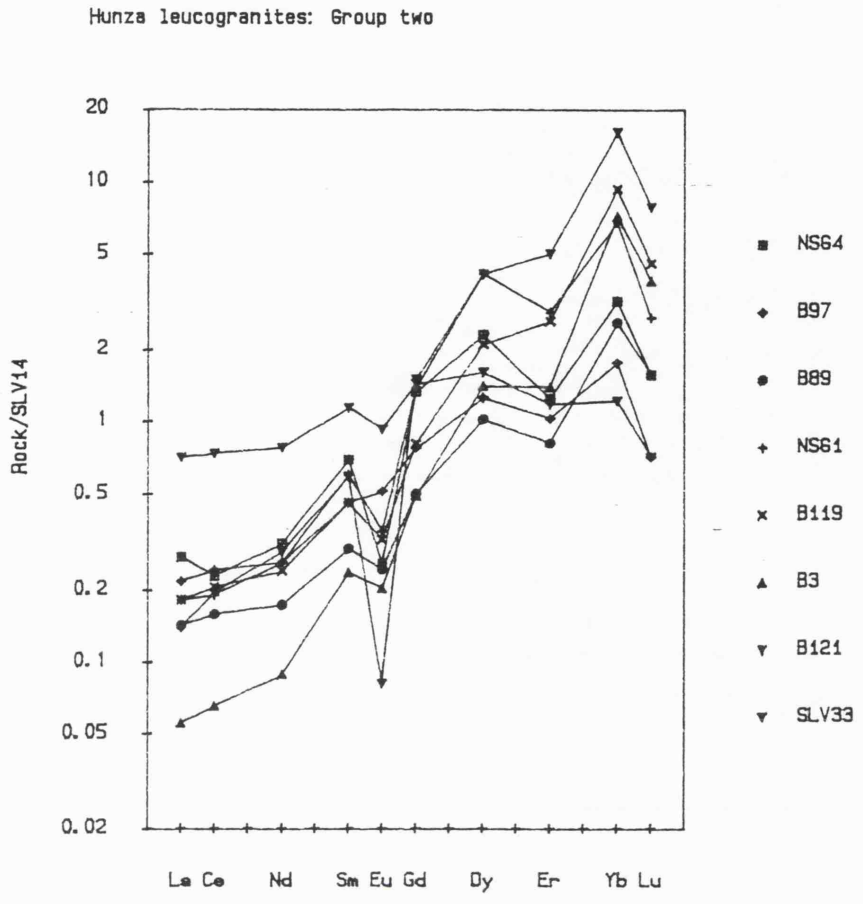

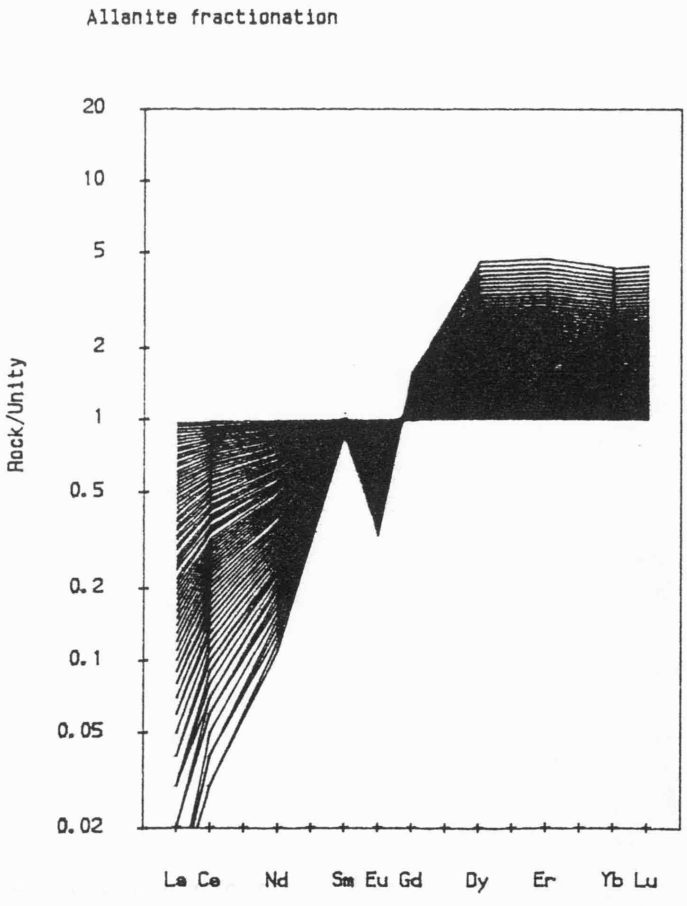

Figure 6.14: Upper diagram shows Group 2 leucogranites from the Hunza dykes normalised to monzogranite SLV14. Lower diagram shows modelled pattern for 80% Rayleigh fractionation of 10% biotite, 30% plagioclase, 59.5% K feldspar, 0.5% allanite. Each line = 1% crystallisation.

monzogranites. Figure 6.16 shows a corresponding similarity between the Hunza and Baltoro leucogranites. Together with the high Ba and Sr abundances in both sets of monzogranites, their temporal and spatial proximity and the comparable Sr and Nd isotope ratios (Baltoro; 0.7078-0.7129; 0.51218-0.51228: Hunza leucogranites; 0.7112-0.7143 (one sample 0.7225); 0.51226-0.51238: fig. 6.17), this suggests a common origin for the Hunza dykes and BPU granites. Therefore, the Hunza dykes are lower crustal melts promoted and contaminated by a LILE-enriched mantle input.

One lacking piece of evidence for such an association is the absence of associated ultra-potassic magmatism, which the petrogenetic model proposed for the Baltoro (chapter 5) requires. However, lamprophyres were reported on the geological map of Hunza made by Schneider (1957), and whilst these were not observed during the present study, it is possible, due to the large area covered and the inaccessibility of a large proportion of the terrain, that any such ultra-potassic dykes present were missed.

6.5.b: The HPC aplite sheets.

The HPC sheets have a lower $^{87}Sr/^{86}Sr$ ratio and higher $^{143}Nd/^{144}Nd$ ratio (0.7065 & 0.51252; B62, fig. 6.17 and appendix 1.3) than the dykes, and this difference, combined with their older K-Ar age and field evidence such as their larger scale and spatial restriction, suggests that the sheets represent a separate magma from a different source to the dykes. However, the similarities in trace element patterns (fig. 6.15), REE patterns (fig. 6.18; cf fig. 6.12) and mineralogy point to a similar petrogenetic history. This is supported by the LILE enriched nature of the sheets (B65; Ba=1828.3 ppm, Sr=449 ppm).

Evolution from granodiorite/monzogranite to leucogranite is again evident from the centres to the margins of the dykes. Here, a genetic relationship is more apparent than it was within the Hunza dykes. The data is again scattered but all trace elements except Rb decrease with fractionation (fig. 6.19). Al_2O_3 is fairly constant, and, apart from the alkalis, all the other major and minor elements decrease with increasing silica. It is likely that biotite, alkali and plagioclase feldspar are again the major fractionating phases.

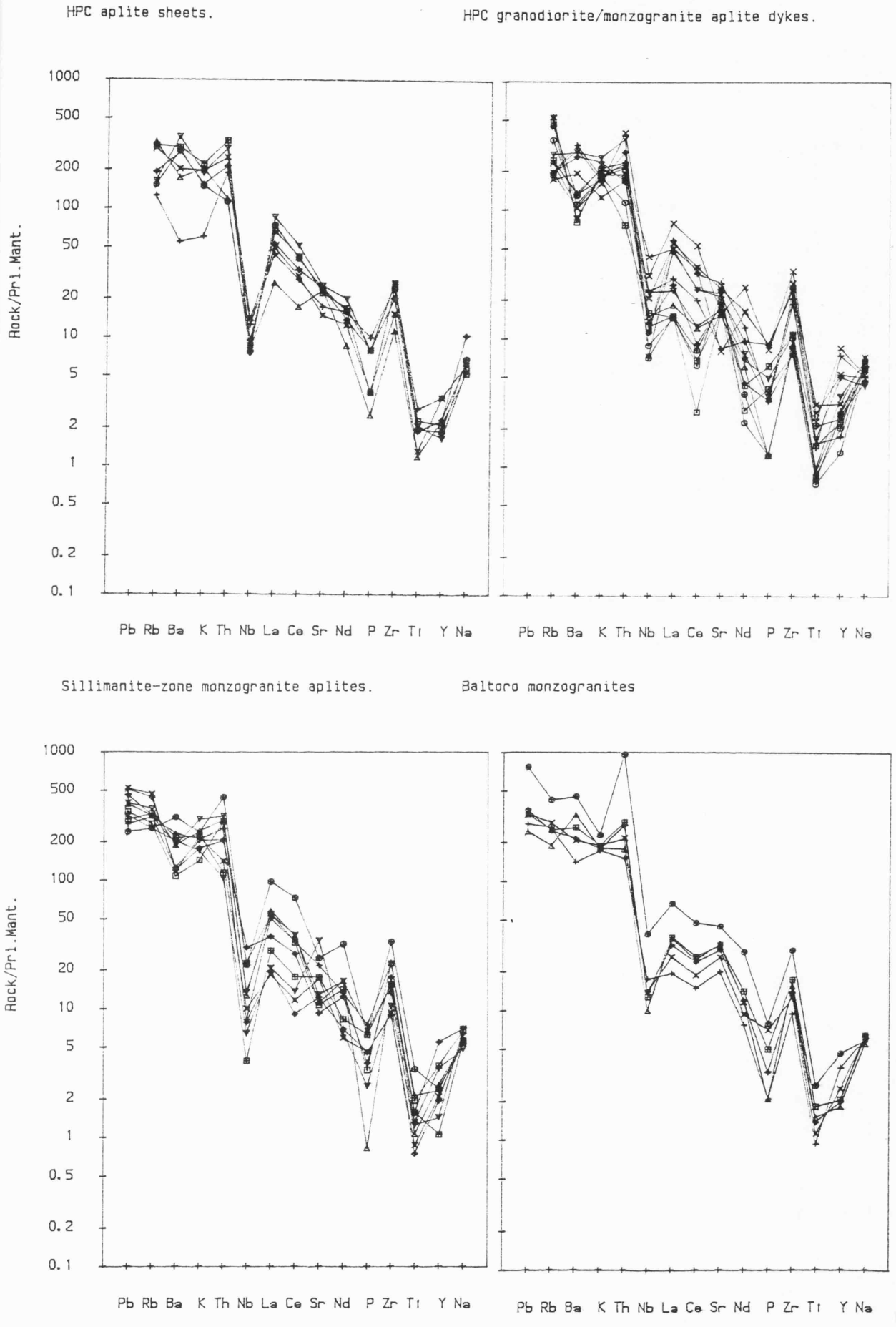

Figure 6.15: Comparitive spider diagrams for post-collisional monzogranites from Hunza and the Baltoro.

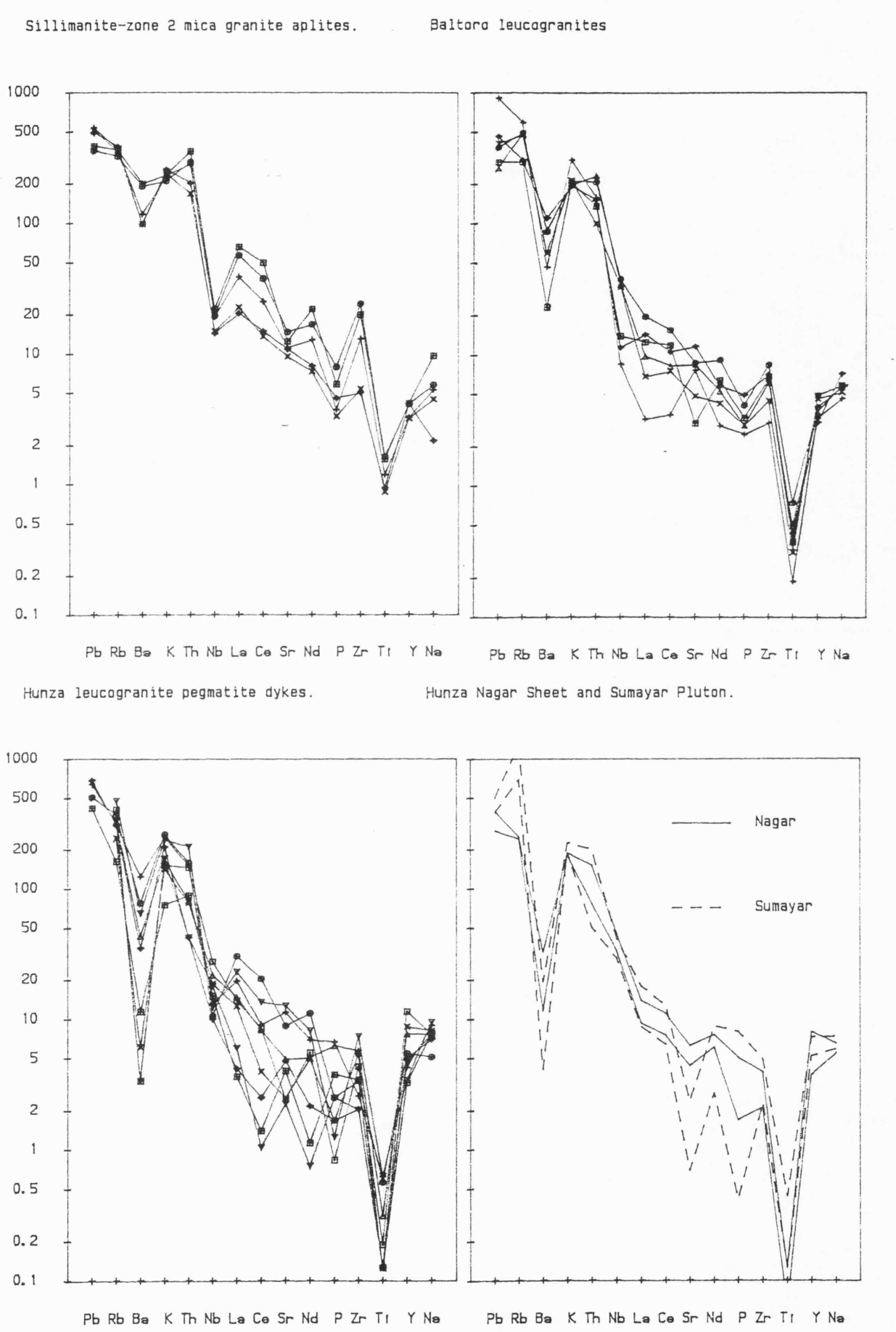

Figure 6.16: Comparitive spider diagrams for two-mica granites and leucogranites from Hunza and the Baltoro.

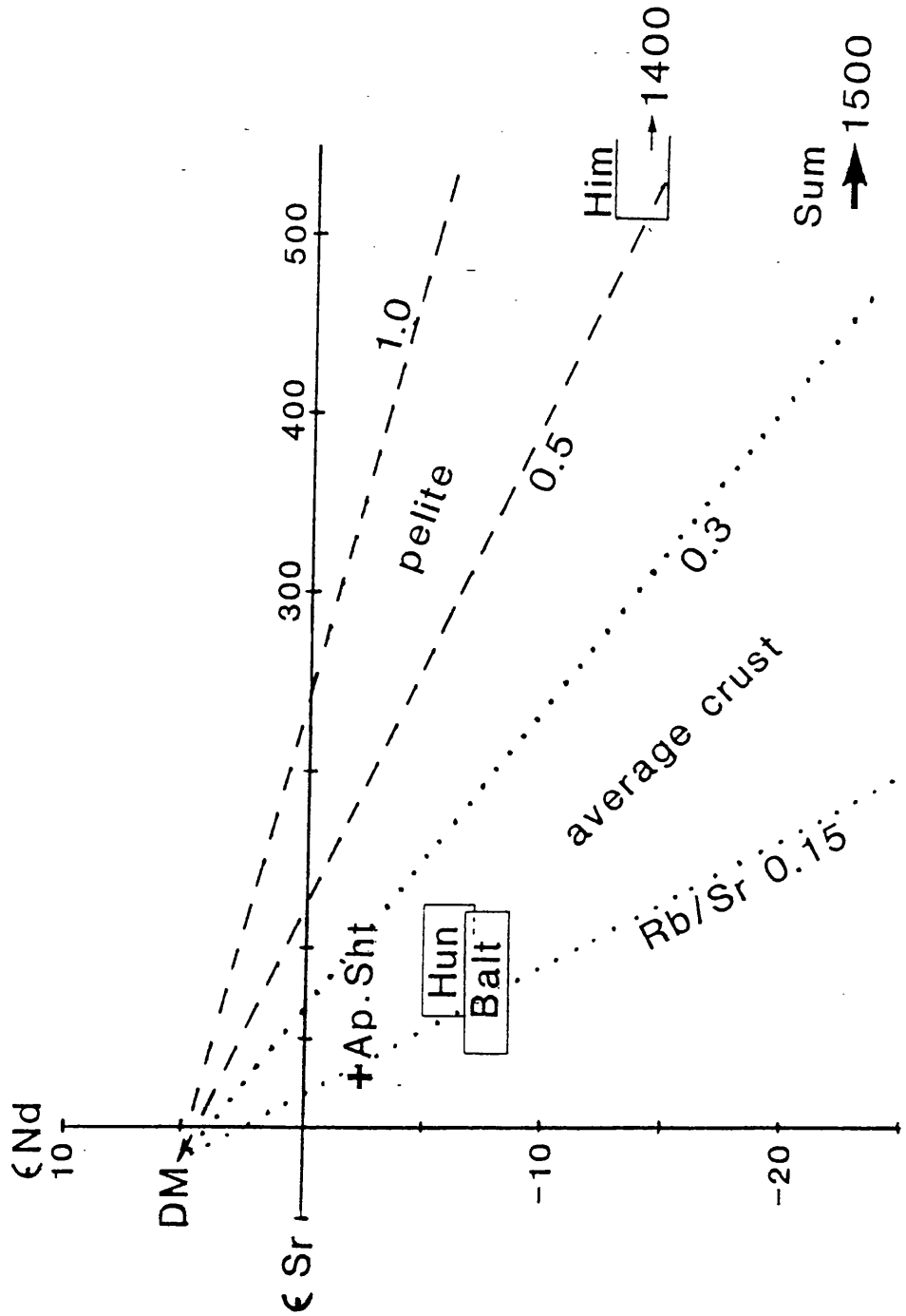

Figure 6.17: εNd vs. εSr diagram for the post-collisional Hunza and Baltoro granites. Lines represent evolution from depleted mantle (DM) of sources with different Rb/Sr ratios (from Miller, 1985). Him = High Himalayan leucogranites (Allegre and Othman, 1980); Sum = Sumayar; Ap. Sht = HPC aplite sheets; Hun = Hunza; Balt = Baltoro.

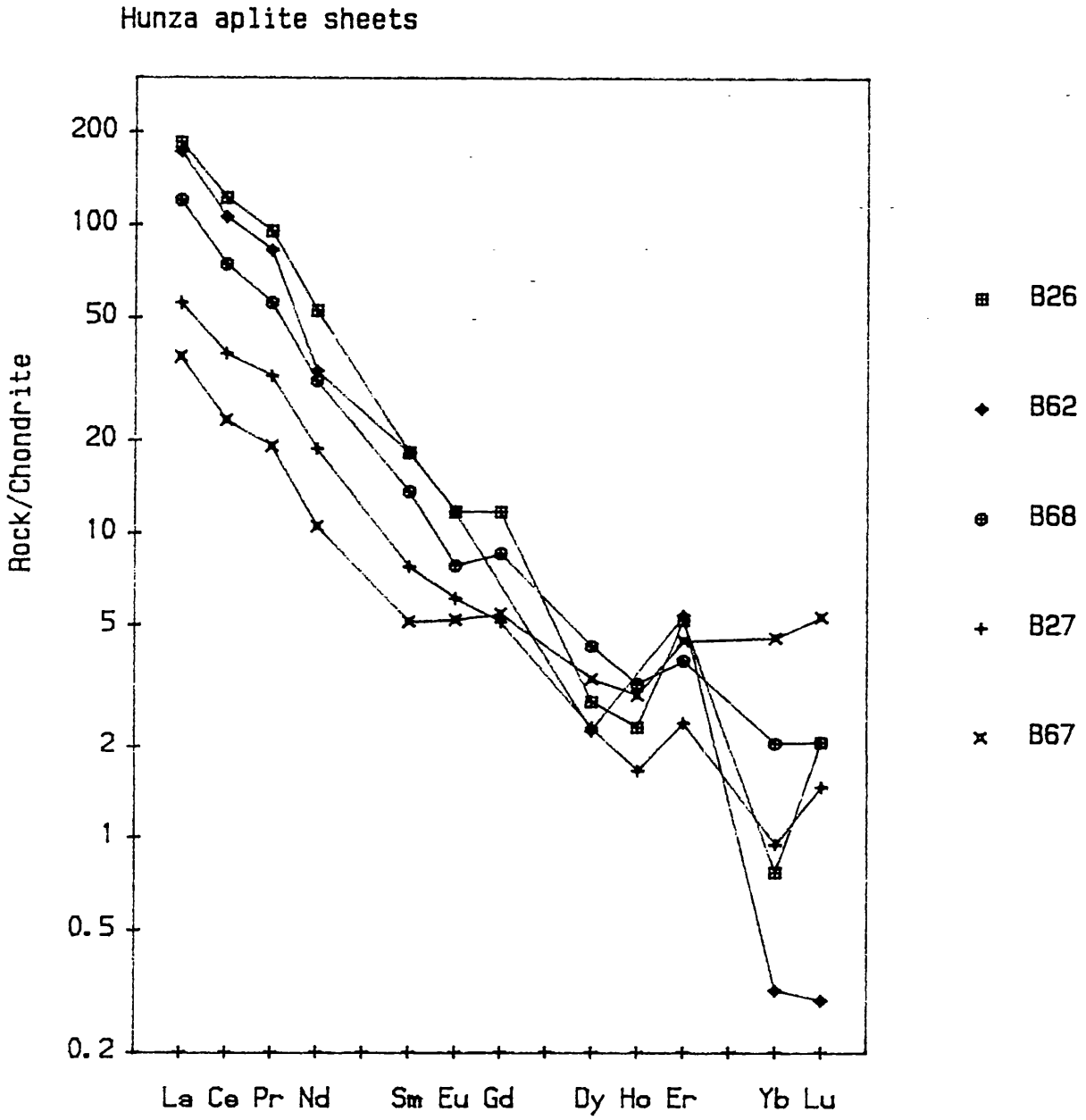

Figure 6.18: Rare earth element patterns for the HPC aplite sheets. B67 = leucogranitic margin to a sheet.

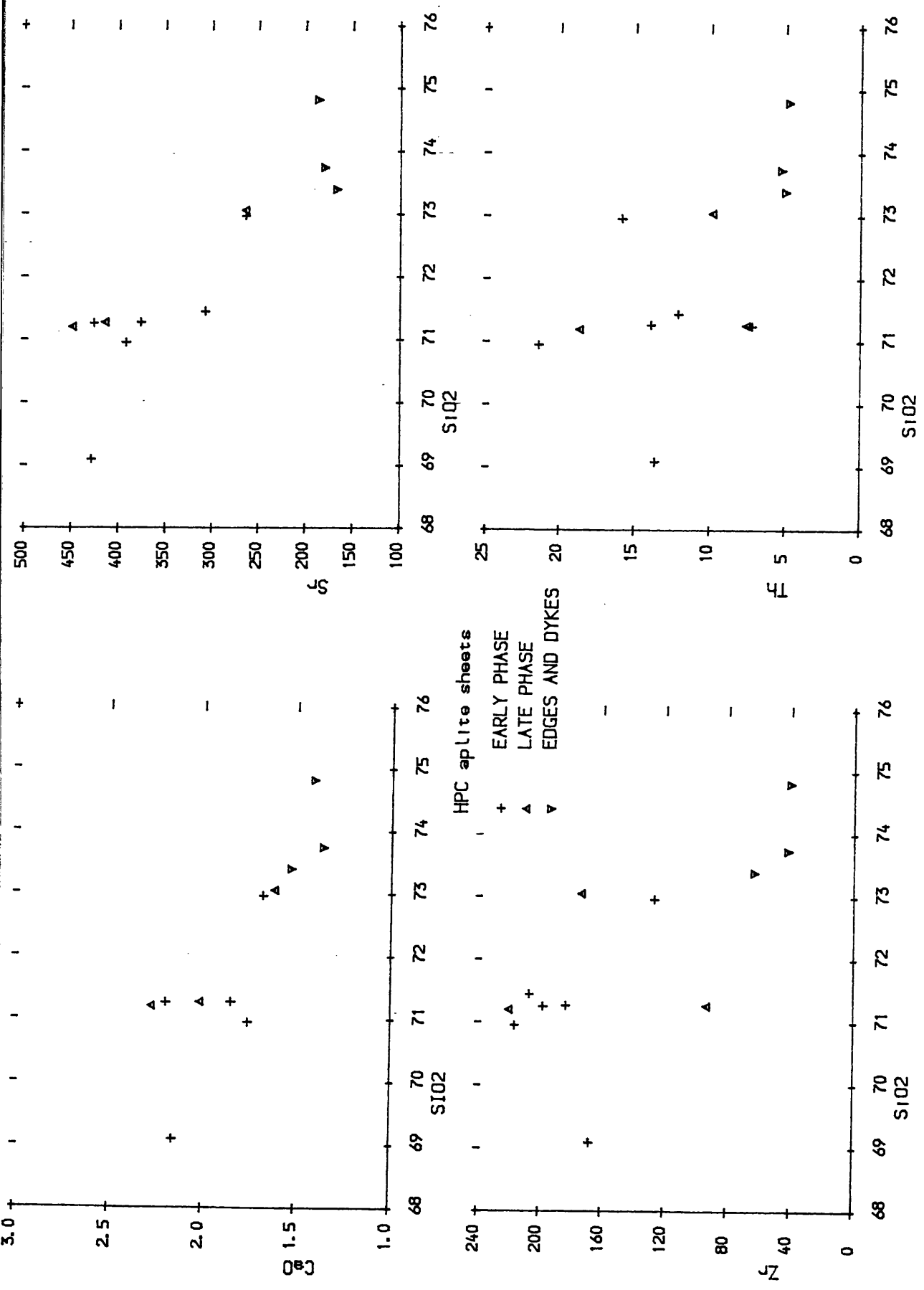

Figure 6.19: 'Harker-type' variation diagrams for the HPC aplite sheets.

The trend in REE from monzogranites to leucogranites (B67, fig. 6.18) is also similar to that in the Baltoro with decreasing LREE, enrichment of HREE, and development of a positive Eu anomaly. This trend was shown earlier to be consistent with a small amount of monazite crystallisation.

6.6: The Sumayar Pluton: Chemistry and petrogenesis - a Manaslu analogue?

6.6.a: Chemistry.

The Sumayar pluton differs from the other studied Hunza leucogranites in its tectonic position, its high Sr isotopic ratio and in the abundance of tourmaline (>2%) in its mineralogy. Figure 6.20(a) shows the position of the Sumayar samples on a Ab-Or-Qtz haplogranitic phase diagram. They do not lie on the trend of the eutectic given by changing PH_2O but they lie close to the eutectic at 1kb if 1% boron (B) is present (Pichavant, 1987). A high boron content not only affects the position of the eutectic but also lowers the wet solidus temperature by about 20°C (Benard et al., 1985). The same authors also consider that to achieve such high concentrations of boron a pelitic source is necessary since pelites may contain a considerable amount of B (up to 2000ppm B_2O_3) due to the substitution of the element for Al in clay minerals. This B will be released at low grades (greenschist facies) forming tourmaline in the potential source rock. For this tourmaline to break down and release the B into the melt temperatures of up to 750°C appear to be necessary, and this will then lead to a B-rich magma which crystallises tourmaline on cooling at low pressures. Hence, the abundance of tourmaline in Sumayar points to a metapelitic source. This is supported by the large Sr (0.8118) and low Nd (0.51146) isotopic ratios which, on a εNd vs. εSr diagram, indicate a source with a high Rb/Sr ratio such as a pelite (fig. 6.17; after Miller, 1985).

The Sumayar pluton is very similar in nature to the High Himalayan granites such as Manaslu (e.g. Le Fort, 1981; Vidal et al., 1982; Le Fort et al., 1987). Figure 6.20(b) shows a Debon and Le Fort (1982) classification diagram for Sumayar with the position of the haplogranitic eutectic under various conditions and the field for the Manaslu granite (Le Fort et al., 1987) superimposed upon it. It can

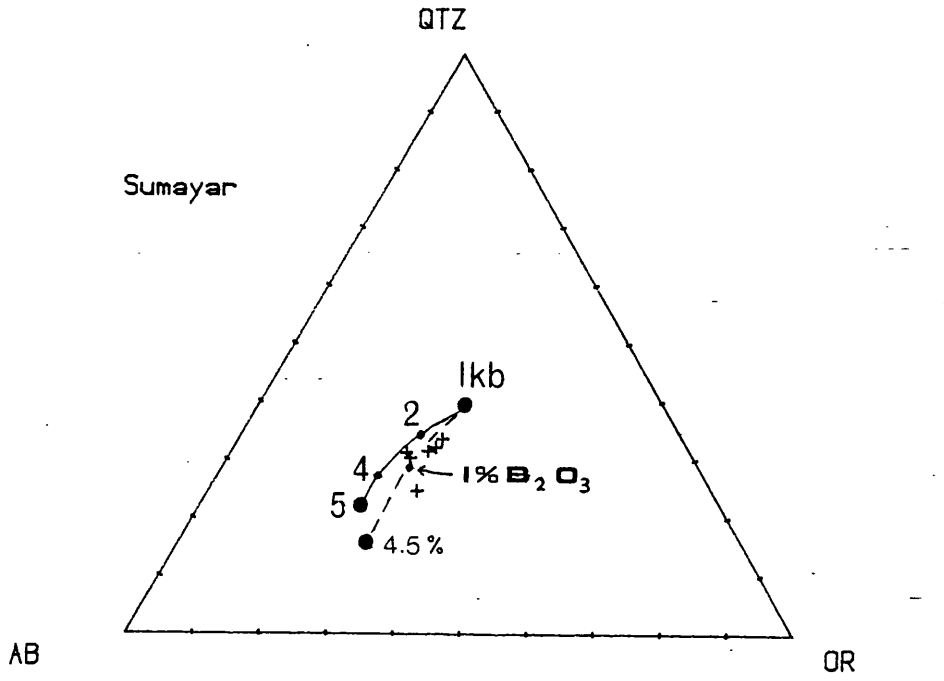

Figure 6.20(a): Qtz-Ab-Or normative diagram for the Sumayar pluton with eutectic positions marked for 1, 2, 4 and 5kb and for 1kb with 1% and 4.5% boron added (from Pichevant, 1987).

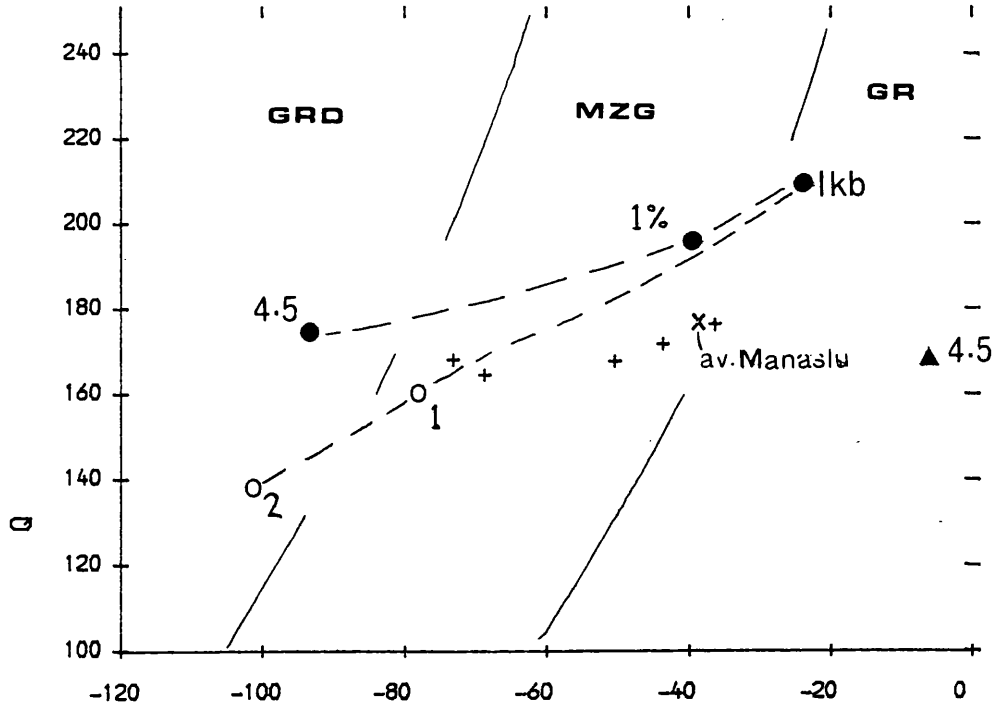

Figure 6.20(b): Debon and Le Fort (1982) classification (Sumayar)

Q = Si/3 - (K+Na+2Ca/3)
P = K - (Ca+Na) in molecular proportions.
Closed circles are eutectic positions at 1kb with 0, 1 and 4.5% boron. Open circles are eutectic positions at 1kb with 0, 1 and 2% fluorine added. Triangle shows the eutectic under dry conditions with 4.5% boron. X shows the average Manaslu composition and plus signs show the Sumayar samples (afterLe Fort et al, 1987).

be seen that the Sumayar defines a similar trend to the Manaslu and is probably a minimum melt with the exact position of the eutectic dependent on pressure, and water, boron and/or fluorine contents of the system.

Small degrees of partial melting giving a eutectic composition would account for the homogeneity of the major element abundances in the Sumayar analyses. Pichavant (1987) states that the addition of boron will not move the position of the eutectic sufficiently to drastically alter the major element composition of the minimum melt, although it may have more effect on the trace element composition. A comparison between the average Manaslu (Le Fort et al, 1987) and Sumayar major element analyses (table 6.5) shows a remarkable similarity between the two within the errors defined by the standard deviation. Trace elements show larger differences reflective of different source abundances for the two magmas.

	Sumayar	St.dev.(n=5)	Manaslu	St.dev.(n=201)
SiO_2	74.09	0.31	73.65	1.18
TiO_2	0.05	0.01	0.10	0.07
Al_2O_3	14.83	0.18	14.87	0.63
Fe_2O_3	0.72	0.11	0.84	0.20
MnO	0.03	0.00	0.03	0.01
MgO	0.01	0.03	0.11	0.09
CaO	0.79	0.03	0.47	0.37
Na_2O	4.37	0.31	4.05	0.34
K_2O	4.54	0.25	4.56	0.44
P_2O_5	0.08	0.06	0.13	-
LOI	0.51	0.04	0.84	0.30
Ba	68	27	213	105
Rb	429.9	32.5	287	158
Sr	32.6	7.3	76	40

Table 6.5: Comparison of mean major (%) and trace element (ppm) data for Sumayar and Manaslu (Le Fort et al., 1987).

Trace element abundances show no correlation with increasing silica, alumina or the alkalis, and poor correlation with less abundant major elements such as iron and calcium. However, when plotted against each other Sr, Ba, Ce, Rb and Zr show linear trends, particularly when an element such as Nb, which has fairly constant values within the pluton, is used as a denominator (fig. 6.21). SG6 was collected from the edge of the pluton and appears to have lost some Sr with respect to the other samples. The Ba and Sr contents in Sumayar vary from 28 to 97ppm and 22 to 41ppm respectively. Melting of a pelitic source would almost certainly involve feldspar and biotite. This is confirmed by the large, negative Eu anomaly and HREE depletion shown by the REE patterns (fig. 6.22) indicating residual plagioclase and garnet. For small degrees of melting these phases in the residue would buffer the Sr and Ba content of the melt as the bulk distribution coefficient between residue and melt would be approximately unity (Miller, 1985; Le Fort et al., 1987). Hence, the three and two-fold changes in Ba and Sr abundances cannot be explained through melting and must represent removal or accumulation of these elements during differentiation within the cooling pluton.

On an AFM phase diagram (fig. 6.23, Benard et al., 1985) the Sumayar pluton plots on the AF side near A ($A=Al_2O_3-K_2O-CaO-Na_2O$ calculated from mole %). During fractional crystallisation of a magma with this bulk composition muscovite, then tourmaline and finally garnet would be crystallising phases. A re-crystallisation experiment on a tourmaline-seeded peraluminous liquid by the same authors showed that the major crystallising phases would be plagioclase, followed by quartz and K-feldspar. A little biotite enclosed in muscovite indicates that this phase crystallised in the early stages when the Mg/Al ratio of the magma was at its highest. The early crystallisation of micas also indicates that the magma was water-saturated (Wyllie et al., 1976). Sr, Ba and Rb will be controlled by the above minerals. Garnet has low K_D values for the LILE elements in acidic magmas (Arth, 1976) and because no distribution coefficient data are available for tourmaline this phase cannot be considered. It can be seen from figure 6.24 that the Ba abundances in Sumayar decrease more rapidly with respect to the Sr abundances and this can be accounted for by the crystallisation of K-feldspar alone. In the case of the other Hunza and BPU granites (see earlier) biotite also played a part in removing Ba but biotite is unlikely to be an

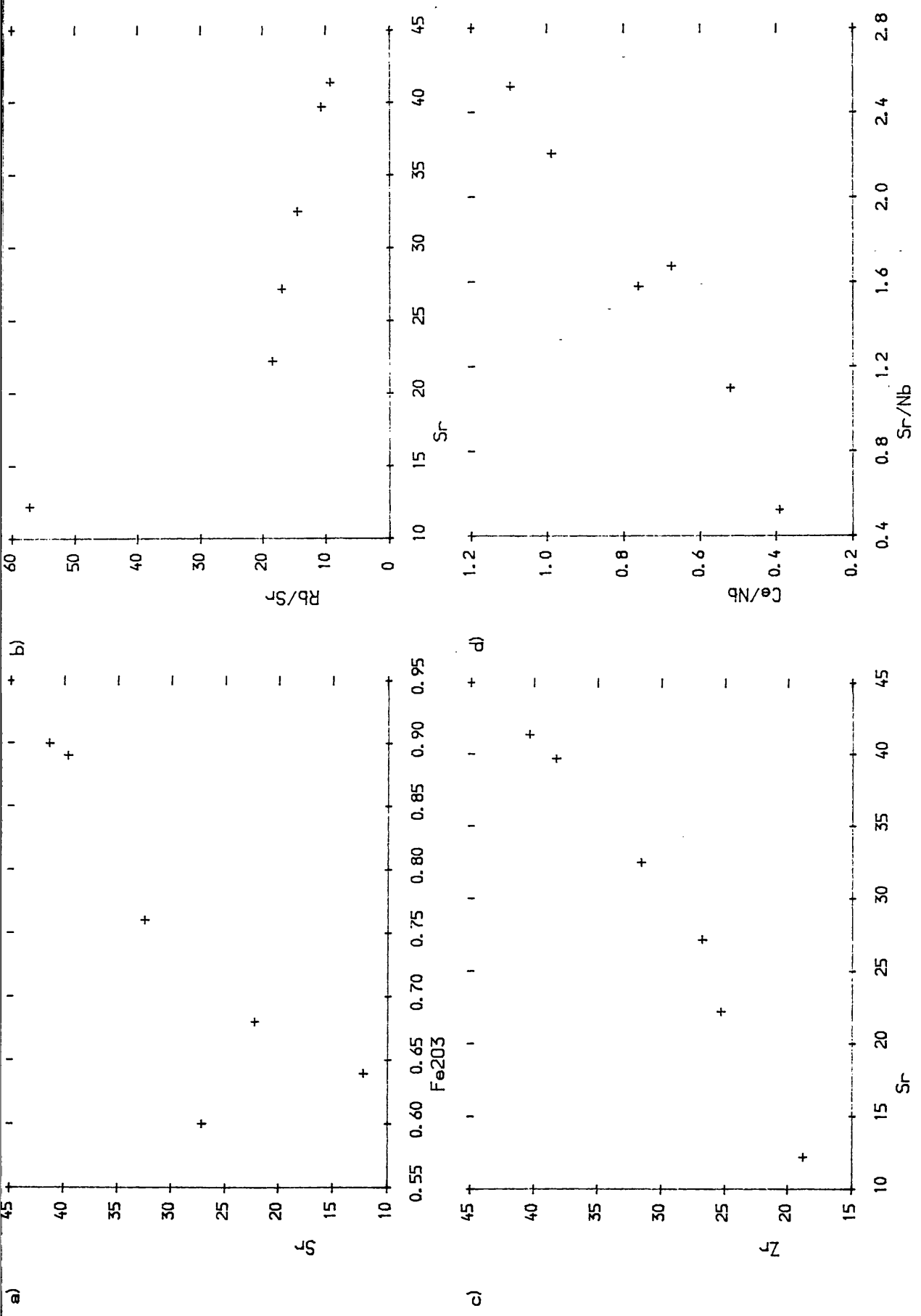

Figure 6.21: 'Harker-type' variation diagrams for the Sumayar pluton. Sample SG6 lies off the trends in graphs a) and b).

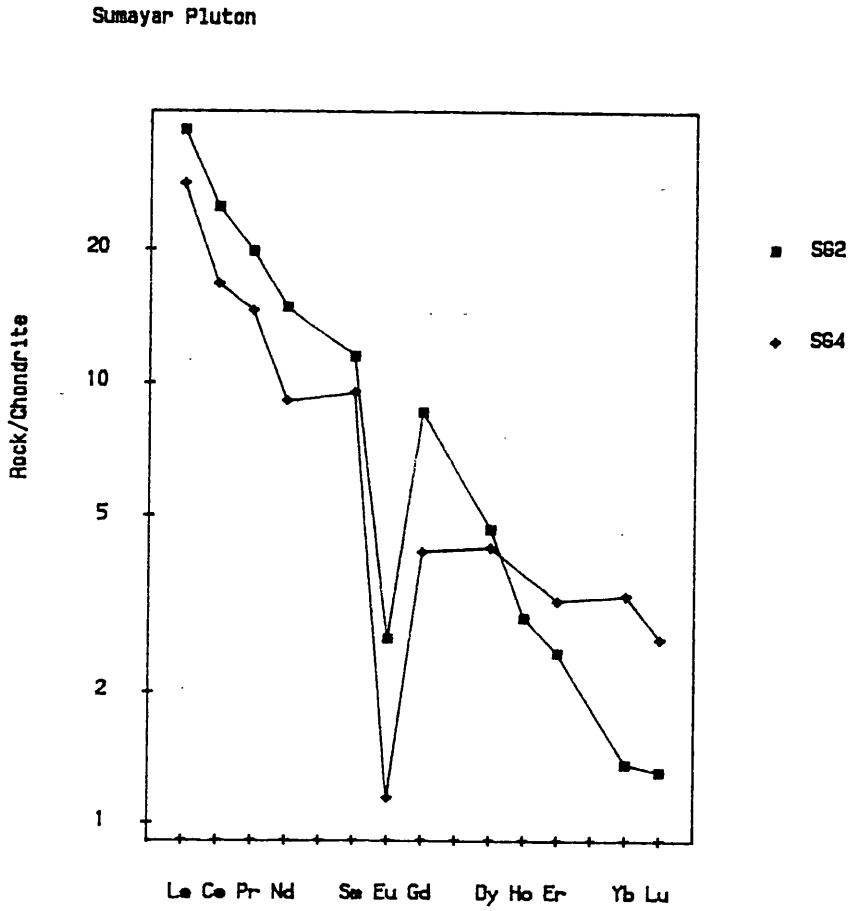

Figure 6.22: Rare earth element patterns for the Sumayar pluton.

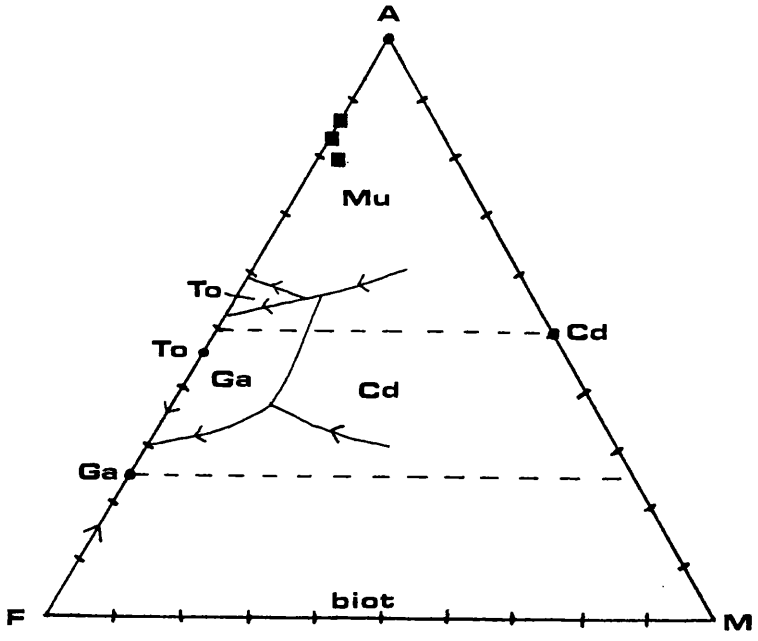

Figure 6.23: AFM plot for the Sumayar pluton (squares) where A = Al_2O_3 - Na_2O - K_2O - CaO; F = FeO + MnO; M = MgO calculated from mole%. Phase relationships from Benard et al. (1985) with the position of tourmaline (To) estimated. Ga = garnet; Cd = cordierite; Mu = muscovite; biot = biotite.

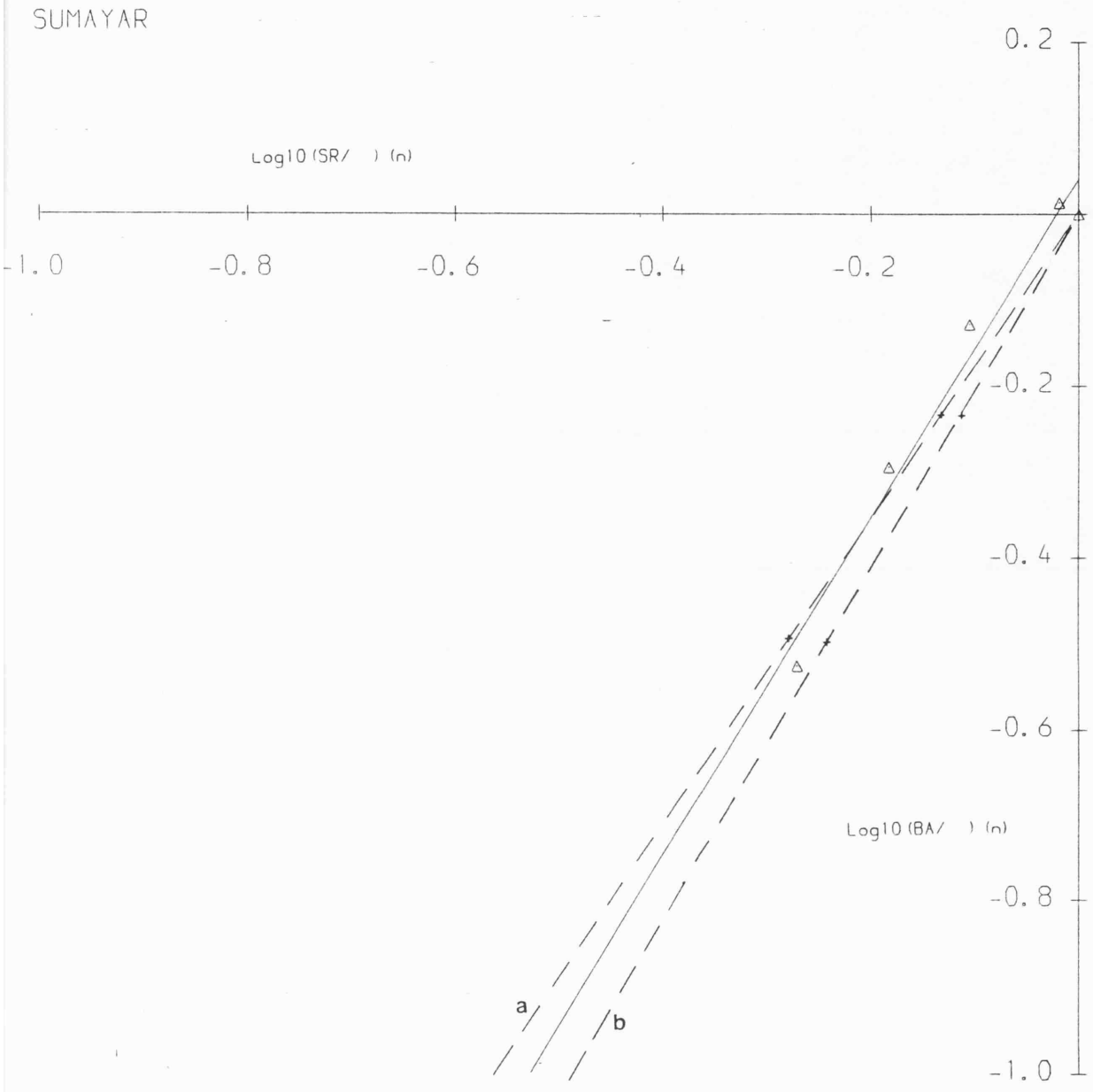

Figure 6.24: log(Ba) vs. log(Sr) for the Sumayar pluton with samples normalised to SG2. Solid line is best-fit regression line. Lines **a** and **b** correspond to Rayleigh fractionation of the respective assemblages 100% K feldspar and 90% K feldspar, 10% biotite using distribution coefficient data from Hanson (1978). Crosses correspond to 10% and 20% crystallisation away from the origin.

important phase here due to its rare occurrence. The variation in Ba and Sr abundances is therefore probably dependent upon the modal proportion of K-feldspar in each sample.

The other trace elements are probably controlled by accessory phases (Watson and Harrison, 1984; Cuney et al., 1984) as shown by the decreasing trend of Zr with Sr indicating the precipitation of zircon.

6.6.b: The Hunza Valley sillimanite-grade metasediments; a source for the Sumayar leucogranites?

The primary nature of the Sumayar leucogranites, their lack of association with other rock types such as monzogranites and their probable metapelitic source with a high Rb/Sr ratio and B content distinguishes them from the other types of leucogranite seen in Hunza and the BPU. They are similar to the High Himalayan leucogranites such as Manaslu and so a similar petrogenesis could be considered. Only the top of the pluton is exposed where it is in metamorphic disequilibrium with the staurolite-grade country rocks causing a thin metamorphic aureole, and a small dyke network emanates from the pluton above its roof. Both these features are observed for the Manaslu pluton (Le Fort, 1981) where the source of the leucogranite is recognised to be deeper-seated sillimanite-grade calc-silicate gneisses, pelitic gneisses and marbles of Formation I of the Tibetan Slab. At the roots of the Manaslu pluton the leucogranite magma is in equilibrium with these gneisses, which were fluxed by fluids coming from dehydration of the overthrust Midland Formation sediments thus lowering the solidus of the gneisses (Le Fort et al., 1987). The regional heat flow due to crustal thickening and localized high heat supply from large concentrations of heat producing elements contained in up to 1% modal zircon, apatite, monazite and xenotime (Hodges et al., in press) could then generate sufficient temperatures to cause local anatexis. That the regional metamorphism needed to be at sillimanite-grade conditions (amphibolite facies) is recognised because where the Tibetan Slab is thin, only kyanite-grade is reached and anatexis is poorly developed. A fluid component is required because temperatures were not sufficiently high to promote large-scale dehydration melting. In the Garwhal Himalaya leucogranite magma

is in equilibrium with kyanite-bearing gneisses which are rich in muscovite and biotite (P. Metcalfe, pers. comm.) indicating these phases have not extensively dehydrated. Therefore, wet melting at lower temperatures in the presence of excess fluid must have generated the leucogranites.

It was shown earlier that the sillimanite-grade metasediments of Hunza did not attain sufficiently high temperatures to melt extensively via dehydration reactions, although temperatures were high enough for wet melting. The high-grade rocks to the north of Sumayar were brought from deeper levels over the top of the staurolite-grade rocks by southward thrusting during the major c.45Ma deformation episode (chapter 3 and Rex et al., in press). It is therefore reasonable to assume that similar sillimanite-grade rocks still underlie the staurolite grade rocks at depth. Also during the 45Ma deformation event Indian, and possibly Kohistan, crust started to underthrust the Eurasian margin along the Main Karakoram Thrust (MKT) or Shyok Suture (Rex et al., in press).

If the underthrust crust dehydrated and fluxed the sillimanite-grade rocks above the MKT then melting could be initiated in a similar manner to the Manaslu model. This could generate a wet, minimum melt at depth which would be fairly immobile and could only rise a short distance, perhaps to the present position of the Sumayar pluton (refer to fig. 6.27, next section). The spatial restriction of this magmatism might be explained by the need for extra heat input from locally high concentrations of heat producing elements. This is supported by the high abundance of U in the pluton compared to other Hunza granites (SG2=17ppm cf 7-9ppm for the Hunza dykes and BPU; Rex et al., in press), suggesting a U-enriched source. This model would mean that the Sumayar pluton would have to have been generated shortly after the deformation (35Ma approx.) which would make it older than the BPU and Hunza dykes.

Unfortunately, the suitability of the Hunza metasediments as a source rock cannot be tested here. A number of samples of the country rock were collected, but because of the wide range of compositions only one lithology was concentrated on. Whilst this lithology showed felsic and mafic segregations in the field subsequent analysis has shown them to be metabasites. The very low Sr isotope ratios (SLG2 &

6; 0.7052) and high Nd isotope ratios (0.51270-0.51284) preclude these rocks as being a source for the Sumayar pluton.

The only rock analysed with a sufficiently high Sr isotope ratio to be a possible source for Sumayar is R-109 from the Dassu Gneiss unit in the Baltoro area (see fig. 5.1) ($^{87}Sr/^{86}Sr$=1.0567; T.Rex, pers. comm.). Figure 6.25 shows SG2 normalised to R-109 (circles) and the lines show a modelled pelitic melt with each line representing a 1% batch melt for a total of 10% melting. The melting fraction is dominated by quartz and feldspar, and the residue is controlled by biotite, plagioclase and some garnet. Initially the model only gave a good fit for the LILE, but the addition of a small amount of residual monazite produced a good fit for the REE. The melting assemblage used in figure 6.25 is supported by the evolving REE patterns. Figure 6.26 shows SG2 normalised to SG4 and a modelled melt using the same assemblage as in figure 6.25 with 0.2% monazite. The model shows a good fit with the data except that the whole pattern is lower. This may be a result of further feldspar fractionation being necessary to generate SG2, but is more likely to reflect loss of some sample during REE preparation resulting in low measured abundances for SG4. There is little point in pursuing the model of figure 6.25 further since, due to their spatial separation, it is unlikely that the Dassu Gneiss is the source for Sumayar. However, the model illustrates that it would be possible to melt a pelite similar to the Dassu Gneiss in the proportions given, and produce some of the trace element signature of the Sumayar pluton. Obtaining a model to fit all the data would be difficult because of the unknown effect of accessory phases on the trace element behaviour e.g. the effect of monazite on the Th abundances in figure 6.25.

6.7: Discussion: a tentative crustal cross-section through Hunza.

It has been shown that there are two main types of post-collisional magmatism in Hunza, and both involve leucogranites. The Sumayar leucogranites are intruded as a pluton which, with its mineralogy of tourmaline and Mn-rich garnet, appears to have been emplaced at a high level (<3kb). The leucogranites are water-saturated minimum melts whose isotope chemistry indicates a pelitic source. It is proposed that the Sumayar pluton is an analogue of the High Himalayan leucogranites with its source being sillimanite-grade

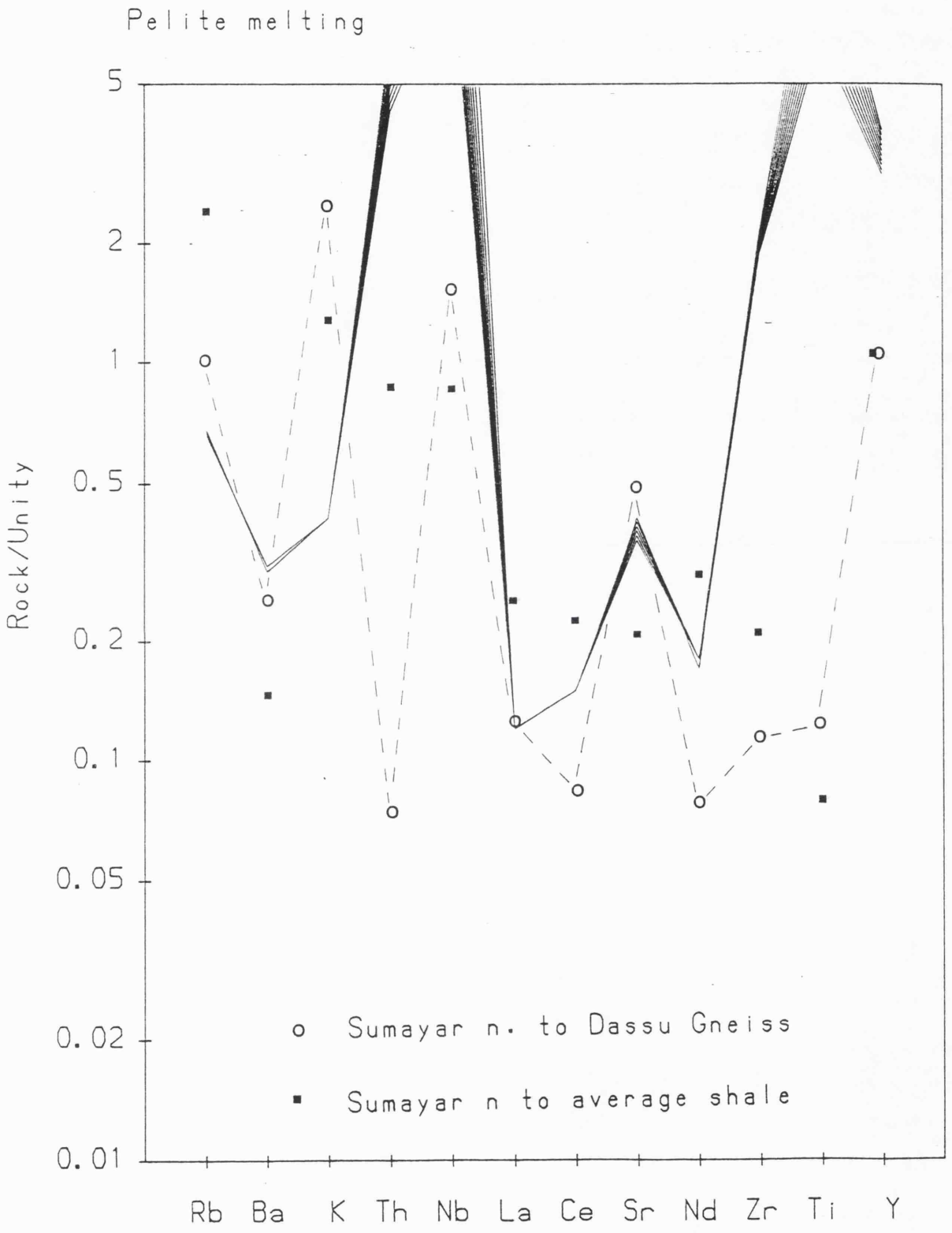

Figure 6.25: Modelled melt for the Sumayar pluton with the source composition represented by unity.
Source proportions = 39.5% biotite, 30% plagioclase, 10% garnet, 10% quartz, 10% K feldspar, 0.5% monazite.
Melting proportions = 5% biotite, 30% plagioclase, 30% K feldspar, 35% quartz.
Average shale composition from Taylor and Mc Lennan (1985).
Distribution coefficients from Henderson (1982).

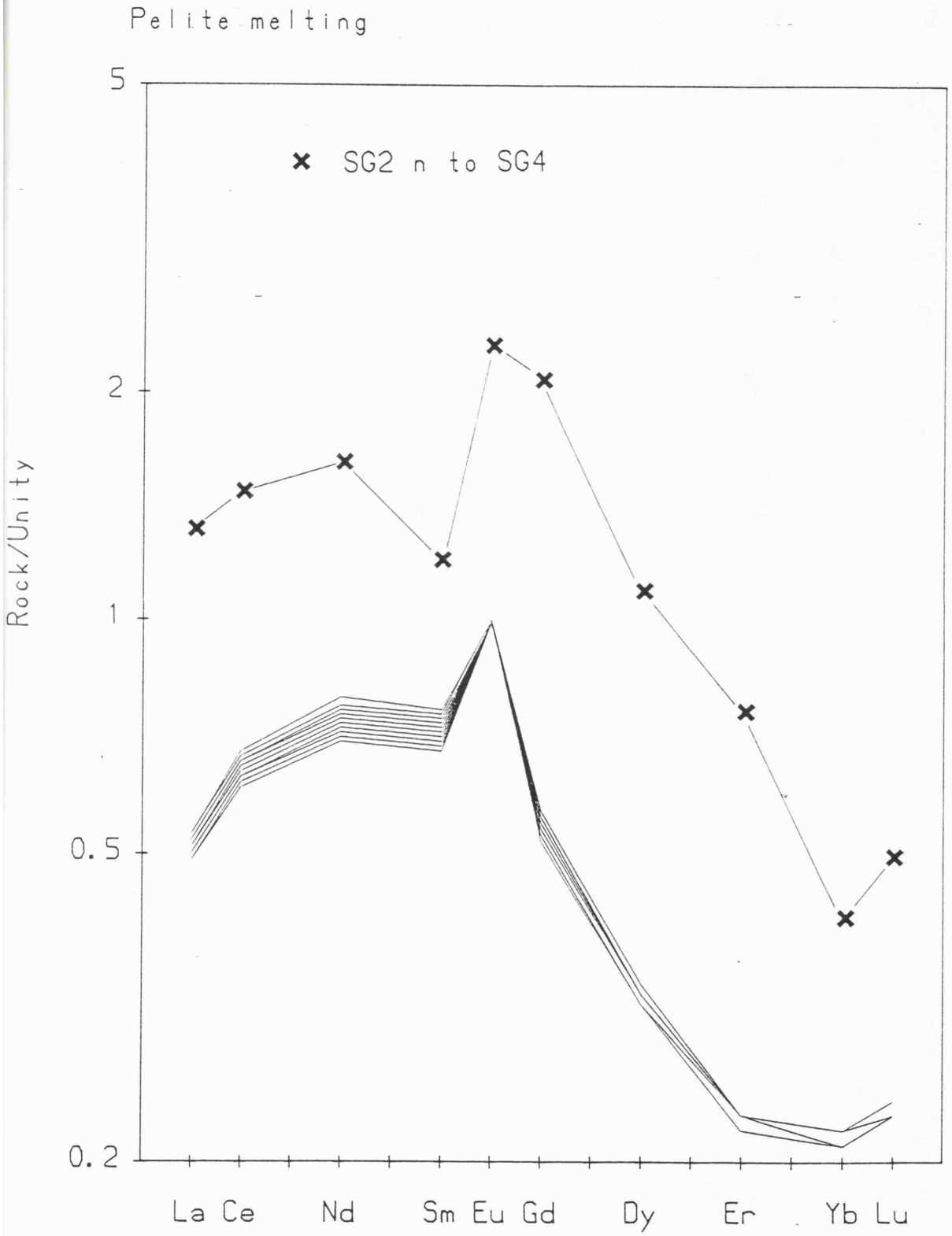

Figure 6.26: Modelled pelitic melt from figure 6.25 compared with the rare earth element pattern of SG2 normalised to SG4.
Source proportions = 40% biotite, 30% plagioclase, 9.8% garnet, 10% quartz, 10% K feldspar, 0.2% monazite.
Melting proportions as for figure 6.25.
Distribution coefficients from Henderson (1984) and estimated for monazite.

metamorphic rocks similar to those seen at the surface further north. As in the model for the Manaslu granite (Le Fort, 1981), it is envisaged that the source rocks were not hot enough for extensive dehydration melting, but that they were fluxed by fluids coming from the dehydrating Kohistan/Indian crust underthrust along the MKT. Figure 6.27 depicts a hypothetical crustal cross-section through the Hunza Valley to show this relationship. The section is based on a similar section for the Baltoro area by Rex et al. (in press), and the depth of the sillimanite-grade rocks below the c.40Ma surface is based on a geothermal gradient of 30°C/km. The large thrusts shown were observed in the field separating the major units (chapter 3). The smaller thrusts are the minimum number necessary to explain the present surface outcrop of the metamorphic rocks, although in reality many more are actually present. Uplift rates in the Hunza Valley increase northwards (Zeitler, 1985) resulting in a sloping c.40Ma surface if the present surface is taken as the horizontal. This section shows that the Sumayar pluton was intruded nearer to the palaeo-surface than the dykes explaining its apparent shallower emplacement depth.

The Hunza leucogranite dykes have been shown to be possible fractionates of the monzogranite dykes. The high Ba and Sr abundances, isotopic and chemical signatures, and mineralogy of these dykes are comparable with the BPU granites. Therefore, a similar origin is proposed with the monzogranites representing primary, lower crustal melts initiated and contaminated by ultra-potassic magmas coming from the enriched mantle beneath the Karakoram (chapter 5).

Two problems which are still apparent in relating the dykes to the BPU are why the Hunza granites only occur as dykes whilst the BPU is intruded as a pluton, and why the dykes are not intruded further north than the deformed part of the HPC batholith. A tentative model is put forward in figure 6.27 to explain this and also explain the break in deformation seen within the HPC (chapter 3).

The juxtaposition of upper- and mid-crustal rocks on opposite sides of the BPU was suggested to be related to northward downthrow along an inferred normal fault; the Karakoram Batholith Linament (KBL; Rex et al., in press). It was also suggested that this fault spatially controlled magmatism along the Karakoram Batholith. The

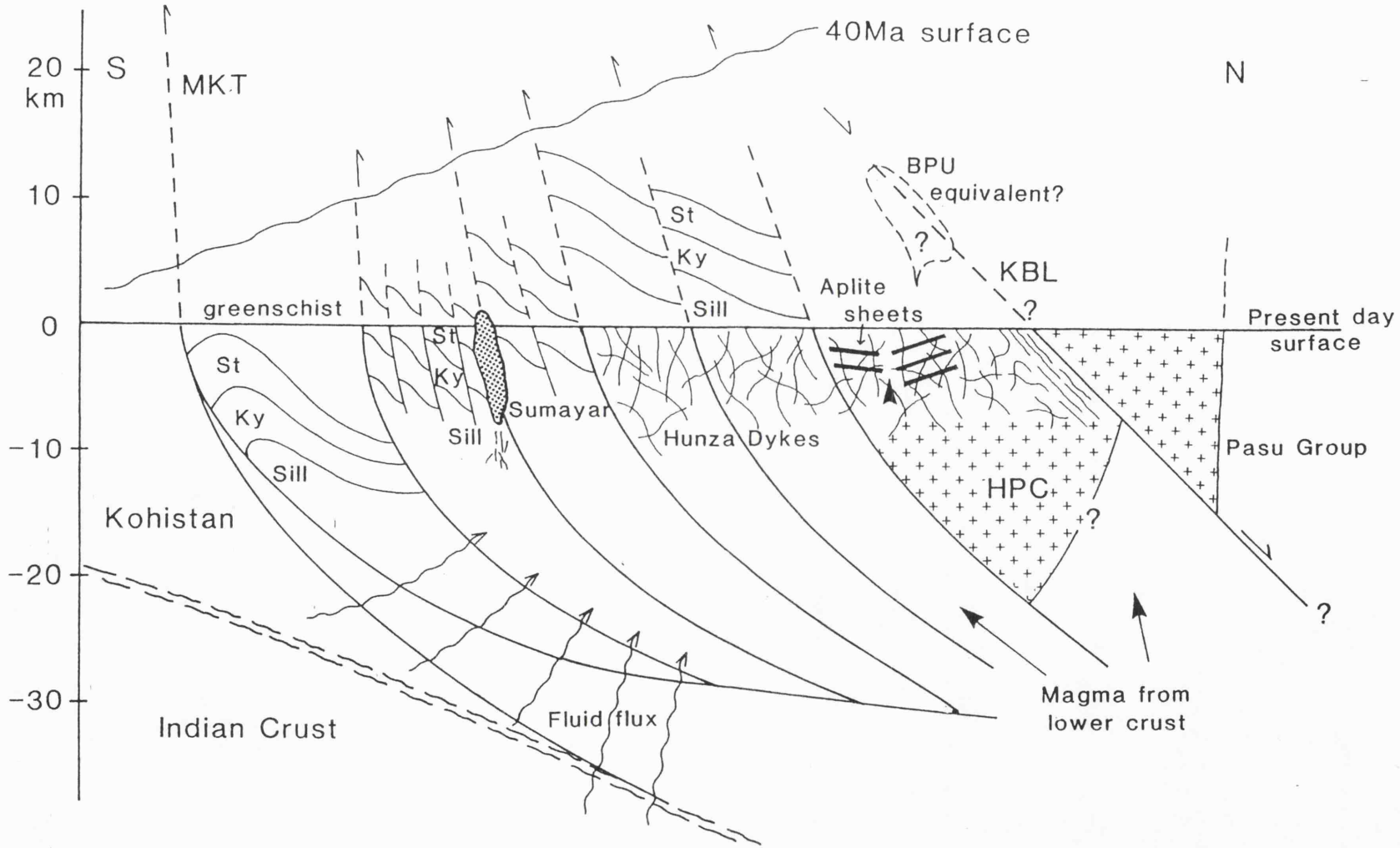

Figure 6.27: Schematic crustal section through Hunza showing the spatial relationships between the Hunza Dykes (squiggles), the Aplite sheets (solid black stripes) and the Sumayar Pluton (dotted). Based on a similar section for the Baltoro area by Rex et al. (in press). MKT (Main Karakoram Thrust or Shyok Suture) represents boundary between Karakoram and underthrust Kohistan and Indian crust. Greenschist, St (staurolite), Ky (kyanite) and Sill (sillimanite) metamorphic zones are shown. Thickness of these zones and the palaeo-40Ma surface are calculated using a geothermal gradient of 30°C/km. Thick black lines are observed major thrusts (except for the inferred KB normal fault). Thinner lines are minimum number of thrusts required to explain surface outcrop (compare with fig 3.4). Horizontal scale = vertical scale.

fault was re-activated after collision by culmination collapse during crustal thickening and uplift of the southern metamorphic complex. Across the KBL, if present, there would be a local high temperature anomaly due to the thermal contrast, with the sedimentary rocks to the north acting as a barrier to lateral heat transfer (see Jaupert and Provost, 1985). This temperature anomaly and thermal contrast would channel the BPU magma which would then be emplaced in the footwall of the KBL. If the BPU magma initially rose via feeder dykes which then merged to form a pluton then these dykes would also only lie to the south (in the footwall) of the KBL and be unexposed at the present day surface.

If, as predicted, the KBL is present in Hunza then it must mark the transition from mid-crustal metamorphic rocks in the south to upper-crustal rocks low-grade rocks in the north. This transition lies in the HPC along the deformation front where the foliation and recrystallisation due to southward-directed thrusting dies out (i.e. around Shishkat bridge, chapter 3). This coincides with the position where the voluminous dyke swarms disappear, with only a few dykes being found to the north of this. It is conceivable that either the Hunza section represents a deeper level in the crust than the Baltoro, or that the magmas in Hunza rose to shallower levels in the crust without merging. This would mean that the Hunza dykes represent the feeder stage to a pluton similar to the BPU. Either this pluton has since been eroded away or it simply did not form to the same extent as the BPU (fig. 6.27).

As well as explaining the location of the dykes just to the south of the inferred KBL or deformation front, this model could also explain one other observed feature in Hunza. Nearing the deformation front the dykes become parallel as opposed to their anastomosing nature further south. This could be a result of the dykes being aligned along the local isotherms caused by the thermal contrast across the KBL. This would facilitate the intrusion of the magma by maintaining a constant temperature.

The major problem with this model is that the KBL is not observed. In the Baltoro it is assumed to be hidden by the intrusion of the BPU, but in Hunza it should be an obvious feature. The rocks of the first HPC phase north and south of the deformation front were

related by fractionation in chapter 4.4. However, this does not preclude this model because the KBL could have simply brought a higher part of the same pluton into contact with a lower part. Whilst no jump in rock type is seen across this zone, there is interfingering of two distinct plutonic phases. This could be explained by movement along the KBL if the deformation was fairly ductile.

Whilst the lack of evidence for the KBL is a major drawback, this is the only model that can be suggested at present to explain the above features. A detailed thermobarometric section across the HPC which indicates a major jump in grade around the proposed position of the KBL would support the model, but the samples from this study are not suitable for such an analysis. In the next chapter, the implications of identifying these two types of post-collisional leucogranite are discussed in a more global context.

CHAPTER SEVEN: Leucogranites of the NW Himalaya: implications for study of leucogranite petrogenesis and magmatic evolution within collisional belts.

7.1: Introduction.

Pitcher (1983) stated that 'the connection between environment and granite type is inescapable. This is because granite arises as a result of several generative processes involving different source rocks, each process and source being appropriate to a particular environment.' With the exception of the few leucogranites that have been related to fractionation from a more basic parent, leucogranites are considered to be the products of crustal anatexis (e.g. Le Fort, 1981; Strong and Hanmer, 1981). Rather than being limited to one environment leucogranites can, therefore, occur wherever conditions are suitable for crustal melting, such as during continental collision and crustal thickening. The classic model for leucogranite formation in collisional belts comes from work on the Manaslu pluton in the High Himalaya by Le Fort and others (e.g. 1975, 1981, 1987). Here melting is induced in sillimanite-grade gneisses by fluids derived from the dehydration of the overthrust Midland Formation metasediments. However, it has been shown (chapter 5) that the Baltoro Plutonic Unit (BPU) leucogranites have a different petrogenesis, forming by fractionation from a monzogranitic parent. These monzogranites are primary melts produced via dehydration melting under water-undersaturated conditions at the base of the crust, promoted and contaminated by an input from the mantle.

Thus, two processes involving two different magmatic triggers but leading to similar magma types have been identified in the same tectonic setting. However, the petrogenetic process does not necessarily imprint a characteristic signature on the granite. The chemistry of the source is much more important in determining the nature of the granite and it follows that it can be difficult to definitively distinguish between the two leucogranite types. However, such separation where possible may have implications for the study of magma genesis, with respect to both process and chronology, during collisional cycles throughout the geological record.

7.2: Leucogranites in collisional belts; the problems of recognition and interpretation.

It can be stated from studies of the BPU and Manaslu that there are at least two types of leucogranite that occur in collisional belts:-

Type-a: Syn-tectonic crustal melts (Manaslu-type): these are small percentage partial melts which are usually of a minimum melt composition i.e. they are essentially primary magmas. They are related to regional metamorphism, usually of sillimanite-grade, and melting is triggered by the influx of fluids lowering the solidus. Melting appears to be controlled by local concentrations of high heat producing (HHP) elements within minor phases in the source (Hodges et al., in press). The generation of such melts is usually associated with thrusts or faults along which the necessary fluids can be released and migrate into the source region. Because the melting is under water-saturated conditions and the granites are minimum melts the magmas are usually fairly immobile and do not travel large distances from their source. This leads to the common association of migmatites with these granites.

Type-b: Post-tectonic crustal melts (Baltoro-type): these originate at the base of the crust where temperatures are elevated by crustal thickening (England and Thompson, 1986). In this case the magmatic trigger is input of heat from the mantle promoting large-scale dehydration melting. These are larger-percentage partial melts allowing the magma to separate from its source and, because of the water-undersaturated conditions, the magmas are hotter and dryer and so can rise for considerable distances through the crust. Because of the larger degrees of melting the magmas need not be minimum melts and so, at least in the case of the Karakoram Axial Batholith (KAB) granites, the first magmas are monzogranitic. The leucogranites evolve from these by differentiation.

A third type of leucogranite, that can occur in any environment, is that which is related by fractionation to a more basic parent such as a calc-alkaline pluton (e.g. Petterson and Windley, submitted). Because the characteristics of such magmas will depend strongly on the composition of the precursor magma they will not be considered

here. However, such a possibilty for the origin of a leucogranite in a collisional setting should be borne in mind.

Hunza is remarkable in that it appears to have both types of leucogranite exposed in near proximity (chapter 6). However, this statement is based upon a number of observations and lines of evidence. Therefore, the following discussion centres on whether, when confronted with a leucogranite exposed in a collisional setting, there are any reliable features which can be used to decide whether the leucogranite is one of the above types.

Classification systems based upon major element or normative compositions (e.g. Streckheisen, 1976; Streckheisen and Le Maitre, 1979; La Roche et al., 1980; Debon and Le Fort, 1982) only separate granites from other major rock types and are not sensitive enough to further subdivide the granite field. The Debon and Le Fort (1982) classification does define a field for leucogranites but because of their homogeneous major element compositions both types of leucogranite plot in the same place in such a system.

Three notable attempts to split the granite field according to environment and genetic process are those by Brown et al. (1984), Chappell and White (e.g. 1974), and Pearce et al. (1984). The system of Brown et al. (1984) deals only with granitoids formed at active continental margins and so is not suitable for dealing with post-collisional leucogranites.

The widely-used discrimination system for granites by Chappell and White (1974) and later expanded on by Pitcher (e.g. 1983, 1987) is based upon various major element abundances and isotopic composition. The original system divided the granitoids of the Lachlan Fold Belt in SE Australia into those with sedimentary (S-type) and those with igneous (I-type) source protoliths. This was later expanded (e.g. White and Chappell, 1983) to include anorogenic (A-type) granites. Pitcher (1987) subdivided the I-type field into four groups and the S-type field into two groups but did not provide any discrimination system with which to identify these groups. Both types of leucogranite have restricted high silica values, high $Al_2O_3/(Na_2O + K_2O + CaO)$ ratios (>1.05), high $d^{18}O$ and $^{87}Sr/^{86}Sr$ normally above 0.708. Both tend to lie in the S-type field (as

defined by White and Chappell, 1983) and so they are not separated. Additionally, it has been shown that whilst the source for the type-b granites may be largely metasedimentary, there is also probably a mantle input and so they are definitely not S-type granites sensu stricto.

Trace elements are much more sensitive to source composition and so might distinguish the two types. Figure 7.1 is a three dimensional plot of the LILE for the Baltoro granites. It shows that Ba and Sr decrease rapidly in the monzogranites with little change in the Rb/Sr ratio. This is a result of Ba and Sr being removed immediately into the crystallising feldspar over a short fractionation interval. Because the amount of liquid does not decrease significantly, Rb, which remains in the liquid as an incompatible element, maintains a fairly constant abundance. Only at larger fractionation values does the Rb/Sr ratio start to increase and the most evolved leucogranites have much lower Ba and Sr and higher Rb values than the monzogranites. Therefore, the high LILE-signature of the monzogranites, inherited via contamination by mantle magmas, is not so apparent in the leucogranites. A comparison between the spidergrams of the type-b leucogranites of the KAB and those of the type-a crustal melts of Manaslu (High Himalaya, Le Fort, 1981) and Sumayar (Hunza) (fig. 7.2) still shows the KAB leucogranites to have higher Ba and Sr and lower Rb. However, on diagrams with a logarithmic scale such as figure 7.2 the differences are not obviously large, and the overall spidergram patterns of the two leucogranite types are similar.

Pearce et al. (1984) developed a Rb vs. (Y+Nb) trace element discrimination diagram to divide granites into volcanic arc (VAG), ocean ridge (ORG), within plate (WPG), and syn-collisional (syn-COLG) types using a large data base to determine the field boundaries. However, on this discrimination diagram they could not define a field for post-collisional granites because such granites do not have a single well-defined source. Harris et al. (1986) later identified two main syn- or post-collisional granite types:

1) Type II syn-collisional e.g. High Himalayan leucogranites. These are crustal melts formed above thrust sheets. Generally, they are muscovite-bearing, enriched in Rb, B, and F by volatiles from wet

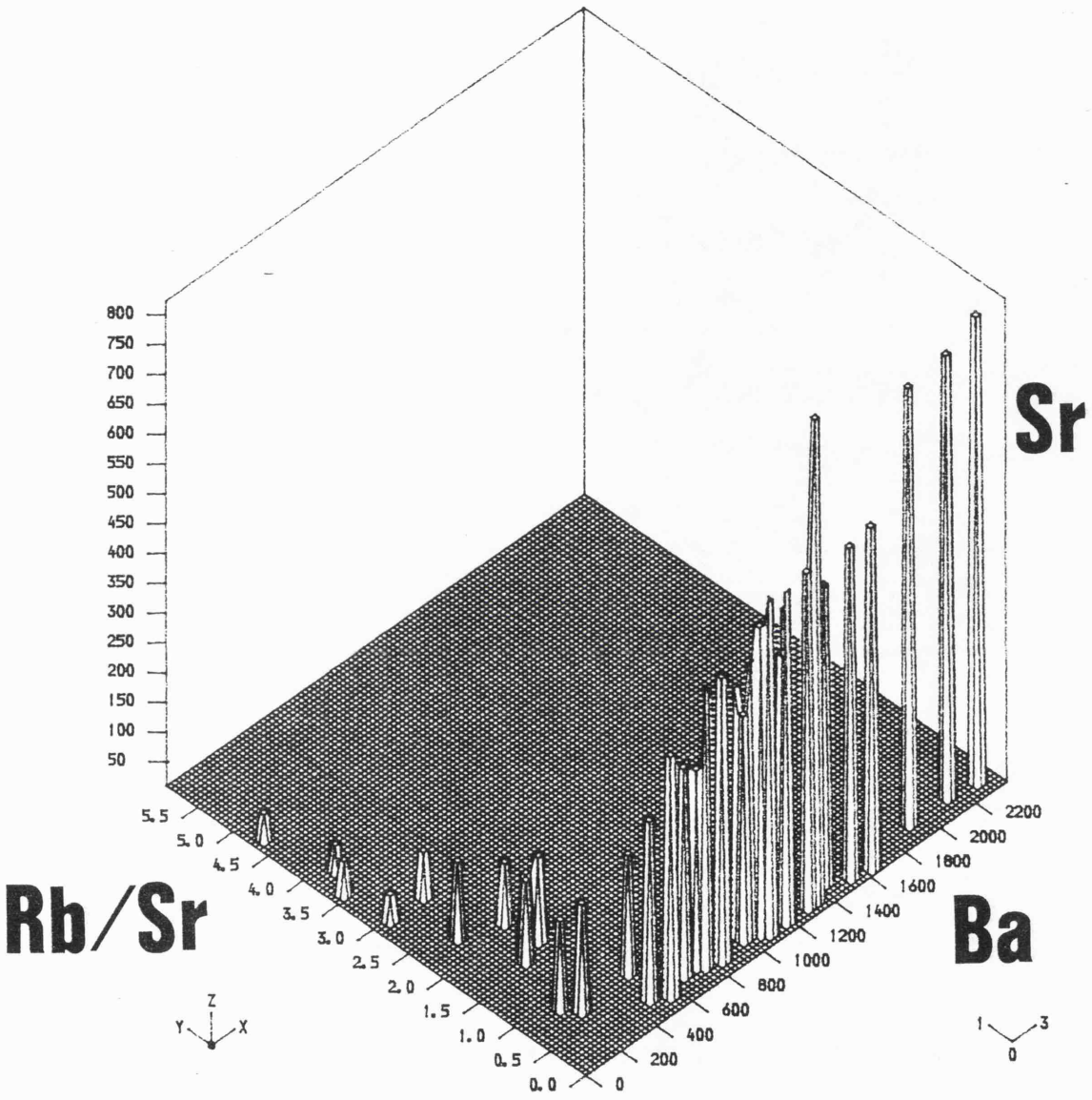

Baltoro Granites

X= BA/
Y= RB/SR
Z= SR/

Figure 7.1: Three dimensional plot of Ba vs. Rb/Sr vs. Sr (vertical) for the Baltoro monzogranites, leucogranites and dykes showing the main fractionation trend. Each spike represents one sample. The monzogranites are the largest spikes along the Ba axis and the leucogranites tend to be the smaller spikes along the Rb/Sr axis. See text for explanation.

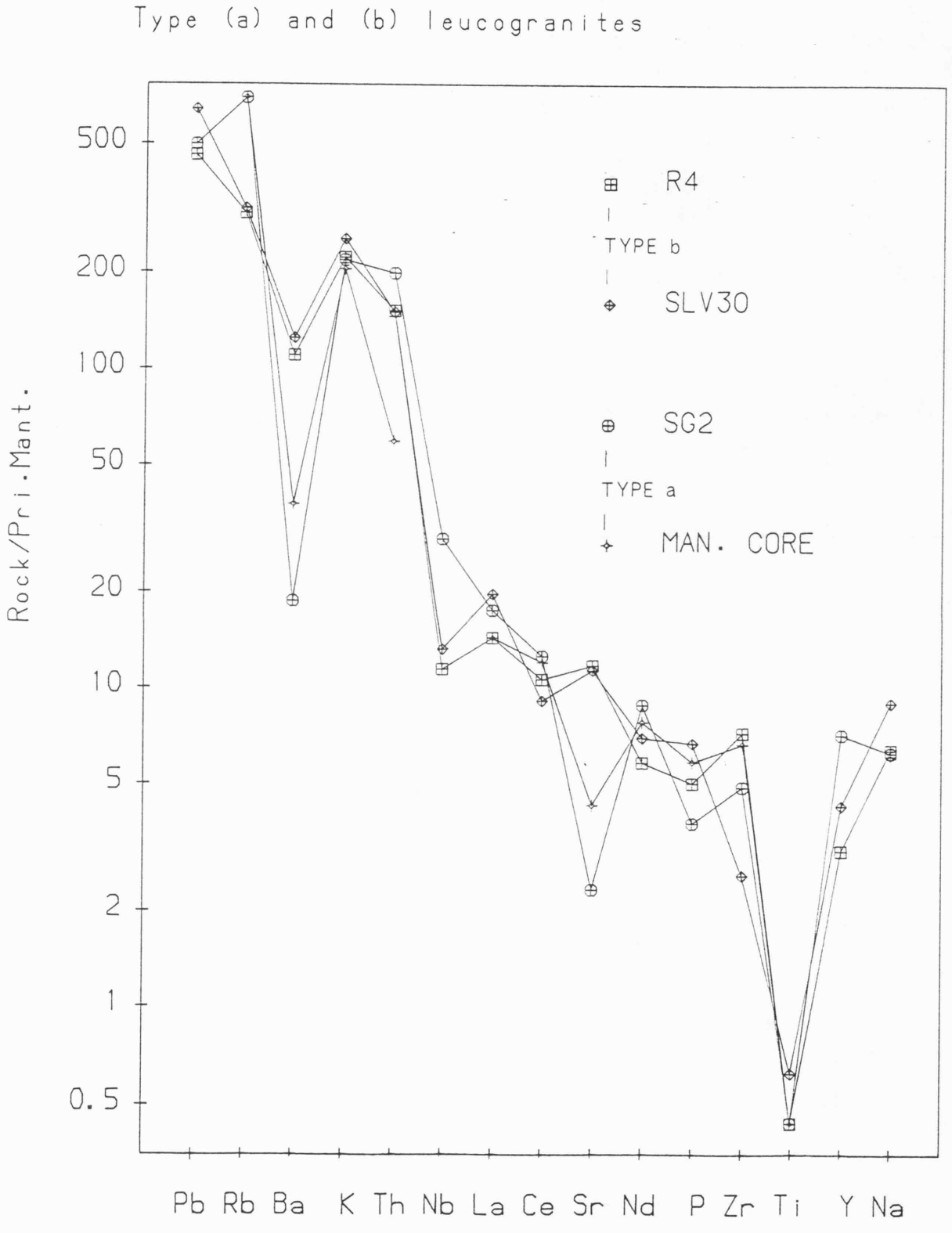

Figure 7.2: Comparison of spidergram patterns for type-a and type-b leucogranites. R4 = Baltoro; SLV30 = Hunza; SG2 = Sumayar; MAN. CORE = Manaslu (data from Le Fort, 1981). Normalised to primitive mantle of Taylor and Mc Lennan (1985).

sedimentary wedges, and depleted in residual Zr, Hf and REE.

2) Type III syn- to post-collisional e.g. Caledonides. These melts originate in the LILE-enriched mantle wedge and are contaminated by crustal melts. The relationship between types II and III is not necessarily sequential but depends upon the rate of crustal thickening. Harris et al. (op.cit) considered that type III has not yet formed in the Himalayan orogeny and will not be emplaced in the upper crust for at least another 10Ma.

The BPU monzogranites appear to fit the description of type III better than type II. However, on the Rb/Zr vs. SiO_2 discrimination diagram for the two types (fig. 7.3) the Baltoro and Hunza type-b monzogranites plot in the type II field and the leucogranites plot in the same place as the High Himalayan leucogranites. Therefore use of such a diagram to try to infer the petrogenesis of the type-b leucogranites would be misleading.

Whereas authors such as Pearce et al. (1984), Harris et al. (1986) and Pitcher (1983) clearly state the limitations and applicability of their systems, systems such as the I-S-A type granite classification are still widely used when they do not adequately or even correctly describe the exact nature of the granitoid body under study. Such problems were experienced in classifying some granites in southwestern N. America where peraluminous, two-mica and garnet bearing plutons were designated as S-type on the basis of mineralogy, isotopes and A/CNK ratios (e.g. Todd and Shaw, 1985). However, in many respects they differ from the S-type granites of the Lachlan Fold Belt by not containing cordierite, having higher abundances of Na and Sr, being associated with migmatites and containing primary muscovite. This led White et al. (1986) to conclude that these granites were products of partial melting of altered basic rocks and were therefore not S-types. The N. American granites have many features in common with the High Himalayan granites which have been shown to have metasedimentary protoliths (Le Fort, 1981) and this demonstrates that non-S-type granites can still show a number of S-type features depending on the nature of their source. This leads to the conclusion that outside the Lachlan Fold Belt (LFB) S-type granites, as defined by Chappell and White (1974), may be rare. If this is because the LFB granites are

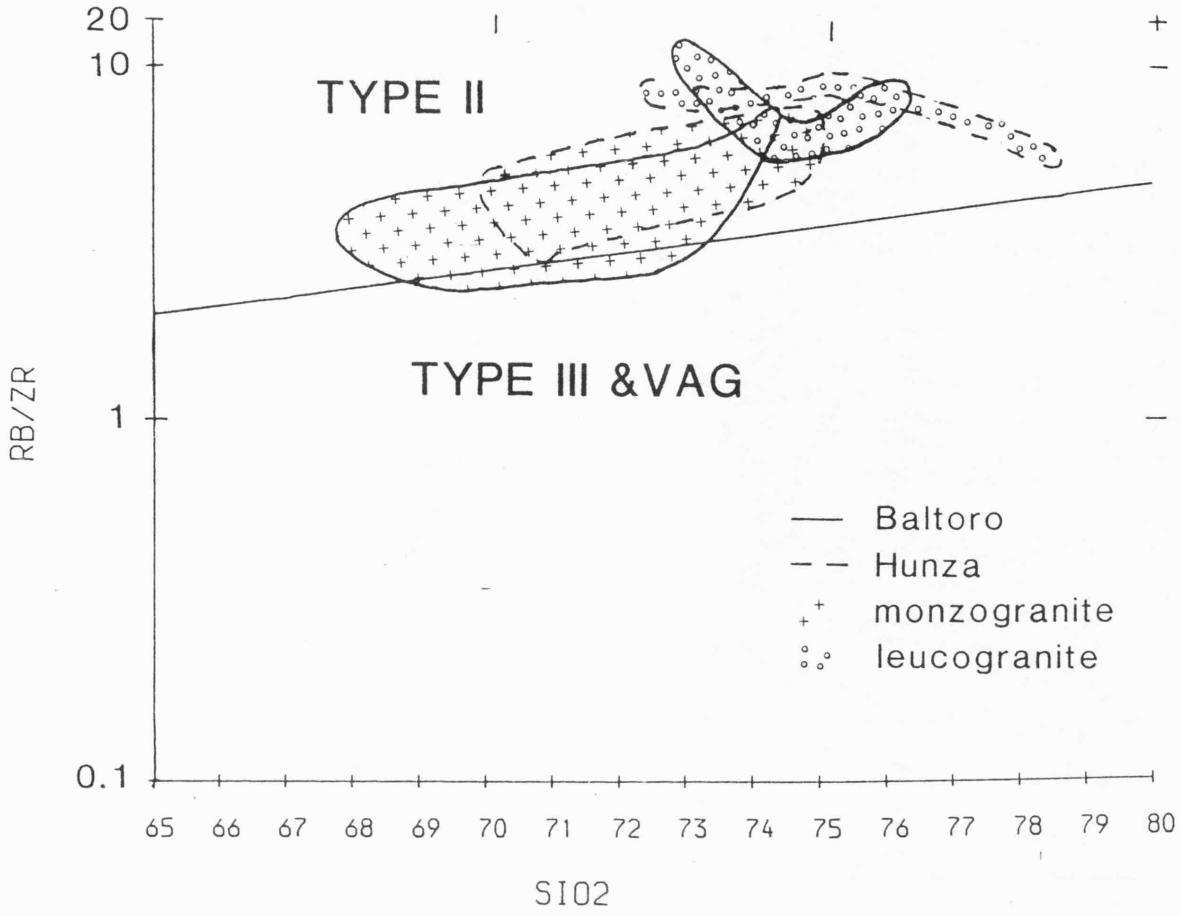

Figure 7.3: Harris et al (1986) discrimination diagram for type II and type III granites (see text for definitions).

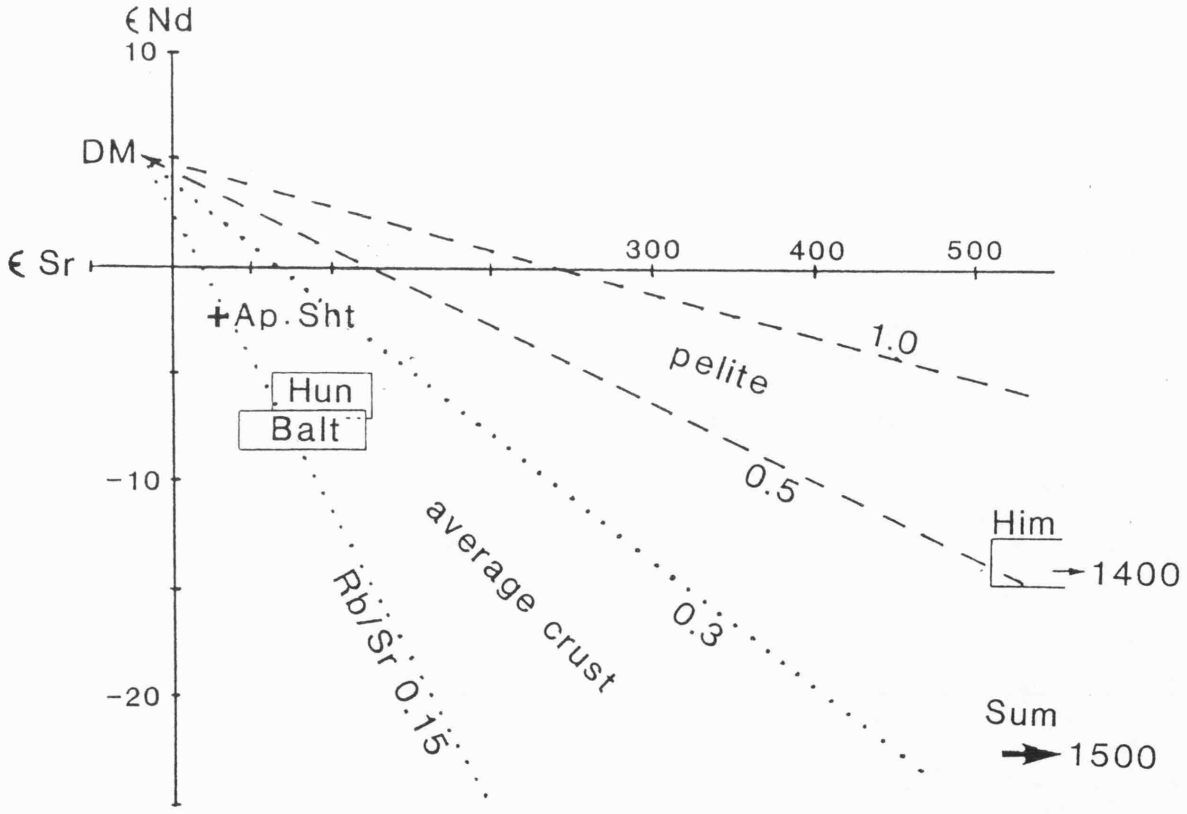

Figure 7.4: εNd vs. εSr diagram adapted from Miller (1985) to show evolution of sources with different Rb/Sr ratios from depleted mantle (DM). Balt = Baltoro; Hun = Hunza; Ap. Sht = HPC aplite sheet; Sum = Sumayar; Him = High Himalayan leucogranites (Allegre and Othman, 1980).

anomalous, being restricted to melting of accretionary prism material within a particular tectonic environment, then a worldwide classification scheme for granites should not be based upon them.

The fallibility of the Rb vs. (Y+Nb) diagram was illustrated by Twist and Harmer (1987) when a group of high Mg felsites were misidentified as subduction-related rather than of within-plate affinity. It was proposed that this was related to the melting and crystallisation histories of their source regions. Therefore, whilst the diagram provided valuable information it did not achieve its primary function of global discrimination.

All the above systems serve only as a first approximation for the subdivision of the granite field and further evidence should be taken into account before any conclusions are reached. Arculus (1987) stated that the juxtaposition of potential magma and fluid sources and the incidence of magma generation processes can take place in more than one tectonic environment. Therefore any trace element signatures taken as diagnostic of one environment are subject to error.

Pearce (1987) has recognised the need to expand on the original systems and has started to develop an Expert System for Classification Of Rock Types (ESCORT). The example given was the further division of the three-fold classification of basalts proposed by Pearce and Cann (1973). Trace elements alone provide insufficient data to do this and geochemical, geological, petrological and mineralogical information is used as input to the expert computer program. Based on all this data the program uses Bajes Decision Rule to take uncertainties into account, give upper and lower probability thresholds and decide whether the interpretation deduced is likely or unlikely. Magma-type membership probability tables constructed using a priori knowledge and a data base containing some 8000 elemental analyses are referred to within the program. Fractionation state is also taken into account resulting in a further basic, intermediate or evolved division.

Whether such a system can be developed for granitoid rocks is beyond the scope of this chapter but a similar qualitative approach can be taken to try to discriminate between the leucogranite types.

To this end differences between the types are discussed below under four headings.

7.2.a: Field relationships and emplacement style.

The association of LILE-enriched monzogranites or other, similar, parental magmas with leucogranites is a clear indication of a type-b origin. Related ultra-potassic rocks are also good evidence for type-b magmatism, but these may not always be present and are not observed in Hunza.

Both leucogranite types in the Himalaya occur as dykes and plutons, and both are seen intruding low- and high-grade metamorphic country rocks. However, the Hunza dykes are intruded into sillimanite-grade metamorphic rocks which do not show any signs of migmatisation, whereas the sillimanite-grade rocks associated with the High Himalayan plutons (type-a) do show in situ anatexis.

7.2.b: Mineralogy.

All the leucogranites studied contain muscovite and garnet. Mn preferentially enters garnet from the melt (Miller and Stoddard, 1981) and so the composition of this phase is dependent upon the composition of the melt and therefore ultimately the source rock. Because there is no consistent difference between the MnO contents of the two granite types it is unlikely that Mn composition of garnets can be used to separate them. This is supported by garnets in the Nagar sheet (type-b; chapter 6) and Kilar (type-a; Searle and Fryer, 1986) leucogranites having similar chemistries.

The same principle of dependence on source composition will control the appearance and chemistry of other accessory phases. Tourmaline is often abundant in type-a granites reflecting high boron concentrations in the source which, as explained earlier, suggests a metapelitic protolith (chapter 6). However, a metapelite could contain tourmaline up to temperatures of 750°C (Benard et al., 1985) and so it is theoretically possible to get tourmaline in the source rocks of type-b granites. Tourmaline was found in small quantities in some Hunza type-b pegmatites. This is thought to be a result of the concentration of boron in the magma during fractionation leading to

relatively high concentrations of the element in the final melt/fluid. However, the ultimate source of the boron might have been small quantities of tourmaline in the source, or contamination of the magma by metapelitic country rocks as it rose through the crust.

One mineralogical feature which might distinguish between the two types is the early crystallisation of mica in type-a indicating a high magmatic water content. In type-b mica is typically one of the last phases to crystallise because a large quantity of the original magma needs to solidify in order to raise the water content to sufficiently high levels. However, the presence of secondary mica might confuse the situation.

As well as the water content of the magma, the pressure and, more especially, the temperature of crystallisation might separate the two types. Type-b magmas are dryer and will therefore tend to be hotter and crystallise at the dry solidus, although there are few phases in leucogranites that can be used to estimate temperature. Green (1977) suggested that garnet, if magmatic and not xenocrystal, can be used for P-T estimates. However, as mentioned above and discussed in chapter 6, it is felt that garnet compositions are more dependent on the magma chemistry, and not the P-T conditions.

7.2.c: Isotope geochemistry.

At first sight isotopic systems would appear to be a good discriminant between the two types of leucogranite since the KAB type-b leucogranites have low initial Sr ratios (0.71-0.72) whilst the High Himalaya type-a have high values (0.74-0.82). However, these values are, like many other characteristics, dependent upon the source and a source with low Rb/Sr ratios could be fluxed by fluids to give type-a leucogranites with low Sr isotope values. This was illustrated by Miller (1985) who, on the basis of trace element and isotope chemistry, showed that many strongly-peraluminous granites that fit the original S-type granite classification of Chappell and White (1974) are in fact not derived from metapelites. Their low εSr and high negative εNd values suggest immature sediments or meta-igneous rocks as more likely crustal sources. Hence, despite being formed by similar mechanisms of crustal anatexis due to fluid fluxing and regional metamorphism, the metapelitic sources of Sumayar and

Manaslu give high initial Sr isotope values (0.74-0.78; Le Fort et al., 1987) whilst the Brittany leucogranites have much lower values (0.708-0.71; Strong and Hanmer, 1981) due to a different source material (fig. 7.4).

Other isotopic systems are also prone to the same problem. Pelites tend to have similar Sm/Nd, U/Pb, and Th/Pb ratios as average continental crust (Miller, 1985) and so it is hard to distinguish particular crustal source materials using Nd and Pb isotopes. $\delta^{18}O$ depends upon the amount of weathering and degree of metamorphism that the source has experienced.

Whilst the above indicates that a type-a leucogranite can have any crustal isotopic signature, it is debatable whether the same applies for the type-b lower crustal melts. Thickened continental crust will experience amphibolite/granulite facies metamorphic conditions at its base. This will lead to loss of Rb through dehydration and partial melting (Taylor and McLennan, 1985) and the lowering of $\delta^{18}O$ (Miller, 1985). This suggests that it is not possible to get type-b leucogranites with high Rb/Sr and initial Sr isotopic ratios, and $\delta^{18}O$ values from the lower crust in collisional environments. Hence, it might be reasonable to propose that a leucogranite with $^{87}Sr/^{86}Sr$ initial ratios of 0.74-0.78 and $d^{18}O$ above +14, such as Manaslu, can only be type-a.

This could be negated if the source of a type-b leucogranite is ancient metasedimentary crust which has not experienced temperatures corresponding to dehydration metamorphism until the recent crustal thickening event which is giving rise to the magma generation. Such a source would have had time to evolve a high $^{87}Sr/^{86}Sr$ ratio prior to metamorphism and so could give a type-b granite with a high initial ratio. However, it is not clear how likely, or how common, it is that a situation like this could arise.

7.2.d: Element geochemistry.

Harris et al. (1986) emphasize that the trace element characteristics of their type II and III granites described earlier will depend upon the chemistries of their crustal component and the fluid or mantle component. The nature of type-a leucogranites will

also be strongly influenced by the melting process and the refractory phases in the source whereas type-b leucogranites will be affected by fractionation.

All the examples of type-b granites found in the literature are associated with LILE-enriched mantle magmas (Nurmi and Haapala, 1986; Rock and Hunter, 1987; Leat et al., 1987; Henney, 1987) and so the process of contamination of type-b granites with LILE might be ubiquitous in their petrogenesis. Alternatively, it may be that this is a consequence of only being able to recognise type-b granites when this association is present. If leucogranites are associated with monzogranites or more basic/ultrapotassic rocks with high Ba and Sr abundances, then this does point to them being type-b, but otherwise Rb, Ba and Sr are not considered reliable discriminating elements. Rb is enriched in type-a rocks by the fluids whilst their Sr and Ba abundances will be similar to, or slightly lower than, those of the source (Le Fort et al., 1987). Lower crust is depleted in these elements with respect to the rest of the crust (Taylor and McLennan, 1985) and so it might be expected that type-b melts will have lower abundances than type-a. However, this is entirely dependent upon the mantle input into the source region of type-b granites. Additionally, it has also been seen how subsequent fractionation will strongly affect the abundances of these elements (fig. 7.1).

Other trace elements such as Th, U, and REE are too dependent upon the presence of accessory phases in both source and melt (Cuney et al., 1984; Gromet and Silver, 1983) to be reliable for discrimination. Refractory elements such as Ni, Cr and V are more abundant in the lower crust but are likely to be retained in the source during melting and so this signature does not appear in the magma. Harris et al. (1986) showed that the Ta/Nb ratios of type II granites tend to be higher than type III, possibly as a result of complexing leading to high ratios in the fluid phase. Type III granites tend to have similar signatures to mature arc rocks except for a higher Ta/Hf ratio due to crustal contamination, although this Ta enrichment was not found to be consistent when studying the post-collisional Caledonian granites. Thus the two types of granites and volcanic arc rocks form separate fields on a Rb/30 vs. Hf vs. Ta triangular diagram. Through a lack of Ta data the above cannot be tested here. However, Zr and Nb have similar behaviour to Hf and Ta

respectively and neither of these elements show any consistent variation between the two leucogranite types (fig. 7.5).

One use of trace elements is to identify fractionation trends within the magma. If this trend correlates with a major element such as silica, and it can be established that the magma is not a minimum melt, then information about a more basic parent and a type-b identification may be established.

7.2.e: Summary: what to look for?

Separating the two leucogranite types is not necessarily straightforward. Obviously, if the source rocks are exposed, as in the case of Manaslu, then this is not such a problem. The presence of co-intruded, LILE-enriched monzogranites or other, more basic granitoid parents and associated mantle-derived magmatism are the best indications of type-b magmatism. However, faced with a suite of leucogranite dykes or a pluton with none of the above features present, it cannot be confidently stated that the magmatism is of a type-a character, and there are few distinctive characteristics from which an identification can be made. This is because the chemistry of the leucogranite is not dependent so much on the process which formed it, but more on the source components. Therefore, type-a is strongly dependent on the crustal source, the melting and residual phases in this source, and the fluid component. Type-b is controlled by both the crustal and mantle components, and subsequent fractionation processes. This means that both types can exhibit a wide, overlapping range of compositions within the broader leucogranite classification field.

In terms of mineralogy, early crystallisation of mica and the presence of abundant tourmaline seem to be the best indicators for type-a. However, tourmaline can occur in type-b, particularly in small quantities, and tourmaline is not always present in type-a (e.g. Manaslu main body; Le Fort, 1981). Higher crystallisation temperatures might also be indicative of type-b magmas but this is hard to quantify. Isotopically it is doubtful whether type-b can exhibit high initial Sr isotope ratios (arbitrarily >0.74) and high $\delta^{18}O$ values (arbitrarily >+14) but both types could show lower values for these variables. Nd and Pb systems are unlikely to be useful

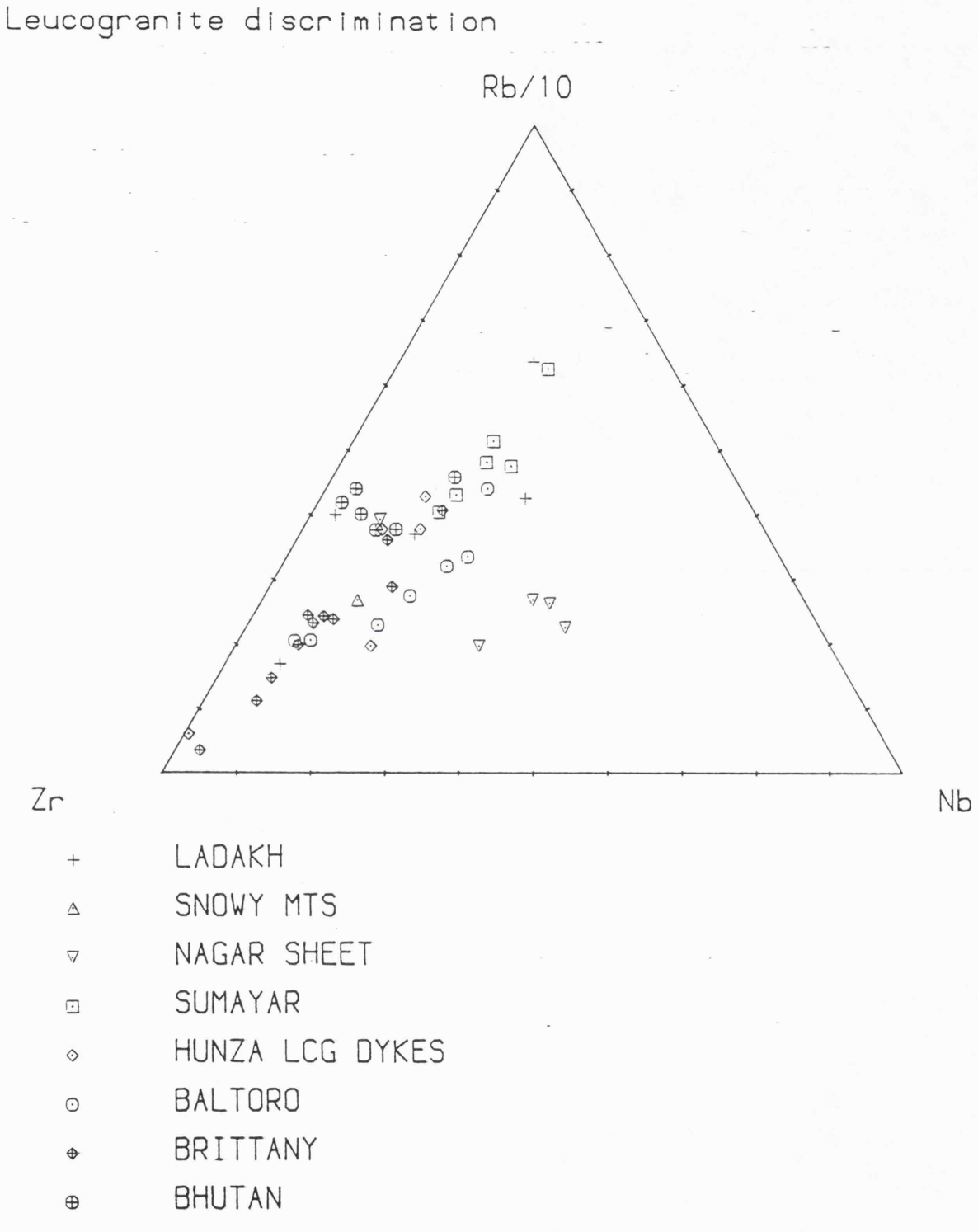

Figure 7.5: Rb/10 vs. Zr vs. Nb triangular plot for various leucogranites. Data for Ladakh from Searle and Fryer (1986); Snowy Mountains (Taylor et al., 1968); Brittany (Strong and Hanmer, 1981); Bhutan (Dietrich and Gansser, 1981).

unless the mantle component for type-b is dominant. Major and trace elements investigated show no reliable differences between the two types. However, if a fractionation trend can be identified and it is apparent that the magma is not a minimum melt then identification of a more basic parent such as a monzogranite will lead to the identification of a type-b leucogranite.

An example of this problem of identification is illustrated by the Kohistan leucogranites in N. Pakistan. Here, in addition to those representing end-fractionation products of more basic plutons such as the Shirot granodiorite, there are two leucogranite suites; the Parri and Indus Confluence acid sheets (Petterson and Windley, 1986). The Parri sheets have low Ba, Sr and Rb concentrations and slightly higher Sr initial isotope ratios (0.7052) compared to the Indus Confluence sheets (0.7045) which have high Ba and Sr abundances (up to 1600 and 600ppm respectively). The Parri sheets are garnet-muscovite pegmatites whilst the Indus Confluence sheets contain biotite ± tourmaline. Both are post-collisional and considering the errors on their Rb/Sr ages (34±14ma and 29±8ma; Petterson and Windley, 1985) could be roughly the same age as the BPU.

Isotopes and mineralogy are of little help in deciding which type these leucogranites might be. Due to their proximity in space and time the Indus Confluence granites could have a similar petrogenesis to the BPU granites which would explain their high Ba and Sr abundances and their low initial Sr isotopic ratios. However, it is also feasible that they formed by anatexis at the base of the Kohistan crust where melting would be promoted by fluids coming from the top of the underthrust Indian plate i.e. type-a. Some of the early basic intrusions in Kohistan which could make up a large proportion of the basement are gabbroic diorites with mono-mineralic layers of hornblende. The gabbros have Ba and Sr abundances of up to 1000ppm whilst the hornblendite layers have much lower concentrations. Melting of the gabbroic diorites leaving a residue dominated by hornblende which did not retain Ba and Sr could generate a melt with the high abundances of these elements seen in the leucogranites.

The lack of associated ultra-potassic and potential, more basic, parental magmas, together with the availability of a mechanism to

explain the trace element chemistry and generation of the Indus Confluence sheets suggests that they are type-a magmas. This would also explain the age difference between the sheets and the BPU, since the sheets would be generated at the time of underthrusting i.e. shortly after collision and before the BPU. Whilst this is not conclusive, it is beyond the scope of this chapter to resolve this problem any further since no field work has been done on these rocks personally. However, the above does shows some of the difficulties that may be encountered when studying other leucogranites in collisional belts, but suggests that some distinction between the two types can usually be made.

7.3: The magmatic evolution of collisional belts: the generation of leucogranites in both space and time.

This section discusses a general model for the magmatic evolution of collisional belt. In principle it is similar to the sequence outlined by Harris et al. (1986), but in this case only the generation of leucogranites at each stage in the evolutionary cycle will be discussed. This is followed in the next section by a consideration of how leucogranites from each stage can be distinguished, which has implications for the study of leucogranites worldwide.

The first stage of any orogenic cycle is the subduction phase prior to collision. Whilst calc-alkaline magmatism is common at this stage, no examples of leucogranites in Andean-type destructive margins have been found in the literature. The leuco-granodiorite unit of the Cordillera Blanca Batholith in Peru shows S-type characteristics, but this is related to fluid interaction with the surrounding sediments and not to any deep-seated source (Atherton and Sanderson, 1987). However, in these settings there is mantle input into the base of an often thickened crust and so it is plausible that leucogranites can form in this environment, via a mechanism similar to that which generates type-b magmas.

Further magmatic evolution of a collisional belt can be explained in terms of recent mathematical modelling by Sonder et al. (1987) which showed that extension and crustal thinning will occur as a consequence of previous thickening and the resultant potential

energy contrast of the lithosphere. Thickened lithosphere is gravitationally unstable and the potential energy stored during thickening will be released by extension once the compressive force is removed. The timing and extent of extension depends strongly upon the initial Moho temperature ($T_M(0)$) and the excess potential energy of the lithospheric column after thickening. If $T_M(0)$ is 750°C then extension will start immediately. Conversely, where $T_M(0)$ is <450°C extension will not start for at least 100Ma and erosion may be the dominant thinning process. This time interval seems to be almost independent of the initial potential energy excess.

Other important parameters include the asthenospheric temperature (T_1), the temperature at the base of the mechanical lithosphere (T_{MBL}), the crustal heat flow (H_0), and the compressional strain (f) although the effect of varying f becomes insignificant if $T_{MBL} < 0.8*T_1$. Sonder et al. (1987) used the Cenozoic extension of western N. America as an example. Where magmatic activity was high prior to collision in the Pacific Northwest extension started soon after compression (about 9Ma) and it is reasonable to assume high initial Moho temperatures. Where there was no magmatic activity in the southern Great Basin extension did not start for 65-75Ma after compression which would indicate Moho temperatures of 500-550°C.

It is of course impossible to accurately determine $T_M(0)$, T_1, T_{MBL}, f, and H_0 for the Himalayan belt. However, E-W extension of the thickened Tibetan plateau via recent N-S grabens is now occurring some 40-50Ma after collision (Chang et al., 1986). The situation is more complicated for the Himalayan chain since compressional forces are still operative but this interval can be used to derive a minimum estimate of $T_M(0)$ of around 550°C. Using values for the other parameters taken from Sonder et al. (1987) this could correspond to their calculated thermal profiles given in figure 7.6. This is obviously subject to large errors but can be used to illustrate the principles given below.

Following collision or zero million years in figure 7.6 type-a leucogranites could be generated syn-tectonically by elevated temperatures and wet melting along thrust/fault planes. Such granites will be purely crustal in origin. From 0 to 30Ma the surface height continues to rise to a maximum. The crustal profile (fig. 7.6(a))

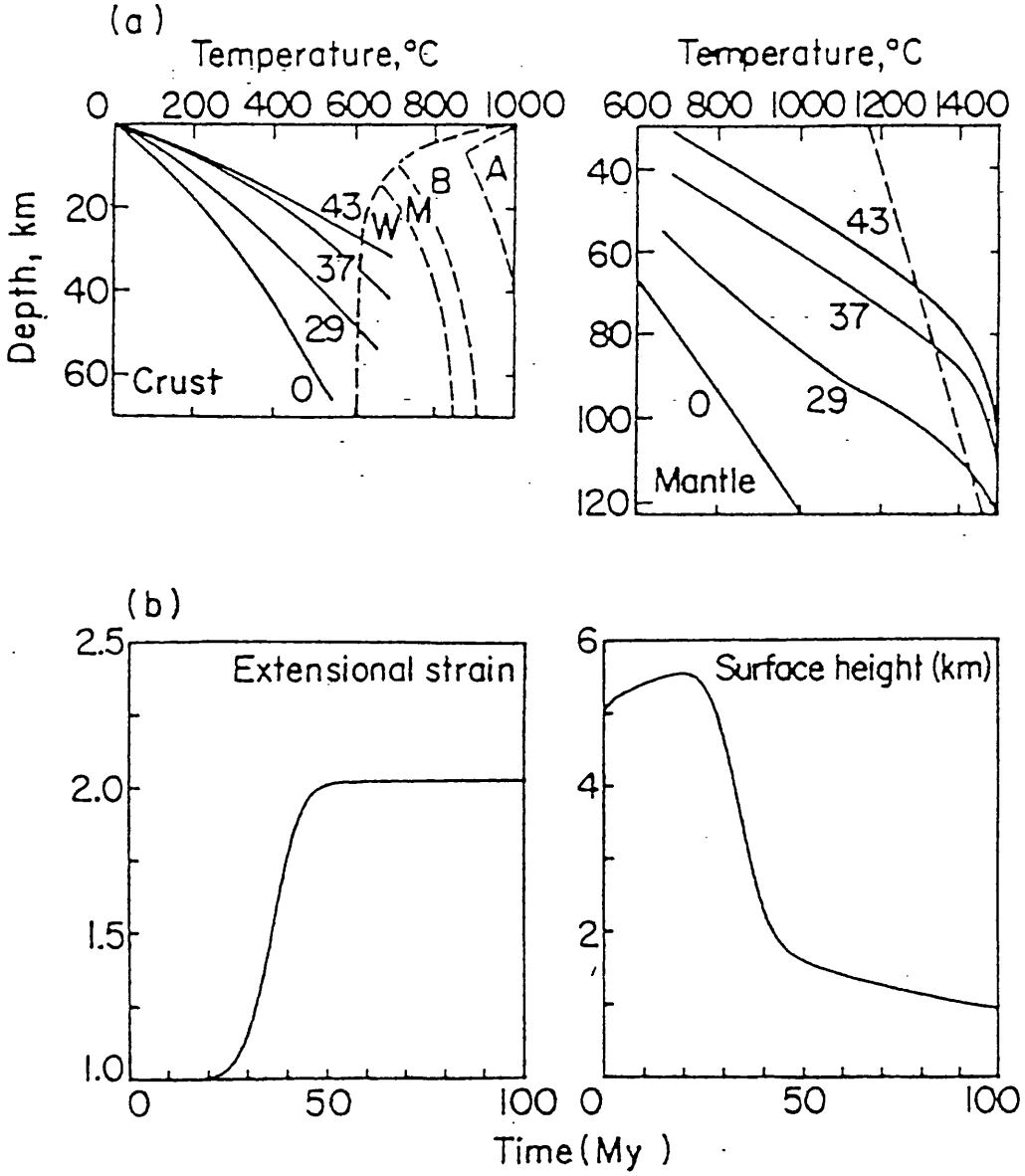

Figure 7.6: (a) Geotherms at selected times for calculations shown in (b) from Sonder et al (1987). Crust/mantle boundary is equivalent to the Moho. Parameters for (b) are T_1=1500°C, H_0=5.9*10^{-7}Wm^{-3}, $T_M(0)$=550°C, T_{MBL}=1000°C, f=1.75. Heat flow is normalised to 52mWm^{-2}. See text for explanation of parameters.

shows that below 50km the temperature is above the granite wet solidus and as deep as 70km dehydration melting will be possible as predicted by the models of England and Thompson (1986). Mantle temperatures (fig. 7.6(b)) lie above the peridotite dry solidus at depths of 110km. It is under these conditions that type-b leucogranites will be generated. A mantle component from either the subduction-modified mantle wedge or subcontinental lithosphere intrudes the crust and promotes sufficient melting under water-undersaturated conditions to allow the magma to separate from its source and rise through the crust. Such granites might not be exposed in Tibet because they have not been able to intrude as far as upper crustal levels. Greater uplift and erosion rates in the Karakoram have led to mid-crustal levels being exposed.

In different belts the timing of the generation of type-a and type-b magmas will vary according to crustal thickening rates, which, as seen above, is strongly dependent on the initial Moho temperature. Type-b magmas may be generated before type-a if there is a long gap between collision and intracontinental thrusting. In the Himalaya the MCT was initiated some 20Ma after collision leading to similar ages for the Manaslu and Baltoro plutons.

Following the peak of crustal thickening after 30Ma in the model of Sonder et al. (1987) extension will start as a result of the crust becoming gravitationally unstable. This leads to melting at higher levels in the asthenosphere. These mantle melts could then intrude the base of the crust. If the crust is sufficiently thinned this will lead to basaltic magmatism at the surface as seen in the Cenozoic of the N. American Cordillera (Wernicke et al., 1987). However, if the crust is thicker the heat from the mantle magmas might trigger melting of the lower crust and generate granitoid magmas i.e. a similar mechanism to that which produced the BPU granites except that the mantle component will be from the asthenosphere. A-type granites are commonly found as final plutonic events in orogenic belts (Whalen et al., 1987) and Rapakivi granites are often dominant within these domains (e.g. Anderson, 1983; Nurmi and Haapala, 1986). Such A-type magmas are thought to represent partial melts of F and/or Cl-enriched, dry granulite residue in the lower crust which has been depleted by the extraction of orogenic magmas (Whalen et al., 1987). The high temperatures indicated (>830°C) require a mantle input, and

mafic-sialic associations with evidence of mixing between the two types occur. The magmas are enriched in highly charged ions such as REE, Nb, Zr, Y, and Ga and Zn. The enrichments of F and Cl are thought to be a result of the enhanced thermal stability of micas and amphiboles containing these elements. If the crustal protolith for these A-type magmas was metasedimentary, then it would be possible to produce leucogranitic melts in such an environment.

Vielzeuf and Holloway (1988) noted that 40% melting of a metapelite would occur via the biotite breakdown reaction between 800-875°C and that this reaction would buffer the metamorphic temperature. This is similar to the mechanism proposed for the generation of the type-b Baltoro magma in chapter 5. Such a reaction would leave a residue of plagioclase, garnet and sillimanite which would require temperatures of up to 1000°C to start melting again (Vielzeuf and Holloway, op.cit.). This temperature is comparable to that predicted for the granulitic source regions of A-type magmas. It is, therefore, not inconceivable that the orogenic magmas removed to create the source regions of these A-type granites might resemble the type-b monzogranites, and that A-type magmas are at present being generated beneath Tibet.

The simple fourfold magmatic evolutionary model outlined above is illustrated in figure 7.7, and is supported by evidence from the Proterozoic of Finland where the granitoids can be divided into four main groups (Nurmi and Haapala, 1986):

1). Syn-kinematic granitoids (1860-1930Ma); these are calc-alkaline granodiorite through to granite batholiths. Characteristic minerals include biotite, hornblende, sphene, and magnetite and mineralisation is porphyry-type Mo and Cu. They are interpreted as subduction-related and mantle-derived with some crustal recycling involved, and are analogous to the first phase of the Hunza Plutonic Complex (HPC).

2). Late-kinematic granites (1800-1850Ma); these are monzogranites and contain biotite, garnet, cordierite, sillimanite, and muscovite. They are associated with migmatites, appear to be S-type and are considered to represent partial melting of supracrustal rocks during metamorphism in thickened crust. These granites are associated with thrusting and thickening and are water-saturated and so are probably

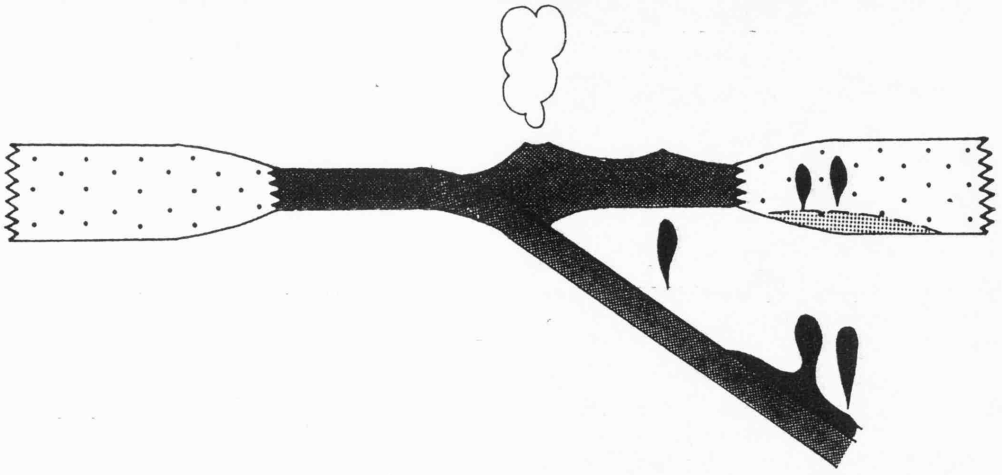

STAGE 1: Syn-subduction, calc-alkaline, mantle derived basic to intermediate magmas, and possible leucogranites.

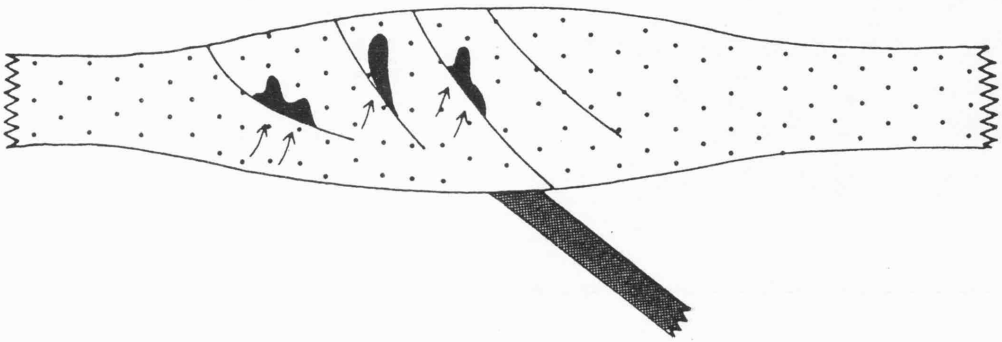

STAGE 2(a): Syn-tectonic, collisional crustal melts associated with high heat flow, high-grade metamorphism and migmatisation triggered by fluid fluxing along thust/fault planes.

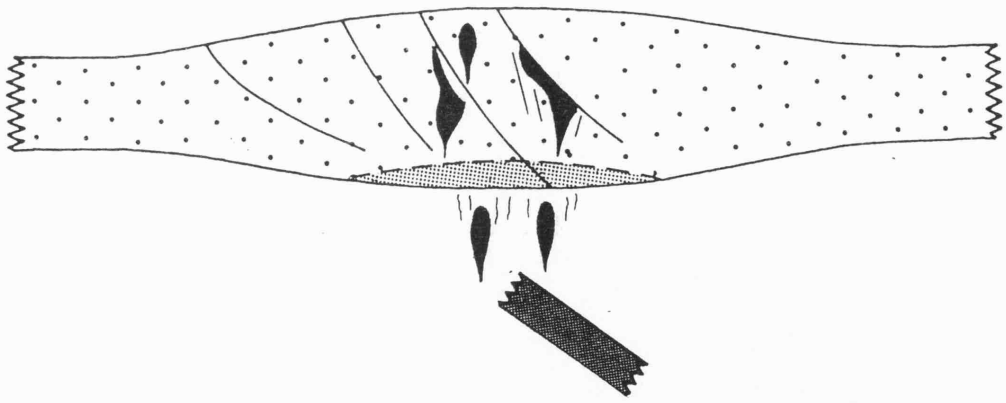

STAGE 2(b): Post-collisional, lower crustal melts triggered and contaminated by intrusion of LILE-enriched mantle melts.

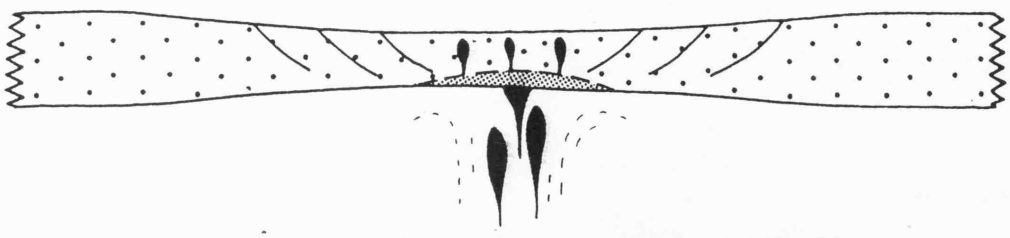

STAGE 3: Anorogenic-type lower crustal melts triggered by intrusion of hot, asthenospheric melts caused by adiabatic upwelling during crustal thinning following thickening during orogenesis.

Figure 7.7: Schematic diagram to illustrate the four-fold magmatic evolution of a collisional belt. Refer to text for a more detailed discussion.

analagous to type-a granites in the High Himalaya although fluid fluxing has not been invoked in their petrogenesis.

3). Post-kinematic granitoids (c1800Ma); granodiorite to granite composite dykes and multiple batholiths with associated lamprophyres. High abundances of Sr and LREE, and $^{87}Sr/^{86}Sr$ values of 0.7088-0.7117 are comparable with the BPU and point to a similar petrogenetic origin.

4). Rapakivi granites (1540-1700Ma); some 150Ma after collision these are A-type granitoids that are interpreted as remelts of granulitic lower crust, initiated by mantle magmas related to rifting.

Most collisional belts do not strictly follow this simple model. The Proterozoic of N. America shows the transition from syn-orogenic, calc-alkaline plutons to anorogenic, A-type Rapakivi granites (Anderson, 1983), but no orogenic type-a and type-b granites have been reported. The Caledonian granitoids of Britain show the development of the subduction-related calc-alkaline stage and post-orogenic type-b stage (Henney, 1987) but no anorogenic granites (particularly Rapakivi types) appear to be present. Such deviations might be due to crucial differences in conditions or tectonic make-up which as yet are not understood. However, the Karakoram appears to be evolving in a similar manner to that shown by the Proterozoic of Finland with the anorogenic stage either yet to start, or hidden beneath Tibet. This indicates that this general process might have been operative for a large period of geological time.

7.4: Discussion: Leucogranites; a collisional signature?

The question now arises as to whether a particular leucogranite can be taken as representative of one of the four stages of magmatic development of a collisional belt. The possible difficulty of separating type-a and type-b leucogranites has already been discussed, but it is felt that there is usually sufficient evidence to be able to assign a magma to one of these two types and that these are indicative of their respective tectonic environments.

As stated earlier, no examples of leucogranites in Andean-type destructive margins have been found in the literature, although in

theory they could form in such an environment. Because the components in both cases are similar such magmas might resemble type-b granites. One distinguishing factor might be the high LILE-contaminated signature of associated monzogranites or more basic rocks in the case of type-b magmas. The stability of amphibole or phlogopite in the pre-collisional mantle wedge (chapter 5) precludes this signature being present in syn-subduction mantle magmas.

Two different examples of peraluminous, anorogenic A-type magmas have been found in the literature. Those from the Proterozoic of N. America belong to the fourth stage of the above model and are two-mica and sillimanite-bearing granite plutons (Anderson and Thomas, 1985). The difference between these and other A-type granites in a similar tectonic setting is thought to be a result of their source being dominantly metasedimentary rather than meta-igneous. However, their high temperature of emplacement (740-760°C) and anhydrous nature points to to a similar petrogenetic mechanism, with the source becoming dehydrated during earlier removal of orogenic magmas (Whalen et al., 1987). The limited data set (Anderson and Thomas, 1985) shows that they are distinguishable from type-b granites in having higher K_2O/Na_2O and Ba/Sr and lower Ba/Rb ratios for similar silica values (fig. 7.8). This is possibly a result of small degrees of partial melting and lack of enrichment in Ba and Sr compared with type-b magmas, although paucity of data precludes an accurate discrimination model being built up.

The Cabo de Santo Agostinho leucogranite in Brazil differs in that it formed in a rifting environment possibly above the ancestral Ascension mantle plume and so is independent of orogeny (Long et al., 1986). Its composition reflects a small degree of partial melting of a quartz-rich source such as an arenite. Ba abundances are compatible with the N. American granites and although Sr is depleted this is a feature of the source and so cannot be taken as diagnostic of the environment. However, Nb and Zr abundances are much higher (216-328 ppm and 650-1280 ppm respectively) than those in other A-type granites (cf Whalen et al., 1987). Whilst data for these elements are not available for the N. American granites it is possible that these abundances are diagnostic since the granite may have picked up this signature from the mantle plume which will be rich in these elements (Saunders et al., in press).

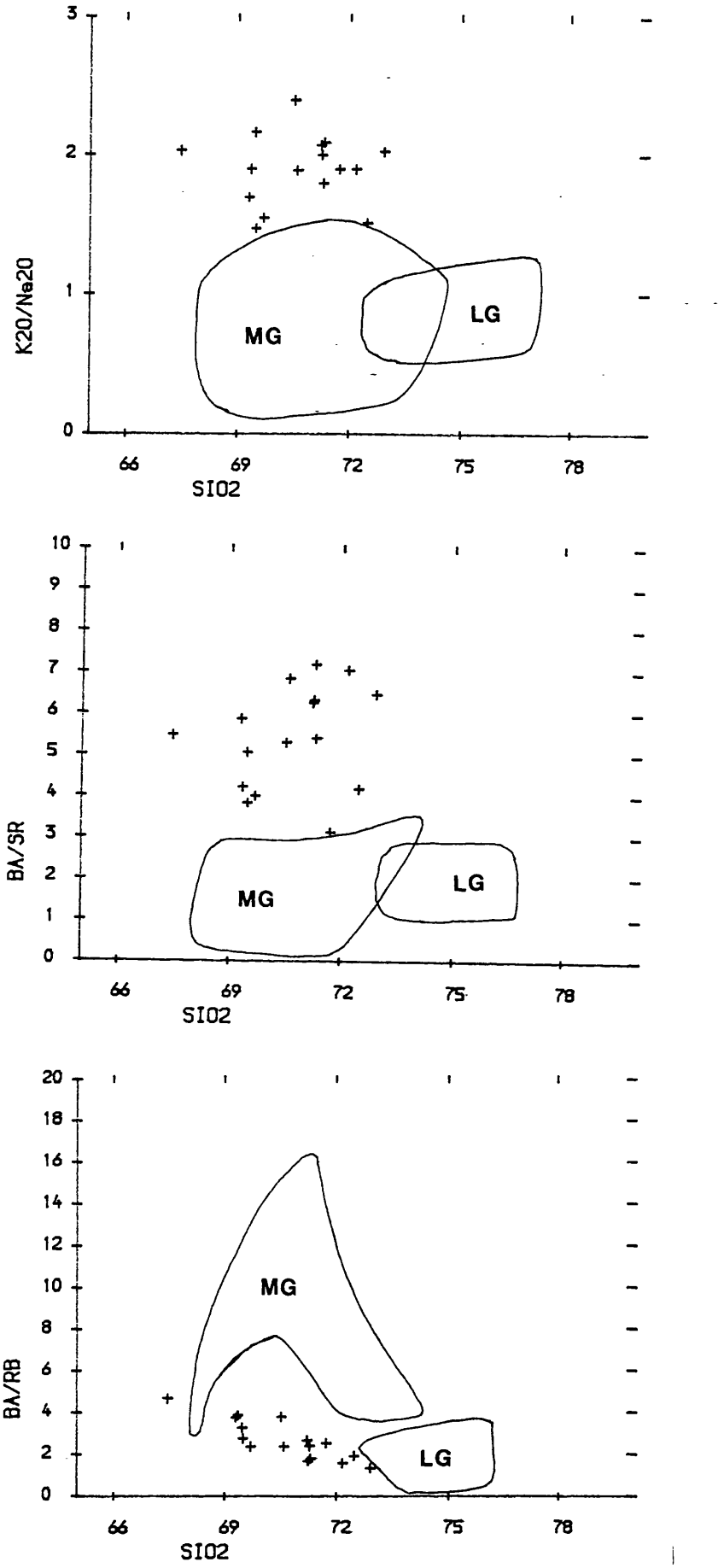

Figure 7.8: Possible discrimination diagrams for type-b and A-type magmas, which follow orogenesis and may come from sources depleted by the extraction of the type-b melts. MG and LG = Baltoro monzogranites and leucogranites respectively; crosses = A-type peraluminous granites from the Proterozoic of Colorado, N. America (Anderson and Thomas, 1985).

In summary it seems that the signature of leucogranites and related rocks can be used to identify a particular environment and the stage of development of that environment. With accurate age dating details of operative processes at the time would be forthcoming. However, it must be stressed that geochemistry alone may often not be a sufficiently powerful tool to uniquely resolve identification problems and all available evidence needs to be synthesized before conclusions can be drawn. Table 7.1 is an attempt at a framework for such a system, but a much larger data set is needed before this can be quantified satisfactorily.

	ENVIRONMENT AND GENESIS	FIELD STYLE	DISTINGUISHING FEATURES
Type-a	Form in a syn-tectonic environment where temperatures are elevated due to crustal thickening and fluid fluxing can occur due to dehydration along thrust/fault planes.	Associated with regional metamorphism of sillimanite grade and migmatisation. Occur as near 'in situ' plutons or dyke networks.	Water saturated, near minimum melts which can have high initial Sr isotope ratios and $d^{18}O$ values. Tourmaline may be a common accessory Often enriched in Rb and depleted in REE.
Type-b	Form in a post-collisional environment at the base of the crust, where large-scale dehydration melting is promoted by mantle input and thickened crust above.	Associated with ultra-potassic magmas, and often lie at the end of fractionation trends from more basic rocks. Occur as plutons or dykes but source is not usually exposed.	Vapour poor, non-minimum melts, usually with low initial Sr isotope ratios and $d^{18}O$ values. Tourmaline is rare and micas crystallise late. Enriched in LILE through contamination by mantle magmas.
A-type	Form in an anorogenic setting some time after collision. Upwelling of asthenosphere in response to crustal thinning causes small scale melting of granulitic lower crust left by removal of type (b) magmas.	Associated with mantle-derived magmas in an extensional rather than compressional environment. Occur as mobile plutons and can have associated layered gabbros and anorthosites.	Anhydrous, hot melts with variable isotope values depending upon the exact nature of their source. Tend to have high K_2O/Na_2O and Ba/Sr ratios and possibly high Nb and Zr abundances.

Table 7.1: Comparison of leucogranites from different environments. For further discussion and explanation see text.

CHAPTER EIGHT: Summary of conclusions.

8.1: Introduction.

The Karakoram Axial Batholith (KAB) records the magmatic evolution of the Eurasian continental margin since the late Jurassic. Neo-Tethyan oceanic crust was subducted beneath this margin until collision of India with Eurasia at c.45Ma, since when northward movement of India has been accommodated by A-type subduction, intracontinental thrusting, strike-slip motion and crustal thickening. The KAB extends E-W for some 600km across N. Pakistan and yet only reaches a maximum width of some 30km. That such a narrow zone has been the focus of magmatic activity for such a long period suggests some form of structural control. To the north of the KAB are low-grade country rocks whereas to the south is a metamorphic complex which reaches sillimanite-grade next to the batholith. This complex decreases in grade southwards to greenschist facies at the margin of the craton, represented by the Shyok Suture Zone. In Hunza the metamorphic sequence has been inverted by southward-directed thrusting. Rex et al. (in press) propose that a major, north-dipping normal fault, the Karakoram Batholith Linament (KBL), initiated by culmination collapse during crustal thickening, has juxtaposed the lower-grade rocks to the north against the high-grade rocks to the south. This fault, considered to be an analogue of the Zanskar Shear Zone to the east, acts as the structural control for the intrusion of the KAB magmas.

The magmatic activity within the KAB can be divided into pre- and post-collisional groups.

8.2: Pre-collisional or syn-subduction magmatism.

This study presented data for the Hunza Plutonic Complex (HPC; 95Ma) and Batura unit (43Ma?) within the KAB, and also for the Khunjerab (105Ma approx.) and N. Sost (age unknown) plutons further to the north. This period of magmatism corresponds with the major plutonic event at 100Ma seen in the Kohistan island arc sequence to the south. All the plutons are dominated by granodioritic lithologies and their chemistry is controlled by high-level fractionation which proceeded via a filter pressing mechanism during cooling. The HPC has

a typical calc-alkaline mineralogy of calcic hornblende, plagioclase and biotite. Salite is found in the more basic rocks (<60% SiO_2) and ilmenite appears in the more acidic samples (>67% SiO_2) recording a drop in $f(O_2)$ during crystallisation. The main fractionating assemblage within the HPC is 43% plagioclase, 44% amphibole and 13% biotite with minor amounts of apatite and sphene. Allanite controls the evolving REE patterns and clinopyroxene is an important early crystallising phase.

N. Sost and Batura appear to be controlled by a similar fractionating assemblage to that of the HPC, but K-feldspar is an important phase in the Khunjerab pluton (40% plagioclase, 30% K-feldspar, 30% mafic phases) with apatite, sphene and allanite controlling the REE distribution.

All the plutons show a typical subduction-related signature. They give calc-alkaline trends on AFM and Debon and Le Fort (1982) characteristic mineral plots, and all have high LILE/HFSE ratios and negative Nb anomalies. Khunjerab and N. Sost have higher LILE/HFSE ratios with respect to the other plutons, and this may relate to either distance from the trench or age. The Rb/Sr and Sm/Nd isotope systematics of the HPC are heterogeneous and an isochron cannot be constructed. This heterogeneity may be a result of contamination of a magma coming from the subducted slab and enriched mantle wedge by a highly Sr radiogenic upper crustal melt/rock. This might proceed by simple, binary mixing or by assimilation-fractional crystallisation, but the ultimate source of the Karakoram pre-collisional granitoids is considered to be the mantle, enriched by a subducted slab component.

8.3: Post-collisional magmatism; type-a.

The Sumayar pluton, which intrudes staurolite-grade rocks to the south of the KAB in Hunza, is the only example of this type of magmatism which has, to date, been found in the Karakoram. Its homogeneous major element chemistry and water-saturated nature suggest that it is a minimum melt. Its isotope chemistry and abundant tourmaline indicate that it is a partial melt of a pelitic source which, together with biotite, garnet, plagioclase, K-feldspar and quartz, must contain a small amount of residual monazite in order to

explain the REE patterns. The sillimanite-grade metamorphic rocks of Hunza were not sufficiently hot to extensively melt by dehydration reactions. However, fluxing of similar rocks beneath the pluton by fluids coming from the underthrusted Kohistan or Indian crust could have triggered wet melting. The restriction of this magma type might be a result of the need for local concentrations of high heat producing elements to promote melting. The Sumayar pluton is, therefore, considered to be an analogue of the High Himalayan leucogranites (e.g. Le Fort et al., 1987). Because the generation of the leucogranite is related to underthrusting and metamorphism, it must have formed shortly after collision (c.35Ma).

8.4: Post-collisional magmatism; type-b.

Post-collisional magmas are found within the HPC and the Baltoro Plutonic Unit (BPU) of the KAB. In Hunza the magmas are intruded as dykes which cross-cut the foliation, whilst the BPU is a pluton dated at 21Ma (U-Pb, Parrich and Tirrul, in press). There are two generations of magma in Hunza with the first being spatially restricted to the HPC, whereas the second also intrudes the sillimanite-grade rocks to the south. All the magmas consist of monzogranites and leucogranites, which are related by fractionation of plagioclase, K-feldspar and biotite. REE chemistry is controlled by accessory phases such as monazite and allanite, and other common accessories include garnet, muscovite and zircon.

The low initial Sr isotope ratios, $\delta^{18}O$ values, and anhydrous nature of the magmas suggest a lower crustal source. However, the high Sr and Ba abundances in the most basic monzogranites cannot be produced by melting of typical lower crust. Additionally, models for melting at the base of thickened crust (England and Thompson, 1986) cannot produce the volume of melt needed for a magma to separate from its source (Clemens and Vielzeuf, 1987; Wickham, 1987). Associated with the BPU magmas are LILE-enriched lamprophyres which are considered to represent melting of the subduction-modified mantle wedge or subcontinental lithosphere during thermal re-equilibration in the mantle following collision. The mantle wedge was enriched during subduction by LILE-bearing fluids or small-scale, siliceous partial melts coming off the subducting slab. Amphibole, stable in the wet, cool pre-collisional wedge, acted as a sink for the LILE,

except for Rb which was released in the syn-subduction magmas. The Sr isotope ratios and the required volume of the lamprophyres seem to preclude the BPU magmas being direct fractionates of the ultra-potassic magmas. However, the LILE-enriched amphibole will dehydrate following collision and release LILE-enriched fluids as precursors to the lamprophyre magmatism. It is considered that these fluids or the lamprophyre magmas themselves could flux the base of the crust, promote melting and contaminate the resultant crustal melts with LILE. The product of such a process will resemble the post-collisional monzogranites.

The spatial restriction of the HPC and BPU magmas is considered to be controlled by the inferred KBL. This will have a conductivity contrast across it because the hanging-wall, low-grade rocks will act as a barrier to lateral heat transfer. This will lead to a thermal maximum along the fault which will channel the dry, monzogranitic magmas and allow them to intrude to higher levels. The BPU pluton, therefore, lies along the KBL whereas the Hunza dykes might be a feeder stage to an eroded pluton, and therefore only lie in the footwall of the KBL.

8.5: Leucogranites; the global context.

There are four general stages for the magmatic evolution of a collisional belt, starting with syn-subduction magmas followed by the two types of post-collisional magmas described above, and then, finally, post-orogenic magmas generated when the thickened crust becomes gravitationally unstable and starts to extend. Leucogranites can be generated in any of these stages, and it is considered that it should be possible to assign a leucogranite suite to one of these four stages (if it actually belongs to one of the four!). Type-b leucogranites are characterized by their association with LILE-enriched, more basic, granitic parents, and with ultra-potassic magmatism. Syn-subduction leucogranites would not be expected to have this LILE-enriched signature since this is a feature of post-collisional mantle magmas, but otherwise their petrogenesis will be similar. Type-a leucogranites are characterised by their wet, minimum melt nature and their common association with pelitic sources with high Sr isotope ratios. Post-orogenic leucogranites are also generated by similar processes to those involved in the production of

type-b magmas. However, their source has already been depleted by the removal of type-b magmas, and they are generated at much higher temperature. Additionally, the mantle signature that these magmas inherit will be from asthenospheric melts and not the LILE-enriched mantle wedge.

The recognition of a particular leucogranite type will give information about the operative processes and environment at the time of formation.

8.6: Suggestions for further work.

Much more isotope data are required on all the magmas of the Karakoram and Kohistan. Only with this data will any chemical variations in the pre-collisional mantle beneath the Karakoram become apparent. Further Nd and Sr isotope analyses are necessary to confirm or invalidate the model given here for the first phase of the HPC. Accurate dating using U-Pb on all the plutons is also essential.

For the post-collisional magmas, an accurate U-Pb date is needed for the Sumayar pluton, and a larger data set is required for the Baltoro lamprophyres. Additionally, more work is needed to investigate the likelihood of the existence of the KBL. It is hoped to fill these three gaps in present knowledge during a further field season.

In a more global context, the association of granites with ultra-potassic magmas needs to be investigated more thoroughly. Leucogranite suites need to be re-appraised in light of the above model to see if they conform, and also whether a satisfactory discrimination system can be built up to link leucogranites with their tectonic setting.

BIBLIOGRAPHY.

ALLEGRE, C.J. & OTHMAN, B.D. (1980). Nd-Sr isotopic relationships in granitoid rocks and continental crust development: a chemical approach to orogenesis. **Nature 286,** pp335-342.

------- ---- et al. (34 authors) (1984). Structure and evolution of the Himalaya-Tibet orogenic belt. **Nature 307,** pp17-22.

ANDERSON, J.L. (1983). Proterozoic anorogenic granite plutonism of North America. **Geol. Soc. America Memoir 161,** pp133-154.

-------- ---- & THOMAS, W.M. (1985). Proterozoic anorogenic two-mica granites: Silver Plume and St. Vrain batholiths of Colorado. **Geology 13,** pp177-180.

ANDO, A., MITA, N. & TERASHIMA, S. (1987). 1986 values for fifteen GSJ rock reference samples, "Igneous rock series". **Geostandards Newsletter XI,** pp159-166.

ARCULUS, R.J. (1987). The significance of source versus process in the tectonic controls of magma genesis. **J. Volcan. Geotherm. Res. 32,** pp1-12.

ARTH, J.G. (1976). Behaviour of trace elements during magmatic processes - a summary of theoretical models and their research applications. **J. Res. U.S. Geol. Survey 4,** pp41-47.

ATHERTON, M.P., McCOURT, W.J., SANDERSON, L.M. & TAYLOR, W.P. (1979). The geochemical character of the segmented Peruvian Coastal Batholith and associated volcanics. in **ATHERTON, M.P & TARNEY, J., (eds) Origin of Granite Batholiths. Shiva Publ.,** pp45-64.

-------- --- & SANDERSON, L.M. (1987). The Cordillera Blanca Batholith: a study of granite intrusion and the relation of crustal thickening to peraluminosity. **Geol. Rundschau 76,** pp213-232.

BARAZANGI, M. & NI, J. (1982). Velocities and propogation characteristics of Pn and Sn beneath the Himalayan Arc and Tibetan Plateau; possible evidence for underthrusting of Indian continental lithosphere beneath Tibet. **Geology 10,** pp179-185.

BARD, J-P. (1983). Metamorphism of an obducted island arc: example of the Kohistan sequence (Pakistan) in the Himalayan collided range. **Earth. Plan. Sci. Lett. 65,** pp133-144.

BARKER, F. (1984). Letter designation of granites; process versus protolith. **Eos 65,** p1151 (abstract).

BARTHOLOMEW, D.S. & TARNEY, J. (1984). Geochemical characteristics of magmatism in the southern Andes (45-46°S). in **HARMON, R.S. & BARREIRO, B.A. (eds) Andean magmatism. Shiva publ.,** pp220-229.

BAUD, A. et al. (11 authors) (1982). Le contact Gondwana-peri-Gondwana dans le Zanskar oriental (Ladakh, Himalaya). **Bull. Geol. Soc. France 7,** pp341-361.

---- --, GAETANI, M., GARZANTI,E., FOIS, E., NICORA, A. & TINTORIA, A. (1984). Geological observations in south eastern Zanskar and adjacent Lahul area (north-western Himalaya). **Ecologae. Geol. Helvet. 77,** pp171-197.

BENARD, F., MOUTOU, P. & PICHAVANT, M. (1985). Phase relations of tourmaline leucogranites and the significance of tourmaline in silicic magmas. **J. Geology 93,** pp271-291.

BESSE, J., COURTILLOT, V., POZZI, J.P., WESTPHAL, M. & ZHOU, Y.X. (1984). Palaeomagnetic estimates of crustal shortening in the Himalayan thrusts and Zangbo suture. **Nature 311,** pp621-626.

BINGHAM, D.K. & KLOOTWIJK, C.T. (1980). Palaeomagnetic constraints on Greater India's underthrusting of the Tibetan Plateau. **Nature 284,** pp336-338.

BLAISE, J., BORDET, P., CARBONNEL, J.P. & MONTENAT, C. (1978). Flyschs et ophiolites dans la region de Panjaw: une suture neocimmerienne en Afghanistan central. **Bull. Soc. Geol. France (7)XX,** pp795-798.

BOULIN, J. (1981). Afghanistan structure, Greater India concept and eastern Tethys evolution. **Tectonophysics 72,** pp261-287.

BOWDEN, P., BATCHELOR, B.A., CHAPPELL, B.W., DIDIER, J. & LAMEYRE, J. (1984). Petrological, geochemical and source criteria for the classification of granitic rocks: a discussion. **Phys. Earth. Plan. Int. 35,** pp1-11.

BROOKFIELD, M.E. & REYNOLDS, P.H. (1981). Late Cretaceous emplacement of the Indus Suture Zone ophiolitic melanges and an Eocene-Oligocene magmatic arc on the northern edge of the Indian plate. **Earth. Plan. Sci. Lett. 55,** pp157-167.

BROUGHTON, R.D., WINDLEY, B.F. & JAN, M.Q. (1985). Reaction isograds and P-T estimates in metasediments on the edge of the Karakorum Plate, Hunza, N. Pakistan. **Geol. Bull. Univ. Peshawar 18,** pp119-136.

BROWN, G.C., THORPE, R.S. & WEBB, P.C. (1984). The geochemical characteristics of granitoids in contrasting arcs and comments on magma sources. **J. Geol. Soc. London 141,** pp413-426.

BURG, J.P., BRUNEL, M., GAPAIS, D., CHEN, G.M. & LUI, G.H. (1984). Deformation of leucogranites of the crystalline Main Central Sheet in southern Tibet (China). **J. Struct. Geol. 6,** pp535-542.

CARMICHEAL, I.S.E. (1967). The iron-titanium oxides of salic volcanic rocks and their associated ferromagnesian silicates. **Contr. Min. Petrology 14,** pp36-64.

CAWTHORN, R.G., STRONG, D.F. & BROWN, P.G. (1976). Origin of corundum-normative intrusive and extrusive magmas. **Nature 259,** pp102-104.

CHAPPELL, B.W. & WHITE, A.J.R. (1974). Two contrasting granite types. **Pacific Geology 8,** pp173-174.

CHENGFA, C. et al. (26 authors) (1986). Preliminary conclusions of the Royal Society and Academic Sinica 1985 geotraverse of Tibet. **Nature 323,** pp501-507.

CLARKE, D.B. (1981). The mineralogy of peraluminous granites: a review. **Can. Mineralogist 19,** pp3-18.

CLEMENS, J.D. & WALL, V.J. (1981). Origin and crystallisation of some peraluminous (S-type) granitic magmas. **Can. Mineralogist 19,** pp111-131.

------- ---- & VIELZEUF, D. (1987). Constraints on melting and magma production in the crust. **Earth. Plan. Sci. Lett. 86,** pp287-306.

COULON, C., MALUSKI, H., BOLLINGER, C. & WANG, S. (1986). Mesozoic and Cenozoic volcanic rocks from central and southern Tibet. ^{39}Ar-^{40}Ar dating, petrological characteristics and geodynamical significance. **Earth. Plan. Sci. Lett. 79,** pp281-302.

COWARD, M.P., JAN, M.Q., REX, D., TARNEY, J., THIRLWALL, M. & WINDLEY, B.F. (1982). Geo-tectonic framework of the Himalaya of N Pakistan. **J. Geol. Soc. London 139,** pp299-308.

------ ---- & BUTLER, R.W.H. (1985). Thrust tectonics and the deep structure of the Pakistan Himalaya. **Geology 13,** pp417-420.

------ ----, WINDLEY, B.F., BROUGHTEN, R.D., LUFF, I.W., PETTERSON, M.G., PUDSEY, C.J., REX, D.C. & ASIF KHAN, M. (1986). Collision tectonics in the NW Himalayas. in **COWARD M.P. & RIES, A.C. (eds) Collision Tectonics. Geol. Soc. Sp. Pub. No. 19,** pp203-219.

COX, K.G., BELL, J.D. & PANKHURST, R.J. (1979). The interpretation of igneous rocks. **pub. George Allen & Unwin, London,** 450p.

CUNEY, M., LE FORT, P. & ZHIXIANG, W. (1984). Uranium and thorium geochemistry and mineralogy in the Manaslu leucogranite (Nepal, Himalaya). in **Geology of granites and their metallogenic relations, Proc. Int. Symp. Nanjing Univ., China,** pp853-873.

CZAMANSKE, G.K. & WONES, D.R. (1973). Oxidation during magmatic differentiation, Finmarka Complex, Oslo area, Norway: Part 2, the mafic silicates. **J. Petrology 14,** pp349-380.

DEBON, F. & LE FORT, P. (1982). A chemical mineralogical classification of common plutonic rocks and associations. **Trans. R. Soc. Edinburgh Earth Sci. 73,** pp135-149.

----- --, -- ---- -- & SONET, J. (1983). Chemical-Mineralogical typology, chronology and geodynamic setting of the Western Hindu Kush-Badakhshan plutonic belt (Afghanistan). in **SHAMS, F.A. (ed) Granites of Himalayas, Karakorum, and Hindu Kush. Punjab Univ. Lahore,** pp407-423.

----- --, -- ---- --, SHEPPARD, S.M.F. & SONET, J. (1986). The four plutonic belts of the Transhimalaya-Himalaya: a chemical, mineralogical and chronological synthesis along a Tibet-Nepal section. **J. Petrology 27,** pp219-250.

DEBON, F., AFZALI, H., LE FORT, P., SONET, J. & ZIMMERMAN, J.L. (1987a). Plutonic rocks and associations in Afghanistan. Typology, age and geodynamic setting. **Memoirs Sci. de la Terre (CNRS Nancy) 49,** 130p.

----- --, LE FORT, P., DAUTEL, D., SONET, J. & ZIMMERMAN, J.L. (1987b). Granites of western Karakorum and northern Kohistan (Pakistan): a composite Mid-Cretaceous to Upper Cenozoic magmatism. **Lithos 20,** pp19-40.

DEER, W.A., HOWIE, R.A. & ZUSSMAN, J. (1966). An introduction to the rock-forming minerals. **Longman Press,** 528p.

DENIEL, C., VIDAL, P., DIETRICH, V. & LE FORT, P. (1985). Origin of the leucogranites of the High Himalaya. **Terra Cognita 5,** p292.

DePAOLO, D.J. (1979). Implications of correlated Nd- and Sr- isotopic variations for the chemical evolution of the crust and mantle. **Earth. Plan. Sci. Lett. 43,** pp210-211.

------- ---- (1981). Trace element and isotopic effects of combined wallrock assimilation and fractional crystallisation. **Earth. Plan. Sci. Lett. 53,** pp189-202.

DESIO, A. (1979). Geologic evolution of the Karakorum. in **FARAH, A. & KEES, A. (eds) Geodynamics of Pakistan, Geol. Surv. Pakistan Quetta,** pp111-124.

----- --, TONGIORGI, E. & FERRARA, G. (1964). On the geological age of some granites of the Karakorum, Hindu Kush and Badakhshan (Central Asia). **Proc. XXII Inter. Geol. Cong. India part XI,** pp479-496.

----- -- & MARTINA, E. (1972). Geology of the Upper Hunza Valley, Karakorum, West Pakistan. **Boll. Soc. Geol. Italiana 91,** pp283-314.

DICKINSON, W.R. (1975). Potash depth (K - h) relations in continental margins and intra-oceanic magmatic arcs. **Geology 3,** pp53-56.

DICKSON, W.L. (1986). S-type granites and their probable absence in south western North America; discussion and reply. (to White et al.'s paper). **Geology 14,** p894.

DIDIER, J., DUTHOU, J.L. & LAMEYRE, J. (1982). Mantle and crustal granites: genetic classification of orogenic granites and the nature of their enclaves. **J. Volcan. Geotherm. Res. 14,** pp125-132.

DIETRICH, V.J. & GANSSER, A. (1981). The leucogranites of the Bhutan Himalaya (crustal anatexis versus mantle melting). **Schweiz. Miner. Petro. Mitt. 61,** pp177-202.

-------- ----, FRANK, W. & HONEGGER, K. (1983). A Jurassic-Cretaceous island arc in the Ladakh Himalayas. **J. Volcan. Geotherm. Res. 18,** pp405-433.

ENGLAND, P.C. & RICHARDSON, S.W. (1977). The influence of erosion upon the mineral facies of rocks from different metamorphic environments. **J. Geol. Soc. London 134,** pp201-213.

ENGLAND, P.C. & SEARLE, M.P. (1986). The Cretaceous-Tertiary deformation of the Lhasa block and its implications for crustal thickening in Tibet. **Tectonics 5,** pp1-14.

------- ---- & THOMPSON, A. (1986). Some thermal and tectonic models for crustal melting in continental collision zone. in **COWARD M.P. & RIES, A.C. (eds) Collision Tectonics. Geol. Soc. Sp. Pub. No. 19,** pp83-94.

FAURE, G. (1986). Principles of isotope geology (2nd edition). **Pub. J. Wiley & Sons, New York,** 589p.

FERRY, J.M. & SPEAR, F.S. (1978). Experimental calibration of the partitioning of Fe and Mg between garnet and biotite. **Contr. Min. Petrology 66,** pp113-117.

FOLEY, S.F., VENTURELLI, G., GREEN, D.H. & TOSCANI, L. (1987). The Ultrapotassic rocks: characteristics, classification and constraints for petrogenetic models. **Earth Sci. Reviews 24,** pp81-134.

FRASER, K.J., HAWKESWORTH, C.J., ERLANK, A.J., MITCHELL, R.H. & SCOTT-SMITH, B.H. (1985/86). Sr, Nd and Pb isotope and minor element geochemistry of lamproites and kimberlites. **Earth. Plan. Sci. Lett. 76,** pp57-70.

FYFE, W.S. (1970). Some thoughts on granitic magmas. in **NEWALL, G. & RAST, N. (eds) Mechanics of igneous intrusion, Geol. J. Spec. Issue no. 2,** pp201-216.

---- ---- (1973). The generation of batholiths. **Tectonophysics 17,** pp273-283.

GAETANI, M., NICORA, A., PREMOLI-SILVA, I., FOIS, E., GARZANTI, E. & TINTORI, A. (1983). Upper Cretaceous and Palaeocene in Zanskar Range (NW Himalaya). **Riv. Ital. Palaeont. Milano 89,** pp81-118.

GANGULY, J. & KENNEDY, G.G. (1974). The energetics of natural garnet solid solution 1: mixing of the aluminosilicate end members. **Contr. Min. Petrology 48,** pp137-148.

GANSSER, A. (1964). Geology of the Himalayas. **Intersci. Publ. Wiley London,** 289p.

GARIEPY, C., ALLEGRE, C.J. & XU, R.H. (1985). The Pb-isotope geochemistry of granitoids from the Himalaya-Tibet collision zone: implications for crustal evolution. **Earth. Plan. Sci. Lett. 74,** pp220-235.

GHENT, E.D. & STOUT, M.Z. (1981). Geobarometry and geothermometry of plagioclase-biotite-garnet-muscovite assemblages. **Contr. Min. Petrology 76,** pp92-97.

GIRARDEAU, J., MARCOUX, J., ALLEGRE, C.J. et al. (1984). Tectonic environment and geodynamic significance of the Neo-Cimmerian Donqiao ophiolite, Bangong-Nu Jiang suture zone, Tibet, China. **Nature 307,** pp27-31.

GRAHAM, C.M. & ENGLAND, P.C. (1976). Thermal regimes and regional metamorphism in the vicinity of overthrust faults: an example of shear heating and inverted metamorphic zonation from Southern California. **Earth. Plan. Sci. Lett. 31,** pp142-152.

------ ---- & POWELL, R. (1984). A garnet-hornblende geothermometer: calibration, testing and application to the Pelona Schist, Southern California. **J. Metamorphic Geol. 2,** pp13-31.

GREEN, T.H. (1977). Garnet in silicic liquids and its possible use as a P-T indicator. **Contr. Min. Petrology 65,** pp59-67.

GROMET, L.P. & SILVER, L.T. (1983). R.E.E. distributions among minerals in a granodiorite and their petrogenetic implications. **Geochim. Cosmochim. Acta 47,** pp925-939.

HANSON, G.N. (1978). The application of trace elements to the petrogenesis of igneous rocks of granitic composition. **Earth. Plan. Sci. Lett. 38,** pp26-43.

HARMON, R.S. & BARRIERO, B.A. (1984) (eds) Andean Magmatism: chemical and isotopic constraints. **Shiva geology series, Shiva Publ., Kent,** 250p.

HARRIS, N.B.W., PEARCE, J.A. & TINDLE, A.G. (1986). Geochemical characteristics of collision-zone magmatism. in **COWARD M.P. & RIES, A.C. (eds) Collision Tectonics. Geol. Soc. Sp. Pub. No. 19,** pp67-81.

HAWKESWORTH, C.J. (1979). $^{143}Nd/^{144}Nd$, $^{87}Sr/^{86}Sr$ and trace element characteristics of magmas along destructive plate margins. in **ATHERTON, M.P & TARNEY, J., (eds) Origin of Granite Batholiths. Shiva Publ.,** pp76-89.

---------- ---- & NORRY, M.J. (1983). (eds). Continental basalts and mantle xenoliths. **Shiva geology series, Pub. Shiva,** 250p.

HENDERSON, P. (1982). Inorganic geochemistry. **Pub. Pergamon Press, Oxford,** 353p.

--------- -- (1984). General geochemical properties and abundances of rare earth elements. in **HENDERSON, P. (ed). Rare earth element geochemistry, Pub. Elsevier,** pp1-29.

HENNEY, P.J. (1987). Granite-lamprophyre association around the Criffel-Dalbeattie Pluton: Implications for mantle endmembers in late Caledonian granitoid petrogenesis. **Unpublished abstract from conference on Caledonian Granites, Univ. of Aston.**

HERREN, E. (1987). Zanskar shear zone: northeast-southwest extension within the Higher Himalayas (Ladakh, India). **Geology 15,** pp409-413.

HIRN, A. et al. (8 authors) (1984). Lhasa block and bordering sutures - a continuation of a 500km Moho traverse through Tibet. **Nature 307,** pp25-27.

HODGES, K.V. & SPEAR, F.S. (1982). Geothermometry, geobarometry and the Al_2SiO_5 triple point at Mt. Moosilauke, New Hampshire. **Am. Mineral. 67,** pp1118-1134.

HODGES, K.V. & CROWLEY, P.C. (1985). Error estimation and empirical geothermobarometry for pelitic systems. **Am. Mineral. 70,** pp702-709.

------ ----, HUBBARD, M.S. & SILVERBURG, D.S. (in press). Metamorphic constraints on the thermal evolution of the Central Himalayan Orogen. **Phil. Trans. R. Soc. London (for 1988).**

HONEGGER, K., DIETRICH, V., FRANF, W., GANSSER, A., THONI, M. & TROMMSDORF, V. (1982). Magmatism and metamorphism in the Ladakh Himalaya (the Indus-Tsangpo suture zone). **Earth. Plan. Sci. Lett. 60,** pp253-292.

HUANG, W.L. & WYLLIE, P.J. (1981). Phase relations of S-type granite with H_2O to 35kbar: muscovite granite from Harney Peak, South Dakota. **J. Geophys. Res. 86,** pp10515-10529.

ISHIHARA, S. (1977). The Magnetite-series and Ilmenite-series granitic rocks. **Mining Geol. (Japan) 27,** pp293-305.

JACOBSSEN, S.B. & WASSERBURG, G.J. (1980). Sm-Nd isotopic evolution of chondrites. **Earth. Plan. Sci. Lett. 50,** pp149-155.

JAN, M.Q. & HOWIE, R.A. (1981). The mineralogy and geochemistry of the metamorphosed basic and ultrabasic rocks of the Jijal complex, Kohistan, NW Pakistan. **J. Petrology 22,** pp85-126.

JAUPART, Cl. & PROVOST, A. (1985). Heat focussing, granite genesis and inverted metamorphic gradients in continental collision zones. **Earth. Plan. Sci. Lett. 73,** pp385-397.

JOHANNES, W. (1985). The significance of experimental studies for the formation of migmatites. in **ASHWORTH, J.R. (ed) Migmatites, Pub. Blackie & Son Ltd, Glasgow,** pp36-85.

JOHANNSEN, A. (1932). A descriptive petrography of the igneous rocks volume II. **Univ. of Chicago Press,** pp120-124.

KAY, S.M., KAY, R.W., BRUECKNER, H.K. & RUBENSTONE, J.L. (1983). Tholeiitic Aleutian arc plutonism: the Finger Bay pluton, Adak, Alaska. **Contr. Min. Petrology 82,** pp99-116.

LAMEYRE, J. & BOWDEN, P. (1982). Plutonic rock-type series: discrimination of various granitoid series and related rock types. **J. Volcan. Geotherm. Res. 14,** pp169-186.

LA ROCHE, H. De, DeLETERNIER, J., GRANDCLAUDE, P. & MARCHEL, M. (1980). A classification of volcanic and plutonic rocks using R_1-R_2 diagrams and major element analyses - its relationships with current nomenclature. **Chem. Geol. 29,** pp183-210.

LEAKE, B.E. (1978). Nomenclature of amphiboles. **Min. Mag. 42,** pp533-563.

LEAT, P.T., THOMPSON, R.N., MORRISON, M.A., TRAYHORN, S.C. & HENDRY, G.L. (1987). Geodynamic significance of post-Variscan intrusive and extrusive potassic magmatism in SW England. **Trans. R. Soc. Edinburgh Earth Sci. 77,** pp349-360.

LE FORT, P. (1975). Himalaya: the collided range. Present knowledge of the continental arc. **Am. J. Sci. 275A,** pp1-44.

-- ---- -- (1981). Manaslu leucogranite: a collision signature of the Himalaya. A model for its genesis and emplacement. **J. Geophys. Res. 86,** pp10545-10568.

-- ---- --, DEBON, F. & SONET, J. (1983). Petrography, geochemistry and geochronology of some samples from the Karakorum Batholith (Northern Pakistan). in **SHAMS, F.A. (ed) Granites of Himalayas, Karakorum, and Hindu Kush. Punjab Univ. Lahore,** pp377-387.

-- ---- --, CUNEY, M., DENIEL, C., FRANCE-LENORD, C., SHEPPARD, S.M.F., UPRETI, B.N. & VIDAL, P. (1987). Crustal generation of the Himalayan leucogranites. **Tectonophysics 134,** pp39-57.

LE MAITRE, R.W. (1976). Some problems of the projection of chemical data into mineralogical classification. **Contr. Min. Petrology 56,** pp181-189.

LONG, L.E., SIAL, A.N., NEKVASIL, H. & BORBA, G.S. (1986). Origin of granite at Cabo de Santo Agostinho, Northeast Brazil. **Contr. Min. Petrology 92,** pp341-350.

MACDONALD, R., THORPE, R.S., GRINDROD, A.R. & GASKARTH, J.W. (1985). Multi-component origin of Caledonian lamprophyres of northern England. **Min. Mag. 49,** pp485-494.

MALUSKI, H. & MATTE, P. (1984). Ages of Alpine tectonometamorphic events in the Northwestern Himlaya (Northern Pakistan) by $^{39}Ar/^{40}Ar$ method. **Tectonics 3,** pp1-18.

------- --, COULON, C. & SONGCHAN, W. (1985). $^{39}Ar/^{40}Ar$ radiometric ages of orogenic volcanics from central and southern Tibet. **Terra Cognita 5,** p279 (abstract).

MARSH, N.G., SAUNDERS, A.D., TARNEY, J. & DICK, H.J.B. (1980). Geochemistry of basalts from the Shikoku and Daito basins, Deep Sea Drilling Project Leg 58. **Init. Rep. DSDP 58,** pp805-842.

McCARTHY, T.S. & HASTY, R.A. (1976). Trace element distribution patterns and their relationship to the crystallisation of granitic melts. **Geochim. Cosmochim. Acta 40,** pp1351-1358.

McINTYRE, G.A., BROOKS, C., COMPSTON, W. & TUREK, A. (1966). The statistical assessment of Rb-Sr isochrons. **J. Geophys. Res. 71,** pp5459-5468.

MEHTA, P.K. (1977). Rb-Sr geochronology of the Kulu-Mandi belt: its implications for the Himalayan tectonogenesis. **Geol. Rundschau 6,** pp156-175.

MENZIES, M. (1983). Mantle ultramafic xenoliths in alkaline magmas: evidence for mantle heterogeneity modified by magmatic activity. in **HAWKESWORTH, C.J. & NORRY, M.J. (eds) Continental Basalts and Mantle Xenoliths, Shiva Publ.,** pp92-110.

MILLER, C.F. (1985). Are strongly peraluminous magmas derived from pelitic sedimentary sources? **J. Geology 93,** pp673-689.

MILLER, C.F. & STODDARD, E.F. (1981). The role of manganese in the paragenesis of magmatic garnet: an example from the Old Woman-Puite Range, California. **J. Geology 89,** pp233-246.

MOLNAR, P. & TAPPONIER, P. (1978). Active tectonics of Tibet. **J. Geophys. Res. 83,** pp5361-5375.

NELSON, D.R., McCULLOCH, M.T. & SUN, S.S. (1986). The origins of ultrapotassic rocks as inferred from Sr, Nd and Pb isotopes. **Geochim. Cosmochim. Acta 50,** pp231-245.

NI, J. & BARAZANGI, M. (1984). Seismotectonics of the Himalayan collision zone: geometry of the underthrusting Indian plate beneath the Himalaya. **J. Geophys. Res. 89,** pp1147-1163.

NICOLAS, A., GIRARDEAU, J. & MARCOUX, J., DUPRE, B., WANG XIBIN, CAU YOUGONG, ZHENG HAIXIANG & XIAO XUCHANG (1981). The Xigaze ophiolite (Tibet): a peculiar oceanic lithosphere. **Nature 294,** pp414-417.

NURMI, P.A. & HAAPALA, I. (1986). The Proterozoic granitoids of Finland: Granite types, metallogeny and relation to crustal evolution. **Bull. Geol. Soc. Finland 58,** pp203-233.

OKRUSCH, M., BUNCH, T.E. & BANK, H. (1976). Paragenesis and petrogenesis of a corundum-bearing marble at Hunza (Kashmir). **Mineral. Deposita 11,** pp278-297.

PANKHURST, R.J. (1979). Isotope and trace element evidence for the origin and evolution of Caledonian granites in the Scottish Highlands. in **ATHERTON, M.P & TARNEY, J., (eds) Origin of Granite Batholiths. Shiva Publ.,** pp18-33.

PARRISH, R.R & TIRRUL, R. (in press). U-Pb geochronology of the Baltoro Granite, northwest Himalaya and implications for zircon inheritance and interpretation of monazite U-Pb systematics. **Geology** (for 1988).

PATRIAT, P. & ACHACHE, J. (1984). India-Eurasia collision chronology has implications for crustal shortening and driving mechanism of plates. **Nature 311,** pp615-621.

PEARCE, J.A. (1983). The role of the sub-continental lithosphere in magma genesis at active plate margins. in **HAWKESWORTH, C.J. & NORRY, M.J. (eds) Continental Basalts and Mantle Xenoliths, Publ. Shiva,** pp230-249.

------ ---- (1987). An expert system for the tectonic characterisation of ancient volcanic rocks. **J. Volcan. Geotherm. Res. 32,** pp51-66.

------ ---- & CANN, J. (1973). Tectonic setting of basic volcanic rocks using trace element analyses. **Earth. Plan. Sci. Lett. 19,** pp290-300.

------ ----, HARRIS, N.B.W. & TINDLE, A.G. (1984). Trace element discrimination diagrams for the tectonic interpretation of granitic rocks. **J. Petrology 25,** pp956-983.

PETTERSON, M.G. & WINDLEY, B.F. (1985). Rb-Sr dating of the Kohistan arc-batholith in the Trans-Himalaya of north Pakistan, and tectonic implications. **Earth. Plan. Sci. Lett. 74,** pp45-57

--------- ---- & ------- ---- (1986). Petrological and geochemical evolution of the Kohistan Arc Batholith, Gilgit, N. Pakistan. **Geol. Bull. Univ. Peshawar 19,** pp121-149.

--------- ---- & ------- ---- (submitted). The leucogranites of Kohistan (N. Pakistan): their age, field relations, geochemistry and petrogenesis. **J. Geol. Soc. London.**

PICHAVANT, M. (1987). Effects of B and H_2O on the liquidus phase relations in the haplogranite system at 1kbar. **Am. Mineral. 72,** pp1056-1070.

--------- -- & MANNING, D.A.C. (1984). Petrogenesis of tourmaline granites and topaz granites; the contribution of experimental data. in **ALLEGRE et al. (eds) Granitoids, Phys. Earth Plan. Int. 35,** pp31-50.

PEIRCE, J.W. (1978). The northward movement of India since the late Cretaceous. **Geophys. J. R. Astr. Soc. 52,** pp277-311.

PINET, C. & JAUPART, C. (1987). A thermal model for the distribution in space and time of the Himalayan granites. **Earth. Plan. Sci. Lett. 84,** pp87-99.

PITCHER, W.S. (1983). Granite type and Tectonic environment. in **HSU, K. (ed) Mountain Building Processes, Academic Press, London,** pp19-40.

------- ---- (1987). Granites and yet more granites forty years on. **Geol. Rundschau 76,** pp51-79.

POWELL, C.McA. & VERNON, R.H. (1979). Growth and rotation history of garnet porphyroblasts with inclusion spirals in a Karakorum schist. **Tectonophysics 54,** pp25-43.

PRIOR, D.J. (1987). Syntectonic porphyroblast growth in phyllites: textures and processes. **J. Metamorphic Geol. 5,** pp27-39.

----- ---- (submitted). Metamorphism, deformation and uplift of the Hunza Valley, Karakorum, N. Pakistan. **J. Metamorphic Geol.**

PUDSEY, C.J. (1986). The Northern Suture, Pakistan: margin of a Cretaceous island arc. **Geol. Mag. 123,** pp405-423.

PUPIN, J-P. (1980). Zircon and granite petrology. **Contr. Min. Petrology 73,** pp207-220.

READ, H.H. (1956). The Granite Contoversy. **Pub. Thomas Murphy & Co., London,** 430p.

REX, A.J., SEARLE, M.P., TIRRUL, R., CRAWFORD, M.B., PRIOR, D.J., REX, D.C. & BARNICOAT, A. (in press). The geochemical and tectonic evolution of the central Karakoram, N. Pakistan. **Phil. Trans. R. Soc. London** (for 1988).

REYNOLDS, P.H., BROOKFIELD, M.E. & McNUTT, R.H. (1983). The age and nature of Mesozoic - Tertiary magmatism across the Indus Suture Zone in Kashmir and Ladakh (NW India and Pakistan). **Geol. Rundschau 72,** pp981-1004.

ROCK, N.M.S. & HUNTER, R.H. (1987). Late Caledonian dyke-swarms of northern Britain: spatial and temporal intimacy between lamprophyric and granitic magmatism around the Ross of Mull pluton, Inner Hebrides. **Geol. Rundschau 76,** pp805-826.

ROGERS, G. & SAUNDERS, A.D. (in press). Magnesian-andesites from Mexico, Chile and the Aleutian Islands: implications for magmatism associated with ridge-trench collision. in **CRAWFORD, A.J. (ed) Boninites and Related Rocks.**

ROGERS, N.W., HAWKESWORTH, C.J., MARSH, J.S. & PARKER, R.J. (1985). The geochemistry of potassic lavas from Vulsini, central Italy and implications for mantle enrichment processes beneath the Roman region. **Contr. Min. Petrology 90,** pp244-257.

RUTTER, M.J. & WYLLIE, P.J. (1988). Melting of vapour-absent tonalite at 10kbar to simulate dehydration-melting in the deep crust. **Nature 331,** pp159-160.

RYBURN, R.J., RAHEIM, A.R. & GREEN, D.H. (1976). Determination of P, T paths of natural eclogites during metamorphism - record of subduction. **Lithos 9,** pp161-164.

SAUNDERS, A.D. & TARNEY, J., MARSH, N.G. & WOOD, D.A. (1980). Ophiolites as ocean crust or marginal basin crust: A geochemical approach. in **PANAYIOTOU, A. (ed) Ophiloites, Proc. Int. Ophiol. Symp. Cyprus,** pp193-204.

-------- ---- & ------ -- (1984). Geochemical characteristics of basaltic volcanism within back-arc basins. in **KOKELAAR, B.P. & HOWELLS, M.F. (eds) Marginal Basin Geology, Geol. Soc. Sp. Pub. no. 16,** pp59-76.

-------- ----, ROGERS, G., MARRINER, F.G., TERELL, D.J. & VERMA, S.P. (1987). Geochemistry of Cenozoic volcanic rocks, Baja California, Mexico: implications for the petrogenesis of post-subduction magmas. **J. Volcan. Geotherm. Res. 32,** pp223-246.

-------- ----, NORRY, M.J. & TARNEY, J. (in press). Origin of MORB and chemically depleted mantle reservoirs. Trace element constraints. **in MENZIES, M.A. & COX, K.G. (eds) Lithosphere volume J. Petrology** (for 1987).

SCHARER, U. & ALLEGRE, C.J. (1983). The Palung granite (Himalaya); high resolution U-Pb systematics in zircon and monazite. **Earth. Plan. Sci. Lett. 63,** pp423-432.

------- --, HAMET, J. & ALLEGRE, C.J. (1984). The Transhimalaya (Gangdese) plutonism in the Ladakh region: a U-Pb and Rb-Sr study. **Earth. Plan. Sci. Lett. 67,** pp327-339.

------- --, XU, R.H. & ALLEGRE, C.J. (1986). U-(Th)-Pb systematics and ages of Himalayan leucogranites, south Tibet. **Earth. Plan. Sci. Lett. 77,** pp35-48.

SCHERMERHORN, L.J.G (1987). The Hercynian gabbro-tonalite-granite-leucogranite suite of Iberia: geochemistry and fractionation. **Geol. Rundschau 76,** pp137-145.

SCHNEIDER, H.J. (1957). Tektonik and Magmatismus in NW Karakorum. **Geol. Rundschau 46,** pp426-476.

SEARLE, M.P. (1982). Stratigraphy, structure and evolution of the Tibetan-Tethys zone in Zanskar and the Indus suture zone in the Ladakh Himalaya. **Trans. R. Soc. Edinburgh Earth Sci. 73** (1983 for 1982), pp205-219.

------ ---- (1986). Structural evolution and sequence of thrusting in the High Himalayas, Tibetan-Tethys and the Indus suture zones of Zanskar and Ladakh, Western Himlaya. **J. Struct. Geol. 8,** pp923-936.

------ ---- & FRYER, B.J. (1986). Garnet, tourmaline and muscovite-bearing leucogranites, gneisses and migmatites of the Higher Himalaya from Zanskar, Kulu, Lahoul and Kashmir. in **COWARD M.P. & RIES, A.C. (eds) Collision Tectonics. Geol. Soc. Sp. Pub. No. 19,** pp185-201.

------ ----, REX, A.J., TIRRUL, R., BARNICOAT, A.C. & REX, D.C. (in press). Metamorphic, magmatic and tectonic evolution of the Central Karakoram in the Biafo-Baltoro-Hushe regions of N. Pakistan. **Geol. Soc. Am. Bull.** (for 1988).

SEKINE, T. & WYLLIE, P.J. (1982). Phase relationships in the system $KAlSiO_4$-Mg_2SiO_4-SiO_2-H_2O as a model for hybridisation between hydrous siliceous melts and peridotite. **Contr. Min. Petrology 79,** pp368-374.

SENGOR, A.M.C. (1986). The dual nature of the Alpine-Himalaya system: progress, problems and prospects. **Tectonophysics 127,** pp177-195.

SHAMS, F.A. (1980). Origin of the Shangla blueschists, Swat Himalaya, Pakistan. **Geol. Bull. Univ. Peshawar Spec. Iss. 13,** pp67-70.

SONDER, L.J., ENGLAND, P.C., CHRISTIANSEN, R.L. & WERNICKE, B.P. (1987). A physical model for the Cenozoic extension of western North America. in **COWARD, M.P., DEWEY, J.F. & HANCOCK, P.L. (eds) Continental Extensional Tectonics, Geol. Soc. Sp. Publ. no. 28,** pp187-201.

STEIGER, R.H. & JAGER, E. (1977). Subcommission on geochronology: Convention on the use of decay constants in geo- and cosmo-chronology. **Earth. Plan. Sci. Lett. 36,** pp359-362.

STEPHENS, W.E. & HALLIDAY, A.N. (1979). Compositional variation in the Galloway plutons. in **ATHERTON, M.P & TARNEY, J., (eds) Origin of Granite Batholiths. Shiva Publ.,** pp9-17.

STOCKLIN, J. (1980). Geology of Nepal and its regional frame. **J. Geol. Soc. London 137,** pp1-34.

STRECKHEISEN, A. (1976). To each plutonic rock its proper name. **Earth Sci. Reviews 12,** pp1-33.

STRECKHEISEN, A. & LE MAITRE, R.W. (1979). A chemical approximation to the modal QAPF classification of the igneous rocks. **Neues Jahr. Min. Abh. 136,** pp169-206.

STRONG, D.F. & HANMER, S.K. (1981). The leucogranites of Southern Brittany: origin by faulting, frictional heating, fluid flux and fractional melting. **Can. Mineralogist 19,** pp163-176.

TAHIRKHELI, R.A. KHAN (1982). Geology of the Himalaya, Karakorum and Hindu Kush in Pakistan. **Geol. Bull. Univ. Peshawar (sp. issue), vol. 15.**

TAPPONIER, P., MATTAUER, M., PROUST, F. & CASSAIGNEAU, C. (1981a). Mesozoic ophiolites, sutures and large scale tectonic movements in Afghanistan. **Earth. Plan. Sci. Lett. 52,** pp355-371.

--------- -- et al. (24 authors) (1981b). The Tibetan side of the India-Eurasia collision. **Nature 294,** pp393-399.

TARNEY, J. & SAUNDERS, A.D. (1979). Trace element constraints on the origin of cordilleran batholiths. in **ATHERTON, M.P & TARNEY, J., (eds) Origin of Granite Batholiths. Shiva Publ.,** pp90-105.

------ --, -------- ----, WEAVER, S.D., DONNELLAN, N.C.B. & HENDRY, G.L. (1979). Minor-element geochemistry of basalts from Leg 49, North Atlantic Ocean. in **LUYENDYK, B.P., CANN, J. et al. (eds) Init. Repts. DSDP 49,** pp657-691.

TAYLOR, S.R., EWART, A. & CAPP, A.C. (1968). Leucogranites and rhyolites: trace element evidence for fractional crystallisation and partial melting. **Lithos 1,** pp179-186.

------ ---- & McLENNAN, S.M. (1981). The composition and evolution of the continental crust: rare earth element evidence from sedimentary rocks. **Phil. Trans. R. Soc. London A301,** p381.

------ ---- & -------- ---- (1985). The continental crust: its composition and evolution. **Blackwell Scientific Publ, Oxford,** 312p.

THAKUR, V.C. (1981). An overview of thrusts and nappes of western Himalaya. in **PRICE, N.C. & McCLAY, K.P. (eds) Thrust and nappe tectonics, Geol. Soc. London Sp. Pub. no. 9,** pp381-392.

THOMPSON, A.B. (1982). Dehydration melting of pelitic rocks and the generation of H_2O-undersaturated granitic liquids. **Am. J. Sci. 282,** pp1567-1595.

THOMPSON, R.N., MORRISON, M.A., DICKIN, A.P. & HENDRY, G.L. (1983). Continental flood basalts ... arachnids rule OK? in **HAWKESWORTH, C.J. & NORRY, M.J. (eds) Continental Basalts and Mantle Xenoliths, Publ. Shiva,** pp158-185.

-------- ----, -------- ----, HENDRY, G.L. & PARRY, S.J. (1984). An assessment of the relative roles of crust and mantle in magma genesis: an elemental approach. **Phil. Trans. R. Soc. London A310,** pp549-590.

THORPE, R.S., COSGROVE, M.E. & VAN CALSTEREN, P.W.C. (1986). Rare earth element, Sr- and Nd-isotope evidence for petrogenesis of Permian basaltic and K-rich volcanic rocks from southwest England. **Min. Mag. 50,** pp481-490.

TINDLE, A.G. & PEARCE, J.A. (1981). Petrogenetic modelling of in situ fractional crystallisation in the zoned Loch Doon pluton, Scotland. **Contr. Min. Petrology 78,** pp196-207.

TODD, V.R. & SHAW, S.E. (1985). S-type granitoids and an I-S line in the Peninsular Ranges batholith, southern California. **Geology 13,** pp231-233.

TRELOAR, P.J., COWARD, M.P. & WILLIAMS, M.P. (1987). Basement-cover imbrication in the footwall of the MMT, Besham, North Pakistan. **Abstract from Himalaya-Karakorum workshop, CNRS, Nancy.**

TWIST, D. & HARMER, R.E.J. (1987). Geochemistry of contrasting siliceous magmatic suites in the Bushveld Complex: genetic aspects and implications for tectonic discrimination diagrams. **J. Volcan. Geotherm. Res. 32,** pp83-98.

VARNE, R. (1985). Ancient subcontinental mantle: a source for K-rich orogenic volcanics. **Geology 13,** pp405-408.

VIDAL, P., COCHERIE, A. & LE FORT, P. (1982). Geochemical investigations of the origin of the Manaslu Leucogranite (Himalaya, Nepal). **Geochim. Cosmochim. Acta 46,** pp2279-2292.

VIELZEUF, D. & HOLLOWAY, J.R. (1988). Experimental determination of the fluid-absent melting reactions in the pelitic system. Consequences for crustal differentiation. **Contr. Min. Petrology 98,** pp257-276.

WALSH, J.N., BUCKLEY, F. & BARKER, J. (1981). The simultaneous determination of the rare-earth elements in rocks using inductively coupled plasma source spectrometry. **Chem. Geol. 33,** pp141-153.

WATSON, E.B. (1979). Zirconium saturation in felsic liquids: experimental results and application to trace element chemistry. **Contr. Min. Petrology 70,** pp407-419.

------ ---- & HARRISON, T.M. (1984). Accessory minerals and the geochemical evolution of crustal magmatic systems: a summary and prospectus of experimental approaches. **Phys. Earth Plan. Int. 35,** pp19-30.

WERNICKE, B.P., CHRISTIANSEN, R.L., SONDER, L.J. & ENGLAND, P.C. (1987). Tectonomagmatic evolution of Cenozoic extension in the North American Cordillera. in **COWARD, M.P., DEWEY, J.F. & HANCOCK, P.L. (eds) Continental Extensional Tectonics, Geol. Soc. Sp. Publ. no. 28,** pp203-221.

WESTPHAL, M. (1983). Palaeomagnetic and plate tectonic constraints on the movement of Tibet. **Tectonophysics 98,** pp1-10.

WHALEN, J.B., CURRIE, K.L. & CHAPPELL, B.W. (1987). A-type granites: geochemical characteristics, discrimination and petrogenesis. **Contr. Min. Petrology 95,** pp407-419.

WHITE, A.J.R. & CHAPPELL, B.W. (1977). Ultrametamorphism and granitoid genesis. **Tectonophysics 43,** pp7-22.

----- ------ & CHAPPELL, B.W. (1983). Granitoid types and their distribution in the Lachlan Fold Belt, southeastern Australia. **Geol. Soc. Am. Memoir 159,** pp21-34.

----- ------, CLEMENS, J.D., HOLLOWAY, J.R., SILVER, L.T., CHAPPELL, B.W. & WALL, V.J. (1986). S-type granites and their probable absence in southwestern North America. **Geology 14,** pp115-118.

WICKHAM, S.M. (1987). The segregation and emplacement of granitic magmas. **J. Geol. Soc. London 144,** pp281-297.

WINDLEY, B.F. (1983). Metamorphism and tectonics of the Himalaya. **J. Geol. Soc. London 140,** pp849-865.

------- ---- & JAN, M.Q. (1981). in **TAHIRKHELI, R.A. KHAN (1982). Geology of the Himalaya, Karakorum and Hindu Kush in Pakistan. Geol. Bull. Univ. Peshawar (sp. issue), vol. 15,** p23.

WONES, D.R. & EUGSTER, H.P. (1965). Stability of biotite: experiment, theory and application. **Am. Mineral. 50,** pp1228-1272.

WRIGHT, T.L. & DOHERTY, P.C. (1970). A linear programming and least squares computer method for solving petrologic mixing problems. **Geol. Soc. Am. Bull. 81,** pp1995-2008.

WYLLIE, P.J. (1984). Sources of granitoid magmas at convergent plate boundaries. **Phys. Earth. Plan. Int. 35,** pp12-18.

------ ----, HUANG, W.L., STERN, C.R. & MAALOE, S. (1976). Granitic magmas: possible and impossible sources, water contents and crystallisation sequences. **Can. J. Earth Sci. 13,** pp1007-1019.

XU, R.H., SCHARER, U. & ALLEGRE, C.J. (1985). Magmatism and metamorphism in the Lhasa Block (Tibet): a geochronological study. **J. Geology 93,** pp41-57.

ZEITLER, P.K. (1985). Cooling history of the NW Himalaya, Pakistan. **Tectonics 1(4),** pp127-151.

ZINDLER, A. & HART, S. (1986). Chemical Geodynamics. **Ann. Rev. Earth Plan. Sci. 14,** pp493-571.

APPENDIX ONE: Analytical techniques

Sample preparation.

The samples were first broken up into small cubes (approx. 1" across) using a hydraulic jaw splitter and any weathered crust was discarded. Enough rock to represent over 1000 times the average grain size by volume (about 1kg for a medium-coarse grained granite) was then further crushed in a fly press to produce a coarse gravel with a grain size of less than 3mm. About 100g of this crush was then ground to a fine powder in an agate Tema mill. All the apparatus was cleaned thoroughly between samples to avoid contamination. Samples which were too small to give a representative amount of crushed material or which were heavily weathered were not used.

A1.2: X-ray Fluorescence (XRF) analysis.

Samples were analysed on the Philips PW 1400 automatic X-ray spectrometer with 72-position sample changer at Leicester University. Fusion beads were prepared from a pre-ignited sample of powder mixed in the proportions one part to five parts (0.9g/4.5g) with dried lithium metaborate/lithium tetraborate flux in a Pt/5%Au crucible. Each batch of flux was dried and a proportion fused to determine its weight loss on fusion so that this could be allowed for. Ignition of samples was carried out in a furnace for 1.5 hours at 900^{o}C and weight loss on ignition (LOI) is included in the major element listings and recalculated totals. Fusion was carried out at 1200^{o}C in a vertical tube furnace for about 20 minutes before the liquid was caste into a 46mm glass disc which was allowed to anneal at 250^{o}C for several hours. Powder pellets were made by mixing 15g of rock powder with around 20 drops of a 7% aqueous solution of polyvinyl alcohol ('Moviol') and then pressing the mixture into 46mm diameter pellets under 15 tons of pressure using a steel dye and hydraulic ram.

A rhodium anode X-ray tube was used with fusion beads for the following major element analysis:

SiO2 TiO2 Al2O3 Fe2O3 MnO MgO CaO Na2O K2O P2O5

Beads which did not give totals between 98.0% and 102.0% were remade. About one dozen samples gave consistently low totals after having been remade three times and so these totals are taken as representative. All iron is determined as Fe2O3. This is recalculated using an FeO/Fe2O3 ratio calculated from the statistical equation of LeMaitre (1976) for the CIPW norm calculation and is given as 'Ferat' in the data tables. This is only an approximate value for the ratio and is probably erroneous but it is only used for the norms and is considered a more accurate method than just assuming a value.

At the fly-press stage of preparation two samples each were taken from two crushed rocks and temed and fused. The results in table A1.1. show little variation indicating the method of preparation gives a representative sample of each rock. To check the reliability of the fusion bead preparation process two beads were made for six samples. Again the results show little variation (table A1.2.).

Sample no.	SLV27(a)	SLV27(b)	B31(a)	B31(b)
SiO2	71.90	71.95	62.30	62.0
TiO2	0.20	0.19	0.70	0.70
Al2O3	14.93	15.09	15.13	15.2
Fe2O3	1.01	0.97	6.46	6.43
MnO	0.02	0.02	0.17	0.17
MgO	0.25	0.17	3.63	3.6
CaO	1.96	1.91	5.53	5.5
Na2O	4.64	4.68	3.94	3.85
K2O	3.69	3.54	2.19	2.22
P2O5	0.06	0.03	0.19	0.27
LOI	0.56	0.57	0.29	0.38
Total	99.20	99.12	100.53	100.24

Table A1.1: To show the homogeneity in major element analyses obtained between two samples (a) and (b) taken from the same crushed rock.

Sample	SG1(1)	SG1(2)	B16(1)	B16(2)	B64(1)	B64(2)
SiO2	73.98	73.78	57.54	57.82	71.2	70.13
TiO2	0.06	0.06	0.69	0.68	0.45	0.43
Al2O3	14.88	14.76	14.70	14.67	15.5	15.23
Fe2O3	0.86	0.88	7.13	6.97	3.3	3.27
MnO	0.03	0.03	0.13	0.13	0.04	0.04
MgO	0.00	0.00	5.08	4.89	0.9	0.81
CaO	0.82	0.79	7.37	7.22	3.9	3.80
Na2O	3.95	3.83	3.03	2.82	4.1	5.25
K2O	4.79	4.77	2.97	2.87	1.33	1.32
P2O5	0.19	0.08	0.23	0.22	0.24	0.24
LOI	0.52	0.52	0.45	0.45	0.32	0.32
Total	100.08	99.57	99.32	98.74	101.28	100.84

Sample	B90(1)	B90(2)	B96(1)	B96(2)	B121(1)	B121(2)
SiO2	53.00	53.20	56.17	57.25	73.22	73.14
TiO2	0.74	0.75	0.79	0.80	0.03	0.03
Al2O3	20.06	20.32	11.69	11.88	14.68	14.70
Fe2O3	6.60	6.57	8.50	8.48	0.79	0.78
MnO	0.12	0.12	0.14	0.15	0.16	0.15
MgO	3.56	3.53	10.68	10.78	0.00	0.00
CaO	9.02	9.02	5.82	5.83	1.00	0.98
Na2O	3.86	3.88	1.43	1.37	5.05	4.54
K2O	2.20	2.21	3.08	3.07	3.33	3.28
P2O5	0.27	0.27	0.07	0.07	0.02	0.01
LOI	0.29	0.29	0.67	0.67	0.43	0.43
Total	99.72	100.16	99.04	100.35	98.71	98.04

Table A1.2: To show variation in the major element oxide analyses between fusion beads (1) and (2) made from the same sample.

Two programs were run on the rhodium (Rh) anode tube and one on a tungsten (W) anode tube in order to analyse powder pellets for the following trace elements:

Rh Traces: Nb Zr Y Sr Rb Th Ga Zn Ni
Rh Ores: Zr Sr Zn Mo W Pb Cu
W Traces: TiO2 V Cr Ba La Ce Nd

The Zr, Sr, and Zn analyses from the Rh Traces program were used as these are more accurate due to higher count times. The Mo and W analyses are not listed as they were usually zero or very small for all samples. The Rh Ores program was not run for all samples. A special program on the rhodium tube was used to measure U for selected samples and this also measured Rb, Th and Pb values which were comparable with those values used from the main programs. Details of the Rh anode excitation technique are given by Marsh et al (1980) and of the W anode excitation technique by Tarney et al (1979). Quality control was maintained on trace element programs by running one international standard for every five samples.

Problems were encountered due to mica becoming aligned to the agate barrel during the tema process which inhibited crushing. This led to the powder not being as fine as usual and because of the resulting coarseness of the powder pellets it was thought that there might be some unreliability in the analyses. Two tests were run:

1) Four pellets were made from one sample (table A1.3.), and two from a selection of others. These show little variation in the Rh Traces elements but a little more in the W Traces elements, particularly in Cr. Again, the separately prepared samples of B31 and SLV27 show good agreement.

Sample	Nb	Zr	Y	Sr	Rb	Th	Ga	Zn	Ni
1B1(1)	14.2	134.5	28.0	289.2	116.7	16.0	17.8	61.5	6.0
1B1(2)	14.4	133.1	29.9	290.3	115.3	15.6	18.2	60.5	5.4
1B1(3)	13.8	130.7	30.2	291.1	115.7	15.0	17.4	61.8	5.4
1B1(4)	13.4	145.1	27.6	288.3	112.9	14.5	19.1	60.8	6.2
SG1(1)	18.0	38.3	22.5	39.7	424.2	12.7	24.9	41.8	1.8
SG1(2)	18.0	37.9	24.8	39.1	428.2	13.5	23.4	38.9	0.0
B16(1)	12.0	96.7	21.9	509.1	113.3	18.0	18.2	68.1	24.4
B16(2)	12.0	84.5	21.3	514.1	111.5	14.2	18.9	68.9	22.5
B64(1)	7.0	206.9	11.7	307.5	69.1	13.5	13.2	52.7	2.9
B64(2)	7.2	211.3	12.3	306.8	69.5	14.0	19.1	52.2	2.9
B90(1)	14.9	223.1	34.3	471.1	60.1	19.3	28.3	73.3	14.0
B90(2)	14.1	205.3	33.4	461.5	57.3	16.6	25.3	71.9	14.8
B96(1)	10.3	38.8	23.1	195.4	121.2	2.4	14.2	80.8	301.4
B96(2)	9.9	44.3	22.3	193.1	125.1	2.7	17.1	78.9	302.7
B121(1)	15.4	36.0	38.7	43.5	225.7	9.3	26.3	25.6	2.2
B121(2)	14.2	40.2	39.1	42.4	225.9	8.2	23.2	24.1	1.3
SLV27(a)	3.6	87.5	4.9	603.3	138.5	6.6	20.4	40.6	0.1
SLV27(b)	3.6	87.8	7.1	614.5	137.3	4.7	19.3	41.4	3.2
B31(a)	37.3	122.2	24.8	383.9	118.0	10.4	20.7	64.5	22.9
B31(b)	35.7	93.3	25.7	374.7	115.7	11.6	18.1	62.7	23.0

Sample	V	Cr	Ba	La	Ce	Nd
1B1(1)	104.0	25.6	644.9	14.3	33.0	15.2
1B1(2)	103.0	23.3	643.8	16.0	37.3	18.8
1B1(3)	105.5	24.2	648.3	15.1	30.2	15.7
1B1(4)	106.0	27.7	635.3	11.1	28.2	10.9
SG1(1)	0.3	0.4	97.9	9.8	17.8	7.6
SG1(2)	0.0	4.8	100.6	10.2	19.1	9.7
B16(1)	156.8	179.3	537.2	17.3	34.2	18.2
B16(2)	158.7	178.4	511.9	18.0	35.1	17.1
B90(1)	159.6	34.4	782.4	36.5	64.0	24.8
B90(2)	156.0	64.6	772.5	34.4	71.0	29.5
B96(1)	199.4	566.1	444.0	8.3	15.8	9.5
B96(2)	201.2	557.0	444.9	5.4	18.7	10.9
B121(1)	0.0	1.6	17.2	7.6	12.1	5.9
B121(2)	0.0	15.3	16.7	9.3	11.2	4.8
SLV27(a)	8.4	0.9	1028.1	11.4	19.5	7.0
SLV27(b)	9.5	1.9	959.6	10.1	15.4	6.0
B31(a)	118.4	133.4	494.9	20.0	40.3	18.0
B31(b)	123.6	143.8	504.4	18.2	37.9	17.6

Table A1.3: To show the variations between results from pellets made from the same sample (1) and (2), and from pellets made from two samples of the same rock (a) and (b) for the Rh and W tube programs.

2) A number of samples were re-temed using the W tema for 20 seconds in an attempt to grind the micas down further (table A1.4.). Again there is little variation for the Rh Traces elements except where Th is low in abundance (4B18) and whilst the W Traces elements show more variation there are no major discrepancies except for Cr in 4B19.

Sample	Nb	Zr	Y	Sr	Rb	Th	Ga	Zn	Ni
1B2	15.0	114.7	38.4	442.2	92.3	7.5	20.9	89.4	110.6
1B2(W)	14.4	112.9	39.4	439.8	90.7	7.7	22.7	89.9	113.6
1B4	15.6	222.9	73.6	331.2	69.6	5.0	19.1	85.6	75.9
1B4(W)	16.0	208.5	74.6	325.3	67.5	5.7	20.2	86.1	76.5
2B8	8.4	65.4	22.8	303.5	69.5	10.1	15.1	64.4	135.8
2B8(W)	8.7	69.5	23.4	305.5	72.8	10.6	16.2	66.4	141.3
4B18	6.2	94.3	23.8	392.9	91.8	1.3	17.8	69.5	155.6
4B18(W)	7.8	104.7	25.9	393.9	92.9	5.1	18.5	70.9	160.3
4B19	9.4	111.7	22.4	377.3	134.9	0.4	19.3	77.9	36.2
4B19(W)	12.0	134.0	24.5	379.8	134.9	2.1	21.0	77.7	37.5
5B25	14.2	151.4	26.7	325.2	105.6	10.2	17.2	63.0	5.2
5B25(W)	15.9	161.4	29.6	325.7	106.9	15.7	19.4	64.9	5.7

Table A1.4. continued overleaf

Sample	V	Cr	Ba	La	Ce	Nd
1B2	159.7	254.1	761.4	9.4	30.3	20.5
1B2(W)	157.2	270.4	719.5	11.2	28.6	19.5
1B4	110.8	195.0	978.0	6.6	26.7	27.4
1B4(W)	104.9	180.2	947.7	9.5	29.5	29.8
2B8	154.4	444.4	249.9	9.2	24.4	13.4
2B8(W)	147.7	428.6	228.5	10.5	25.8	15.1
4B18	195.1	322.6	365.9	7.1	21.5	12.6
4B18(W)	188.1	320.6	649.5	8.2	19.3	11.8
4B19	125.2	105.6	583.5	7.5	15.7	12.6
4B19(W)	124.5	190.5	568.8	4.4	23.3	12.6
5B25	116.8	43.3	624.9	17.2	35.8	17.0
5B25(W)	108.1	32.8	632.9	20.4	44.8	20.7

Table A1.4: To show the difference between pellets from the same sample after the powder for one pellet (W) has been re-temed in the W tema.

This reasonably good correlation suggested that the data was reliable. However, when the La, Ce and Nd values from neutron activation analyses were compared with W Trace analyses for the Baltoro differences of up to 100% were observed (table A1.5.)

Sample	La(XRF)	La(INAA)	Ce(XRF)	Ce(INAA)	Nd(XRF)	Nd(INAA)
R1	6.9	13.4	17.1	31.5	6.9	15.0
R33	36.9	66.1	68.3	141.5	30.3	56.8
R35	10.8	19.7	22.3	44.6	9.9	18.3
R36	1.8	4.7	5.1	9.3	3.1	4.2
R45	36.6	66.9	67.9	152.5	27.4	54.2
R68	0.9	5.7	2.6	20.2	2.6	13.5
R70	1.4	1.3	0.1	2.2	1.0	1.1
R88	17.6	33.8	34.0	71.4	12.8	26.7
R91	13.2	25.6	23.9	60.2	9.4	21.6
R95	39.6	67.8	76.8	161.0	32.6	59.8
R-13	39.1	45.4	81.5	103.0	31.1	44.0
R-14	33.3	44.2	68.8	103.0	31.1	44.0
R-53	24.0	36.4	47.2	84.1	20.6	32.0
R-103	4.6	11.0	9.5	4.5	4.3	10.8
R-109	77.7	144.0	217.9	416.0	121.6	214.0

Table A1.5: Comparison of XRF and INAA data for some Baltoro samples.

Values for R88 from the ICP at King's College, London agreed with the INAA data but an analysis run on a fusion bead on the XRF at Southampton University agreed with the XRF values obtained at Leicester (T. Rex, pers.comm.). This suggested that the problem lay with the different analytical techniques and not with the coarseness of the powder pellets. To support this, the finer powders still show the same problem. To try to solve this problem the W Traces program was run on fusion beads which are completely homogeneous. These also showed major discrepancies with the La, Ce and Nd values of the powder pellets (table A1.6.) showing these results to be unreliable, but showed lesser differences with the other elements indicating the V, Ba and probably Cr are reliable.

Sample	V	Cr	Ba	La	Ce	Nd
6B27	154.0	46.8	530.4	19.2	42.1	21.4
GEO	142.6	42.7	540.5	34.3	103.3	43.7
USGS	129.9	42.7	541.7	49.6	98.3	543.9
6B31	132.3	66.9	229.2	16.8	34.5	15.2
GEO	114.6	54.8	209.1	25.2	77.6	30.8
USGS	102.4	54.8	211.4	40.0	73.9	32.6
6B32	34.9	13.4	468.9	11.6	24.3	11.2
GEO	23.4	11.5	498.4	11.0	48.1	19.3
USGS	12.5	11.5	499.7	24.9	45.8	22.4

Table A1.6. continued overleaf.

Sample	V	Cr	Ba	La	Ce	Nd
8B37	73.2	51.5	264.0	19.4	37.2	15.4
GEO	54.4	34.1	266.7	23.7	70.4	25.6
USGS	43.1	34.1	268.8	38.4	67.0	28.0
8B39	85.4	28.9	646.6	18.4	39.1	16.6
GEO	64.5	17.5	647.0	22.2	80.6	28.2
USGS	53.0	17.5	647.8	36.8	76.7	30.2
8B42	122.0	38.1	515.1	13.7	26.9	13.1
GEO	107.3	37.2	482.4	6.7	52.6	20.8
USGS	95.2	37.2	483.8	20.4	50.1	23.8
9B44	40.2	6.2	780.9	22.4	41.8	16.0
GEO	31.2	7.9	837.8	22.9	66.9	24.5
USGS	20.3	7.9	838.0	37.5	63.7	27.0
9B47	144.9	122.6	544.9	15.5	36.7	17.7
GEO	129.9	105.4	547.0	13.3	69.0	26.5
USGS	117.5	105.4	548.1	27.3	65.7	28.8
UV23	103.3	33.2	484.9	16.4	30.9	14.7
GEO	86.2	30.9	527.7	23.0	76.3	29.3
USGS	74.4	30.9	528.9	37.6	72.6	31.2
GC1	17.1	9.7	1230.8	36.5	56.4	15.8
GEO	12.3	5.3	1318.1	48.8	95.1	23.8
USGS	1.6	5.3	1316.6	65.1	90.5	26.4

Table A1.6 : Selection of samples to illustrate the discrepancies between results from the W traces program for the XRF run on pellets (first line of each set) and on beads using two sets of calibrations, the USGS and GEO standards.

However, the fusion bead results could not be used instead because the two sets of standards, USGS and Geostds, gave two different sets of values (table A1.6.). This problem is still under investigation but for the purpose of this study it is considered that the XRF values for La, Ce and Nd are internally consistent in relation to each other and therefore can be used in multi-element plots such as spidergrams. However, care must be taken when comparing data for these three elements from this study with data from elsewhere. It is hoped to solve this problem soon but, until then, the above will be stressed in any publication.

A1.2: REE analysis.

Rare-earth elements for some Baltoro samples were measured using instrumental neutron activation analysis (INAA) on the powdered sample (T. Rex, pers. comm.). For the rest of the samples the REE were measured simultaneously using an inductively coupled plasma (ICP) source spectrometer. Sample preparation involved the standard HF - $HClO_4$ attack followed by dissolution in HCl (Walsh et al, 1981) as outlined below.

0.5g of ignited powder (see above) is accurately weighed into a PTFE beaker and dampened with a few drops of distilled and deionised water (ddH_2O). 15ml of HF and 4ml of $HClO_4$ are added and the mixture is then evaporated to incipient dryness at 180°C on a hotplate. A further 4ml of $HClO_4$ is added and the mixture again taken down to incipient dryness. By this stage any undissolved material may be apparent and, if this is the case, the process from the addition of the first batch of acid is repeated. The final residue is redissolved in 20ml of warmed 25% HCl, transferred to a 100ml pyrex beaker, rinsing out with ddH_2O and finally made up to 50ml with ddH_2O.

Chromatographic glass columns with an internal diameter of 20mm were used for the REE separation. They were filled with Dowex AG 50W-XB(H), 200-400 mesh resin to a settled height of approx. 12cm in a distilled water medium. 250ml of ddH_2O is initially run through the columns followed by a 250ml 4N HCl wash and a 250ml 1N HCl wash. The sample solution is now added followed by 450ml of 1.7N HCl. The REEs and Y are eluted with 600ml of 4N HCl and the solution is evaporated to dryness, being transferred to a 50ml pyrex beaker when only a small amount remains. At this stage 2ml of concentrated nitric acid is also added. When the samples come to be run the nitrate residue is redissolved in 10% HCl for injection into the ICP.

Problems with this method of preparation include possible loss of some REE giving low abundances, failure of the acid attack to completely dissolve accessory phases, particularly zircon, which can contain significant amounts of REE, and the apparently random development of a white precipitate in some solutions. Because of the problems with measuring the LREE on the XRF (see above) no comparison can be made between results from the two methods in order to indicate erroneous analyses. Therefore only a few analyses which were exceedingly incompatible with the rest were discarded. The white precipitate was reported by T. Rex (unpublished thesis,

University of Leicester) and on analysis appeared to contain no REE. Therefore, this is not considered to be a problem. However, any residual accessory phases could lead to serious errors in the analysis. For isotope analyses (see later) samples were left in the acid at 200°C for four to five days to dissolve, whilst in this method they were only left overnight at room temperature.

Three controls were run to try to highlight any errors:

a). Each batch of six samples included one blank, whereby the above method is followed exactly except that no sample is added. At least one blank was run through each column and all yielded negligible results when run through the ICP. This indicates that there is minimal contamination during the preparation process.

b). Four samples comprising two granodiorites, one monzogranite and one leucogranite, were prepared twice. Each sample was run through the same column each time. These samples were run on the ICP at Leicester University and the chondrite normalised results are shown in fig. A1.1. All four samples show good agreement between the two runs except for elements Gd and Er. Slight differences in abundances can be attributed to small losses of all REE during preparation. However, the similarity of the patterns indicates that all accessories had dissolved otherwise these would affect one part of the pattern more than another part e.g. undissolved zircon would lower the HREE more than the LREE. The discrepancies in Gd and Er were due to spectrometer error at Leicester, and because of this the rest of the samples were run at Royal Holloway and Bedford New College, London.

c). Each batch of six samples contained one international standard. JR-1 (rhyolite) or JG-1a (granite) were used as these are considered comparable to the majority of samples. Table A1.7. shows the average analysis, with errors, obtained for each of these standards and compares them with the recommended Leicester analysis and values from Ando et al (1987). In general the results show good agreement with the Leicester analysis indicating that the preparation technique was adequate.

	JR-1 (n=11)				JG-1a (n=6)			
	Mean	±Error	Leics	Ando	Mean	±Error	Leics	Ando
La	18.31	0.9	17.95	21.0	21.48	0.63	21.47	23.0
Ce	43.92	2.24	41.73	49.0	46.41	1.32	45.71	46.6
Pr	5.38	0.25	5.07	6.1	5.19	0.21	4.78	4.5
Nd	21.97	1.16	21.28	25.5	19.87	0.54	19.06	20.0
Sm	5.01	0.24	5.40	6.2	3.94	0.14	4.14	5.1
Eu	0.26	0.01	0.25	0.31	0.67	0.01	0.70	0.76
Gd	5.56	0.25	5.30	4.8	3.90	0.15	3.56	3.70
Dy	5.99	0.28	5.80	6.2	3.19	0.06	3.06	4.6
Ho	1.24	0.06	1.17	1.1	0.59	0.01	0.54	0.75
Er	4.06	0.2	3.82	3.9	1.70	0.14	1.68	1.69
Yb	4.48	0.24	4.46	4.6	1.58	0.02	1.50	2.7
Lu	0.71	0.05	0.67	0.68	0.28	0.02	0.23	0.46

Table A1.7: Comparison of average analyses for international standards JR-1 and JG-1a from this study with recommended Leicester analysis and data from Ando et al (1987).

ICP machine drift was monitored by running an in-house composite standard, for which REE concentrations are accurately known, for every 6-8 samples. The sensitivity of this method of REE determination is affected by interference from spectral lines for the elements Ba, Sr, Zr, Ca and Fe. Therefore the following corrections were applied to each analysis according to the intensities of the peaks for the above elements:

	Corrections in ppm per (x) intensity units of:-			
	Ba	Sr	Ca	Fe
(x)	620000	240000	4000	18000
Ce	+0.1	-0.7	-0.3	+0.25
Pr	+0.1	0.0	-0.3	+0.2
Nd	-0.15	-0.4	-0.4	+0.5
Sm	+0.1	+0.1	+0.12	0.0
Eu	+0.01	-0.01	0.0	-0.01
Gd	+0.05	0.0	-0.3	+0.05
Dy	+0.01	0.0	+0.02	+0.01
Er	+0.05	+0.05	-0.7	-0.6
Yb	+0.01	0.0	0.0	_0.01

No corrections were applied for Zr as the intensity of the Zr peak was always so low as to make corrections negligible.

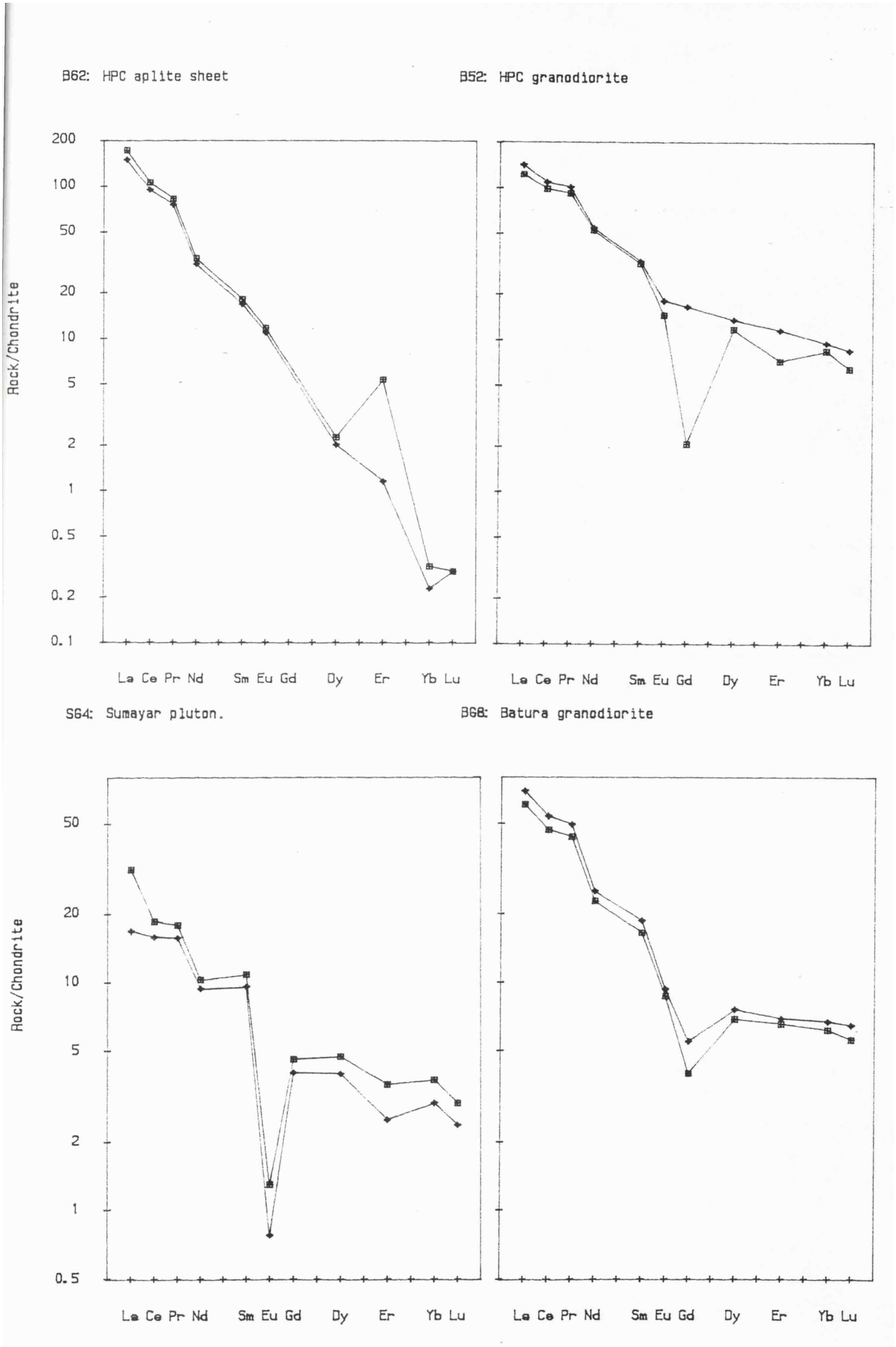

Figure A1.1: Comparison of chondrite normalised REE patterns obtained from repeat preparations of four representative samples from the Hunza Valley. Er and Gd discrepancies are due to ICP error.

The types in the following listings of XRF, ICP and INAA data are based on the Debon and Le Fort (1982) classification and also the nature of the sample in the field (e.g. dyke or xenolith etc.). Sample localities and further details about samples are given in appendix 2. Where the classification system fails to separate rock types e.g. monzogranites and leucogranites the type is based upon the nature of the hand specimen. A list of the type abbreviations used is given below:

Mzg = monzogranite (adamellite)
Lcg = leucogranite
2MG = two-mica granite
Grd = granodiorite
QzDi = quartz diorite
Mz.DQ = monzo-quartz diorite
Mz.Go = monzogabbro
Porph = porphyry
Gneiss = gneiss
Aug.Gn = augen gneiss
Lamp = lamprophyre
Peg or Pg = pegmatite dyke
Ap = aplite dyke
Xen = xenolith
Amph = amphibolite
M.Bas = metabasite country rock

The groups of rocks used in plots within the text are defined below. Sample localities are given in Appendix Two.

Baltoro.

Monzogranites:	R2 R3 R33 R34 R37 R38 R45 R49 R55 R57 R58 R59 R60 R61 R62 R63ii R65 R71 R79 R80 R81 R84 R85 R88 R89 R93 R94 R95
Leucogranites:	R1 R4 R35 R40 R51 R56 R64
Ap/Peg Dykes:	R36 R52 R66 R68 R70 R77 R78 R86 R90 R91 R92
Porphyries:	R-6 R-9 R-10 R-12 R-13 R-14 R-15
K2 Gneiss:	R-53 GNEISS

Khunjerab and Sost.

Khunj. Granodiorites:	K203 K204 K205 K206 K207
Khunj. Xenolith:	K208
Khunj. Mzgranite:	K209 K210
N. Sost Shap-type:	K211
N. Sost Pluton:	K212 K213 K214 K215
S. Sost Mzg Pluton:	K216 K217

Hunza Dykes.

Early HPC lcg's:	B3 B4 B105 B119 B120
Late HPC lcg's:	B12 B69 B89 B95 B103 B110 B118 B121
Early HPC aplites:	B21 B30 B53 B70 B94 B104 B109
Late HPC aplites:	B19 B29 B47 B54 B78 B97 B98
Mixing zone aplites:	B35 B41 B42 B59 B87
Sill. zone lcg pegs:	SLV19 SLV20 SLV26 SLV30 DPHUN3 DPHUN4
Sill. zone 2mg ap's:	SLV3 SLV5 SLV32 SLV33 SLV34 GC1
Sill.zone mzg ap's:	SLV7 SLV8 SLV13 SLV14 SLV18 SLV23 SLV24 SLV25 SLV27 SLV28 SLV31 DPHUN1
Leucogranite sheets:	NSG1 NSG2 NSG3 NSG4 NSG5 SLV21 9SLV35 9SLV36 DPHUN2
Sumayar pluton:	SG1 SG2 SG3 SG4 SG5

HPC Aplite sheets.

Early phase:	9B44 B26 B61 B62 B64 B68 B73
Later phase:	B27 B65 B72
Edges & rims (Lcg's):	B66 B67 B74

HPC first phase.

Northern granodiorite:	2B11 3B13 3B16 3B17 B1 B2 B14 B15 B100 B101 B111 B112 B113 B114
Gulmit granodiorite:	1B1 1B4 1B6 4B19 5B22 RBSR3 RBSR4 RBSR5 B5 B9 B90 B99
Gulmit quartz diorite:	1B2 2B8 4B18 RBSR1 RBSR7 B8 B11 B91 B96
North of mixing zone:	5B25 6B27 8B37 8B39 8B41 8B42 B28 B60 B63 B71 B88 B108
South of mixing zone:	7B36 9B47 B46 B48 B49 B51 B52 B77
Southern contact:	B16 B17 B18 B20 B25 B102
Granodiorite sheets:	SLV4 SLV9 SLV12 SLV15 SLV17 3SLV35 3SLV36 UV23
Augen gneisses:	SLV29 SLG4 SLG5 SLG7
Xenoliths:	5B23 B92 B93 B115 B116 B117

Batura.

Main granodiorite:	BG1 BG2 BG3 BG4 BG5
Leucogranitoids:	BG6 BG9 BG10
Xenolith:	BG11
Pegmatite:	BG7
Foliated s:ample	BG8

HPC Mixing Zone.

Normal granodiorite:	6B27 7B36 8B37 8B41 9B47 B28 B46 B48 B60 B63 B71 B77 B88
Granodiorite host:	6B29 6B31 9B43 B31 B36 B55 B56
Fsp megacrystic grd:	B80 B84
Basic gneiss:	B34 B37 B44 B81 B82
Acidic gneiss:	B32 B38 B40 B57 B83
Pegmatite sweats:	B34 B45 B58 B85 B86
Aplite sheets:	9B44 B26 B61 B62 B64 B68 B73

Karakoram pre-collisional granodiorites.

HPC:	1B1 2B11 3B16 5B22 6B27 8B39 8B41 8B42 9B47 RBSR3 RBSR4 RBSR5 RBSR7 B1 B2 B5 B11 B14 B15 B16 B17 B20 B28 B46 B51 B60
Khunjerab:	K203 K204 K205 K206 K207
North Sost:	K212 K213 K214 K215
Batura pluton:	BG1 BG2 BG3 BG4

Baltoro granites

Rock no.	R1	R2	R3	R4	R33	R34	R35	R36	R37
Pellet	L7491	L7492	L7493	L7494	L7553	L7554	L7555	L7556	L7557
Type	Lcg	Mzg	Mzg	Lcg	Mzg	Mzg	Lcg	Lcg	Mzg
SiO2	74.5	70.6	71.4	75.6	69.4	72.4	73.9	72.8	70.0
TiO2	0.06	0.29	0.28	0.07	0.42	0.21	0.12	0.03	0.46
Al2O3	14.3	14.9	15.0	14.1	14.7	14.0	14.2	14.1	14.5
Fe2O3	0.7	1.6	1.4	0.6	2.1	1.3	1.0	0.3	2.3
MnO	0.05	0.03	0.03	0.04	0.04	0.02	0.05	0.08	0.03
MgO	0.0	0.3	0.2	0.0	0.7	0.3	0.1	0.0	0.7
CaO	0.8	1.9	1.7	0.9	1.7	1.3	0.8	0.6	1.7
Na2O	4.5	4.1	3.6	4.3	5.0	4.5	4.6	6.8	4.5
K2O	3.97	4.36	5.33	4.88	3.98	4.60	3.87	3.15	4.29
P2O5	0.08	0.12	0.04	0.12	0.19	0.10	0.10	0.06	0.20
LOI	0.32	0.15	0.25	0.19	0.18	0.24	0.42	0.16	0.18
Total	99.32	98.48	99.23	100.83	98.35	98.98	99.21	98.05	98.89
Trace elements in parts per million									
Rb	161.8	136.4	133.4	168.1	233.6	197.2	271.6	326.1	234.4
Ba	117.5	1332.0	1108.4	561.4	2317.0	1285.4	442.4	238.6	2169.6
Th	8.7	18.3	35.4	9.7	61.7	38.1	13.3	10.1	84.5
Pb	35.3	39.4	46.7	55.6	92.4	73.5	45.8	109.8	93.2
Nb	7.8	7.1	7.8	6.4	21.8	10.0	21.1	4.8	19.6
La	6.9	20.3	29.5	7.9	36.9	14.0	10.8	1.8	37.4
Ce	17.1	37.5	54.0	15.2	68.3	25.8	22.3	5.1	73.7
Sr	53.9	573.3	570.6	208.4	795.6	505.0	155.8	138.4	755.2
Nd	6.9	15.0	19.4	6.2	30.3	11.2	9.9	3.1	30.3
Zr	55.3	144.8	138.6	59.6	244.2	135.9	70.8	25.5	257.1
Y	16.9	7.0	5.8	10.5	15.9	7.8	13.7	11.4	16.0
V	2.5	19.6	18.8	4.4	31.9	18.5	5.1	1.8	34.1
Cr	8.9	9.5	7.7	10.7	22.6	16.3	15.8	10.6	30.6
Ni	1.7	2.2	2.2	2.2	10.3	9.6	2.6	3.0	10.4
Cu	0.0	0.0	1.2	0.0	4.1	3.8	5.0	5.0	7.8
Zn	22.1	44.6	34.8	12.9	54.5	26.7	33.4	6.1	55.6
Ga	23.1	18.3	17.6	18.7	19.6	17.2	22.3	21.3	19.3
Rb/Sr	3.0	0.2	0.2	0.8	0.3	0.4	1.7	2.4	0.3
La/Y	0.4	2.9	5.1	0.8	2.3	1.8	0.8	0.2	2.3
C.I.P.W. norms with calculated FeO/Fe2O3 ratio (Ferat)									
Ferat	0.62	0.65	0.61	0.62	0.70	0.65	0.63	0.77	0.67
Qtz	31.65	25.47	25.93	30.29	20.83	25.79	30.31	21.90	22.84
Cor	1.41	0.31	0.35	0.40	--	--	1.14	--	--
Or	23.52	25.83	31.56	28.90	23.58	27.24	22.99	18.67	25.41
Ab	37.99	34.95	30.55	36.22	42.31	37.99	39.26	54.85	38.42
An	3.40	8.44	8.12	3.83	5.86	4.58	3.46	--	6.63
Ac	--	--	--	--	--	--	--	0.42	--
Ns	--	--	--	--	--	--	--	0.52	--
Di	--	--	--	--	1.15	1.17	--	0.83	0.28
Wol	--	--	--	--	--	--	--	0.65	--
Hy	0.65	1.66	1.30	0.43	2.08	0.78	0.98	--	2.55
Mt	0.36	0.89	0.71	0.32	1.17	0.71	0.55	--	1.28
Ilm	0.11	0.55	0.53	0.13	0.80	0.40	0.23	0.06	0.87
Ap	0.19	0.28	0.09	0.28	0.44	0.23	0.23	0.14	0.46
Rare Earth Elements in ppm: INAA analysis (ICP for R3 & R34).									
La	13.4	--	54.23	--	66.1	27.58	19.7	4.72	--
Ce	31.5	--	79.89	--	141.0	44.72	44.6	9.25	--
Pr	na	--	10.87	--	na	6.14	na	na	--
Nd	15.0	--	33.64	--	56.8	20.93	18.3	4.24	--
Sm	2.64	--	4.93	--	8.92	3.54	3.03	0.91	--
Eu	0.29	--	0.81	--	1.89	1.01	0.58	0.35	--
Gd	na	--	2.85	--	na	2.29	na	na	--
Tb	0.40	--	na	--	0.37	na	0.34	0.16	--
Dy	na	--	1.19	--	na	1.29	na	na	--
Ho	na	--	0.18	--	na	0.21	na	na	--
Er	na	--	0.56	--	na	na	na	na	--
Yb	2.23	--	0.24	--	1.22	0.53	0.64	1.59	--
Lu	0.24	--	0.04	--	0.14	0.07	0.13	0.24	--

Baltoro granites

Rock no.	R38	R45	R46	R49	R50	R51	R52	R55	R56
Pellet	L7558	L7546	L7547	L7549	L7550	L7551	L7552	L7495	L7496
Type	Mzg	Mzg	Mzg Ap	Mzg	Lcg	Lcg	Lcg Peg	Mzg	Lcg
SiO2	68.8	70.1	72.7	73.8	72.5	75.5	74.8	71.3	72.9
TiO2	0.44	0.38	0.15	0.15	0.06	0.05	0.07	0.23	0.03
Al2O3	14.4	14.7	14.0	13.8	15.1	13.6	14.0	14.9	14.1
Fe2O3	2.3	2.0	1.1	1.1	1.4	0.7	0.5	1.6	0.8
MnO	0.03	0.03	0.03	0.03	0.36	0.05	0.01	0.03	0.20
MgO	0.6	0.6	0.2	0.2	0.0	0.1	0.0	0.3	0.0
CaO	1.6	1.9	1.5	1.2	1.3	0.7	1.1	1.8	0.6
Na2O	4.3	4.4	3.7	4.3	3.9	4.7	4.3	3.4	3.7
K2O	4.70	3.96	4.32	4.01	3.78	3.50	3.44	4.42	5.46
P2O5	0.27	0.21	0.05	0.08	0.20	0.07	0.08	0.08	0.18
LOI	0.31	0.65	0.76	0.31	0.54	0.72	0.34	0.67	0.28
Total	97.72	98.87	98.54	99.04	99.19	99.66	98.74	98.67	98.34
Trace elements in parts per million									
Rb	259.4	154.3	148.1	189.5	149.0	262.3	146.8	138.0	238.0
Ba	1957.4	1221.5	856.9	771.2	235.9	305.8	287.6	874.9	385.1
Th	52.8	27.6	7.4	11.8	6.5	6.4	3.0	14.0	3.5
Pb	91.1	74.2	40.0	46.4	38.7	49.3	42.6	36.8	49.2
Nb	20.7	16.3	7.3	9.7	11.0	18.5	7.5	10.6	11.9
La	54.3	36.6	10.2	10.7	3.1	3.8	3.2	16.0	1.0
Ce	98.0	67.9	19.4	19.6	8.2	10.9	5.8	30.2	2.0
Sr	745.3	611.0	317.4	270.7	157.5	87.3	190.2	486.3	128.1
Nd	33.5	27.4	7.3	8.6	4.9	4.6	2.9	12.8	1.8
Zr	268.4	164.3	70.9	69.9	18.8	37.5	1.0	106.6	18.5
Y	14.8	10.2	8.1	9.8	43.3	16.0	17.7	8.9	13.4
V	30.6	27.7	7.5	4.9	1.7	1.6	2.4	21.2	1.4
Cr	23.7	11.8	13.8	9.4	10.5	15.7	16.3	10.2	10.2
Ni	9.5	2.8	2.5	2.1	1.0	1.0	1.3	2.9	2.0
Cu	7.2	7.9	6.1	7.4	6.9	4.0	1.9	0.0	0.0
Zn	48.1	47.9	29.5	35.6	7.5	18.3	12.3	36.3	9.5
Ga	20.6	18.1	15.6	16.3	26.4	18.3	18.8	17.9	20.8
Rb/Sr	0.3	0.3	0.5	0.7	0.9	3.0	0.8	0.3	1.9
La/Y	3.7	3.6	1.3	1.1	0.1	0.2	0.2	1.8	0.1
C.I.P.W. norms with calculated FeO/Fe2O3 ratio (Ferat)									
Ferat	0.64	0.67	0.61	0.63	0.61	0.64	0.63	0.60	0.55
Qtz	21.81	24.96	30.96	30.39	32.37	33.34	34.20	30.31	29.54
Cor	--	0.33	0.58	0.38	2.73	0.99	1.40	1.54	1.52
Or	27.84	23.58	25.71	23.76	22.46	20.86	20.39	26.30	32.39
Ab	36.64	37.15	31.82	36.89	33.43	39.94	36.89	29.03	31.06
An	6.06	8.10	7.16	5.33	5.04	3.11	4.88	8.26	1.90
Di	0.13	--	--	--	--	--	--	--	--
Hy	2.42	2.30	1.24	1.15	1.78	0.73	0.38	1.68	1.02
Mt	1.22	1.11	0.59	0.61	0.72	0.39	0.25	0.82	0.40
Ilm	0.84	0.72	0.28	0.28	0.11	0.09	0.13	0.44	0.06
Ap	0.63	0.49	0.12	0.19	0.46	0.16	0.19	0.19	0.42
Rare Earth Elements in ppm: INAA analysis.									
La	--	66.9	--	--	--	--	--	--	--
Ce	--	152.0	--	--	--	--	--	--	--
Nd	--	54.2	--	--	--	--	--	--	--
Sm	--	7.7	--	--	--	--	--	--	--
Eu	--	1.03	--	--	--	--	--	--	--
Tb	--	0.46	--	--	--	--	--	--	--
Yb	--	0.23	--	--	--	--	--	--	--
Lu	--	0.024	--	--	--	--	--	--	--

Baltoro granites

Rock no.	R57	R58	R59	R60	R61	R62	R63ii	R64	R65
Pellet	L7497	L7483	L7482	L7481	L7480	L7479	L7478	L7560	L7561
Type	Mzg	Mzg	Mzg	Mzg	Mzg	Mzg	Mzg	Lcg	Mzg
SiO2	72.2	71.9	72.7	72.7	73.0	73.2	74.4	74.8	74.0
TiO2	0.11	0.18	0.21	0.19	0.16	0.17	0.14	0.08	0.11
Al2O3	14.1	14.6	15.0	14.2	14.4	13.4	13.8	14.6	14.0
Fe2O3	0.9	1.3	1.4	1.2	1.3	1.2	1.1	0.9	1.2
MnO	0.02	0.03	0.03	0.02	0.03	0.03	0.02	0.07	0.05
MgO	0.1	0.2	0.2	0.2	0.2	0.2	0.1	0.0	0.2
CaO	1.5	1.4	1.6	1.5	1.4	1.0	0.9	0.8	0.8
Na2O	3.7	4.1	3.7	4.2	4.4	4.9	3.5	4.3	4.8
K2O	4.38	4.28	4.54	4.17	4.05	3.73	4.97	3.92	3.88
P2O5	0.05	0.17	0.06	0.07	0.15	0.08	0.16	0.07	0.05
LOI	0.65	0.33	0.35	0.34	0.41	0.38	0.42	1.49	0.36
Total	97.68	98.60	99.89	98.77	99.43	98.21	99.44	100.99	99.26
Trace elements in parts per million									
Rb	129.6	155.8	151.5	149.1	166.5	193.8	158.3	267.4	248.6
Ba	813.3	1052.0	1016.2	1024.2	745.8	1140.2	833.1	453.9	413.6
Th	7.0	13.8	17.4	12.3	11.0	18.1	14.1	14.9	4.9
Pb	41.0	40.1	38.3	37.8	37.6	45.5	40.8	31.8	38.7
Nb	6.5	7.7	7.8	6.5	8.1	7.9	9.1	19.3	15.5
La	5.9	14.3	20.3	14.3	12.3	19.2	15.3	5.4	6.0
Ce	10.8	27.0	37.0	25.7	22.1	38.2	30.3	11.9	12.1
Sr	324.1	463.0	451.2	466.3	351.3	314.6	212.9	151.4	112.1
Nd	4.4	10.0	13.4	10.3	9.5	14.6	12.2	5.7	6.1
Zr	59.4	105.4	118.8	97.8	85.5	113.9	76.2	51.8	54.9
Y	6.8	8.5	7.4	6.7	9.8	7.8	10.9	12.6	15.1
V	7.0	10.3	12.9	12.5	12.3	8.1	5.3	3.3	5.7
Cr	10.1	12.5	7.8	27.3	7.3	7.3	6.4	11.5	14.7
Ni	1.0	2.5	2.3	3.4	1.7	2.4	2.8	2.3	2.2
Cu	0.0	5.2	5.0	5.3	5.8	4.8	5.1	4.2	1.1
Zn	25.4	37.7	38.0	31.2	34.1	30.7	27.4	37.1	38.9
Ga	14.4	17.7	17.7	16.8	17.1	15.5	17.6	21.6	19.3
Rb/Sr	0.4	0.3	0.3	0.3	0.5	0.6	0.7	1.8	2.2
La/Y	0.9	1.7	2.7	2.1	1.3	2.5	1.4	0.4	0.4
C.I.P.W. norms with calculated FeO/Fe2O3 ratio (Ferat)									
Ferat	0.60	0.63	0.62	0.64	0.65	0.66	0.56	0.62	0.64
Qtz	30.72	28.45	29.87	28.87	29.18	28.10	33.43	33.43	29.30
Cor	0.70	1.02	1.10	0.26	0.74	--	1.51	1.98	0.65
Or	26.06	25.35	26.95	24.70	24.05	22.10	29.49	23.52	22.99
Ab	31.48	35.03	31.48	35.54	37.06	41.89	29.62	36.73	40.62
An	7.02	5.98	7.79	6.93	5.87	3.33	3.27	3.71	3.49
Di	--	--	--	--	--	1.01	--	--	--
Hy	0.82	1.26	1.32	1.23	1.12	0.55	0.89	0.80	1.20
Mt	0.49	0.69	0.75	0.63	0.67	0.64	0.53	0.47	0.61
Ilm	0.21	0.34	0.40	0.36	0.30	0.32	0.27	0.15	0.21
Ap	0.12	0.39	0.14	0.16	0.35	0.19	0.37	0.16	0.12
Rare Earth Elements in ppm: ICP analyses.									
La	--	21.4	--	--	--	--	--	8.7	--
Ce	--	40.76	--	--	--	--	--	18.2	--
Pr	--	4.34	--	--	--	--	--	2.23	--
Nd	--	14.9	--	--	--	--	--	7.5	--
Sm	--	2.33	--	--	--	--	--	1.47	--
Eu	--	0.57	--	--	--	--	--	0.19	--
Gd	--	1.79	--	--	--	--	--	1.68	--
Dy	--	1.03	--	--	--	--	--	1.06	--
Ho	--	0.17	--	--	--	--	--	0.16	--
Er	--	0.49	--	--	--	--	--	0.66	--
Yb	--	0.21	--	--	--	--	--	0.44	--
Lu	--	0.07	--	--	--	--	--	0.11	--

Baltoro granites

Rock no.	R66	R68	R70	R71	R75	R76	R77	R78	R79
Pellet	L7562	L7563	L7564	L7565	L7490	L7489	L7488	L7487	L7486
Type	Lcg Peg	Lcg	Lcg Peg	Mzg	Mzg Ap	Mzg Ap	Lcg Ap	Lcg Ap	Mzg
SiO2	74.8	73.6	76.1	72.7	72.1	71.2	75.6	75.2	72.4
TiO2	0.05	0.02	0.09	0.17	0.27	0.22	0.13	0.04	0.15
Al2O3	14.1	14.5	13.1	14.3	14.8	14.5	13.5	13.4	14.4
Fe2O3	0.7	1.1	0.6	1.2	1.8	1.5	0.6	0.3	1.1
MnO	0.04	0.36	0.01	0.02	0.04	0.04	0.01	0.00	0.03
MgO	0.0	0.0	0.1	0.2	0.3	0.3	0.1	0.0	0.2
CaO	0.6	0.4	1.0	1.6	1.8	1.7	0.8	0.4	1.8
Na2O	4.3	4.0	4.4	3.8	4.4	3.6	4.5	3.7	3.8
K2O	5.51	4.24	3.98	4.45	3.73	4.33	3.72	5.77	4.06
P2O5	0.08	0.09	0.03	0.04	0.10	0.09	0.03	0.03	0.05
LOI	0.25	0.44	0.20	1.00	0.26	0.26	0.24	0.27	0.38
Total	100.33	98.78	99.50	99.41	99.59	97.79	99.20	99.11	98.32
Trace elements in parts per million									
Rb	212.1	273.2	111.9	115.8	171.6	166.3	236.4	243.1	142.7
Ba	154.6	9.8	521.2	589.2	712.0	796.4	325.8	80.7	718.8
Th	3.7	8.2	0.3	12.8	16.0	13.2	45.0	20.7	9.6
Pb	32.8	22.2	44.9	40.5	32.8	30.7	135.7	183.8	33.5
Nb	14.1	20.9	3.5	5.4	10.4	9.2	17.0	17.4	9.8
La	2.9	0.9	1.4	9.2	16.8	14.4	15.2	6.0	10.7
Ce	8.3	2.6	0.1	21.3	33.8	26.1	36.3	14.1	21.5
Sr	54.1	8.8	308.9	412.7	465.7	474.5	145.3	67.4	358.1
Nd	4.3	2.6	1.0	8.0	13.8	10.1	16.6	5.0	8.3
Zr	31.4	29.9	0.0	83.0	118.2	105.6	115.6	70.4	79.2
Y	13.3	13.0	5.4	6.0	10.5	9.2	10.6	5.8	12.4
V	3.6	1.5	5.7	12.8	23.3	20.5	8.0	1.8	7.8
Cr	10.6	11.7	6.9	7.7	16.1	10.9	9.6	7.0	9.7
Ni	1.0	1.3	2.2	0.0	3.5	2.6	5.5	4.5	2.3
Cu	6.1	3.6	3.7	3.1	0.0	0.0	0.0	11.6	4.5
Zn	17.4	16.2	17.5	32.5	41.5	36.5	10.0	3.7	33.7
Ga	18.0	27.0	13.4	16.1	19.2	17.7	18.1	21.6	16.3
Rb/Sr	3.9	31.0	0.4	0.3	0.4	0.4	1.6	3.6	0.4
La/Y	0.2	0.1	0.3	1.5	1.6	1.6	1.4	1.0	0.9
C.I.P.W. norms with calculated FeO/Fe2O3 ratio (Ferat)									
Ferat	0.59	0.56	0.63	0.62	0.68	0.61	0.62	0.54	0.63
Qtz	27.67	32.92	33.37	30.12	27.54	29.51	33.48	30.68	30.62
Cor	0.21	2.81	--	0.51	0.47	0.98	0.72	0.35	0.63
Or	32.62	25.18	23.58	26.53	22.10	25.65	22.04	34.22	24.11
Ab	36.22	33.93	36.89	32.41	37.74	30.63	37.99	31.56	32.16
An	2.40	1.55	4.48	7.53	8.13	7.94	3.72	1.74	8.60
Di	--	--	0.20	--	--	--	--	--	--
Hy	0.54	1.54	0.40	1.19	1.78	1.55	0.59	0.23	1.13
Mt	0.35	0.53	0.30	0.62	0.98	0.79	0.30	0.17	0.59
Ilm	0.09	0.04	0.17	0.32	0.51	0.42	0.25	0.08	0.28
Ap	0.19	0.21	0.07	0.09	0.23	0.21	0.07	0.07	0.12
Rare Earth Elements in ppm: INAA analyses.									
La	--	5.71	1.3	--	--	--	--	--	--
Ce	--	20.2	2.2	--	--	--	--	--	--
Nd	--	13.5	1.14	--	--	--	--	--	--
Sm	--	1.57	0.19	--	--	--	--	--	--
Eu	--	1.02	0.43	--	--	--	--	--	--
Tb	--	0.21	0.063	--	--	--	--	--	--
Yb	--	1.27	0.25	--	--	--	--	--	--
Lu	--	0.19	0.024	--	--	--	--	--	--

Baltoro granites

Rock no.	R80	R81	R82	R84	R85	R86	R88	R89	R90
Pellet	L7485	L7484	L7498	L7499	L7500	L7501	L7502	L7503	L7504
Type	Mzg	Mzg	Mzg Ap	Mzg	Mzg	Lcg Ap	Mzg	Mzg	Lcg Ap
SiO2	71.4	72.2	73.0	71.4	67.9	76.0	70.2	72.4	72.0
TiO2	0.30	0.20	0.12	0.24	0.41	0.04	0.22	0.22	0.17
Al2O3	15.3	15.2	14.5	14.4	15.6	14.2	14.8	14.4	14.8
Fe2O3	1.8	1.4	1.0	1.6	2.3	0.6	1.5	1.5	1.2
MnO	0.03	0.04	0.03	0.02	0.03	0.06	0.02	0.03	0.03
MgO	0.4	0.2	0.1	0.3	0.8	0.0	0.3	0.2	0.2
CaO	2.6	2.2	1.5	2.2	2.3	0.7	1.7	1.5	2.4
Na2O	4.3	3.7	4.3	3.9	4.6	4.8	3.9	4.2	2.7
K2O	2.72	3.39	4.18	3.74	4.10	3.87	4.25	3.91	4.27
P2O5	0.10	0.06	0.12	0.05	0.20	0.10	0.08	0.17	0.04
LOI	0.21	0.25	0.33	0.28	0.24	0.45	0.21	0.30	0.44
Total	99.19	98.86	99.08	98.18	98.39	100.90	97.12	98.82	98.37

Trace elements in parts per million

Rb	110.6	184.1	124.2	103.0	188.4	250.3	133.8	167.5	112.9
Ba	1206.1	1467.0	790.2	1676.7	1369.4	80.0	1089.9	1019.1	1580.4
Th	11.8	6.6	7.4	11.3	36.1	7.5	17.3	18.8	4.7
Pb	28.1	27.6	41.8	29.2	55.5	91.5	42.9	39.6	26.1
Nb	8.2	11.2	6.4	5.6	15.4	25.0	7.8	10.2	4.5
La	16.9	13.5	5.8	19.8	41.6	5.8	17.6	19.0	9.9
Ce	32.6	23.5	10.0	35.5	79.7	14.8	34.0	35.2	15.2
Sr	567.4	512.2	339.1	586.3	821.9	52.8	527.0	425.8	567.1
Nd	12.0	6.4	4.7	12.5	27.7	7.5	12.8	14.3	5.0
Zr	151.8	111.0	66.1	130.0	218.9	48.1	114.5	110.7	88.2
Y	7.3	5.6	10.6	6.2	10.4	15.9	6.8	10.0	4.5
V	19.9	6.6	5.6	12.7	32.2	2.2	16.6	14.3	8.3
Cr	15.2	7.5	16.3	9.0	15.0	8.8	14.1	10.6	16.8
Ni	2.4	2.4	2.0	2.2	5.2	1.6	3.3	1.8	2.3
Cu	5.1	4.7	4.5	6.8	6.3	7.2	6.6	6.3	7.9
Zn	46.9	40.0	20.2	35.2	50.0	31.5	34.2	40.8	29.6
Ga	18.7	19.1	15.3	14.6	21.0	22.4	17.2	18.5	15.1
Rb/Sr	0.2	0.4	0.4	0.2	0.2	4.7	0.3	0.4	0.2
La/Y	2.3	2.4	0.5	3.2	4.0	0.4	2.6	1.9	2.2

C.I.P.W. norms with calculated FeO/Fe2O3 ratio (Ferat)

Ferat	0.72	0.65	0.65	0.67	0.71	0.64	0.62	0.64	0.60
Qtz	29.98	32.58	28.79	28.91	19.82	31.99	27.27	29.55	34.24
Cor	0.86	1.58	0.43	0.08	--	1.08	0.97	0.91	1.45
Or	16.13	20.09	24.76	22.16	24.29	22.99	25.18	23.17	25.35
Ab	36.05	31.31	36.47	33.51	38.67	40.62	32.92	35.88	23.19
An	12.34	10.57	6.71	10.49	9.95	3.02	7.76	6.28	11.74
Di	--	--	--	--	0.16	--	--	--	--
Hy	1.89	1.38	0.83	1.49	2.84	0.52	1.56	1.34	1.27
Mt	1.03	0.74	0.53	0.87	1.29	0.34	0.76	0.79	0.63
Ilm	0.57	0.38	0.23	0.46	0.78	0.08	0.42	0.42	0.32
Ap	0.23	0.14	0.28	0.12	0.46	0.23	0.19	0.39	0.09

Rare Earth Elements in ppm: ICP analyses.

La	--	--	--	32.53	76.1	--	33.83	--	--
Ce	--	--	--	46.78	145.37	--	52.82	--	--
Pr	--	--	--	7.38	15.31	--	6.93	--	--
Nd	--	--	--	20.39	51.42	--	22.38	--	--
Sm	--	--	--	2.93	6.93	--	3.66	--	--
Eu	--	--	--	0.86	1.25	--	0.65	--	--
Gd	--	--	--	1.75	4.3	--	2.49	--	--
Dy	--	--	--	0.92	2.09	--	1.34	--	--
Ho	--	--	--	0.16	0.39	--	0.2	--	--
Er	--	--	--	0.56	1.0	--	0.56	--	--
Yb	--	--	--	0.4	0.69	--	0.32	--	--
Lu	--	--	--	0.06	0.13	--	0.05	--	--

Baltoro granites and Broad Peak porphyries (R-6 to R-12)

Rock no.	R91	R92	R93	R94	R95	R-6	R-9	R-10	R-12
Pellet	L7505	L7506	L7507	L7508	L7509	L8271	L8274	L8275	L8273
Type	Lcg Ap	Lcg Ap	Mzg	Mzg	Mzg	Porph	Porph	Porph	Porph
SiO2	71.4	73.1	68.3	68.5	68.7	59.9	62.5	61.9	63.2
TiO2	0.18	0.13	0.48	0.48	0.49	0.81	0.76	0.77	0.75
Al2O3	14.1	14.5	16.0	15.8	13.4	16.0	15.7	15.4	15.2
Fe2O3	1.3	1.0	2.4	2.7	2.4	6.4	5.9	5.6	5.6
MnO	0.03	0.03	0.06	0.06	0.05	0.10	0.10	0.10	0.10
MgO	0.2	0.1	0.6	0.5	0.6	2.9	2.7	2.8	2.6
CaO	1.6	1.8	2.9	2.5	2.6	5.2	5.5	4.3	5.0
Na2O	4.2	3.5	1.5	2.4	1.3	2.6	2.6	3.4	2.7
K2O	4.00	4.39	5.41	5.13	4.42	2.31	2.48	2.87	2.72
P2O5	0.12	0.03	0.16	0.17	0.17	0.21	0.20	0.20	0.20
LOI	0.44	0.43	0.20	0.20	4.77	2.74	1.26	2.47	1.48
Total	97.48	98.99	98.03	98.47	98.81	99.33	99.64	99.80	99.51
Trace elements in parts per million									
Rb	135.5	127.0	104.0	133.4	87.4	97.0	109.7	91.5	100.6
Ba	1030.3	1206.5	315.3	838.1	358.8	650.8	684.7	897.8	636.2
Th	10.5	7.5	27.6	15.6	21.8	15.9	18.9	17.6	13.7
Pb	30.7	33.0	27.1	29.9	20.1	na	na	na	na
Nb	7.2	5.1	12.3	14.6	12.9	14.8	15.1	16.2	14.5
La	13.2	9.5	33.8	26.0	39.6	33.2	39.0	38.0	38.5
Ce	23.9	14.4	63.5	51.6	76.8	72.6	84.4	79.7	77.4
Sr	386.6	455.0	812.3	677.4	718.9	478.3	405.6	456.8	375.9
Nd	9.4	4.0	26.6	21.4	32.6	32.9	35.8	35.1	34.7
Zr	88.2	74.2	221.5	194.4	214.5	225.6	240.3	234.2	227.0
Y	7.7	5.6	9.3	15.4	12.4	25.3	27.5	27.7	25.8
V	8.1	5.4	40.2	33.9	39.8	114.9	110.6	106.0	105.9
Cr	12.7	6.9	12.6	10.5	13.3	72.5	64.7	72.0	71.6
Ni	0.5	0.9	3.9	3.4	3.7	13.0	12.1	13.2	11.4
Cu	8.4	6.0	8.2	7.9	7.0	na	na	na	na
Zn	20.9	24.7	63.2	53.2	45.2	99.5	69.3	71.2	69.7
Ga	13.7	14.3	22.0	22.2	20.3	19.0	17.9	18.6	17.0
Rb/Sr	0.4	0.3	0.1	0.2	0.1	0.2	0.3	0.2	0.3
La/Y	1.7	1.7	3.6	1.7	3.2	1.3	1.4	1.4	1.5
C.I.P.W. norms with calculated FeO/Fe2O3 ratio (Ferat)									
Ferat	0.64	0.62	0.53	0.57	0.52	0.77	0.79	0.77	0.76
Qtz	28.29	31.84	31.73	28.37	39.79	20.27	22.07	18.01	23.00
Cor	0.34	0.81	2.80	2.14	2.43	0.29	--	--	--
Or	23.76	26.06	32.03	30.38	27.42	14.01	14.83	17.37	16.31
Ab	35.54	29.79	12.61	20.65	11.25	22.59	22.51	29.36	22.76
An	7.00	8.78	13.29	11.29	12.12	25.20	23.90	18.70	21.83
Di	--	--	--	--	--	--	1.83	1.58	1.62
Hy	1.14	0.81	2.98	2.86	3.01	10.53	8.63	9.04	8.40
Mt	0.70	0.52	1.14	1.31	1.17	3.94	3.60	3.43	3.34
Ilm	0.34	0.25	0.91	0.91	0.97	1.58	1.46	1.50	1.44
Ap	0.28	0.07	0.37	0.39	0.42	0.51	0.46	0.46	0.46
Rare Earth Elements in ppm: INAA analysis.									
La	25.6	--	--	--	67.8	--	--	--	--
Ce	60.2	--	--	--	161.0	--	--	--	--
Nd	21.6	--	--	--	59.8	--	--	--	--
Sm	3.15	--	--	--	8.21	--	--	--	--
Eu	0.57	--	--	--	1.31	--	--	--	--
Tb	0.22	--	--	--	0.57	--	--	--	--
Yb	0.75	--	--	--	1.32	--	--	--	--
Lu	0.11	--	--	--	0.23	--	--	--	--

Broad Peak Porphyries (R-13,14,15), K2 Gneiss (R-53), MMC pegmatites (R-103,104) and Dassu Gneiss (R-109,110) and pegmatite (R-111).

Rock no.	R-13	R-14	R-15	R-53	R-103	R-104	R-109	R-110	R-111
Pellet	L8270	L8272	L8276	L8268	L8267	L8263	L8264	L8265	L8266
Type	Porph	Porph	Porph	Gneiss	Lcg Peg	Lcg Peg	Gneiss	Gneiss	Lcg Peg
SiO2	63.2	61.1	58.4	70.6	70.8	73.1	67.2	70.4	77.0
TiO2	0.74	0.77	0.77	0.28	0.01	0.17	0.58	0.30	0.02
Al2O3	15.7	15.0	15.3	16.2	14.8	14.9	16.4	16.1	13.4
Fe2O3	5.6	6.7	6.2	2.2	1.6	1.2	3.9	2.1	0.1
MnO	0.09	0.10	0.09	0.06	0.24	0.02	0.02	0.01	0.00
MgO	2.8	4.0	2.9	0.4	0.0	0.3	1.1	0.5	0.1
CaO	4.9	3.9	4.9	2.1	2.1	2.8	0.8	1.0	2.1
Na2O	3.0	2.2	2.1	3.8	3.1	1.1	5.8	6.2	0.6
K2O	2.39	2.18	3.30	3.76	4.07	5.25	1.94	2.30	5.03
P2O5	0.20	0.19	0.21	0.13	0.02	0.01	0.36	0.35	0.04
LOI	1.41	2.74	5.38	0.21	0.13	0.33	0.52	0.47	0.33
Total	100.06	98.93	99.46	99.77	96.81	99.01	98.60	99.71	98.73
Trace elements in parts per million									
Rb	133.0	86.3	73.4	181.9	73.0	43.6	380.5	329.6	38.9
Ba	696.8	549.5	599.3	624.8	395.1	215.6	377.7	488.3	14.5
Th	18.5	17.0	13.8	19.0	38.0	3.0	173.9	99.6	9.8
Nb	14.7	14.9	14.0	16.9	1.9	7.0	10.8	5.7	3.8
La	39.1	33.3	36.1	24.0	4.6	3.6	77.7	47.4	11.0
Ce	81.5	68.8	74.0	47.2	9.5	3.6	217.9	133.4	18.6
Sr	385.0	315.3	337.7	209.9	237.2	432.6	85.7	112.2	80.0
Nd	35.1	31.1	32.9	20.6	4.3	3.1	121.6	75.0	9.8
Zr	231.9	236.7	214.9	120.9	113.0	13.6	357.7	214.5	2.2
Y	26.7	26.1	24.4	11.4	64.8	0.7	23.5	17.1	28.5
V	103.5	104.4	118.3	25.3	0.2	15.2	34.0	16.5	0.0
Cr	78.3	76.8	72.8	7.0	0.0	5.7	20.9	12.3	2.9
Ni	12.6	12.5	11.5	3.5	2.8	1.2	12.5	6.7	1.0
Zn	68.4	90.7	76.0	44.5	5.7	18.0	95.3	50.5	4.1
Ga	18.1	17.8	17.9	15.7	16.1	14.0	27.9	18.3	19.5
Rb/Sr	0.3	0.3	0.2	0.9	0.3	0.1	4.4	2.9	0.5
La/Y	1.5	1.3	1.5	2.1	0.1	5.1	3.3	2.8	0.4
C.I.P.W. norms with calculated FeO/Fe2O3 ratio (Ferat)									
Ferat	0.79	0.65	0.72	0.64	0.60	0.52	0.69	0.75	0.46
Qtz	21.70	24.83	18.95	29.05	32.04	40.07	23.16	23.26	49.90
Cor	--	2.29	--	2.50	1.47	2.40	4.20	2.42	3.30
Or	14.30	13.24	20.63	22.28	24.11	31.14	11.52	13.65	29.84
Ab	25.98	19.55	18.96	31.99	26.06	9.31	49.08	52.89	5.25
An	22.57	18.78	23.77	9.42	10.44	13.68	1.67	2.62	10.01
Di	0.82	--	0.20	--	--	--	--	--	--
Hy	9.04	14.14	10.75	2.40	1.70	1.46	4.64	2.14	0.24
Mt	3.43	3.68	3.74	1.16	0.82	0.54	2.15	1.23	0.06
Ilm	1.42	1.50	1.54	0.53	0.02	0.32	1.10	0.57	0.04
Ap	0.46	0.46	0.51	0.30	0.05	0.02	0.83	0.81	0.09
Rare Earth Elements in ppm: INAA analysis.									
La	45.4	44.2	--	36.4	11.0	--	--	--	144.0
Ce	103.0	103.0	--	84.1	4.52	--	--	--	416.0
Nd	41.9	44.0	--	32.0	10.8	--	--	--	214.0
Sm	7.34	7.09	--	5.36	1.76	--	--	--	29.3
Eu	1.60	1.53	--	0.94	0.66	--	--	--	1.29
Tb	0.81	0.68	--	0.45	0.96	--	--	--	0.54
Yb	2.66	2.52	--	1.03	7.61	--	--	--	2.88
Lu	0.35	0.39	--	0.19	1.03	--	--	--	0.18

K2 Gneiss (GNEISS), Baltoro lamprophyres (R11,R74) and Khunjerab (K203-208)

Rock No.	GNEISS	R11	R74	K203	K204	K205	K206	K207	K208
Pellet	L8269	L10132	L10148	L9026	L9027	L9028	L9029	L9030	L9031
Type	Gneiss	Lamp	Lamp	Grd	Grd	Grd	Grd	Grd	Xen
SiO2	70.6	52.9	51.7	60.3	66.9	62.6	61.9	62.5	52.0
TiO2	0.33	1.62	1.13	0.73	0.57	0.72	0.67	0.71	1.17
Al2O3	15.4	10.3	11.2	16.2	15.9	16.1	16.1	16.2	18.5
Fe2O3	2.5	6.9	6.5	5.5	4.4	5.4	5.0	5.3	8.5
MnO	0.06	0.12	0.11	0.09	0.09	0.09	0.08	0.09	0.15
MgO	0.6	11.1	9.6	3.0	2.2	2.8	2.6	2.7	4.7
CaO	2.6	6.0	7.3	5.1	4.4	5.4	5.1	5.0	7.8
Na2O	3.7	1.1	1.9	2.9	2.9	2.9	2.7	2.5	2.9
K2O	3.72	7.95	8.57	3.54	3.94	3.44	3.46	3.47	2.48
P2O5	0.14	1.70	1.47	0.34	0.24	0.24	0.23	0.25	0.40
LOI	0.19	na	na	0.83	0.55	1.26	0.84	1.47	1.07
Total	99.76	99.69	99.48	98.45	102.00	100.90	98.60	100.27	99.63
Trace elements in parts per million									
Rb	160.6	358.4	659.7	126.7	145.2	117.8	131.3	123.4	119.2
Ba	808.4	3679.5	6502.1	963.2	828.3	837.3	867.9	761.8	997.5
Th	11.0	76.0	60.2	11.5	19.9	11.0	11.4	10.6	6.1
U	na	7.2	6.0	na	na	na	na	na	na
Pb	0.0	105.9	131.6	11.5	17.2	16.0	19.1	18.7	8.8
Nb	13.5	46.3	27.6	10.9	10.7	11.7	11.9	12.0	12.5
La	18.0	114.1	85.5	26.4	34.3	29.7	27.6	24.4	31.0
Ce	32.0	265.6	216.2	56.8	68.8	64.1	59.4	51.9	74.9
Sr	258.5	1221.4	917.8	529.3	430.5	494.3	511.1	502.2	635.5
Nd	13.0	135.6	121.5	27.6	28.8	30.9	26.7	27.8	42.0
Zr	132.6	692.3	526.3	176.3	161.7	164.6	200.3	201.5	176.3
Y	9.1	34.3	54.7	25.7	24.8	25.3	22.5	24.9	34.3
V	29.8	134.9	119.5	137.1	100.6	129.2	128.1	125.0	223.0
Cr	7.0	580.5	501.5	71.7	44.8	62.8	64.1	65.2	50.7
Ni	3.6	402.8	351.4	6.6	2.5	6.1	5.3	7.2	5.5
Cu	0.0	na	na	0.0	0.0	0.0	0.6	1.5	0.0
Zn	52.4	153.3	64.6	54.6	46.0	48.3	57.2	57.2	90.2
Ga	16.1	18.7	22.4	20.2	17.6	18.8	20.8	19.1	24.7
Rb/Sr	0.6	0.3	0.7	0.2	0.3	0.2	0.3	0.2	0.2
La/Y	2.0	3.3	1.6	1.0	1.4	1.2	1.2	1.0	0.9
C.I.P.W. norms with calculated FeO/Fe2O3 ratio (Ferat)									
Ferat	0.68	0.66	0.82	0.77	0.74	0.81	0.76	0.75	0.99
Qtz	28.25	--	--	15.05	22.31	17.71	18.48	19.70	3.03
Cor	0.89	--	--	--	--	--	--	--	--
Or	22.04	46.98	37.51	21.10	23.40	20.57	20.63	20.80	14.83
Ab	31.23	8.73	--	24.62	24.88	24.79	22.85	21.83	25.22
An	12.03	--	--	20.99	18.80	21.19	21.87	22.78	30.19
Lu	--	--	10.30	--	--	--	--	--	--
Ne	--	--	5.37	--	--	--	--	--	--
Ac	--	0.51	5.43	--	--	--	--	--	--
Di	--	14.67	21.04	1.79	1.13	3.46	1.71	0.55	5.11
Hy	2.85	4.32	--	9.08	7.04	7.60	7.97	9.20	11.77
Ol	--	13.57	12.62	--	--	--	--	--	--
Mt	1.37	3.46	1.29	3.29	2.55	3.33	2.97	3.15	5.86
Ilm	0.63	3.08	2.15	1.41	1.08	1.39	1.29	1.37	2.24
Ap	0.32	3.94	3.41	0.79	0.56	0.56	0.53	0.58	0.93
Rare Earth Elements in ppm: ICP analyses.									
La	--	--	--	40.0	--	--	--	--	40.2
Ce	--	--	--	80.75	--	--	--	--	91.38
Pr	--	--	--	9.39	--	--	--	--	11.41
Nd	--	--	--	35.0	--	--	--	--	46.47
Sm	--	--	--	6.06	--	--	--	--	8.67
Eu	--	--	--	1.48	--	--	--	--	2.03
Gd	--	--	--	6.5	--	--	--	--	8.26
Dy	--	--	--	4.56	--	--	--	--	6.37
Ho	--	--	--	0.89	--	--	--	--	1.23
Er	--	--	--	2.54	--	--	--	--	3.51
Yb	--	--	--	2.06	--	--	--	--	2.83
Lu	--	--	--	0.4	--	--	--	--	0.47

Khunjerab (K209-210), N. Sost Shap-type (K211), N. Sost (K212-215), S. Sost (K216-217).

Rock No.	K209	K210	K211	K212	K213	K214	K215	K216	K217
Pellet	L9032	L9033	L9034	L9035	L9036	L9037	L9038	L9039	L9040
Type	Mzg	Mzg	Mzg	Mzg	Mzg	QzDi	QzDi	Mzg	Mzg
SiO2	71.6	71.9	69.6	67.0	67.6	58.6	55.1	69.7	69.5
TiO2	0.26	0.26	0.35	0.39	0.41	0.79	0.90	0.29	0.33
Al2O3	13.8	13.6	14.2	15.1	15.3	16.0	15.9	14.3	14.8
Fe2O3	2.1	2.0	2.9	3.3	3.4	6.7	7.6	2.2	2.4
MnO	0.05	0.04	0.07	0.07	0.08	0.12	0.13	0.05	0.06
MgO	0.7	0.8	1.7	1.2	1.3	3.4	4.2	0.7	0.8
CaO	2.1	1.8	3.3	2.8	2.8	5.3	6.2	2.0	2.1
Na2O	3.1	3.3	3.4	4.3	3.8	3.5	3.4	3.5	4.6
K2O	4.64	4.55	4.82	4.17	4.10	3.29	3.40	4.80	4.80
P2O5	0.08	0.17	0.20	0.20	0.18	0.44	0.42	0.17	0.23
LOI	0.92	1.32	0.46	0.42	0.39	1.07	0.69	0.47	0.48
Total	99.31	99.68	101.01	98.95	99.34	99.22	97.99	98.13	100.27
Trace elements in parts per million									
Rb	182.8	168.1	278.0	159.7	167.2	136.1	133.1	280.6	286.9
Ba	565.4	548.0	768.4	1172.6	1201.3	1323.3	1373.0	667.8	757.4
Th	23.9	24.4	22.6	17.6	14.8	10.5	9.3	17.7	11.2
Pb	21.0	24.4	26.0	32.3	32.8	37.1	19.1	21.5	24.4
Nb	9.2	9.8	13.2	9.6	9.8	12.4	11.6	12.8	14.4
La	29.8	27.8	22.2	25.5	22.7	29.2	23.2	13.2	14.5
Ce	54.6	52.1	40.5	48.9	39.7	62.2	49.8	27.1	26.4
Sr	264.9	271.4	496.9	592.2	608.7	751.9	752.2	393.2	423.4
Nd	20.9	19.6	16.9	18.1	17.8	32.1	23.9	11.9	12.7
Zr	97.7	75.3	63.3	92.3	93.5	64.0	48.0	107.9	125.6
Y	22.1	17.6	16.9	16.5	16.9	29.8	25.0	13.6	15.4
V	37.9	37.2	51.4	65.2	66.7	167.6	221.2	37.5	42.3
Cr	36.9	29.1	62.4	31.7	48.1	58.0	67.2	35.6	30.3
Ni	0.3	1.8	11.5	8.3	8.2	13.5	15.0	5.5	7.0
Cu	0.0	0.0	9.6	4.9	11.2	24.4	20.8	0.0	0.0
Zn	27.6	26.3	33.5	46.2	45.7	78.4	80.4	31.1	33.9
Ga	14.8	14.7	16.8	16.8	17.5	18.6	19.5	16.8	18.2
Rb/Sr	0.7	0.6	0.6	0.3	0.3	0.2	0.2	0.7	0.7
La/Y	1.3	1.6	1.3	1.5	1.3	1.0	0.9	1.0	0.9
C.I.P.W. norms with calculated FeO/Fe2O3 ratio (Ferat)									
Ferat	0.61	0.60	0.70	0.73	0.68	0.84	0.89	0.61	0.71
Qtz	30.07	30.64	23.18	18.61	21.85	10.25	4.83	25.93	19.43
Cor	0.02	0.39	--	--	0.05	--	--	0.24	--
Or	27.66	27.24	28.60	24.76	24.35	19.68	20.21	28.49	28.49
Ab	26.66	28.09	28.69	36.73	31.99	30.04	28.86	29.45	39.26
An	9.89	7.97	9.52	9.63	12.71	18.47	18.42	8.66	5.60
Di	--	--	4.38	2.48	--	4.25	7.90	--	2.94
Hy	3.12	3.27	3.72	3.47	5.11	9.39	9.69	3.14	1.86
Mt	1.08	1.05	1.63	1.88	1.89	4.22	4.96	1.14	1.39
Ilm	0.49	0.49	0.66	0.74	0.78	1.52	1.73	0.55	0.63
Ap	0.19	0.39	0.46	0.46	0.42	1.02	0.97	0.39	0.53
Rare Earth Elements in ppm: ICP analyses.									
La	--	37.5	--	--	48.2	58.4	--	--	--
Ce	--	68.1	--	--	85.9	112.0	--	--	--
Pr	--	6.89	--	--	9.33	12.39	--	--	--
Nd	--	23.0	--	--	31.6	45.74	--	--	--
Sm	--	3.76	--	--	4.97	7.91	--	--	--
Eu	--	0.71	--	--	1.26	1.83	--	--	--
Gd	--	3.44	--	--	4.99	7.1	--	--	--
Dy	--	2.8	--	--	3.21	5.28	--	--	--
Ho	--	0.55	--	--	0.62	1.01	--	--	--
Er	--	1.65	--	--	1.89	3.23	--	--	--
Yb	--	1.56	--	--	1.46	2.38	--	--	--
Lu	--	0.28	--	--	0.33	0.39	--	--	--

Hunza sillimanite-zone dykes, Hassanabad (SLV4) and Ultar (SLV9 & 12) sheets.

Rock no.	SLV3	SLV4	SLV5	SLV7	SLV8	SLV9	SLV12	SLV13	SLV14
Pellet	L9452	L9453	L9454	L9455	L9456	L9457	L9458	L9459	L9460
Type	2MG Ap	Mzg	2MG Ap	Grd Ap	Mzg Ap	Grd	Grd	Grd Ap	Grd Ap
SiO2	71.3	71.8	74.1	69.7	72.1	67.2	69.1	70.4	70.7
TiO2	0.25	0.35	0.15	0.25	0.25	0.55	0.58	0.54	0.34
Al2O3	14.2	14.7	14.0	14.7	15.0	15.4	14.7	14.8	15.1
Fe2O3	1.6	1.8	0.9	1.3	2.1	4.3	4.1	2.5	1.8
MnO	0.03	0.02	0.02	0.01	0.03	0.08	0.06	0.03	0.02
MgO	0.2	0.4	0.1	0.4	0.4	1.7	1.6	0.6	0.5
CaO	1.3	1.8	1.2	1.8	1.6	3.9	2.6	1.7	2.0
Na2O	6.4	3.9	1.4	3.7	4.7	3.1	2.7	3.6	3.9
K2O	5.11	4.84	5.62	4.91	3.90	3.56	4.47	5.12	4.58
P2O5	0.14	0.07	0.11	0.15	0.09	0.23	0.16	0.15	0.18
LOI	0.49	0.43	0.59	0.35	0.49	0.30	0.36	0.50	0.68
Total	101.04	100.10	98.33	97.37	100.54	100.40	100.36	99.96	99.73

Trace elements in parts per million

Rb	197.6	174.8	210.1	182.0	175.6	131.6	158.6	139.8	172.3
Ba	1013.0	1180.1	498.8	1085.7	608.8	667.2	657.4	1576.0	1175.1
Th	22.5	27.5	12.9	7.3	13.0	23.2	19.9	28.3	16.2
Pb	46.4	32.9	59.0	35.6	55.0	35.4	43.7	28.5	33.0
Nb	12.2	5.9	8.0	2.2	16.7	14.8	15.7	12.2	4.6
La	36.2	35.9	11.2	15.5	20.0	24.5	19.1	53.6	27.8
Ce	71.2	58.4	21.2	25.3	38.1	54.1	38.6	104.0	47.3
Sr	221.0	354.8	192.0	311.1	163.7	280.1	214.1	438.8	385.3
Nd	23.4	20.8	8.6	8.8	13.2	23.7	18.3	33.8	14.1
Zr	164.5	208.2	41.9	127.1	145.0	152.9	178.5	273.7	189.6
Y	14.2	7.7	14.1	3.6	18.7	45.1	25.3	8.1	7.9
V	12.5	26.9	3.3	46.5	24.4	82.4	82.6	35.4	31.7
Cr	5.6	15.7	4.0	9.9	12.3	42.7	41.8	12.4	14.0
Ni	1.1	0.2	1.1	0.0	3.5	7.5	13.3	2.7	0.3
Cu	2.2	0.8	1.0	41.6	0.0	0.0	0.0	4.5	6.6
Zn	41.6	49.8	24.9	47.3	56.1	53.8	45.8	69.2	47.5
Ga	22.3	20.5	18.5	20.1	18.5	14.7	18.5	20.7	19.3
Rb/Sr	0.9	0.5	1.1	0.6	1.1	0.5	0.7	0.3	0.4
La/Y	2.5	4.7	0.8	4.3	1.1	0.5	0.8	6.6	3.5

C.I.P.W. norms with calculated FeO/Fe2O3 ratio (Ferat).

Ferat	0.80	0.63	0.45	0.62	0.68	0.72	0.60	0.61	0.65
Qtz	17.22	26.30	41.89	25.01	25.74	24.21	27.94	25.18	25.94
Cor	--	0.12	3.78	0.32	0.40	--	1.08	0.49	0.61
Or	30.38	28.72	33.39	29.14	23.17	21.10	26.53	30.44	27.24
Ab	44.70	32.92	12.19	31.73	39.94	26.49	22.68	30.72	33.26
An	--	8.27	5.09	8.05	7.15	17.57	12.00	7.65	8.60
Ac	1.93	--	--	--	--	--	--	--	--
Ns	1.79	--	--	--	--	--	--	--	--
Di	3.55	--	--	--	--	0.34	--	--	--
Wol	0.60	--	--	--	--	--	--	--	--
Hy	--	1.90	0.98	1.52	2.16	6.37	6.30	2.67	1.96
Mt	--	0.93	0.40	0.69	1.16	2.49	2.09	1.28	0.95
Ilm	0.47	0.66	0.28	0.47	0.47	1.04	1.10	1.03	0.65
Ap	0.32	0.16	0.25	0.35	0.21	0.53	0.37	0.35	0.42

Rare Earth Elements in ppm: ICP analyses.

La	--	--	21.5	--	--	--	--	--	45.1
Ce	--	--	40.65	--	--	--	--	--	76.5
Pr	--	--	4.44	--	--	--	--	--	7.58
Nd	--	--	16.0	--	--	--	--	--	24.8
Sm	--	--	3.24	--	--	--	--	--	2.96
Eu	--	--	0.73	--	--	--	--	--	0.74
Gd	--	--	3.45	--	--	--	--	--	2.09
Dy	--	--	2.27	--	--	--	--	--	1.05
Ho	--	--	0.34	--	--	--	--	--	0.19
Er	--	--	0.81	--	--	--	--	--	0.6
Yb	--	--	0.4	--	--	--	--	--	0.22
Lu	--	--	0.08	--	--	--	--	--	0.07

Hunza sillimanite-zone dykes, Ultar (SLV 15 & 17) and Aliabad (SLV21) sheets.

Rock no.	SLV15	SLV17	SLV18	SLV19	SLV20	SLV21	SLV23	SLV24	SLV25
Pellet	L9461	L9518	L9519	L9520	L9521	L9522	L9524	L9525	L9526
Type	Mz.DQ	Mz.DQ	Mzg Ap	Lcg Pg	Lcg Pg	Lcg	Mzg Ap	Mzg Ap	Mzg
SiO2	57.6	59.1	73.1	77.8	74.6	72.3	73.5	71.5	76.8
TiO2	0.84	0.92	0.14	0.02	0.02	0.18	0.17	0.21	0.02
Al2O3	16.6	16.3	14.8	13.6	14.9	15.0	14.5	14.5	13.0
Fe2O3	7.1	7.2	0.8	0.5	0.5	1.7	1.1	1.3	0.4
MnO	0.13	0.13	0.01	0.07	0.06	0.06	0.02	0.02	0.01
MgO	4.1	3.9	0.2	0.0	0.0	0.2	0.2	0.2	0.0
CaO	6.9	6.6	1.6	1.1	0.9	1.9	1.4	1.3	1.4
Na2O	3.2	3.0	3.7	5.2	4.6	4.1	3.7	3.3	4.5
K2O	2.61	2.54	4.77	1.65	4.59	3.82	5.29	6.55	3.25
P2O5	0.23	0.25	0.11	0.09	0.04	0.21	0.02	0.16	0.12
LOI	0.39	0.43	0.85	0.50	0.43	0.31	0.54	0.33	0.18
Total	99.70	100.36	100.05	100.56	100.63	99.77	100.53	99.37	99.71
Trace elements in parts per million									
Rb	99.5	112.1	258.1	89.1	168.4	161.9	174.3	197.9	106.2
Ba	670.6	607.5	600.7	58.2	177.8	529.6	958.5	949.3	100.1
Th	5.0	10.8	9.0	5.7	2.7	9.6	18.9	20.3	0.0
Pb	19.0	16.3	62.4	50.0	82.0	51.4	46.9	47.9	41.4
Nb	12.6	16.0	5.6	8.4	5.6	11.3	7.1	7.5	3.4
La	18.8	24.3	10.1	2.0	2.3	18.0	31.9	29.7	2.9
Ce	39.8	49.5	16.7	2.0	3.6	33.1	52.6	53.4	0.7
Sr	415.0	373.3	304.0	71.7	85.9	229.0	198.1	227.6	99.9
Nd	15.9	20.1	6.3	1.2	2.3	13.4	17.5	17.5	1.7
Zr	169.8	160.2	76.5	28.3	17.0	90.9	113.1	128.3	0.0
Y	23.8	27.3	7.1	11.0	16.8	17.1	8.7	11.7	5.3
V	152.9	156.2	6.9	0.6	0.0	10.6	6.8	9.0	0.0
Cr	87.2	80.1	19.8	2.9	9.3	8.1	10.3	4.6	8.6
Ni	14.7	12.7	2.5	0.0	0.0	1.1	1.9	0.0	0.1
Cu	9.2	10.1	3.2	2.3	2.4	1.3	0.6	3.0	4.4
Zn	73.4	74.2	31.0	8.4	5.4	39.0	27.7	32.8	12.3
Ga	19.8	19.6	21.3	17.1	15.8	17.2	20.9	17.8	14.9
Rb/Sr	0.2	0.3	0.8	1.2	2.0	0.7	0.9	0.9	1.1
La/Y	0.8	0.9	1.4	0.2	0.1	1.1	3.7	2.5	0.5
C.I.P.W. norms with calculated FeO/Fe2O3 ratio (Ferat).									
Ferat	0.95	0.91	0.62	0.71	0.64	0.66	0.61	0.56	0.68
Qtz	9.84	13.34	30.02	39.26	28.03	29.81	28.13	24.50	35.33
Cor	--	--	0.86	1.54	0.68	1.25	0.17	--	--
Or	15.48	15.07	28.43	9.81	27.24	22.63	31.44	38.83	19.27
Ab	26.99	25.30	31.56	44.09	39.52	34.53	31.82	27.67	38.42
An	23.49	23.75	7.32	4.92	4.30	8.10	6.76	5.49	5.61
Di	7.51	6.11	--	--	--	--	--	0.09	0.50
Wol	--	--	--	--	--	--	--	--	0.04
Hy	9.09	9.38	0.89	0.41	0.44	1.62	1.21	1.28	--
Mt	4.78	4.69	0.41	0.26	0.25	0.90	0.56	0.65	0.21
Ilm	1.60	1.75	0.27	0.04	0.04	0.34	0.32	0.40	0.04
Ap	0.53	0.58	0.25	0.21	0.09	0.49	0.05	0.37	0.28
Rare Earth Elements in ppm: ICP analyses.									
La	31.5	--	--	4.3	2.8	--	--	55.9	--
Ce	63.8	--	--	8.2	5.63	--	--	100.4	--
Pr	7.37	--	--	0.94	0.87	--	--	9.83	--
Nd	28.17	--	--	3.0	2.35	--	--	32.5	--
Sm	4.87	--	--	0.63	0.62	--	--	4.81	--
Eu	1.3	--	--	0.27	0.39	--	--	0.81	--
Gd	5.49	--	--	0.89	1.14	--	--	3.38	--
Dy	4.3	--	--	0.96	1.84	--	--	1.96	--
Ho	0.86	--	--	0.19	0.34	--	--	0.34	--
Er	2.52	--	--	0.98	1.42	--	--	0.82	--
Yb	2.15	--	--	1.1	1.16	--	--	0.46	--
Lu	0.35	--	--	0.18	0.22	--	--	0.08	--

Hunza sillimanite-zone intrusions and augen gneiss (SLV29)

Rock no.	SLV26	SLV27	SLV28	SLV29	SLV30	SLV31	SLV32	SLV33	SLV34
Pellet	L9527	L9528	L9529	L9530	L9531	L9639	L9640	L9641	L9642
Type	Lcg Pg	Mzg Ap	Mzg Ap	Aug.Gn	Lcg Pg	Mzg Ap	2MG Ap	2MG Ap	2MG Ap
SiO2	72.9	71.9	71.0	68.5	71.7	71.4	70.8	72.1	73.1
TiO2	0.09	0.20	0.31	0.42	0.10	0.12	0.26	0.19	0.14
Al2O3	13.3	14.9	14.6	16.8	14.8	14.3	14.6	14.5	14.7
Fe2O3	1.2	1.0	2.3	2.6	0.6	0.8	1.7	1.4	0.9
MnO	0.05	0.02	0.03	0.05	0.01	0.02	0.02	0.02	0.01
MgO	0.1	0.2	0.4	0.9	0.1	0.1	0.4	0.1	0.1
CaO	0.8	2.0	1.8	3.7	1.2	1.4	1.6	1.4	1.2
Na2O	3.4	4.6	4.5	5.1	5.9	4.3	3.8	3.5	3.0
K2O	5.75	3.69	3.12	1.28	5.53	4.49	4.61	5.11	5.22
P2O5	0.06	0.06	0.08	0.04	0.16	0.11	0.19	0.09	0.08
LOI	0.31	0.56	0.71	0.34	0.85	0.18	0.44	0.45	0.68
Total	97.94	99.20	98.93	99.73	100.98	97.12	98.43	98.93	99.10
Trace elements in parts per million									
Rb	203.6	138.5	151.0	91.8	173.8	241.2	176.9	202.1	193.3
Ba	395.9	1028.1	548.1	463.8	635.3	635.3	970.2	595.9	500.7
Th	10.1	6.6	18.4	8.1	9.6	13.2	18.7	18.0	10.7
Pb	60.8	38.1	41.0	19.7	77.2	61.2	42.9	64.2	61.6
Nb	5.9	3.6	12.6	16.7	7.4	4.4	10.9	10.7	8.3
La	16.7	11.4	30.1	17.2	10.8	10.8	31.2	21.4	12.5
Ce	29.1	19.5	46.9	28.4	13.0	13.0	53.9	36.1	19.4
Sr	157.6	603.3	189.7	481.6	201.2	218.5	260.4	198.5	169.3
Nd	11.8	7.0	15.1	10.2	7.4	7.4	17.9	13.7	7.8
Zr	27.9	87.5	186.3	119.4	21.4	74.5	200.2	108.7	44.7
Y	18.5	4.9	12.3	12.0	14.5	6.6	14.0	11.1	10.9
V	0.0	8.4	25.1	39.9	3.6	6.3	23.2	11.1	3.4
Cr	2.0	0.9	8.0	6.2	6.8	3.8	13.5	10.5	4.2
Ni	0.9	0.1	3.4	4.6	0.4	4.1	0.1	0.7	0.0
Cu	0.7	5.0	2.2	6.1	2.6	3.6	1.6	0.0	0.8
Zn	25.8	40.6	63.2	42.2	16.2	34.6	46.3	37.0	23.5
Ga	13.2	20.4	18.6	18.9	22.3	20.4	21.0	21.1	20.2
Rb/Sr	1.3	0.2	0.8	0.2	0.9	1.1	0.7	1.0	1.1
La/Y	0.9	2.3	2.4	1.4	0.7	1.6	2.2	1.9	1.1
C.I.P.W. norms with calculated FeO/Fe2O3 ratio (Ferat).									
Ferat	0.54	0.71	0.68	0.88	0.75	0.63	0.62	0.58	0.54
Qtz	29.08	26.40	28.25	24.50	17.26	26.27	26.99	28.80	33.26
Cor	0.19	--	0.78	0.40	--	0.15	0.77	0.92	2.20
Or	34.10	21.93	18.56	7.56	32.98	26.59	27.36	30.32	31.09
Ab	28.86	39.52	38.50	43.50	45.85	36.47	32.66	30.13	25.39
An	3.63	9.05	8.36	17.99	--	6.08	6.84	6.21	5.38
Ac	--	--	--	--	0.71	--	--	--	--
Ns	--	--	--	--	0.96	--	--	--	--
Di	--	0.27	--	--	1.23	--	--	--	--
Wol	--	--	--	--	1.41	--	--	--	--
Hy	1.15	0.89	2.29	3.04	--	0.59	1.84	1.20	0.84
Mt	0.55	0.57	1.28	1.70	--	0.42	0.90	0.71	0.43
Ilm	0.17	0.38	0.59	0.80	0.19	0.23	0.49	0.36	0.27
Ap	0.14	0.14	0.19	0.09	0.37	0.25	0.44	0.21	0.19
Rare Earth Elements in ppm: ICP analyses.									
La	--	--	--	--	--	--	34.1	32.1	16.5
Ce	--	--	--	--	--	--	60.6	56.55	31.1
Pr	--	--	--	--	--	--	6.43	5.69	3.31
Nd	--	--	--	--	--	--	20.15	19.42	11.92
Sm	--	--	--	--	--	--	2.87	3.4	2.28
Eu	--	--	--	--	--	--	0.67	0.69	0.66
Gd	--	--	--	--	--	--	3.48	3.02	2.23
Dy	--	--	--	--	--	--	1.85	1.7	1.34
Ho	--	--	--	--	--	--	0.29	0.25	0.19
Er	--	--	--	--	--	--	0.85	0.71	0.5
Yb	--	--	--	--	--	--	0.35	0.27	0.22
Lu	--	--	--	--	--	--	0.1	0.05	0.04

Bar (3SLV35 & 36), Aliabad (9SLV35 & 36), and Nagar (DPHUN2 & NSG1) intrusions, and Hunza sillimanite-zone dykes (DPHUN1,3 & 4).

Rock no.	3SLV35	3SLV36	9SLV35	9SLV36	DPHUN1	DPHUN2	DPHUN3	DPHUN4	NSG1
Pellet	L9643	L9644	L9645	L9646	L9022	L9023	L9024	L9025	L9425
Type	Mzg	Mzg	Lcg	Lcg	Mzg Ap	Lcg	Lcg Pg	Lcg Pg	Lcg
SiO2	67.2	70.5	72.4	72.3	67.6	74.2	73.1	73.2	73.7
TiO2	0.53	0.46	0.22	0.21	0.36	0.01	0.08	0.03	0.01
Al2O3	15.8	14.8	14.7	14.7	15.8	14.4	14.0	14.5	14.3
Fe2O3	3.7	3.1	2.1	1.8	3.1	0.8	1.2	0.8	0.8
MnO	0.07	0.05	0.07	0.06	0.04	0.09	0.03	0.12	0.09
MgO	1.0	0.8	0.2	0.3	0.5	0.0	0.0	0.0	0.0
CaO	2.8	2.8	1.9	1.7	2.4	1.1	0.9	0.6	1.1
Na2O	3.7	3.3	3.9	3.7	5.8	4.3	2.8	3.1	4.1
K2O	4.36	3.88	3.77	3.87	1.47	4.01	5.56	6.51	4.00
P2O5	0.20	0.16	0.15	0.13	0.22	0.03	0.27	0.20	0.12
LOI	0.52	0.26	0.40	0.40	0.38	0.43	0.53	0.43	0.47
Total	99.95	100.17	99.71	99.21	97.76	99.41	98.44	99.47	98.78
Trace elements in parts per million									
Rb	171.5	137.9	178.9	160.5	121.7	138.7	230.4	251.0	131.8
Ba	823.7	654.0	458.6	433.2	71.2	52.9	60.4	138.3	102.1
Th	12.0	11.6	12.8	10.3	12.1	5.4	2.2	1.9	4.9
Pb	26.8	25.2	37.5	46.5	23.2	29.8	34.8	53.0	37.2
Nb	20.6	14.2	16.5	12.5	24.5	20.3	18.5	3.5	22.3
La	35.1	22.1	20.6	22.7	27.2	7.3	3.8	1.4	5.1
Ce	67.7	42.8	37.1	41.0	48.6	16.6	7.7	3.8	10.7
Sr	291.8	308.9	223.6	203.9	173.2	89.9	65.9	61.5	95.1
Nd	24.8	16.0	13.9	16.2	17.6	8.4	4.9	1.9	6.5
Zr	222.4	207.2	111.3	103.2	247.0	19.8	42.4	36.9	32.0
Y	14.1	10.6	15.3	17.5	22.6	13.8	23.2	9.0	27.2
V	47.7	38.3	15.3	13.9	30.3	0.2	0.0	0.0	0.0
Cr	6.8	11.9	1.3	1.1	18.5	5.0	9.1	0.9	5.8
Ni	3.7	1.6	0.1	0.3	2.1	0.8	0.9	0.8	0.4
Cu	6.2	6.0	0.1	2.0	0.0	0.0	0.0	0.0	0.5
Zn	75.3	52.9	49.1	44.8	90.9	34.7	32.0	10.1	21.0
Ga	19.7	17.6	19.5	18.8	22.4	18.8	18.6	14.7	22.6
Rb/Sr	0.6	0.4	0.8	0.8	0.7	1.5	3.5	4.1	1.4
La/Y	2.5	2.1	1.3	1.3	1.2	0.5	0.2	0.2	0.2
C.I.P.W. norms with calculated FeO/Fe2O3 ratio (Ferat).									
Ferat	0.68	0.66	0.64	0.62	0.82	0.63	0.51	0.51	0.61
Qtz	21.48	29.05	31.10	31.66	22.25	31.26	33.92	29.37	32.25
Cor	0.46	0.46	1.23	1.53	0.82	1.03	2.37	1.86	1.57
Or	25.88	22.99	22.40	22.99	8.75	23.82	33.04	38.65	23.76
Ab	31.31	28.09	32.83	31.56	49.42	36.64	24.20	26.15	35.12
An	12.68	12.94	8.25	7.83	10.57	5.36	2.50	1.57	4.52
Hy	4.40	3.54	1.92	1.87	2.68	0.75	1.00	0.92	0.78
Mt	2.05	1.67	1.10	0.95	1.90	0.41	0.55	0.39	0.42
Ilm	1.01	0.87	0.42	0.40	0.68	0.02	0.15	0.06	0.02
Ap	0.46	0.37	0.35	0.30	0.51	0.07	0.63	0.46	0.28
Rare Earth Elements in ppm: ICP analyses.									
La	--	47.0	--	29.8	--	--	--	--	8.2
Ce	--	87.33	--	55.85	--	--	--	--	14.6
Pr	--	8.83	--	6.19	--	--	--	--	1.67
Nd	--	31.13	--	21.1	--	--	--	--	6.45
Sm	--	4.7	--	3.52	--	--	--	--	1.79
Eu	--	1.01	--	0.76	--	--	--	--	0.26
Gd	--	3.7	--	4.17	--	--	--	--	2.91
Dy	--	1.96	--	2.87	--	--	--	--	4.37
Ho	--	0.34	--	0.54	--	--	--	--	0.82
Er	--	0.89	--	1.71	--	--	--	--	1.72
Yb	--	0.51	--	1.34	--	--	--	--	1.5
Lu	--	0.09	--	0.25	--	--	--	--	0.19

Nagar Sheet (NSG2 - NSG5) and Sumayar Pluton (SG1 - SG5).

Rock no.	NSG2	NSG3	NSG4	NSG5	SG1	SG2	SG3	SG4	SG5
Pellet	L9426	L9427	L9428	L9429	L9430	L9431	L9432	L9433	L9434
Type	Lcg	Lcg	Lcg	Lcg	Lcg	Lcg	Lcg	Lcg	Lcg
SiO2	72.8	75.0	72.4	73.6	74.0	74.3	73.5	74.2	74.4
TiO2	0.01	0.02	0.01	0.02	0.06	0.07	0.05	0.03	0.04
Al2O3	14.1	14.8	14.1	14.2	14.9	14.8	14.5	14.8	15.1
Fe2O3	0.9	0.9	0.8	0.9	0.9	0.9	0.8	0.7	0.6
MnO	0.15	0.12	0.09	0.12	0.03	0.03	0.03	0.04	0.03
MgO	0.0	0.0	0.0	0.0	0.0	0.0	0.1	0.0	0.0
CaO	0.9	1.2	1.1	1.1	0.8	0.8	0.8	0.8	0.7
Na2O	3.3	4.3	3.7	4.1	3.9	4.2	4.3	4.7	4.7
K2O	5.78	4.03	4.05	4.15	4.79	4.78	4.60	4.16	4.35
P2O5	0.04	0.12	0.11	0.04	0.19	0.09	0.08	0.03	0.01
LOI	0.35	0.41	0.38	0.36	0.52	0.52	0.57	0.51	0.44
Total	98.30	100.85	96.71	98.67	100.11	100.45	99.27	100.03	100.40
Trace elements in parts per million									
Rb	163.5	132.9	131.8	136.4	424.2	383.2	470.3	409.8	462.1
Ba	165.4	151.4	58.7	164.0	97.9	95.0	70.8	28.3	48.2
Th	4.4	9.6	5.8	6.7	12.7	12.7	10.8	7.7	9.8
Pb	56.9	44.0	33.6	47.6	56.2	60.0	53.7	56.4	54.2
Nb	4.1	19.9	25.3	18.7	18.0	16.4	19.4	20.2	17.2
La	3.2	7.6	7.2	6.9	9.8	9.6	7.5	4.8	6.9
Ce	6.6	15.7	12.3	13.7	17.8	18.0	13.1	10.5	13.1
Sr	117.0	108.1	76.9	109.9	39.7	41.4	32.5	22.2	27.2
Nd	3.8	8.1	7.3	7.3	7.6	9.4	6.9	5.8	6.4
Zr	21.3	17.6	20.2	18.7	38.3	40.4	31.6	25.3	26.8
Y	30.1	14.5	14.4	12.7	22.5	24.2	24.6	17.7	23.6
V	0.0	0.0	0.0	0.0	0.3	0.0	0.0	0.0	0.0
Cr	7.7	6.8	3.0	12.8	0.4	0.4	2.7	11.9	2.3
Ni	1.0	1.4	1.0	0.0	1.8	1.2	0.2	1.6	0.9
Cu	1.3	0.8	0.8	1.0	0.0	2.4	1.2	0.0	0.0
Zn	8.3	20.1	48.3	16.1	41.8	38.5	39.7	36.3	31.4
Ga	15.7	19.1	20.0	17.0	24.9	25.7	25.9	25.8	23.0
Rb/Sr	1.4	1.2	1.7	1.2	10.7	9.3	14.5	18.5	17.0
La/Y	0.1	0.5	0.5	0.5	0.4	0.4	0.3	0.3	0.3
C.I.P.W. norms with calculated FeO/Fe2O3 ratio (Ferat).									
Ferat	0.54	0.64	0.57	0.61	0.58	0.60	0.60	0.64	0.63
Qtz	29.20	32.15	33.28	31.12	31.30	30.16	29.30	29.27	28.61
Cor	0.85	1.53	1.99	1.02	2.18	1.49	1.30	1.25	1.33
Or	34.28	23.93	24.05	24.64	28.49	28.37	27.36	24.70	25.83
Ab	28.35	36.47	31.14	34.95	33.59	35.46	36.56	40.03	40.20
An	4.00	5.07	4.69	5.39	2.83	3.48	3.30	3.72	3.56
Hy	1.02	0.86	0.82	0.89	0.67	0.65	0.74	0.54	0.44
Mt	0.43	0.47	0.41	0.47	0.44	0.46	0.39	0.36	0.32
Ilm	0.02	0.04	0.02	0.04	0.11	0.13	0.09	0.06	0.08
Ap	0.09	0.28	0.25	0.09	0.44	0.21	0.19	0.07	0.02
Rare Earth Elements in ppm: ICP analyses.									
La	--	--	12.4	--	--	13.7	--	10.34	--
Ce	--	--	17.45	--	--	23.8	--	15.98	--
Pr	--	--	2.02	--	--	2.71	--	1.99	--
Nd	--	--	7.75	--	--	10.5	--	6.47	--
Sm	--	--	2.06	--	--	2.65	--	2.2	--
Eu	--	--	0.19	--	--	0.23	--	0.1	--
Gd	--	--	2.79	--	--	2.63	--	1.27	--
Dy	--	--	2.43	--	--	1.78	--	1.62	--
Ho	--	--	0.39	--	--	0.25	--	na	--
Er	--	--	0.75	--	--	0.61	--	0.8	--
Yb	--	--	0.7	--	--	0.34	--	0.82	--
Lu	--	--	0.11	--	--	0.05	--	0.1	--

Sumayar Pluton (SG6) and Hunza Plutonic Complex;
first season samples (all 95 ma phase).

Rock no.	SG6	1B1	1B2	1B4	1B6	2B8	2B11	3B13	3B16
Pellet	L9435	L8753	L8754	L8755	L9016	L8756	L8757	L8758	L8759
Type	Lcg	Grd	Mz.DQ	Grd	QzDi	Mz.DQ	Grd	Grd	Grd
SiO2	71.6	63.1	50.9	58.3	56.0	55.9	63.3	66.7	61.1
TiO2	0.02	0.66	1.07	0.70	0.98	0.72	0.70	0.56	0.72
Al2O3	15.4	15.7	17.1	15.3	17.1	14.1	15.5	15.8	15.9
Fe2O3	0.6	5.3	8.0	8.0	7.1	7.0	5.3	4.4	5.8
MnO	0.11	0.09	0.14	0.17	0.09	0.13	0.09	0.07	0.10
MgO	0.0	2.2	6.7	4.9	3.4	8.9	2.3	1.8	2.3
CaO	0.4	4.9	8.1	7.4	5.9	7.9	5.0	3.8	5.2
Na2O	4.9	2.8	2.8	2.6	3.3	2.2	2.6	3.0	2.8
K2O	4.95	3.20	2.13	1.91	1.11	1.74	2.82	2.89	2.69
P2O5	0.03	0.14	0.22	0.19	0.21	0.10	0.17	0.28	0.18
LOI	0.37	0.49	0.47	0.56	2.56	0.45	0.44	0.44	0.46
Total	98.44	98.54	97.63	100.02	97.72	99.15	98.14	99.68	97.26
Trace elements in parts per million									
Rb	697.4	116.7	92.3	69.6	57.8	69.5	113.9	118.1	108.3
Ba	21.0	644.9	761.4	978.0	314.4	249.9	632.9	615.1	639.9
Th	3.2	11.9	2.8	2.2	17.1	6.7	13.1	3.8	10.4
U	na	2.7	na	2.0	na	0.7	na	1.4	3.4
Pb	46.4	23.7	13.6	18.8	16.1	15.8	22.3	24.8	27.2
Nb	23.3	14.2	15.0	15.6	10.3	8.4	15.2	16.4	17.2
La	9.6	14.3	9.4	6.6	25.2	9.2	18.2	8.0	15.4
Ce	9.1	33.0	30.3	26.7	53.9	24.4	43.2	17.7	36.2
Sr	12.2	289.2	442.2	331.2	432.5	303.5	327.2	247.8	348.5
Nd	2.9	15.2	20.5	27.4	25.1	13.4	15.4	9.5	22.9
Zr	18.8	134.5	114.7	222.9	177.5	65.4	164.3	123.4	158.1
Y	24.4	28.0	38.4	73.6	32.4	22.8	19.6	23.2	42.4
V	0.0	104.0	159.7	110.8	174.0	154.4	115.2	83.1	121.1
Cr	15.6	25.6	254.1	195.0	43.4	444.4	44.4	26.5	27.6
Ni	0.3	6.0	110.6	75.9	9.9	135.8	7.0	5.4	4.9
Cu	1.3	1.8	0.0	0.0	28.4	6.0	3.0	0.9	1.7
Zn	24.1	61.5	89.4	85.6	73.7	64.4	63.4	57.3	64.1
Ga	28.1	17.8	20.9	19.1	19.7	15.1	18.9	19.8	19.4
Rb/Sr	57.2	0.4	0.2	0.2	0.1	0.2	0.3	0.5	0.3
La/Y	0.4	0.5	0.2	0.1	0.8	0.4	0.9	0.3	0.4
C.I.P.W. norms with calculated FeO/Fe2O3 ratio (Ferat).									
Ferat	0.61	0.76	0.99	0.95	0.87	0.94	0.74	0.70	0.77
Qtz	23.14	20.79	1.20	14.01	14.93	8.66	23.05	27.18	19.58
Cor	1.26	--	--	--	0.38	--	--	1.41	--
Or	29.37	19.03	12.65	11.35	6.74	10.34	16.72	17.14	15.96
Ab	41.63	23.52	23.69	22.34	28.35	18.45	22.00	25.56	23.86
An	1.89	21.02	27.97	24.37	28.53	23.75	22.49	17.27	23.09
Di	--	2.15	8.55	9.09	--	11.89	0.97	--	1.40
Hy	0.67	7.02	15.09	11.32	11.30	19.46	7.75	6.66	7.78
Mt	0.33	3.10	5.50	5.35	4.62	4.64	3.10	2.49	3.46
Ilm	0.04	1.25	2.05	1.33	1.92	1.37	1.33	1.06	1.37
Ap	0.07	0.32	0.51	0.44	0.51	0.23	0.39	0.65	0.42
Rare Earth Elements in ppm: ICP analyses.									
La	--	--	--	--	--	--	--	--	--
Ce	--	--	--	--	--	--	--	--	--
Pr	--	--	--	--	--	--	--	--	--
Nd	--	--	--	--	--	--	--	--	--
Sm	--	--	--	--	--	--	--	--	--
Eu	--	--	--	--	--	--	--	--	--
Gd	--	--	--	--	--	--	--	--	--
Dy	--	--	--	--	--	--	--	--	--
Ho	--	--	--	--	--	--	--	--	--
Er	--	--	--	--	--	--	--	--	--
Yb	--	--	--	--	--	--	--	--	--
Lu	--	--	--	--	--	--	--	--	--

Hunza Plutonic Complex; first season samples - all 95ma phase.

Rock no.	3B17	4B18	4B19	5B22	5B23	5B25	6B27	6B29	6B31
Pellet	L9201	L9002	L9003	L9202	L9203	L9004	L9005	L9204	L9006
Type	Grd	QzDi	Grd	Grd	Xen	Grd	Grd	Mz.Go	Grd
SiO2	62.2	53.3	59.0	68.6	48.2	63.8	57.3	44.9	63.0
TiO2	0.81	1.01	0.70	0.47	1.26	0.77	0.97	1.76	0.79
Al2O3	16.0	16.2	16.9	15.0	19.3	16.0	17.5	17.1	15.7
Fe2O3	6.2	8.0	5.6	3.7	9.1	5.8	7.4	13.3	6.2
MnO	0.10	0.12	0.10	0.06	0.13	0.10	0.12	0.18	0.11
MgO	2.7	7.8	4.5	1.5	6.5	2.5	3.3	6.7	3.1
CaO	5.6	7.8	6.1	3.7	9.9	5.3	6.3	8.7	5.2
Na2O	2.7	3.5	3.1	2.7	3.1	2.9	2.7	2.0	3.6
K2O	2.48	2.16	2.32	3.80	2.02	2.69	2.66	3.22	2.08
P2O5	0.20	0.13	0.24	0.13	0.25	0.27	0.23	0.49	0.16
LOI	0.55	0.66	0.53	0.35	0.45	0.39	0.61	0.55	0.39
Total	99.51	100.65	98.95	100.14	100.22	100.49	99.08	98.91	100.24
Trace elements in parts per million									
Rb	95.8	91.8	134.9	104.5	93.1	105.6	115.6	161.5	138.9
Ba	781.3	365.9	583.5	1042.6	520.9	624.9	530.4	805.4	229.2
Th	4.0	1.3	0.4	13.9	1.7	10.2	9.6	24.8	14.4
Pb	19.1	19.0	22.4	24.8	15.9	24.7	18.1	13.6	18.4
Nb	12.5	6.2	9.4	9.9	11.9	14.2	18.5	22.5	16.3
La	12.0	7.1	7.5	17.4	13.5	17.2	19.2	50.7	16.8
Ce	27.0	21.5	15.7	38.4	32.5	35.8	42.1	104.9	34.5
Sr	352.2	392.9	377.3	332.9	488.2	325.2	348.3	224.8	197.8
Nd	11.5	12.6	11.5	15.5	19.2	17.0	21.4	44.6	15.2
Zr	135.1	94.3	111.7	87.3	32.0	151.4	183.7	341.1	150.6
Y	17.6	23.8	22.4	14.8	33.7	26.7	34.1	60.4	34.9
V	126.6	195.1	125.2	65.7	186.2	116.8	154.0	284.6	132.3
Cr	54.6	322.6	105.6	38.7	90.7	43.3	46.8	96.3	66.9
Ni	6.8	155.6	36.2	3.2	51.5	5.2	7.5	16.6	11.5
Cu	4.7	31.8	0.0	0.0	5.8	0.7	0.0	0.0	0.0
Zn	71.6	69.5	77.9	45.7	84.4	63.0	85.8	138.7	76.1
Ga	19.2	17.8	19.3	16.4	23.0	17.8	22.1	24.7	19.0
Rb/Sr	0.3	0.2	0.4	0.3	0.2	0.3	0.3	0.7	0.7
La/Y	0.7	0.3	0.3	1.2	0.4	0.6	0.6	0.8	0.5
C.I.P.W. norms with calculated FeO/Fe2O3 ratio (Ferat).									
Ferat	0.81	1.06	0.86	0.68	1.22	0.80	0.84	0.94	0.85
Qtz	20.84	--	12.98	27.53	--	21.79	12.76	--	18.82
Or	14.72	12.82	13.77	22.52	12.00	15.96	15.84	19.15	12.35
Ab	23.02	30.21	25.98	23.02	22.75	24.37	23.10	14.63	30.21
An	24.27	22.02	25.71	17.75	32.77	22.87	27.95	28.13	20.79
Ne	--	--	--	--	2.16	--	--	1.43	--
Di	1.97	12.76	2.33	0.04	11.60	1.41	1.57	9.62	3.22
Hy	8.55	11.92	12.42	5.79	--	8.16	10.41	--	8.72
Ol	--	2.57	--	--	8.56	--	--	11.88	--
Mt	3.79	5.70	3.56	2.07	6.97	3.51	4.64	8.86	3.92
Ilm	1.54	1.94	1.33	0.89	2.41	1.46	1.86	3.36	1.50
Ap	0.46	0.30	0.56	0.30	0.58	0.63	0.53	1.14	0.37
Rare Earth Elements in ppm: ICP analyses.									
La	--	--	--	--	--	--	--	--	--
Ce	--	--	--	--	--	--	--	--	--
Pr	--	--	--	--	--	--	--	--	--
Nd	--	--	--	--	--	--	--	--	--
Sm	--	--	--	--	--	--	--	--	--
Eu	--	--	--	--	--	--	--	--	--
Gd	--	--	--	--	--	--	--	--	--
Dy	--	--	--	--	--	--	--	--	--
Ho	--	--	--	--	--	--	--	--	--
Er	--	--	--	--	--	--	--	--	--
Yb	--	--	--	--	--	--	--	--	--
Lu	--	--	--	--	--	--	--	--	--

Hunza Plutonic Complex; first season samples - all 95ma phase except 9B44.
9B44 = aplite sheet; 6B32 & 34 = mixing zone gneisses.

Rock no.	6B32	6B34	7B36	8B37	8B39	8B41	8B42	9B43	9B44
Pellet	L9007	L9205	L9206	L9008	L9009	L9010	L9011	L9207	L9012
Type	Gneiss	Gneiss	Grd	Grd	Grd	Grd	Grd	Grd	Mzg Ap
SiO2	72.6	62.8	67.5	67.4	67.7	62.4	62.9	68.1	68.5
TiO2	0.26	0.83	0.51	0.51	0.64	0.80	0.77	0.52	0.42
Al2O3	14.7	16.4	15.4	16.0	15.6	16.8	16.0	14.8	15.4
Fe2O3	2.4	5.7	3.6	3.8	4.4	6.4	5.8	3.7	2.6
MnO	0.04	0.12	0.08	0.05	0.07	0.11	0.10	0.07	0.04
MgO	0.6	2.3	1.7	1.3	1.4	2.8	2.5	1.6	0.7
CaO	2.5	5.2	4.0	3.3	3.9	5.2	5.2	3.3	2.6
Na2O	3.4	4.1	3.3	4.7	3.7	3.0	2.5	4.1	4.4
K2O	3.89	1.99	2.84	1.92	2.23	2.33	1.96	1.77	3.27
P2O5	0.11	0.30	0.15	0.25	0.19	0.17	0.18	0.14	0.13
LOI	0.24	0.44	0.30	0.43	0.40	0.36	0.45	0.35	0.35
Total	100.60	100.20	99.34	99.60	100.26	100.36	98.36	98.40	98.33
Trace elements in parts per million									
Rb	118.9	110.2	114.9	119.0	101.6	131.8	93.8	125.4	74.5
Ba	468.9	500.8	1696.8	264.0	646.6	453.9	515.1	592.8	780.9
Th	9.7	3.2	6.4	9.2	6.6	8.5	3.8	14.4	6.7
Pb	30.1	15.0	23.9	21.9	13.9	16.2	15.1	12.9	16.6
Nb	18.6	12.3	11.2	20.2	12.6	13.7	14.9	15.4	10.8
La	11.6	17.4	17.6	19.4	18.4	17.3	13.7	23.2	22.4
Ce	24.3	36.5	28.8	37.2	39.1	39.5	26.9	46.9	41.8
Sr	176.0	303.8	385.7	196.8	271.0	291.6	321.9	260.4	450.8
Nd	11.2	14.9	10.2	15.4	16.6	19.0	13.1	19.1	16.0
Zr	86.5	118.1	69.7	152.0	165.5	148.7	169.2	140.7	190.6
Y	10.2	16.9	15.2	14.2	16.1	30.4	24.1	17.9	8.3
V	34.9	117.9	85.9	73.2	85.4	131.0	122.0	70.1	40.2
Cr	13.4	27.8	40.2	51.5	28.9	41.1	38.1	46.9	6.2
Ni	2.0	6.0	7.0	6.0	3.3	6.2	5.2	12.2	2.3
Cu	0.0	0.0	0.0	0.0	0.0	0.0	0.9	0.0	0.0
Zn	37.4	64.7	46.8	67.1	57.5	85.8	70.5	52.2	52.0
Ga	15.9	19.3	16.5	20.7	18.1	20.6	18.0	18.4	19.8
Rb/Sr	0.7	0.4	0.3	0.6	0.4	0.5	0.3	0.5	0.2
La/Y	1.1	1.0	1.2	1.4	1.1	0.6	0.6	1.3	2.7
C.I.P.W. norms with calculated FeO/Fe2O3 ratio (Ferat).									
Ferat	0.65	0.90	0.74	0.80	0.77	0.80	0.75	0.75	0.72
Qtz	31.67	17.73	26.17	23.77	27.03	19.87	25.48	27.95	23.69
Cor	0.64	--	0.03	0.76	0.51	0.25	0.74	0.57	0.21
Or	23.05	11.82	16.84	11.41	13.24	13.83	11.64	10.52	19.38
Ab	28.43	34.44	27.76	40.03	31.31	25.56	20.90	34.53	37.49
An	11.73	20.77	18.86	14.79	18.16	24.88	24.92	15.51	11.90
Di	--	2.62	--	--	--	--	--	--	--
Hy	2.90	6.54	6.05	4.76	5.50	9.78	9.05	5.60	2.92
Mt	1.28	3.71	2.10	2.32	2.61	3.91	3.41	2.19	1.47
Ilm	0.49	1.58	0.97	0.97	1.22	1.52	1.46	0.99	0.80
Ap	0.25	0.70	0.35	0.58	0.44	0.39	0.42	0.32	0.30
Rare Earth Elements in ppm: ICP analyses.									
La	--	--	--	--	--	--	--	--	--
Ce	--	--	--	--	--	--	--	--	--
Pr	--	--	--	--	--	--	--	--	--
Nd	--	--	--	--	--	--	--	--	--
Sm	--	--	--	--	--	--	--	--	--
Eu	--	--	--	--	--	--	--	--	--
Gd	--	--	--	--	--	--	--	--	--
Dy	--	--	--	--	--	--	--	--	--
Ho	--	--	--	--	--	--	--	--	--
Er	--	--	--	--	--	--	--	--	--
Yb	--	--	--	--	--	--	--	--	--
Lu	--	--	--	--	--	--	--	--	--

Hunza Plutonic Complex 95ma phase (9B47, RBSR1-7, B1); Ultar Sheet (UV23); Hunza sillimanite-zone dyke (GC1). B1 = first of second season HPC samples.

Rock no.	9B47	GC1	UV23	RBSR1	RBSR3	RBSR4	RBSR5	RBSR7	B1
Pellet	L9013	L9014	L9015	L9017	L9018	L9019	L9020	L9021	L9656
Type	Grd	2Mg Ap	Grd	QzDi	Grd	Grd	Grd	Mz.DQ	Grd
SiO2	58.0	71.8	65.1	55.7	61.5	63.0	61.7	57.0	68.0
TiO2	0.77	0.30	0.66	0.85	0.76	0.75	0.75	0.86	0.70
Al2O3	16.8	14.7	15.6	15.8	16.7	17.1	16.1	17.6	15.5
Fe2O3	6.6	1.8	5.1	7.0	5.8	5.7	5.9	6.0	4.3
MnO	0.11	0.02	0.10	0.13	0.08	0.08	0.09	0.09	0.07
MgO	3.8	0.3	2.1	7.0	2.8	2.7	2.6	5.2	1.4
CaO	6.4	1.5	4.6	7.1	5.9	6.0	5.2	6.9	3.6
Na2O	3.3	3.6	3.0	2.8	3.1	3.1	2.8	3.1	2.5
K2O	2.19	4.09	3.02	2.17	1.93	1.86	2.61	2.37	2.44
P2O5	0.21	0.16	0.17	0.15	0.24	0.16	0.16	0.24	0.31
LOI	0.44	0.61	0.31	0.49	0.49	0.39	0.46	0.46	0.92
Total	98.69	98.90	99.70	99.13	99.26	100.76	98.45	99.71	99.66
Trace elements in parts per million									
Rb	108.1	137.1	141.6	145.9	81.0	72.9	98.5	94.8	103.0
Ba	544.9	1230.8	484.9	427.1	691.3	626.8	1007.1	488.1	619.3
Th	6.6	22.7	13.5	0.7	18.7	12.1	14.2	7.1	11.6
Pb	21.5	60.1	26.1	14.8	18.8	16.3	17.8	15.1	22.5
Nb	11.9	4.3	17.0	10.2	10.7	9.6	12.1	9.5	11.6
La	15.5	36.5	16.4	3.0	31.0	25.4	24.1	19.2	23.9
Ce	36.7	56.4	30.9	14.0	66.0	49.0	48.6	43.9	46.6
Sr	416.4	377.0	270.8	343.8	380.2	393.2	365.9	436.5	250.7
Nd	17.7	15.8	14.7	9.5	26.9	19.9	16.7	20.1	21.4
Zr	149.1	206.7	154.5	73.2	134.0	128.1	150.3	102.6	179.7
Y	27.0	7.9	45.5	26.7	23.8	20.9	22.5	24.5	18.7
V	144.9	17.1	103.3	147.9	135.1	123.8	121.7	142.5	54.1
Cr	122.6	9.7	33.2	378.5	59.2	35.8	50.8	168.4	14.1
Ni	21.1	4.9	7.4	144.3	7.2	5.0	6.6	70.0	3.6
Cu	12.8	0.0	0.0	0.4	0.7	0.0	1.9	0.0	6.7
Zn	77.3	42.5	61.1	78.5	66.1	60.6	69.3	62.6	73.0
Ga	22.6	20.4	20.3	19.1	19.3	19.5	19.0	19.0	20.7
Rb/Sr	0.3	0.4	0.5	0.4	0.2	0.2	0.3	0.2	0.4
La/Y	0.6	4.6	0.4	0.1	1.3	1.2	1.1	0.8	1.3
C.I.P.W. norms with calculated FeO/Fe2O3 ratio (Ferat).									
Ferat	0.92	0.59	0.75	0.91	0.86	0.88	0.78	0.93	0.65
Qtz	11.65	31.84	23.15	7.10	19.60	20.67	19.86	8.40	34.71
Cor	--	2.06	--	--	--	--	--	--	3.00
Or	13.00	24.35	17.91	12.88	11.46	11.05	15.48	14.07	14.54
Ab	28.43	30.38	25.13	23.44	26.15	26.74	23.69	26.66	21.07
An	24.54	6.40	20.46	24.33	26.09	27.04	23.93	26.97	15.93
Di	4.81	--	1.09	8.02	1.41	1.38	0.90	4.45	--
Hy	9.58	1.87	7.02	16.43	8.51	8.10	8.89	12.69	5.74
Mt	4.36	0.94	2.99	4.58	3.71	3.67	3.54	3.96	2.33
Ilm	1.46	0.57	1.25	1.61	1.44	1.42	1.42	1.63	1.35
Ap	0.49	0.37	0.39	0.35	0.56	0.37	0.37	0.56	0.72
Rare Earth Elements in ppm: ICP analyses.									
La	--	--	--	--	--	--	--	--	--
Ce	--	--	--	--	--	--	--	--	--
Pr	--	--	--	--	--	--	--	--	--
Nd	--	--	--	--	--	--	--	--	--
Sm	--	--	--	--	--	--	--	--	--
Eu	--	--	--	--	--	--	--	--	--
Gd	--	--	--	--	--	--	--	--	--
Dy	--	--	--	--	--	--	--	--	--
Ho	--	--	--	--	--	--	--	--	--
Er	--	--	--	--	--	--	--	--	--
Yb	--	--	--	--	--	--	--	--	--
Lu	--	--	--	--	--	--	--	--	--

Hunza Plutonic Complex; B6 = basic dyke opposite Gulmit.
95 ma phase (B2, B5, B8, B9, B11 from around Gulmit); later dykes (B3, B4, B12)

Rock no.	B2	B3	B4	B5	B6	B8	B9	B11	B12
Pellet	L9657	L9658	L9659	L9660	L9661	L9662	L9663	L9665	L9666
Type	Grd	Lcg Pg	Mzg Ap	Grd	Dyke	QzDi	Grd	Mz.DQ	Lcg Pg
SiO2	67.0	75.0	74.4	65.5	48.9	57.2	62.8	56.2	73.1
TiO2	0.73	0.01	0.08	0.69	0.97	1.05	0.79	0.96	0.01
Al2O3	15.7	14.4	13.3	15.2	15.2	15.9	16.4	12.4	14.5
Fe2O3	4.7	0.6	0.8	4.5	11.5	8.2	5.4	8.7	1.2
MnO	0.08	0.21	0.06	0.07	0.26	0.11	0.06	0.17	0.41
MgO	1.5	0.0	0.1	1.4	5.9	4.8	2.7	9.3	0.0
CaO	4.1	0.6	1.5	4.0	9.6	6.7	5.5	8.1	0.4
Na2O	2.8	1.7	5.1	2.9	2.8	2.5	3.0	1.9	6.1
K2O	2.38	7.28	4.43	2.55	2.40	2.09	2.00	1.61	2.90
P2O5	0.19	0.17	0.07	0.19	0.17	0.22	0.23	0.09	0.10
LOI	0.81	0.50	0.51	1.34	0.83	0.76	0.68	0.68	0.24
Total	100.10	100.59	100.34	98.37	98.63	99.44	99.60	100.12	98.95
Trace elements in parts per million									
Rb	123.8	182.9	155.4	128.4	93.6	86.5	78.5	58.6	281.8
Ba	657.8	159.7	149.0	584.9	342.8	668.0	696.4	317.7	2.7
Th	15.3	2.8	14.5	11.5	11.0	23.4	33.6	6.8	5.2
Pb	20.9	57.5	60.9	23.6	16.8	13.8	19.4	16.9	30.4
Nb	13.3	7.3	11.4	13.0	23.8	13.5	10.0	9.9	17.3
La	29.2	3.4	9.5	20.4	23.4	38.4	47.1	12.2	3.1
Ce	60.0	2.4	18.2	39.9	58.8	70.5	84.2	35.0	2.5
Sr	268.7	73.8	82.9	266.3	230.0	340.0	387.5	234.4	3.1
Nd	26.8	1.5	10.1	19.5	39.7	26.1	25.5	23.2	1.1
Zr	207.6	20.1	42.3	195.1	134.1	188.5	148.4	139.3	69.3
Y	24.0	10.3	46.8	22.5	89.3	36.5	19.5	37.6	24.0
V	57.3	0.4	4.5	56.6	207.8	191.6	117.7	217.5	0.0
Cr	17.1	8.4	10.3	20.6	77.4	113.0	50.7	464.2	7.9
Ni	6.8	0.0	0.9	4.8	11.8	25.1	13.6	209.0	0.0
Cu	17.7	5.8	2.1	0.0	17.4	14.0	4.1	5.9	0.0
Zn	75.9	3.1	9.3	66.5	124.6	72.2	43.9	84.2	27.0
Ga	19.5	15.7	15.2	20.5	18.4	15.1	15.5	15.9	26.1
Rb/Sr	0.5	2.5	1.9	0.5	0.4	0.3	0.2	0.3	90.9
La/Y	1.2	0.3	0.2	0.9	0.3	1.1	2.4	0.3	0.1
C.I.P.W. norms with calculated FeO/Fe2O3 ratio (Ferat).									
Ferat	0.71	0.44	0.71	0.71	1.16	0.85	0.82	0.94	0.71
Qtz	30.44	35.97	26.25	27.89	--	13.90	21.93	10.74	25.33
Cor	1.58	3.00	--	0.79	--	--	--	--	0.75
Or	14.18	43.26	26.30	15.25	14.30	12.47	11.88	9.57	17.20
Ab	23.78	14.55	42.99	25.30	24.12	20.99	25.47	16.25	51.53
An	19.20	2.11	0.57	18.85	21.98	26.25	25.69	20.55	1.58
Di	--	--	1.58	--	19.94	4.55	0.11	15.35	--
Wol	--	--	1.82	--	--	--	--	--	--
Hy	6.09	0.98	--	5.66	2.28	13.06	8.80	19.36	1.57
Ol	--	--	--	--	4.59	--	--	--	--
Mt	2.70	0.26	0.48	2.57	8.61	5.24	3.36	5.79	0.68
Ilm	1.41	0.02	0.15	1.33	1.86	2.01	1.52	1.84	0.02
Ap	0.44	0.39	0.16	0.44	0.39	0.51	0.53	0.21	0.23
Rare Earth Elements in ppm: ICP analyses.									
La	--	2.5	--	--	37.8	68.4	93.1	--	--
Ce	--	5.0	--	--	89.15	119.65	151.62	--	--
Pr	--	0.53	--	--	11.88	12.58	13.69	--	--
Nd	--	2.2	--	--	54.0	45.6	44.0	--	--
Sm	--	0.7	--	--	13.59	7.52	5.67	--	--
Eu	--	0.15	--	--	1.58	1.47	1.21	--	--
Gd	--	1.03	--	--	16.59	9.42	5.47	--	--
Dy	--	1.49	--	--	16.8	6.88	3.82	--	--
Ho	--	0.24	--	--	3.38	1.38	0.76	--	--
Er	--	0.84	--	--	9.85	3.79	2.01	--	--
Yb	--	1.59	--	--	9.02	3.25	1.81	--	--
Lu	--	0.27	--	--	1.3	0.58	0.3	--	--

Hunza Plutonic Complex; 95ma phase except for later dykes B19 & B21.
B14 & B15 = N. granodiorite; B16 - B25 from S. contact.

Rock no.	B14	B15	B16	B17	B18	B19	B20	B21	B25
Pellet	L9667	L9668	L9669	L9670	L9671	L9672	L9673	L9674	L9676
Type	Grd	Grd	Mz.DQ	Grd	Mzg	Mzg Ap	Grd	Mzg Ap	Grd
SiO2	66.1	68.2	57.5	60.7	70.5	68.6	64.4	70.1	65.5
TiO2	0.69	0.68	0.69	0.64	0.34	0.50	0.65	0.24	0.70
Al2O3	15.2	15.3	14.7	15.1	14.7	16.1	16.3	15.2	15.3
Fe2O3	4.4	4.4	7.1	6.2	2.5	3.0	5.1	1.6	4.9
MnO	0.07	0.07	0.13	0.11	0.04	0.04	0.09	0.03	0.08
MgO	1.4	1.3	5.1	3.8	1.0	0.9	2.0	0.5	1.9
CaO	3.6	3.7	7.4	5.9	2.7	3.2	4.5	2.5	4.1
Na2O	2.9	2.8	3.0	2.9	2.7	4.9	3.4	3.9	3.4
K2O	3.22	2.64	2.97	3.33	4.89	2.77	2.88	3.86	2.02
P2O5	0.17	0.19	0.23	0.14	0.15	0.22	0.24	0.15	0.23
LOI	2.80	0.88	0.45	0.56	0.49	0.30	0.31	0.22	0.37
Total	100.54	100.14	99.30	99.52	100.08	100.48	99.86	98.21	98.54
Trace elements in parts per million									
Rb	150.0	100.7	113.3	120.8	168.5	95.6	134.9	134.3	128.0
Ba	604.6	652.6	537.2	681.1	1528.1	991.6	697.7	677.3	150.9
Th	9.9	14.5	18.0	9.0	15.7	11.0	13.3	4.9	23.3
Pb	20.8	21.2	24.1	18.8	na	na	na	na	na
Nb	13.6	13.7	12.0	11.1	10.3	11.7	17.5	9.0	21.6
La	20.9	26.6	17.3	19.7	17.2	30.8	17.4	8.1	26.7
Ce	46.0	56.3	34.2	37.6	26.9	52.5	33.9	9.9	49.7
Sr	301.4	266.7	509.1	463.6	330.7	441.6	307.2	290.8	251.3
Nd	19.4	23.8	18.2	16.7	13.3	17.7	14.3	4.7	22.2
Zr	179.2	206.3	96.7	121.8	114.6	204.5	140.8	92.0	157.4
Y	30.1	19.9	21.9	19.7	17.3	10.8	25.5	7.8	19.0
V	54.9	53.3	156.8	136.6	42.1	44.9	96.7	18.3	94.0
Cr	15.8	18.9	179.3	94.1	23.6	3.4	31.4	9.1	30.5
Ni	4.8	4.9	24.4	15.6	2.7	3.8	4.7	0.6	4.0
Cu	0.0	18.7	33.3	27.4	na	na	na	na	na
Zn	65.7	65.6	68.1	67.6	36.5	59.0	63.9	35.4	65.7
Ga	26.9	28.8	18.2	19.4	14.5	19.9	21.0	18.1	19.4
Rb/Sr	0.5	0.4	0.2	0.3	0.5	0.2	0.4	0.5	0.5
La/Y	0.7	1.3	0.8	1.0	1.0	2.9	0.7	1.0	1.4
C.I.P.W. norms with calculated FeO/Fe2O3 ratio (Ferat).									
Ferat	0.70	0.68	0.98	0.85	0.62	0.81	0.78	0.68	0.75
Qtz	27.20	31.91	8.45	14.03	28.55	21.60	20.68	26.52	26.07
Cor	0.79	1.65	--	--	0.33	--	--	0.35	0.58
Or	19.56	15.72	17.61	19.80	29.02	16.43	17.08	22.87	12.00
Ab	25.64	23.86	25.72	24.79	23.27	41.55	28.94	33.26	29.03
An	17.13	17.06	17.86	18.52	12.51	13.72	20.63	11.42	18.94
Di	--	--	13.77	8.18	--	0.58	0.11	--	--
Hy	5.69	5.48	8.80	8.38	3.93	3.11	7.31	2.00	6.90
Mt	2.51	2.44	4.86	3.93	1.31	1.86	3.03	0.89	2.87
Ilm	1.35	1.31	1.31	1.22	0.65	0.95	1.23	0.46	1.33
Ap	0.42	0.44	0.53	0.32	0.35	0.51	0.56	0.35	0.53
Rare Earth Elements in ppm: ICP analyses.									
La	--	39.0	34.5	--	--	--	--	--	--
Ce	--	79.7	66.9	--	--	--	--	--	--
Pr	--	9.41	7.64	--	--	--	--	--	--
Nd	--	35.3	27.2	--	--	--	--	--	--
Sm	--	5.78	4.7	--	--	--	--	--	--
Eu	--	1.37	1.23	--	--	--	--	--	--
Gd	--	7.0	4.67	--	--	--	--	--	--
Dy	--	3.71	3.64	--	--	--	--	--	--
Ho	--	0.64	0.73	--	--	--	--	--	--
Er	--	1.73	2.37	--	--	--	--	--	--
Yb	--	1.21	1.93	--	--	--	--	--	--
Lu	--	0.26	0.4	--	--	--	--	--	--

Hunza Plutonic Complex; Aplite sheets (B26 & 27); mixing zone (B31 - B36).
B28 = 95ma phase from southern part of HPC; B29 and B30 = later dykes.

Rock no.	B26	B27	B28	B29	B30	B31	B34	B35	B36
Pellet	L9677	L9678	L9679	L9680	L9681	L9682	L9683	L9684	L9685
Type	Mzg Ap	Mzg Ap	Grd	Mzg Ap	Mzg Ap	Grd	Peg	Mzg Ap	Grd
SiO2	70.6	70.7	58.9	71.5	73.2	62.3	73.7	73.0	63.4
TiO2	0.36	0.19	0.76	0.15	0.13	0.70	0.08	0.16	0.61
Al2O3	14.6	14.7	15.6	14.8	13.9	15.1	14.3	15.1	13.7
Fe2O3	1.8	1.0	6.7	1.0	1.0	6.5	0.6	1.1	6.2
MnO	0.02	0.02	0.12	0.02	0.01	0.17	0.01	0.03	0.14
MgO	0.5	0.2	4.4	0.1	0.2	3.6	0.1	0.1	4.4
CaO	1.8	2.0	6.5	1.6	1.8	5.5	1.8	1.6	5.5
Na2O	3.5	4.3	3.0	4.3	3.2	3.9	3.7	4.5	3.2
K2O	4.82	4.44	2.39	4.37	5.23	2.18	5.11	4.10	1.75
P2O5	0.19	0.06	0.30	0.03	0.08	0.19	0.09	0.12	0.18
LOI	0.47	0.77	0.51	0.21	0.20	0.29	0.19	0.27	0.42
Total	98.64	98.37	99.12	98.15	98.89	100.52	99.64	100.13	99.52

Trace elements in parts per million

Rb	168.9	179.6	100.2	292.7	107.8	118.0	136.9	288.4	144.2
Ba	1504.5	877.1	711.6	430.5	1333.6	494.9	394.1	439.5	192.6
Th	21.4	7.6	13.2	14.2	10.7	10.4	1.6	12.4	9.6
Nb	4.8	4.5	15.3	8.4	7.5	37.3	5.1	13.0	16.3
La	36.7	14.6	20.1	10.2	14.6	20.0	6.5	13.2	10.0
Ce	60.6	24.7	34.8	17.6	13.2	40.3	9.2	18.1	21.8
Sr	392.0	414.6	405.0	278.4	336.8	383.9	184.2	307.9	209.8
Nd	17.9	9.2	18.6	6.6	4.9	18.0	4.4	7.4	11.9
Zr	216.4	93.7	142.4	75.5	64.4	122.2	16.0	91.4	97.4
Y	7.1	7.8	24.4	9.6	8.8	24.8	6.7	12.3	25.3
V	30.2	11.3	145.4	8.9	9.3	118.4	2.1	11.7	130.9
Cr	8.1	6.8	155.4	4.0	12.3	133.4	0.2	3.6	115.5
Ni	2.6	0.0	27.6	1.2	3.3	22.9	0.0	1.1	13.4
Zn	46.9	34.3	72.9	44.6	13.6	64.5	10.2	38.3	81.9
Ga	20.0	22.3	19.0	26.6	18.5	20.7	16.9	26.6	18.5
Rb/Sr	0.4	0.4	0.2	1.1	0.3	0.3	0.7	0.9	0.7
La/Y	5.2	1.9	0.8	1.1	1.7	0.8	1.0	1.1	0.4

C.I.P.W. norms with calculated FeO/Fe2O3 ratio (Ferat).

Ferat	0.60	0.68	0.90	0.65	0.59	0.91	0.63	0.68	0.84
Qtz	27.47	24.87	13.12	26.38	30.68	15.10	28.85	27.38	20.96
Cor	0.84	--	--	0.27	--	--	--	0.50	--
Or	28.60	26.42	14.18	25.88	30.97	12.94	30.26	24.29	10.40
Ab	29.96	36.39	25.89	36.05	26.74	33.43	31.73	38.50	26.82
An	7.49	7.92	21.89	7.79	8.25	17.20	7.07	7.40	18.10
Di	--	1.42	6.76	--	0.17	7.26	0.98	--	6.62
Wol	--	--	--	--	--	--	0.04	--	--
Hy	2.10	0.23	10.40	0.81	1.09	8.24	--	0.82	10.78
Mt	0.94	0.57	4.37	0.56	0.49	4.23	0.31	0.60	3.91
Ilm	0.68	0.36	1.44	0.28	0.25	1.33	0.15	0.30	1.16
Ap	0.44	0.14	0.70	0.07	0.19	0.44	0.21	0.28	0.42

Rare Earth Elements in ppm: ICP analyses.

La	60.7	18.4	--	--	--	--	--	--	--
Ce	105.5	33.05	--	--	--	--	--	--	--
Pr	10.66	3.62	--	--	--	--	--	--	--
Nd	33.15	11.8	--	--	--	--	--	--	--
Sm	3.69	1.57	--	--	--	--	--	--	--
Eu	0.9	0.47	--	--	--	--	--	--	--
Gd	3.22	1.41	--	--	--	--	--	--	--
Dy	0.96	0.79	--	--	--	--	--	--	--
Ho	0.18	0.13	--	--	--	--	--	--	--
Er	1.17	0.54	--	--	--	--	--	--	--
Yb	0.17	0.21	--	--	--	--	--	--	--
Lu	0.07	0.05	--	--	--	--	--	--	--

Hunza Plutonic Complex; mixing zone (B37 - B45);
B46 = 95ma phase; B47 = later dyke.

Rock no.	B37	B38	B40	B41	B42	B44	B45	B46	B47
Pellet	L9686	L9687	L9688	L9689	L9690	L9691	L9692	L9693	L9694
Type	Gneiss	Gneiss	Gneiss	Mzg Ap	Mzg Ap	Gneiss	Peg	Grd	Mzg Ap
SiO2	68.2	73.3	66.1	71.9	71.7	55.0	74.6	63.8	70.7
TiO2	0.61	0.25	0.63	0.13	0.35	1.53	0.07	0.70	0.27
Al2O3	15.1	14.0	15.7	14.7	15.4	17.2	13.4	15.4	14.7
Fe2O3	4.1	2.0	5.7	0.9	2.1	7.3	0.6	5.4	1.5
MnO	0.07	0.04	0.11	0.02	0.04	0.12	0.01	0.10	0.02
MgO	0.9	0.4	1.0	0.0	0.5	2.6	0.0	2.4	0.5
CaO	3.2	1.9	3.8	1.7	2.4	5.7	1.7	4.8	2.0
Na2O	4.5	3.7	5.0	4.2	4.7	4.7	4.0	2.8	2.9
K2O	1.96	4.23	1.57	4.65	2.80	2.70	3.93	3.27	5.65
P2O5	0.30	0.08	0.31	0.10	0.12	0.88	0.08	0.26	0.08
LOI	0.21	0.22	0.19	0.50	0.29	0.40	0.21	0.30	0.28
Total	99.08	100.15	100.08	98.88	100.45	98.01	98.59	99.30	98.61
Trace elements in parts per million									
Rb	130.0	131.7	86.0	256.8	144.2	112.1	137.8	125.1	149.5
Ba	288.2	645.9	281.8	412.0	977.8	543.6	349.5	735.9	1448.7
Th	15.8	20.4	12.4	11.5	17.9	10.0	5.4	13.6	23.2
Nb	26.1	30.4	24.5	7.0	12.5	52.7	8.1	17.1	4.1
La	15.9	20.5	35.7	8.4	39.5	35.1	6.8	21.4	27.7
Ce	29.3	39.6	68.3	3.9	64.3	69.1	9.5	42.0	35.1
Sr	205.5	211.2	318.3	291.0	402.3	730.3	190.5	321.6	403.3
Nd	15.2	13.6	26.3	3.0	19.2	32.5	5.2	18.0	8.3
Zr	193.4	146.0	339.2	65.5	222.0	294.0	89.0	188.7	197.5
Y	25.0	18.7	26.8	9.0	11.0	35.3	11.1	30.4	17.4
V	67.1	19.8	69.8	7.9	24.1	140.5	3.5	107.8	19.3
Cr	12.5	5.6	1.5	0.6	11.4	2.6	7.6	51.9	5.0
Ni	2.1	2.0	1.9	0.3	4.7	13.6	0.7	7.2	3.1
Zn	58.9	27.0	58.8	30.8	55.5	99.5	12.5	66.3	26.2
Ga	18.2	15.5	18.9	25.6	22.1	22.4	16.0	19.3	16.3
Rb/Sr	0.6	0.6	0.3	0.9	0.4	0.2	0.7	0.4	0.4
La/Y	0.6	1.1	1.3	0.9	3.6	1.0	0.6	0.7	1.6
C.I.P.W. norms with calculated FeO/Fe2O3 ratio (Ferat).									
Ferat	0.78	0.64	0.86	0.66	0.75	0.96	0.65	0.75	0.58
Qtz	26.70	30.53	21.55	26.05	27.90	4.39	32.85	21.38	26.96
Cor	0.50	0.15	--	--	0.54	--	--	--	0.28
Or	11.58	25.06	9.28	27.60	16.61	16.02	23.28	19.38	33.51
Ab	37.74	31.56	41.97	36.13	39.60	39.52	34.02	23.44	24.79
An	14.01	8.70	15.92	7.41	11.32	18.06	6.97	20.10	9.55
Di	--	--	0.95	0.24	--	3.63	0.77	1.70	--
Hy	4.04	2.30	4.54	0.45	2.15	6.12	0.02	7.87	1.97
Mt	2.42	1.07	3.64	0.46	1.25	4.92	0.32	3.18	0.75
Ilm	1.16	0.47	1.20	0.25	0.66	2.92	0.13	1.33	0.51
Ap	0.70	0.19	0.72	0.23	0.28	2.04	0.19	0.60	0.19
Rare Earth Elements in ppm: ICP analyses.									
La	33.8	--	--	--	--	--	--	38.8	--
Ce	67.15	--	--	--	--	--	--	75.1	--
Pr	7.6	--	--	--	--	--	--	8.19	--
Nd	28.0	--	--	--	--	--	--	31.0	--
Sm	5.11	--	--	--	--	--	--	5.48	--
Eu	0.93	--	--	--	--	--	--	1.39	--
Gd	5.06	--	--	--	--	--	--	5.75	--
Dy	4.21	--	--	--	--	--	--	5.1	--
Ho	0.79	--	--	--	--	--	--	0.99	--
Er	2.2	--	--	--	--	--	--	2.83	--
Yb	1.79	--	--	--	--	--	--	2.47	--
Lu	0.28	--	--	--	--	--	--	0.37	--

Hunza Plutonic Complex; 95ma phase south of mixing zone (B48 - B52); Mixing zone (B56 & 57); later dykes (B53, B54, B55).

Rock no.	B48	B49	B51	B52	B53	B54	B55	B56	B57
Pellet	L9695	L9696	L9698	L9699	L9700	L9701	L9702	L9703	L9704
Type	Grd	Grd	Grd	Grd	Mzg Ap	Mzg Ap	Mzg	Grd	Gneiss
SiO2	63.9	63.7	66.3	63.6	72.7	73.4	74.8	61.2	72.8
TiO2	0.83	0.84	0.63	0.77	0.14	0.16	0.21	0.97	0.27
Al2O3	15.7	16.9	15.4	16.2	15.1	15.4	13.1	16.6	14.2
Fe2O3	6.0	6.1	4.7	5.8	0.8	1.0	1.4	6.2	2.1
MnO	0.11	0.09	0.07	0.09	0.02	0.02	0.02	0.13	0.03
MgO	2.8	2.6	1.9	2.4	0.1	0.1	0.3	2.8	0.4
CaO	5.3	4.4	4.3	5.1	1.7	1.8	1.0	5.4	1.8
Na2O	2.8	3.4	3.2	3.0	4.6	7.5	2.7	4.1	3.8
K2O	2.85	2.71	3.07	2.59	4.70	4.59	6.33	2.01	4.33
P2O5	0.25	0.23	0.24	0.20	0.03	0.02	0.07	0.44	0.19
LOI	0.31	0.34	0.26	0.42	0.29	0.58	0.47	0.41	0.36
Total	100.62	101.30	100.16	100.18	100.14	104.55	100.45	100.42	100.34
Trace elements in parts per million									
Rb	111.2	116.8	106.7	108.6	249.2	273.3	167.2	123.0	128.6
Ba	845.6	542.2	770.3	533.0	663.5	499.9	634.1	335.6	810.3
Th	17.6	4.8	14.1	13.4	0.0	7.5	21.1	2.1	17.6
Nb	14.7	13.2	13.4	16.9	4.0	6.9	11.9	34.5	19.7
La	40.9	10.1	26.4	27.7	8.4	9.1	29.1	23.9	30.2
Ce	80.7	12.1	52.6	48.9	11.8	7.2	57.5	49.2	49.6
Sr	322.1	366.0	295.2	319.5	350.5	341.2	163.7	390.3	199.7
Nd	30.5	6.8	20.2	21.1	4.0	2.7	21.6	22.6	18.8
Zr	208.3	175.4	165.3	161.5	86.1	88.3	105.6	214.8	188.1
Y	34.0	22.3	14.3	18.4	7.0	9.3	10.3	25.7	15.9
V	115.5	132.9	89.6	112.0	4.9	9.0	5.8	117.0	16.9
Cr	57.9	54.8	34.6	35.6	0.3	1.8	7.0	58.6	4.9
Ni	8.8	16.7	7.5	7.0	0.6	1.7	0.4	15.9	1.5
Zn	72.0	79.8	45.7	72.1	41.3	42.3	27.9	87.1	34.2
Ga	19.6	18.7	17.5	19.6	21.9	24.9	15.3	23.7	17.9
Rb/Sr	0.3	0.3	0.4	0.3	0.7	0.8	1.0	0.3	0.6
La/Y	1.2	0.5	1.8	1.5	1.2	1.0	2.8	0.9	1.9
C.I.P.W. norms with calculated FeO/Fe2O3 ratio (Ferat).									
Ferat	0.78	0.77	0.75	0.79	0.68	0.96	0.52	0.91	0.64
Qtz	21.70	19.59	23.97	21.63	24.67	15.01	32.13	14.81	29.51
Cor	--	0.85	--	--	--	--	0.21	--	0.39
Or	16.90	16.07	18.20	15.37	27.84	27.30	37.59	11.94	25.71
Ab	23.36	29.11	26.82	25.22	39.01	53.92	23.02	35.03	32.66
An	22.01	20.42	18.87	23.21	6.61	--	4.45	20.89	7.79
Ac	--	--	--	--	--	1.36	--	--	--
Ns	--	--	--	--	--	2.04	--	--	--
Di	2.05	--	0.92	0.75	1.08	1.79	--	2.65	--
Wol	--	--	--	--	0.09	2.76	--	--	--
Hy	8.52	9.13	6.55	8.21	--	--	1.74	7.80	2.09
Mt	3.58	3.64	2.79	3.53	0.46	--	0.65	4.11	1.11
Ilm	1.58	1.60	1.20	1.46	0.27	0.30	0.40	1.84	0.51
Ap	0.58	0.53	0.56	0.46	0.07	0.05	0.16	1.02	0.44
Rare Earth Elements in ppm: ICP analyses.									
La	--	--	--	46.57	7.4	--	39.0	38.9	57.1
Ce	--	--	--	93.86	12.3	--	75.6	77.0	104.9
Pr	--	--	--	11.31	1.4	--	8.13	8.26	10.56
Nd	--	--	--	34.33	4.6	--	28.35	32.95	35.8
Sm	--	--	--	6.66	0.65	--	5.24	7.7	5.33
Eu	--	--	--	1.39	0.27	--	0.78	1.52	0.81
Gd	--	--	--	4.56	0.63	--	4.97	5.39	4.63
Dy	--	--	--	4.66	0.42	--	1.98	4.3	3.23
Ho	--	--	--	na	0.06	--	0.29	0.81	0.6
Er	--	--	--	2.61	0.1	--	0.78	2.41	1.71
Yb	--	--	--	2.11	0.1	--	0.27	2.04	1.16
Lu	--	--	--	0.29	0.04	--	0.08	0.31	0.17

Hunza Plutonic Complex; B58 = mixing zone; Aplite sheets (B61, B62, B64 - B66).
B60 & B63 = 95ma phase near mixing zone; B59 = later dyke.

Rock no.	B58	B59	B60	B61	B62	B63	B64	B65	B66
Pellet	L9705	L9706	L9707	L9708	L9709	L9710	L9711	L9712	L9713
Type	Peg Sw	Mzg Ap	Grd	Mzg	Mzg	Grd	Mzg	Mzg	Mzg
SiO2	77.4	69.7	59.9	68.9	70.9	62.1	71.2	71.0	72.9
TiO2	0.05	0.34	0.87	0.30	0.31	0.79	0.45	0.33	0.08
Al2O3	13.4	14.6	15.9	14.7	14.7	16.1	15.5	14.7	15.2
Fe2O3	0.4	2.1	6.7	1.8	1.8	6.3	3.3	2.0	0.8
MnO	0.01	0.02	0.12	0.03	0.02	0.10	0.04	0.02	0.02
MgO	0.0	0.5	2.9	0.4	0.4	2.7	0.9	0.5	0.1
CaO	1.1	2.2	5.8	2.2	2.2	5.6	3.9	2.3	1.5
Na2O	3.3	4.2	5.1	6.9	4.5	2.9	4.1	3.7	4.8
K2O	5.16	3.75	2.15	3.35	3.24	2.72	1.33	4.12	4.00
P2O5	0.01	0.22	0.23	0.19	0.09	0.28	0.24	0.19	0.08
LOI	0.15	0.36	0.37	0.29	0.52	0.43	0.32	0.27	0.63
Total	100.99	97.94	99.95	98.96	98.80	100.11	101.28	99.05	100.07
Trace elements in parts per million									
Rb	116.5	105.7	112.4	104.9	83.5	113.5	69.1	89.5	177.0
Ba	523.0	1531.9	489.4	1401.5	1444.2	686.0	280.5	1828.3	445.9
Th	2.9	18.3	14.1	13.6	7.2	7.0	12.1	18.7	5.0
Nb	3.6	6.3	18.3	5.3	4.3	19.6	7.0	4.2	17.3
La	4.0	26.4	14.1	29.2	40.7	13.1	24.4	47.2	9.3
Ce	2.0	35.2	32.2	48.0	58.6	29.2	40.2	74.2	14.5
Sr	191.4	380.8	291.8	428.4	425.9	338.0	307.5	449.0	166.7
Nd	1.6	10.3	17.0	14.6	17.0	18.2	16.7	21.1	7.3
Zr	45.1	211.2	192.8	167.7	198.1	161.7	206.9	220.4	63.3
Y	4.1	8.3	28.8	7.8	6.3	42.3	11.7	5.6	20.5
V	6.2	24.3	131.6	26.9	22.9	121.4	54.7	23.2	4.0
Cr	4.9	11.3	41.5	8.6	7.1	43.9	13.2	4.1	4.4
Ni	1.0	0.5	6.6	0.5	1.3	8.3	2.9	2.4	2.7
Zn	0.0	21.5	75.6	49.4	49.0	71.0	50.9	41.5	20.8
Ga	17.1	20.1	21.1	19.6	20.2	21.4	17.9	20.3	24.2
Rb/Sr	0.6	0.3	0.4	0.2	0.2	0.3	0.2	0.2	1.1
La/Y	1.0	3.2	0.5	3.7	6.5	0.3	2.1	8.4	0.5
C.I.P.W. norms with calculated FeO/Fe2O3 ratio (Ferat).									
Ferat	0.57	0.68	1.04	0.91	0.71	0.82	0.82	0.65	0.69
Qtz	36.33	26.07	8.23	13.13	26.75	18.93	32.73	28.51	26.47
Cor	0.54	0.28	--	--	--	--	0.80	0.55	0.34
Or	30.55	22.22	12.77	19.86	19.27	16.13	7.86	24.41	23.82
Ab	27.67	35.37	42.99	56.93	38.67	24.79	35.03	31.14	40.96
An	5.24	9.38	14.27	--	10.22	23.02	17.73	10.07	7.07
Ac	--	--	--	1.74	--	--	--	--	--
Di	--	--	10.28	3.91	0.08	2.59	--	--	--
Wol	--	--	--	1.99	--	--	--	--	--
Hy	0.30	2.15	4.18	--	1.84	8.23	3.47	2.11	0.60
Mt	0.22	1.18	4.72	0.31	1.05	3.90	2.06	1.07	0.43
Ilm	0.09	0.65	1.65	0.57	0.59	1.50	0.85	0.63	0.15
Ap	0.02	0.51	0.53	0.44	0.21	0.65	0.56	0.44	0.19
Rare Earth Elements in ppm: ICP analyses.									
La	3.5	--	22.7	--	56.73	--	--	--	--
Ce	5.3	--	51.15	--	91.53	--	--	--	--
Pr	0.62	--	6.63	--	9.24	--	--	--	--
Nd	1.9	--	26.2	--	21.08	--	--	--	--
Sm	0.29	--	4.88	--	3.67	--	--	--	--
Eu	0.6	--	1.29	--	0.9	--	--	--	--
Gd	0.46	--	6.75	--	na	--	--	--	--
Dy	0.29	--	4.87	--	0.77	--	--	--	--
Ho	0.05	--	0.96	--	na	--	--	--	--
Er	0.37	--	2.52	--	1.21	--	--	--	--
Yb	0.13	--	2.49	--	0.07	--	--	--	--
Lu	0.03	--	0.46	--	0.01	--	--	--	--

Hunza Plutonic Complex; Aplite sheets (B67, B68, B72 - B74);
B69 & B74 = later dykes.

Rock no.	B67	B68	B69	B70	B71	B72	B73	B74	B77
Pellet	L9714	L9715	L9716	L9717	L9718	L9719	L9720	L9721	L9724
Type	Lcg	Mzg	Lcg Pg	Mzg Ap	Grd	Mzg	Mzg	Lcg	Grd
SiO2	74.6	72.7	73.6	71.2	69.6	72.8	71.0	73.5	64.4
TiO2	0.04	0.21	0.02	0.25	0.41	0.28	0.32	0.06	0.84
Al2O3	13.8	14.7	14.7	14.7	16.1	13.9	14.7	15.1	16.2
Fe2O3	0.5	1.3	0.5	1.6	3.2	1.9	1.9	0.5	5.3
MnO	0.04	0.03	0.08	0.03	0.05	0.03	0.02	0.01	0.06
MgO	0.0	0.2	0.0	0.3	0.8	0.5	0.5	0.0	2.4
CaO	1.4	1.7	1.0	2.0	3.5	1.6	1.8	1.4	4.4
Na2O	4.2	4.1	5.4	4.3	6.4	3.6	3.5	4.1	3.4
K2O	4.31	4.28	3.13	3.98	1.63	4.60	4.98	5.48	2.44
P2O5	0.00	0.09	0.04	0.08	0.23	0.20	0.11	0.13	0.23
LOI	0.24	0.38	0.47	0.28	0.34	0.33	0.32	0.31	0.51
Total	99.11	99.66	99.00	98.71	102.37	99.75	99.25	100.54	100.15
Trace elements in parts per million									
Rb	144.7	161.2	135.7	108.4	91.1	197.7	171.3	262.7	123.9
Ba	471.4	1029.9	31.3	1649.1	118.2	692.6	1218.2	261.3	495.1
Th	4.8	15.9	5.0	15.1	11.9	9.9	13.9	5.3	1.4
Nb	6.3	7.8	10.4	6.5	15.2	18.0	6.5	6.7	26.9
La	7.5	27.3	6.9	32.6	22.9	11.4	24.6	10.4	11.5
Ce	3.0	42.8	5.7	46.6	43.1	13.3	35.7	16.1	17.7
Sr	187.0	263.8	44.4	487.4	231.8	264.5	376.4	179.8	296.4
Nd	1.5	13.3	5.3	13.3	16.1	4.8	10.8	6.4	11.3
Zr	40.5	127.1	45.5	158.0	198.3	173.9	183.3	42.0	175.3
Y	9.5	11.6	29.7	6.0	17.1	11.8	7.5	16.8	23.7
V	2.0	12.1	0.2	16.7	45.2	31.2	34.1	2.5	119.5
Cr	0.4	1.8	0.0	4.2	5.2	7.2	13.1	1.5	55.4
Ni	0.0	2.0	1.6	1.3	2.7	5.0	3.7	0.6	13.2
Zn	11.7	33.2	18.9	28.7	62.5	41.3	40.1	15.7	77.4
Ga	19.5	6.9	12.8	15.4	15.7	15.7	14.7	17.9	16.2
Rb/Sr	0.8	0.6	3.1	0.2	0.4	0.7	0.5	1.5	0.4
La/Y	0.8	2.4	0.2	5.4	1.3	1.0	3.3	0.6	0.5
C.I.P.W. norms with calculated FeO/Fe2O3 ratio (Ferat).									
Ferat	0.64	0.65	0.70	0.68	1.00	0.61	0.61	0.63	0.77
Qtz	30.83	28.63	28.08	26.18	19.01	30.15	26.68	26.28	22.30
Cor	--	0.48	0.72	--	--	0.48	0.43	0.36	0.60
Or	25.53	25.41	18.56	23.58	9.69	27.30	29.55	32.50	14.48
Ab	35.63	34.86	45.78	36.47	53.99	30.63	29.96	34.53	28.52
An	6.01	7.75	4.90	9.04	10.65	6.73	8.46	5.90	20.37
Di	0.67	--	--	0.46	4.33	--	--	--	--
Wol	0.10	--	--	--	--	--	--	--	--
Hy	--	1.12	0.50	1.34	1.00	2.36	2.24	0.28	8.27
Mt	0.25	0.72	0.31	0.88	2.23	0.98	0.96	0.25	3.17
Ilm	0.08	0.40	0.04	0.47	0.78	0.53	0.61	0.11	1.60
Ap	--	0.21	0.09	0.19	0.53	0.46	0.25	0.30	0.53
Rare Earth Elements in ppm: ICP analyses.									
La	12.3	39.5	--	--	--	--	--	--	--
Ce	20.1	64.3	--	--	--	--	--	--	--
Pr	2.14	6.24	--	--	--	--	--	--	--
Nd	6.6	19.6	--	--	--	--	--	--	--
Sm	1.04	2.76	--	--	--	--	--	--	--
Eu	0.4	0.6	--	--	--	--	--	--	--
Gd	1.5	2.36	--	--	--	--	--	--	--
Dy	1.14	1.46	--	--	--	--	--	--	--
Ho	0.23	0.25	--	--	--	--	--	--	--
Er	1.0	0.86	--	--	--	--	--	--	--
Yb	1.0	0.45	--	--	--	--	--	--	--
Lu	0.18	0.04	--	--	--	--	--	--	--

Hunza Plutonic Complex; B80 - B86 = mixing zone; B78 & B79 = later dykes.

Rock no.	B78	B79	B80	B81	B82	B83	B84	B85	B86
Pellet	L9725	L9726	L9727	L9728	L9729	L9730	L9731	L9732	L9733
Type	Mzg Ap	Lcg Pg	Mzg	Gneiss	Gneiss	Gneiss	Mzg	Peg Sw	Peg Sw
SiO2	65.7	74.2	71.1	57.2	65.3	67.4	71.2	75.0	74.6
TiO2	0.67	0.08	0.45	1.23	0.75	0.48	0.51	0.08	0.18
Al2O3	16.6	15.0	14.4	17.3	16.1	15.4	14.7	13.6	13.6
Fe2O3	3.4	0.7	2.9	7.2	5.2	5.1	3.1	1.0	1.5
MnO	0.05	0.01	0.05	0.18	0.10	0.16	0.06	0.11	0.03
MgO	1.2	0.1	0.8	3.3	1.9	0.8	0.9	0.0	0.3
CaO	3.7	1.4	2.5	4.8	4.7	3.7	2.4	1.6	1.9
Na2O	5.0	4.0	4.0	4.4	2.2	4.7	3.9	3.5	3.7
K2O	1.95	5.27	3.44	3.10	1.78	1.55	3.69	4.80	3.94
P2O5	0.20	0.07	0.21	0.55	0.29	0.28	0.22	0.13	0.08
LOI	0.67	0.29	0.28	0.97	0.40	0.25	0.34	0.27	0.43
Total	99.20	101.20	100.12	100.25	98.63	99.74	101.04	100.21	100.13

Trace elements in parts per million

Rb	78.2	190.6	135.5	235.6	133.9	94.6	147.3	132.5	132.3
Ba	285.4	270.3	656.0	288.8	491.0	218.5	618.6	413.9	368.6
Th	5.6	9.7	17.3	11.9	9.7	23.6	16.8	6.3	14.6
Nb	10.3	11.2	15.2	85.7	17.3	70.5	11.9	12.0	29.5
La	31.5	12.7	17.7	21.8	18.7	36.2	17.3	4.4	17.6
Ce	57.3	24.1	31.0	37.9	37.1	64.7	33.6	0.0	27.9
Sr	582.9	131.7	203.7	278.7	297.7	259.2	189.7	157.7	147.5
Nd	20.3	10.2	14.6	13.5	15.7	25.8	16.2	0.0	11.3
Zr	264.0	55.9	137.6	151.5	183.1	310.1	159.2	32.1	77.7
Y	12.4	30.0	23.9	39.1	23.8	44.7	28.7	49.2	14.6
V	59.1	2.7	41.8	95.0	94.6	60.0	47.5	6.2	14.5
Cr	27.5	11.4	24.0	52.9	16.9	7.7	22.1	3.7	3.6
Ni	7.6	2.4	1.4	33.5	4.8	0.3	2.4	0.0	1.2
Zn	66.3	13.6	42.1	75.8	77.0	56.7	46.2	11.0	24.2
Ga	17.2	16.8	17.4	19.0	20.6	19.2	17.8	15.9	16.1
Rb/Sr	0.1	1.4	0.7	0.8	0.4	0.4	0.8	0.8	0.9
La/Y	2.5	0.4	0.7	0.6	0.8	0.8	0.6	0.1	1.2

C.I.P.W. norms with calculated FeO/Fe2O3 ratio (Ferat).

Ferat	0.86	0.63	0.69	0.87	0.70	0.83	0.68	0.61	0.64
Qtz	19.58	27.58	28.09	5.47	32.82	24.91	27.80	32.85	33.76
Cor	0.03	0.28	0.07	--	2.84	0.04	0.35	0.03	0.11
Or	11.58	31.26	20.39	18.50	10.58	9.16	21.87	28.43	23.40
Ab	42.90	33.93	34.10	37.66	18.53	39.52	33.17	29.70	31.23
An	17.00	6.64	10.88	18.35	21.27	16.48	10.67	7.19	8.70
Di	--	--	--	1.76	--	--	--	--	--
Hy	3.99	0.78	3.47	9.83	7.25	4.63	3.79	0.98	1.52
Mt	2.18	0.38	1.61	4.64	2.91	3.15	1.73	0.52	0.79
Ilm	1.27	0.15	0.85	2.36	1.42	0.91	0.97	0.15	0.34
Ap	0.46	0.16	0.49	1.30	0.67	0.65	0.51	0.30	0.19

Rare Earth Elements in ppm: ICP analyses.

La	--	15.4	28.1	42.9	32.7	--	35.0	5.3	25.6
Ce	--	30.9	58.75	75.25	65.35	--	70.05	9.68	48.25
Pr	--	3.43	6.63	7.85	7.62	--	7.72	1.12	5.37
Nd	--	12.1	24.85	29.0	28.1	--	29.35	3.7	17.3
Sm	--	2.78	4.97	5.26	4.79	--	5.88	0.7	2.82
Eu	--	0.55	0.89	1.51	1.39	--	0.97	0.57	0.58
Gd	--	3.01	5.26	6.02	5.93	--	5.94	1.36	3.83
Dy	--	1.77	3.97	6.24	4.06	--	4.9	4.13	2.35
Ho	--	0.26	0.73	1.29	0.77	--	0.93	1.56	0.41
Er	--	0.65	2.12	4.1	2.05	--	2.84	8.67	1.15
Yb	--	0.37	1.31	4.27	1.47	--	2.02	17.29	0.67
Lu	--	0.07	0.22	0.66	0.26	--	0.35	3.31	0.18

Hunza Plutonic Complex; B88 - B95 from south of Gulmit;
B87, B89, B94 & B95 = later dykes.

Rock no.	B87	B88	B89	B90	B91	B92	B93	B94	B95
Pellet	L9734	L9735	L9736	L9737	L9738	L9739	L9740	L9741	L9742
Type	Mzg Ap	Grd	Lcg Pg	Mz.Go	Mz.Go	Xen	Xen	Mzg Ap	Lcg Pg
SiO2	73.4	62.0	74.3	53.0	51.3	52.8	57.1	74.2	74.3
TiO2	0.12	0.94	0.05	0.74	1.09	0.88	1.22	0.06	0.03
Al2O3	14.9	16.1	14.5	20.1	14.9	14.4	14.8	13.6	15.1
Fe2O3	0.9	6.7	0.7	6.6	8.9	9.0	8.0	0.4	0.9
MnO	0.02	0.11	0.04	0.12	0.17	0.18	0.13	0.01	0.20
MgO	0.2	3.1	0.0	3.6	10.1	9.5	6.2	0.0	0.1
CaO	2.0	5.7	1.3	9.0	8.6	8.3	6.4	1.5	0.8
Na2O	3.9	2.9	5.0	3.9	2.1	2.4	2.3	3.3	5.6
K2O	4.01	2.52	3.62	2.20	2.44	2.21	2.97	4.95	3.09
P2O5	0.03	0.27	0.15	0.27	0.11	0.13	0.15	0.01	0.11
LOI	0.59	0.44	0.42	0.29	0.65	0.64	0.53	0.15	0.31
Total	100.08	100.86	100.09	99.72	100.19	100.41	99.75	98.34	100.66
Trace elements in parts per million									
Rb	193.4	125.0	181.2	60.1	124.5	102.9	135.8	94.0	259.4
Ba	566.8	488.5	220.6	782.4	469.5	390.8	537.9	1054.1	27.7
Th	7.4	61.9	5.2	19.3	2.6	0.0	5.6	6.1	0.0
Nb	5.0	20.9	12.1	14.9	15.0	13.8	10.7	8.1	16.3
La	8.1	28.8	8.1	36.5	11.6	2.7	11.8	7.1	2.4
Ce	9.0	62.6	11.8	64.0	35.0	6.3	24.4	7.1	0.0
Sr	434.0	339.9	87.7	471.1	312.9	260.4	302.4	220.2	28.5
Nd	2.4	26.4	5.4	24.8	23.7	13.2	12.3	4.2	0.5
Zr	73.2	222.6	47.0	223.1	111.1	64.7	110.9	42.4	27.4
Y	4.5	27.0	26.1	34.3	38.1	46.4	27.2	12.9	14.2
V	6.4	141.3	1.9	159.6	190.7	185.1	116.5	3.3	6.2
Cr	2.2	66.4	7.0	52.8	484.3	535.2	335.2	3.3	13.5
Ni	1.2	9.4	2.8	14.0	198.8	220.0	104.3	3.8	4.8
Zn	29.7	77.3	19.0	73.3	94.5	95.6	84.6	5.3	24.5
Ga	21.6	19.9	18.6	28.3	19.6	19.6	71.8	33.7	20.7
Rb/Sr	0.4	0.4	2.1	0.1	0.4	0.4	0.4	0.4	9.1
La/Y	1.8	1.1	0.3	1.1	0.3	0.1	0.4	0.6	0.2
C.I.P.W. norms with calculated FeO/Fe2O3 ratio (Ferat).									
Ferat	0.67	0.83	0.70	1.24	0.97	0.98	0.81	0.59	0.71
Qtz	30.57	18.90	28.69	0.26	--	1.44	10.57	32.46	27.66
Cor	0.48	--	0.40	--	--	--	--	0.05	1.23
Or	23.82	14.95	21.51	13.06	14.54	13.12	17.67	29.31	18.32
Ab	33.51	24.54	42.90	32.75	17.77	20.06	19.46	28.35	47.81
An	9.92	23.67	5.27	31.01	24.22	22.35	21.48	7.43	3.50
Di	--	2.56	--	9.57	14.08	14.46	7.33	--	--
Hy	0.93	9.25	0.46	5.66	18.87	20.38	15.16	0.36	1.24
Ol	--	--	--	--	1.88	--	--	--	--
Mt	0.50	4.19	0.37	5.07	6.02	6.15	4.93	0.22	0.53
Ilm	0.23	1.79	0.09	1.41	2.09	1.69	2.34	0.11	0.06
Ap	0.07	0.63	0.35	0.63	0.25	0.30	0.35	0.02	0.25
Rare Earth Elements in ppm: ICP analyses.									
La	9.5	--	6.4	--	--	--	19.3	--	--
Ce	18.0	--	12.1	--	--	--	43.8	--	--
Pr	2.37	--	1.29	--	--	--	5.21	--	--
Nd	6.93	--	4.3	--	--	--	21.1	--	--
Sm	1.07	--	0.88	--	--	--	4.15	--	--
Eu	0.32	--	0.18	--	--	--	1.18	--	--
Gd	1.11	--	1.05	--	--	--	4.89	--	--
Dy	0.47	--	1.08	--	--	--	4.41	--	--
Ho	0.09	--	0.17	--	--	--	0.86	--	--
Er	0.59	--	0.49	--	--	--	2.73	--	--
Yb	0.12	--	0.57	--	--	--	2.23	--	--
Lu	0.13	--	0.11	--	--	--	0.34	--	--

Hunza Plutonic Complex; Malamgodhi Glacier (B100 & 101).
B96, B99, B102 = 95ma phase; B97, B98, B103 & B104 = later dykes.

Rock no.	B96	B97	B98	B99	B100	B101	B102	B103	B104
Pellet	L9743	L9744	L9745	L9746	L9747	L9748	L9749	L9750	L9751
Type	Mz.DQ	Mzg Ap	Mzg Ap	Mz.DQ	Grd	Grd	Grd	Mzg Pg	Mzg Ap
SiO2	56.2	72.5	73.1	59.2	68.3	69.5	66.7	66.5	70.0
TiO2	0.78	0.10	0.23	0.94	0.50	0.49	0.60	0.10	0.43
Al2O3	11.7	14.7	13.9	17.1	14.7	15.0	15.6	19.3	15.1
Fe2O3	8.5	1.0	1.9	6.8	2.9	2.8	4.7	0.7	3.2
MnO	0.14	0.03	0.04	0.11	0.06	0.06	0.08	0.02	0.04
MgO	10.7	0.1	0.3	3.0	0.8	0.8	1.8	0.0	0.9
CaO	5.8	1.0	1.8	6.2	2.2	2.4	2.9	1.8	3.3
Na2O	1.4	4.5	3.4	5.0	3.6	3.5	2.8	6.3	3.4
K2O	3.08	5.18	4.70	2.47	3.59	3.62	4.45	5.19	3.53
P2O5	0.06	0.22	0.09	0.24	0.20	0.20	0.18	0.03	0.20
LOI	0.67	0.24	0.19	0.47	1.78	0.64	0.51	1.02	0.44
Total	99.03	99.61	99.69	101.51	98.54	98.95	100.40	100.98	100.39

Trace elements in parts per million

Rb	121.2	181.9	133.5	107.8	158.6	157.4	192.7	263.3	107.8
Ba	444.0	252.9	695.2	608.1	616.3	607.8	848.3	330.6	529.2
Th	2.4	5.4	15.2	16.7	18.3	14.1	25.7	13.5	25.8
Nb	10.3	17.3	13.1	21.1	18.7	18.2	20.8	6.9	17.5
La	8.3	8.2	16.3	28.7	36.4	32.7	33.7	12.7	43.9
Ce	15.8	7.5	28.8	63.9	68.0	60.0	63.9	19.3	77.1
Sr	195.4	96.3	151.6	370.4	294.0	310.7	245.5	224.6	282.9
Nd	9.5	4.9	10.5	29.0	26.8	25.5	25.5	8.7	27.2
Zr	38.8	46.9	172.8	194.1	168.4	165.1	132.4	61.2	228.8
Y	23.1	13.2	25.6	48.1	18.3	18.7	24.5	11.6	18.3
V	199.4	4.0	19.0	141.2	33.9	33.2	88.5	5.8	41.1
Cr	566.1	1.9	7.6	37.3	10.9	11.7	35.8	0.0	5.8
Ni	301.4	1.8	1.6	9.9	3.0	3.4	10.4	1.3	2.4
Zn	80.8	35.4	28.1	84.3	47.6	62.5	64.0	25.7	58.1
Ga	14.2	17.9	14.1	19.6	16.9	18.0	18.4	23.6	17.1
Rb/Sr	0.6	1.9	0.9	0.3	0.5	0.5	0.8	1.2	0.4
La/Y	0.4	0.6	0.6	0.6	2.0	1.7	1.4	1.1	2.4

C.I.P.W. norms with calculated FeO/Fe2O3 ratio (Ferat).

Ferat	0.69	0.63	0.61	1.08	0.63	0.64	0.62	0.81	0.70
Qtz	8.26	24.40	30.75	5.51	28.39	29.20	23.85	6.32	28.46
Cor	--	0.37	0.09	--	1.56	1.53	1.37	0.17	0.23
Or	18.32	30.67	27.84	14.66	21.63	21.51	26.42	30.97	20.98
Ab	12.19	38.33	28.94	42.31	30.72	29.62	23.78	53.65	28.60
An	16.50	3.67	8.39	17.20	9.56	10.65	13.36	8.78	15.01
Di	9.65	--	--	9.64	--	--	--	--	--
Hy	27.20	0.89	1.93	4.66	3.50	3.38	7.35	0.37	3.84
Mt	4.75	0.52	0.99	4.87	1.55	1.49	2.43	0.43	1.79
Ilm	1.50	0.19	0.44	1.79	0.97	0.93	1.14	0.19	0.82
Ap	0.14	0.51	0.21	0.56	0.46	0.46	0.42	0.07	0.46

Rare Earth Elements in ppm: ICP analyses.

La	--	9.8	--	55.8	--	--	--	--	--
Ce	--	18.48	--	113.15	--	--	--	--	--
Pr	--	1.87	--	13.19	--	--	--	--	--
Nd	--	6.47	--	51.3	--	--	--	--	--
Sm	--	1.37	--	9.8	--	--	--	--	--
Eu	--	0.38	--	1.84	--	--	--	--	--
Gd	--	1.63	--	10.77	--	--	--	--	--
Dy	--	1.33	--	8.84	--	--	--	--	--
Ho	--	0.2	--	1.73	--	--	--	--	--
Er	--	0.62	--	5.02	--	--	--	--	--
Yb	--	0.39	--	3.65	--	--	--	--	--
Lu	--	0.05	--	0.57	--	--	--	--	--

Hunza Plutonic Complex; B110 - B115 from N. Grd around Pasu and Ghulkin.

Rock no.	B105	B108	B109	B110	B111	B112	B113	B114	B115
Pellet	L9752	L9755	L9756	L9757	L9758	L9759	L9760	L9761	L9762
Type	Lcg Pg	Grd	Mzg Ap	Lcg Pg	Grd	Grd	Grd	Grd	Xen
SiO2	74.8	60.6	70.7	74.3	68.1	68.8	68.0	67.6	59.9
TiO2	0.09	0.89	0.37	0.02	0.69	0.65	0.71	0.71	1.01
Al2O3	13.7	16.6	14.4	14.5	15.4	15.2	15.2	15.5	16.2
Fe2O3	1.3	6.5	3.1	0.6	4.4	4.2	4.5	4.5	6.8
MnO	0.08	0.10	0.06	0.02	0.07	0.08	0.07	0.07	0.10
MgO	0.1	2.8	0.6	0.0	1.4	1.3	1.4	1.3	2.6
CaO	1.1	5.8	2.4	0.9	3.9	3.5	3.7	3.7	4.8
Na2O	2.6	3.1	3.6	5.1	2.8	2.8	2.7	2.9	2.2
K2O	6.78	2.52	4.01	3.76	2.56	2.88	2.75	2.89	3.71
P2O5	0.02	0.24	0.22	0.06	0.18	0.17	0.18	0.18	0.21
LOI	0.34	0.48	0.44	0.49	0.98	0.65	0.79	0.66	2.81
Total	100.88	99.56	99.98	99.68	100.45	100.38	99.96	99.87	100.28

Trace elements in parts per million

Rb	177.9	121.9	129.7	182.4	100.6	101.2	101.5	104.0	140.4
Ba	586.8	617.8	538.2	17.3	633.1	608.0	637.5	691.5	563.7
Th	14.5	15.6	13.9	2.7	9.8	13.3	11.4	14.1	9.5
Nb	16.0	17.2	24.4	10.0	12.9	14.0	13.9	14.4	15.1
La	13.4	23.8	28.1	3.3	20.8	25.3	27.0	26.3	18.7
Ce	18.2	48.9	49.6	1.5	43.7	54.9	54.3	53.5	37.0
Sr	121.7	355.6	144.1	40.3	254.4	250.6	262.9	268.9	261.5
Nd	7.7	20.9	17.5	0.8	20.0	25.7	23.2	24.9	17.4
Zr	71.2	212.1	283.4	16.7	183.2	179.7	196.5	207.2	146.3
Y	39.8	26.5	29.5	16.0	25.1	34.4	22.1	22.1	17.8
V	1.6	128.5	36.7	0.2	53.8	50.6	56.8	51.5	105.6
Cr	0.0	42.7	6.8	3.4	19.0	18.3	16.7	25.1	17.1
Ni	1.8	8.2	1.0	0.8	4.8	8.1	7.8	5.4	5.1
Zn	19.8	78.0	45.9	22.1	70.4	69.8	65.5	69.1	103.4
Ga	14.4	19.4	15.3	15.2	17.8	19.1	16.4	20.5	18.9
Rb/Sr	1.5	0.3	0.9	4.5	0.4	0.4	0.4	0.4	0.5
La/Y	0.3	0.9	1.0	0.2	0.8	0.7	1.2	1.2	1.1

C.I.P.W. norms with calculated FeO/Fe2O3 ratio (Ferat).

Ferat	0.52	0.84	0.66	0.67	0.70	0.68	0.68	0.69	0.70
Qtz	30.88	16.94	28.44	28.52	31.43	31.44	31.47	29.64	18.43
Cor	0.14	--	0.31	0.62	1.39	1.41	1.54	1.31	0.34
Or	40.19	14.95	23.82	22.34	15.31	17.14	16.37	17.20	22.58
Ab	22.00	26.06	30.29	43.24	24.03	24.20	23.36	24.37	19.21
An	5.43	24.12	10.77	3.97	18.22	16.55	17.13	17.38	23.07
Di	--	2.56	--	--	--	--	--	--	--
Hy	1.36	8.22	3.30	0.44	5.56	5.40	5.57	5.45	9.85
Mt	0.59	4.10	1.66	0.33	2.50	2.34	2.47	2.49	3.91
Ilm	0.17	1.69	0.70	0.04	1.33	1.23	1.37	1.35	1.98
Ap	0.05	0.56	0.51	0.14	0.42	0.39	0.42	0.42	0.51

Rare Earth Elements in ppm: ICP analyses.

La	--	39.8	--	--	36.4	--	--	--	30.4
Ce	--	77.75	--	--	72.8	--	--	--	60.67
Pr	--	8.57	--	--	8.18	--	--	--	6.91
Nd	--	32.9	--	--	31.4	--	--	--	27.5
Sm	--	5.65	--	--	5.38	--	--	--	4.94
Eu	--	1.51	--	--	1.36	--	--	--	1.53
Gd	--	5.68	--	--	6.09	--	--	--	5.05
Dy	--	4.56	--	--	3.82	--	--	--	3.47
Ho	--	0.88	--	--	0.68	--	--	--	0.6
Er	--	2.58	--	--	1.97	--	--	--	1.59
Yb	--	2.13	--	--	1.34	--	--	--	0.97
Lu	--	0.33	--	--	0.23	--	--	--	0.13

Hunza Plutonic Complex (B116 - B121); Country rocks (SLG2 - SLG4).
B118-B121 = late dykes south of Gulmit.

Rock no.	B116	B117	B118	B119	B120	B121	SLG2	SLG3	SLG4
Pellet	L9763	L9764	L9765	L9766	L9767	L9768	L9647	L9648	L9649
Type	Xen	Xen	Lcg Pg	Lcg Pg	Mzg Pg	Lcg Pg	M.Bas	M.Bas	Aug.Gn
SiO2	63.8	59.5	75.5	74.8	68.0	73.2	43.8	48.2	57.9
TiO2	0.89	1.25	0.01	0.03	0.05	0.03	3.12	2.52	0.83
Al2O3	16.2	16.6	14.5	14.1	17.4	14.7	11.8	15.4	17.2
Fe2O3	6.0	7.1	0.6	0.7	0.4	0.8	13.1	8.2	7.3
MnO	0.09	0.13	0.01	0.10	0.01	0.16	0.25	0.17	0.11
MgO	1.9	2.6	0.0	0.0	0.0	0.0	8.2	2.4	4.0
CaO	4.2	5.1	0.7	0.8	1.9	1.0	17.3	15.9	6.9
Na2O	3.0	4.4	4.9	3.6	2.8	5.0	1.1	1.1	1.3
K2O	2.71	2.90	3.87	5.89	9.50	3.33	0.64	2.00	2.93
P2O5	0.14	0.45	0.07	0.05	0.44	0.02	0.46	0.68	0.17
LOI	0.86	0.47	0.39	0.24	0.50	0.43	0.87	2.86	1.17
Total	99.83	100.54	100.59	100.36	100.94	98.70	100.66	99.48	99.87
Trace elements in parts per million									
Rb	117.7	90.7	204.6	197.3	221.3	225.7	8.5	58.0	129.2
Ba	561.4	452.9	11.2	191.2	1563.4	17.2	148.6	1035.1	399.3
Th	13.3	10.1	7.2	6.4	1.3	9.3	3.1	7.3	10.6
Pb	na	na	na	na	na	na	6.0	9.6	14.7
Nb	16.5	60.5	16.3	10.8	5.0	15.4	48.1	83.1	13.0
La	21.3	32.9	4.7	7.6	3.8	7.6	21.8	40.9	17.6
Ce	42.8	55.5	6.7	9.0	0.0	12.1	47.9	85.9	38.9
Sr	285.0	366.4	19.9	81.4	296.3	43.5	530.5	763.0	201.7
Nd	20.2	24.3	3.5	4.3	0.5	5.9	25.7	38.2	18.8
Zr	209.9	237.7	50.3	44.8	9.1	36.0	184.6	279.3	145.7
Y	19.7	38.8	23.8	23.7	24.0	38.7	26.4	32.8	22.1
V	81.2	107.4	0.0	2.2	5.3	0.0	320.0	146.5	173.9
Cr	26.4	21.4	2.2	3.7	0.0	1.6	551.5	8.0	245.1
Ni	8.8	14.0	0.0	1.2	0.7	2.2	158.3	8.9	106.6
Cu	na	na	na	na	na	na	0.0	0.0	29.3
Zn	93.1	72.3	26.0	16.2	11.6	25.6	123.6	82.7	102.9
Ga	21.0	17.5	17.4	16.0	16.9	26.3	21.0	22.4	23.6
Rb/Sr	0.4	0.2	10.3	2.4	0.7	5.2	0.0	0.1	0.6
La/Y	1.1	0.8	0.2	0.3	0.2	0.2	0.8	1.2	0.8
C.I.P.W. norms with calculated FeO/Fe2O3 ratio (Ferat).									
Ferat	0.72	0.90	0.65	0.56	0.55	0.67	2.25	2.06	0.78
Qtz	23.35	9.51	30.72	29.63	12.49	28.81	--	7.74	17.52
Cor	1.04	--	1.07	0.55	0.16	1.02	--	--	--
Or	16.13	17.20	22.99	34.87	56.44	19.74	3.84	12.17	17.49
Ab	25.64	37.74	41.72	30.46	23.78	42.90	7.96	9.90	11.42
An	20.22	16.85	3.11	3.54	6.40	4.83	25.32	32.06	32.68
Ne	--	--	--	--	--	--	1.01	--	--
Di	--	4.37	--	--	--	--	44.48	13.21	0.71
Wol	--	--	--	--	--	--	0.38	11.55	--
Hy	7.60	6.40	0.45	0.75	0.33	0.82	--	--	13.22
Mt	3.44	4.65	0.32	0.34	0.21	0.43	4.37	1.64	4.41
Ilm	1.71	2.39	0.02	0.06	0.09	0.06	5.98	4.92	1.60
Hm	--	--	--	--	--	--	5.83	4.36	--
Ap	0.32	1.04	0.16	0.12	1.02	0.05	1.07	1.62	0.39
Rare Earth Elements in ppm: ICP analyses.									
La	--	--	--	8.2	4.5	6.3	31.1	--	--
Ce	--	--	--	15.75	10.7	14.93	68.2	--	--
Pr	--	--	--	1.66	1.15	1.96	8.6	--	--
Nd	--	--	--	5.95	6.0	7.18	36.4	--	--
Sm	--	--	--	1.37	1.77	1.76	6.57	--	--
Eu	--	--	--	0.24	1.0	0.06	2.25	--	--
Gd	--	--	--	1.7	2.89	3.16	8.07	--	--
Dy	--	--	--	2.22	3.5	4.35	5.41	--	--
Ho	--	--	--	0.45	0.66	0.88	1.01	--	--
Er	--	--	--	1.58	2.13	3.03	2.46	--	--
Yb	--	--	--	2.06	1.21	3.56	1.93	--	--
Lu	--	--	--	0.32	0.27	0.55	0.3	--	--

Hunza Country rocks (SLG5 - 7); Batura Pluton (BG1 - 6); BG1-5 = main grd.

Rock no.	SLG5	SLG6	SLG7	BG1	BG2	BG3	BG4	BG5	BG6
Pellet	L9650	L9651	L9652	L9441	L9442	L9443	L9444	L9445	L9446
Type	Aug.Gn	M.Bas	Aug.Gn	Grd	Grd	Grd	Grd	Grd	Mzg
SiO2	58.9	37.6	74.4	67.5	65.0	64.8	67.0	63.9	73.5
TiO2	0.77	2.93	0.54	0.52	0.63	0.63	0.60	0.61	0.25
Al2O3	16.2	12.3	11.7	14.7	15.6	16.0	14.8	15.5	13.6
Fe2O3	7.0	13.3	3.4	4.3	4.8	4.8	4.8	5.5	1.9
MnO	0.13	0.18	0.07	0.08	0.08	0.09	0.09	0.11	0.05
MgO	3.8	5.0	1.1	1.7	2.0	2.0	2.0	2.3	0.3
CaO	6.6	17.8	1.3	3.9	4.5	4.6	4.1	5.5	1.3
Na2O	3.1	2.9	2.3	2.9	3.1	3.2	1.4	3.2	3.9
K2O	2.53	0.64	3.04	3.54	3.43	3.26	3.58	2.03	4.79
P2O5	0.22	0.45	0.14	0.05	0.09	0.15	0.11	0.19	0.06
LOI	0.51	5.29	0.67	0.35	0.33	0.33	0.35	0.68	0.17
Total	99.84	98.38	98.60	99.51	99.55	99.96	98.75	99.44	99.73
Trace elements in parts per million									
Rb	90.8	9.9	132.5	147.3	140.4	140.5	155.6	139.4	187.9
Ba	533.4	102.1	643.2	595.9	665.9	613.0	631.8	151.3	373.8
Th	1.6	0.7	13.6	26.6	13.6	10.1	13.5	11.6	21.9
Pb	17.2	3.8	26.7	32.5	28.6	28.8	29.0	21.6	23.6
Nb	13.4	36.5	10.8	14.3	14.9	16.4	15.2	17.7	29.8
La	17.8	21.4	25.8	36.7	20.1	19.1	22.5	11.8	20.8
Ce	38.9	40.8	49.0	76.0	44.8	40.1	45.3	29.4	40.6
Sr	452.0	405.0	153.7	249.3	294.5	294.1	253.5	289.2	100.8
Nd	19.3	22.4	21.4	30.8	20.5	19.6	22.0	17.8	14.8
Zr	125.6	216.9	241.3	156.2	175.9	140.4	160.7	153.0	137.7
Y	24.0	32.1	27.2	33.9	28.5	28.1	36.5	44.8	22.8
V	157.7	263.5	57.4	79.9	99.1	98.0	91.0	94.4	17.9
Cr	79.9	392.7	62.8	25.9	36.2	31.7	30.3	45.3	12.5
Ni	14.0	174.1	18.3	5.4	6.1	5.4	6.4	8.2	1.5
Cu	18.6	0.0	9.0	0.0	2.7	1.0	0.5	0.0	0.0
Zn	79.4	107.6	43.6	54.2	59.8	60.0	59.5	68.8	31.1
Ga	20.5	22.5	15.6	17.8	18.0	20.3	19.2	19.9	16.3
Rb/Sr	0.2	0.0	0.9	0.6	0.5	0.5	0.6	0.5	1.9
La/Y	0.7	0.7	0.9	1.1	0.7	0.7	0.6	0.3	0.9
C.I.P.W. norms with calculated FeO/Fe2O3 ratio (Ferat).									
Ferat	0.92	3.42	0.51	0.70	0.75	0.77	0.60	0.84	0.61
Qtz	12.54	--	44.64	25.94	21.30	20.89	32.44	23.11	29.12
Cor	--	--	2.63	--	--	--	1.47	--	--
Or	15.01	1.79	18.08	20.98	20.33	19.32	21.22	12.06	28.37
Ab	26.57	--	19.72	24.37	26.15	26.99	11.93	26.91	32.92
An	22.81	19.82	5.48	16.84	18.57	19.77	19.57	22.17	5.51
Lu	--	1.74	--	--	--	--	--	--	--
Ne	--	13.93	--	--	--	--	--	--	--
Di	6.94	28.47	--	2.01	2.47	1.91	--	3.21	0.63
Wol	--	14.15	--	--	--	--	--	--	--
Hy	9.00	--	4.91	5.61	6.20	6.35	7.98	6.60	1.50
Mt	4.62	1.63	1.56	2.40	2.84	2.89	2.44	3.49	0.96
Ilm	1.46	5.87	1.03	0.99	1.20	1.20	1.14	1.16	0.47
Hm	--	9.45	--	--	--	--	--	--	--
Ap	0.51	1.09	0.32	0.12	0.21	0.35	0.25	0.44	0.14
Rare Earth Elements in ppm: ICP analyses.									
La	28.7	36.0	--	62.4	--	--	40.6	--	--
Ce	59.77	75.0	--	111.2	--	--	79.85	--	--
Pr	7.09	10.0	--	11.7	--	--	8.66	--	--
Nd	27.3	43.8	--	41.55	--	--	32.8	--	--
Sm	4.86	8.66	--	6.55	--	--	5.9	--	--
Eu	1.28	3.11	--	1.1	--	--	1.07	--	--
Gd	6.0	10.12	--	6.84	--	--	5.94	--	--
Dy	4.22	7.27	--	5.54	--	--	5.65	--	--
Ho	0.84	1.35	--	1.11	--	--	1.13	--	--
Er	2.49	3.38	--	3.39	--	--	3.7	--	--
Yb	2.11	2.57	--	3.19	--	--	3.81	--	--
Lu	0.36	0.39	--	0.53	--	--	0.6	--	--

Batura Pluton (BG7 - 11); Hushe samples (K238 - 249).

Rock no.	BG7	BG8	BG9	BG10	BG11	K238	K245	K248	K249
Pellet	L9447	L9448	L9449	L9450	L9451	L9189	L9190	L9191	L9192
Type	Lcg Pg	Lcg	Lcg	Lcg	Xen	Mzg	Qz.Di	Amph	Lcg
SiO2	74.0	73.9	75.1	75.6	69.8	72.5	58.3	55.8	73.0
TiO2	0.17	0.16	0.10	0.13	0.39	0.22	0.87	1.17	0.06
Al2O3	12.8	13.4	13.3	13.1	14.5	13.8	18.7	18.1	14.4
Fe2O3	1.4	1.5	0.7	1.0	3.2	1.4	6.1	7.8	0.9
MnO	0.05	0.04	0.01	0.02	0.06	0.03	0.08	0.14	0.18
MgO	0.1	0.3	0.2	0.2	1.4	0.3	2.1	3.6	0.0
CaO	0.9	2.0	1.8	1.8	3.3	1.5	5.2	6.7	0.8
Na2O	4.3	3.3	2.6	2.6	3.0	4.1	4.4	3.2	3.7
K2O	4.66	4.54	5.50	5.21	3.97	4.24	2.08	2.12	4.49
P2O5	0.13	0.06	0.01	0.04	0.08	0.07	0.33	0.33	0.10
LOI	0.26	0.26	0.25	0.21	0.33	0.28	0.26	0.31	0.57
Total	98.79	99.37	99.58	99.93	100.19	98.39	98.30	99.36	98.17
Trace elements in parts per million									
Rb	200.9	164.7	118.9	153.0	136.0	121.8	81.9	117.9	240.6
Ba	289.3	642.7	1013.2	412.2	468.8	630.0	974.5	642.6	148.5
Th	29.7	28.2	18.9	24.6	21.2	11.0	7.7	5.6	6.0
Pb	23.8	44.8	25.5	48.7	44.2	23.9	7.9	10.3	33.8
Nb	35.4	9.8	3.0	7.2	15.5	15.0	9.3	13.8	30.1
La	19.1	11.3	3.5	7.7	18.9	15.6	26.2	18.4	3.8
Ce	37.3	23.1	5.3	13.0	36.9	31.6	51.1	35.8	6.9
Sr	77.7	196.0	244.9	174.1	233.7	296.0	639.6	473.5	73.0
Nd	13.6	10.6	2.2	6.9	16.9	12.3	19.5	16.8	4.3
Zr	120.8	92.2	23.0	69.6	108.5	72.2	175.4	103.8	40.1
Y	22.5	15.7	4.1	12.7	26.7	8.5	13.3	27.5	12.7
V	7.3	16.5	11.4	14.6	58.7	24.0	109.6	153.3	3.2
Cr	8.3	11.1	2.5	8.2	52.8	7.3	18.4	37.0	8.1
Ni	1.0	1.3	0.0	0.1	8.4	1.8	3.7	10.1	0.3
Cu	1.6	1.7	2.0	1.8	26.7	1.9	13.2	0.0	0.0
Zn	25.0	24.0	9.3	11.3	36.0	27.3	79.1	77.7	9.4
Ga	16.0	14.2	11.3	5.8	8.8	15.4	26.1	21.5	28.6
Rb/Sr	2.6	0.8	0.5	0.9	0.6	0.4	0.1	0.2	3.3
La/Y	0.8	0.7	0.9	0.6	0.7	1.8	2.0	0.7	0.3
C.I.P.W. norms with calculated FeO/Fe2O3 ratio (Ferat).									
Ferat	0.61	0.61	0.56	0.56	0.68	0.63	0.89	0.91	0.56
Qtz	29.52	32.87	34.71	36.24	27.77	29.06	10.69	9.69	32.50
Cor	--	--	--	0.03	--	--	0.60	--	2.22
Or	27.60	26.89	32.56	30.85	23.52	25.12	12.35	12.59	26.71
Ab	36.22	27.67	22.42	22.00	25.47	34.44	37.23	26.99	31.48
An	1.93	8.51	8.24	8.62	14.50	6.81	23.54	29.06	3.46
Di	1.65	0.73	0.44	--	1.29	0.02	--	1.77	--
Hy	0.42	1.37	0.61	1.29	4.72	1.52	7.19	10.71	0.97
Mt	0.74	0.79	0.34	0.50	1.79	0.75	3.95	5.14	0.42
Ilm	0.32	0.30	0.19	0.25	0.74	0.42	1.65	2.22	0.11
Ap	0.30	0.14	0.02	0.09	0.19	0.16	0.76	0.76	0.23
Rare Earth Elements in ppm: ICP analyses.									
La	--	22.85	--	--	28.5	--	50.3	--	--
Ce	--	46.36	--	--	55.8	--	96.77	--	--
Pr	--	5.53	--	--	6.21	--	10.62	--	--
Nd	--	15.84	--	--	23.0	--	36.23	--	--
Sm	--	3.79	--	--	4.04	--	4.92	--	--
Eu	--	0.72	--	--	0.86	--	1.35	--	--
Gd	--	na	--	--	4.78	--	3.96	--	--
Dy	--	2.61	--	--	3.95	--	2.44	--	--
Ho	--	na	--	--	0.81	--	0.48	--	--
Er	--	1.56	--	--	2.58	--	1.71	--	--
Yb	--	1.48	--	--	2.52	--	1.2	--	--
Lu	--	0.22	--	--	0.42	--	0.3	--	--

Hushe Valley samples (K256 - K266).

Rock no.	K256	K258	K259	K262	K263	K264	K265	K266
Pellet	L9193	L9194	L9195	L9196	L9197	L9198	L9199	L9200
Type	Qz.Di	Mzg	Mzg	Gneiss	Gneiss	Gneiss	Lcg	Lcg
SiO2	65.7	73.0	68.7	70.3	69.4	72.5	73.0	73.8
TiO2	0.67	0.10	0.33	0.53	0.53	0.32	0.08	0.05
Al2O3	15.9	15.1	15.3	14.7	14.3	14.6	14.5	14.2
Fe2O3	4.4	0.8	2.4	3.1	3.1	2.8	0.7	0.6
MnO	0.09	0.02	0.05	0.06	0.05	0.08	0.02	0.06
MgO	1.7	0.1	0.7	1.0	0.9	0.6	0.0	0.0
CaO	3.8	1.6	2.5	2.5	2.4	2.1	1.6	0.9
Na2O	3.2	4.7	3.8	4.5	4.0	4.3	4.4	3.7
K2O	2.97	3.60	4.59	3.27	3.20	2.98	3.76	4.26
P2O5	0.35	0.06	0.13	0.30	0.37	0.13	0.02	0.06
LOI	0.41	0.30	0.26	0.29	0.22	0.27	0.34	0.27
Total	99.12	99.24	98.64	100.62	98.41	100.65	98.52	97.96
Trace elements in parts per million								
Rb	130.3	123.0	128.3	188.1	171.5	213.9	111.8	190.5
Ba	709.4	1111.6	880.7	904.2	1384.6	427.2	905.7	109.7
Th	2.7	7.8	10.1	14.7	41.8	16.6	3.5	12.5
Pb	18.9	30.9	27.6	32.4	53.3	30.3	34.2	68.1
Nb	10.8	11.9	11.9	10.6	12.6	17.7	2.3	18.2
La	7.3	7.6	16.2	18.5	41.8	25.7	2.4	5.7
Ce	15.5	9.8	32.7	38.7	80.3	47.9	2.6	11.4
Sr	402.3	410.9	281.0	239.4	851.2	206.3	356.6	74.9
Nd	8.0	3.6	13.7	15.6	33.1	18.8	1.5	5.8
Zr	113.5	42.0	103.6	74.7	92.8	122.1	17.1	32.9
Y	18.0	4.7	14.3	10.9	12.1	15.8	4.6	25.1
V	101.5	5.0	36.8	26.9	59.1	28.1	5.3	1.6
Cr	47.1	6.9	22.1	12.7	24.8	18.9	20.6	7.8
Ni	9.5	0.9	1.9	1.4	4.5	0.7	0.0	0.0
Cu	3.9	0.0	0.0	0.0	14.2	0.0	0.0	0.0
Zn	68.5	13.6	37.5	31.2	64.5	58.9	12.7	17.3
Ga	20.1	15.7	16.3	15.4	18.8	18.3	12.2	23.7
Rb/Sr	0.3	0.3	0.5	0.8	0.2	1.0	0.3	2.5
La/Y	0.4	1.6	1.1	1.7	3.5	1.6	0.5	0.2
C.I.P.W. norms with calculated FeO/Fe2O3 ratio (Ferat).								
Ferat	0.70	0.69	0.66	0.73	0.68	0.69	0.67	0.57
Qtz	25.58	28.63	22.79	24.95	27.67	30.26	29.30	33.75
Cor	1.52	0.79	0.01	--	0.72	0.77	0.27	1.94
Or	17.61	21.33	27.18	19.38	18.97	17.67	22.28	25.23
Ab	26.91	39.52	31.90	38.50	34.02	36.73	37.66	31.73
An	16.42	7.59	11.35	10.20	9.54	9.52	7.96	4.12
Di	--	--	--	0.20	--	--	--	--
Hy	6.25	0.57	3.00	3.69	3.76	3.08	0.42	0.60
Mt	2.49	0.43	1.33	1.81	1.69	1.55	0.39	0.30
Ilm	1.27	0.19	0.63	1.01	1.01	0.61	0.15	0.09
Ap	0.81	0.14	0.30	0.70	0.86	0.30	0.05	0.14
Rare Earth Elements in ppm: ICP analyses.								
La	--	10.0	--	--	--	--	--	7.3
Ce	--	18.46	--	--	--	--	--	15.7
Pr	--	2.29	--	--	--	--	--	1.99
Nd	--	6.9	--	--	--	--	--	6.82
Sm	--	0.97	--	--	--	--	--	1.76
Eu	--	0.39	--	--	--	--	--	0.29
Gd	--	0.91	--	--	--	--	--	1.41
Dy	--	0.5	--	--	--	--	--	1.6
Ho	--	0.1	--	--	--	--	--	0.36
Er	--	0.59	--	--	--	--	--	1.54
Yb	--	0.23	--	--	--	--	--	2.4
Lu	--	0.12	--	--	--	--	--	0.49

A1.3: Isotope analysis.

$^{87}Sr/^{86}Sr$ and $^{143}Nd/^{144}Nd$ isotopic ratios were measured at the isotope laboratories of the Earth Science Department at Leeds University. Eighteen samples were run for both ratios. Approximately 0.2g of unspiked powder was initially added to a mixture of hydrofluoric and concentrated nitric acids in PTFE beakers. The beakers were placed in bombs and kept at over 200°C in an oven for four to five days to ensure that all the accessory phases, which may contain the bulk of the Nd, dissolved. The sample was then evaporated to dryness and redissolved in concentrated nitric acid to check that there was no undissolved residue. After evaporating the nitric acid off, 6M hydrochloric acid was added and the samples were placed back in the bombs for a further two days in order to convert all the fluoride complexes to chloride complexes. After evaporating the samples down to dryness again, 2ml of 2.5M hydrochloric acid was added and wet chemical, ion exchange techniques were used to extract the Sr and Nd from the sample.

Sr was loaded onto a single Ta filament prepared with phosphoric acid, and the samples were run on an automated VG 54E mass spectrometer. Nd was loaded onto two Ta side filaments separated by a single rhenium filament, and the samples were run on a manual Micromass 30 mass spectrometer. One sample failed to give a result for Sr with sufficiently small errors and five failed for Nd. This is presumed to be a result of low Nd abundances and loss of the sample during preparation, since the stage at which Nd is removed is sensitive to temperature. Due to a lack of time these samples could not be rerun.

$^{87}Rb/^{86}Sr$ and $^{147}Sm/^{144}Nd$ ratios given in the following tables were calculated from XRF (Rb/Sr) and ICP (Sm/Nd) single element abundances using the equations given in chapter 1.3.d:.

Sample	Lithology	Rb ppm	Sr ppm	$^{87}Rb/^{86}Sr$	$^{87}Sr/^{86}Sr$
Hunza Plutonic Complex (HPC) 95my phase					
B16	Contact QzDi	113.3	509.1	0.6438	0.706373±14
B52	Granodiorite	108.6	319.5	0.9838	0.711343±12
B111	N. Grd.	100.6	254.4	1.1450	0.715577±12
B115	Xenolith	140.4	261.5	1.5546	0.715692±14
HPC mixing zone					
B84	Acidic gneiss	147.3	189.7	2.2490	0.718833±10
B85	Peg. sweat	132.5	157.7	2.4314	0.709949±12
B62	Aplite sheet	83.5	425.9	0.5672	0.706524±10
Hunza Dykes					
B120	Leucogranite	221.3	296.3	2.1616	0.711242±10
B121	Leucogranite	225.7	43.5	15.020	0.713361±10
SLV20	Leucogranite	168.4	85.9	5.6801	0.722537±10
SLV33	Leucogranite	202.1	198.5	2.9474	0.713772±10
NSG1	Nagar sheet	131.8	95.1	4.0123	0.714359±10
Other Hunza litholgies					
SG2	Sumayar	383.2	41.4	27.070	0.818818±10
SLG2	Country rock	8.5	530.5	0.0463	0.705214±14
Baltoro Plutonic Unit					
R-58	Monzogranite	155.8	463.0	0.9736	0.707700±12
R-85	Monzogranite	188.4	821.9	0.6633	0.709775±10
R-64	Leucogranite	267.4	151.4	5.1107	0.709393±10

Sample	Lithology	Sm ppm	Nd ppm	$^{147}Sm/^{144}Nd$	$^{143}Nd/^{144}Nd$
Hunza Plutonic Complex (HPC) 95my phase					
B16	Contact QzDi	4.7	27.2	0.10446	0.512551±22
B52	Granodiorite	6.66	34.3	0.11727	0.512202±21
B111	N. Grd.	5.38	31.4	0.10357	0.512087±22
HPC mixing zone					
B85	Peg. sweat	0.7	3.7	0.11437	0.512514±20
B62	Aplite sheet	3.67	21.1	0.10525	0.512516±12
Hunza Dykes					
B120	Leucogranite	1.77	6.0	0.17833	0.512278±30
SLV33	Leucogranite	3.4	19.4	0.10584	0.512258±18
NSG1	Nagar sheet	1.79	6.45	0.16777	0.512378±22
Other Hunza litholgies					
SG2	Sumayar	2.65	10.5	0.15254	0.511461±24
SLG2	Country rock	2.25	6.57	0.20704	0.512708±30
SLG6	Country rock	8.66	43.8	0.11954	0.512843±29
Baltoro Plutonic Unit					
R-85	Monzogranite	6.93	51.4	0.08147	0.512278±17
R-64	Leucogranite	1.47	7.5	0.11848	0.512185±26

Appendix 1.3: Isotope data from this study.

Sample	Lithology	Rb ppm	Sr ppm	$^{87}Rb/^{86}Sr$	$^{87}Sr/^{86}Sr$
Baltoro Plutonic Unit					
R-2	Monzogranite	136.4	573.3	0.6884	0.708307
R-3	Monzogranite	130.0	588.3	0.6396	0.708443
R-33	Monzogranite	233.6	795.6	0.8499	0.712845
R-34	Monzogranite	197.2	505.0	1.1303	0.712497
R-37	Monzogranite	234.4	755.2	0.8984	0.712919
R-45	Monzogranite	154.3	611.0	0.7307	0.708285
R-49	Monzogranite	185.2	277.9	1.9288	0.711115
R-55	Monzogranite	138.0	486.3	0.8210	0.707355
R-58	Monzogranite	152.7	472.5	0.9350	0.707648
R-62	Monzogranite	193.8	314.6	1.7824	0.708590
R-65	Monzogranite	146.7	193.2	2.1978	0.710693
R-79	Monzogranite	139.9	366.1	1.1060	0.710065
R-93	Monzogranite	104.0	812.3	0.3705	0.708912
R-95	Monzogranite	87.4	718.9	0.3518	0.708721
R-1	Leucogranite	156.9	53.7	8.4536	0.711438
R-4	Leucogranite	168.1	208.4	2.3338	0.708307
Masherbrum Migmatite Complex					
R-52	Pegmatite	247.2	115.5	6.1970	0.709776
R-56	Pegmatite	235.6	130.0	5.2450	0.709490
R-64	Pegmatite	260.3	151.5	4.9706	0.709386
R-66	Pegmatite	209.2	55.4	10.931	0.710623
Other Baltoro lithologies					
R-53	K2 Gneiss	181.9	209.9	2.5081	0.711151
R-13	Porphyry	133.0	385.0	1.0000	0.711991
R-14	Porphyry	86.3	315.3	0.7923	0.712624
R-39	Muztagh Tower	-	-	1.2768	0.713123
R-42	Muztagh Tower	-	-	1.0343	0.711865
Baltoro Lamprophyres					
R-11	Lamprophyre	358.4	1221.4	0.8497	0.716574
R-74	Lamprophyre	659.7	917.8	2.0823	0.721261

Appendix 1.3: Rb-Sr isotope data for the Baltoro area, N. Pakistan. All analyses carried out by A.J. Rex (pers. comm).

A1.4: Electron microprobe analysis.

All probe analyses were carried out at Leicester University. A new probe was installed at the start of 1988 resulting in a gap from September, 1987 to March, 1988 when no analyses could be done. Prior to September, 1987, measurements were made on a Cambridge Scientific Microscan 5 instrument with a Link Analytical 860 series 1 energy dispersive system (ED). Operating voltage was 15kV with a specimen current of 3E-9 A and count time of 100 seconds. After March, 1988, analyses were carried out on a JEOL JXA-8600S Superprobe with a wavelength dispersive system (WD). Operating voltage was again 15kV with a probe current of 3E-8 A. A standard program of 10 elements (SiO_2, TiO_2, Al_2O_3, Cr_2O_3, FeO, MnO, MgO, CaO, Na_2O, K_2O) was used with each element being measured twice using a peak count of 10 seconds and a background count for 5 seconds.

In the following tables total iron is given as FeO except for amphibole and Fe-oxide analyses. Fe_2O_3 is calculated for amphiboles by assuming 13 cations excluding Ca, Na and K and then adjusting the FeO/Fe_2O_3 ratio to bring the oxygen total upto 23. This gives a maximum estimate of Fe^{3+} and is the method recommended by Leake (1978). Fe_2O_3 in Fe-oxides is calculated using the charge balance method of Carmicheal (1967). For the geothermometry and barometry discussed in chapter 6.4. only the average analyses were used, and not all the individual analyses are given. Error data is also presented for some averages. The proportion of Fe_2O_3 in garnet was calculated within the geothermo-barometry programs using the charge balance method of Ryburn et al (1976) and is not given here.

The garnet-biotite geothermometer of Hodges and Spear (1982) was used because the Hunza samples often exceed the chemical limits set by Ferry and Spear (1978) in their original thermometer. The Hodges and Spear calculation allows for this by applying corrections to account for non-ideality in garnet solid solutions. The free energy interaction or Margueles parameter for the bounding binary solution between Mn and Mg in garnet was assumed to be zero following Hodges and Spear (1982) who showed that the value of 3500 cal/mol (taken from Ganguly and Kennedy, 1974) led to considerable overestimates of metamorphic conditions. The value of zero gives reasonable temperatures with the smallest range in values. The geobarometer of Hodges and Crowley (1985) was used since the garnet-biotite-muscovite-plagioclase assemblage was most common in the rocks studied. This applies the equation of Ghent and Stout (1981) but with the coefficients ∆H and ∆S recalibrated using a larger data set and a wider range in P and T. Hodges and Crowley (op.cit) found that this equation gave good results for sillimanite-grade metapelites. Some error may be inherent since the equation was calibrated using the garnet-biotite geothermometer of Ferry and Spear (1978) which, as mentioned above, does not allow for non-ideality in garnet solid solution. The Fe-endmember equation of Ghent and Stout (1981) is used since the Hunza garnets are Fe-rich and this is the equation that was recalibrated.

The samples which were used for probe analyses are:

B16	Southern contact quartz diorite
1PS3	Northern granodiorite
B8	Gulmit quartz diorite
1B1	Gulmit granodiorite
4B18	Gulmit quartz diorite
5B25	North of mixing zone granodiorite
6B31	Mixing zone granodiorite
8B42	North of mixing zone granodiorite
UV24	Ultar sheet granodiorite
1PS6	Carbonate-rich inclusion
2PS14	Mafic dyke opposite Gulmit
2PS8	Mafic inclusion near Gulmit
B117	Xenolith from Ghulkin
B17	Southern contact granodiorite
3B13	Northern granodiorite
8B37	North of mixing zone granodiorite
9PS55	Southern granodiorite
B70	HPC monzogranite dyke
B72	Leucogranite margin to HPC aplite sheet
B64	HPC monzogranite/granodiorite aplite sheet
SLV34	Hunza sillimanite-zone two-mica granite aplite
SG6	Sumayar leucogranite pluton
B67	Leucogranite margin to HPC aplite sheet
B121	Late leucogranite dyke in HPC
NSG4	Nagar Sheet leucogranite

B83 & BPS34 mixing zone gneisses for geothermometry

SL36, SL11, SL32, SL38, SL24, SL20, SL13, SL21 & SILL10 are all country rock, metapelitic biotite-garnet schists from south of the HPC.

HPC Clinopyroxenes: B16(1-6)

	1	2	3	4	5	6
SiO2	53.23	53.21	51.32	53.51	53.20	53.14
TiO2	0.05	0.10	0.13	0.07	0.04	0.10
Al2O3	1.05	1.06	1.18	1.12	1.17	1.17
FeO	9.59	9.17	8.35	8.21	8.88	8.26
MnO	0.45	0.41	0.42	0.38	0.34	0.41
MgO	12.96	12.86	12.71	13.20	13.13	13.21
CaO	23.52	23.64	23.07	24.33	24.02	24.34
Na2O	0.42	0.44	0.45	0.48	0.45	0.47
Total	101.29	100.91	97.73	101.32	101.27	101.15
Cations recalculated on the basis of 6 oxygens						
Si	1.975	1.978	1.968	1.975	1.970	1.968
Ti	0.001	0.003	0.004	0.002	0.001	0.003
Al	0.046	0.046	0.053	0.049	0.051	0.051
Fe2	0.298	0.285	0.268	0.253	0.275	0.256
Mn	0.014	0.013	0.014	0.012	0.011	0.013
Mg	0.717	0.713	0.727	0.726	0.725	0.729
Ca	0.935	0.942	0.948	0.962	0.953	0.966
Na	0.030	0.032	0.033	0.034	0.032	0.034
Sum	4.016	4.012	4.020	4.015	4.019	4.021

HPC Ilmenite: 1PS3(1-8)

	1	2	3	4	5	6	7	8
TiO2	54.02	53.98	54.00	53.98	54.21	54.26	54.37	54.30
Cr2O3	-	0.04	-	0.04	0.07	0.01	0.02	0.03
FeO	42.85	43.29	43.02	43.44	43.17	43.24	43.22	43.24
Fe2O3	-	-	-	-	-	-	-	-
MnO	2.23	2.16	2.10	2.11	2.37	2.09	2.06	2.06
MgO	0.33	0.39	0.39	0.37	0.27	0.40	0.40	0.39
CaO	0.11	0.01	0.02	0.01	0.09	0.05	-	0.04
Total	99.57	99.87	99.55	99.95	100.19	100.06	100.08	100.06
Cations calculated on the basis of 3 oxygens.								
Ti	1.019	1.016	1.019	1.016	1.017	1.018	1.020	1.019
Cr	-	0.001	-	0.001	0.001	-	-	0.001
Fe2	0.899	0.906	0.902	0.909	0.901	0.902	0.901	0.902
Fe3	-	-	-	-	-	-	-	-
Mn	0.047	0.046	0.045	0.045	0.050	0.044	0.044	0.044
Mg	0.012	0.015	0.015	0.014	0.010	0.015	0.015	0.015
Ca	0.003	-	0.001	-	0.002	0.001	-	0.001
Sum	1.981	1.984	1.981	1.984	1.982	1.982	1.980	1.981

HPC Magnetite: B8(1-5)

	1	2	3	4	5
SiO2	2.55	2.05	3.25	3.69	3.44
TiO2	0.09	0.01	0.02	-	0.02
Al2O3	0.03	0.04	0.05	0.02	0.02
FeO	27.73	26.33	29.06	29.63	28.93
Fe2O3	50.34	49.00	50.22	49.56	49.95
MnO	0.04	0.05	0.03	0.02	0.04
MgO	0.04	0.19	0.13	0.29	0.48
CaO	0.85	0.23	0.88	0.76	0.72
Total	81.67	77.93	83.66	83.98	83.60
Cations calculated on the basis of 4 oxygens					
Si	0.118	0.100	0.146	0.165	0.155
Ti	0.003	-	0.001	-	0.001
Al	0.002	0.002	0.003	0.001	0.001
Fe2	1.075	1.073	1.095	1.109	1.087
Fe3	1.756	1.796	1.702	1.668	1.689
Mn	0.002	0.002	0.001	0.001	0.002
Mg	0.003	0.014	0.009	0.019	0.032
Ca	0.042	0.012	0.042	0.036	0.035
Sum	3.000	3.000	3.000	3.000	3.000

HPC Amphiboles

1B1(1-4), 4B18(5-9), 5B25(10-12), 6B31(13-14), 8B42(15-18), UV24(19)
1PS6(20-22), 2PS14(23-24), 2PS8(24-26),B117(27)

	1	2	3	4	5	6	7	8	9
SiO2	44.66	43.30	42.95	42.99	51.22	49.77	48.86	48.51	51.28
TiO2	0.53	1.00	0.89	0.81	0.41	0.82	0.66	0.87	0.37
Al2O3	11.88	11.18	10.52	10.94	4.81	7.14	7.21	8.48	5.95
FeO	17.54	17.43	17.64	17.40	11.06	11.57	11.61	12.09	10.53
Fe2O3	1.00	0.20	0.42	0.47	-	0.01	-	-	-
MnO	0.42	0.51	0.49	0.45	-	-	-	-	-
MgO	8.51	8.77	8.49	8.36	15.42	14.33	13.64	12.90	14.71
CaO	12.25	11.92	11.79	11.72	12.62	12.58	12.51	12.63	12.89
Na2O	1.05	1.50	1.38	1.32	0.95	0.88	0.94	0.99	0.71
K2O	1.17	1.25	1.24	1.16	0.18	0.29	0.42	0.54	0.34
Total	99.01	97.06	95.81	95.62	96.67	97.39	95.85	97.01	96.78
Cations calculated on the basis of 23 oxygens.									
Si	6.633	6.587	6.634	6.634	7.439	7.201	7.200	7.084	7.414
Ti	0.059	0.114	0.103	0.094	0.045	0.089	0.073	0.096	0.040
Al	2.080	2.005	1.915	1.990	0.823	1.218	1.252	1.460	1.014
Fe2	2.179	2.217	2.279	2.246	1.343	1.400	1.431	1.477	1.273
Fe3	0.112	0.023	0.049	0.055	-	0.001	-	-	-
Mn	0.053	0.066	0.064	0.059	-	-	-	-	-
Mg	1.884	1.989	1.955	1.923	3.339	3.091	2.996	2.808	3.170
Ca	1.950	1.943	1.951	1.938	1.964	1.950	1.975	1.976	1.997
Na	0.302	0.442	0.413	0.395	0.268	0.247	0.269	0.280	0.199
K	0.222	0.243	0.244	0.228	0.033	0.054	0.079	0.101	0.063
Sum	15.474	15.628	15.609	15.561	15.255	15.251	15.275	15.281	15.170

	10	11	12	13	14	15	16	17	18
SiO2	44.89	43.71	42.74	42.25	44.04	41.83	42.05	42.63	42.47
TiO2	0.63	0.83	0.69	0.86	1.15	0.93	1.13	1.23	1.07
Al2O3	10.56	10.74	11.77	11.41	11.32	11.86	12.39	12.80	12.48
FeO	16.64	16.50	16.33	16.40	17.20	14.49	17.84	18.21	17.85
Fe2O3	0.50	1.40	1.58	-	0.28	4.26	-	0.02	-
MnO	0.32	0.31	0.58	-	-	0.42	0.70	0.50	0.43
MgO	9.56	9.23	8.65	8.34	9.28	8.10	7.82	8.42	7.83
CaO	11.99	11.91	11.89	11.41	11.82	11.00	11.89	12.21	11.83
Na2O	1.41	1.50	1.47	1.20	1.38	0.92	1.31	1.70	1.39
K2O	1.01	1.01	1.11	1.52	1.55	1.60	1.72	1.53	1.47
Total	97.51	97.14	96.81	93.39	98.02	95.41	96.85	99.25	96.82
Cations calculated on the basis of 23 oxygens.									
Si	6.737	6.618	6.509	6.634	6.605	6.453	6.448	6.380	6.489
Ti	0.071	0.095	0.079	0.102	0.130	0.108	0.130	0.138	0.123
Al	1.868	1.917	2.113	2.112	2.001	2.157	2.240	2.258	2.247
Fe2	2.088	2.089	2.080	2.154	2.157	1.870	2.288	2.279	2.281
Fe3	0.056	0.160	0.181	-	0.032	0.495	-	0.002	-
Mn	0.041	0.040	0.075	-	-	0.055	0.091	0.063	0.056
Mg	2.139	2.083	1.964	1.952	2.075	1.863	1.788	1.879	1.783
Ca	1.928	1.932	1.940	1.920	1.900	1.818	1.954	1.958	1.937
Na	0.410	0.440	0.434	0.365	0.401	0.275	0.390	0.493	0.412
K	0.193	0.195	0.216	0.305	0.297	0.315	0.337	0.292	0.287
Sum	15.532	15.568	15.590	15.543	15.598	15.408	15.665	15.744	15.614

	19	20	21	22	23	24	25	26	27
SiO2	42.85	53.99	49.33	50.63	43.57	43.32	42.73	41.65	41.03
TiO2	0.76	0.13	0.21	0.22	0.58	0.33	0.34	0.32	0.60
Al2O3	11.93	2.11	6.78	3.53	10.05	9.39	10.65	11.12	11.36
FeO	16.82	10.86	12.48	11.54	16.67	11.99	15.70	16.16	17.65
Fe2O3	-	-	-	-	-	4.86	-	-	3.78
MnO	-	-	-	0.30	-	-	0.53	0.54	0.55
MgO	8.94	16.00	13.30	14.25	9.13	10.09	9.06	8.59	7.42
CaO	12.11	13.16	12.76	12.65	11.89	10.78	12.31	12.50	11.73
Na2O	1.54	0.43	1.00	0.41	1.01	1.16	0.97	1.01	1.54
K2O	1.47	0.20	0.43	0.24	1.04	0.81	1.03	1.25	1.50
Total	96.42	96.88	96.29	93.77	93.94	92.73	93.36	93.15	97.16
Cations calculated on the basis of 23 oxygens.									
Si	6.538	7.786	7.266	7.607	6.784	6.756	6.698	6.588	6.350
Ti	0.087	0.014	0.023	0.025	0.068	0.039	0.040	0.038	0.070
Al	2.146	0.359	1.177	0.625	1.844	1.726	1.968	2.073	2.072
Fe2	2.146	1.310	1.537	1.450	2.171	1.564	2.058	2.138	2.284
Fe3	-	-	-	-	-	0.570	-	-	0.440
Mn	-	-	-	0.038	-	-	0.070	0.072	0.072
Mg	2.033	3.440	2.920	3.192	2.119	2.346	2.117	2.026	1.712
Ca	1.980	2.034	2.014	2.036	1.984	1.801	2.068	2.119	1.945
Na	0.456	0.120	0.286	0.119	0.305	0.351	0.295	0.310	0.462
K	0.286	0.037	0.081	0.046	0.207	0.161	0.206	0.252	0.296
Sum	15.673	15.099	15.305	15.138	15.482	15.313	15.526	15.617	15.703

HPC Amphiboles

B17(1-4), Overall Mean(5).

	1	2	3	4	5
SiO2	43.24	43.00	43.76	43.30	44.92 +- 7.02
TiO2	1.17	1.18	1.22	1.19	0.75 +- 0.68
Al2O3	10.92	10.42	10.04	9.91	9.73 +- 5.41
FeO	14.20	14.55	14.05	14.38	15.01 +- 5.09
Fe2O3	1.78	0.81	1.44	1.01	0.77 +- 2.60
MnO	0.41	0.36	0.34	0.35	0.27 +- 0.47
MgO	10.43	10.56	10.94	10.84	10.38 +- 5.11
CaO	11.96	12.04	11.99	12.08	12.09 +- 1.02
Na2O	1.31	1.34	1.33	1.34	1.17 +- 0.63
K2O	1.46	1.34	1.31	1.31	1.05 +- 0.96
Total	96.93	95.64	96.43	95.80	96.16

Cations calculated on the basis of 23 oxygens.

Si	6.526	6.574	6.619	6.608	6.794
Ti	0.133	0.136	0.139	0.137	0.085
Al	1.942	1.878	1.790	1.783	1.735
Fe2	1.792	1.861	1.777	1.835	1.899
Fe3	0.202	0.093	0.164	0.116	0.087
Mn	0.052	0.047	0.044	0.045	0.035
Mg	2.346	2.407	2.467	2.466	2.341
Ca	1.934	1.972	1.943	1.975	1.959
Na	0.383	0.397	0.390	0.397	0.344
K	0.281	0.261	0.253	0.255	0.202
Sum	15.599	15.631	15.586	15.627	15.483

HPC Plagioclases

1B1(1-5), 3B13(5-10), 4B18(11-15), 5B25(16-18)

	1	2	3	4	5	6	7	8	9
SiO2	55.5	54.6	56.1	54.2	55.0	58.2	55.5	56.8	58.1
Al2O3	26.4	27.2	26.1	27.8	26.3	25.6	26.0	25.8	24.5
CaO	9.5	10.5	9.1	10.8	9.5	7.9	9.2	8.2	6.6
Na2O	5.8	5.5	6.1	5.1	5.4	7.1	6.2	6.0	7.3
K2O	-	-	-	-	-	0.2	0.1	-	0.2
Total	97.2	97.8	97.4	97.9	96.3	98.9	97.0	96.8	96.6

Cations calculated on the basis of 8 oxygens

Si	2.559	2.514	2.580	2.493	2.560	2.629	2.569	2.616	2.676
Al	1.436	1.474	1.414	1.504	1.442	1.363	1.419	1.398	1.330
Ca	0.471	0.516	0.447	0.532	0.474	0.382	0.454	0.404	0.325
Na	0.516	0.492	0.543	0.454	0.487	0.618	0.552	0.536	0.648
K	-	-	-	-	-	0.010	0.008	-	0.009
Sum	4.982	4.995	4.984	4.982	4.963	5.003	5.002	4.953	4.988
An	47.7	51.2	45.1	54.0	49.3	37.8	44.8	43.0	33.1

An = 100*Ca/(Ca+Na+K)

	10	11	12	13	14	15	16	17	18
SiO2	59.0	56.3	57.6	49.7	57.8	57.9	55.3	55.2	55.1
Al2O3	22.2	28.0	26.4	31.9	26.5	26.6	27.2	26.9	27.6
CaO	4.9	10.4	9.1	15.4	9.2	8.7	10.0	10.2	10.4
Na2O	7.6	5.6	6.7	2.8	6.6	6.3	5.7	5.4	5.4
K2O	0.2	-	0.1	-	-	-	-	-	-
Total	93.9	100.3	99.9	99.9	100.1	99.4	98.1	97.8	98.5

Cations calculated on the basis of 8 oxygens

Si	2.777	2.521	2.587	2.270	2.587	2.601	2.529	2.536	2.513
Al	1.230	1.477	1.397	1.720	1.400	1.406	1.466	1.458	1.485
Ca	0.247	0.499	0.436	0.756	0.439	0.417	0.489	0.500	0.506
Na	0.695	0.486	0.580	0.249	0.573	0.546	0.506	0.483	0.482
K	0.012	-	0.008	-	-	-	-	-	-
Sum	4.962	4.983	5.008	4.995	4.999	4.969	4.991	4.977	4.986
An	25.9	50.6	42.6	75.2	43.4	43.3	49.2	50.9	51.2

HPC Plagioclases

5B25(1-3), 8B37(4-6), 8B42(7-10), UV24(11-13), 2PS14(14-17)
9PS55(18-22), 2PS8(23-25), B117(26)

	1	2	3	4	5	6	7	8	9
SiO2	57.3	55.3	55.8	62.0	60.9	62.4	55.8	57.3	57.9
Al2O3	26.1	27.2	26.8	22.6	23.1	23.4	26.3	26.0	27.2
FeO	-	-	-	-	0.3	-	-	-	-
CaO	8.4	9.7	6.7	4.9	4.8	5.1	9.3	8.4	9.1
Na2O	7.0	5.6	4.5	8.5	7.8	8.4	6.4	6.6	6.2
K2O	-	0.3	-	0.3	0.3	0.2	0.3	0.2	0.3
Total	98.8	98.2	93.8	98.2	97.3	99.6	98.2	98.5	100.7
Cations calculated on the basis of 8 oxygens									
Si	2.595	2.532	2.617	2.792	2.769	2.773	2.558	2.605	2.574
Al	1.396	1.468	1.483	1.199	1.240	1.227	1.422	1.390	1.428
Fe2	-	-	-	-	0.011	-	-	-	-
Ca	0.409	0.477	0.338	0.236	0.235	0.245	0.457	0.411	0.434
Na	0.614	0.500	0.406	0.746	0.691	0.724	0.568	0.580	0.536
K	-	0.018	-	0.016	0.020	0.012	0.018	0.011	0.014
Sum	5.014	4.993	4.844	4.989	4.966	4.982	5.023	4.996	4.987
An	40.0	47.9	45.4	23.6	24.9	24.9	43.8	41.0	44.1

An = 100*Ca/(Ca+Na+K)

	10	11	12	13	14	15	16	17	18
SiO2	56.6	57.5	57.1	58.4	57.1	59.3	55.6	55.5	57.4
TiO2	-	-	-	0.3	-	-	-	-	-
Al2O3	26.0	25.5	25.7	26.0	23.6	24.8	27.0	27.3	25.9
CaO	8.8	8.6	8.1	8.2	6.5	6.6	9.9	10.0	8.2
Na2O	6.2	6.4	6.3	6.6	7.4	7.4	6.2	6.0	6.7
K2O	0.2	0.2	0.3	0.3	0.1	0.2	-	-	0.3
Total	97.8	98.2	97.4	99.8	94.7	98.3	98.7	98.9	98.5
Cations calculated on the basis of 8 oxygens									
Si	2.591	2.619	2.617	2.615	2.684	2.682	2.534	2.525	2.607
Ti	-	-	-	0.010	-	-	-	-	-
Al	1.404	1.370	1.388	1.374	1.308	1.324	1.451	1.466	1.388
Ca	0.432	0.417	0.395	0.395	0.328	0.321	0.482	0.487	0.400
Na	0.552	0.566	0.563	0.574	0.673	0.648	0.543	0.530	0.594
K	0.010	0.013	0.015	0.014	0.008	0.011	-	-	0.015
Sum	4.988	4.986	4.978	4.982	5.002	4.986	5.012	5.007	5.004
An	43.4	41.9	40.7	40.2	32.5	32.8	47.0	47.9	39.7

	19	20	21	22	23	24	25	26
SiO2	57.0	58.2	56.9	55.8	58.65	60.12	57.41	61.91
Al2O3	25.6	26.3	25.5	25.9	25.51	22.77	25.96	22.34
Cr2O3	-	-	-	-	-	0.04	0.01	0.02
FeO	-	-	-	-	0.01	0.37	0.06	0.09
MnO	-	-	-	-	0.03	0.01	0.04	0.01
MgO	-	-	-	-	-	0.36	-	-
CaO	8.1	8.3	8.2	9.0	8.15	5.85	8.78	5.20
Na2O	6.3	6.4	6.4	5.8	7.03	7.91	6.81	8.87
K2O	0.3	0.2	0.3	0.2	0.15	0.14	0.15	0.18
Total	97.4	99.5	97.2	96.7	99.54	97.58	99.23	98.63
Cations calculated on the basis of 8 oxygens								
Si	2.616	2.612	2.615	2.585	2.635	2.741	2.596	2.787
Al	1.386	1.393	1.383	1.414	1.351	1.224	1.384	1.185
Cr	-	-	-	-	-	0.001	-	0.001
Fe2	-	-	-	-	-	0.014	0.002	0.003
Mn	-	-	-	-	0.001	-	0.002	-
Mg	-	-	-	-	-	0.024	-	-
Ca	0.397	0.400	0.405	0.445	0.392	0.286	0.425	0.251
Na	0.565	0.558	0.568	0.518	0.612	0.699	0.597	0.774
K	0.018	0.012	0.015	0.011	0.009	0.008	0.009	0.010
Sum	4.982	4.976	4.985	4.972	5.000	4.999	5.015	5.012
An	40.5	41.2	41.0	45.7	38.7	28.8	41.3	24.2

HPC Biotites

1B1(1-4), 3B13(5-7), 4B18(8-10), 5B25(10-11), 6B31(13-14), 8B37(15-17)
8B42(18-19), UV24(20), 2PS14(21-23), 9PS55(24-26), 2PS8(27)

	1	2	3	4	5	6	7	8	9
SiO2	35.9	36.2	36.1	36.3	34.4	36.3	35.6	37.9	37.6
TiO2	1.9	1.7	1.9	1.5	1.8	2.3	2.4	2.1	2.1
Al2O3	16.1	16.1	16.0	16.2	16.8	17.7	17.0	16.5	16.4
FeO	19.9	19.9	20.3	20.0	19.5	20.2	19.9	15.4	15.4
MnO	0.4	0.5	-	-	-	-	-	-	-
MgO	9.7	9.3	9.7	9.6	8.6	9.2	8.4	13.1	13.0
K2O	9.2	9.7	9.7	9.5	9.4	9.8	9.7	9.6	9.6
Total	93.2	93.3	93.8	93.2	90.4	95.4	93.0	94.6	94.0
Cations calculated on the basis of 22 oxygens									
Si	5.623	5.667	5.635	5.680	5.559	5.543	5.586	5.688	5.674
Ti	0.227	0.203	0.223	0.178	0.219	0.265	0.286	0.232	0.243
Al	2.970	2.966	2.946	2.987	3.191	3.178	3.138	2.917	2.911
Fe2	2.609	2.601	2.652	2.618	2.633	2.577	2.615	1.934	1.939
Mn	0.054	0.062	-	-	-	-	-	-	-
Mg	2.261	2.182	2.247	2.237	2.061	2.087	1.967	2.932	2.932
K	1.843	1.931	1.933	1.898	1.927	1.905	1.935	1.834	1.854
Sum	15.586	15.612	15.636	15.598	15.590	15.555	15.527	15.538	15.554
Mg No.	46.4	45.6	45.9	46.1	43.9	44.8	42.9	60.3	60.2

Mg No. = 100*Mg/(Fe2+Mg)

	10	11	12	13	14	15	16	17	18
SiO2	38.3	36.3	36.4	36.7	36.2	35.3	35.1	36.0	36.1
TiO2	1.9	2.0	1.7	2.4	2.3	3.7	2.9	3.3	1.4
Al2O3	16.9	16.1	16.3	16.0	15.6	16.8	16.2	16.9	15.7
FeO	15.5	19.7	19.8	18.8	19.3	20.6	20.4	20.9	19.2
MnO	-	0.3	0.3	-	-	-	-	-	0.3
MgO	13.7	9.6	9.7	10.9	10.9	7.8	8.8	8.5	9.6
Na2O	0.7	0.6	-	0.8	0.6	0.5	-	-	-
K2O	9.8	9.5	9.7	9.7	9.8	9.8	9.1	9.9	8.4
Total	96.8	94.2	93.8	95.3	94.6	94.7	92.6	95.6	90.8
Cations calculated on the basis of 22 oxygens									
Si	5.624	5.633	5.653	5.600	5.587	5.483	5.547	5.528	5.747
Ti	0.212	0.237	0.194	0.271	0.266	0.431	0.343	0.385	0.172
Al	2.928	2.940	2.980	2.881	2.832	3.073	3.024	3.055	2.954
Fe2	1.908	2.554	2.575	2.401	2.486	2.680	2.700	2.685	2.552
Mn	-	0.041	0.046	-	-	-	-	-	0.045
Mg	3.002	2.230	2.255	2.480	2.507	1.802	2.065	1.941	2.284
Na	0.202	0.171	-	0.228	0.174	0.145	-	-	-
K	1.845	1.879	1.918	1.883	1.933	1.944	1.836	1.931	1.700
Sum	15.723	15.685	15.622	15.744	15.784	15.594	15.515	15.525	15.454
Mg No.	61.1	46.6	46.7	50.8	50.2	40.2	43.3	42.0	47.2

	19	20	21	22	23	24	25	26	27
SiO2	36.3	36.5	35.8	35.7	34.2	36.3	35.4	35.8	37.18
TiO2	1.9	1.8	1.3	1.5	1.5	3.0	2.7	3.2	1.26
Al2O3	16.0	15.7	16.0	15.7	15.2	17.3	17.2	17.1	16.98
FeO	19.3	18.9	19.4	18.3	17.7	20.1	20.7	20.3	17.74
MgO	10.5	10.5	10.3	10.5	10.3	9.6	9.1	9.3	11.81
CaO	-	-	-	-	0.3	-	-	0.2	0.01
Na2O	0.7	-	-	-	-	0.7	-	-	0.08
K2O	9.7	9.6	9.6	9.8	8.3	9.8	9.9	9.7	9.65
Total	94.4	93.0	92.3	91.6	87.4	96.8	94.9	95.6	95.05
Cations calculated on the basis of 22 oxygens									
Si	5.601	5.698	5.644	5.665	5.653	5.482	5.467	5.471	5.631
Ti	0.217	0.208	0.152	0.180	0.183	0.340	0.316	0.366	0.144
Al	2.920	2.889	2.980	2.937	2.959	3.079	3.127	3.088	3.031
Fe2	2.498	2.462	2.557	2.433	2.440	2.538	2.672	2.593	2.247
Mg	2.422	2.441	2.416	2.478	2.528	2.150	2.096	2.120	2.666
Ca	-	-	-	-	0.050	-	-	0.033	0.002
Na	0.213	-	-	-	-	0.214	-	-	0.023
K	1.912	1.904	1.929	1.987	1.747	1.886	1.950	1.899	1.865
Sum	15.784	15.602	15.678	15.680	15.559	15.688	15.628	15.569	15.653
Mg No.	49.2	49.8	48.6	50.5	50.9	45.9	44.0	45.0	54.3

HPC Biotites

2PS8(1-4), B117(5), B17(6-8)

	1	2	3	4	5	6	7	8
SiO2	36.98	37.05	36.99	37.25	36.28	37.15	36.47	37.07
TiO2	1.36	1.40	1.20	1.43	2.09	3.06	3.60	3.34
Al2O3	16.68	16.51	16.71	16.41	14.78	14.72	14.54	14.96
FeO	17.89	17.75	17.90	18.00	20.94	17.49	16.97	17.09
MnO	0.28	0.39	0.40	0.34	0.43	0.21	0.20	0.25
MgO	11.59	11.44	11.50	11.23	9.94	11.78	11.62	11.72
Na2O	0.09	0.08	0.06	0.14	0.09	0.07	0.09	0.09
K2O	9.83	9.67	9.76	9.76	9.51	10.01	9.95	9.70
Total	94.76	94.34	94.57	94.61	94.16	94.55	93.48	94.27
Cations calculated on the basis of 22 oxygens								
Si	5.634	5.663	5.646	5.684	5.669	5.683	5.641	5.667
Ti	0.156	0.161	0.138	0.164	0.246	0.352	0.419	0.384
Al	2.995	2.975	3.007	2.952	2.722	2.654	2.651	2.695
Fe2	2.280	2.269	2.285	2.297	2.736	2.238	2.195	2.185
Mn	0.036	0.050	0.052	0.044	0.057	0.027	0.026	0.032
Mg	2.632	2.607	2.617	2.555	2.315	2.686	2.679	2.671
Na	0.027	0.024	0.018	0.041	0.027	0.021	0.027	0.027
K	1.911	1.886	1.901	1.900	1.896	1.954	1.964	1.892
Sum	15.679	15.642	15.669	15.644	15.684	15.622	15.607	15.559
Mg No.	53.6	53.5	53.4	52.7	45.8	54.6	55.0	55.0

Mg No. = 100*Mg/(Fe2+Mg)

HPC Sphene

1B1(1-2), 3B13(3), 4B18(4), 5B25(5), 8B42(6-7), 2PS14(8)

	1	2	3	4	5	6	7	8
SiO2	30.0	30.9	29.7	30.4	30.3	30.7	30.9	29.4
TiO2	36.2	37.2	36.6	38.5	37.8	27.3	36.9	36.5
Al2O3	2.1	2.2	2.5	1.3	1.8	2.6	2.7	2.1
FeO	-	0.6	-	-	0.4	0.7	0.5	0.6
CaO	28.5	28.8	28.4	28.8	28.5	28.3	29.6	28.7
Total	96.7	99.7	97.2	99.1	98.6	89.6	100.5	97.3
Cations calculated on the basis of 20 oxygens								
Si	4.034	4.043	3.978	4.006	3.999	4.457	4.005	3.956
Ti	3.666	3.652	3.691	3.816	3.756	2.972	3.602	3.697
Al	0.327	0.344	0.393	0.197	0.276	0.437	0.410	0.330
Fe2	-	0.069	-	-	0.043	0.087	0.058	0.066
Ca	4.109	4.027	4.073	4.061	4.032	4.398	4.115	4.133
Sum	12.136	12.134	12.135	12.080	12.106	12.352	12.189	12.182

HPC Zoisite (1-4); Apatite (5-7); Chlorite (8)

	1	2	3	4	5	6	7	8
SiO2	37.3	38.5	38.6	38.1	-	-	0.4	25.0
Al2O3	26.3	27.1	27.5	27.3	-	0.3	-	19.9
FeO	6.8	7.2	6.6	7.3	-	0.6	0.4	26.7
MnO	-	-	-	0.6	-	-	-	0.4
CaO	24.2	24.0	24.5	23.9	56.4	56.6	54.9	-
K2O	-	-	-	-	-	-	-	0.2
P2O5	-	-	-	0.5	41.2	41.2	41.1	-
Total	94.7	96.9	97.6	98.0	97.6	98.7	96.8	72.2
Cations calculated on the basis of the following oxygens								
O	13.000	13.000	13.000	13.000	26.000	26.000	26.000	28.000
Si	3.176	3.195	3.169	3.135	-	-	0.067	6.476
Al	2.640	2.650	2.668	2.643	-	0.062	-	6.083
Fe2	0.483	0.497	0.454	0.502	-	0.086	0.064	5.800
Mn	-	-	-	0.040	-	-	-	0.092
Ca	2.205	2.137	2.155	2.103	10.643	10.596	10.415	-
K	-	-	-	-	-	-	-	0.063
P	-	-	-	0.036	6.143	6.090	6.155	-
Sum	8.504	8.480	8.472	8.523	16.786	16.834	16.700	18.514

HPC Sheet and Hunza dyke phases

Averages: B70 monzogranite dyke (1-3); B72 aplite sheet lcg margin (4-6); B64 aplite sheet (5-6); SLV34 2-mica granite aplite (9-11).

	1 BIOT(n=9)	2 KFSP(n=2)	3 PLAG(n=9)	4 KFSP(n=5)
SiO2	36.10 +- 0.17	64.41 +- 0.68	63.07 +- 0.65	64.91 +- 0.48
TiO2	3.89 +- 0.61	0.04 +- 0.02	-	-
Al2O3	17.25 +- 0.67	18.39 +- 0.17	22.88 +- 0.68	18.29 +- 0.49
FeO	21.63 +- 1.69	-	-	-
MnO	0.35 +- 0.10	0.03 +- 0.01	-	-
MgO	7.01 +- 0.49	-	-	-
CaO	-	-	4.65 +- 0.30	-
Na2O	0.07 +- 0.04	0.88 +- 0.25	9.01 +- 0.41	1.07 +- 0.44
K2O	9.83 +- 0.42	15.57 +- 0.32	0.21 +- 0.10	15.47 +- 0.62
Total	96.13	99.32	99.82	99.74

Cations calculated on the basis of 22 (biotite) or 32 (feldspar) oxygens

Si	5.526	11.969	11.185	12.002
Ti	0.448	0.006	-	-
Al	3.112	4.028	4.783	3.986
Fe2	2.769	-	-	-
Mn	0.045	0.005	-	-
Mg	1.600	-	-	-
Ca	-	-	0.884	-
Na	0.021	0.317	3.098	0.384
K	1.920	3.691	0.048	3.649
Sum	15.440	20.016	19.997	20.021

	5 PLAG(n=4)	6 BIOT(n=5)	7 PLAG(n=10)	8 BIOT(n=10)
SiO2	64.47 +- 2.68	35.77 +- 0.99	60.17 +- 1.99	35.95 +- 0.73
TiO2	-	3.23 +- 1.10	-	3.46 +- 0.76
Al2O3	22.51 +- 1.30	17.30 +- 0.66	24.83 +- 1.08	16.67 +- 0.60
FeO	-	20.48 +- 2.15	-	21.74 +- 1.16
MnO	-	0.42 +- 0.12	-	0.29 +- 0.08
MgO	-	7.49 +- 0.90	-	7.51 +- 0.60
CaO	3.93 +- 1.26	-	7.03 +- 1.32	-
Na2O	9.44 +- 0.58	-	7.61 +- 0.79	-
K2O	0.20 +- 0.14	9.55 +- 1.06	0.24 +- 0.09	9.80 +- 0.22
Total	100.55	94.24	99.88	95.42

Cations calculated on the basis of 22 (biotite) or 32 (feldspar) oxygens

Si	11.321	5.553	10.738	5.552
Ti	-	0.377	-	0.402
Al	4.659	3.165	5.223	3.035
Fe2	-	2.659	-	2.808
Mn	-	0.055	-	0.038
Mg	-	1.733	-	1.729
Ca	0.739	-	1.344	-
Na	3.214	-	2.633	-
K	0.045	1.891	0.055	1.931
Sum	19.979	15.433	19.994	15.494

	9 BIOT(n=7)	10 KFSP(n=8)	11 PLAG(n=4)
SiO2	35.39 +- 0.81	65.16 +- 2.16	64.93 +- 2.61
TiO2	3.04 +- 0.53	-	-
Al2O3	17.43 +- 0.55	18.39 +- 0.61	23.03 +- 1.46
FeO	22.77 +- 1.34	-	-
MnO	0.32 +- 0.12	-	-
MgO	6.38 +- 0.41	-	-
CaO	-	-	4.16 +- 1.99
Na2O	-	0.99 +- 0.33	9.23 +- 1.27
K2O	9.65 +- 0.41	15.56 +- 0.63	-
Total	94.98	100.10	101.35

Cations calculated on the basis of 22 (biotite) or 32 (feldspar) oxygens

Si	5.516	12.003	11.293
Ti	0.356	-	-
Al	3.202	3.993	4.721
Fe2	2.968	-	-
Mn	0.042	-	-
Mg	1.482	-	-
Ca	-	-	0.775
Na	-	0.354	3.113
K	1.919	3.657	-
Sum	15.486	20.006	19.903

SG6 (Sumayar) Garnet Analyses: rim to centre = 1 - 7

	1	2	3	4	5	6	7
SiO2	35.63	35.45	35.83	35.63	36.04	35.98	36.41
TiO2	0.02	0.01	0.06	0.03	0.07	0.04	0.05
Al2O3	20.55	20.50	20.52	20.30	20.56	20.53	20.55
Cr2O3	0.01	0.02	0.04	0.03	0.01	0.01	0.01
FeO	13.75	18.42	25.21	25.73	25.53	25.74	26.59
MnO	27.41	23.06	17.01	16.20	16.11	16.33	15.46
MgO	0.08	0.14	0.12	0.13	0.12	0.13	0.14
CaO	1.09	0.81	0.77	0.79	0.81	0.82	0.83
Total	98.56	98.42	99.57	98.86	99.28	99.60	100.06
Cations calculated on the basis of 24 oxygens							
Si	5.953	5.941	5.948	5.958	5.981	5.964	5.998
Ti	0.003	0.001	0.007	0.004	0.009	0.005	0.006
Al	4.047	4.049	4.015	4.001	4.022	4.011	3.990
Cr	0.001	0.003	0.005	0.004	0.001	0.001	0.001
Fe2	1.921	2.582	3.500	3.598	3.543	3.569	3.663
Mn	3.879	3.274	2.392	2.295	2.265	2.293	2.157
Mg	0.020	0.035	0.030	0.032	0.030	0.032	0.034
Ca	0.195	0.145	0.137	0.142	0.144	0.146	0.147
Sum	16.024	16.033	16.037	16.039	16.004	16.027	16.003

Average Garnet Analyses for Thermobarometry.

Sample	SL36 n=8	BPS34 n=4	SL11 n=7	SL32 n=3	SL38 n=5	SL24 n=14
SiO2	37.59	37.8	37.1	38.9	37.3	36.3
Al2O3	21.23	21.0	21.0	21.1	21.0	20.1
FeO	25.72	21.5	34.5	22.1	22.5	32.6
MnO	9.72	5.9	3.5	5.8	6.2	4.6
MgO	1.82	1.9	2.7	0.8	1.5	1.1
CaO	3.91	11.3	1.4	13.8	11.0	3.6
Total	99.99	99.3	100.2	102.5	99.4	98.3
Cations calculated on the basis of 24 oxygens						
Si	6.040	6.028	5.993	6.050	5.972	6.010
Al	4.021	3.941	3.998	3.857	3.959	3.933
Fe2	3.456	2.869	4.661	2.877	3.013	4.522
Mn	1.323	0.796	0.480	0.757	0.839	0.650
Mg	0.436	0.445	0.643	0.190	0.370	0.264
Ca	0.673	1.924	0.234	2.292	1.895	0.645
Sum	15.949	16.002	16.008	16.022	16.048	16.024

Sample	SL20 n=6	SL13 n=6	SL21 n=8	SILL10 n=11
SiO2	37.23 +- 1.36	36.84 +- 0.69	37.68 +- 1.27	38.07 +- 0.90
Al2O3	21.31 +- 0.40	20.73 +- 0.60	21.59 +- 0.67	21.72 +- 0.45
Cr2O3	-	0.04 +- 0.03	-	-
FeO	32.16 +- 0.72	35.29 +- 1.07	31.83 +- 0.78	31.51 +- 1.35
MnO	4.19 +- 0.71	-	3.24 +- 1.40	2.52 +- 0.57
MgO	4.20 +- 0.43	2.86 +- 0.12	4.80 +- 1.73	5.23 +- 0.98
CaO	0.96 +- 0.09	3.03 +- 0.59	1.44 +- 0.32	1.81 +- 0.49
Total	100.05	98.79	100.58	100.86
Cations calculated on the basis of 24 oxygens				
Si	5.962	5.998	5.965	5.981
Al	4.022	3.978	4.029	4.022
Cr	-	0.005	-	-
Fe2	4.307	4.805	4.214	4.140
Mn	0.568	-	0.434	0.335
Mg	1.003	0.694	1.133	1.225
Ca	0.165	0.529	0.244	0.305
Sum	16.027	16.010	16.020	16.008

Average Garnet Analyses for Thermobarometry.

Sample	B83 n=5	B67 n=6	B121 n=4	NSG4 n=4
SiO2	37.10 +- 2.37	37.10 +- 1.09	36.30 +- 1.30	36.19 +- 2.54
Al2O3	20.60 +- 1.09	20.96 +- 0.51	20.61 +- 0.99	20.51 +- 0.75
FeO	22.92 +- 1.57	26.14 +- 0.44	28.58 +- 0.52	33.43 +- 2.08
MnO	6.27 +- 2.44	12.62 +- 0.97	12.21 +- 1.22	6.74 +- 1.15
MgO	0.94 +- 0.51	1.18 +- 0.12	0.51 +- 0.01	0.62 +- 0.18
CaO	11.51 +- 4.54	2.50 +- 0.19	1.62 +- 0.50	1.79 +- 0.79
Na2O	-	-	0.05 +- 0.04	-
Total	99.34	100.50	99.88	99.28
Cations calculated on the basis of 24 oxygens				
Si	5.982	6.006	5.974	5.984
Al	3.915	4.000	3.998	3.997
Fe2	3.091	3.539	3.934	4.623
Mn	0.856	1.731	1.702	0.944
Mg	0.226	0.285	0.125	0.153
Ca	1.989	0.434	0.286	0.317
Na	-	-	0.016	-
Sum	16.060	15.994	16.035	16.018

Average Biotite Analyses for Thermobarometry

Sample	SL36 n=5	BPS34 n=5	SL11 n=8	SL32 n=2	SL38 n=6	SL24 n=17	SL20 n=6
SiO2	35.91	35.5	35.0	36.8	35.5	34.0	35.54 +- 0.96
TiO2	2.83	2.9	4.2	2.2	2.5	2.7	2.29 +- 0.63
Al2O3	17.40	16.4	18.1	16.5	16.1	16.8	18.51 +- 1.64
FeO	20.42	20.0	21.5	25.0	20.5	26.9	16.50 +- 0.57
MnO	0.42	0.3	-	0.3	-	0.2	0.13 +- 0.06
MgO	7.82	9.5	7.1	7.1	9.3	4.3	10.37 +- 0.61
K2O	9.71	9.4	9.6	9.3	9.4	9.6	9.40 +- 0.32
Total	94.51	94.0	95.5	97.1	93.3	94.5	93.20
Cations calculated on the basis of 22 oxygens							
Si	5.559	5.523	5.388	5.631	5.569	5.463	5.465
Ti	0.329	0.334	0.486	0.256	0.297	0.328	0.265
Al	3.175	3.012	3.288	2.974	2.981	3.175	3.355
Fe2	2.644	2.593	2.764	3.195	2.684	3.612	2.122
Mn	0.055	0.038	-	0.035	-	0.033	0.017
Mg	1.804	2.206	1.619	1.627	2.177	1.028	2.377
K	1.918	1.862	1.876	1.815	1.869	1.968	1.844
Sum	15.483	15.568	15.420	15.533	15.578	15.606	15.563
Mg No.	40.6	46.0	36.9	33.7	44.8	22.2	52.8

Mg No. = 100*Mg/(Fe2+Mg)

Sample	SL13 n=4	SL21 n=5	SILL10 n=11	B83 n=4
SiO2	34.17 +- 2.94	35.84 +- 1.11	36.16 +- 3.12	34.42 +- 1.52
TiO2	1.68 +- 1.24	2.44 +- 0.54	2.11 +- 1.24	3.57 +- 0.80
Al2O3	17.94 +- 1.22	18.24 +- 1.45	18.68 +- 1.47	15.02 +- 1.70
FeO	19.86 +- 2.33	15.63 +- 2.27	15.52 +- 2.66	23.61 +- 2.82
MnO	0.03 +- 0.02	-	-	0.31 +- 0.10
MgO	8.87 +- 1.09	11.28 +- 1.34	12.47 +- 1.85	6.01 +- 1.23
Na2O	0.29 +- 0.04	0.23 +- 0.06	0.27 +- 0.14	-
K2O	8.75 +- 1.45	9.61 +- 0.24	8.39 +- 2.88	9.35 +- 0.61
Total	91.59	93.27	93.60	92.29
Cations calculated on the basis of 22 oxygens				
Si	5.435	5.482	5.460	5.580
Ti	0.201	0.281	0.240	0.435
Al	3.364	3.288	3.325	2.870
Fe2	2.642	1.999	1.960	3.201
Mn	0.004	-	-	0.043
Mg	2.103	2.572	2.807	1.452
Na	0.089	0.068	0.079	-
K	1.776	1.875	1.616	1.934
Sum	15.614	15.565	15.486	15.516
Mg No.	44.3	56.3	58.9	31.2

Various Average Analyses for Thermobarometry

Sample	B67	B121	SL32	SL11	SL24	SL20
Phase	BIOT	BIOT	AMPH	MUSC	MUSC	MUSC
	n=3	n=1	n=3	n=2	n=1	n=6
SiO2	34.19 +- 2.64	32.72	41.3	45.6	43.2	45.67 +- 1.64
TiO2	2.69 +- 1.45	2.05	0.3	1.5	0.3	0.71 +- 0.40
Al2O3	16.95 +- 1.48	16.92	13.4	33.5	31.0	33.31 +- 1.74
FeO	22.07 +- 1.29	28.54	21.6	1.6	6.2	1.11 +- 0.24
MnO	0.50 +- 0.18	0.42	0.5	-	-	-
MgO	6.16 +- 0.37	2.58	6.2	0.4	1.0	0.81 +- 0.21
CaO	-	0.03	12.0	-	-	-
Na2O	0.16 +- 0.10	0.12	1.5	-	0.8	0.73 +- 0.10
K2O	9.38 +- 1.07	9.36	1.7	11.0	10.1	10.49 +- 0.31
Total	92.10	92.78	98.4	93.6	92.7	92.83
Cations calculated on the basis of the following oxygens						
O	22.000	22.000	23.000	22.000	22.000	22.000
Si	5.507	5.426	6.346	6.205	6.112	6.247
Ti	0.326	0.256	0.035	0.149	0.031	0.073
Al	3.218	3.307	2.418	5.376	5.166	5.371
Fe2	2.973	3.958	2.778	0.182	0.738	0.127
Mn	0.068	0.059	0.060	-	-	-
Mg	1.479	0.638	1.412	0.089	0.211	0.165
Ca	-	0.005	1.979	-	-	-
Na	0.050	0.039	0.438	-	0.214	0.194
K	1.927	1.980	0.329	1.912	1.820	1.831
Sum	15.547	15.672	15.794	13.914	14.291	14.007

Sample	SL13	SL21	B67	B121
Phase	MUSC	MUSC	MUSC	MUSC
	n=2	n=5	n=1	n=3
SiO2	45.03	46.24 +- 2.42	46.47	45.29 +- 1.84
TiO2	0.92	-	1.32	0.28 +- 0.05
Al2O3	32.75	33.28 +- 4.24	30.63	31.84 +- 1.00
FeO	1.33	1.08 +- 0.72	2.20	3.08 +- 0.56
MnO	0.03	-	0.05	0.06 +- 0.05
MgO	0.62	0.87 +- 0.14	1.08	0.51 +- 0.22
Na2O	1.02	0.61 +- 0.26	0.28	0.49 +- 0.30
K2O	9.75	10.55 +- 0.72	10.91	10.84 +- 0.42
Total	91.51	92.63	92.98	92.39
Cations calculated on the basis of 22 oxygens				
Si	6.243	6.325	6.396	6.303
Ti	0.096	-	0.137	0.029
Al	5.352	5.365	4.969	5.223
Fe2	0.154	0.124	0.253	0.359
Mn	0.004	-	0.006	0.007
Mg	0.128	0.177	0.222	0.106
Na	0.274	0.162	0.075	0.132
K	1.725	1.841	1.916	1.925
Sum	13.982	13.994	13.976	14.084

Average Plagioclase Analyses for Thermobarometry

Sample	SL11	SL24	SL20	SL13	SL21	B67	B121
	n=2	n=1	n=1	n=1	n=2	n=2	n=1
SiO2	61.8	55.3	60.68	59.70	59.48	64.11	64.74
Al2O3	22.4	24.0	22.00	22.88	23.63	20.82	19.00
CaO	5.1	3.3	4.89	6.39	6.80	3.19	1.49
Na2O	8.5	6.6	8.93	8.19	7.91	9.86	10.84
K2O	0.3	1.0	0.11	0.10	0.13	0.23	0.08
Total	98.1	90.1	96.83	97.32	98.03	98.38	96.23
Cations calculated on the basis of 8 oxygens							
Si	2.792	2.703	2.783	2.733	2.706	2.876	2.954
Al	1.192	1.385	1.189	1.235	1.267	1.101	1.022
Ca	0.248	0.176	0.240	0.313	0.331	0.153	0.073
Na	0.741	0.622	0.794	0.727	0.698	0.858	0.959
K	0.019	0.060	0.006	0.006	0.008	0.013	0.005
Sum	4.992	4.946	5.021	5.016	5.012	5.008	5.016

APPENDIX TWO: Sample Localities.

The following lists include all geochemical samples from the Baltoro and Hunza for which analyses were given in appendix 1. The lists are accompanied by three maps to show the locations given. The first map is for the Baltoro area (A2-1) and is taken from Searle et al. (in press). The second map (A2-2) shows those samples which were not collected from along the road section through the Hunza Plutonic Complex which is shown in the thrid map (A2-3). Samples from Khunjerab, Sost and Hushe (K203-K217 & K238-K266) were collected by M. Searle and are not included. For location of these plutons the reader is referred to figures 4.1 and 5.1 and Searle et al. (in press).

BALTORO.

Sample.	Description.	Locality.	Map.
R1	Leucogranite, rich in garnet. Some biotite.	Paiyu, S. contact.	1
R2	Monzogranite, Plag>Kfsp, some megacrysts.	Paiyu	1
R3	Monzogranite, one or two fsp megacrysts.	Paiyu	1
R4	Leucogranite, rich in garnet, biot>musc.	Paiyu, S. contact.	1
R33	Monzogranite, biotite aggregates.	Biange, N. contact	1
R34	Monzogranite, representative of area.	Biange, N. contact.	1
R35	Two-mica granite, late cross-cutting sheet.	Biange	1
R36	Aplitic leucogranite, lineations of biotite.	N. of Biange.	1
R37	Monzogranite, large aggregates of biotite, some megacrysts and iron stained.	Biange	1
R38	As R37.	Biange	1
R45	Monzogranite, K fsp. megacrysts.	Yermanandu.	1
R46	Monzogranite, from vein cutting main granite.	Yermanandu.	1
R49	Monzo-syenogranite, Kfsp>Plag, two-mica. (R49-52 collected from moraine).	Yermanandu.	1
R50	Leucogranite late-stage dyke. Rich in garnet, muscovite "books" and Kfsp megacrysts.	Yermanandu.	1
R51	Leucogranite, more biotite, less garnet than R50.	Yermanandu.	1
R52	Two-mica pegmatite with Kfsp megacrysts.	Yermanandu.	1
R55	Monzogranite, Kfsp megacrysts with biotite rims.	Yermanandu.	1
R56	Leucogranite, aplitic but rich in garnet, from glacier moraine. Ubiquitous of this region.	Yermanandu.	1
R57	Monzogranite, same locality as R56.	Yermanendu.	1
R58	Monzogranite, Kfsp>Plag, biot>>musc.	Urdukas.	1
R59	Monzogranite, as R58 except finer grained.	Urdukas	1
R60	Monzogranite, as R58 but with Kfsp megacrysts.	Urdukas	1
R61	Monzogranite, as R60 but a little garnet.	Urdukas	1
R62	Monzogranite, as R58 with Kfsp megacrysts.	Urdukas	1
R63.ii	Monzogranite, as R61 but strongly foliated.	Urdukas	1
R64	Leucogranite, garnet "strings" enclosing biotite devoid areas, (R64-73 collected from moraine).	Yermanandu	1
R65	Monzogranite, same locality as R64.	Yermanandu	1
R66	Leucogranite pegmatite with biotite-rich rim.	Yermanandu	1
R68	Aplitic leucogranite, moraine sample rich in small garnets and mica "books". Ubiquitous.	Yermanandu	1
R70	Pegmatite, with biotite and Kfsp>Plag.	Yermanandu	1
R71	Monzo-syenogranite, coarse graines.	Yermanandu	1
R75	Monzogranite vein in Kfsp megacrystic granite.	Vigne Glacier.	1
R76	Monzogranite, as R75 but more muscovite.	Vigne Glacier.	1
R77	Aplite in contact hornfels, biot>>musc.	Vigne & Mitre area.	1
R78	Aplite as R77, finer grained, less biotite.	Vigne & Mitre area.	1
R79	Monzogranite, Biot>>musc.	Vigne Glacier	1
R80	Monzogranite, rich in biotite.	Vigne Glacier	1
R81	Monzogranite, less biotite than R80.	Vigne Glacier.	1
R82	Monzogranite, large garnet crystals, from late vein. (R82-86 from moraine).	Trango area.	1
R84	Monzogranite, large Kfsp crystals.	Trango-Dunge area	1
R85	Monzogranite, pinkish Kfsp megacrysts.	Trango-Dunge area.	1
R86	Two-mica aplite, musc>biot.	Trango-Dunge area	1
R88	Monzogranite, representative.	Urdukas-Paiyu.	1
R89	Monzoganite, as R88 but a little garnet ± musc.	Urdukas-Paiyu.	1
R90	Late-stage aplite, two-mica but no garnet.	Urdukas-Paiyu	1
R91	Aplite in Kfsp megacrystic granite, as R90.	Urdukas-Paiyu	1
R92	Monzogranite/aplite, as R90 but little garnet.	Urdukas-Paiyu	1
R93	Monzogranite, Kfsp megacrysts and biotite-rich.	Urdukas-Paiyu	1
R94	Coarse grained, Kfsp megacrystic syenogranite.	Liligs	1
R95	Monzogranite, as R94 but no megacrysts, some garnet crystals.	Liligs.	1
R-6	Quartz dacite, subvolcanic porphyry-tuff.	Broad Peak	1
R-9	Prophyry with siliceous clasts (S. fan)	Concordia	1
R-10	Chloritised porphyry, as R-9.	Concordia	1
R-12	As R-9 (middle fan).	Concordia	1
R-14	As R-9 (N. fan).	Concordia	1
R-15	Homogeneous, lithic-poor tuff.	Concordia.	1
R-103	Garnet-biotite granitic migmatite	Gneiss dome in south.	1
R-104	Biotite-rich pegmatite, dominant in dome.	Gneiss dome in south	1
R-109	Sillimanite-gneiss.	East of Dassu	1
R-110	As R-109	East od Dassu	1
R-111	Muscovite pegmatite cutting R-109 (no garnet).	East of Dassu	1
R-11	Lamprophyre.	Concordia	1
R-74	Lamprophyre.	Gasherbrum area.	1

HUNZA. - OUTSIDE THE PLUTONIC COMPLEX.

Sample	Description	Locality	Map
BG1	Granodiorite, typical, coarse grained, clumps of hornblende and biotite (25%). All BG samples from terminal moraine.	Batura Glacier	2
BG2–BG5	Granodiorites, as BG1	Batura Glacier	2
BG6	Leucocratic granite, 50% less mafics than BG1.	Batura Glacier	2
BG7	Pegmatitic monzogranite, Kfsp megacrysts.	Batura Glacier	2
BG8	Foliated, leucocratic granite (15% mafic).	Batura Glacier	2
BG9 & 10	Leucocratic granites but with a little hbl.	Batura Glacier	2
BG11	Xenolith, rich in mafics with some cpx.	Batura Glacier	2
SG1–5	Sumayar Pluton, tourmaline-garnet-muscovite leucogranites with a little biotite.	Sumayar	2
SG6	Contact of Sumayar pluton. More garnet and altered compared to SG1–5.	Sumayar	2
NSG1–5	Nagar sheet leucogranite, rich in musc-garnet.	Nagar bridge	2
SLV3	Two-mica granite aplite, biot>musc, no garnet.	Hassanabad	2
SLV4	Monzogranite, large sheet, biotite only mafic.	Hassanabad	2
SLV5	Two-mica granite aplite, musc>biot.	Hassanabad	2
SLV7	Granodiorite/monzogranite dyke.	Altit	2
SLV8	Monzogranite, aplitic part of pegmatite boss.	Ultar	2
SLV9	Granodiorite sheet, well foliated, Plag>Kfsp.	Ultar	2
SLV12	Lower granodiorite sheet in Ultar. As with SLV9 biotite defines a foliation. Slightly weathered.	Ultar	2
SLV13	Granodiorite aplite near HPC contact.	Nr. Sarrat	2
SLV14	Granodiorite aplite, biotite as only mafic.	Hassanabad	2
SLV15	Quartz diorite, large sheet, some hbl and cpx.	Ultar	2
SLV17	As SLV15, biotite still dominant mafic.	Ultar	2
SLV18	Monzogranite aplite near HPC contact (5% biot).	Road	3
SLV19	Leucogranite pegmatite at Ky/Sill boundary, rich in garnet and muscovite.	Hassanabad	2
SLV20	As SLV19 with a little tourmaine.	Hassanabad	2
SLV21	Aliabad leucogranite sheet.	Hassanabad	2
SLV23	Concordant monzogranite aplite, biotite = 5–10%.	Road nr. Baltit.	2
SLV24	Monzogranite aplite opposite Mohammedabad.	Road	2
SLV25	Biotite-rich pegmatite ± tourmaline.	Road opp. M'abad.	2
SLV26	As SLV25, pegmatite boss rather than dyke.	Road opp. M'abad.	2
SLV27	Aplitic part of SLV26 pegmatite boss (5% biot).	Road	2
SLV28	Monzogranite aplite in pegmatite (15% biot.).	Road nr. Sarrat.	3
SLV29	Augen gneiss sheet near HPC contact.	Road nr. Sarrat.	3
SLV30	Leucogranite pegmatite, musc>biot ± tourmaline.	Nagar	2
SLV31	Monzogranite aplite, biotite (10%) only mafic.	Gharesa.	2
SLV32-34	Two-mica aplite in sill. gneiss. 32=edge (15% biot), 33=midway (biot=musc), 34=centre.	Hassanabad	2
3SLV35	Bar monzoganite sheet, Fsp megacrysts.	Bar Valley	2
3SLV36	As 3SLV35, biotite-rich matrix.	Bar Valley	2
9SLV35	Aliabad leucogranite sheet, two-mica.	Hassanabad	2
9SLV36	As 9SLV35, sporadic garnet.	Hassanabad	2
UV23	Ultar granodiorite sheet, as SLV15	Ultar	2
GC1	Monzogranite aplite, two-mica.	Road S of Baltit.	2
SLG2	Metabasic gneiss, hbl-biot-cpx (75%) + plag. Foliated with qtz in mm wide felsic bands.	Road S of contact.	3
SLG3	Interlayered basic gneiss/calc-gneiss, rich in garnet, cpx, hbl and biotite.	Road S of contact	3
SLG4	Augen gneiss, rich in biot + plag ± hbl, cpx.	Road opp. M'abad	2
SLG5	Augen gneiss as SLG4	Road nr. Baltit	2
SLG6	Layered mafic/felsic gneiss with 80/20% hbl and biotite rich layers ± cpx.	Hassanabad	2
SLG7	Augen gneiss, as SLG4 with sporadic garnet.	Road S of Baltit.	2

HUNZA PLUTONIC COMPLEX.

Sample	Description	Locality	Map
1B1	Granodiorite, rich in hbl + biot (30–40%)	Shishkat Bridge	3
1B2	Quartz diorite (55% mafics)	Shishkat Bridge	3
1B4	Granodiorite (fsp>mafics). Some hbl-rich pods.	Shishkat Bridge	3
1B6	Quartz diorite (40% mafics, 50% plag).	Shishkat Bridge	3
2B8	Quartz diorite from near N contact. Fsp=mafics, unusually mafic for this area.	N. Contact at river.	2
2B11	Granodiorite, typical, leucocratic.	Opp. Gulmit.	2
3B13	Northern granodiorite, biotite lineations.	Above Ghulkin	2
3B16	N. granodiorite, fsp>mafics (biot + hbl).	Gulmit Glacier	2
3B17	N. granodiorite (mafic = 35%).	S. side Gulmit Gl.	2
4B18	Quartz diorite, mafics>fsp (hbl, biot, cpx).	Nr Shishkat Bridge.	3
4B19	Granodiorite, euhedral hbl, mafics=fsp.	Shishkat Bridge	3
5B22	Typical granodiorite, 35% biot + hbl.	Above Shishkat.	3

Sample	Description	Locality	Map
5B23	Xenolith, dioritic and sharp-edged (60% mafics.).	Above Shishkat	3
5B25	Typical, mid-batholith granodiorite.	N. of Ayeen.	3
6B27	Typical granodiorite, fsp=mafics, faintly foliated. (large cutting = S of Ayeen).	Large cutting.	3
6B29	Monzogabbro, mafics = 65% (hbl, cpx, biot)	Mixing Zone.	3
6B31	Foliated granodiorite.	Large cutting	3
6B32	Acidic gneiss, fsp>mafics (biot + hbl).	Mixing zone	3
6B34	Gneissic, large fsp crystals, mafics=fsps.	Mixing zone.	3
7B36	Typical S. granodiorite, 35-40% mafics, foliated.	Sarrat	3
8B37	Granodiorite, mafics=fsps, coarse grained.	Ayeen	3
8B39	Leucocratic granodiorite, rich in biotite.	S. of Ayeen.	3
8B41	Granodiorite, 50% mafics, foliated.	S. of Ayeen	3
8B42	Granodiorite, mafics=fsps, typical.	Nr. large cutting.	3
9B43	Typical mixing zone granodiorite.	Mixing zone	3
9B44	Centre of HPC monzogranite aplite sheet.	Large cutting.	3
9B47	Typical S. granodiorite, fsps=mafics.	Opp. Sarrat	3
RBSR1	Quartz diorite, 60% mafics, euhedral plag.	Shishkat Bridge	3
RBSR3	Gulmit granodiorite, 40% mafics (biot + hbl).	Shishkat Bridge	3
RBSR4 & 5	As RBSR3.	Shishkat Bridge	3
RBSR7	Quartz diorite, 50% mafics, coarse grained.	Shishkat Bridge	3
B1	Typical N. granodiorite, 30% mafics (hbl+biot).	N. Contact	2
B2	As B1. Faint foliation.	250m from N. contact	2
B3	Leucogranite pegmatite, little garnet.	Nr N. contact.	2
B4	Monzogranite aplite, 5% biotite in clumps.	Opp. Gulmit.	2
B5	Northern granodiorite, 30% mafics.	Opp. Gulmit.	2
B6	Basic dyke, euhedral hbl and plag.	Opp. Gulmit.	2
B8	Quartz diorite, 50% plag, 50% hbl+biot.	Above Gulmit	2
B9	Granodiorite, 40% mafics, coarse grained.	Above Gulmit.	2
B11	Monzo-quartz diorite, 70% mafics (biot, hbl, and cpx) with rest = plag.	Above Gulmit	2
B12	Large leucogranite pegmatite rich in garnet "strings" and "books" of muscovite.	Above Gulmit	2
B14	N. granodiorite, 30% mafics.	N. contact.	2
B15	Typical N. granodiorite, as B14.	N. side Ghulkin Gl.	2
B16	Quartz diorite, 60% mafics (biot, hbl, cpx).	S. contact nr. Sarrat	2
B17	Granodiorite with fsp-rich band and cpx.	S. contact in M'abad	2
B18	Well foliated granodiorite/monzogranite.	S. contact in M'abad	2
B19	Monzogranite aplite, 20% biot as only mafic.	S. contact in Ultar	2
B20	Granodiorite, 50% mafics and large fsp crystals.	S. contact on road.	3
B21	Monzogranite aplite, parallel to F, 15% biot.	S. contact on road	3
B25	Granodiorite, 40% mafics, above thrust sheet.	S. contact on road	3
B26	Early part of HPC aplite sheet, monzogranite.	Opp. Sarrat.	3
B27	Late part of B26 sheet (10% biotite).	Opp. Sarrat.	3
B28	Granodiorite, 50% mafics.	At spring.	3
B29	Monzogranite aplite, biotite only mafic - layered with gnt-musc pegmatite.	At spring.	3
B30	Early monzogranite aplite dyke, biot>>musc.	At spring	3
B31	Granodiorite host, 50% mafics, small fsp augen.	Mixing zone	3
B34	Pegmatite sweat, 15% biot as mafic phase.	Mixing zone	3
B35	Late monogranite aplite dyke, 15% biotite	Mixing zone	3
B36	Banded granodiorite, 70% mafic layers (hbl, biot and cpx) on inch scale with 30% mafic layers.	Mixing zone	3
B37	Basic gneiss, biot + plag rich, little garnet.	Mixing zone	3
B38	Acidic gneiss, 15% biotite only mafic.	Mixing zone	3
B40	Acidic gneiss, 35% mafics (biot+hbl), unfoliated.	Mixing zone	3
B41	Late aplitic monzogranite dyke, 10% biot>>musc.	Mixing zone	3
B42	As B41, little muscovite.	Mixing zone	3
B44	Gneiss, 40-50% mafics (biot ± hbl), fsp forms mm wide monomineralic bands.	Mixing zone	3
B45	Pegmatite sweat, 10% biot = only mafic.	Mixing zone	3
B46	S. granodiorite, typical, 50% mafics, foliated.	Opp. Sarrat	3
B47	Aplitic centre of layered dyke, 10% biotite.	Opp. Sarrat	3
B48	S. granodiorite, 40% mafics (hbl + biot).	Opp. Sarrat	3
B49	As B48, foliated, biotite-rich layer.	Opp. Sarrat.	3
B51	As B48, partly altered.	Opp. Sarrat	3
B52	As B48, rich in hbl, rest = euhedral plag ± qtz.	Opp. Sarrat	3
B53	Early, aplitic monzogranite dyke, 10% biot, with pegmatitic margin.	Opp. Sarrat	3
B54	As B53, but later (cross-cutting).	Opp. Sarrat	3
B55	Monzogranitic, coarse grained, 15% biotite.	Mixing zone	3
B56	Granodiorite host for B55 & 57, 50% mafics.	Mixing zone	3
B57	Acidic gneiss, fsp-rich bands and augen, well foliated, biotite = only mafic.	Mixing zone	3
B58	Pegmatite sweat, 10% biotite only mafic	Mixing zone	3
B59	Aplitic monzogranite dyke, 15% biotite.	Mixing zone	3
B60	Typical granodiorite, 50% mafics, foliated.	Large cutting	3
B61	Rim of HPC aplite sheet, 20% biotite, mzg.	Large cutting	3
B62	Centre of B61 sheet, monzogranite.	Large cutting	3

Sample	Description	Locality	Map
B63	Typical granodiorite, 50% mafics.	Large cutting	3
B64	HPC aplite sheet, mzg, 20% biotite, some fsp-rich bands, unfoliated.	Large cutting	3
B65	Later part of B64 sheet, as B64.	Large cutting	3
B66	Layered aplite/pegmatite at edge of HPC sheet. Pegmatites rich in garnet and tourmaline.	Large cutting	3
B67	Sample of pegmatite from B66.	Large cutting	3
B68	HPC sheet with B66,67 as margin, mzg, 15% biot.	Large cutting.	3
B69	Large garnet-musc, leucogranite pegmatite.	Large cutting	3
B70	Early, aplitic monzogranite dyke, 20% biotite.	Large cutting	3
B71	Granodiorite, 35% mafics (biot + hbl).	Large cutting	3
B72	HPC aplite sheet monzogranite, 15% biot.	Large cutting	3
B73	More mafic part of B72 sheet, 20% biot.	Large cutting	3
B74	Late differentiate leucogranite dyke in B72 sheet, layered ap/peg, biotite only mafic (5%).	Large cutting	3
B77	Granodiorite, 50% mafics, unfoliated.	S. of mixing zone.	3
B78	Monzogranite, aplite dyke, 20% biotite, has granodiorite xenolith.	S. of mixing zone	3
B79	Leucogranite, layered ap/peg, 5% biotite.	S. of mixing zone	3
B80	Fsp megacrystic monzogranite, foliated, biot and hbl as mafics, biot included in fsps.	Mixing zone	3
B81	Basic gneiss, 60% mafics, well foliated.	Mixing zone	3
B82	Gneiss, 50% mafics, homogeneous, typical.	Mixing zone	3
B83	Gneiss, 35% mafics, some large garnets.	Mixing zone	3
B84	As B80, biot>>hbl.	Mixing zone	3
B85	Pegmatite sweat, 5% musc, large garnets, lcg.	Mixing zone	3
B86	Pegmatite sweat, mafics = biotite, mzg.	Mixing zone	3
B87	Monzogranitic, aplite dyke, 10% biotite.	Mixing zone	3
B88	Granodiorite, 45% mafics, faint foliation.	Nr. Ayeen	3
B89	Large, leucogranite layered ap/peg. Aplite rich in biotite (15%), pegs in muscovite.	Nr. Ayeen	3
B90	Monzogabbro, coarse grained hbl.	Shishkat Bridge	3
B91	As B90, 60-70% mafics (hbl>>cpx + biot)	Shishkat Bridge	3
B92	Xenolith, 50% biot+hbl, 50% plag. Equigranular.	Shishkat Bridge	3
B93	Gneissic xenolith as B92, richer in hbl.	Shishkat Bridge	3
B94	Early monzogranite aplite, biot>musc (10%).	Shishkat Bridge	3
B95	Large, leucogranite pegmatite, 5% musc, garnet in zones, some granodiorite enclaves.	Shishkat Bridge	3
B96	Quartz diorite, 60% mafics (hbl, cpx, biot) form matrix with plag as euhedral crystals.	Shishkat Bridge	3
B97	Monzogranite dyke, 10% biotite	Shishkat Bridge	3
B98	Monzogranite aplite dyke, 15% biotite.	Shishkat Bridge	3
B99	Typical Gulmit Granodiorite, 40% mafics, biot = hbl, faintly foliated.	Shishkat Bridge	3
B100	Granodiorite, 25% mafics, rich in white fsp.	Malamgodhi Gl.	2
B101	As B100, N. contact.	Malamgodhi Gl.	2
B102	Granodiorite, 50% mafics, well foliated.	S. contact, Gharesa	2
B103	2-mica pegmatite, mzg, musc=biot, sporadic gnt.	S. contact, Gharesa	2
B104	Monzogranite aplite dyke (early)	S. of Ayeen	3
B105	Early pegmatite, 10% biotite and garnet.	2km S. of Ayeen	3
B108	Granodiorite, 35% mafics, typical.	N. of Ayeen.	3
B109	Early monzogranite aplite, 20% biotite.	N. of Ayeen	3
B110	Large leucogranite pegmatite, two-mica and rare garnet. One part of sample has tourmaline.	Above Shishkat	3
B111	Typical N. granodiorite, 30% mafics, unfoliated.	Pasu Glacier	2
B112	As B111, some weathering.	Pasu Glacier	2
B113	As B111, faint foliation.	N. side of Ghulkin Gl.	2
B114	As B113	N. side of Ghulkin Gl.	2
B115	Gneissic xenolith, 50% biot + hbl, 50% plag, some black phenocrysts (hbl), slightly foliated.	N. side of Ghulkin Gl.	2
B116	As B115 but no phenocrysts.	N. side of Ghulkin Gl.	2
B117	As B115, cut by small, felsic veins.	N. side of Ghulkin Gl.	2
B118	Large leucogranite pegmatite, 15% mica (musc = biot), sporadic garnet.	Shishkat Bridge	3
B119	Earlier leucogranite pegmatite, biot = only mafic, some tourmaline.	Shishkat Bridge	3
B120	Two-mica granite pegmatite, 10% mica (musc>biot) Some tourmaline and rare garnet.	Large cutting	3
B121	Large, late leucogranite pegmatite, 10% mica (musc>>biot), musc forms "books", garnet-rich.	Large cutting	3

Figure A2-1: Geological map of the Baltoro area, N. Pakistan, (from Searle et al., in press) to show the localities of geochemical samples.

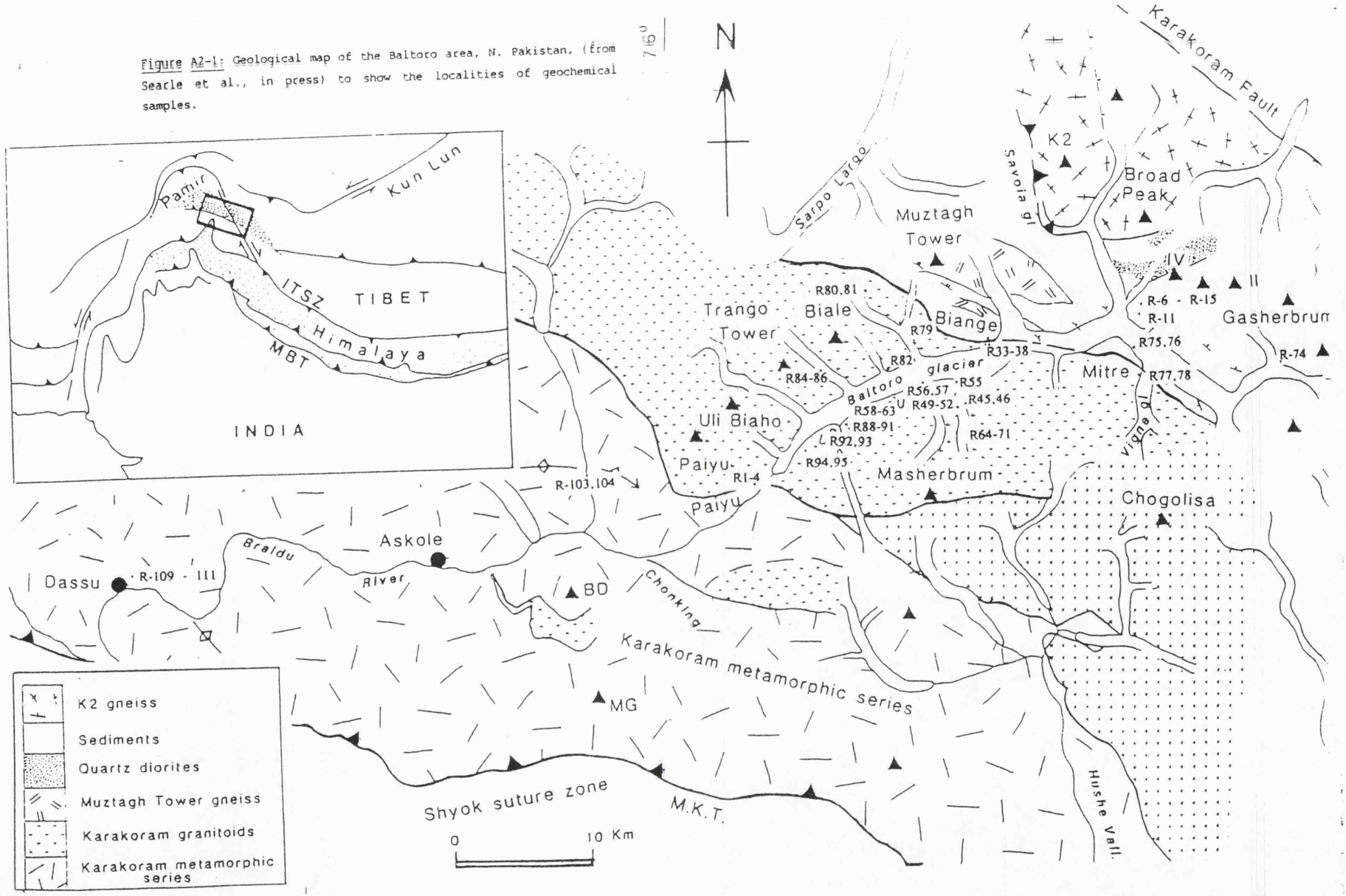

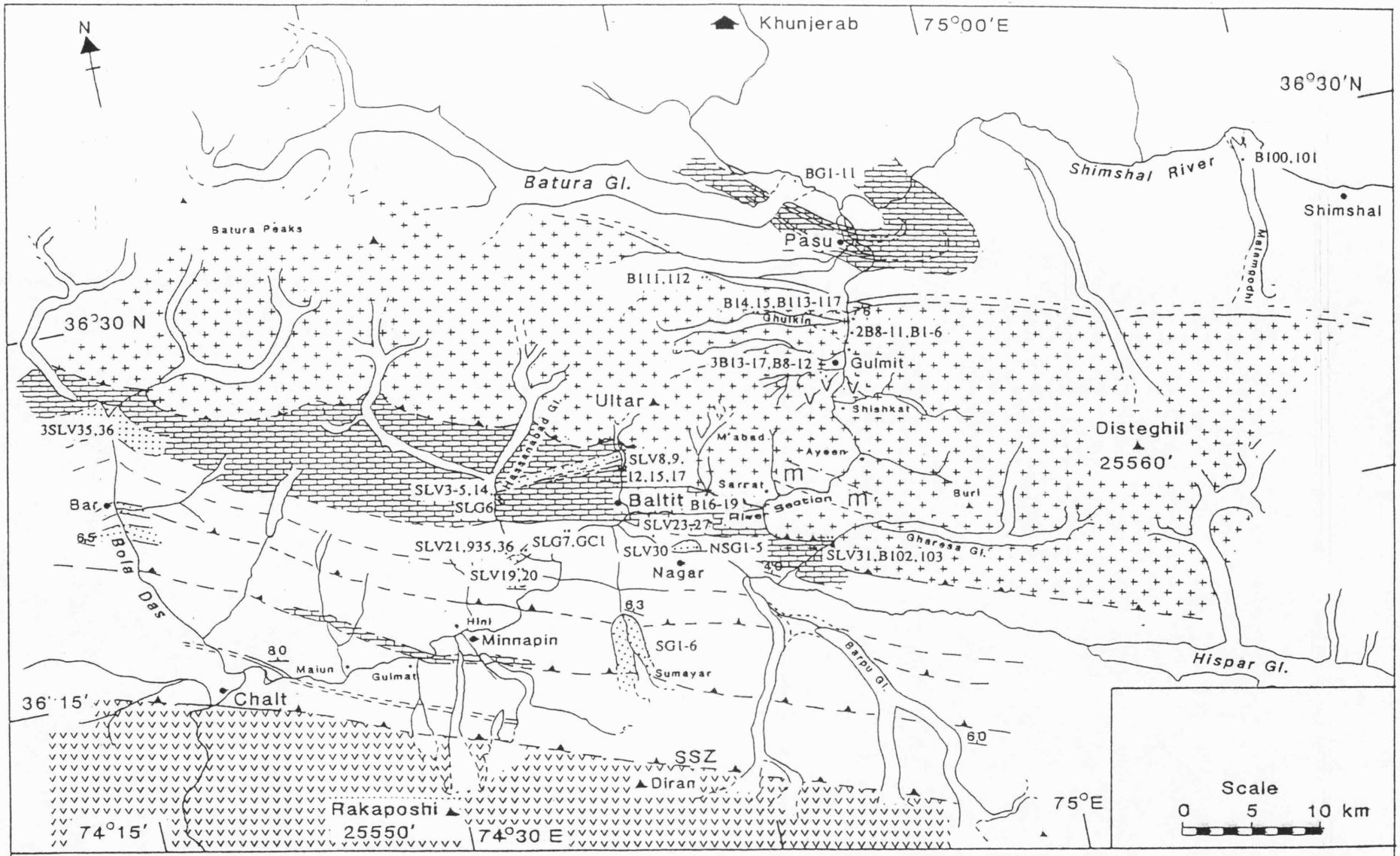

Figure A2-2: Geological map of the middle Hunza Valley to show the localities of geochemical samples not collected along the road section through the plutonic complex. See figure 3.2 for key to geological units.

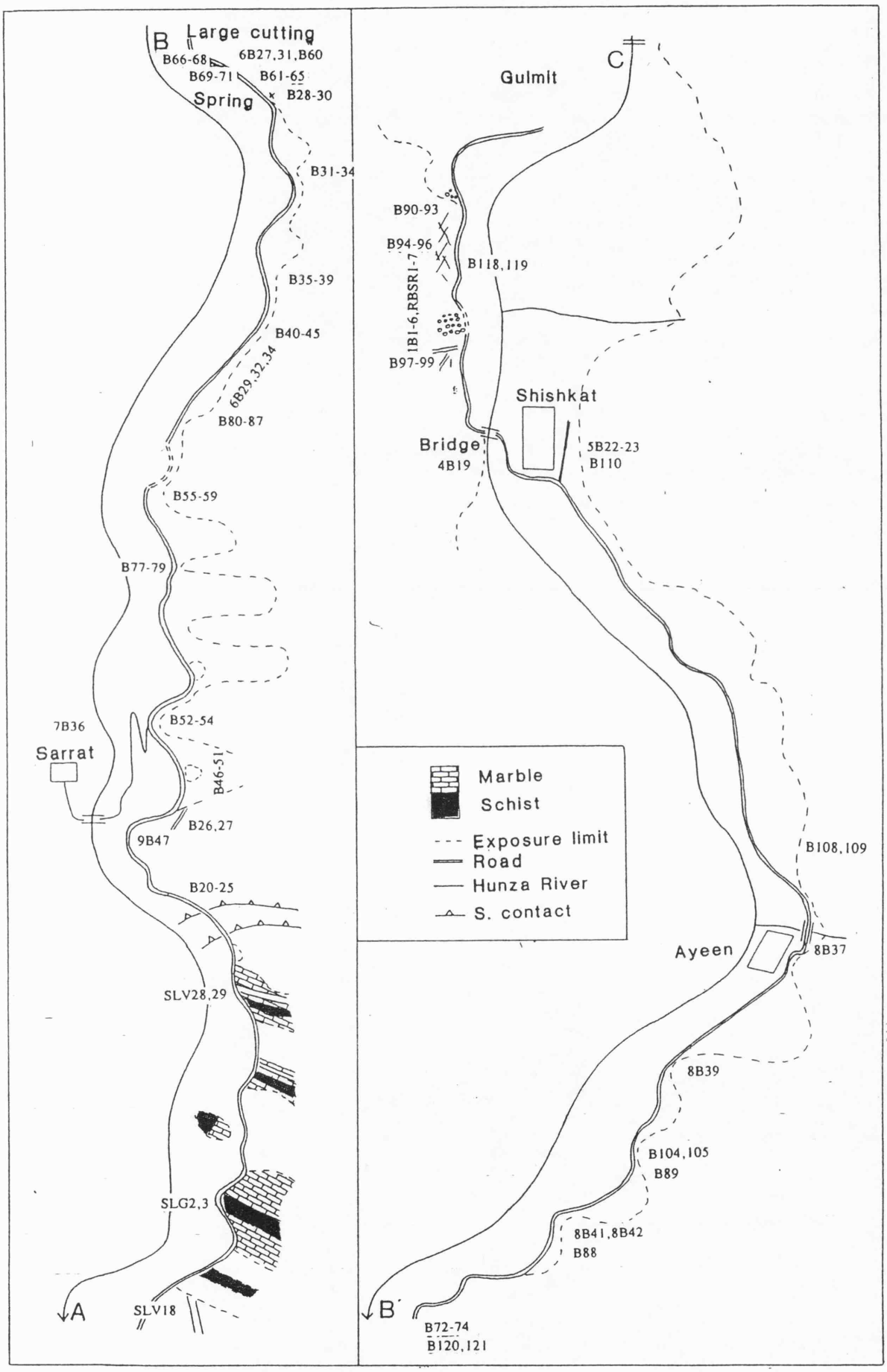

Figure A2-3: Sketch map of road section through the Hunza Plutonic Complex to show the localities of geochemical samples. A to C is south to north, B connects with B'. Not to scale.